Universidad de Oviedo

**Departamento de Química Física y Analítica**

**Programa de Doctorado en Química Teórica y Modelización Computacional**

# Reactivity and Photoactivity of Rhenium and Molybdenum Complexes: A Theoretical Study

# Reactividad y Fotoactividad de Complejos de Renio y Molibdeno: Un Estudio Teórico

**Tesis Doctoral**

**Daniel Álvarez Lorenzo**

**2021**

Universidad de Oviedo
*Universidá d'Uviéu*
*University of Oviedo*

# RESUMEN DEL CONTENIDO DE TESIS DOCTORAL

| **1.- Título de la Tesis** | |
|---|---|
| Español/Otro Idioma: Reactividad y Fotoactividad de Complejos de Renio y Molibdeno: Un Estudio Teórico | Inglés: Reactivity and Photoactivity of Rhenium and Molybdenum Complexes: A Theoretical Study |

| **2.- Autor** | |
|---|---|
| Nombre: Daniel Álvarez Lorenzo | DNI/Pasaporte/NIE: |
| Programa de Doctorado: Química Teórica y Modelización Computacional (Interuniversitario) | |
| Órgano responsable: Universidad de Oviedo | |



## RESUMEN (en español)

En esta Tesis se ha estudiado la reactividad y fotoactividad de una serie de complejos carbonílicos de renio(I) con ligandos diimina (N-N). En menor medida, también se ha investigado la reactividad de complejos carbonílicos de molibdeno(II) con ligandos N-N y de metalocenos de molibdeno(IV). Para ello, se han empleado métodos de la teoría del funcional de la densidad (DFT) y su variante dependiente del tiempo (TD-DFT) y de clústers acoplados (CC) combinados con diferentes bases de cálculo y métodos de simulación de Dinámica Molecular. Los efectos del disolvente se tuvieron en cuenta mediante modelos de solvatación continuos, explícitos o mixtos dependiendo de los objetivos marcados en cada problema químico investigado. Además, con el objeto de interpretar los resultados obtenidos en términos químicos más intuitivos, se han utilizado diferentes tipos de análisis teóricos.

En concreto, se ha investigado la reactividad de complejos tricarbonílicos de renio(I) con una selección de ligandos monodentados nucleofílicos y varios bidentados N-N frente a acetilenos activados, racionalizando los diferentes productos obtenidos experimentalmente y analizando la influencia de dichos ligandos. Se han estudiado las reacciones frente a bases fuertes de complejos de renio(I) y molibdeno(II) con ligandos bipiridina/fenantrolina sustituidos y ligandos monodentados de tipo imidazol. En este caso, además de esclarecer la selectividad experimentalmente observada, se han hecho predicciones teóricas de los efectos de nuevos sustituyentes que se han confirmado posteriormente de forma experimental. También se ha investigado la reactividad de complejos de renio(I), ahora con un ligando aqua, frente a dianas biológicas de tipo guanina e histidina para adquirir un conocimiento más profundo de la actividad citotóxica de este tipo de complejos y comprender la influencia del ligando bidentado en dicha actividad. Así, se ha descrito teóricamente un nuevo mecanismo de acción compatible con observaciones experimentales. Por último, los resultados alcanzados en nuestro estudio mecanístico sobre la hidrólisis de éteres catalizada por molibdocenos, han permitido racionalizar con éxito la diferente reactividad de éteres mono- y difuncionales encontrada experimentalmente.

En el marco de fotoactividad, se han diseñado y caracterizado una serie de compuestos de Re(I) de diferente naturaleza con el fin de poder ser usados como fotosensibilizadores en terapia fotodinámica o en celdas solares. Por un lado, se han realizado modificaciones en un complejo piridil tricarbonílico de renio(I) con un ligando piridocarbazol consistentes en alterar dicho ligando y/o en reemplazar uno de los ligandos carbonilo por fosfinas, con el fin de desplazar la absorción de dicho complejo a la conocida como ventana terapéutica de interés en terapia fotodinámica contra el cáncer y otras enfermedades. Por otro lado, se han analizado las propiedades estructurales, electrónicas y espectroscópicas de un conjunto de diadas formadas por BODIPY y oxasmaragdirina unidos por diferentes puentes, lo que ha permitido elegir los tipos de puentes óptimos para la aplicación de estas diadas en celdas solares. Después, se han intentado mejorar las propiedades de la BODIPY al unirlas al ligando bipiridina de un complejo tricarbonílico de renio(I). En este estudio, se han investigado paso a paso los cambios producidos al unir una o dos de estas moléculas a la bipiridina, y las consecuencias de coordinar dichos aductos al centro metálico.

Universidad de Oviedo
*Universidá d'Uviéu*
*University of Oviedo*

**RESUMEN (en Inglés)**

In this PhD thesis we have studied the reactivity and photoactivity of a series of rhenium(I) carbonyl complexes bearing diimine ligands (N-N). To a lesser extent, we have also investigated the reactivity of molybdenum(II) carbonyl complexes with N-N ligands and metallocenes of molybdenum(IV). For that purpose, we have employed density functional theory (DFT) methods, its time-dependent variant (TD-DFT), and the coupled clusters method (CC), combined with different basis sets, as well as molecular dynamics simulations. The solvent effects have been considered through implicit, explicit or hybrid models depending on the objectives of each chemical problem investigated. On top of that, with the aim of converting our results into more intuitive chemical terms, several methods of analysis have been employed.

Specifically, the reactivity of rhenium(I) tricarbonyl complexes bearing various nucleophilic monodentate ligands and bidentate N-N ligands towards activated alkynes has been investigated, rationalizing the different products obtained experimentally and analysing the influence of such ligands. Furthermore, we have theoretically studied of reaction between rhenium(I) and molybdenum(II) complexes bearing bipyridine/phenantroline substituted ligands and imidazole monodentate ligands with strong bases. In this case, in addition to clarify the reported experimental selectivity, we have made some theoretical predictions for the effect of new substituents at the bidentate ligand that have been later confirmed by the experimentalists. Moreover, we have also investigated the reactivity of rhenium(I) complexes with an aquo ligand towards guanine and histidine biological targets with the goal of acquiring a deeper knowledge of the cytotoxic activity of these complexes and to understand the influence of the bidentate ligand in such an activity. Hence, a new mechanism of action in accordance with the experimental findings has been described. Finally, the results from our mechanistic study on the hydrolysis of ethers catalysed by molybdocenes have shed light on the divergent reactivity of mono- and bifunctional ethers experimentally found.

Concerning the photoactivity field, a series of rhenium(I) complexes of different nature have been designed and assessed for their use as photosensitisers in photodynamic therapy or solar cells. On the one hand, we have made different modifications to a tricarbonyl pyridyl rhenium(I) complex bearing a pyridocarbazole ligand consisting in altering such a ligand and/or replacing one of the carbonyl ligands by phosphines. The goal of such changes is to shift the absorption of the complex to the so-called therapeutic window, which is important in the photodynamic therapy against cancer and other diseases. On the other hand, we have analysed the structural, electronic, and spectroscopic properties of a set of BODIPY-oxasmaragdyrin dyads linked by different bridges. This investigation has allowed us to choose the optimal bridges for the application of these dyads in dye-sensitized solar cells. Then, we have focused on improving the properties of the BODIPY by attaching it to the bipyridine ligand of a rhenium(I) tricarbonyl complex. In this theoretical study, we have explored step by step the changes produced by linking one or two of these molecules to the bipyridine as well as the consequences of coordinating those adducts to the metal center.

**SR. PRESIDENTE DE LA COMISIÓN ACADÉMICA DEL PROGRAMA DE DOCTORADO EN QUÍMICA TEÓRICA Y MODELIZACIÓN COMPUTACIONAL (INTERUNIVERSITARIO)**

# Agradecimientos

En primer lugar, quiero agradecer a mis directores Isabel Menéndez y Ramón López por todo el apoyo recibido a lo largo de estos años, por sus enseñanzas en todos los campos y por la confianza que han depositado en mí. El científico que soy y el que llegaré a ser es gracias a vosotros.

También quiero agradecer a Pablo Campomanes por todo lo que he aprendido en mi estancia en Suiza y por la ayuda y el buen trato recibidos.

Gracias también a todas las personas que me han ido acompañando en el laboratorio y a todos mis compañeros del Máster.

Mi más sincero agradecimiento a todos los profesores que me han brindado su colaboración desinteresada en cuestiones de docencia, habéis hecho mucho más fácil que me enamore de la profesión.

No puedo olvidarme de mis amigos, muchas gracias por todos los buenos momentos y por hacerme disfrutar también fuera de la ciencia.

Asimismo, a Carolina por ser mi mayor pilar y convertir estos años de doctorando en la mejor etapa de mi vida.

Para terminar quiero darles las gracias a mi familia. Todo lo que soy os lo debo a vosotros, me habéis ayudado cuando más lo necesitaba y siempre me habéis hecho ir hacia adelante. Ni una palabra de esta Tesis habría sido posible sin vosotros.

A todos, gracias.

*A mi familia*

# Contents

# List of Schemes

# List of Figures

# List of Tables

# 1 Introduction

Transition metal complexes are cationic, neutral or anionic species in which a transition metal center is coordinated by molecules and/or ions called ligands. The properties of these compounds can be altered drastically or fine-tuned depending on the metal center and its oxidation state, the geometry and coordination number, and the nature of the ligands. Hence, tuning the colour, magnetism, reactivity, light absorption or catalytic activity, among other properties, of the transition metal complexes provide a wide range of options to make them potential candidates in countless diverse fields such as catalysis,[1–4] materials science,[5,6] photophysics and photochemistry,[7] biological systems,[8,9] medicine,[10–12] etc. Consequently, many families of transition metal complexes are being actively investigated. Among them, rhenium(I) complexes bearing three carbonyl ligands in facial (*fac*) disposition, one diimine (N–N) bidentate ligand, such as 2,2′-bipyridine (bpy), 1,10-phenanthroline (phen) or derivatives, and another neutral (n = +1) or anionic (n = 0) monodentate (L) ligand (see $[Re(CO)_3(N–N)L]^n$ in Scheme 1.1) have attracted significant attention since 1983, when it was discovered that complexes $[Re(CO)_3(N–N)L]$ (L = Cl, Br) are capable of reducing $CO_2$ to CO by either visible light irradiation[13] or electrocatalysis.[14] Many groups have worked in altering these compounds to enhance their catalytic activity, mainly changing the bidentate ligand and/or the ligand L. Apart from the numerous catalytic applications,[15] this type of Re(I) complexes are of interest in organic light-emitting diodes[16–18] and materials,[19] dye-sensitized solar cells,[20,21] sensors,[22] biological applications,[23,24] bioimaging,[25–27] chemotherapy and photodynamic therapy against cancer,[23,27–30] etc. The possibility of modifying the N–N and/or L ligands in order to synthesize new Re(I) tricarbonyl complexes with specific or improved properties has also aroused interest in investigating the reactivity of $[Re(CO)_3(N–N)L]^n$ complexes as well as that of the analogous molybdenum(II) complexes (see $[Mo(\eta^3\text{–allyl})(CO)_2(N–N)(L)]^n$ in Scheme 1.1) towards different organic substrates.[31,32]

Metallocenes are another important family of transition metal compounds wherein the metal center (M) is bonded to two aromatic rings, typically two cyclopentadienyl anions (Cp) or derivatives.[33] The general formula for these compounds with M in the oxidation state +2 is $Cp_2M$, whereas for the ones in the oxidation state +4 is $Cp_2MX_2$ (Scheme 1.2), where X is a halide or a *pseudo*-halide, such as carboxylates. Metallocenes have been employed as chemical intermediates, antiknock additives to gasoline, lubricants, etc.,[33] but their main current applications are as anticancer agents[34–37] and homogeneous catalysts in plastics industry, especially in olefin polymerization.[33] Among them, molybdocene dihalides of the general formula $Cp_2MoX_2$ have received a lot of attention in homogeneous catalysis.[37,38] This is mainly due to their potential in green chemistry as water-soluble catalysts, minimizing the pollution from the use of organic solvents.

In this PhD Thesis we have focused mostly on the reactivity and photoactivity of rhenium(I) tricarbonyl diimine complexes and, to a lesser extent, on

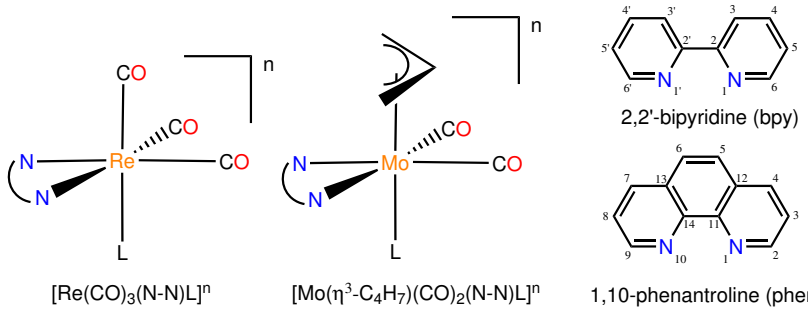


**Scheme 1.1.** General structure of the Re(I) complex $[Re(CO)_3(N{-}N)L]^n$ and the Mo(II) complex $[Mo(\eta^3{-}allyl)(CO)_2(N{-}N)(L)]^n$ (N–N = bpy, phen; L = monodentate ligand; n = 0, +1). The numbering of the diimine ligands is also included.

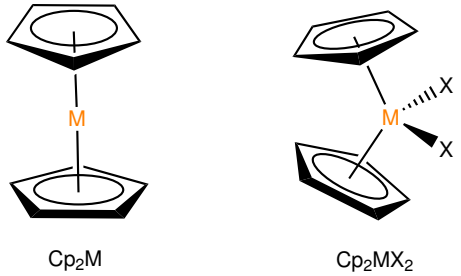


**Scheme 1.2.** General structure of metallocenes, with M being the metal center, Cp the cyclopentadienyl and X a halide or a *pseudo*-halide.

the reactivity of molybdenum(II) allyl dicarbonyl diimine complexes and metallocenes of molybdenum(IV).

## 1.1 Reactivity

Rhenium has a number of advantages over other metals, including diverse oxidation states, from -1 to +7,[39] and air and moisture tolerance.[40] In addition, being in the group 7, just in between early and late transition metals, it has a versatile hard and soft Lewis acidity.[41] In this context, it has lower electronegativity than the late transition metals, so it forms polarized metal-ligand bonds that favor the nucleophilic addition to polar organic substrates. This aspect has been widely exploited to investigate the reactivity of complexes $[ReX(CO)_3(N{-}N)]$ and the analogous ones $[MoX(\eta^3{-}allyl)(CO)_2(N{-}N)]$ (N–N = bpy, phen or derivatives; X = OH, $PPh_2$,...) towards a variety of neutral organic electrophiles (esters, ketenes, isocyanates, carbon disulfide, activated alkynes, etc.).[31] The possibility of tuning the L and the N–N ligands has allowed to explore other reactivities and applications mostly of Re(I) tricarbonyl complexes. Thus, it has been found

a rich reactivity when Re(I)/Mo(II) carbonyl diimine complexes bearing neutral ligands such as imidazoles, phosphines or dimethyl sulphide react towards strong bases.[31] In addition, the reactivity of Re(I) tricarbonyl complexes against biological targets has awakened interest in their acticancer activities.[23,42]

On the other hand, the study on the aqueous chemistry of molybdocene dichlorides, $Cp_2MoCl_2$, has shown that the chloro ligands are exchanged by water molecules, forming the diaquo complex $[Cp_2Mo(OH_2)_2]^{2+}$ in unbuffered pH solution and instantaneously when the pH is brought to 7.4.[38] Then, it occurs a two-step deprotonation of $[Cp_2Mo(H_2O)_2]^{2+}$ with pKa values of 5.5 and 8.5 ascribed to the generation of the cationic monoaquated molybdocene $[Cp_2Mo(OH)(H_2O)]^+$ and the neutral molybdocene $[Cp_2Mo(OH)_2]$, respectively. Therefore, $[Cp_2Mo(OH)(H_2O)]^+$ is the predominant species at neutral pH, but this species can lose its aquo ligand to form $[Cp_2Mo(OH)]^+$, as confirmed by a theoretical study from our group.[43] $[Cp_2Mo(OH)]^+$ is especially active due to an empty coordination site and the presence of a hydroxo ligand, explaining thus the interest in investigating the reactivity of aqueous molybdocenes towards a variety of organic substrates.[37,38,44–46]

### 1.1.1 Reactivity of Re(I) and Mo(II) Carbonyl Complexes towards Organic Electrophiles

The synthesis of transition metal complexes bearing a hydroxo ligand is important due to their rich OH-centered reactivity, which is dominated by the nucleophilic character of the hydroxo ligand.[47] The chemistry of hydroxo complexes of middle (groups 6 and 7) transition metal fragments began to be explored mainly at the beginning of the 21st century.[44–52] Pérez and co-workers have investigated the reactivity of the complexes $[Re(OH)(CO)_3(Me_2\text{–}bpy)]$ and $[Mo(OH)(\eta^3\text{–}C_4H_7)(CO)_2(phen)]$ towards a variety of organic substrates, including esters, carbon disulfide, ketenes, activated alkynes, etc.,[44–46,49] Then, this group explored the influence of replacing the hydroxo ligand by other anionic ligands such as alkoxo, amido, and phosphanido at the Re(I) and Mo(II) carbonyl diimine complexes when reacted with activated alkynes.[53–57] To illustrate this, herein we will focus on the case of the results obtained for the Re(I) complexes, although similar trends were found for the analogous Mo(II) ones.

Pérez and co-workers proposed that the reaction between the complexes $[ReX(CO)_3(N\text{–}N)]$ (X = OH, OMe, NH*p*Tol, $PPh_2$; N–N = bpy, phen) and activated alkynes, such as methyl propiolate (HMAD) or dimethylacetylenedicarboxylate (DMAD), starts with an initial nucleophilic attack from the heteroatom of the ligand X to one of the acetylenic carbon atoms (to the non-substituted one in the case of HMAD).[31] However, the subsequent steps change for each complex (see Scheme 1.3). If the nucleophilic ligand contains a hydrogen atom, which is the case of the OH and NH*p*Tol ligands, the other acetylenic carbon of the alkyne binds to a CO ligand in *cis* disposition, forming a stable zwitterionic five-membered metallacycle, denoted as **P*coo***, that transforms into a stable and neutral complex by migration of the hydrogen to the oxygen atom of the carbonyl, **P*cooh***.[45,55] The outcome of the reaction changes to an insertion of the

alkyne into the Re-X bond, forming a new Re-C bond, if the nucleophilic ligand is OMe, **P*ins***.[53,54] Finally, the diphenylphosphanido complex forms instead a coupling product with the bidentate ligand, in which a new bond between a external *ortho* carbon of the bidentate ligand and the acetylenic carbon is formed, **P*ccb***.[56,57] Nevertheless, the diverging reactivity of these complexes could not been rationalized just with experimental evidences.

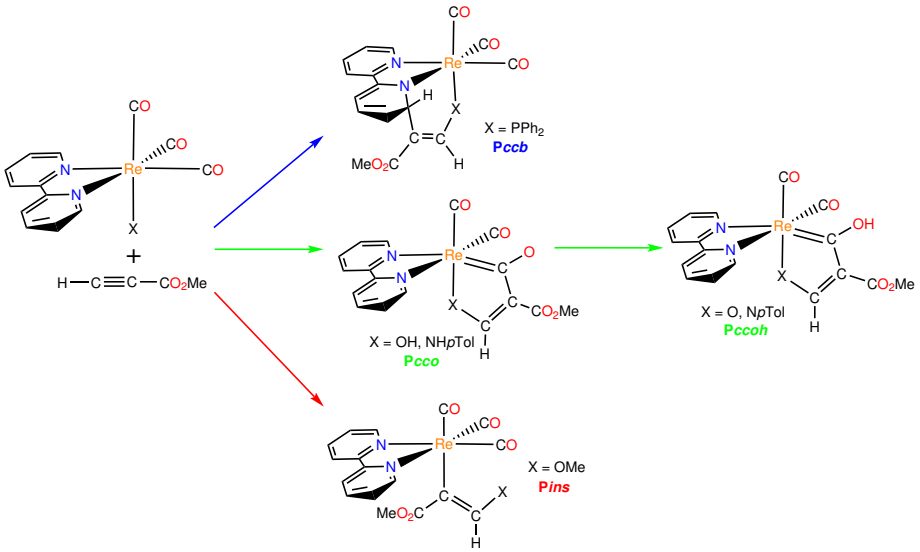


**Scheme 1.3.** Kinds of products obtained for the reaction of $[ReX(CO)_3(N{-}N)]$ (X = OH, OMe, NH*p*Tol, $PPh_2$; N–N = bpy, phen) complexes with HMAD.

The **P*ccb*** type of product is especially remarkable because of the usual inertness of the bpy and phen ligands. Such type of coupling had not been reported in analogous reactions of complexes with Fe,[58] Mo, W,[59] and Ir[60] containing a $PPh_2$ ligand and activated alkynes, which resulted in a product similar to **P*coo*** (see a, b and c in Scheme 1.4), or in the same reaction with a diphenylphosphanido Nb complex,[61] which formed an insertion product instead (see d in Scheme 1.4).

Indeed, the good $\sigma$ donor and $\pi$ acceptor properties, along with their tendency to form five-membered metallacycles, make the aromatic diimine ligands, bpy and phen, capable of stabilizing complexes of metals in every oxidation state. These properties explain the fact that this type of ligands is one of the most used in transition metal chemistry.[62] Despite this, the reports of reactivity towards coordinated bpy/phen are very scarce. In 1973, Gillard and Lyons suggested a nucleophilic attack from a hydroxide anion in water to the external *ortho* carbon of bpy and phen.[63,64] Although the nucleophilic addition to the same position of an isolated pyridine is well-known, Gillard's hypothesis produced a lot of controversy.[65–67] It was not until 2002 that Zhang *et al.* demonstrated the feasibility of such attack, but in hydrothermal conditions.[68]

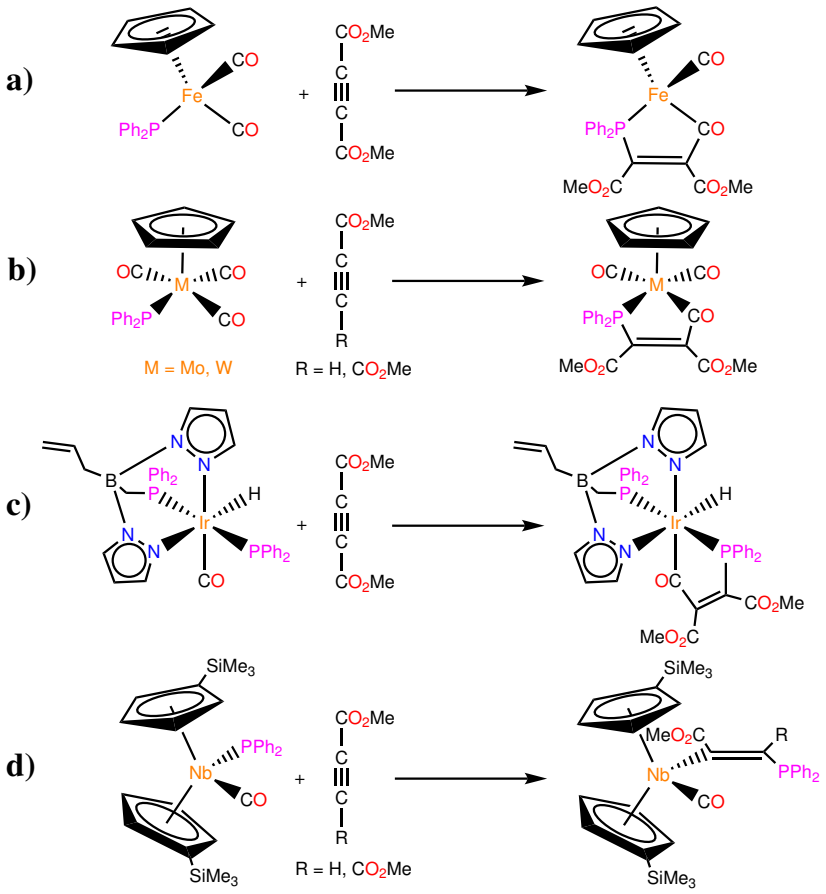


**Scheme 1.4.** Products formed by the reaction of diphenylphosphanido Fe, Mo, W, Ir, and Nb complexes with activated alkynes.

Apart from this example, there were only some reports of alkylation to bpy and phen.[69–72] In Section 1.1.3 we will present other examples of coupling to the diimine ligands in reactions of rhenium(I) and molybdenum(II) complexes towards strong bases.

### 1.1.2 Reactivity of Molybdocenes towards Organic Electrophiles

The aqueous molybdocenes $Cp_2MoCl_2$ and derivatives have been proven as efficient catalysts of several important organic reactions, including H/D exchange in alcohols,[73–75] hydrogenation of olefins,[76] nitrile hydration,[38,52,77–80] carbon monoxide oxidation,[52] and hydrolysis of ethers,[52] esters of carboxylic acids,[52,76,77] and various organophosphates.[52,77,80–85] According to the experimental results, it has been proposed that the general operative mechanism (see

Scheme 1.5) starts with the coordination of the organic substrate to the metal, followed by an intramolecular nucleophilic attack from the hydroxo ligand to the corresponding organic electrophile. The four-membered metallacycle formed by this attack is readily opened by adding water from the medium. In the final step, the organic substrate is displaced by another water molecule, forming the final product and recovering thus the initial catalyst. This mechanism has been corroborated by theoretical studies on the hydrolysis of ethyl acetate,[86] the acrylonitrile hydration,[87] and the carbon monoxide oxidation[88] catalyzed by $[Cp_2Mo(OH)(OH_2)]^+$. These studies have shown that the rate-determining step of these processes depend on the corresponding organic substrate. For instance, the intramolecular nucleophilic attack from the hydroxo ligand presents the largest energy barrier in the case of the acrylonitrile hydration and the CO oxidation, whereas the release of ethanol after the formation of the metallacycle in the hydrolysis of ethyl acetate competes with the acetic acid formation step to be the rate-determining one.

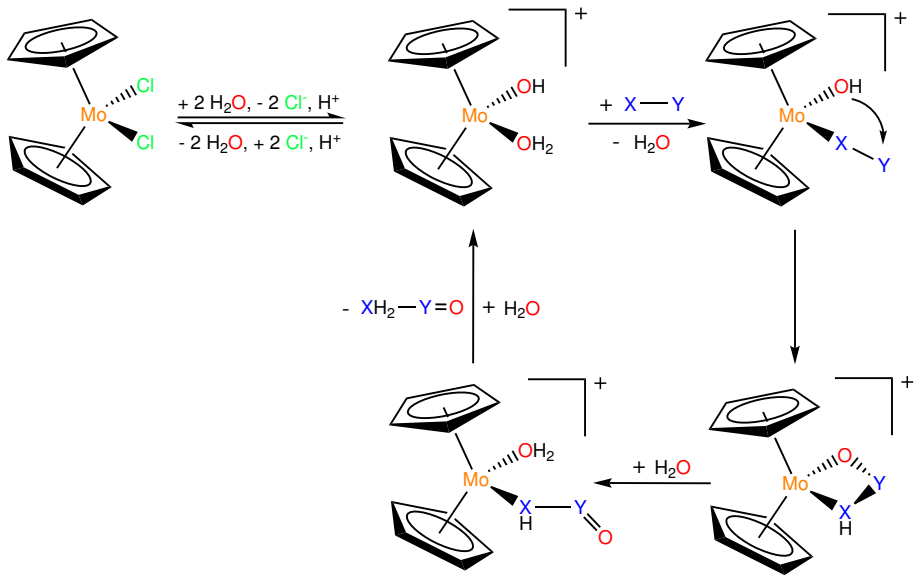


**Scheme 1.5.** General mechanism proposed for the intramolecular nucleophilic attack of the hydroxo ligand in the reaction of $[Cp_2Mo(OH)(OH_2)]^+$ towards different organic substrates (X−Y).

The reaction of aqueous molybdocenes towards ethers is particularly relevant due to the high availability and low preparation cost of such substrates. Apart from the interest in carrying out ether hydrolysis in environmentally benign conditions, the study of this reaction in the presence of aqueous molybdocenes is also interesting because it can provide information on the mechanisms of biomass decomposition into fuels and chemicals. Breno and co-workers have reported the hydrolysis of ethyl vinyl ether and 2-methoxyacetonitrile in water

catalyzed by $[(MeCp)_2Mo(OH)(OH_2)]^+$ (MeCp = $\eta^5$-$C_5H_4CH_3$).[52] However, they have found that such a reaction does not occur with monofunctional ethers, like diethyl ether. They explained this divergent reactivity owing to the weak and hindered character of the ether functionality, which would prevent the coordination of the ether to the metal center through the oxygen atom. As a consequence, the coordination must take place via other functionalities of the ether substrate, like the alkenyl or the nitrile functionalities of vinyl ethyl ether and 2-methoxyacetonitrile, respectively, which are not present in the monofunctional ether. However, it remains unclear if a monofunctional ether with such functionalities, like divinyl ether, would hydrolyze in the same conditions. In this PhD Thesis this issue will be investigated.

### 1.1.3 Reactivity of Re(I) and Mo(II) Carbonyl Complexes towards Bases

Besides the coupling of activated alkynes to a Re-coordinated phen mentioned in Section 1.1.1, Pérez and co-workers have also found other reactions wherein the bidentate ligands bpy and phen are not inert, specifically when different Re(I) and Mo(II) carbonyl diimine complexes react towards strong bases. For instance, they have shown that the reaction between $[Re(CO)_3(bpy)(SMe_2)]OTf$ and $KN(SiMe_3)_2$ deprotonates one of the methyl groups of $SMe_2$, which then couples to the C2 atom of the bpy (see a in Scheme 1.6).[89] In contrast, the same reaction with a trimethylphosphane ligand yields a coupling between a P-bonded $CH_2$ group and the C6 position of bpy as one of the products (see b in Scheme 1.6).[90] In 2016, they have also reported an addition of MeLi to the trimethylphosphane complex, which occurs in the C2 and C4 positions of the phen ligand, and only in the C2 position with the bpy ligand (see c in Scheme 1.6).[91] In the same paper, they have described a reversible addition of $KN(SiMe_3)_2$ (the $N(SiMe_3)_2$ moiety) to the C4 position of phen, which then evolve through $PMe_3$ deprotonation to yield an intramolecular addition of the deprotonated methyl group to the C2 position of phen (see b in Scheme 1.6). Very recently, they have also investigated the addition of *t*BuLi to the same complex bearing bpy and phen (see d in Scheme 1.6). In the case of the bpy complex, it underwent an unprecedented addition to the C5 position. In contrast, the addition took place in the C2 and C4 positions when the bidentate ligand was phen.[92]

In 2008, they have reported couplings with the bidentate ligand when treating $[Re(CO)_3(N{-}N)(RIm)]OTf$ (N–N = bpy, phen; RIm = *N*-methylimidazole (MeIm), *N*-mesitylimidazole (MesIm)), with $KN(SiMe_3)_2$ (see Scheme 1.7).[93] This reaction starts with a deprotonation of the C2 carbon of the imidazole, which then attacks to the external *ortho* carbon of the bidentate ligand. It is also remarkable that when they treated the product that contains bpy and MeIm with MeOTf, one of the pyridine rings of the bpy ligand underwent nitrogen exclusion, forming a 2,4-cyclopentadienyldimethylamine unit. Such a product has been observed as well for the reaction of similar complexes with bpy ligands bearing substituents in the C4 and C4′ positions, $[Re(CO)_3(4,4'{-}R'_2bpy)(RIm)]OTf$

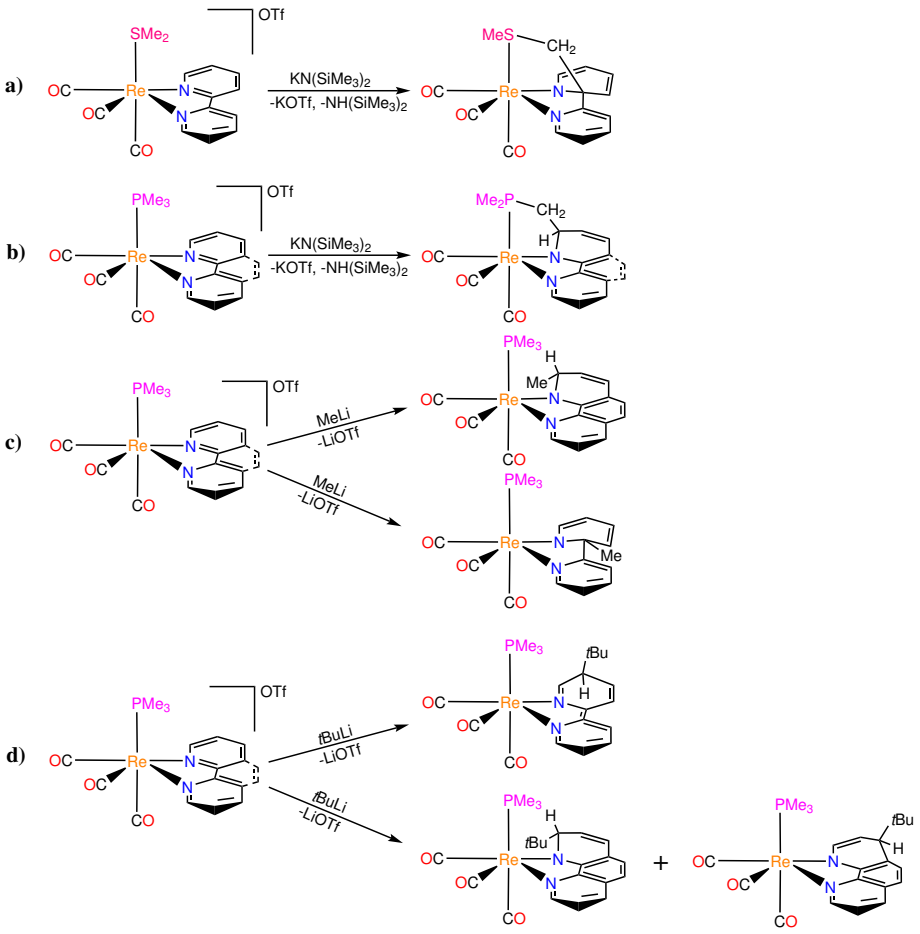


**Scheme 1.6.** Products from the reactions of Re(I) tricarbonyl complexes bearing bpy/phen and $SMe_2$/$PMe_3$ towards different bases: $KN(SiMe_3)_2$, MeLi, and *t*BuLi.

(R′ = OMe, *t*Bu; R = Me, Mes) and [Re(CO)$_3$(4,4′−(NMe$_2$)$_2$bpy)(MesIm)]OTf, under the same conditions.[94,95]

They have also described the deprotonation of an $\alpha$-methyl group of 1,2-dimethylimidazole, 2-methyloxazoline or 2-methylpyridine by $KN(SiMe_3)_2$ in Re(I) tricarbonyl complexes with bpy/phen, which in all cases resulted in a C−C coupling with the external *ortho* carbon of the bidentate ligand (see Scheme 1.8).[96]

Interestingly, the reaction of [Re(CO)$_3$(bpy)(RIm)]OTf with $KN(SiMe_3)_2$ ends up with a C−C coupling with bpy, as seen in Scheme 1.7, but the deprotonation with the same base of the analogous Mo(II) allyl carbonyl complex, [Mo($\eta^3$−C$_4$H$_7$)(CO)$_2$(bpy)(RIm)]OTf (R = Me, Mes), transforms the

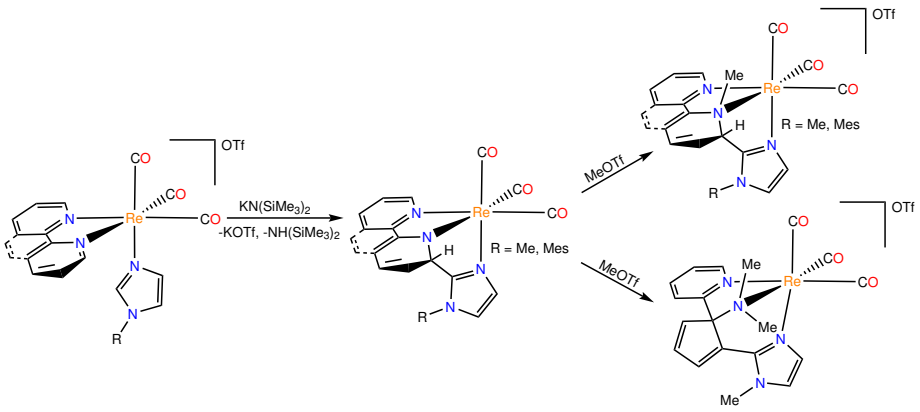


**Scheme 1.7.** Reaction of $[Re(CO)_3(N{-}N)(RIm)]OTf$ (N–N = bpy, phen; R = Me, Mes) with $KN(SiMe_3)_2$ and the products obtained after treatment with MeOTf.

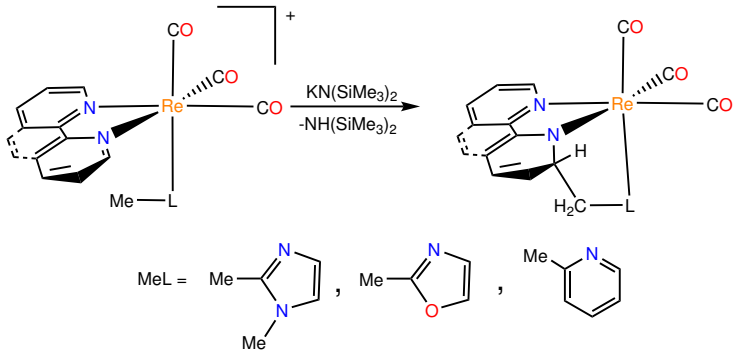


**Scheme 1.8.** Reaction of $[Re(CO)_3(N{-}N)L]OTf$ (N–N = bpy, phen; MeL = 1,2-dimethylimidazole, 2-methyloxazoline, 2-methylpyridine) with $KN(SiMe_3)_2$.

*N*-alkylimidazole to a NHC ligand (see a in Scheme 1.9).[97] A similar outcome had been previously observed in a comparable manganese(I) complex, $[Mn(CO)_3(bpy)(PhIm)]^+$, in a deprotonation/protonation sequence (see b in Scheme 1.9).[98] These differences were rationalized, along with their corresponding reaction mechanisms, by DFT calculations carried out in our group, which showed that the formation of the NHC-type product was more kinetically accessible in the Mo and Mn complexes.[97] Nevertheless, when the bpy ligand of the Mo(II) complex is replaced by py-2-CH=NR, with R = $C_6H_5$, $C_6H_4$-4-Me, $C_6H_3$-3,5-$Me_2$, *i*Pr, *t*Bu, the deprotonation affords a C–C coupling product between the central carbon atom of the imidazole (C2) and the imine carbon atom of the pyridylimino bidentante ligand (C1) instead (see c in Scheme 1.9).[99] In addition, if the imidazole ligand is changed by 1-methyl-1,2,3-triazole, the re-

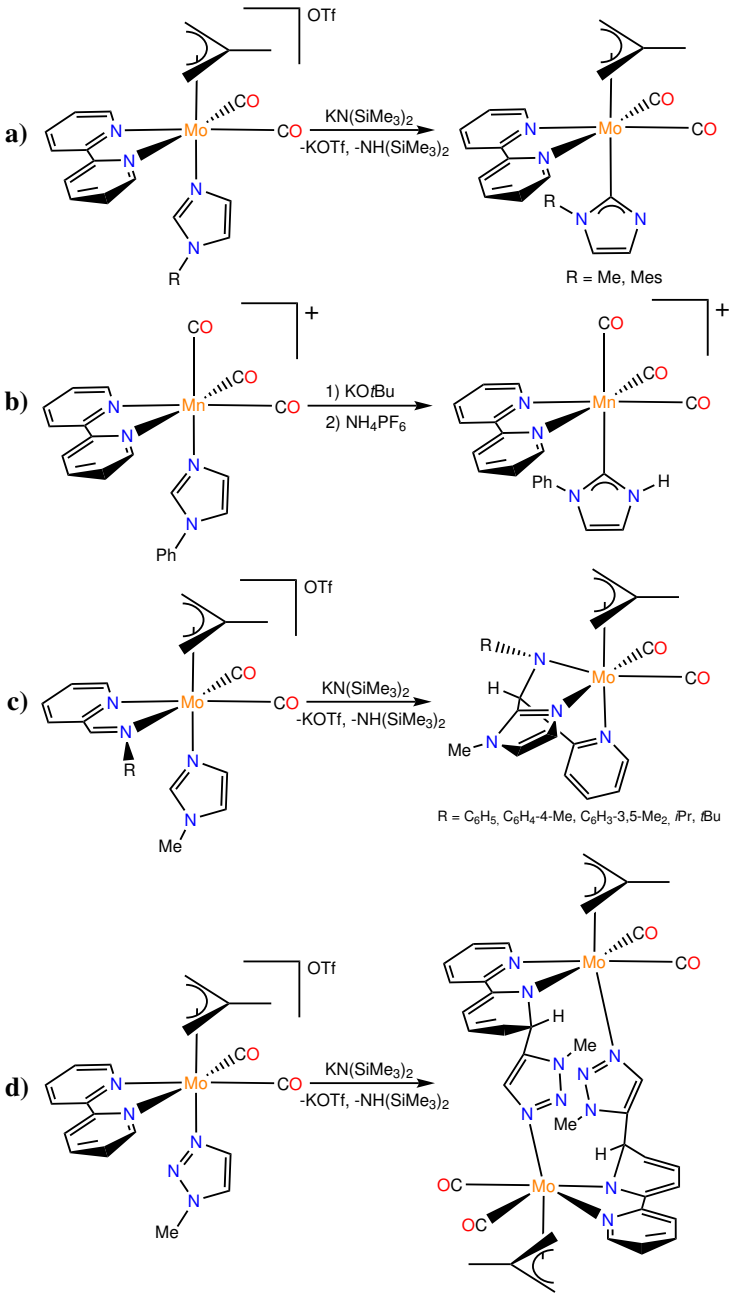


**Scheme 1.9.** Reaction of Mo(II) and Mn(I) complexes towards bases.

action towards $KN(SiMe_3)_2$ produces a deprotonation in the C5 carbon of the

triazole, followed by an intermolecular C−C coupling with the *ortho* carbon of either bpy or phen, forming a bimetallic compound with dearomatized bidentate ligands (see d in Scheme 1.9).[100]

In subsequent works, Julio Pérez and co-workers also investigated the effect of adding certain electron donors and acceptors to the 4,4′ positions of bpy and the 4,7 positions of phen in the reaction of $[Re(CO)_3(N{-}N)(RIm)]OTf$ and $[Mo(\eta^3{-}C_4H_7)(CO)_2(N{-}N)(RIm)]OTf$ with $KN(SiMe_3)_2$ (Scheme 1.10).[94,95] As a result, they corroborated that the outcome of the reaction greatly depends on the bidentate ligand as well as in the presence of a methyl or a mesithyl group in the imidazole. In this sense, three types of products were reported depending on those for both metals: the formation of a NHC-type product, a C−C coupling between the C2 atom of imidazole and the C2 carbon of bpy (the internal *ortho* carbon), and the coupling with the C2 carbon of phen or the C6 carbon of bpy (the external *ortho* carbons). A theoretical investigation of these reactions could shed light on the effect of the substituents in the formation of the different types of products, and it will be done in the present Thesis.

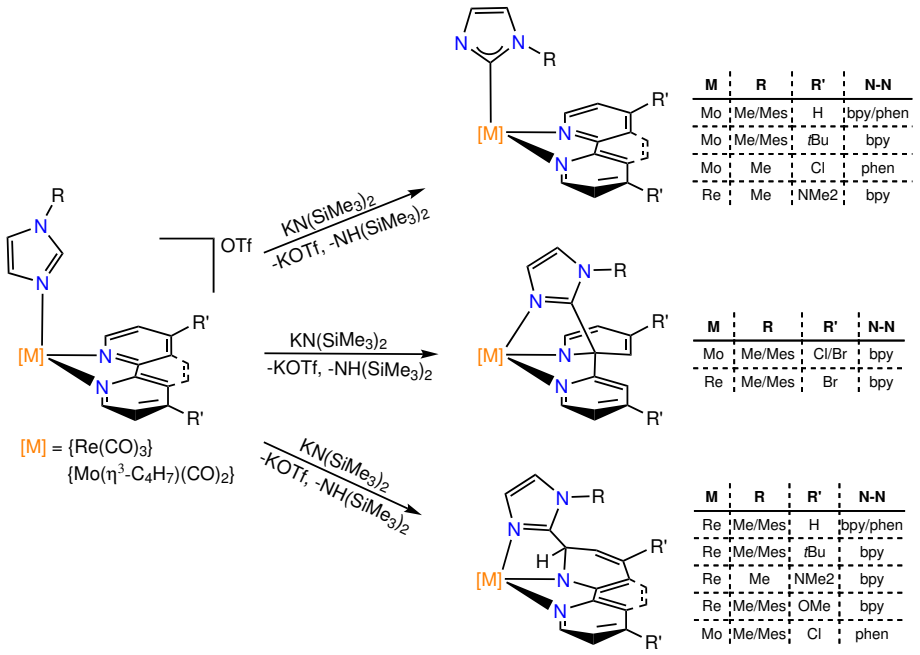


**Scheme 1.10.** Reaction of Re(I) tricarbonyl complexes and Mo(II) allyl dicarbonyl complexes bearing MeIm/MesIm and bpy/phen with different substituents towards $KN(SiMe_3)_2$.

### 1.1.4 Reactivity of Re(I) Carbonyl Complexes towards Biological Targets Related to Cancer

Despite the huge research effort of all the scientific world, cancer remains as one of the leading causes of death in the world, especially in high-income countries. For instance, according to "Instituto Nacional de Estadística (INE)", cancer is the second leading cause of death in 2018 in Spain, very close to the circulatory system diseases. Therefore, the development of new treatments is vital.

Nowadays, most cancer patients receive a chemotherapy treatment either as main treatment or in combination with surgery and/or radiotherapy. One of the first metal-based chemotherapeutic agents is *cis*-diaminodichloroplatinum (II), commonly known as cisplatin (see Scheme 1.11).[101,102] Since it was approved for the treatment of testicular and ovarian cancer by the US Food and Drug Administration (FDA) in 1978, it remains as the most popular chemotherapeutic agent, being employed in about 50 % of all cancer patients, including testicular, ovarian, bladder, lung, cervical, head and neck, and other types of cancer.[103]

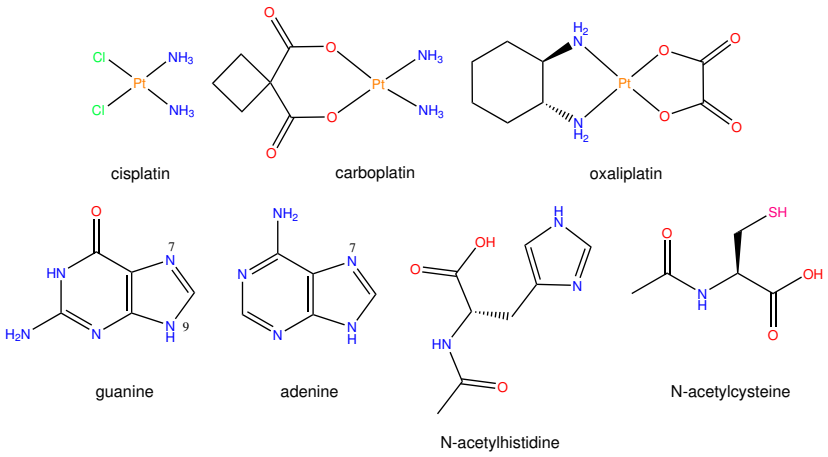


**Scheme 1.11.** Pt(II) anticancer drugs and some biological targets.

Cisplatin is inoculated intravenously to the patients, keeping all its structure intact within the bloodstream due to the high concentration of chloride in blood. However, once it enters the cell, the low concentration of chloride in the cytoplasm activates the drug by replacing one of its chloro ligands by water. Water is a good leaving group and, hence, cisplatin can react with nucleophiles within the cell, especially with nitrogen donor atoms of nucleic acids.[104] It has been reported that the preference binding site of cisplatin is the N7 position of the imidazole ring of guanine in DNA (see Scheme 1.11), followed by the analogous nitrogen atom of adenine (Scheme 1.11). The preference of binding to guanine over adenine is due to the formation of a hydrogen bond between one of the amine groups bonded to Pt and the oxo group of guanine.[105] The monofunctional DNA adduct formed by this binding may evolve to a bifunc-

tional adduct by ring closure, either directly from the monoadduct or just after replacing the other chloro ligand by water. Most of the bifunctional adducts are a consequence of intrastand binding with two adjacent guanine bases (around 65 %), although other adducts, especially adenine-guanine (approximately 25 %) are also formed.[106] It is thought that 1,2-intrastand adducts produce cell death more efficiently than 1,3-intrastand adducts. This distortion of DNA is recognized by DNA binding proteins, which can either initiate the DNA damage repair or signal for apoptosis (controlled cell death).

After the success of cisplatin, a large number of Pt(II) anticancer drugs have been synthesized and tested, but only a few of them have been approved for commercialization, such as carboplatin and oxaliplatin (Scheme 1.11). All Pt based drugs are based on the same mechanism of action as cisplatin. There are two major drawbacks in this type of drugs: the side effects (nephrotoxicity, ototoxicity, hepatotoxicity, gastrointestinal toxicity,...), and the drug resistance, which limit their application and effectiveness.[101] The main causes of resistance are inactivation of the drug by binding to glutathione and metallothioneins, and faster DNA repair. These drawbacks have prompted the search for other metal based anticancer drugs with less side effects and different mechanisms of action than cisplatin. Many metals have been investigated as new candidates, including Ag, Au, Ir, Pd, Os, Ru, Rh, Re and even Ti, some of them entering clinical trials.[107–110] Among them, rhenium(I) tricarbonyl complexes are catching a lot of attention in recent years due to their interesting properties, easily tuned by altering their ligands.[23,111]

The excellent review by Gasser *et al.* from 2014 covers all the cytotoxic examples in the literature to that date.[23] In general, the cytotoxicity of these complexes increases with their lipophilicity, due to an improved capacity for entering the cells. This is seen, for example, in the recent work by Wilson and co-workers.[112] They reported the synthesis and cytotoxic activity of a series of $[ReCl(CO)_3(N{-}N)]$ complexes, where (N–N) are pyridyl imine ligands with different lengths of alkyl chains, from two to twelve carbons. Their results show that the complexes with longer chains, which are the most lipophilic, produce *in vitro* cell death at a much faster rate. Despite the huge number of Re(I) tricarbonyl complexes with cytotoxic activity, there are few examples with reported antitumor activity *in vivo*.

The first anticancer *in vivo* testing of a Re(I) tricarbonyl complex was made by d'Angelo's group, and it remains as the most extensively studied.[42] In 2011, they synthesized four complexes of the formula $[ReCl(CO)_3(Se{-}Se)]$ (see **1-4** in Scheme 1.12), where Se–Se is a diseleno bidentate ligand with different functionalities, and tested their antiproliferative activity against human tumor cells (i.e., the ability to inhibit cellular growth), aiming at combining the cytotoxic ability of Re with the apoptotic modulator properties of Se.[113] The water soluble disodium salts of the complexes with carboxylic acids in the bidentate ligand (**5** and **6** in Scheme 1.12) showed marked activity against breast cancer cells, especially **6** due to the longest alkyl chain between the Se atoms. Then, they investigated the cellular uptake of **6** and its tissue distribution in mice, reporting that the complex was incorporated into the nucleus of malignant cells, allegedly

forming adducts with DNA.[114] After that, in 2015, they tested the activity of **6** in tumors transplanted in mice, showing a reduction in the tumor growth.[115] In this work, they also confirmed the effects on DNA due to the Re atom by describing its interaction with 9-methylguanine (9-MeG), a popular molecule used as a model for guanine.

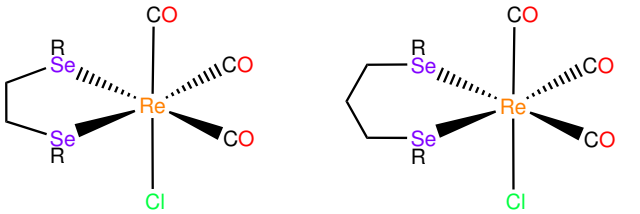


**1** R = Ph
**2** R = $CH_2COOH$
**5** R = $CH_2COONa$

**3** R = Ph
**4** R = $CH_2COOH$
**6** R = $CH_2COONa$

**Scheme 1.12.** Schematic representation of Re(I) cytotoxic complexes **1-6** bearing diseleno ligands.

As another example, the group of Mao and Tan synthesized and tested the cytotoxic activity of two phosphorescent Re(I) tricarbonyl complexes bearing pyridine and a bidentate $\beta$-carboline derivative ligand (**7** and **8** in Scheme 1.13).[116] Both complexes displayed better anticancer activity than cisplatin for several cell lines, in particular against cisplatin-resistant human lung carcinoma cells. Since **8** showed higher activity it was selected for further testing *in vivo*. The mice treated with this complex presented a 60 % tumor growth inhibition compared to the untreated group, with low systemic toxicity. They also reported that the cell death occurs through lysosomal disfunction that causes autophagy, being the first time that this mechanism is found for a Re(I) complex. The same group synthesized and investigated the anticancer activity, both *in vitro* and *in vivo*, of two binuclear rhenium(I) complexes of the formula $[Re_2(CO)_6(dip)_2L](PF_6)_2$ (dip = 4,7-diphenyl-1,10-phenantroline; L = 4,4′-azopyridine, 4,4′-dithiodipyridine) (**9** and **10** in Scheme 1.13, respectively).[117] When tested against various cell lines, both complexes showed more anticancer activity than cisplatin, especially the complex with sulphur atoms (**10**). They are able to inhibit tumor growth *in vivo*, but their activity was not higher than cisplatin, although they did not produce any side effects. It was reported that both complexes accumulate in the mitochondria, causing oxidative stress and mitochondrial disfunction, and induce cell death via necroptosis and caspase-dependent apoptosis.

In 2017, Wilson *et al.* reported the synthesis and cytotoxic activity of various Re(I) tricarbonyl complexes of the formula $[Re(CO)_3(N{-}N)(OH_2)]^+$, where (N−N) is either a bpy or a phen ligand with different substituents (**11-17** in Scheme 1.14).[118] After testing their antiproliferative activity against HeLA cells *in vitro*, they found that the complex **17**, with methyl groups in the C2 and

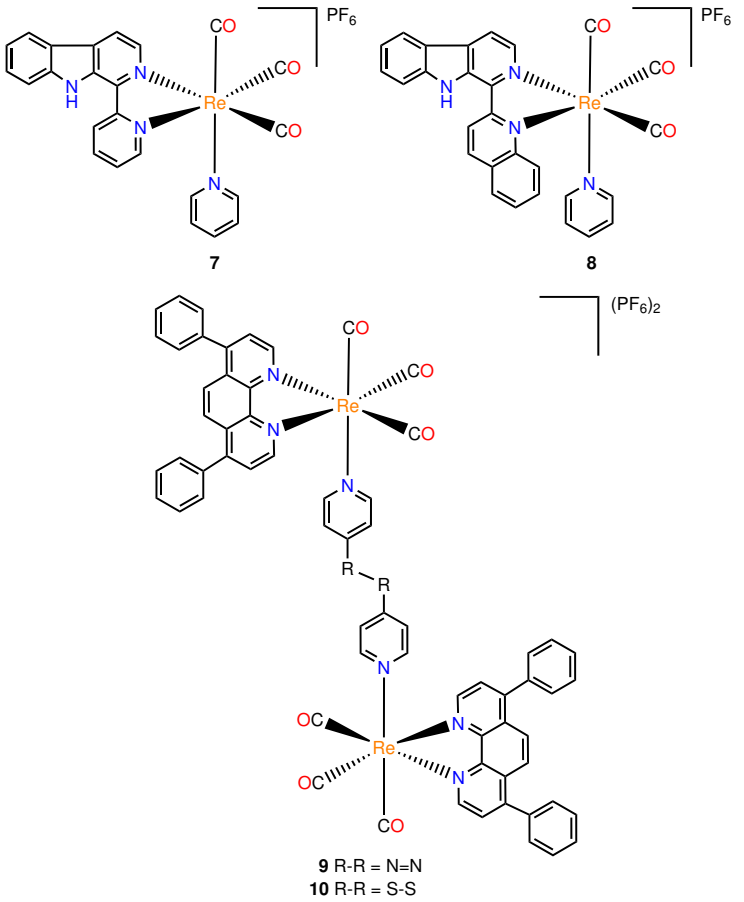


**Scheme 1.13.** Anticancer Re(I) complexes **7-10** synthesized by the group of Mao and Tan.

C9 positions of phen, was the most potent, even more than cisplatin. They also tested this complex in other cancer cell lines, showing cytotoxic activity in all of them, including the ones that were cisplatin-resistant, which indicates that it is able to overcome cisplatin resistance. To elucidate the action mechanism, they studied the reaction of **17** with several biomolecules. They reported the formation of adducts with 9-EtG, *N*-acetylhistidine, and *N*-acetylcysteine (see Scheme 1.11), being the reaction with 9-EtG faster than with the other compounds. This indicates the potential interaction of **17** with DNA and/or proteins, although the specific biological target remains unclear. On the other hand, it did not interact with methionine, serine, and glycine. After that, they described the *in vivo* antitumor properties of **17** in mice bearing patient-derived ovarian cancer tumor xenografts.[119] In this study, **17** was able to inhibit the tumor growth efficiently without adverse side effects. They also identified that

the complex accumulated in the mitochondria rather than in the nucleus, but the mechanism of action is still unknown.

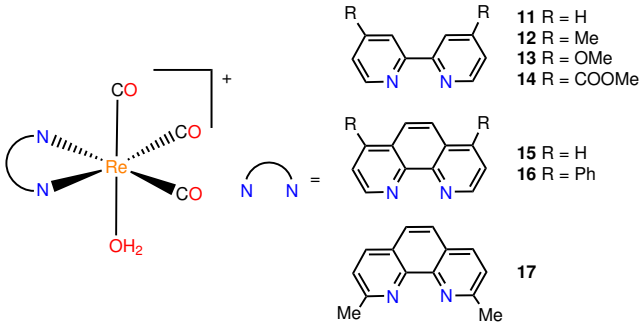


**Scheme 1.14.** Cytotoxic Re(I) tricarbonyl aqua complexes **11-17**.

In a subsequent work, Wilson's group described the anticancer activity of $[Re(CO)_3(dmphen)(p\text{-tol-ICN})]^+$, where the bidentate ligand dmphen is the same as the one in **17**, 2,9-dimethyl-1,10-phenanthroline, and *p*-tol-ICN is *para*-tolyl isonitrile (see **18** in Scheme 1.15).[120] They evaluated its cytotoxicity against a series of cancer cell lines *in vitro*, finding that **18** had similar or greater toxicity than cisplatin and **17**. They also concluded that this complex produces cell death by causing an accumulation of misfolded proteins, which induces endoplasmic reticulum stress and activates the unfolded protein response. To rationalize the structure-activity relationship, they varied the bidentate and isonitrile ligands by adding different substituents (see **19-28** in Scheme 1.15).[121] As a result, they reported that the more lipophilic and electron-rich complexes display the higher cytotoxicities, being the more active ones **18** and the complex with *t*Bu substituents in C4 and C4′ positions of bpy (**24**). In this study, they also investigated the *in vivo* antitumor activity of **18**, which was able to slow tumor growth, but caused severe local inflammations. To analyse its axial ligand stability, they synthesized $[Re(CO)_3(dmphen)(para\text{–iodobenzeneisonitrile})]^+$ (**29** in Scheme 1.15) and followed its biodistribution by using X-ray fluorescence microscopy.[122] As a conclusion, they verified that the axial ligand does not act as a leaving group in these complexes, remaining intact within the cells.

These are the only examples of Re(I) tricarbonyl complexes with reported tumor growth inhibition *in vivo* to date. Although scarce, they show the potential of this type of complexes as chemotherapeutic agents. Currently, many efforts are underway to try to elucidate their action mechanisms and biological targets and to optimize their ligands to maximize the cytotoxic properties.

In this Thesis, we will investigate the cytotoxic properties of the complex bearing an aqua ligand reported by Wilson and co-workers.[118,119] This complex has antiprofilerative activity both *in vitro* and *in vivo* and it is able to overcome cisplatin resistance, although its mechanism of action remains unknown. Our main goal will be unraveling this mechanism.

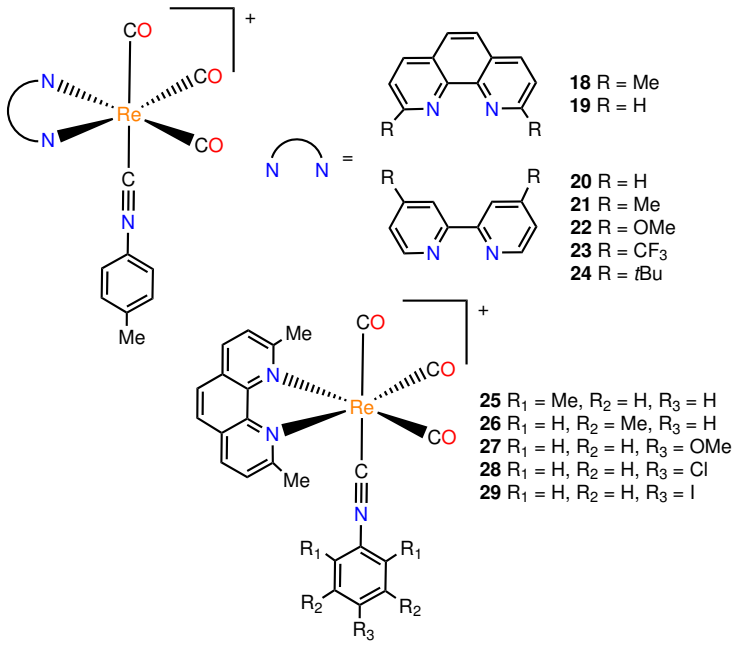


**Scheme 1.15.** Schematic representation of the Re(I) tricarbonyl isonitrile complexes **18-29**.

## 1.2 Photoactivity

Photoactivity is the effect produced when a substance or system is exposed to light. The complexes $[Re^{I}(CO)_3(N{-}N)L]^n$ (N–N = bpy, phen, or derivatives) possess interesting photophysical and photochemical properties, including high quantum yields for the formation of triplet metal-to-ligand charge transfer ($^3$MLCT) excited states, phosphorescence in solution, long-lived excited states, and strong reactivity of the $^3$MLCT states.[123] As a consequence, they have been investigated in many diverse fields and applications, for example as labeling and imaging agents of biomolecules,[27,124] as photocatalysts for the reduction of $CO_2$,[125] as emitting centers in organic light-emitting diodes (OLED),[16,18] as dyes for dye-sensitized solar cells (DSSC),[20,21] or as photodynamic therapy (PDT) and photoactivated chemotherapy (PACT) agents.[28,30] In the present work, we have focused on the use of Re(I) tricarbonyl diimine complexes in PDT and DSSC.

### 1.2.1 Re(I) Carbonyl Complexes as Phosensitisers in Photodynamic Therapy

PDT is a treatment that uses light to activate non-toxic molecules, commonly known as photosensitizers (PSs), to induce the generation of cytotoxic reactive oxygen species (ROS) and/or singlet oxygen, producing the cell death. In PDT,

the patient is treated with the PS, which is allowed to accumulate through all parts of the body, although, ideally, it would have higher selectivity for the target cells. Then, the patient is irradiated with light of the proper wavelength, depending on the absorption profile of the PS and the depth of tissue penetration. The light absorption promotes the PS from its ground singlet state ($S_0$) to an excited singlet state ($S_1$), which is an unstable and short-lived state. As a consequence, the excited PS ($S_1$) can return to its ground state ($S_0$) by converting its energy into heat or fluorescence. Alternatively, the PS can evolve from the $S_1$ state through an intersystem crossing (ISC) to its first triplet excited state ($T_1$) that can transfer its energy by phosphorescence or colliding with other molecules to generate chemically reactive species (CRS), which kill cells. The mechanisms for CRS formation in PDT are generally classified into two types. In the so-called type I mechanism the PS in its $T_1$ state reacts with $^3O_2$ to generate reactive oxygen species ($O_2^-$, $H_2O_2$, etc.), whereas in the mechanism known as type II it produces $^1O_2$. The latter is supposed to be the predominant process.[126] Additionally, there is another oxygen-independent mechanism where a cytotoxic chemical compound is released upon irradiation, this is known as photoactivated chemotherapy (PACT).[127] As type I and II mechanisms lead to cell death, PDT is mainly employed to combat a variety of cancers, but it has also been used against wars, acne, or psoriasis. PDT can only be applied efficiently in superficial regions of the body, where the light can penetrate easily. The main advantage of PDT is that its use is local, which means that the PS only acts where it is required to, minimizing the side effects and maximizing the selectivity. In addition, it does not cause resistance or hypersensitivity, so it can be applied many times in the same area. Currently, there is a number of PSs with approval from the Food and Drug Administration (FDA) for its use in the treatment of many types of cancer (lung, skin, bladder, breast,...). Most of them are porphyrin derivatives, such as Verteporfin,[128] Temoporfin,[129] Padeliporfin,[130] or Photofrin,[131] among others. The main disadvantages of these PSs is their water insolubility and their lack of efficacy in hypoxic tumors, where there is a low concentration of oxygen.

Apart from the non-toxicity in absence of light and other common characteristics of drugs such as solubility and stability in physiological environments, an ideal PS must also fulfill other requirements.[30] It should absorb in the so-called therapeutic window, which falls into the near-infrared (NIR) region of the spectrum at, approximately, 620-850 nm.[132–134] This is important because the light at the therapeutic window has its maximum depth of penetration in the tissue. Shorter wavelengths could also increase the possibility of damage from the light in the body of the patient. Since molecular oxygen interacts with the PS in $T_1$, this excited state must have long lifetimes and high yields, which implies that the ISC between the singlet and triplet states must be efficient. Finally, in order to produce cytotoxic oxygen, the energy of the triplet state of the PS is transferred to $^3O_2$. This requires that the energy gap between the singlet and triplet states of the PS must be at least 0.98 eV to have a good singlet oxygen quantum yield.[126,135]

The complexes $[Re(CO)_3(N{-}N)L]^n$ (N–N = bpy, phen, or derivatives) have

properties that fulfill most of these requirements, including stability and biocompatibility, due to their $d^6$ electron configuration. However, their absorption bands are not located in the therapeutic window, so the wavelength required to activate these complexes is too short, with low tissue penetration. In recent years, many efforts have been put in tuning these complexes to enhance their absorption profiles and phototoxicity as well as other properties, such as selectivity or solubility.

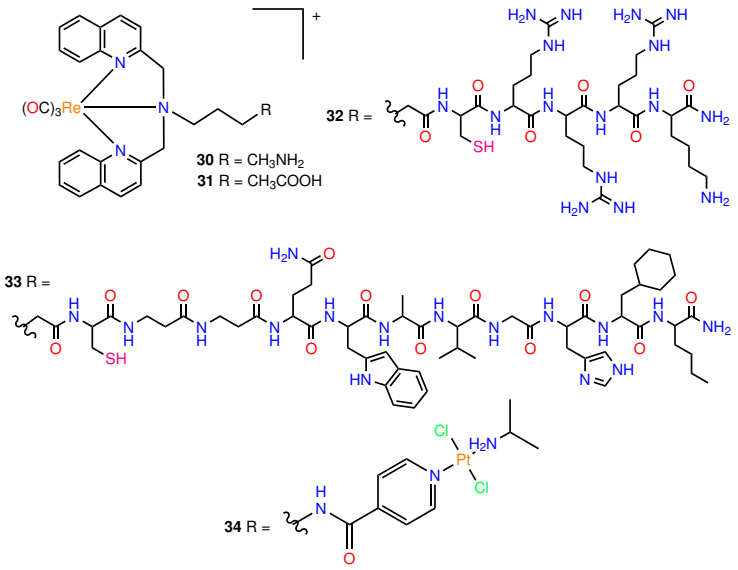


**Scheme 1.16.** Re(I) tricarbonyl complexes with different tridentate nitrogen ligands designed by Gasser and co-workers.

The work of Gasser *et al.* included examples of structural modifications to improve the characteristics of these complexes without aiming for a red-shifted absorption profile.[23] First, they reported Re(I) tricarbonyl complexes with bisquinoline (BQ) (**30** and **31** in Scheme 1.16), a tridentate nitrogen ligand, which showed phototoxicity in cancer cells upon irradiation at 350 nm.[136] Their selectivity was improved by coupling two different targeting peptides: a short nuclear localization signal (NLS) to target the nucleus (**32** in Scheme 1.16), and a derivative of the neuropeptide bombesin to enhance the selectivity towards cancer cells over the healthy ones (**33**). The cytotoxicity of these complexes upon 10 min irradiation with 350 nm light is greater than the one of cisplatin. Even better cytotoxicities were achieved by coupling similar Re(I) complexes to Pt(II) cytotoxic complexes (**34** in Scheme 1.16), hence mixing the intrinsic cytotoxic nature of Pt with the photoproperties of Re.[137]

In a different direction, a series of porphyrin-Re(I) conjugates have been synthesised,[138] with the goal of combining the properties of porphyrins, especially the absorption at the visible region, with those of the rhenium(I) tricarbonyl

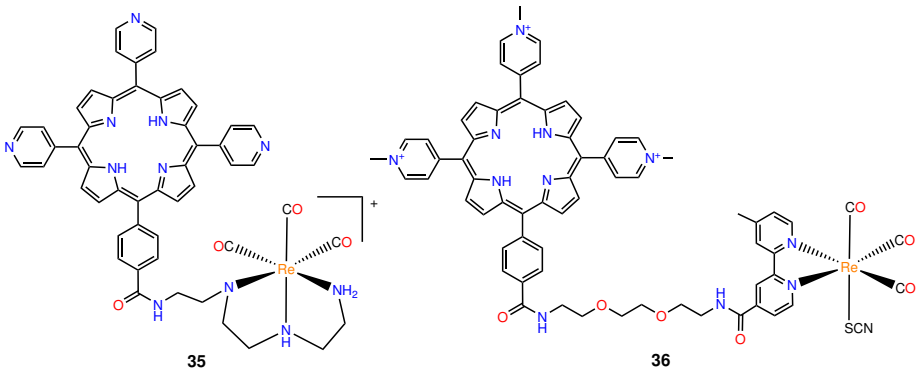


**Scheme 1.17.** Porphyrin-Re(I) conjugates with phototoxic properties.

complexes (see Scheme 1.17). These conjugates showed cytotoxicity upon irradiation at 590-700 nm. However, the phototoxicity of these compounds is only due to the porphyrin moiety, as explained by the fact that the singlet oxygen quantum yields with red light irradiation in the Re(I) conjugate are similar to those in the corresponding parent porphyrin.

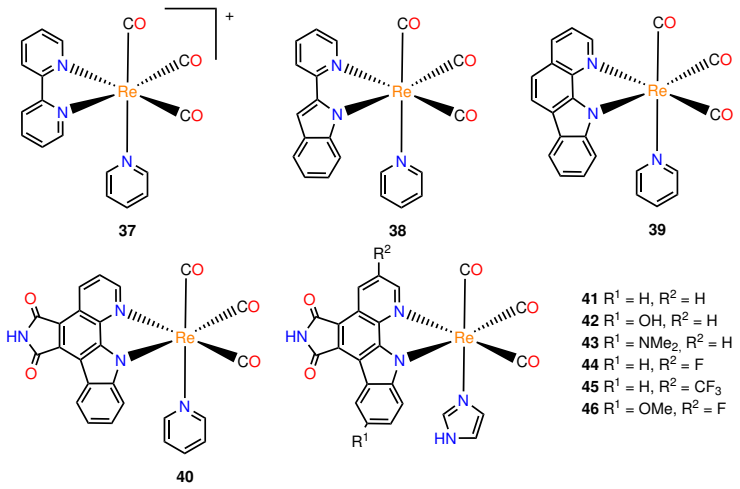


**Scheme 1.18.** Re(I) tricarbonyl complexes synthesized by Megger's group for their use in PDT.

The first examples of Re(I) tricarbonyl complexes with anticancer activity triggered by visible light were reported by Meggers and co-workers.[139] In their work, they replaced the bpy ligand from $[Re(CO)_3(bpy)py]^+$ (py = pyridine) (**37** in Scheme 1.18) by some derivatives of 2-(2′-pyridyl)indolato (**38-40** in Scheme 1.18). Remarkably, these neutral complexes showed no cytotoxic activity in the dark but, when irradiated with visible light ($\lambda \geq 505$ nm), the cell

survival decreased dramatically. They have also shown that complex **40** is able to produce singlet oxygen with $\lambda \geq 505$ nm irradiation, whereas compound **37** requires UV light.

The same group has been able to improve the properties of **40** even further by incorporating substituents in the bidentate ligand (**41-46** in Scheme 1.18).[140] To achieve a red shift of the lowest-lying absorption band, they incorporated $\pi$-donating substituents (OH, $NMe_2$, OMe) in the indole and $\sigma$-accepting substituents in the pyridine ring of the bidentate ligand (F, $CF_3$). All complexes suffered a bathochromic shift in their absorption bands, although the $\pi$-donating substituents completely suppress (OH, $NMe_2$) or diminish (OMe) the formation of singlet oxygen upon irradiation with visible light. However, the complexes bearing a $\sigma$-accepting substituent, even the one with OMe in the indole (**46**), displayed cytotoxicity upon irradiation with red light ($\lambda \geq 620$ nm), which makes them great candidates for their use in PDT, especially complex **44** (with a F substituent).

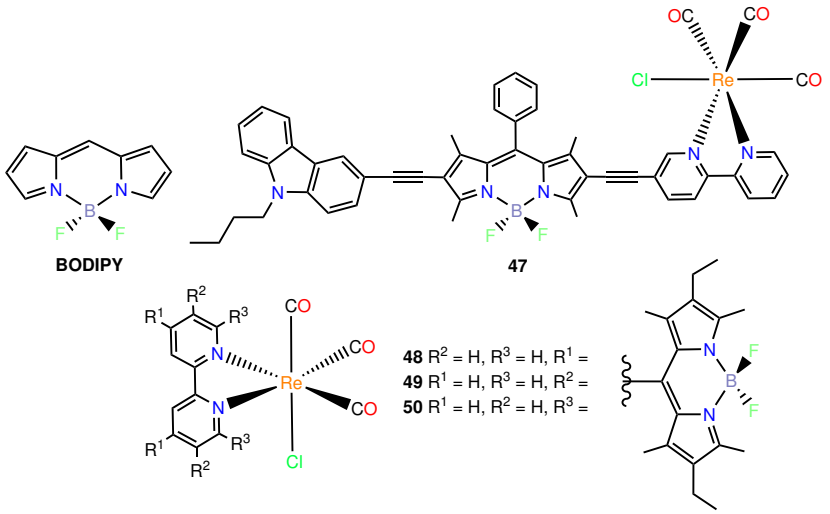


**Scheme 1.19.** General structure of a BODIPY and Re(I)-BODIPY conjugates designed by Zhong (**47**) and Rosenthal (**48-50**).

Boron dipyrromethenes (BODIPYs) (see Scheme 1.19) are compounds known for their interesting luminiscent properties, including high fluorescence quantum yields, photostability and, especially, strong visible light absorption.[141–143] However, the population of their triplet states is practically negligible, which avoids their application as PSs in PDT. These properties along with the ease to modify these compounds have prompted many groups to couple BODIPY moieties to heavy metal complexes, including Re(I) complexes, in order to benefit from the heavy atom effect that promotes the ISC. In this context, Zhong *et al.* reported a rhenium(I) tricarbonyl complex with a bpy ligand bonded to a carbazole-styrylBODIPY (**47** in Scheme 1.19), increasing the lowest-lying

absorption band from 399 nm without the BODIPY moiety to 624 nm with it, as well as producing a triplet state with longer lifetime. Nevertheless, complex **47** did not show significant phototoxicity upon 625 nm irradiation against lung cancer cells.[144]

Rosenthal and co-workers have synthesized a series of $[ReCl(CO)_3(N-N)]$ complexes where N−N is a bpy ligand with BODIPY moieties (**48-50** in Scheme 1.19) attached to the 4,4′ (**48**), 5,5′ (**49**), or 6,6′ (**50**) positions.[20] They paid special attention to the influence of the distance between BODIPY and the metal center in the production of singlet oxygen. As expected, they have reported that complex **50**, which has the shortest BODIPY-Re distance, is the one that exhibits the highest quantum yield for $^1O_2$ production due to an enhanced ISC. In addition, this complex absorbs light at a maximum wavelength of 585 nm, close to the therapeutic window.

Since the lowest-lying absorption band of the complexes $[Re^I(CO)_3(bpy/phen)L]^n$ has a $^1$MLCT character, mainly due to a transition from the Re occupied *d* orbitals to the $\pi^*$ antibonding orbitals of the bidentate ligand, it has also been sought to stabilize the bidentate $\pi^*$ orbitals to induce a bathochromic shift. This can be done by either increasing its conjugation or coupling electron-withdrawing groups, but this also have the side effect of stabilizing the $^3$MLCT excited state. Therefore, other groups have focused on the opposite task: adding electron-donating groups to the bidentate ligand to enhance the reactivity and lifetime of the triplet state.[145]

In 1991, Meyer's group reported the synthesis and photoproperties of a series of $[ReCl(CO)_3(4,4'-R_2bpy)]$ complexes, with electron-donating R =$NEt_2$, $NH_2$, $NHCOCH_3$, OMe, $CH_3$ (**51-55** in Scheme 1.20) and electron-withdrawing groups (R = Ph, Cl, $CO_2Et$, $NO_2$) (**57-60** in Scheme 1.20).[146] Unsurprisingly, compared to the $[ReCl(CO)_3(bpy)]$ complex (**56** in Scheme 1.20), which has the lowest energy absorption maximum at 370 nm, the electron-donating substituents produced a hypsochromic shift whereas the complexes with electron-withdrawing substituents underwent a bathochromic one. Accordingly, they found that both the emission quantum yields and the excited state lifetimes are larger with the electron-donating groups. Their results show that the bathochromic shift induced by the introduction of electron-withdrawing groups is moderate, with a maximum of 78 nm ($NO_2$) in a bpy ligand. Furthermore, if the $\pi^*$ orbitals of the diimine ligand suffer too much stabilization, this ligand may dissociate from the complex.

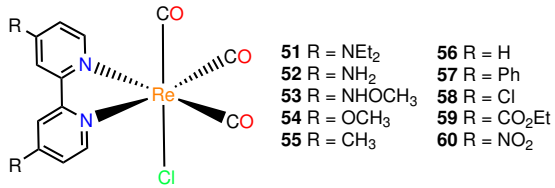


**Scheme 1.20.** Re(I) tricarbonyl complexes with different substituents in the C4 and C4′ positions of the bpy ligand.

A less explored alternative consists of destabilizing the Re *d* orbitals, which mostly form the HOMO of these complexes, to reduce the HOMO-LUMO gap and hence produce a red shift in the lowest-lying absorption band. With this in mind, Kurtz *et al.* varied the carbonyl and acetonitrile ligands in *cis* disposition to the bidentate ligand of $[Re(CO)_3(deeb)(NCCH_3)]^+$ (deeb = 4,4′-diethylesterbpy) (**61** in Scheme 1.21) to examine its influence on the absorption spectra.[147] First, they replaced the acetonitrile ligand by $Cl^-$ to form a neutral complex (**62**). The $\pi$ donation by the $Cl^-$ ligand gives rise to a destabilization of the occupied frontier orbitals, shifting the main absorption band from 365 to 410 nm. In addition, the CO ligand in *cis* disposition to the diimine was substituted by $PMe_3$ (**63**). Carbonyl ligands are known for stabilizing the occupied *d* orbitals of the metal center due to their $\pi$-accepting properties. Therefore, changing this ligand by $PMe_3$, a strong $\sigma$-donor and a weak $\pi$-acceptor, causes a large destabilization of the *d* orbitals. This is reflected in the absorption spectrum, with a lowest energy absorption maximum of 465 nm in the complex with the phosphine ligand. The complex with both ligands, $[ReCl(CO)_2(PMe_3)(deeb)]$ (**64**), combines the two destabilizing effects to achieve a bathochromic shift of 168 nm compared to the original complex.

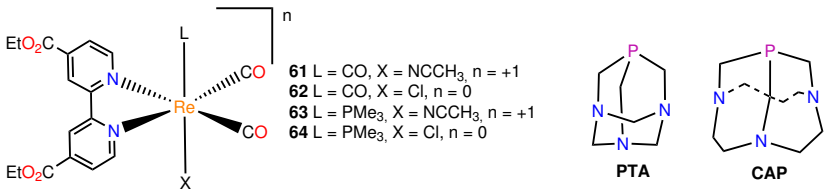


**Scheme 1.21.** Re(I) complexes **61-64** and schematic representation of the phosphine ligands PTA and CAP.

Since an ideal PS must also be soluble in water, the use of a phosphine ligand that, apart from destabilizing the *d* orbitals of the metal center, increases the solubility of the complex, should be desirable. There are some examples of this type of ligands in the literature. PTA (1,3,5-Triaza-7-phosphaadamantane) is a ligand known for its high water solubility (see Scheme 1.21), and has already been incorporated in Re(I) tricarbonyl complexes.[28,148] Another phosphine ligand (1,4,7-triaza-9-phosphatricyclo [5.3.2.1$^{4,9}$]tridecane), known as CAP for the cap-like characteristic shape of its cage (Scheme 1.21), seems also promising. This ligand combines the stability and water solubility of PTA with the electron donating power of the strongest phosphines.[149]

In this Thesis, we will focus on the effects of changing and tuning the bidentate ligand to produce bathochromic shifts. In addition, and aiming at improving even further the absorption profile of these compounds, we will take the idea of Kurtz *et al.* of replacing the carbonyl ligand in *cis* disposition to the bidentate ligand by a phosphine. In this sense, we will employ the trimethylphosphine and the more water soluble and electron-donating ligand CAP.

### 1.2.2 Re(I) Carbonyl Complexes as Dyes in Dye-Sensitized Solar Cells

Renewable energies, including solar energy (photovoltaic and thermic), wind energy, and hydroelectric energy, provide a good alternative for the production of energy based on burning fossil fuels, such as oil, coal, and gas. In addition to the contamination and climate change problems associated with these resources, they will be eventually drained. The production of energy from renewable resources does not emit greenhouse effect gases or pollutants, and represents a secure supply of energy. Despite these advantages, in January 2021, according to "Red Eléctrica Española (REE)", only 47.7 % of the electricity generated in Spain came from renewable sources, and hardly a 4 % from solar energy. This fact can be explained by the relative large costs of photovoltaic cells and their low efficiency, aggravated by the variability of solar light, which depends on the atmospheric conditions as well as the hour of the day. As a consequence, the search for a cheap and efficient way of converting solar energy into electricity has been a goal of the scientific world for decades.

So far, three generations of solar cells have been developed.[150] The first generation, which accounts for the vast majority of solar cells in the market, encompasses a series of silicon solar cells (monocristalline silicon, polycristalline silicon, ribbon silicon, ...). These cells are formed by two layers of silicon, one with extra holes ($p$-type), and another one with extra electrons ($n$-type), forming a $p-n$ junction. When photons with energy greater than the band gap of silicon hit the cell, a electron-hole pair is formed. Therefore, it starts generating electricity. The efficiency of this generation of cells is limited, with a theoretical maximum of 31 %, and their costs are relatively large.

The second generation is formed by thin film solar cells, whose main appeal is the lower cost compared to the first generation, reducing the active material in a cell. There are three main types of cells in this generation: amorphous silicon, copper indium galium diselenide (CIGS), and cadmium telluride. However, these cells are not very efficient and use toxic (Cd) or scarce materials (In), which limit their mass production.

The third generation of solar cells differ from the others in that they are not based on $p-n$ junctions for generating electricity. This generation includes perovskite solar cells, organic solar cells, quantum dot solar cells, and Dye-Sensitized Solar Cells (DSSCs), among others. DSSCs were invented by O'Regan and Grätzel in 1991[151] and have attracted a lot of attention in recent years in view of their low costs, a simple and flexible fabrication process, high efficiencies, and the possibility of using them as building integrated photovoltaics (BIPV).[152] The main difference between DSSCs and silicon solar cells is that in the latter the silicon is responsible for both the generation of photoelectrons and the charge transport, whereas in the former a dye absorbs light and injects an electron into the conduction band of a semiconductor, transferring it to an electrode.

A DSSC consists of a monolayer of dye adsorbed to a semiconductor oxide film over a conductive glass, in contact with a redox electrolyte, and a counter electrode.[152,153] Although other oxides, such as ZnO and $Nb_2O_5$, have been

investigated, $TiO_2$ remains as the material of choice for the semiconductor, which must have a wide band gap. The process of converting solar energy into electricity in a DSSC starts with the photoexcitation of the dye by solar light. Then, the excited electrons of the dye are injected into the conduction band of the $TiO_2$ semiconductor. The oxidized dye recovers its ground state by taking electrons from the electrolyte, which is, typically, the $I^-/I_3^-$ redox couple dissolved in an organic electrolyte. The electrolyte is readily reduced by accepting electrons from the counter electrode, recovering also its initial state. Analogously, the dye and the electrolyte could be regenerated from the electrons injected in the semiconductor, although these side reactions must be avoided. In the final step, the conduction band of $TiO_2$ transfers the electrons to the conductive glass, which is normally fluorine-doped tin dioxide (FTO) or tin-doped indium oxide (ITO), and the electrons reach the external circuit. The voltage of this cell corresponds to the difference between the Fermi level of the electron in the solid and the redox potential of the electrolyte.

The key component in a DSSC is the dye, since it is responsible for absorbing the incoming photons as well as injecting the electrons into the semiconductor. Therefore, the dye must meet some requirements:[153–155] (1) its HOMO must lie below the energy level of the redox couple, so that the oxidized dye can accept the electrons from the electrolyte, (2) the energy level of its LUMO must be above the conduction band of the semiconductor to permit the electron injection in the latter after excitation, (3) the adsorption on the surface of the semiconductor must be strong, which is usually achieved by adding anchoring groups, such as carboxylic acids, into the structure of the dye, (4) the absorption profile of the dye should cover as much visible and IR region as possible for an efficient light harvesting, (5) to increase the useful lifetime of the cell, the dye must be non-corrosive and non-toxic, and should also be stable in both its ground and excited states, (6) aggregation on the semiconductor surface must be avoided. There are other characteristics that improve even further the performance of the dye. For example, the LUMO of the PS should involve the anchoring groups for an optimal injection process into the conduction band of the semiconductor. In addition, the hole on the dye after the injection should locate as far as possible from the surface of the semiconductor to minimize the recombination between the oxidized dye and the injected electrons. Nowadays, there are two main groups of dyes, metal and non-metal based compounds.

The properties of $d^6$ transition metal complexes make them interesting candidates for their use as dyes. In fact, the first device operating as a DSSC used a Ru(II) complex with three 4,4′-dicarboxylate-2,2′-bipyridyl ligands (dcbpy) (see $[Ru(dcbpy)_3]^{2+}$ Scheme 1.22).[156] Ru(II) complexes with pyridines or bipyridines remain as the prime choice for conventional dyes, with different modifications in their ligands to adjust the HOMO and LUMO energy levels and to enhance the absorption at the visible region.[157] For example, one of the most popular dyes is a *cis*-di(thiocyanato)bis(dcbpy) Ru(II) complex, N3 in Scheme 1.22.[158] It was the first dye to achieve a power conversion efficiency (PCE) of 10 %. Recently, a dye coded as RC-62 (see Scheme 1.22), similar to N3 but replacing the carboxylic groups of one of the bpy ligands by thiophene substituents

with acetyl groups, outperformed the PCE of N3.[159] This improvement was attributed to the $\pi$-acceptor properties and extended $\pi$-conjugation with the new substituents, stabilizing both the HOMO and the LUMO, and producing a 30-50 nm red shift in the absorption spectrum.

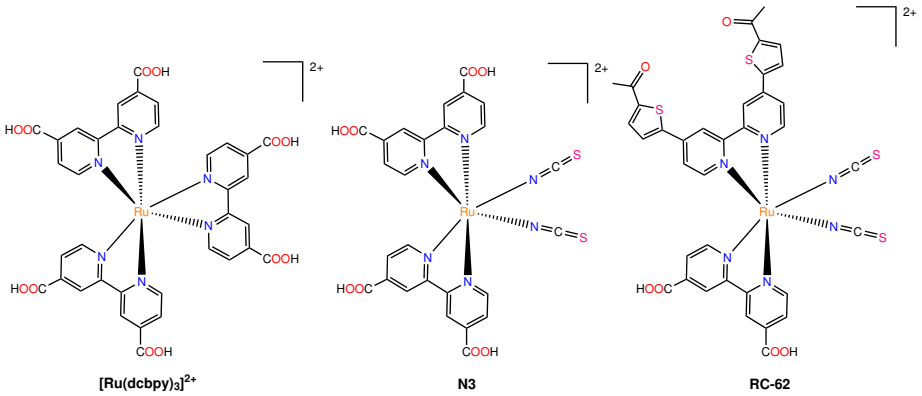


**Scheme 1.22.** Examples of Ru(II) complexes used as dyes in DSSCs.

Despite the interesting photoproperties of Re(I) complexes, there are very few examples of their use as dyes in DSSCs, and all of them are still less efficient than the more popular Ru(II) PSs. Hasselmann and Meyer were the first to explore the performance of these complexes in DSSCs, motivated by the Re(I/II) reduction potential and the facial geometry, which favours the control of the sensitiser orientation.[160] They anchored two Re(I) tricarbonyl complexes to $TiO_2$, $[Re(CO)_3(deeb)py]^+$ (deeb = 4,4′-$(CO_2Et)_2$-bpy; py = pyridine) (**65** in Scheme 1.23) and $[Re(CO)_3(bpy)ina]^+$ (ina = isonicotinic acid) (**66**). The former complex was adsorbed on $TiO_2$ through the deeb ligand whereas the latter was anchored to the semiconductor through the ina ligand. Their incident photon-to-current efficiency (IPCE) was low due to their poor harvesting of photons, although the absorbed photon-to-current efficiency was larger. The same group also tested a series of $[ReX(CO)_3(deeb)]$ complexes (X = I, Br, Cl, CN) (**67-70** in Scheme 1.23), with efficient conversion of absorbed protons to electrons.[161] Recently, Komreddy and co-workers studied the analogous complexes bearing dcbpy instead of deeb (adding also X = SCN) (**71-75**) in acidic and basic media to find that complex $[Re(I)(CO)_3(dcbpy)]$ (**71**) is the most red-shifted in absorption and presents the largest IPCE.[21] The relative poor performance of these complexes compared to N3 was attributed to the lower absorption in the red region of the spectrum.

In 2009, Chen *et al.* investigated the performance as dyes of Re(I) tricarbonyl complexes with bidentate ligands containing COOMe or COOH moieties in sulphur-rich pendants (**76-83** in Scheme 1.24).[162] The lower performance of these complexes compared to N3 was ascribed again to their poor efficiency of light-harvesting. In relation to that work, Zhang and co-workers carried out a theoretical study on two of these complexes (**78** and **82**) to elucidate the influ-

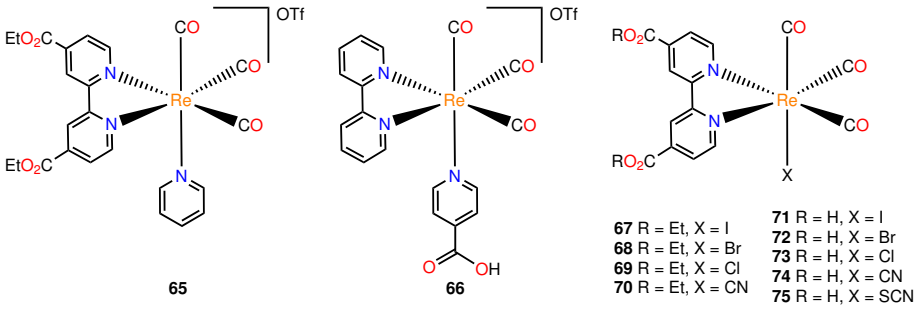


**Scheme 1.23.** Schematic structure of complexes **65-75**.

ence of the COOH groups in their absorption profiles, electronic structure, and performance as a dye.[163] Furthermore, they also reported two new complexes with additional COOH groups attached to the diimine ligand (**84** and **85**), these modifications induce a red-shift in the absorption spectrum and could enhance their performance in DSSCs.

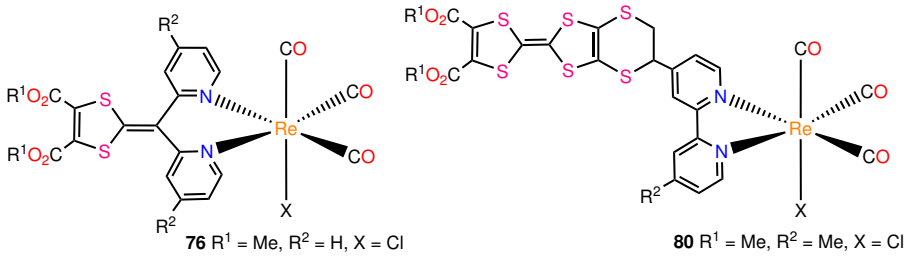


**Scheme 1.24.** Re(I) tricarbonyl complexes **76-85** bearing sulphur-rich moieties attached to the diimine ligand.

To this date, the last example in the literature is the work of Veronese and co-workers. In 2016, they investigated the possible use of some dinuclear Re(I) carbonyl complexes as dyes in DSSCs (**86-88** in Scheme 1.25).[164] These complexes present two $Re(CO)_3$ units connected by different bridging ligands and a pyridazine-4-COOH moiety. They observed conversion to electricity, but with a PCE lower than 1 %, mainly due to poor injection of electrons into $TiO_2$. In a subsequent work, they improved the performance of these complexes by introducing an organic dye (DN-F04 in Scheme 1.25) to extend their photon harvesting capacity, and an alkyl chain in the pyridazine moiety to raise the LUMO level of the dye (**89** and **90**).[165] Thus, the PCE raised from less than 1 % to 3.5 % with the best dye.

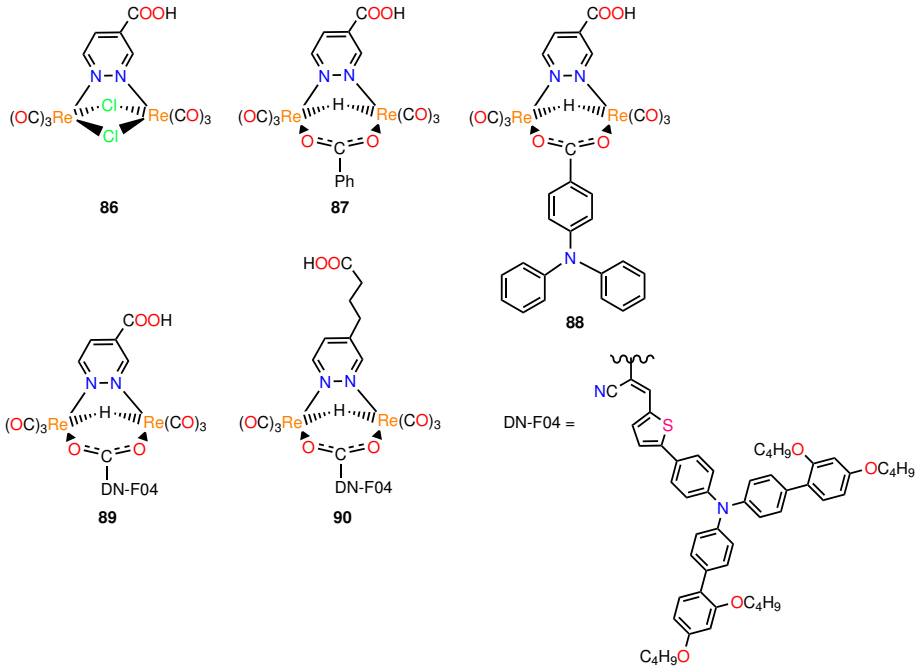


**Scheme 1.25.** Dinuclear Re(I) carbonyl complexes **86-90** reported by Veronese and co-workers.

The high cost, poor light harvesting, and limited availability of dyes based on metal complexes have motivated the search for metal-free organic dyes.[153] These sensitisers are normally designed with a D-$\pi$-A structure. In this sense, an electron-accepting group (A) is connected to an electron-donating group (D) through a $\pi$-conjugated linker. This facilitates the overlap between the $\pi$ orbitals and, hence, produces a bathochromic shift in the absorption spectrum. It also minimizes the recombination between the electron and the hole within the sensitiser.[155] The operating principle of these dyes is to induce an intramolecular charge transfer (ICT) from the donor to the acceptor moieties through the $\pi$ bridge upon irradiation. That is, the HOMO must be located on the D and the linker, while the LUMO must be centered on the A moiety. Then, the acceptor, which should be anchored to the semiconductor, transfers the electrons to $TiO_2$. Among them, porphyrin based D-$\pi$-A dyes have shown the greatest efficiencies. For instance, a PCE of 12.3 % was achieved with a porphyrin dye supplemented by an organic co-sensitiser, developed by Grätzel and co-workers.[166] The highest PCE reported for a DSSC (13 %) with no co-sensitiser has been achieved using a porphyrin dye, coded as SM315.[167] Although it is not a metal-free dye, since it contains a Zn atom, it is a great example of the potential of D-$\pi$-A porphyrins as dyes in DSSCs. Nowadays, the best PCE (14.2 %) has been obtained in a co-sensitized DSSC based on an organic and a porphyrin dye, with a D-$\pi$-A

structure.[168]

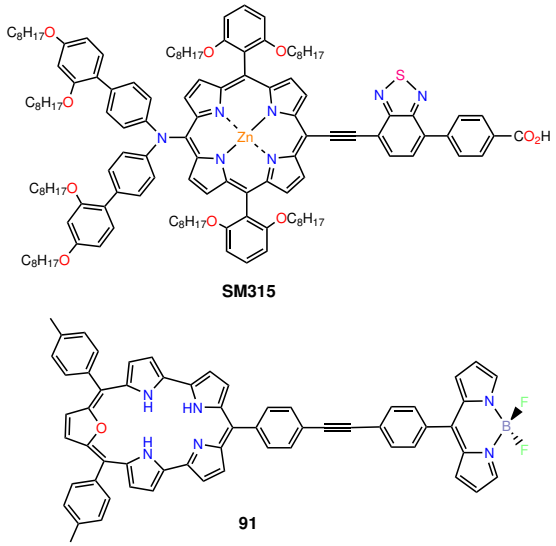


**Scheme 1.26.** SM315 dye and the BODIPY-oxasmaragdyrin dyad synthesized by Kalita *et al.*

BODIPYs are another family of metal-free compounds with growing interest in their use as dyes in DSSCs due to their spectroscopic properties. As already mentioned, BODIPYs have strong light absorption, versatile structural modification capability, high fluorescence quantum yields, and photostability.[141–143] However, their PCEs are still far below the ones reported in porphyrin dyes, with a maximum of 6.43 %.[169] The main reason for that general poor performance is a narrow absorption profile, that is, BODIPYs exhibit strong absorption but not in a broad range of the spectrum, so most of the incident photons are not captured. There are some strategies that are being used to improve the light harvesting of these compounds.[141] These include modifying their structure by adding electron acceptor and/or donor groups,[143,170,171] or employing dyes with an increasing number of BODIPY moieties.[142] In another direction, the coupling of BODIPY with porphyrins have shown promising results. For example, Kalita *et al.* have synthesized a dyad consisting in a BODIPY moiety covalently linked to oxasmaragdyrin through a phenylethynyl bridge (see **91** in Scheme 1.26).[172] Oxasmaragdyrin is a porphyrin-like compound with a $\pi$-extended system, which produces a red-shift in the absorption bands compared to regular porphyrins. This dyad presents broad and strong absorption in the visible region, in the range of 449-706 nm.

In this PhD Thesis we will explore the properties of a series of dyads formed by a oxasmaragdyrin molecule and a BODIPY moiety, linked through different bridges. Our goal is to examine the potential use of the dyads as dyes in DSSCs, paying special attention to the influence of the bridges and the relation between

the geometrical and electronic features, such as planarity and ring currents, with the spectroscopic properties.

The lack of rhenium(I) carbonyl complexes as dyes in DSSCs has prompted us to contribute to this field. According to the literature, the main drawback of these complexes as dyes is the poor absorption in the visible region. Note that the tuning of the HOMO and LUMO levels described in their use for PDT is not suitable here, since, as mentioned before, they have to meet some requirements. If the HOMO is too much destabilized or the LUMO too much stabilized, the reduction of the oxidized dye by the electrolyte or the injection of the electrons to the semiconductor could be seriously affected. A clever solution may consist of coupling a rhenium(I) tricarbonyl complex with a diimine ligand to BODIPY units, as in complexes **48-50**, synthesized by Rosenthal and co-workers.[20] In this way, the BODIPY can help to improve the light harvesting in the visible region without an excessive adjustment of the energy levels of the complex. With that purpose in mind, BODIPY molecules with some structural modifications will be coupled in different positions to the bpy ligand of a Re(I) tricarbonyl complex. We will carry out a computational study on the properties of these compounds and their potential use in DSSCs. Additionally, we will also test their possible use as PS in PDT.

## 1.3 Objectives of the Present Study

Having seen the context of various fields in which Re(I) and Mo(II) carbonyl complexes and molybdocenes play an important role, the objectives covered in this PhD Thesis are detailed herein.

- The reactions of $[ReX(CO)_3(N{-}N)]$ (N–N = bpy and phen; X = OH, OMe, OPh, $NH_2$, NHMe, NH*p*Tol, SH, SMe, SPh, $PH_2$, PHMe, $PMe_2$, PHPh, $PPh_2$, and PMePh) complexes with methyl propiolate (HMAD) render different products coming from the coupling of activated HMAD to the CO ligand, the bidentate ligand or from its insertion into the Re-X bond. In this work we aim to elucidate the general reaction mechanisms and the influence of such ligands that explains the product obtained in each system.

- Mono- and difunctional ethers present different behavior in their hydrolisis catalyzed by the aqueous molybdocene $[Cp_2Mo(OH)(OH_2)]^+$. Through the theoretical analysis of the reaction between $[Cp_2Mo(OH)(OH_2)]^+$ and ethyl vinyl ether, diethyl ether, and divinyl ether we aim to unveil the hydrolysis mechanism and the role played by the unsaturated moieties of the ethers

- The reactions between $[Re(CO)_3(4,4'{-}R'_2bpy)(RIm)]OTf$ ($R' = t$Bu, $NMe_2$, Br; R = Me, Mes) and $KN(SiMe_3)_2$, and that of the analogous Mo(II) complex $[Mo(\eta^3{-}C_4H_7)(CO)_2(4,7{-}Cl_2phen)(RIm)]OTf$ (R = Me, Mes) with the same base may yield three different products, two derived from the coupling of the imidazole ligand to two different positions of the bidentate

ligand and a third one where the imidazole ligand rearranges to form an imidazol-2-yl complex. In this Thesis we focus on understanding the effect of donor/acceptor substituents in the bidentate ligand and of those in the imidazole ligand on the selectivity of the reaction.

- The Re(I) tricarbonyl complex bearing an aqua ligand and a dimethylphen bidentate ligand reported by Wilson and co-workers shows cytotoxic properties. Since it may interact with DNA bases or with some amino acids, we model its reaction towards guanine and histidine to elucidate its preferred biological target.

- Re(I) carbonyl complexes are potential candidates to be used in the PDT against cancer. Among the required features, these complexes should absorb light in therapeutic window, which is located in the visible and the near-infrarred regions of the electromagnetic spectrum, and present high solubility in water. Herein, we seek to understand the main features of a variety of ligands that are able to produce bathochromic shifts and increase the water solubility of the complexes.

- Re(I) carbonyl complexes could be used in DSSC to transform sunlight into electricity. To obtain the desired features of an ideal dye, the ligands of the complex must fulfill several requirements. As an initial step in the study of a Re(I) complex in this field, we aim to study the spectroscopic, geometrical, and electronic properties of dyads formed by oxasmaragdyrin and a BODIPY linked by different bridges as dyes in DSSCs.

- Finally, we select the same BODIPY as in the previous study to link to different positions in the bpy ligand of the $[ReCl(CO)_3(R_2bpy)]$ complex with the aim of testing the potential use of these complexes in PDT as well as in DSSCs.

# 2 Methods

## 2.1 Elementary Quantum Mechanics

### 2.1.1 The Schrödinger Equation

The movement of the electrons in matter cannot be described by Classical Mechanics (Newton equations) and must be described instead by Quantum Mechanics (QM), in which the dynamic state of an electronic system (atom, molecule ...) is defined by a wave function, $\Psi$, which contains all its physical information.

The time-dependent Schrödinger equation (TDSE)[173,174] gives the description of the system evolving with time $t$

$$i\hbar\frac{\partial}{\partial t}\Psi(r,t) = \hat{H}(r,t)\Psi(r,t) \tag{1}$$

where the other variable $r$ represents the space coordinates, $\hat{H}(r,t)$ is the time-dependent Hamiltonian operator, and $\hbar$ is the Planck constant $h$ divided by $2\pi$. When $\hat{H}$ does not depend on time, it is possible to separate the time-dependent part of the wave function as a phase factor wherein $E$ is a constant with dimensions of energy and the system is therefore in a stationary state, with all its observable properties constant in time

$$\Psi(r,t) = \Psi(r)e^{-iEt/\hbar} \tag{2}$$

In this context, the combination of equations (1) and (2) leads to the time-independent Schrödinger equation (3), whose resolution is the aim of most quantum chemical methods

$$\hat{H}(r)\Psi(r) = E\Psi(r) \tag{3}$$

In a system formed by $N$ electrons and $M$ nuclei, the non-relativistic Hamiltonian contains terms for the kinetic energy of the nuclei ($\hat{T}_n$) and the electrons ($\hat{T}_e$), for the repulsion between nuclei ($\hat{V}_{nn}$) and between electrons ($\hat{V}_{ee}$), and for the coulomb attraction between electrons and nuclei ($\hat{V}_{en}$)

$$\hat{H} = \hat{T}_n + \hat{T}_e + \hat{V}_{en} + \hat{V}_{ee} + \hat{V}_{nn} \tag{4}$$

where, in atomic units,

$$\hat{T}_n = -\sum_{A=1}^{M}\frac{1}{2M_A}\nabla_A^2 \tag{5}$$

$$\hat{T}_e = -\frac{1}{2}\sum_{i=1}^{N}\nabla_i^2 \tag{6}$$

$$\hat{V}_{en} = -\sum_{i=1}^{N}\sum_{A=1}^{M}\frac{Z_A}{R_{iA}} \tag{7}$$

$$\hat{V}_{ee} = \sum_{i=1}^{N} \sum_{j>i}^{N} \frac{1}{r_{ij}} \tag{8}$$

$$\hat{V}_{nn} = \sum_{A=1}^{M} \sum_{B>A}^{M} \frac{Z_A Z_B}{R_{AB}} \tag{9}$$

being $M_A$ the ratio of the mass of nucleus $A$ to the mass of an electron $i$, $Z_A$ the atomic number of nucleus $A$, $r_{ij}$ the distance between electrons $i$ and $j$, $R_{AB}$ the distance between nucleus $A$ and $B$, $R_{iA}$ the distance between electron $i$ and nucleus $A$, and $\nabla^2$ the Laplacian of the coordinates of either the nuclei, $\nabla_A^2$, or the electrons, $\nabla_i^2$

$$\nabla_i^2 = \left( \frac{\partial^2}{\partial x_i^2} + \frac{\partial^2}{\partial y_i^2} + \frac{\partial^2}{\partial z_i^2} \right) \tag{10}$$

$$\nabla_A^2 = \left( \frac{\partial^2}{\partial x_A^2} + \frac{\partial^2}{\partial y_A^2} + \frac{\partial^2}{\partial z_A^2} \right) \tag{11}$$

### 2.1.2 The Born-Oppenheimer Approximation

Normally, the non-relativistic Hamiltonian (see eq. (4)) is split into terms depending on the nuclear coordinates $R$ (the kinetic energy of the nuclei and the repulsion between them) and the electronic coordinates $r$ (the kinetic energy of the electrons, their mutual repulsion, and the attraction between electrons and nuclei). The electron-dependent terms are usually grouped in the so-called electronic Hamiltonian, $\hat{H}_e$

$$\hat{H}(r, R) = \hat{T}_n(R) + \hat{V}_{nn}(R) + \hat{H}_e(r; R) \tag{12}$$

$$\hat{H}_e = -\frac{1}{2} \sum_{i=1}^{N} \nabla_i^2 - \sum_{i=1}^{N} \sum_{A=1}^{M} \frac{Z_A}{R_{iA}} + \sum_{i=1}^{N} \sum_{j>i}^{N} \frac{1}{r_{ij}} \tag{13}$$

The notation $\hat{H}_e(r; R)$ is used to indicate that the electronic Hamiltonian depends explicitly on the coordinates of the electrons $r$, but only parametrically on the coordinates of the nuclei $R$. The hermiticity of $\hat{H}_e(r; R)$ allows to express the time-independent Schrödinger equation corresponding to the electronic problem as

$$\hat{H}_e(r; R)\Psi_{e,k}(r; R) = E_{e,k}\Psi_{e,k}(r; R) \qquad k = 1, 2, \ldots, \infty \tag{14}$$

where $\Psi_{e,k}$ and $E_{e,k}$ are the electronic wave function and energy for a given electronic state $k$, respectively. Both of them depend parametrically on $R$ in the sense that altering the positions of the nuclei changes the dependence on the electronic coordinates. This is due to the electron-nuclei potential, where $R$ is no longer a variable but a parameter.

Since the electronic wave functions form a complete and orthonormal set of functions in the $r$ space for any value of $R$, the total wave function $\Psi(r, R)$ can be written as a linear combination of them, taking as coefficients functions of

the nuclear coordinates, $\Xi_k(R)$, which describe the nuclear movement in the electronic state $k$

$$\Psi(r,R) = \sum_{i=1}^{\infty} \Psi_{e,k}(r;R)\Xi_k(R) \tag{15}$$

thus, the Schrödinger equation (3) becomes

$$\sum_{k=1}^{\infty} \left(\hat{T}_n + \hat{V}_{nn} + \hat{H}_e\right) \Psi_{e,k}(r;R)\Xi_k(R) = E \sum_{k=1}^{\infty} \Psi_{e,k}(r;R)\Xi_k(R) \tag{16}$$

Multiplying this equation by an electronic wave function $\Psi^*_{e,l}$ and integrating over the electron coordinates, a set of equations with coupling elements between two electronic states is obtained

$$\hat{T}_n\Xi_k + \hat{V}_{nn}\Xi_k + E_{e,l}\Xi_k + \sum_{k=1}^{\infty} \left[2\langle\Psi_{e,l}|\nabla_n|\Psi_{e,k}\rangle \left(\nabla_n\Xi_k\right) + \langle\Psi_{e,l}|\nabla_n^2|\Psi_{e,k}\rangle\Xi_k\right] = E\Xi_l \tag{17}$$

where the electronic wave function has been removed from the first three terms due to the orthonormality condition, whereas two different coupling terms appear, the first- and second-order non-adiabatic coupling terms.

In the adiabatic approximation,[173] only the diagonal coupling terms (i.e., the ones corresponding to the same electronic state,¡) are not neglected. Unless the wave function is spatially degenerated, the diagonal first-order non-adiabatic coupling element is also set to zero and, consequently, only a coupling term is preserved, which is called diagonal correction

$$\left(\hat{T}_n + \hat{V}_{nn} + E_{e,l} + \langle\Psi_{e,l}|\nabla_n^2|\Psi_{e,l}\rangle\right) \Xi_l = E\Xi_l \tag{18}$$

In the Born-Oppenheimer (BO) approximation,[175,176] the diagonal correction on the left-hand side of the above equation is also neglected

$$\left(\hat{T}_n + \hat{V}_{nn} + E_{e,k}\right) \Xi_k = E\Xi_k \tag{19}$$

The qualitative meaning of this assumption is that the variation of the electronic wave functions with respect to the movement of the nuclei is negligible, separating the electronic and nuclear movements, and that the different electronic states are distant in energy. Therefore, the BO approximation fails in systems with degenerated or *quasi*-degenerated electronic states, where the term $\langle\Psi_{e,l}|\nabla_n|\Psi_{e,k}\rangle$ acquires importance. Within the BO picture, the electronic energies $E_{e,l}$, which depend parametrically on $R$, provide the potentials on which the nuclei move.

In this PhD Thesis the BO approximation is considered valid for all the studied molecular systems. Therefore, henceforth, the subscript $e$ will be removed from the electronic Hamiltonian, energy, and wave function.

### 2.1.3 Potential Energy Surface

An important consequence of the BO approximation is that the movement of the nuclei is described by the coulomb repulsion between nuclei and the electronic

energy. In this sense, they define a Potential Energy Surface (PES) for a given electronic state that depends on the nuclear coordinates

$$E(R) = V_{nn}(R) + E_{e,k}(R) \tag{20}$$

Therefore, the analysis of the PES gives qualitative and quantitative information about all the chemical changes that may occur in the molecular system. Since the PES depends on all the nuclear coordinates, its exploration for all the possible nuclear configurations is only feasible in small systems. However, from a chemical point of view, the most relevant information can be extracted from the critical points ($R_c$) of the PES.[177] These points are identified by the following condition,

$$g(R_c) = \nabla E(R_c) = \left( \frac{\partial E}{\partial R_1}, \frac{\partial E}{\partial R_2}, \ldots, \frac{\partial E}{\partial R_{3M}} \right) = 0 \tag{21}$$

which means that the gradient of the energy $E$ at that point ($R_c$) must be null.

According to the Hellmann-Feynman theorem, the derivative of the energy with respect to the nuclear coordinates can be interpreted as the force acting upon that atom. As a consequence, the critical points, where all these derivatives are zero, correspond to equilibrium geometries.

The second derivatives of the energy form a real and symmetric matrix known as the Hessian matrix **H**. The elements of this matrix are defined as

$$H_{ij} = \frac{\partial^2 E}{\partial R_i \partial R_j} \tag{22}$$

This matrix can be diagonalized and the number of negative eigenvalues at the critical point $\lambda(R_c)$ is used to classify them:

- If $\lambda = 0$, the critical point is a local minimum of the PES. Therefore, it corresponds to a stable nuclear configuration, such as reactants, products, and reaction intermediates.
- If $\lambda = 1$, the critical point is a first order saddle point, as it represents a maximum in the direction defined by the eigenvector related to the negative eigenvalue, the so-called transition vector, and a minimum in all the other directions. This corresponds to a Transition State (TS), which connects two minima of the PES through the transition vector.
- The critical points with $\lambda > 1$ do not correspond to significant chemical points. However, they may have some importance in certain situations (e.g. $\lambda = 2$ may be a bifurcation point in the PES).

### 2.1.4 Geometry Optimization

The search for critical points within the PES, called geometry optimization, can not be performed analytically, since there is not an explicit expression for $E(R)$. However, there are many available numerical methods for this purpose. These

methods are normally classified according to the information that they employ to perform the optimization: some of them only use the energy function, others also its gradients, and there are other methods that add the Hessian matrix as well.

Most of the geometry optimization algorithms are based on the Newton-Raphson method.[178] This method starts with a Taylor series expansion of the energy with respect to a initial nuclear configuration $R_0$

$$E(R) = E(R_0) + g(R_0)(R - R_0)^t + \frac{1}{2}(R - R_0)\mathbf{H}(R_0)(R - R_0)^t \tag{23}$$

where $g(R_0)$ and $\mathbf{H}(R_0)$ are the gradient and the Hessian evaluated at the reference geometry, respectively. Deriving the previous equation with respect to $R$, the following expression is obtained

$$\frac{dE}{dR} = g(R_0) + \mathbf{H}(R_0)(R - R_0)^t \tag{24}$$

As at a critical point $dE/dR = 0$, equation (25) provides the prescription for the next geometry, $R$, from the gradient and the inverse of the Hessian

$$R = R_0 - \mathbf{H}^{-1}(R_0)g(R_0) \tag{25}$$

In principle, the new geometry $R$ should be a critical point of the PES, with $g(R) = 0$. However, since the Taylor expansion has been truncated at the second order, these equations are only approximations. Thus, this procedure must be repeated iteratively until convergence is achieved (i.e., the geometry of the next point is similar enough to the previous one).

There are two major disadvantages in the Newton-Raphson method. The first one is the use of the inverse Hessian for the computation of the next step. This implies that, if one of the Hessian eigenvalues is close to zero, the size of the step approaches infinity. There are some methods to control that the step size remains in the region of the PES where the Taylor expansion is valid, such as Rational Function Optimization (RFO)[179–182] and Trust Radius Method (TRM).[183] Furthermore, the Newton-Raphson method involves the calculation of the Hessian matrix in every step of the optimization, which must be stored and diagonalized to calculate its inverse. This implies a large computational cost. In general, the optimization algorithms based on the Newton-Raphson method employ approximated Hessian matrices, in which case they are called *pseudo*-Newton-Raphson methods. Typically, they use an updating scheme, starting with an unit Hessian matrix that it is then refined during the optimization, using the gradients from the previous points. As a consequence, the convergence of the *pseudo*-Newton-Raphson methods is linear, whereas the true Newton-Raphson methods converge quadratically.

In the Gaussian set of programs,[184] the default method is called Berny optimization algorithm, which is based on the original algorithm proposed by H. B. Schlegel in 1982.[185] This method employs an updating scheme algorithm for the computation of the Hessian matrix: Broyden-Fletcher-Goldfarb-Shanno

(BFGS) for the minima, and an iterated Bofill for TS. The determination of the step size uses the RFO approach. The convergence is achieved when the criteria for the maximum force component, the root-mean square force, the maximum step component, and the root-mean-square step are fulfilled. For the optimization of TSs, this algorithm must check the presence of a negative eigenvalue in the Hessian matrix for every step. The Hessian matrix for the search of a TS should be calculated analytically at least in the first step.

### 2.1.5 Reaction Path

As already mentioned, any chemical process in a system can be described in the PES through the change in nuclear coordinates associated with that process. The trajectory of the PES that connects two minima, normally associated with reactants and products, is called reaction path.

A reaction path could, in principle, be defined by a reaction coordinate or a set of coordinates able to represent the change in the geometry of the reactive system during the reaction. However, this coordinate/s is usually arbitrary determined and may not be associated with the actual changes occurring in the system. Therefore, the reaction paths are normally defined according to the fulfillment of some properties.

The most popular choice for this path is called Mininum Energy Path (MEP), which connects the two minima through their corresponding TS.[186] The reaction coordinate for this path is normally determined with the Steepest Descent (SD) path, also called Intrinsic Reaction Coordinate (IRC) in mass weighted coordinates.[187] Hence, the reaction path is defined from the TS, following the direction of its gradient towards the two minima. For that purpose, since the gradient at the TS is null, the first point is determined using the transition vector. Then, the tangent vector at each point of the path, $v(R)$, is computed as the normalized gradient vector at that point

$$v(R) = \frac{dR}{ds} = -\frac{g(R)}{|g(R)|} \tag{26}$$

where $s$ is the arc length of the curve.

Euler's method is the simplest choice for solving equation (26). However, it is normally useless for this particular problem, since it gives points outside the MEP due to its finite linear steps.[173] The algorithm proposed by Schlegel and González corrects this problem by forcing each step to remain in a hypersphere of a given radius and correcting it through an energy minimization along the transition vector in each point.[188,189]

### 2.1.6 The Slater Determinant

Coming back to the solution of the electronic Schrödinger equation (14), most methodologies construct the ground state wave function as a Slater determi-

nant[190] for the most stable electron configuration (single-reference methods),

$$\Psi(x_1, x_2, \ldots, x_N) = (N!)^{-1/2} \begin{vmatrix} \phi_1(x_1) & \phi_2(x_1) & \ldots & \phi_N(x_1) \\ \phi_1(x_2) & \phi_2(x_2) & \ldots & \phi_N(x_2) \\ \vdots & \vdots & \ddots & \vdots \\ \phi_1(x_N) & \phi_2(x_N) & \ldots & \phi_N(x_N) \end{vmatrix} = (N!)^{-1/2} \sum_{p=0}^{N-1} (-1)^p \hat{P}\Pi \tag{27}$$

where $\phi_i(x_i)$ are the one-electron functions (or spinorbitals), given by the product of spatial orbitals and spin ($\alpha$ or $\beta$), the variable $x_i$ contains information about the position and the spin of an electron $i$, $\hat{P}$ is the permutation operator (to generate all possible permutations of the electrons), $p$ is 0 or 1 depending on the order of permutation (even or odd), and $\Pi$ represents the diagonal product of the Slater determinant. The most common representation of a Slater determinant only includes the diagonal elements, as in the following expression

$$\Psi \equiv |\Pi\rangle = |\phi_1(x_1)\phi_2(x_2)\phi_3(x_3)\ldots\phi_N(x_N)\rangle \tag{28}$$

The expectation value for the energy using the Slater determinant for the wave function is then:

$$E = \langle\Psi|\hat{H}|\Psi\rangle = \sum_{p=0}^{N-1} (-1)^p \langle\Pi|\hat{H}|\hat{P}\Pi\rangle \tag{29}$$

The permutation operator $\hat{P}$ only appears once since the presence at both sides of the integral leads to a $N!$ counting, from which the prefactor $(N!)^{-1}$ cancels out. It contains sums over all electrons and pairs of electrons, but all the terms with a permutation of more than two electrons are zero. Thus, the Hamiltonian can be expressed as

$$\hat{H} = \sum_{i=1}^{N} \hat{h}_i + \sum_{i=1}^{N} \sum_{j>i}^{N} \hat{g}_{ij} \tag{30}$$

where $\hat{h}_i$ is the set of one-electron operators, describing the movement of electrons in the field created by the nuclei, and $\hat{g}_{ij}$ is the two-electron operator for the electron-electron interaction

$$\hat{h}_i(r_i; R) = \hat{T}_e(r_i) + \hat{V}_{en}(r_i; R) = -\frac{1}{2}\nabla_i^2 - \sum_{A=1}^{M} \frac{Z_A}{R_{iA}} \tag{31}$$

$$\hat{g}_{ij}(r_i, r_j) = \hat{V}_{ee}(r_i, r_j) = \frac{1}{r_{ij}} \tag{32}$$

The integrals involving the one-electron operator, $\hat{h}_i$, only differ from zero when there is no permutation, so there will be $N$ of these terms, which are denoted as $h_i$

$$\langle\Psi|\hat{h}_i|\Psi\rangle = \langle\Pi|\hat{h}_i|\Pi\rangle = \langle\phi_i(x_i)|\hat{h}_i|\phi_i(x_i)\rangle = h_i \tag{33}$$

On the other hand, there are two types of contributions resulting from the two-electron operator, $\hat{g}_{ij}$, with and without the permutation operator between two electrons, $\hat{P}_{ij}$

$$\langle\Psi|\hat{g}_{ij}|\Psi\rangle = \langle\Pi|\hat{g}_{ij}|\Pi\rangle - \langle\Pi|\hat{g}_{ij}|\hat{P}_{ij}\Pi\rangle \tag{34}$$

The first integral in equation (34) is called coulomb integral, denoted as $J_{ij}$, and represents the classical repulsion between two charge distributions

$$\langle\Pi|\hat{g}_{ij}|\Pi\rangle = \langle\phi_i(x_i)\phi_j(x_j)|\hat{g}_{ij}|\phi_i(x_i)\phi_j(x_j)\rangle = J_{ij} \tag{35}$$

The second integral in equation (34) is called exchange integral, represented as $K_{ij}$, and it has no classical analogy. The sign of this integral is negative due to the $(-1)^p$ factor

$$\langle\Pi|\hat{g}_{ij}|\hat{P}_{ij}\Pi\rangle = \langle\phi_i(x_i)\phi_j(x_j)|\hat{g}_{ij}|\phi_j(x_i)\phi_i(x_j)\rangle = K_{ij} \tag{36}$$

Putting together equations (33), (35), and (36), and adding the contributions from all the $N$ electrons, and the nuclei repulsion term (9), the following expression for the total energy is obtained,

$$E = \sum_{i=1}^{N} h_i + \sum_{i=i}^{N}\sum_{j>i}^{N} (J_{ij} - K_{ij}) + \sum_{A=1}^{M}\sum_{B>A}^{M} \frac{Z_A Z_B}{R_{AB}} \tag{37}$$

where the sum involving the two-electron contributions runs over unique pairs of electrons.

Usually, for closed shell systems, the spinorbitals are grouped in pairs with the same spatial wave function. $\psi_i$ is the spatial orbital of an an electron with $\alpha$ spin function and $\bar{\psi}_i$ is the same spatial orbital of another electron with $\beta$ spin function

$$\begin{aligned} \phi_1(x_1) &= \psi_1(r_1)\alpha(1) = \psi_1(r_1) \\ \phi_2(x_2) &= \psi_1(r_2)\beta(2) = \bar{\psi}_1(r_2) \end{aligned} \tag{38}$$

Each of these pairs would represent a doubly filled molecular orbital (MO). With this notation, equation (28) transforms into the following one,

$$\Psi = |\psi_1(r_1)\bar{\psi}_1(r_2)\psi_2(r_3)\bar{\psi}_2(r_4)\ldots\psi_{N/2}(r_{N-1})\bar{\psi}_{N/2}(r_N)\rangle \tag{39}$$

As a consequence of the orthonormality of the spin functions, only the exchange integrals, $K_{ij}$, involving two electrons with the same spin will be different from zero. This is related to the Pauli principle, since the probability of finding two electrons with the same spin close in space is reduced.[178] Therefore, there will be a $(J_{ij} - K_{ij})$ term for each pair of electrons having the same spin and a $J_{ij}$ term for each pair of electrons with different spin. Hence, in terms of these orbitals, the total energy can be written as

$$E = 2\sum_{i=1}^{N/2} h_i + \sum_{i=i}^{N/2}\sum_{j=1}^{N/2} (2J_{ij} - K_{ij}) + \sum_{A=1}^{M}\sum_{B>A}^{M} \frac{Z_A Z_B}{R_{AB}} \tag{40}$$

where the sum involving the two-electron integral now runs over all possible pairs of spatial orbitals, including the '$ii$', and the '$ij$' and '$ji$' pairs. Note that $J_{ii} = K_{ii}$, so the only two-electron contribution for the pair of electrons with the same spatial orbital is $J_{ii}$.

The expression (40) is only valid for closed-shell systems with the same number of $\alpha$ and $\beta$ electrons. The energy in equation (40) is already corrected to account for the double counting of the electron-electron interactions. As already mentioned, each pair of different spatial orbitals is considered twice, but there are eight pairs of electrons between every pair of spatial orbitals, so half of the two-electron contributions are removed from the equation, exactly the ones necessary to correct the double counting. From this point, all the equations will be presented in terms of spatial orbitals, $\psi(r_i)$.

### 2.1.7 The Hartree-Fock Methodology

The Hartree-Fock (HF) methodology[176] is based on the so-called Fock operator, $\hat{f}_i$, which introduces an effective one-electron potential $\hat{V}_{eff}$ simulating the behaviour of the two-electron operator defined in (32). Hence, each electron feels an average field created by the other electrons and the nuclei. The HF method applied to closed-shell systems with the same spatial function for two different spins is called Restricted Hartree-Fock (RHF)

$$\hat{f}_i(r_i, R) = \hat{T}_e(r_i) + \hat{V}_{en}(r_i, R) + \hat{V}_{eff}(r_i) \tag{41}$$

The effective potential groups the coulomb, $\hat{J}_i$, and exchange, $\hat{K}_i$, one-electron operators

$$\hat{J}_i|\psi_j(r_j)\rangle = \langle\psi_i(r_i)|\hat{g}_{ij}|\psi_i(r_i)\rangle|\psi_j(r_j)\rangle \tag{42}$$

$$\hat{K}_i|\psi_j(r_j)\rangle = \langle\psi_i(r_i)|\hat{g}_{ij}|\psi_j(r_i)\rangle|\psi_i(r_j)\rangle \tag{43}$$

Therefore, the Fock operator for an electron $i$ is

$$\hat{f}_i = \hat{h}_i + \sum_{j=1}^{N/2}\left(2\hat{J}_j - \hat{K}_j\right) \tag{44}$$

which is normally written as

$$\hat{f}_i = \hat{h}_i + \hat{V}_i^{HF} \tag{45}$$

$$\hat{V}_i^{HF} = \sum_{j=1}^{N/2}\left(2\hat{J}_j - \hat{K}_j\right) \tag{46}$$

Using this Fock operator along with Lagrange multipliers under the orthonormality constraint, and considering the variational principle, a series of eigenvalue equations are generated, the so-called Hartree-Fock equations. The orthonormality constraint between the (spatial) orbitals is written as

$$\langle\psi_i|\psi_j\rangle - \delta_{ij} = 0 \tag{47}$$

where the first term is the overlap integral, $S_{ij}$. Taking as the Lagrange multipliers for this constraint the constants $\epsilon_{ij}$, the following functional of the orbitals must be optimized,

$$\mathcal{L}[\{\psi_i\}] = E[\{\psi_i\}] - 2\sum_{ij}^{N/2} \epsilon_{ij} \left(S_{ij} - \delta_{ij}\right) \tag{48}$$

where $E$ is the expectation value of the energy for the total wave function, as defined in equation (40).The variation of $\mathcal{L}$ with respect to the orbitals, which must be zero, is

$$\delta\mathcal{L} = \delta E[\{\psi_i\}] - 2\sum_{ij}^{N} \epsilon_{ij}\delta S_{ij} = 0 \tag{49}$$

Inserting now the definition of $E$

$$\delta\mathcal{L} = 2\sum_{i=1}^{N/2} \delta h_i + \sum_{i=i}^{N/2}\sum_{j=1}^{N/2} (2\delta J_{ij} - \delta K_{ij}) - 2\sum_{ij}^{N} \epsilon_{ij}\delta S_{ij} = 0 \tag{50}$$

where the variation of the overlap integral is

$$\delta S_{ij} = \langle\delta\psi_i|\psi_j\rangle + \langle\psi_i|\delta\psi_j\rangle \tag{51}$$

The variation of the other terms can be simplified due to the hermitian nature of the operators. For instance, the variation of the one-electron part of the energy is given by the expression

$$\delta h_i = \langle\delta\psi_i|\hat{h}_i|\psi_i\rangle + \langle\psi_i|\hat{h}_i|\delta\psi_i\rangle = \langle\delta\psi_i|\hat{h}_i|\psi_i\rangle + \langle\delta\psi_i|\hat{h}_i|\psi_i\rangle^* \tag{52}$$

where the last integral is the complex conjugate (c.g.) of the previous one.

Repeating the same procedure for the remaining terms of equation (50),

$$\delta J_{ij} = \langle\delta\psi_i\psi_j|\hat{g}_{ij}|\psi_i\psi_j\rangle + \langle\psi_i\delta\psi_j|\hat{g}_{ij}|\psi_i\psi_j\rangle + \text{ c.g.} \tag{53}$$

$$\delta K_{ij} = \langle\delta\psi_i\psi_j|\hat{g}_{ij}|\psi_j\psi_i\rangle + \langle\psi_i\delta\psi_j|\hat{g}_{ij}|\psi_j\psi_i\rangle + \text{c.g.} \tag{54}$$

and using the notation from equations (42) and (43), with the coulomb and exchange one-electron operators

$$\delta J_{ij} = \langle\delta\psi_i|\hat{J}_j|\psi_i\rangle + \langle\delta\psi_j|\hat{J}_i|\psi_j\rangle + \text{c.g.} \tag{55}$$

$$\delta K_{ij} = \langle\delta\psi_i|\hat{K}_j|\psi_i\rangle + \langle\delta\psi_j|\hat{K}_i|\psi_j\rangle + \text{c.g.} \tag{56}$$

Putting together all the previous equations

$$2\sum_{i=1}^{N/2}\langle\delta\psi_i| \left[\hat{h}_i|\psi_i\rangle + \sum_{j=1}^{N/2}\left(2\hat{J}_j - \hat{K}_j\right)|\psi_i\rangle - \sum_{j=1}^{N/2}\epsilon_{ij}|\psi_j\rangle\right] + \text{c.g.} = 0 \tag{57}$$

where all the complex conjugates have been grouped into the last term, along with the second term of equation (51), due to the hermitian nature of the operators and the relation $\epsilon_{ij}\langle\psi_i|\delta\psi_j\rangle = \epsilon_{ji}\langle\psi_j|\delta\psi_i\rangle = (\epsilon_{ij}\langle\delta\psi_i|\psi_j\rangle)^*$ (the complex conjugate for the variation of the overlap integral).

Since $\delta\psi_i^*$ is arbitrary, the quantity in square brackets must be zero to fulfill the equation (57),

$$\left(\hat{h}_i + \sum_{j=1}^{N/2}\left(2\hat{J}_j - \hat{K}_j\right)\right)|\psi_i\rangle - \sum_{j=1}^{N/2}\epsilon_{ij}|\psi_j\rangle = 0 \tag{58}$$

in which the term in parenthesis can be identified as the Fock operator (44), so the previous equation can be rearranged to

$$\hat{f}_i|\psi_i\rangle = \sum_{j=1}^{N/2}\epsilon_{ij}|\psi_j\rangle \tag{59}$$

which resembles an eigenvalue equation, but it is not. However, the orbitals from this equation can be changed by means of unitary transformations to achieve an eigenvalue equation, wherein the new set of $N/2$ orbitals $\{\psi_i'\}$ can be written as

$$\psi_i' = \sum_j \psi_j U_{ji} \tag{60}$$

being $U_{ji}$ the unitary transformation that converts $psi_j$ to $\psi_i'$. In matrix notation,

$$\psi' = \mathbf{U}\psi \tag{61}$$

where $\psi'$ and $\psi$ represent the column vectors of the new and the old set of orbitals, respectively, and $\mathbf{U}$ is the unitary transformation matrix of $N/2 \times N/2$ dimensions, which fulfills $\mathbf{U}\mathbf{U}^\dagger = \mathbf{U}^\dagger\mathbf{U} = \mathbf{1}$.

Using this notation, equation (59) transforms into

$$\hat{F}\psi = \mathbf{E}\psi \tag{62}$$

being $\mathbf{E}$ a non-diagonal $N/2 \times N/2$ matrix. Multiplying this equation by $\mathbf{U}$ from the left

$$\hat{F}\mathbf{U}\psi = \mathbf{U}\mathbf{E}\psi \tag{63}$$

inserting $\mathbf{U}^\dagger\mathbf{U}$ between $\mathbf{E}$ and $\psi$,

$$\hat{F}\mathbf{U}\psi = \mathbf{U}\mathbf{E}\mathbf{U}^\dagger\mathbf{U}\psi \tag{64}$$

and identifying $\mathbf{U}\psi$ as $\psi'$

$$\hat{F}\psi' = \mathbf{U}\mathbf{E}\mathbf{U}^\dagger\psi' \tag{65}$$

Since $\mathbf{E}$ is a Hermitian matrix, it can be diagonalized ($\mathbf{E}'$) using a unitary transformation matrix. Choosing $\mathbf{U}$ as this matrix, an eigenvalue equation is formed:

$$\hat{F}\psi' = \mathbf{E}'\psi' \tag{66}$$

The set of spatial orbitals $\{\psi_i'\}$ is called the set of canonical orbitals.

Dropping the primes from equation (66), the so-called Hartree-Fock equations (there are $N/2$ equations, $N$ considering spin-orbitals instead of spatial orbitals) are obtained

$$\hat{f}_i|\psi_i\rangle = \epsilon_i|\psi_i\rangle \tag{67}$$

To solve these equations, Roothaan proposed[191] a basis set representation . If the basis functions are centered on the atoms of the system, this approximation is called Linear Combination of Atomic Orbitals (LCAO),

$$\psi_i = \sum_{\mu=1}^{k} C_{\mu i}\chi_\mu \tag{68}$$

where $\chi_\mu$ are the atomic orbitals, which act as basis functions, $C_{\mu i}$ are their corresponding coefficients, and $k$ is the size of the basis set (the number of basis functions). Combining equations (67) and (68), and multiplying by $\chi_\nu^*$,

$$\sum_{\mu=1}^{k} C_{\mu i}\langle\chi_\nu(r_i)|\hat{f}_i|\chi_\mu(r_i)\rangle = \epsilon_i \sum_{\mu=1}^{k} C_{\mu i}\langle\chi_\nu(r_i)|\chi_\mu(r_i)\rangle \tag{69}$$

These equations are called the Roothaan-Hall equations,[192] which are normally written with the notation $F_{\nu\mu}$ for the integral at the left-hand side and $S_{\nu\mu}$ for the one at the right-hand side,[176]

$$\sum_{\mu=1}^{k} C_{\mu i}F_{\nu\mu} = \epsilon_i \sum_{\mu=1}^{k} C_{\mu i}S_{\nu\mu} \tag{70}$$

or in matrix notation, where $\mathbf{F}$ is the matrix containing all the $F_{\nu\mu}$ integrals, and $\mathbf{S}$ is the one formed by the $S_{\nu\mu}$ integrals. Both of them are $k \times k$ symmetric matrices

$$\mathbf{FC} = \mathbf{SC}\epsilon \tag{71}$$

If the basis set functions are orthonormalised, which is not the general case, the overlap matrix $\mathbf{S}$ is reduced to the identity matrix and equation (71) is transformed into an eigenvalue equation. Therefore, one of the first steps in the solution of the Roothaan-Hall equations is usually to find the transformation matrix that orthonormalises $\mathbf{S}$.

However, the solution, either with orthonormal basis functions or not, cannot be obtained as in a standard eigenvalue equation, since the Fock matrix, $\mathbf{F}$, depends on the coefficients of the orbitals and its diagonalization will lead to a new set of coefficients. The following determinant must be solved

$$\begin{vmatrix} F_{11}-\epsilon S_{11} & F_{12}-\epsilon S_{12} & \dots & F_{1k}-\epsilon S_{1k} \\ F_{21}-\epsilon S_{21} & F_{22}-\epsilon S_{22} & \dots & F_{2k}-\epsilon S_{2k} \\ \vdots & \vdots & \ddots & \vdots \\ F_{k1}-\epsilon S_{k1} & F_{k2}-\epsilon S_{k2} & \dots & F_{kk}-\epsilon S_{kk} \end{vmatrix} = 0 \tag{72}$$

all the $F_{\nu\mu}$ and $S_{\nu\mu}$ elements in the secular matrix can be computed explicitly, combining equations (44), (68), and (69), and expanding the $\phi_j$ orbitals. Each of these matrix elements is calculated according to the following equations,

$$\begin{aligned} F_{\nu\mu} =& \langle\chi_\nu|\hat{h}_i|\chi_\mu\rangle + \sum_{j=1}^{N/2}\langle\chi_\nu|\left(2\hat{J}_j - \hat{K}_j\right)|\chi_\mu\rangle \\ =& \langle\chi_\nu|\hat{h}_i|\chi_\mu\rangle + \sum_{j=1}^{N/2}\sum_{\lambda\sigma}^{k} P_{\lambda\sigma}\left(\langle\chi_\lambda\chi_\nu|\hat{g}_{ij}|\chi_\mu\chi_\sigma\rangle - \frac{1}{2}\langle\chi_\lambda\chi_\nu|\hat{g}_{ij}|\chi_\sigma\chi_\mu\rangle\right) \end{aligned} \tag{73}$$

$$S_{\nu\mu} = \langle\chi_\nu|\chi_\mu\rangle \tag{74}$$

The $P_{\lambda\sigma}$ elements act as a weight factor for the two-electron integrals and form the so-called density matrix $\mathbf{P}$. They are computed as

$$P_{\lambda\sigma} = 2\sum_{i=1}^{N/2} C_{\lambda i}C_{\sigma i} \tag{75}$$

being $C_{\mu i}$ the coefficient representing the contribution of the basis function $\chi_\mu$ to the MO $i$. In the first step of every HF calculation, a guess for the density matrix must be made.

Once the basis functions are orthonormalised, the solution of the secular equation (71) consists of diagonalizing the Fock matrix (transformed to the new orthonormal basis set)

$$\mathbf{F'C'} = \mathbf{C'}\epsilon \tag{76}$$

As solution, a set of $k$ energies, $\epsilon_i$, will be obtained as eigenvalues, which correspond to the energy of each MO of the system, along with their associated eigenvectors as sets of coefficients.

Then, the total electronic energy of the system can be calculated as the sum of energies for each occupied MO (77) multiplied by 2 due to the double occupancy. Although this energy must be corrected to account for the double counting of the electron-electron interactions, since the Fock operator for each electron (44) takes into account its interaction with all the other electrons, even if it has been already included. The total energy of the system will be the result of also adding the nuclei repulsion term. In terms of spatial orbitals,

$$E_{HF} = 2\sum_{i=1}^{N/2}\epsilon_i - \sum_{ij}^{N/2}(2J_{ij} - K_{ij}) \tag{77}$$

and in terms of spinorbitals

$$E_{HF} = \sum_{i=1}^{N}\epsilon_i - \frac{1}{2}\sum_{ij}^{N}(J_{ij} - K_{ij}) \tag{78}$$

After solving equation (76), the set of eigenvectors are used to build up the new density matrix. With the new $\mathbf{P}$, the Fock matrix must be computed again, leading to a new set of eigenvectors, and so on. This iterative procedure must be repeated until self-consistency is achieved.

If a different spatial orbital is considered for each electron (changing the number of occupied MOs from $N/2$ to $N$) the HF method is called Unrestricted Hartree-Fock (UHF). UHF is specially useful for open-shell molecules, where the number of $\alpha$ and $\beta$ electrons ($N^\alpha$ and $N^\beta$, respectively) differ. There will be now two different sets of spatial orbitals, one for the electrons with $\alpha$ spin, $\{\phi_i^\alpha\}$, and another one for the $\beta$ electrons, $\{\phi_i^\beta\}$

$$\begin{aligned} \hat{f}_i|\psi_i^\alpha\rangle|\alpha\rangle &= \epsilon_i^\alpha|\psi_i^\alpha\rangle|\alpha\rangle \\ \hat{f}_i|\psi_i^\beta\rangle|\beta\rangle &= \epsilon_i^\beta|\psi_i^\beta\rangle|\beta\rangle \end{aligned} \tag{79}$$

Multiplying the previous equations by $\langle\alpha|$ and $\langle\beta|$, respectively

$$\begin{aligned} \hat{f}_i^\alpha|\psi_i^\alpha\rangle &= \epsilon_i^\alpha|\psi_i^\alpha\rangle \\ \hat{f}_i^\beta|\psi_i^\beta\rangle &= \epsilon_i^\beta|\psi_i^\beta\rangle \end{aligned} \tag{80}$$

where $\hat{f}_i^\alpha = \langle\alpha|\hat{f}_i|\alpha\rangle$ is the operator used to obtain the kinetic energy, the electron-nuclei attraction, and the effective potential of an electron of $\alpha$ spin. The exchange integrals ($K_{ij}^{\alpha\beta}$) with $\beta$ electrons vanish. However, the coulomb integrals ($J_{ij}^{\alpha\beta}$) do not.

$$\begin{aligned} \hat{f}_i^\alpha &= \hat{h}_i + \sum_{j=1}^{N^\alpha}\left(\hat{J}_j^\alpha - \hat{K}_j^\alpha\right) + \sum_{j=1}^{N^\beta}\hat{J}_j^\beta \\ \hat{f}_i^\beta &= \hat{h}_i + \sum_{j=1}^{N^\beta}\left(\hat{J}_j^\beta - \hat{K}_j^\beta\right) + \sum_{j=1}^{N^\alpha}\hat{J}_j^\alpha \end{aligned} \tag{81}$$

The total unrestricted electronic energy, $E_{UHF}$, is the result of adding all the terms, correcting for the double-counting of the electron-electron interactions with a 1/2 factor,

$$\begin{aligned} E_{UHF} = &\sum_{i=1}^{N^\alpha}\hat{h}_i^\alpha + \sum_{i=1}^{N^\beta}\hat{h}_i^\beta + \frac{1}{2}\sum_{i=1}^{N^\alpha}\sum_{j=1}^{N^\alpha}\left(J_{ij}^{\alpha\alpha} - K_{ij}^{\alpha\alpha}\right) \\ &+\frac{1}{2}\sum_{i=1}^{N^\beta}\sum_{j=1}^{N^\beta}\left(J_{ij}^{\beta\beta} - K_{ij}^{\beta\beta}\right) + \sum_{i=1}^{N^\alpha}\sum_{j=1}^{N^\beta}J_{ij}^{\alpha\beta} \end{aligned} \tag{82}$$

wherein there is no double counting in the last term, since $J_{ij}^{\alpha\beta} \neq J_{ji}^{\alpha\beta}$, and there is not self-interaction either ($J_{ii}^{\alpha\alpha} = K_{ii}^{\alpha\alpha}$).

The same applies for the Roothaan-Hall equations in the UHF case. There will be two matrix equations, one for the $\alpha$ electrons and another one for the $\beta$

electrons

$$\begin{aligned} \mathbf{F}^{\alpha}\mathbf{C}^{\alpha} &= \mathbf{S}\mathbf{C}^{\alpha}\epsilon^{\alpha} \\ \mathbf{F}^{\beta}\mathbf{C}^{\beta} &= \mathbf{S}\mathbf{C}^{\beta}\epsilon^{\beta} \end{aligned} \tag{83}$$

### 2.1.8 Correlation Energy

HF energies, $E_{HF}$, are usually quite good (around 99% of the exact energy in the basis set limit),[173] but the results are still above the exact energies $E_{exact}$ (always above because of the variational theorem used in the derivation of the HF equations) due to the lack of correlation energy $E_{corr}$, which is defined as[176]

$$E_{corr} = E_{exact} - E_{HF} \tag{84}$$

There are two kinds of correlation effects (two contributions to the correlation energy, the part of the energy that Hartree-Fock methodology does not include), static and dynamic.

- The lack of static correlation comes from the error introduced for considering only one electronic configuration, since only one Slater determinant is used for the construction of the wave function, as seen in equation (27), regardless if there are other configurations necessary to describe the state of the system.
- The dynamic correlation refers to the correlated movement of the electrons, which is simplified at the moment of introducing the concept of average field, $V_{eff}$. Only the correlation between electrons with parallel spin is considered in Hartree-Fock, since they cannot be found in the same point of space due to the mathematical properties of the Slater determinant.

The order of magnitude of the correlation energy is comparable with the differences in energy in chemical problems, thus, it must be taken into account for a proper description of the system.[193]

Some *post* HF methods (e.g. MP2, CISD, CCSD...) include correlation energy using different strategies, but their computational cost is large for big systems. They are all based on the wave function, which depends on $4N$ coordinates (spin and the 3 spatial coordinates of each electron). Some of these methods will be covered in section 2.3.

## 2.2 Basis Sets

As already seen in section 2.1.7, the spinorbitals (or the spatial orbitals) that form the wave function of the system are normally expanded in terms of basis functions, in the so-called LCAO. In this section, a range of possible mathematical representations for these basis functions will be presented.

### 2.2.1 Slater and Gaussian Type Orbitals

The most common basis functions (AOs) are Slater and Gaussian Type Orbitals (STO and GTO, respectively), which are centered on the atoms.

The STOs,[194] defined in equation (85), have an exponential dependence on the distance between the electrons and the atomic nuclei ($r$), which mirrors the exact orbitals from the solution of the hydrogen atom. To introduce nodes in the radial part, STOs are put together in linear combinations. The major problem of STOs is that the calculation of two-electron integrals with three and four centers cannot be performed analytically

$$\chi^{STO}_{\zeta,n,l,m}(r,\theta,\varphi) = NY_{l,m}(\theta,\varphi)r^{n-1}e^{-\zeta r} \tag{85}$$

where $\zeta$ is an exponent that is chosen according to a set of rules that depend on the atomic number, $N$ is a normalization constant, $n$ is the principal quantum number, and $Y_{l,m}(\theta,\varphi)$ is the spherical harmonic function, which depends on the angular quantum numbers $l$ and $m$.

Therefore, the only practical use for STOs is in mono- and diatomic systems and in semi-empirical methods, where the two-electron integrals with three our four centers are neglected.

On the other hand, GTOs do not present this problem, since the dependence on the electron-nuclei distance is $r^2$ instead of $r$, allowing the analytical solution of all the integrals.[195] However, this change creates some disadvantages of GTOs over STOs: GTOs don't represent well the behaviour near the nuclei (absence of cusps that are present with STOs), and the stronger dependence on $r$ makes GTOs to fall off too rapidly when the distance is large. The sum of $l_x$, $l_y$ and $l_z$ determines the type of orbital (0 in an $s$-orbital, 1 a $p$-orbital,...).

$$\chi^{GTO}_{\zeta,n,l,m}(r,\theta,\varphi) = NY_{l,m}(\theta,\varphi)r^{2n-2-l}e^{-\zeta r^2} \tag{86}$$

$$\chi^{GTO}_{\zeta,n,l,m}(x,y,z) = Nx^{l_x}y^{l_y}z^{l_z}e^{-\zeta r^2} \tag{87}$$

The intrinsic problems of GTOs can be attenuated making linear combinations of $L$ GTOs, which are named Primitive GTOs (PGTOs), to mimic STOs, forming the so-called Contracted GTOs (CGTOs)

$$\chi^{CGTO}(r,\theta,\varphi) = \sum_{p=1}^{L} d_p \chi^{PGTO}_p(r,\theta,\varphi) \tag{88}$$

The total number of CGTOs and PGTOs employed in their expansions depends on the balance between accuracy and computational cost

The so-called minimal basis sets only include one CGTO for each Atomic Orbital (AO). For example, carbon atom has the electron configuration $1s^2 2s^2 2p^2$, so there will be 5 CGTOs with a minimal basis set, corresponding to the $1s$, $2s$, $2p_x$, $2p_y$, and $2p_z$ AOs. An option to get more flexible basis sets is to increase the number of CGTOs per AO. These basis sets are represented with notation $XZ$, being $X$ (D, T, Q ...) the number of CGTOs, each one 'mimics' a STO

with a different $\zeta$ exponent, to describe an orbital. To lower the computational cost, 'split-valence' basis sets differentiate between the core and the valence orbitals. Each core orbital is described with minimal basis sets, whereas the valence orbitals are formed by linear combination of CGTOs.

To improve the description of the system, some polarization functions can be added, these functions correspond to unoccupied orbitals with higher angular momentum than the occupied AOs (i.e. $p$ functions are added to the $s$ orbitals, $d$ to the $p\ldots$). This addition allows more flexibility on the atomic charge distribution, specially useful when describing bonds, where the electron density is usually polarized.

Other improvement consists of adding diffuse functions, which are functions with the same angular momentum as the valence AOs but with a lower exponent ($\zeta$). They help to describe molecules with weakly-bonded electrons, where the MOs tend to be more diffuse. This is particularly crucial when studying anions, excited states, or atoms with lone pairs.

### 2.2.2 Pople Basis Sets

Pople *et al.*[196] were the first ones in optimizing the coefficients and exponents for reproducing STOs using CGTOs. The result are the famous Pople minimal basis sets, which are denoted as STO-$n$G, where $n$ is the number of PGTOs used in the expansion of each CGTO (typically between 2 and 6) to simulate a STO. For example, with STO-3G, there are 3 PTGOs for each AO (CGTO), this minimal basis set gives the best combination of computational cost and accuracy of the STO-$n$G family.

Nevertheless, the most popular basis sets from Pople *et al.* are their split-valence basis sets,[196–198] which use the notation $c-v_1v_2\ldots v_NG(p_1,p_2)$, being $c$ the number of PGTOs in the contraction of each core AO (only one contraction per core AO), $N$ the number of CGTOs included in each valence orbital, $v_i$ the number of PGTOs forming each of these CGTOs, $p_1$ and $p_2$ the polarization functions (if present) for the heavy and hydrogen atoms, respectively. The inclusion of diffuse functions in this type of basis sets[199] is indicated by adding before the '$G$' the notation '+' for the presence of diffuse $s$ and $p$ functions with lower exponents on heavy atoms (non-hydrogen atoms), and '++' for indicating that diffuse $s$-functions are also added to hydrogen atoms.

The exponents and coefficients for the contracted functions were determined using the variational principle, optimizing them to yield the minimum possible HF energy over a set of molecules and atoms. The contraction scheme employed in the Pople basis sets is called 'segmented', because the primitives used in each CGTO are unique (i.e., they are not used in more than one expansion).[178]

### 2.2.3 Correlation-consistent basis sets

Dunning[200] has proposed another popular family of basis sets, specifically designed for *post* Hartree-Fock calculations. They are called correlation-consistent (cc) basis sets. The name comes from the fact that the functions with similar

contributions to the correlation energy are included at the same stage. They all present polarization functions and use the following notation: cc-pVXZ (correlation consistent polarized valence X zeta), where X is D (double), T (triple), Q (quadruple) .... If there is interest in recovering the correlation from the core, and not only from the valence electrons as in cc-pVXZ, the cc-pCVXZ basis sets are able to do that (C stands for core).

As the Pople basis sets, the coefficients and exponents were obtained variationally but, in this case, they also employed calculations including the electron correlation. The contraction scheme differs from the one used by Pople. It is called 'general' contraction, because the PGTOs are shared in all the expansions, appearing with different coefficients in each CGTO. This allows a more efficient calculation of the integrals involving the same primitives, specially important in the computationally demanding *post* Hartree-Fock calculations.

The addition of diffuse functions to the cc-pVXZ basis sets is indicated by the 'aug' prefix (aug-cc-pVXZ). It includes diffuse functions for all the angular momentum ($s$, $p$, $d$, $f$ on heavy atoms, and $s$, $p$, $d$ on hydrogen atoms).

Another important feature of this family of basis sets is the extrapolation to the complete basis set (CBS) limit. Unlike the Pople basis sets, the cc-pVXZ basis sets are specifically designed for this purpose. The procedure consists of carrying out calculations with increasing number of CGTOs, like cc-pVDZ, cc-pVTZ, cc-pVQZ,... and then, extrapolate the result to the one that would be obtained with an infinite basis set, hence removing the error associated with the LCAO approximation.

### 2.2.4 Pseudopotentials

Heavy atoms (third row or higher of the periodic table) have a large number of core electrons that do not participate in breaking or forming bonds, but make computations very demanding, both in time and storage capacity, since it's necessary to include them anyway in the expansion of the orbitals to have a good description of the electron–electron repulsion.

One solution for considering core electrons with little computational cost comes from representing all these electrons with an Effective Core Potential (ECP), also called pseudopotential, modelling the core electrons with a suitable function, whereas the treatment of the valence electrons remains explicit.[201,202] In addition to the computational benefits of removing a huge amount of basis functions, some relativistic effects, present in heavy transition metal atoms, can be included through ECPs.

In an ECP basis set, the valence orbitals from an all-electron wave function are replaced by a set of *pseudo*-orbitals, which are designed to be smooth and nodeless in the core region, and the coulomb and exchange contributions of the core electrons are replaced by a potential $U_{ECP}(r)$.[173] This potential is typically constructed on a grid using the numerical HF procedure and fitted to a suitable set of analytical functions, with parameters $a_i$, $n_i$, $\alpha_i$ that depend on

the angular momentum

$$U_{ECP}(r) = \sum_i a_i r^{n_i} r^{-\alpha_i r^2} \tag{89}$$

Some of the most popular pseudopotentials have been developed by Los Alamos' group, such as LANL2DZ,[203] mostly used for transition metals, and LANL2TZ+*f*,[204] which contains polarization functions.

### 2.2.5 Karlsruhe Basis Sets

The Karlsruhe basis sets, developed by Ahlrichs and coworkers,[205] are called 'def2' basis sets, because is the second generation of default basis sets in the Turbomole program.[206] They are designed to be used in connection with ECPs in atoms from Rb to Rn, which reduces the required basis set size and accounts for scalar relativistic effects.

These basis sets have a 'segmented' contraction scheme, whose exponents and coefficients are minimized with respect to HF energies, although with some variations due to the presence of ECPs.

Their notation starts with the 'def2' prefix, followed by 'SV', if they are split-valence, or 'TZV/QZV' for valence triple/quadruple-zeta. Then, they indicate the presence of one set ('P') or two sets ('PP') of polarization functions. If they also add diffuse functions it is indicated by 'D' afterwards. For example, the basis set def2-QZVPPD is a valence quadruple-zeta with two sets of polarization functions and diffuse functions.

## 2.3 *post* Hartree-Fock Methods

### 2.3.1 Configuration Interaction

Configuration Interaction (CI)[207] is a method based on the ground state Slater determinant. From it, a series of Slater determinants associated with excited states are constructed, where some of the virtual orbitals are now occupied, and the wave function is expressed as a linear combination of them. The number of determinants $M$ that can be obtained from a certain reference determinant depends on the number of electrons $N$ and MOs $K$ (occupied and virtual)

$$M = \binom{K}{N} = \frac{K!}{N!(K-N)!} \tag{90}$$

These $M$ determinants correspond to different electronic configurations, which are the result of exciting a given number of electrons from occupied $(i, j, \ldots)$ to virtual $(a, b, \ldots)$ orbitals. Note, however, that some configurations are not defined by a single determinant but by a linear combination of determinants.

The so-called Full CI (FCI) wave function is the result of the combination of all the possible determinants, which are grouped according to the number of electrons that populate the (previous) virtual orbitals. This wave function, $\Psi^{FCI}$, with an infinite basis set, gives the exact solution for the non-relativistic

time-independent Schrödinger equation, within the BO approximation. Hence, $\Psi_{FCI}$ includes all the possible configuration state functions of the system

$$\Psi^{FCI} = c_0\Psi_0 + \sum_{i<a} c_i^a \Psi_i^a + \sum_{\substack{i<a \\ a<b}} c_{ij}^{ab}\Psi_{ij}^{ab} + \dots \tag{91}$$

The first term in the previous equation corresponds to the HF reference wave function, which is taken as the starting point to construct all the wave functions with single-excitations ($\Psi_i^a$), double-excitations ($\Psi_{ij}^{ab}$) and so on until the determinant where all the electrons have been excited is reached. Each of them has an expansion coefficient, $c$, that can be calculated through the diagonalization of the Hamiltonian matrix, obtaining a set of $M$ roots with their associated sets of coefficients.

As previously stated, this method is exact, but its computational cost for molecules of more than few atoms is unaffordable. In practice, an infinite basis set can not be employed either, although the FCI calculation would still give us the best possible solution for the Schrödinger equation for that choice of basis set. On top of that, even with basis sets of moderate size, the number of basis functions in a FCI calculation is too large for the majority of systems. As a consequence, the number of configuration state functions must be truncated.

In order to choose where to truncate the expansion at equation (91), the Slater-Condon rules[190,208] are useful for evaluating the Hamiltonian terms involving determinants with different levels of excitation, (equations (93) and (94)), where $\phi_i$ are the MOs, which are already eigenfunctions of the Fock operator, $\hat{f}_i$. For instance, since the determinants are formed by the product of orthonormal MOs, all the integrals from $\langle\Psi_0|\hat{F}|\Psi_i^a\rangle$ are zero, since $\phi_i \neq \phi_a$. This result is called Brillouin's theorem, which states that all the matrix elements of the Hamiltonian involving the HF reference wave function and a single excited determinant are zero: $\langle\Psi_0|\hat{H}|\Psi_i^a\rangle = 0$. This theorem does not apply to matrix elements without $\Psi_0$. Also note that all the integrals with determinants differing by 3 or more orbitals vanish

$$\langle\Psi_0|\hat{H}|\Psi_0\rangle = \sum_{i=1}^{N}\langle\phi_i|\hat{f}|\phi_i\rangle \tag{92}$$

$$\langle\Psi_0|\hat{H}|\Psi_i^a\rangle = \langle\phi_i|\hat{h}|\phi_a\rangle + \sum_{j=1}^{N}\langle\phi_i\phi_j|\hat{g}|\phi_a\phi_j\rangle = \langle\phi_i|\hat{f}|\phi_a\rangle = \epsilon_a\delta_{ia} \tag{93}$$

$$\langle\Psi_0|\hat{H}|\Psi_{ij}^{ab}\rangle = \langle\phi_i\phi_j|\hat{g}|\phi_a\phi_b\rangle \tag{94}$$

$$\langle\Psi_0|\hat{H}|\Psi_{ijk}^{abc}\rangle = 0 \tag{95}$$

Using a simplified notation, with $S$ for a single-excited determinant, $D$ for a doubly-excited, and $H_{AB}$ for $\langle A|\hat{H}|B\rangle$, the FCI matrix is shown below (only one determinant for each level of excitation is depicted)

$$\Psi^{FCI} = c_0|0\rangle + \sum_{i,a} c_i^a|S\rangle + \sum_{ij,ab} c_{ij}^{ab}|D\rangle + \dots \tag{96}$$

$$\mathbf{H} = \begin{pmatrix} H_{00} & H_{0S} & H_{0D} & \dots \\ H_{S0} & H_{SS} & H_{SD} & \dots \\ H_{D0} & H_{DS} & H_{DD} & \dots \\ \vdots & \vdots & \vdots & \ddots \end{pmatrix} = \begin{pmatrix} E_0 & 0 & H_{0D} & 0 \\ 0 & H_{SS} & H_{SD} & \dots \\ H_{D0} & H_{DS} & H_{DD} & \dots \\ 0 & \vdots & \vdots & \ddots \end{pmatrix} \tag{97}$$

Therefore, if the CI matrix is truncated at the single excitations, **H** is a block diagonal matrix. Diagonalization of the block corresponding to the ground state wave function would yield again the HF energy, $E_0$.[178] Consequently, the CI matrix must be truncated, at least, at the double electronic excitations. The CI method where the excitations are truncated at the doubles is known as CISD. It is worth noting that, although the single excited configurations do not interact with the ground state, they do interact with the double excited determinants and, hence, they can slightly influence on the lowest root of the CI matrix and, specially, they can be important in the calculation of other properties, such as the charge distribution. On the other hand, the inclusion of triple excitations is not generally worthy since, normally, this would add too many determinants to the matrix and their contributions to the lowest eigenvalue are very sparse. These are the reasons why the CISD method is the most popular truncation of FCI.

One of the main advantages of CISD is that it is variational, each of the energies obtained through the diagonalization of the CISD matrix represents an upper bound to the corresponding exact energy (of the ground state or some excited state). However, this method has some serious drawbacks, specially its computational cost, with a scaling of $M^6$ ($M$ now refers to the number of basis functions), is much worse than HF and prevents its use in very large systems. In addition, a problem of all the truncated CI methods is the consistency. The energy of two fragments separated by an infinite distance should be equal to the addition of the energies of each fragment, but this is not fulfilled when using CISD[176]

$$E_A + E_B \neq E_{AB}(r \to \infty) \tag{98}$$

There are some variations to the CISD method that correct this size consistency problem, such as spin-flip CISD (SF-CISD).[209] Nevertheless, its computational cost is still at the same order as CISD.

Other method related to CI is known as Multireference CI (MRCI). This method uses a multi-determinant wave function as reference to improve the calculation of energies corresponding to excited states and the inclusion of non-dynamic correlation.

### 2.3.2 Perturbation Theory

The aim of Perturbation Theory (PT) is to solve a problem that slightly differs from a problem that can be solved exactly, through a correction term to the latter. In this sense, the part without analytical solution is called perturbation, and must be small compared to the other one. Hence, using the eigenvectors and eigenvalues of the operator from the original problem, it is possible to obtain

corrected eigenvectors and eigenvalues for the operator of the more complicated problem.

The Rayleigh-Schrödinger Perturbation Theory (RS-PT)[210] applies the PT to solve the Schrödinger equation. The Hamiltonian is thus split into two terms, one operator with an exact solution, $\hat{H}^{(0)}$, for which the eigenvalue $E_0$ and eigenfunction $\Psi_0$ are obtained (the subscript 0 refers to the lowest eigenvalue of $H_0$), and the perturbation operator, $\hat{V}$, without analytical solution

$$\hat{H} = \hat{H}^{(0)} + \lambda\hat{V} \tag{99}$$

In the previous equation, a parameter $\lambda$ has been introduced. This is a dimensionless parameter, with values from 0 to 1, that determines the weight of the perturbation into the total operator. For instance, if $\lambda = 0$, there is no perturbation and the original problem is recovered.

When $\lambda \neq 0$, the Hamiltonian operator presents a perturbation and the expressions for the new eigenvalue and eigenfunction will depend on this parameter. These equations can be obtained from a Taylor expansion to the original $\Psi_0$ and $E_0$

$$E_0 = E_0^{(0)} + \lambda\left(\frac{\partial E_0^{(0)}}{\partial\lambda}\right)_{\lambda=0} + \frac{1}{2!}\lambda^2\left(\frac{\partial^2 E_0^{(0)}}{\partial\lambda^2}\right)_{\lambda=0} + \ldots \tag{100}$$

$$\Psi_0 = \Psi_0^{(0)} + \lambda\left(\frac{\partial \Psi_0^{(0)}}{\partial\lambda}\right)_{\lambda=0} + \frac{1}{2!}\lambda^2\left(\frac{\partial^2 \Psi_0^{(0)}}{\partial\lambda^2}\right)_{\lambda=0} + \ldots \tag{101}$$

The superscript (0) indicates that $E_0^{(0)}$ and $\Psi_0^{(0)}$ are the original (without perturbation) eigenvalue and eigenfunction of the ground state. These equations are usually presented as

$$E_0 = E_0^{(0)} + \lambda E_0^{(1)} + \lambda^2 E_0^{(2)} + \ldots \tag{102}$$

$$\Psi_0 = \Psi_0^{(0)} + \lambda\Psi_0^{(1)} + \lambda^2\Psi_0^{(2)} + \ldots \tag{103}$$

where the superscripts $(1), (2), \ldots$ refer to the perturbative correctionn of order $1, 2, \ldots$ to either $E_0^{(0)}$ or $\Psi_0^{(0)}$.

Inserting these equations into the Schrödinger equation

$$\left(\hat{H}^{(0)} + \lambda\hat{V}\right)|\Psi_0^{(0)} + \lambda\Psi_0^{(1)} + \lambda^2\Psi_0^{(2)} + \ldots\rangle = \left(E_0^{(0)} + \lambda E_0^{(1)} + \lambda^2 E_0^{(2)} + \ldots\right)|\Psi_0^{(0)} + \lambda\Psi_0^{(1)} + \lambda^2\Psi_0^{(2)} + \ldots\rangle \tag{104}$$

It is possible to group the resulting terms according to the power of $\lambda$. For instance, if the truncation is made at the second order of perturbation, three

equations can be obtained:

$$\hat{H}^{(0)}\Psi_0^{(0)} = E_0^{(0)}\Psi_0^{(0)} \tag{105}$$

$$\hat{H}^{(0)}\Psi_0^{(1)} + \hat{V}\Psi_0^{(0)} = E_0^{(0)}\Psi_0^{(1)} + E_0^{(1)}\Psi_0^{(0)} \tag{106}$$

$$\hat{H}^{(0)}\Psi_0^{(2)} + \hat{V}\Psi_0^{(1)} = E_0^{(0)}\Psi_0^{(2)} + E_0^{(1)}\Psi_0^{(1)} + E_0^{(2)}\Psi_0^{(0)} \tag{107}$$

To solve these equations and thus determine the first and second order corrections, intermediate normalization to $\Psi$ is a good start,

$$\langle\Psi_0|\Psi_0^{(0)}\rangle = 1 \tag{108}$$

consequently, the overlap integrals between $\Psi_0^{(n)}$ of different $n$ are zero. The equations (105), (106), and (107) are multiplied by $\langle\Psi_0^{(0)}|$ and, then, integrated. When this step is applied to equation (106), the first order correction to the energy is obtained

$$E_0^{(1)} = \langle\Psi_0^{(0)}|\hat{V}|\Psi_0^{(0)}\rangle \tag{109}$$

Analogously, the second correction to the energy, obtained from equation (107), is

$$E_0^{(2)} = \langle\Psi_0^{(0)}|\hat{V}|\Psi_0^{(1)}\rangle \tag{110}$$

hence, extrapolating to the $nth$ correction to the energy

$$E_0^{(n)} = \langle\Psi_0^{(0)}|\hat{V}|\Psi_0^{(n-1)}\rangle \tag{111}$$

Therefore, in order to know the correction of order $n$ to the energy, the correction of order $n-1$ to the wave function is needed. This is achieved through a linear expansion of $\Psi_0^{(n)}$ in terms of the complete set of eigenfunctions of $\hat{H}_0$, which is a hermitian operator,

$$\Psi_0^{(n)} = \sum_k C_{0,k}^{(n)}\Psi_k^{(0)} \tag{112}$$

where the coefficients are:

$$C_{0,k}^{(n)} = \langle\Psi_k^{(0)}|\Psi_0^{(n)}\rangle \tag{113}$$

Hence, the coefficients for $\Psi_0^{(1)}$ can be determined multiplying equation (106) by $\langle\Psi_k^{(0)}|$ and integrating,

$$\left(E_0^{(0)} - E_k^{(0)}\right)\langle\Psi_k^{(0)}|\Psi_0^{(1)}\rangle = \langle\Psi_k^{(0)}|\hat{V}|\Psi_0^{(0)}\rangle \tag{114}$$

substituting $\Psi_0^{(1)}$ by equation (112), and taking into account the orthonormality between $\Psi_k^{(0)}$ and $\Psi_0^{(0)}$

$$C_{0,k}^{(1)} = \frac{\langle\Psi_k^{(0)}|\hat{V}|\Psi_0^{(0)}\rangle}{E_0^{(0)} - E_k^{(0)}} \tag{115}$$

The equations for the coefficients of the corrections of higher orders are computed following the same procedure, although their expressions are increasingly more complicated.

So far, expressions for the corrected eigenvalues and eigenfunctions of the Hamiltonian with a perturbation have been presented. However, when applying this method, a prescription for the original Hamiltonian $\hat{H}^{(0)}$ and its perturbation $\hat{V}$ is needed. The Møller-Plesset PT (MPPT) provides these prescriptions.[211] It applies the RS-PT to the HF method, defining the original Hamiltonian as the sum of monoelectornic Fock operators, and the perturbation as the difference between the exact Hamiltonian $\hat{H}$ and $\hat{H}^{(0)}$. Recall from equation (77) that the sum of the monoelectronic Fock operators does not give the Hartree-Fock energy of the system, but an energy that must be corrected with a term for the double counting of the electron-electron interactions (78).

$$\hat{H}^{(0)} = \sum_{i=1}^{N} \hat{f}_i \tag{116}$$

Therefore, the non-perturbated wave function, $\Psi^{(0)}$, is the wave function obtained from the HF calculation, a Slater determinant of the occupied orbitals, and the zero-order energy, $E_0^{(0)}$, is the sum of energies of these orbitals.

The perturbation $\hat{V}$ is then the difference between the real electron-electron interactions and the sum of effective potentials $\hat{V}_i^{HF}$ for all the electrons

$$\hat{V} = \sum_{i=1}^{N} \sum_{j>i}^{N} \frac{1}{r_{ij}} - \sum_{i=1}^{N} \hat{V}_i^{HF} \tag{117}$$

Hence, the first-order correction to the energy, $E_0^{(1)}$, defined in equation (109) and evaluated with the HF wave function, is just the negative of the electron - electron interaction energy. Indeed, this is the correction term to account for the double counting of the electron-electron interactions in HF. As a consequence, the energy resulting from adding $E_0^{(1)}$ to the zero-order energy, usually denoted as MP1, is the Hartree-Fock energy of the system (78). Therefore, MP1 does not provide an advantage over HF.

To obtain the first correction to the HF energy, the second-order correction, $E_0^{(2)}$, must be included. This method is called MP2,[212] the most popular one from MPPT because it provides a good estimation of the correlation energy at a moderately low computational cost.

To get $E_0^{(2)}$, $\Psi^{(1)}$ must be known, but the expansion from equation (112) runs over all the eigenfunctions of the Hamiltonian, which implies that all the excited states from the system must be considered. However, bringing back again the Slater-Condon rules, the integral at the numerator of equation (115) is only different from zero when $\Psi_k^{(0)}$ corresponds to a doubly excited determinant. So getting $E_0^{(2)}$ is not too computationally demanding, as it can be obtained from evaluating the bielectronic integrals with the newly occupied virtual orbitals,

as in equation (94), and the difference in energy between the excited and the ground state wave functions can be evaluated as the difference in energy between the previously occupied orbitals $\epsilon_i, \epsilon_j$ and the virtual orbitals with promoted electrons, $\epsilon_a, \epsilon_b$.

The scaling of MP2 is approximately $M^5$, although in practice, since only the bielectronic integrals involving two virtual and two occupied MOs have to be evaluated, the second order correction to the energy can be computed at a computational cost similar to a HF calculation. In addition, MP2 accounts for a large percentage of the correlation energy and it is size-consistent. The main disadvantage of MPn methods is assuming that the HF wave function is a good reference state. If it is not a good description of the system, the perturbation would be too large and convergence problems may arise. On top of that, these methods are not variational. This means that the inclusion of correlation energy may be overestimated, ending with an energy lower than $E_{exact}$.

### 2.3.3 Coupled-cluster Theory

The Coupled-Cluster theory (CC)[213] fixes the consistency and separability (size consistency) problems of the truncated CI methods by building the wave function as an exponential *ansatz*. Similarly to the CI method, it is based on taking the HF wave function, $\Psi_0$, as starting point

$$\Psi^{FCI} = \hat{\Omega}^{FCI}\Psi_0 \tag{118}$$

$$\Psi^{CC} = \hat{\Omega}^{CC}\Psi_0 \tag{119}$$

In FCI, the operator $\hat{\Omega}^{FCI}$, which acts on the reference wave function, $\Psi_0$, would be the one that generates all the excited configurations as in equation (91). The only difference between this operator and the one used in CC, $\hat{\Omega}^{CC}$, is that the former is linear whereas the latter is exponential

$$\hat{\Omega}^{CC} = e^{\hat{T}} \tag{120}$$

$$\hat{T} = \hat{T}_1 + \hat{T}_2 + \hat{T}_3 + \dots \tag{121}$$

The operator $\hat{T}_n$ introduces $n$ excitations into the reference determinant. Thus $\hat{T}$ generates all the possible excitations. If the operator $\hat{T}$ is not truncated, the CC and FCI methods are equivalent, giving both of them the exact solution to the time-independent Schrödinger equation if an infinite basis set is used. This operator can be written, in the second-quantization notation, as

$$\hat{T}_1 = \sum_{i,a}^{N} t_i^a \hat{a}_i \hat{a}_a^\dagger \tag{122}$$

$$\hat{T}_2 = \frac{1}{4}\sum_{ij,ab}^{N} t_{ij}^{ab} \hat{a}_i \hat{a}_j \hat{a}_a^\dagger \hat{a}_b^\dagger \tag{123}$$

where $\hat{a}_i$ are the annhilitation operators, which remove an electron from the orbital $i$, and the adjoints, $\hat{a}_a^\dagger$, are the creation operators, which promote an electron to the orbital $a$. The expansion coefficients $t$ are called cluster amplitudes.

The CC operator $\hat{\Omega}^{CC}$ can be written as a Taylor expansion

$$e^{\hat{T}} = \sum_{k=0}^{\infty} \frac{1}{k!} \hat{T}^k \tag{124}$$

$$\hat{\Omega}^{CC} = 1 + \left(\hat{T}_1\right) + \left(\frac{1}{2}\hat{T}_1^2 + \hat{T}_2\right) + \left(\frac{1}{6}\hat{T}_1^3 + \hat{T}_2\hat{T}_1 + \hat{T}_3\right) + \dots \tag{125}$$

where the terms have been arranged in brackets according to the order of excitation that they induce. The first term leaves the HF reference wave function as it was, the second generates all the single excited determinants, the third all the doubly excited determinants, distinguishing between connected ($\hat{T}_2$) and disconnected ($\hat{T}_1^2$) excitations. The next ones are the triple excitations, again both connected ($\hat{T}_3$) and disconnected ($\hat{T}_2\hat{T}_1$, $\hat{T}_1^3$), and so on.

CC energy is calculated as $\langle\Psi_0|\hat{H}\hat{\Omega}^{CC}|\Psi_0\rangle$. Taking into account again the Slater-Condon rules, only the first and the bielectronic excitation terms of equation (125) will result in integrals different from zero. Therefore, the CC ground state energy only depends on the singles (because of the disconnected double excitations) and doubles amplitudes, in addition to the two-electron integrals associated and the HF energy $E_0$

$$E_0^{CC} = E_0 + \sum_{i<j}\sum_{a<b} \left(t_{ij}^{ab} + t_i^a t_j^b - t_i^b t_j^a\right) \langle\phi_i\phi_j|\hat{g}|\phi_a\phi_b\rangle \tag{126}$$

Nevertheless, CC energy does depend on higher order excitations in the sense that the calculation of singles and doubles amplitudes involves them. Consequently, the CC calculation becomes too computationally demanding even for small systems and the number of cluster operators included in $\hat{T}$ must be truncated. As for previous methods, the inclusion of $\hat{T}_1$ does not improve the HF energy. Therefore, the lowest truncation that takes into account part of correlation energy must include $\hat{T}_2$, either with or without $\hat{T}_1$ (CCSD and CCD, respectively).

The CCSD method is the most popular truncated CC method. Its computational cost is comparable to that of CCD but gives better results, although both of them scale as $M^6$, being $M$ the number of basis functions. The computational cost is even larger if the truncation is made at $\hat{T}_3$ (CCSDT), with $M^8$ scaling. An alternative for taking into account the triples contribution to the energy at a lower computational cost is to evaluate this contribution with perturbation theory, through the formula given by MP4,[214] but using the CCSD cluster amplitudes for the corrections to the wave function. This hybrid method, known as CCSD(T), is normally taken as reference for calculations of the ground state energy of systems with moderate size. It scales as $M^7$.

Despite the many advantages of the CCSD and CCSD(T) methods, including size-consistency, its computational cost is still too demanding for many applications, specially compared to the DFT methods that will be covered in the next section. In recent years, a lot of effort has been put in order to develop accurate approximations to these methods, with the ultimate goal of achieving a cost similar to the initial HF calculation.

The methods known as DLPNO-CCSD and DLPNO-CCSD(T) provide efficient and accurate calculations for large systems.[215,216] They use the concept of PNOs, which refers to Pair Natural Orbitals. It has been proved that the use of Natural Orbitals (section 2.11.3) ordered according to their occupation numbers can speed up the calculations.[217] The idea of PNO is to benefit from this by providing separate sets of NOs for each electron pair of the system. This concept is combined with local correlation ideas (LPNO), which assume that the electron correlation is mainly local, permitting a truncation of PNOs.[218] DLPNO (Domain-based Local Pair Natural Orbital) takes these concepts and expand the PNOs into local correlation domains to speed up the CCSD and CCSD(T) calculations without sacrificing much accuracy.

### 2.3.4 Resolution of Identity

In all the quantum chemical methods above described, the calculation of two-electron integrals is a mandatory step. Even using GTOs, this step involves a large computational cost, which is normally reduced with the use of some algorithms, such as the Resolution of the Identity (RI).[219–221]

As seen in equation (73), the coulomb part of the Fock operator, in terms of the basis functions, can be written as a sum of four indexes

$$\sum_{\lambda\nu\mu\sigma}^{M} P_{\lambda\sigma}\langle\chi_\lambda\chi_\nu|\hat{g}_{ij}|\chi_\mu\chi_\sigma\rangle \tag{127}$$

The RI algorithm reduces the computational cost for these integrals by introducing a new auxiliary basis set, which separates the sum into a product of two terms with three indices each. It achieves this by representing the density, which in terms of the basis functions is calculated according to

$$\rho(r) = \sum_{\lambda\nu}^{M} P_{\lambda\nu}\chi_\lambda(r)\chi_\nu(r) \tag{128}$$

as a linear combination of one electron auxiliary functions $\{\alpha(r)\}$[222]

$$\rho(r) \approx \rho_{aux}(r) = \sum_{\alpha}^{M_{aux}} c_\alpha\alpha(r) \tag{129}$$

The coefficients $c_\alpha$ must be obtained through some fitting. There are many possible metrics for minimizing the error introduced with this approximation. Two of them are the so-called density fitting and the coulomb fitting.[223]

The density fitting minimizes the integrated residual error of the density $|\delta\rho(r)|$ with respect to the coefficients,[224]

$$|\delta\rho(r)|^2 = \int \left| \rho(r) - \sum_{\alpha}^{M_{aux}} c_\alpha \alpha(r) \right|^2 dr \tag{130}$$

obtaining the following equation for these coefficients

$$c_\alpha = \sum_{\alpha'} S^{-1}_{\alpha\alpha'} \langle \alpha' | \rho \rangle \tag{131}$$

where the integral is

$$\langle \alpha' | \rho \rangle = \int \alpha'(r) \chi_\lambda(r) \chi_\nu(r) dr \tag{132}$$

and $S^{-1}_{\alpha\alpha'}$ is the inverse of the overlap integral of the auxiliary basis functions ($S_{\alpha\alpha'} = \langle \alpha | \alpha' \rangle$).

On the other hand, the coulomb fitting minimizes the self-interaction of the residual density with respect to the coefficients , $\langle \delta\rho | \hat{g} | \delta\rho \rangle$, resulting in

$$c_\alpha = \sum_{\alpha'} V^{-1}_{\alpha\alpha'} \langle \alpha' | \hat{g} | \rho \rangle \tag{133}$$

where $V^{-1}_{\alpha\alpha'}$ is the inverse of the coulomb integral of the auxiliary basis, $\langle \alpha | \hat{g} | \alpha' \rangle$. This fitting provides better results than those of the density fitting at the expense of a larger computational cost.[223] The quality of the auxiliary basis set is also important for both metrics, although if this basis set reproduces exactly the original density, both fitting techniques are equivalent.

## 2.4 Foundations of Density Functional Theory (DFT)

Density Functional Theory (DFT)[225] accounts for correlation energy with a lower computational cost than the *post* HF methods by using an alternative approach to these wave function-based methods: it focuses on the electron density $\rho(r)$.

### 2.4.1 Electron density

The electron density is defined as the integral over all the electron spin coordinates ($s$) and over the three spatial coordinates ($r$) of all but one electron ($dr_1$)

$$\rho(r) = N \int \Psi^*(x_1, \ldots, x_N) \Psi(x_1, \ldots, x_N) ds_1 ds_2 dr_2 \ldots dr_N \tag{134}$$

Hence, $\rho(r)$ determines the probability of finding any of the $N$ electrons of the system in a differential volume $dr_1$, and it only depends on the three spatial

coordinates. So, from both a methodological and a computational viewpoint, it would be desirable to calculate the energy using the electron density instead of the wave function. In addition, unlike the wave function, the electron density is a physical observable and can be measured experimentally (e.g., through X-ray diffraction).

The electron density has some other properties of interest:

- By integration over the whole space it gives the total number of electrons. Furthermore, it decays to zero at infinite distance from the nuclei (asymptotic decay)

$$\int \rho(r) = N \tag{135}$$

$$\rho(r \to \infty) = 0 \tag{136}$$

- It is maximum at the positions of the atoms, $R_A$, due to the attractive potential of the positive charge in the nuclei towards the electrons.
- It is possible to relate it to the nuclear charge, $Z_A$, at the nuclear positions, according to the following equation

$$\lim_{r \to R_A} \left[ \left( \frac{d}{dr} + 2Z_A \right) \bar{\rho}(r) \right] = 0 \tag{137}$$

where $\bar{\rho}(r)$ is the spherically averaged density.

As already seen in equation (13), the electronic Hamiltonian is an operator that can be constructed with only three variables of the system: $N$, $Z_A$, and $R_A$. Since the electron density contains enough information to specify these three variables, it should be sufficient to define the Hamiltonian and hence, the energy of the system and its wave function. In principle, every observable can be obtained exactly from the electron density.

### 2.4.2 The Thomas-Fermi Model

The first known use of the electron density for calculating the energy of a system is the Thomas-Fermi model,[226, 227] which is based on a uniform electron density (uniform gas of electrons) instead of the wave function. The accuracy of this model is low and its applicability limited, but it can be considered as the first and simplest DFT method

$$E^{TF}[\rho(r)] = \frac{3}{10}(3\pi^2)^{2/3} \int \rho^{5/3}(r) dr - Z \int \frac{\rho(r)}{r} dr + \frac{1}{2} \iint \frac{\rho(r_1)\rho(r_2)}{r_{12}} dr_1 dr_2 \tag{138}$$

$E^{TF}[\rho(r)]$ is the Thomas-Fermi functional. The first term corresponds to the kinetic energy, the second is the nuclear-nuclear potential, and the third is the electron-electron potential.

The energy in this model only depends on the electron density, which is obtained applying the variational method under the constraint that it must integrate to the total number of electrons.

### 2.4.3 The Hohenberg-Kohn theorems

The electronic Hamiltonian can be written as the sum of kinetic energy, $\hat{T}(r)$, electron-electron repulsion potential, $\hat{V}_{ee}(r)$ and a term that can be called external potential, $\hat{V}_{ext}$, which refers to the potential acting on an electron (normally just the potential of nuclear charges, $\hat{V}_{en}$)

$$\hat{H}(r) = \hat{T}(r) + \hat{V}_{ee}(r) + \hat{V}_{ext}(r) \tag{139}$$

The first Hohenberg-Kohn[228] theorem states that the external potential is determined, within a trivial additive constant, by the ground state electron density $\rho(r)$. There is a unique external potential for a given density, but not all electron densities have an associated external potential. The ones that have it are called $v$-representable. The ground state densities for a Hamiltonian with an external potential are always $v$-representable.

Since the Hamiltonian is a functional of the ground state density, the ground state energy, $E_0$, must also be $v$-representable

$$E_0[\rho(r)] = \underbrace{T[\rho(r)] + V_{ee}[\rho(r)]}_{F_{HK}[\rho(r)]} + \int \rho(r) V_{en}(r) dr \tag{140}$$

In the previous equation, the Hohenberg-Kohn functional, $F_{HK}[\rho(r)]$, has been defined, and it includes functionals for the kinetic energy of the electrons and the electron-electron repulsion (the terms that are independent of the nuclei). If this universal functional was known, the time-independent Schrödinger equation could be solved exactly for any type of system, but its explicit form is still unknown.

Nevertheless, the classical coulomb interaction, $J[\rho(r)]$, from the electron-electron repulsion term can be calculated exactly as a functional of the electron density,

$$V_{ee}[\rho(r)] = J[\rho(r)] + V_{ncl}[\rho(r)] = \frac{1}{2} \iint \frac{\rho(r_1)\rho(r_2)}{r_{12}} dr_1 dr_2 + V_{ncl}[\rho(r)] \tag{141}$$

the second term refers to the non-classical contribution to the electron-electron interaction, containing the self-interaction correction, the exchange, and the electron correlation (the electrons do not feel a mean average potential as in HF). Both explicit forms of the functionals $V_{ncl}[\rho(r)]$ and $T[\rho(r)]$ are still unknown.

The second Hohenberg-Kohn theorem relates to the problem of not knowing the exact electron density for the ground state. It states that the functional $E_0[\rho(r)]$ only delivers the lowest energy if the input density is the true ground state density.

Hence, introducing in equation (140) any trial density $\tilde{\rho}(r)$ that fulfils the boundary conditions and that is $v$-representable, the energy obtained will represent an upper bound to the ground state energy (similar to the variational principle). The energy obtained from the trial density will be the ground state energy only if this density is the true ground state density $\tilde{\rho}(r) = \rho(r)$

$$E_0 \leq E[\tilde{\rho}(r)] = T[\tilde{\rho}(r)] + V_{ee}[\tilde{\rho}(r)] + V_{en}[\tilde{\rho}(r)] \tag{142}$$

Therefore, the ground state energy of an $N$-electron system is obtained by minimizing the following equation, varying only the electron density with the constraint that it must integrate to the total number of electrons

$$E_0 = \min_{\rho \to N} \left( F_{HK}[\rho(r)] + \int \rho(r) V_{ext}(r) dr \right) \tag{143}$$

As previously seen in equation (140), the functional $F_{HK}[\rho(r)]$ includes the kinetic energy and the electron-electron potential (coulomb and exchange), but only the coulomb interaction $J[\rho(r)]$ is known.

### 2.4.4 The Kohn-Sham equations

In 1965, Khon and Sham[229] proposed a procedure that allows to apply the second Hohenberg-Kohn theorem efficiently (Thomas-Fermi applied it but only in the case of a model without chemical bonds).

Their idea was to calculate the HF kinetic energy for a fictitious non interacting system but with the same density as the real (interacting) one. The kinetic energy obtained, $T_S$, is not equal to the true kinetic energy $T$ of the system (subscript $S$ in $T_S$ refers to the fact that the kinetic energy is calculated for a Slater determinant), although the difference $T - T_S$ is usually small

$$T_S = \sum_{i=1}^{N} \langle \phi_i | - 1/2 \nabla_i^2 | \phi_i \rangle \tag{144}$$

In the previous equation, $\phi_i$ are the spin-orbitals of the non-interacting system. Although the wave function is not exact, it is possible to build the exact electron density with these orbitals

$$\rho_S(r) = \sum_{i=1}^{N} |\phi_i(x_i)|^2 = \rho_{exact}(r) \tag{145}$$

where the summation runs over all orbitals and spins (all the electrons in the system).

Then, Kohn and Sham introduced an exchange-correlation functional, which contains everything that is still unknown, as

$$E_{XC}[\rho(r)] = (T[\rho(r)] - T_S[\rho(r)]) + (V_{ee}[\rho(r)] - J[\rho(r)]) \tag{146}$$

This functional includes the self-interaction error correction, the correlation energy related to the electron-electron interactions, the exchange energy, and the part of the real kinetic energy that is missing in equation (144).

The ground state energy can thus be calculated as

$$E[\rho(r)] = T_S[\rho(r)] + V_{en}[\rho(r)] + J[\rho(r)] + E_{XC}[\rho(r)] \tag{147}$$

where the exchange-correlation functional, $E_{XC}[\rho(r)]$, is now the only term without an explicit form.

Applying the variational principle as in HF to get the orbitals that minimize the energy, with the same constraint of orthogonality of the orbitals, the so-called Khon-Sham equations are obtained:

$$\left(-\frac{1}{2}\nabla_i^2 + \left[\int \frac{\rho(r)}{r_{ij}} dr_j + E_{XC}(r_i) - \sum_{A=1}^{M} \frac{Z_A}{r_{iA}}\right]\right)\phi_i = \epsilon_i \phi_i \tag{148}$$

$$V_{eff}(r_i) = J(r_i) + E_{XC}(r_i) + V_{en}(r_i) \tag{149}$$

$$\left(-\frac{1}{2}\nabla_i^2 + V_{eff}(r_i)\right)\phi_i = \epsilon_i \phi_i \tag{150}$$

The shape of these equations resembles that of HF methodology (one electron operator with an effective potential) and the procedure for solving them is similar as well: an iterative process to get the orbitals (and hence the electron density) that minimize the ground state energy (so far DFT follows the variational theorem) under the orthogonality constraint until self-consistency is achieved. The LCAO approximation is also be applied to the spin-orbitals within DFT.

The Kohn-Sham (KS) orbitals and eigenvalues belong to a fictitious system, a non-interacting system, so they are not directly related to the real system. However, they are used to construct the exact electron density, which is associated with the one-electron potential that includes all the missing effects in the fictitious picture. Furthermore, the energy of the Kohn-Sham Highest Occupied Molecular Orbital (HOMO) is equal to the negative of the exact ionization energy (Koopmans' Theorem).

Note that a KS system may or may not exist for a given $v$-representable density, this is called the non-interacting $v$-representability problem.

## 2.5 Approximate Exchange-Correlation functionals

The accuracy of the results in DFT depends on the approximation used for the exchange-correlation functional. However, there is not any guidance for improving these approximations. There are some physical constraints that must be fulfilled, but there are functionals that violate these rules with better results than others that fulfil them.

The only way to check the accuracy and usefulness of a specific functional is to compare its performance to a reference, like, for instance, to experimental data or high level calculations.

### 2.5.1 Local Density Aproximation

The local density approximation (LDA) is the basis of most of the exchange-correlation functionals.[230] Thomas-Fermi model is an example of LDA and, as already mentioned, it is based on the uniform electron gas (UEG) model to represent the system. This model is electrically neutral with $N$ electrons in a volume $V$ that move on a positive background charge distribution, hence, the

density $\rho$ is finite

$$\rho = \frac{N}{V} \tag{151}$$

The main idea of LDA is to write the exchange-correlation energy as

$$E_{XC}^{LDA}[\rho(r)] = \int \rho(r)\epsilon_{XC}[\rho(r)]dr \tag{152}$$

where $\epsilon_{XC}$ is the exchange-correlation energy per particle of a UEG with density $\rho(r)$. It is then split into exchange (the exactly form is known) and correlation (approximation with high accuracy) contributions

$$\epsilon_{XC}[\rho(r)] = \epsilon_X[\rho(r)] + \epsilon_C[\rho(r)] \tag{153}$$

The following equation for the exchange energy contribution was derived by Block[231] and Dirac[232]

$$\epsilon_X[\rho(r)] = -\frac{3}{4}\left[\frac{3\rho(r)}{\pi}\right]^{1/3} \tag{154}$$

Inserting this expression into equation (152)

$$E_X^{LDA}[\rho(r)] = -\frac{3}{4}\left(\frac{3}{\pi}\right)^{1/3}\int \rho^{4/3}(r)dr \tag{155}$$

Unlike the exchange contribution, no explicit expression for the correlation part is known. However, highly accurate quantum Monte-Carlo simulations of the homogeneous electron gas have been employed to obtain expressions for $\epsilon_C[\rho(r)]$.

There is an extension for LDA where $\alpha$ and $\beta$ spins are independently treated. It is especially useful for open-shell systems where there are un-paired electrons and LDA functionals that do not depend on the spin densities would lead to large errors. This 'unrestricted' LDA is known as Local Spin-Density-Approximation (LSDA).

In open-shell systems, the electron density for each spin is different,

$$\rho_\alpha(r) \neq \rho_\beta(r) \tag{156}$$

and the exchange-correlation energy depends on the $\alpha$ electron density, $\rho_\alpha(r)$, and the $\beta$ electron density, $\rho_\beta(r)$, as follows,

$$E_{XC}^{LSDA}[\rho_\alpha(r), \rho_\beta(r)] = \int \rho(r)\epsilon_{XC}[\rho_\alpha(r), \rho_\beta(r)]dr \tag{157}$$

like in UHF, the Kohn-Sham equations are evaluated separately for the two spins.

One of the first forms for the LSDA correlation potential was given by Vosko, Wilk, and Nusair (VWN),[233] reproducing the uniform electron gas for high and

low density limits. It depends on two variables: $r_S$ and $\zeta$. $r_S$ is the Seitz radius, related to the inverse of the electron density, and $\zeta$ is the spin polarization

$$\frac{4}{3}\pi r_S^3 = \frac{V}{N} = \frac{1}{\rho} \tag{158}$$

$$\zeta = \frac{\rho_\alpha - \rho_\beta}{\rho} \tag{159}$$

The VWN correlation functional has been constructed using an analytic interpolation formula. It interpolates between the unpolarized ($\zeta = 0$, same number of electrons in both spins) and spin polarised ($\zeta = 1$, all electrons with $\alpha$ spin) limits,

$$\epsilon_C(r_S,\zeta) = \epsilon_C(r_S,0) + \alpha_C(r_S)\frac{f(\zeta)}{f''(0)}\left(1-\zeta^4\right) + \left[\epsilon_C(r_S,1) - \epsilon_C(r_S,0)\right] f(\zeta)\zeta^4 \tag{160}$$

being $\alpha_C(r_S)$ a function called spin stiffness, defined as

$$\alpha_C(r_S) = \left[\frac{\partial^2 \epsilon_C(r_S,\zeta)}{\partial \zeta^2}\right]_{\zeta=0} \tag{161}$$

and $f(\zeta)$

$$f(\zeta) = \frac{(1+\zeta)^{4/3} + (1-\zeta)^{4/3} - 2}{2\left(2^{1/3}-1\right)} \tag{162}$$

The different $\epsilon_C(r_S,\zeta)$ functionals are parametrized according to the following equation,

$$\begin{aligned}\epsilon_C^{VWN}(x) = A\Bigg\{&\ln\frac{x^2}{X(x)} + \frac{2b}{Q}\tan^{-1}\left(\frac{Q}{2x+b}\right) \\ &-\frac{bx_0}{X(x_0)}\left[\ln\frac{(x-x_0)^2}{X(x)} + \frac{2\left(b-2x_0\right)}{Q}\tan^{-1}\left(\frac{Q}{2x+b}\right)\right]\Bigg\}\end{aligned} \tag{163}$$

where $x$, $X(x)$, and Q are defined as follows

$$x = \sqrt{r_S} \tag{164}$$

$$X(x) = x^2 + bx + c \tag{165}$$

$$Q = \sqrt{4c - b^2} \tag{166}$$

In the previous equations, $A$, $x_0$, $b$, and $c$ are parameters, also known as fitting constants, with different values for $\epsilon_C(r_S,0)$, $\epsilon_C(r_S,1)$, and $\alpha_C(r_S)$.

A different parametrization for $\epsilon_C$ and $\alpha_C$ was proposed by Perdew and Wang (PW92)[234] as displayed here,

$$\epsilon_C^{PW92} = -2A\left(1+\alpha_1 r_S\right)\ln\left[1 + \frac{1}{2A\left(\beta_1 r_S^{1/2} + \beta_2 r_S + \beta_3 r_S^{3/2} + \beta_4 r_S^2\right)}\right] \tag{167}$$

in which now the parameters are $A$, and $\beta_n$, also taking different values for $\epsilon_C(r_S, 0)$, $\epsilon_C(r_S, 1)$, and $\alpha_C(r_S)$. PW92 uses the VWN interpolation formula (160) and this combination is the most accurate functional for LSDA correlation energy available at the moment.

### 2.5.2 The Generalized Gradient Approximation

LSDA is exact for a uniform electron gas and quite accurate for solids. However, it fails for atoms and molecules since the electron density in them is not homogeneous. The obvious improvement for LSDA is to include some dependence on the gradient of the electron density, $\nabla\rho(r)$, in the exchange-correlation functional (similar to adding extra terms from a Taylor expansion of the density), to account for the inhomogeneity of the real system. This is known as Gradient Expansion Approximation (GEA).

The GEA exchange-correlation energy is then,

$$E_{XC}^{GEA}[\rho_\alpha(r), \rho_\beta(r)] = \int f\left(\rho_\alpha(r), \rho_\beta(r), \nabla\rho_\alpha(r), \nabla\rho_\beta(r)\right) dr \tag{168}$$

and applying this concept for the exchange energy,

$$E_X^{GEA}[\rho(r)] = E_X^{LDA}[\rho(r)] + \int f(x)\rho^{4/3}(r)dr \tag{169}$$

where $f(x)$ is a function of the electron density gradient, as $x$ is defined as

$$x = \frac{|\nabla\rho(r)|}{\rho^{4/3}(r)} \tag{170}$$

Introducing the expansion for the exchange-correlation functional in an UEG (the terms that vanish are not shown),

$$E_{XC}[\rho(r)] = \int \rho(r)\epsilon_{XC}^{LDA}[\rho(r)]dr + \int |\nabla\rho(r)|^2\epsilon_{XC}^{(2)}[\rho(r)]dr + \dots \tag{171}$$

where $\epsilon_{XC}^{(2)}$ are coefficients with appropriate dimension.

Applying this expansion to the GEA exchange energy in terms of the reduced density gradient, $x$,

$$E_X^{GEA}[\rho(r)] = E_X^{LDA}[\rho(r)] - \beta_X \int \rho^{4/3}(r)x^2 dr + \dots \tag{172}$$

being $\beta_X$ the second-order GEA exchange coefficient. Some terms ($\rho^{4/3}x^n$) of this expansion diverge, so it may fail when applied and it does not provide an improvement over LSDA.

Gradient Corrected or Generalized Gradient Approximation (GGA) is the name of GEA including a corrected dependency on the derivatives of the density that leads indeed to a better description than LSDA. Sometimes, GGA methods

are called non-local methods, but this is not correct since they only depend on the density (and its gradient) at a given point of space.

As in LDA (see eq. (153)), there is usually a separation between the exchange and correlation contributions. The GGA functionals that approximate exchange and correlation together are called Nonseparable Gradient Approximation (NGA) functionals.

First, some GGA exchange functionals, depending on $F_X[x]$, a functional of $x$, will be presented herein

$$E_X^{GGA}[\rho(r)] = \int \rho(r)\epsilon_X^{LDA}[\rho(r)]F_X[x]dr \tag{173}$$

One of the first GGA exchange functionals was proposed by Perdew and Wang in 1986 (PW86),[235] with three $a$, $b$, and $c$ suitable constants. As all the GGA exchange functionals, it must be combined with some expression for the correlation energy

$$F_X^{PW86}[x] = \left(1 + ax^2 + bx^4 + cx^6\right)^{1/15} \tag{174}$$

Perdew also participated in the development of another popular GGA exchange functional, the so-called PBE,[236]

$$F_X^{PBE}[x] = 1 + \kappa - \frac{\kappa^2}{\mu p} \tag{175}$$

where $p = s^2$ ($s$ depends on $x$ according to the following equation), $\mu = 0.21951$, and $\kappa = 0.804$

$$s(x) = \frac{x}{2\left(3\pi^2\right)^{1/3}} \tag{176}$$

Almost simultaneously to PW86, in 1986, Becke[237] proposed a functional for GGA exchange energy, whose form was the basis for future functionals

$$F_X^{B86}[s] = 1 + \frac{\beta c_2 c_1^2 s^2}{1 + \gamma c_1^2 s^2} \tag{177}$$

$$c_1 = 2\left(6\pi^2\right)^{1/3} \tag{178}$$

$$c_2 = 2\left(C_X 2^{1/3}\right)^{-1} \tag{179}$$

$$C_X = \frac{3}{4}\left(\frac{3}{\pi}\right)^{1/3} \tag{180}$$

where the constants $\beta$ and $\gamma$ have 0.0036 and 0.004 values, respectively.

In 1988, Becke[238] improved this exchange GGA functional with some corrections that satisfy the asymptotic constraint for the exchange density

$$\lim_{r\to\infty} \epsilon_X = -\frac{\rho(r)}{2r} \tag{181}$$

This exchange functional is known as B88. Its value for $\gamma$ is 0.0042, which has been obtained from fitting of the exchange energy for the six noble gases

$$F_X^{B88}[s] = 1 + \frac{\gamma c_2 c_1^2 s^2}{1 + 6\gamma s c_1 \sinh^{-1}(s c_1)} \tag{182}$$

Other popular GGA exchange functionals are LG,[239] FT97,[240] G96,[241] and PW91.[242–244]

There is also a huge number of GGA correlation functionals, one of the most used was developed by Lee, Yang, and Parr (LYP)[245] using the Colle-Salvetti formula for calculating the correlation energy,

$$E_C^{LYP}[\rho(r)] = \int \rho(r)\epsilon_C^{LYP}[\rho(r)]dr \tag{183}$$

$$\begin{aligned}\epsilon_C^{LYP}[\rho(r)] = -a\frac{\gamma}{\left(1+d\rho^{-1/3}\right)} - ab\frac{\gamma e^{-c\rho^{-1/3}}}{9\left(1+d\rho^{-1/3}\right)\rho^{8/3}}\Big[18\left(2^{2/3}\right)C_F \\ \left(\rho_\alpha^{8/3}+\rho_\beta^{8/3}\right) - 18\rho t_W + \rho_\alpha\left(2t_W^\alpha + \nabla^2\rho_\alpha\right) + \rho_\beta\left(2t_W^\beta + \nabla^2\rho_\beta\right)\Big]\end{aligned} \tag{184}$$

$a$, $b$, $c$, and $d$ are parameters fitted for the helium atom, $t_W^\sigma$ is the local Weizsacker kinetic energy with spin $\sigma$ ($\alpha$ or $\beta$),

$$t_W^\sigma = \frac{1}{8}\left(\frac{|\nabla\rho_\sigma|^2}{\rho_\sigma} - \nabla^2\rho_\sigma\right) \tag{185}$$

and $\gamma$ is a function, defined as

$$\gamma = 2\left(1 - \frac{\rho_\alpha^2 + \rho_\beta^2}{\rho^2}\right) \tag{186}$$

It becomes zero when all the spins are aligned, so LYP functional does not predict any correlation energy for parallel spins orientations.

Perdew proposed two different functionals for the GGA correlation energy: one with Wang (PW91),[242–244] and another one with Burke and Ernzerhof (PBE).[236] Their starting points are the equations shown below,

$$E_C^{GGA}[\rho_\alpha(r), \rho_\beta(r)] = \int \rho(r)H(r_S, \zeta, t)dr \tag{187}$$

$$t = \frac{|\nabla\rho|}{2\phi(\zeta)k_S\rho} \tag{188}$$

$$k_S = \left(\frac{4k_F}{\pi}\right)^{1/2} \tag{189}$$

$$k_F = \left(3\pi^2\rho\right)^{1/3} \tag{190}$$

where $H(r_S, \zeta, t)$ is a numerically defined gradient correction, $r_S$ is the Seitz radius (158), $\zeta$ is the relative spin polarization (159), and $t$ is the reduced

density gradient generalized to spin-polarized systems. In equation (188), $\phi$ is a scaling factor, defined as

$$\phi(\zeta) = \left[(1+\zeta)^{2/3} + (1-\zeta)^{2/3}\right]/2 \tag{191}$$

In the case of PW91, $H(r_S, \zeta, t)$ is expressed as

$$H^{PW91}(r_S, \zeta, t) = H_0^{PW91}(r_S, \zeta, t) + H_1^{PW91}(r_S, \zeta, t) \tag{192}$$

wherein the $H_1$ term is negligible unless $s$, defined in eq. (176), is close to zero.

On the other hand, the PBE correlation functional defines $H(r_S, \zeta, t)$ as

$$H^{PBE}(r_S, \zeta, t) = H_0^{PBE}(r_S, \zeta, t) \tag{193}$$

In both functionals, PW91 and PBE, $H_0$ has the same expression

$$H_0(r_S, \zeta, t) = \gamma\phi^3(\zeta) \ln\left[1 + at^2\left(\frac{1+At^2}{1+At^2+A^2t^4}\right)\right] \tag{194}$$

where $a$ is a suitable constant and $A$ is

$$A = \frac{a}{e^{-\epsilon_C^{LSDA}(r_S,\zeta)/\gamma\phi^3(\zeta)} - 1} \tag{195}$$

$H_0^{PW91}$ and $H_0^{PBE}$ only differ in the value given for $\gamma$, which is 0.024734 and 0.031091, respectively. $\epsilon_C^{LSDA}(r_S, \zeta)$ is the LSDA correlation energy with the PW92[234] parameterization (see eq. (167)).

Other functionals for GGA correlation energy are, for example, B95,[246] P86,[247] and WL.[248]

### 2.5.3 *Meta*-GGA

The next obvious improvement for GGA functionals is to include an extra term in the expansion of the density, the Laplacian of the electron density, $\nabla^2\rho(r)$. Therefore, the functionals now depend on the density and its first and second derivatives, thus, the system is described with more accuracy

$$E_{XC}^{mGGA}[\rho(r), \nabla\rho(r), \nabla^2\rho(r)] \tag{196}$$

Alternatively, GGA functionals can be improved by including the dependence on the kinetic energy density $\tau(r)$[230] rather than the Laplacian of the density. Both types of improvements are commonly called *meta*-GGA ($m$GGA), or *meta*-NGA for the functionals that do not separate the exchange and correlation contributions

$$E_{XC}^{mGGA}[\rho_\alpha(r), \rho_\beta(r), \nabla\rho_\alpha(r), \nabla\rho_\beta(r), \tau_\alpha(r), \tau_\beta(r)] \tag{197}$$

$$\tau(r) = \frac{1}{2}\sum_{i=1}^{N} |\nabla\phi_i(r,s)|^2 \tag{198}$$

One of the most popular *m*GGA functionals is TPSS, proposed by Tao, Perdew, Staroverov, and Scuseria in 2003.[249] It depends on the density, its gradient, and the orbital kinetic energy density, satisfying some constraints without using empirical parameters.

The development of TPSS was based on a previous *m*GGA functional called PKZB, proposed by Perdew, Kurth, Zupan, and Blaha in 1999[250]

$$E_X^{mGGA}[\rho(r)] = \int \rho(r)\epsilon_X^{LDA}[\rho(r)]F_X(p,z)dr \tag{199}$$

The function $F_X$ depends on two dimensionless inhomogeinity parameters, $p$ and $z$,

$$p = s^2 \tag{200}$$

$$z = \frac{\tau^W}{\tau} \leq 1 \tag{201}$$

$$\tau^W = \frac{1}{8}\frac{|\nabla\rho|^2}{\rho} \tag{202}$$

and has the following expression,

$$F_X = 1 + \kappa - \frac{\kappa}{1 + x/\kappa} \tag{203}$$

where $\kappa = 0.804$, and $x$ is a function that depends on $p$ and $z$.

The exchange functional was chosen according to the fulfilment of the following constraint criteria:[249]

- The expression for $F_X$ when $p$ tends to an infinity value is maintained as $F_X^{PBE}$ (eq. (175)).
- For a slowly variant density, $F_X$ has the following expression

$$F_X = 1 + \frac{10}{81}p + \frac{146}{2025}q^2 - \frac{73}{146}qp + Dp^2 + O(\nabla^6) \tag{204}$$

$$q = \frac{\nabla^2\rho}{4\left(3\pi^2\right)^{2/3}\rho^{5/3}} \tag{205}$$

  that recovers the fourth-order gradient expansion of Svendsen and von Barth,[251] being $q$ the reduced Laplacian of the density and $D$ a parameter that is set to zero in TPSS, but in other functionals, such as PKZB, $D = 0.113$.

- Recovery of the exact exchange energy for the ground state density of the hydrogen atom, which is $-0.3125$ hartree.
- The Laplacian of the density diverges at the nuclei ($s \approx 0.4$) unless its coefficient, proportional to $dF_X/ds$, vanishes there.

$$\left(\frac{dF_X}{ds}\right)_{s\approx 0.4} = 0 \tag{206}$$

Hence, $x$ must fulfil all of these constraints, in the case of TPSS,

$$x = \left\{ \left[ \frac{10}{81} + c\frac{z^2}{(1+z^2)^2} \right] p + \frac{146}{2015}\tilde{q}_b^2 - \frac{73}{405}\tilde{q}_b \sqrt{\frac{1}{2}\left(\frac{3}{5}z\right)^2 + \frac{1}{2}p^2} + \frac{1}{\kappa}\left(\frac{10}{81}\right)^2 p^2 + 2\sqrt{e}\frac{10}{81}\left(\frac{3}{5}z\right)^2 + e\mu p^3 \right\} \left(1+\sqrt{e}p\right)^{-2} \tag{207}$$

in this expression, $\tilde{q}_b$ is a parameter that tends to the reduced Laplacian $q$ in the slowly varying limit; $c = 1.59096$ and $e = 1.537$ are constants, which assure that the constraint related to the exchange energy of the hydrogen atom is fulfilled, and the constant $\mu = 0.21951$ comes from the PBE exchange functional (175).

For the correlation contribution, PKZB is a nonempirical self-interaction-free functional, which is also the basis for TPSS correlation[249]

$$E_C^{mGGA}[\rho(r)] = \int \rho \epsilon_C^{revPKZB} dr \left[1 + d\epsilon_C^{revPKZB} \left(\tau_W/\tau\right)^3\right] \tag{208}$$

being $d = 2.8$ hartree$^{-1}$ and $\epsilon_C^{revPKZB}$ a revised version of the PKZB correlation energy

$$\epsilon_C^{revPKZB} = \epsilon_C^{PBE}[\rho_\alpha(r), \rho_\beta(r), \nabla\rho_\alpha(r), \nabla\rho_\beta(r)] \left[1 + C(\zeta,\xi)\left(\tau^W/\tau\right)^2\right] - \left[1 + C(\zeta,\xi)\left(\tau^W/\tau\right)^2\right] \sum_\sigma \frac{\rho_\sigma}{\rho}\tilde{\epsilon}_C \tag{209}$$

with $C(\zeta,\xi)$ a function that depends on two variables, $\zeta$ the spin polarization (159), and $\xi = |\nabla\zeta|/2\left(3\pi^2\rho\right)^{1/3}$. In PKZB, $\tilde{\epsilon}_C = \epsilon_C^{PBE}[\rho_\sigma(r), 0, \nabla\rho_\sigma(r), 0]$, but in this revised version is chosen to be

$$\tilde{\epsilon}_C = \max\left\{\epsilon_C^{PBE}[\rho_\sigma(r), 0, \nabla\rho_\sigma(r), 0], \epsilon_C^{PBE}[\rho_\alpha(r), \rho_\beta(r), \nabla\rho_\alpha(r), \nabla\rho_\beta(r)]\right\} \tag{210}$$

### 2.5.4 Hybrid functionals

Another advance in exchange-correlation functionals came in 1993. It was derived from the adiabatic connection, which models the connection between the two systems involved in Khon-Sham equations (non-interacting system and the actual interacting system). Hence, the exchange correlation functional is obtained by integration over a parameter $\lambda$ that describes the 'amount' of electron-electron interactions included ($\lambda = 0$ in the non-interacting system) as displayed below

$$E_{XC} = \int_0^1 \langle\Psi_\lambda|V_{XC}(\lambda)|\Psi_\lambda\rangle d\lambda \tag{211}$$

If $V_{XC}(\lambda)$ is taken to be linear in $\lambda$, the integral gives the following expression

$$E_{XC} \approx \frac{1}{2}\langle\Psi_0|V_{XC}(0)|\Psi_0\rangle + \frac{1}{2}\langle\Psi_1|V_{XC}(1)|\Psi_1\rangle \tag{212}$$

which is just the average value between the two limits. The first term in this equation can be calculated exactly, since the HF methodology provides an expression for the exact exchange energy of a non-interacting system

$$E_X^{HF} = -\sum_{i=1}^{N}\sum_{j>i}^{N} K_{ij} = -\sum_{i=1}^{N}\sum_{j>i}^{N}\langle\phi_i(x_i)\phi_j(x_j)|g_{ij}|\phi_j(x_i)\phi_i(x_j)\rangle \tag{213}$$

Now, $\phi_i(x_i)$ are the Khon-Sham spinorbitals, which play an identical role to their analogues in the HF methodology for this type of system.

Although the expression for the second term in equation (212) is not known exactly, some approximations for the exchange-correlation potential in an interacting system have already been presented.

In 1993, Becke proposed the so-called Half-and-Half methods,[252] whose idea is splitting the exchange energy exactly in two halves, one for the HF exchange (exact for the non-interacting system) and the other half for the exchange from LSDA, as depicted below

$$E_X = \frac{1}{2}E_X^{HF} + \frac{1}{2}E_X^{LSDA} \tag{214}$$

It must be combined with another functional for correlation energy

In this framework, Becke proposed several functionals.[252] For example, the BHandH functional combines the Half-and-Half method with the GGA functional LYP for correlation.

$$E_{XC}^{BHandH} = \frac{1}{2}E_X^{HF} + \frac{1}{2}E_X^{LSDA} + E_C^{LYP} \tag{215}$$

Another one is the BHandHLYP functional, also known as BHLYP,[252] which includes a GGA correction (B88) for the exchange energy as well

$$E_{XC}^{BHandHLYP} = \frac{1}{2}E_X^{HF} + \frac{1}{2}E_X^{LSDA} + \frac{1}{2}\Delta E_X^{B88} + E_C^{LYP} \tag{216}$$

This kind of functionals did not greatly improve the GGA results. Therefore, the next step was to introduce some GGA exchange-correlation energy in equation (214) along with some experimental (or from high-level calculations) parameters. Becke[253] proposed the following general expression for this kind of functionals, usually called hybrid functionals,

$$E_{XC}^{B3} = aE_X^{HF} + (1-a)E_X^{LSDA} + b\Delta E_X^{B88} + cE_C^{LSDA} + (1-c)E_C^{GGA} \tag{217}$$

in which $a$, $b$, and $c$ are the parameters (the dependence on these parameters may vary depending on the hybrid functional). The name of the functional (B3) comes from the number of parameters.

The famous hybrid functional B3LYP is the result of combining equation (217) with VWN[233] (eq. (163)), and LYP[245] (eq. (183)) correlation energies, and using a set of parameters fitted from experimental data

$$E_{XC}^{B3LYP} = 0.2E_X^{HF} + 0.8E_X^{LSDA} + 0.72\Delta E_X^{B88} + 0.19E_C^{VWN} + 0.81E_C^{LYP} \tag{218}$$

B3LYP is by far the widest used hybrid functional (and DFT functional in general), with successful results for a wide variety of chemical problems.[254,255] However, there are many other hybrid functionals that have been developed. For instance, another popular hybrid functional is PBE0,[256] which is based on the GGA exchange-correlation functional PBE, incorporating a quarter of exact (HF) exchange energy

$$E_{XC}^{PBE0} = 0.25E_X^{HF} + 0.75E_X^{PBE} + E_C^{PBE} \tag{219}$$

The $E_C^{GGA}$ term in the expression of hybrid functionals (217) can be substituted by the correlation energy of a *meta*-GGA functional, $E_C^{mGGA}$. This type of functionals are known as hybrid *meta*-GGA functionals. TPSSh,[257] defined in the equation (220), is an example. It combines the TPSS exchange-correlation functional[249] ($m$GGA) with the HF exchange energy,

$$E_{XC}^{TPSSh} = 0.10E_X^{HF} + 0.90E_X^{TPSS} + E_C^{TPSS} \tag{220}$$

It only has one parameter, $a$, which has been obtained by fitting to theoretical enthalpies of formation of 223 molecules.

Truhlar *et al.* have developed several hybrid functionals (also known as Minnesota functionals) mostly based on the *meta*-GGA approximation (e.g., M05,[258] M06,[259] ...). One of the last functionals proposed by this group is called MN15.[260] It is a hybrid *meta*-NGA functional with 58 empirical parameters fitted to a large set of data and which incorporates 44 % of HF exchange. This functional showed remarkable performance for a wide range of properties.

One of the key aspects in hybrid functionals is the choice of parameters. It is usually done by fitting to experimental data. Many functionals have included a higher number of parameters to improve this fitting. For example, the B97 functional uses 10 parameters,[261] and there are some functionals with even higher level of parameterization, such as VS98.[262] The Minnesota functionals have a great number of parameters as well, which are fitted to many chemical species, leading to an impressive performance in many areas.

### 2.5.5 Beyond-hybrid functionals

Despite the huge number of hybrid functionals, all the exchange-correlation functionals reported in the literature present some limitations, specially in systems containing transition metals as well as in the calculation of barrier heights. In this sense, many new developments in functionals based on different assumptions have emerged in recent years.[263] Some of the most important ones will be covered in this section.

#### Local hybrids

One of the main problems of hybrid functionals is the lack of flexibility in the ratio between the exact and the approximated exchange energies (they usually include 20-25 % of exact HF exchange), which is fixed for all the different regions

of the system of interest. Furthermore, there exist a self-interaction error in this kind of functionals, since the self-coulomb energy ($J_{ii}$) is only partially cancelled by the exchange energy ($K_{ii}$, the HF exchange).

Jaramillo et al. proposed in 2003[264] a new approximation based on the hybrid methods but changing the parameter $a$, which gives the amount of exact exchange included, to a local function $a(r)$. For example, a local hybrid (LH) functional[263] with a shape similar to B3LYP is

$$E_{XC}^{LH} = \int \left[a(r)\epsilon_X^{HF}(r) + (1-a(r))\epsilon_X^{LDA}(r)\right] dr + b\Delta E_X^{GGA} + E_C^{GGA} \quad (221)$$

One choice for this function that helps to correct the self-interaction error is,

$$a(r) = \frac{\tau^W}{\tau} \quad (222)$$

where $\tau$ and $\tau^W$ have already been defined in equations (198) and (202), respectively. Note that $\tau = \tau^W$ in regions with one electron. Therefore, 100% of the exchange energy comes from the exact HF exchange and hence, there is no self-interaction error for one-electron regions ($J_{ii} = K_{ii}$). Alternatively, for homogeneous regions (with uniform densities), $|\nabla\rho|^2 = 0$, so $\tau^W = 0$, $a(r) = 0$, and all the exchange energy will come from DFT exchange.

The flexibility of this kind of functionals is very attractive and there are many examples of local-hybrid functionals with different choices for the local mixing function.

**Adiabatic connection functionals**

The local hybrid functionals create a smooth mixing of exchange energy between the non-interacting and the full-interacting systems. Alternatively, there are other ways of improving the connection between the two kind of systems. Unlike in hybrid (and local-hybrid) functionals in which only the two extreme limits ($\lambda = 0$, $\lambda = 1$) are considered, in adiabatic connection functionals,[263,265] a smooth transformation from non-interacting to full-interacting system is represented

$$E_{XC} = \int_0^1 W_\lambda d\lambda \quad (223)$$

$$W_\lambda = \langle\Psi_\lambda|V_{XC}(\lambda)|\Psi_\lambda\rangle - J[\rho(r)] \quad (224)$$

There are many approximations to $W_\lambda$. The simplest one was proposed by Becke[252] and it is based on the knowledge of the exact $W_0$ (HF), and $W_1$ (approximated with LSDA), with a linear model

$$W_\lambda = a + b\lambda \quad (225)$$

Other models used different forms of $W_\lambda$, for example $W_0'$, $W_\infty$, $W_\infty'$ (Perdew *et al.*)[266–268]

$$W_0' = 2\lim_{\lambda\to 0} E_C[\rho_{1/\lambda}] \quad (226)$$

Mori-Sánchez, Cohen, and Yang[269] have developed a functional from $W_0$, $W_0'$, and a chosen point $W_{\lambda p}$ from an approximate DFA

$$W_\lambda = a + \frac{b\lambda}{1 + c\lambda} \tag{227}$$

**Range-separated (RS) functionals**

The nature of the two-electron operator $1/r_{ij}$ creates an incorrect behaviour when the interelectronic distance tends to zero ($r_{ij} \to 0$). This is usually known as correlation cusp problem. One way to solve this issue[270,271] is to introduce a suitable cut-off function $g(r_{ij})$ for short interelectronic distances,

$$\frac{1}{r_{ij}} = \frac{g(r_{ij})}{r_{ij}} + \frac{1 - g(r_{ij})}{r_{ij}} \tag{228}$$

hence, the two-electron operator is split in two parts, one for long-range interactions (first term) and the other one for short-range interactions (second term).

A good choice for this function, $g(r_{ij})$, is the standard error function, $\mathrm{erf}(x)$. It also depends on a parameter $\mu$, which moves the system from the non-interacting picture with $\mu \to 0$ to the full-interacting one when $\mu \to \infty$

$$\mathrm{erf}(x) = \frac{2}{\sqrt{\pi}} \int_0^x dx' e^{-x'^2} \tag{229}$$

$$g(r_{ij}) = \mathrm{erf}(\mu r_{ij}) \tag{230}$$

$$1 - g(r_{ij}) = \mathrm{erfc}(\mu r_{ij}) \tag{231}$$

Therefore, when the interelectronic distance tends to zero, the long-range interaction approaches to $2\mu/\sqrt{\pi}$, whereas when that distance tends to infinite, the short-range interaction approaches zero.

Within this approximation, the long-range and short-range parts should be treated with different functionals. The HF exchange potential is correct in the asymptotic limit,[272] so it can be used to calculate the long-range interaction combined with a density functional (DF) to calculate the short-range interaction and the correlation.

The short-range ($sr$) exchange energy is calculated as the difference between the total exchange energy and the long-range ($lr$) exchange energy,

$$E_X^{sr} = E_X - E_X^{lr} \tag{232}$$

$$E_{XC}^{RS} = E_X^{lr-HF} + \left(E_X^{DF} - E_X^{lr-DF}\right) + E_C^{DF} \tag{233}$$

wherein the density functional (DF) can belong to any of the previous approximations (LDA, GGA,...). There are many examples of range-separated functionals.[273–276] It is a field of growing interest, since they are especially useful for calculating excitation energies.[277]

One of the most popular range-separated functionals is CAM-B3LYP, which includes two extra parameters in the short-range and long-range separation as displayed in equation (234). CAM are the initials of 'Coulomb-Attenuating Method', termed by Yanai, Tew, and Handy in 2004[274]

$$\frac{1}{r_{ij}} = \frac{\alpha + \beta \mathrm{erf}(\mu r_{ij})}{r_{ij}} + \frac{1 - [\alpha + \beta \mathrm{erf}(\mu r_{ij})]}{r_{ij}} \tag{234}$$

The presence of two extra parameters provides more flexibility. The parameter $\alpha$ multiplies the HF exchange contribution over the whole range, and the parameter $\beta$ allows the same with the DFT counterpart by a factor of $1-(\alpha+\beta)$. Note that in the hybrid functional B3LYP, $\alpha$ (the analogous of the parameter $a$) and $\beta$ are constant with 0.2 and 0.0 values, respectively.

In this type of hybrid functionals, the percentage of HF exchange energy depends on the interelectronic distance. To distinguish the range-separated hybrids from the previous hybrid functionals, where the amount of HF exchange is constant, the latter are normally called global hybrids.

#### Functionals involving unoccupied orbitals

The next step in the improvement of density functionals is to involve unoccupied orbitals.[278–280] Prior to the success of DFT, the cheapest and simplest way of incorporating correlation effects into the electronic structure calculations was the second order Perturbation Theory (PT2). Then, the idea is to introduce this method (or an alternative perturbation-theory method) in the general expression of hybrid functionals. Therefore, some part of PT2 correlation is mixed with GGA (or *meta*-GGA) correlation, whereas the exchange part does not change. For example, B2x-PLYP[279] is one of the most successful functionals in this field,

$$E_{XC}^{B2xPLYP} = aE_X^{HF} + (1-a)E_X^{GGA} + bE_C^{GGA} + (1-b)E_C^{PT2} \tag{235}$$

the parameters $a$ and $b$ may vary depending on the B2x functional (B2, B2K, B2T...). In the case of the most common one, B2PLYP,[279] $a$ and $b$ are equal to 0.53 and 0.73, respectively.

## 2.6 Time-Dependent DFT

The time-dependent version of DFT, commonly known as Time-Dependent Density Functional Theory (TD-DFT) aims to solve the TDSE (equation (1)) employing the electron density instead of the wave function.[281] Its theory is similar to the one for the time-independent version: the electron density $\rho(r,t)$ is associated with the external potential $\hat{V}_{ext}(r,t)$, then being able to construct the Hamiltonian $\hat{H}(r,t)$, solve the TDSE and get the wave function of the system $\Psi(r,t)$, from which any physical observable can be obtained.[282]

The electronic time-dependent Hamiltonian can be written as

$$\hat{H}(r,t) = \hat{T}(r) + \hat{V}_{ee}(r) + \hat{V}_{ext}(r,t) \tag{236}$$

where $\hat{T}(r)$ is the kinetic energy of the electrons, $\hat{V}_{ee}(r)$ the interelectronic repulsion between the pairs of electrons, and $\hat{V}_{ext}(r,t)$ the total time-dependent external potential acting on the electrons (this includes the coulomb interactions of the electrons with the nuclei and with any external field, if present)

$$\hat{V}_{ext}(r,t) = \sum_{i=1}^{N} \upsilon(r_i,t) \tag{237}$$

### 2.6.1 Runge-Gross Theorem

The Runge-Gross theorem[283] is analogous to the first Hohenberg-Khom theorem in the time-dependent scenario. It proves that there exists a one-to-one correspondence between the electron density and the external potential acting upon the electrons.

The proof is based on the idea that, if two external potentials $\upsilon(r,t)$ and $\upsilon'(r,t)$ differ by more than a purely time dependent function $c(t)$, they can not lead to the same density $\rho(r,t)$. Note here that if two potentials differ only by $c(t)$, they will give rise to wave functions only differing by a phase factor, which is cancelled while calculating the density (238) or any other observable

$$\begin{aligned} \upsilon(r,t) &\rightarrow \Psi(r,t) \rightarrow \rho(r,t) \\ \upsilon'(r,t) + c(t) &\rightarrow \mathrm{e}^{-ic(t)}\Psi(r,t) \rightarrow \rho'(r,t) = \rho(r,t) \end{aligned} \tag{238}$$

$$\upsilon(r,t) \neq \upsilon'(r,t) + c(t) \rightarrow \rho(r,t) \neq \rho'(r,t) \tag{239}$$

If the densities produced by the different external potentials must be different, there is a unique one-to-one correspondence between the potential and the density for a fixed initial state $\Psi_0$. This implies that, knowing the electron density and the initial state, the external potential can be obtained as a functional of both of them (240) and hence, the TDSE can be solved

$$\upsilon(r,t) = \upsilon[\rho, \Psi_0](r,t) \tag{240}$$

The Runge-Gross theorem assumes that the external potential can be expanded in a Taylor series with respect to the initial time $t_0$,

$$\upsilon(r,t) = \sum_{k=0}^{\infty} c_k(r)(t-t_0)^k \tag{241}$$

being the expansion coefficients the corresponding derivatives evaluated at the initial time

$$c_k(r) = \frac{1}{k!}\frac{\partial^k}{\partial t^k}\upsilon(r,t)\bigg|_{t=t_0} \tag{242}$$

If the two potentials differ by more than $c(t)$, there is an integer $k \geq 0$ such that the function $u_k(r)$, defined below, is not constant in space

$$u_k(r) = \frac{\partial^k}{\partial t^k}\left[\upsilon(r,t) - \upsilon'(r,t)\right]\bigg|_{t=t_0} \neq constant \tag{243}$$

In the first step of the proof, it is demonstrated that if the two potentials differ by more than a purely time-dependent function, the current densities $j(r,t)$ and $j'(r,t)$ generated by them must also be different. The current density is defined as the expectation value of the current density operator $\hat{j}(r)$

$$j(r,t) = \langle \Psi(t)|\hat{j}(r)|\Psi(t)\rangle \tag{244}$$

$$\hat{j}(r) = -\frac{1}{2i}\sum_{i=1}^{N}\left[\nabla_i \delta(r-r_i) + \delta(r-r_i)\nabla_i\right] \tag{245}$$

To get the time evolution of the current densities, the equation of motion for the expectation value of a general operator $\hat{O}(t)$

$$i\frac{\partial}{\partial t}\langle \Psi(t)|\hat{O}(t)|\Psi(t)\rangle = \langle \Psi(t)|i\frac{\partial}{\partial t}\hat{O}(t) + \left[\hat{O}(t),\hat{H}(t)\right]|\Psi(t)\rangle \tag{246}$$

must be applied to the current densities, obtaining

$$i\frac{\partial}{\partial t}j(r,t) = \langle \Psi(t)|\left[\hat{j}(r),\hat{H}(t)\right]|\Psi(t)\rangle \tag{247}$$

$$i\frac{\partial}{\partial t}j'(r,t) = \langle \Psi'(t)|\left[\hat{j}(r),\hat{H}'(t)\right]|\Psi'(t)\rangle \tag{248}$$

Since the initial state for the primed and unprimed systems is the same, the wave functions at $t_0$ have to be equal, this is also true for the electron density ($\rho_0$) and the current density ($j_0$).

$$|\Psi(t_0)\rangle = |\Psi'(t_0)\rangle \equiv |\Psi_0\rangle \tag{249}$$

Subtracting the equations of motion for the primed (247) and unprimed (248) current densities at $t_0$, and taking into account that the Hamiltonians at the initial time only differ in the external potentials,

$$\begin{aligned} i\frac{\partial}{\partial t}\left[j(r,t)-j'(r,t)\right]_{t=t_o} &= \langle \Psi_0|\left[\hat{j}(r),\hat{H}(t_0)-\hat{H}'(t_0)\right]|\Psi_0\rangle \\ &= \langle \Psi_0|\left[\hat{j}(r),\upsilon(r,t_0)-\upsilon'(r,t_0)\right]|\Psi_0\rangle \\ &= i\rho_0(r)\nabla\left[\upsilon(r,t_0)-\upsilon'(r,t_0)\right] \end{aligned} \tag{250}$$

if the equation (243) is already fulfilled for $k=0$, i.e., the external potentials differ at the initial time, the right-hand side of (250) must be different from zero. This implies that the two current densities $j$ and $j'$ on the left-hand side will deviate infinitesimally after $t_0$. However, the two potentials $\upsilon$ and $\upsilon'$ may be equal at the initial time and hence, only fulfill the equation (243) for $k>0$. In this case, the equation of motion (246) is applied $(k+1)$ times to get

$$\frac{\partial^{k+1}}{\partial t^{k+1}}\left[j(r,t)-j'(r,t)\right]_{t=t_o} = -\rho_0(r)\nabla u_k(r) \tag{251}$$

since the right-hand side is not zero, the current densities must differ for $t>t_0$.

Having proved the first step of the Runge-Gross theorem, the second step consists of showing that having two different current densities $j$ and $j'$ implies different electron densities $\rho$ and $\rho'$. To achieve this, the continuity equation, which relates the current and electron densities, is useful

$$\frac{\partial}{\partial t}\rho(r,t) = -\nabla j(r,t) \tag{252}$$

Taking the difference between the primed and unprimed densities,

$$\frac{\partial}{\partial t}\left[\rho(r,t) - \rho'(r,t)\right] = -\nabla\left[j(r,t) - j'(r,t)\right] \tag{253}$$

and calculating the $(k+1)th$ derivative of the previous equation

$$\begin{aligned}\frac{\partial^{k+2}}{\partial t^{k+2}}\left[j(r,t) - j'(r,t)\right]_{t=t_o} &= -\nabla\left[j(r,t) - j'(r,t)\right] \\ &= \nabla\left[\rho_0(r)\nabla u_k(r)\right]\end{aligned} \tag{254}$$

where equation (251) has been used in the second step. Since $u_k(r)$ in eq. (243) is not constant, it is possible to prove that if the last term $\nabla\left[\rho_0(r)\nabla u_k(r)\right]$ is not zero, the electron densities $\rho$ and $\rho'$ must be different. For this, a demonstration via *reductio ad absurdum* is used, assuming that $\nabla\left[\rho_0(r)\nabla u_k(r)\right] = 0$ and considering the following integral

$$\begin{aligned}\int d^3r\rho_0(r)\left[\nabla u_k(r)\right]^2 = &-\int d^3r u_k(r)\nabla\left[\rho_0(r)\nabla u_k(r)\right] \\ &+\oint dS\rho_0(r)u_k(r)\nabla u_k(r)\end{aligned} \tag{255}$$

where Green's theorem has been employed. Gross and Kohn have shown in 1990 that the second term on the right-hand side vanishes for physically realistic potentials (this is the case of potentials arising from normalizable external charge densities) as they decay to zero at least as fast as $1/r$. Since the integrand on the left-hand side $\rho_0(r)\left[\nabla u_k(r)\right]^2$ is always positive (or zero if $u_k(r)$ is constant, but this would contradict equation (243)), the first term on the right-hand side cannot be zero as assumed, so $\nabla\left[\rho_0(r)\nabla u_k(r)\right] \neq 0$. This completes the proof of the Runge-Gross theorem.

Therefore, for a fixed initial state $\Psi_0$, the electron densities evolving under different external potentials must also be different. Consequently, the time-dependent density determines the external potential and hence, the wave function. Any expectation value of an observable will then be a functional of the density and the initial state. However, note that, as happened in the ground-state case, the $v$-representability problem is also present in TD-DFT, i.e., the Runge-Gross theorem does not prove the existence of the potential associated to a given electron density.

### 2.6.2 Time-Dependent Kohn-Sham Equations

In TD-DFT there is no variational principle for the energy. Nevertheless, there is a quantity analogous to the energy that plays its role in time-dependent systems. This quantity is called quantum mechanical action, $\mathcal{A}$, defined as

$$\mathcal{A}[\Psi] = \int_{t_0}^{t_1} dt \langle \Psi(t) | i\frac{\partial}{\partial t} - \hat{H} | \Psi(t) \rangle \tag{256}$$

Hence, the problem is reduced to calculate the stationary point of the action (the derivative with respect to the density must be zero). In this way, the wave function $\Psi(t)$ that makes the action stationary will be the solution of the TDSE, since the wave function itself is a functional of the density and the initial state $\Psi(t)\,[\rho, \Psi_0]$, the action will also be a functional of the density $\mathcal{A}[\rho]$.

There is not a recipe for calculating the electron density of the system, which will determine the external potential and thus, the wave function. However, this problem is attenuated when, in analogy with the ground state DFT, a Kohn-Sham auxiliary system is considered. That is a system of non-interacting electrons with the same density as the original interacting system, subject to a time-dependent external local potential, $\upsilon_{KS}$. Note that, as in the ground state, the time-dependent density is also subject to the non-interacting $v$-representability problem. Therefore, the density can be calculated from the time-dependent occupied Kohn-Sham orbitals $\phi_i(r,t)$,

$$\rho(r,t) = \sum_{i}^{occ} |\phi_i(r,t)|^2 \tag{257}$$

which obey the TDSE

$$i\frac{\partial}{\partial t}\phi_i(r,t) = \left[-\frac{\nabla^2}{2} + \upsilon_{KS}(r,t)\right]\phi_i(r,t) \tag{258}$$

If the exact Kohn-Sham potential was known, $\upsilon_{KS}(r,t)$, equation (258) could be solved exactly, obtaining thus the orbitals and the true electron density of the system. But, as in the ground-state case, there is not an exact expression for all the contributions to this potential, which are the external time-dependent field acting upon the system $\upsilon_{ext}$, the time-dependent Hartree potential (coulomb potential) $\upsilon_{Hartree}$, and a exchange-correlation potential $\upsilon_{xc}$ that includes all the non-trivial many-body effects. The exact form of this potential is unknown and in practice, it has to be approximated as a functional of the density

$$\upsilon_{KS}(r,t) = \upsilon_{ext}(r,t) + \upsilon_{Hartree}(r,t) + \upsilon_{xc}(r,t) \tag{259}$$

$$\upsilon_{Hartree} = \int \frac{\rho(r,t)}{|r-r'|} d^3r' \tag{260}$$

The Time-Dependent Kohn-Sham (TDKS) calculation starts with an initial choice of KS orbitals $\phi_i(r,0)$ that reproduces the exact density of the true initial state $\rho_0(r)$ and its first-time derivative and then, the TDKS equations (258)

propagate these initial orbitals under the KS potential, employing an approximation for the exchange-correlation potential.

There are some approximations to $v_{xc}(r,t)$, such as those based on adiabatic approximations, a time-dependent exact-exchange (EXX) functional[284] or a functional with memory.[285] In the next section, the adiabatic approximations, which are the most widely used, will be presented.

### 2.6.3 Adiabatic Approximations

The adiabatic approximation for exchange-correlation functionals in TD-DFT, $v_{xc}^{A}(r,t)$, is based on the idea that, if the perturbation that acts on the system is sufficiently slow (small time-dependence), the system will remain in its initial stationary state, (i.e., the ground state). Therefore, any of the many available approximations to the ground-state exchange-correlation functional can be employed, $v_{xc}^{gs}[\rho]$, to get the time-dependent one, just evaluating $v_{xc}^{gs}[\rho]$ at the instantaneous time-dependent density $\rho(r,t)$

$$v_{xc}^{A}(r,t) = v_{xc}^{gs}[\rho(r)]\Big|_{\rho(r)=\rho(r,t)} \tag{261}$$

The main drawback of this type of functionals is the lack of memory. The functional will be local in time and hence, all the memory of the exchange-correlation potential is erased. In addition, it will also retain the drawbacks of the chosen ground-state functional. For example, one of the most used time-dependent exchange-correlation potentials is called ALDA, which is based on LDA (Adiabatic Local Density Approximation). It takes the exchange-correlation potential for the ground state as the one of an homogeneous-electron gas (HEG). This functional is, consequently, local in both time and space. Nevertheless, it still yields good results for excitation energies. The same can be done with the other approximations of ground-state functionals, like GGA and *meta*-GGA.

$$v_{xc}^{ALDA}(r,t) = v_{xc}^{HEG}[\rho(r)]\Big|_{\rho(r)=\rho(r,t)} \tag{262}$$

### 2.6.4 Linear Response Theory

If the system is only subject to a small perturbation, there is no need to solve the full time-dependent KS equations. Considering that the system will not deviate strongly from its initial state, the focus can be put into calculating just the response of the system to first order in the perturbation. This is called linear response (LR) theory,[286] since the response of the observable, such as the density, to the first order perturbation, $v^{(1)}$, will depend linearly on it.

Hence, the total time-dependent electron density can be calculated as

$$\rho(r,t) = \rho^{(0)}(r) + \rho^{(1)}(r,t) \tag{263}$$

being $\rho^{(0)}(r)$ the initial unperturbed density, which corresponds to the ground state density, $\rho_0(r)$, and $\rho^{(1)}(r,t)$ the first order response to the perturbation.

In addition, the total external potential will consist now of

$$\upsilon_{ext}(r,t) = \upsilon^{(0)}(r) + \upsilon^{(1)}(r,t) \tag{264}$$

where $\upsilon^{(0)}(r)$ is the initial potential, i.e., the nuclear potential, and, after the initial time, the perturbation is 'turned on', $\upsilon^{(1)}$, inducing a linear response in the density,

$$\rho^{(1)}(r,t) = \int_{-\infty}^{\infty} dt' \int d^3r' \chi(r,r',t-t')\upsilon^{(1)}(r',t') \tag{265}$$

Normally, the focus is the frequency-dependent response, which is obtained through the Fourier transformation of equation (265), being $\omega$ the frequency

$$\rho^{(1)}(r,\omega) = \int d^3r' \chi(r,r',\omega)\upsilon^{(1)}(r',\omega) \tag{266}$$

The function $\chi$ is the linear density-density response function of the system. Within the Lehmann representation, $\chi$ is given by

$$\begin{aligned}\chi(r,r',\omega) = \lim_{\eta\to 0^+} \sum_{n=1}^{\infty} \Bigg[ &\frac{\langle\Psi_0|\hat{\rho}(r)|\Psi_n\rangle\langle\Psi_n|\hat{\rho}(r')|\Psi_0\rangle}{\omega - \Omega_n + i\eta} \\ &- \frac{\langle\Psi_0|\hat{\rho}(r')|\Psi_n\rangle\langle\Psi_n|\hat{\rho}(r)|\Psi_0\rangle}{\omega + \Omega_n + i\eta}\Bigg]\end{aligned} \tag{267}$$

where each $\Psi_n$ is an eigenstate of the system with energy $E_n$, and $\Omega_n$ is the excitation energy, i.e., the difference between the corresponding energy $E_n$ and the ground state energy $E_0$

$$\Omega_n = E_n - E_0 \tag{268}$$

From equation (267) it is obvious that the density-density response function has poles at frequencies corresponding to the exact excitation energies of the system. However, the response function of the interacting system is difficult to calculate and the KS system must be used instead, whose response function $\chi_{KS}$ has poles at the frequencies corresponding to the excitation energies of the non-interacting system, i.e., at the energy differences between the KS orbitals $\phi_j$ and $\phi_k$, $(\epsilon_j - \epsilon_k)$, with occupation numbers $f_j$ and $f_k$, respectively

$$\chi_{KS}(r,r',\omega) = \lim_{\eta\to 0^+} \sum_{j,k}^{\infty} (f_k - f_i)\, \frac{\phi_j(r)\phi_k^*(r)\phi_j^*(r')\phi_k(r')}{\omega - (\epsilon_j - \epsilon_k) + i\eta} \tag{269}$$

Since the KS system has the same density as the real interacting one, the linear response of the density (266) can be computed from this system

$$\rho^{(1)}(r,\omega) = \int d^3r' \chi_{KS}(r,r',\omega)\upsilon_{KS}^{(1)}(r',\omega) \tag{270}$$

The linear change of the KS potential, $v_{KS}^{(1)}$, can be calculated explicitly as

$$v_{KS}^{(1)}(r,t) = v_{ext}^{(1)}(r,t) + v_{Hartree}^{(1)}(r,t) + v_{xc}^{(1)}(r,t) \tag{271}$$

$$v_{Hartree}^{(1)}(r,t) = \int d^3r' \frac{\rho^{(1)}(r',t)}{|r-r'|} \tag{272}$$

$$v_{xc}^{(1)}(r,t) = \int dt' \int d^3r' f_{xc}(r,t,r',t')\rho^{(1)}(r',t') \tag{273}$$

where $f_{xc}$ is the so-called exchange-correlation kernel, which is defined as the derivative of the exchange-correlation potential with respect to the density

$$f_{xc}(r,t,r',t') = \frac{\delta v_{xc}(r,t)}{\delta\rho(r',t')} \tag{274}$$

Combining equations (270) and (271) with equation (266), a self-consistent equation that permits the calculation of the exact response function of the interacting system $\chi$ is obtained

$$\begin{aligned}\chi(r,r',\omega) =& \chi_{KS}(r,r',\omega) \\ &+ \int d^3x \int d^3x' \chi(r,x,\omega) \left[\frac{1}{|x-x'|} + f_{xc}(x,x',\omega)\right] \chi_{KS}(x',r',\omega)\end{aligned} \tag{275}$$

Note that equation (275), which plays the main role in LR-TDDFT calculations, is exact. However, as a consequence of not knowing the exact exchange-correlation kernel, the solution must rely on approximations.

As for the exchange-correlation functionals, there are many different approximations to the exchange-correlation kernel. The most trivial one is the random phase approximation (RPA), which sets the exchange-correlation kernel to zero. The most popular approximation coincides with the one used for the exchange-correlation potentials, the adiabatic approximation (section 2.6.3).

Equation (275) is often transformed into a matrix equation, as first derived by Casida in 1995.[287] Casida's equations are the most popular implementation in electronic structure codes to get excitation energies within the TDDFT linear response formalism and the adiabatic approximation. These matrix equations are usually written as

$$\begin{pmatrix} A & B \\ B^* & A^* \end{pmatrix} \begin{pmatrix} X \\ Y \end{pmatrix} = \omega \begin{pmatrix} -1 & 0 \\ 0 & 1 \end{pmatrix} \begin{pmatrix} X \\ Y \end{pmatrix} \tag{276}$$

where the eigenvalues $\omega_n$ are the excitation energies of the system and $A$ and $B$ are matrices with their elements defined as

$$\begin{aligned}A_{ia,jb} =& \delta_{ij}\delta_{ab}\left(\epsilon_a - \epsilon_i\right) + \\ &2\int d^3r \int d^3r' \phi_i(r)\phi_a^*(r) \left[\frac{1}{|r-r'|} + f_{xc}(r,r',\omega)\right] \phi_j^*(r')\phi_b(r')\end{aligned} \tag{277}$$

$$B_{ia,jb} = 2\int d^3r \int d^3r' \phi_i(r)\phi_a^*(r) \left[\frac{1}{|r-r'|} + f_{xc}(r,r',\omega)\right] \phi_b^*(r')\phi_j(r') \tag{278}$$

These equations are only valid for discrete spectra, and a previous ground-state DFT calculation is required to obtain the occupied and unoccupied KS orbitals, $\phi(r)$. Once equation (276) is solved the oscillator strength for each transition can be computed. This quantity measures the probability of absorption/emission for the transition. The sum of oscillator strengths calculated in a such way equals the total number of electrons in the system, thus obeying the Thomas-Reiche-Kuhn sum rule.

The so-called Tamm-Dancoff approximation (TDA),[288] neglects the backward transitions of electrons, thus setting the off-diagonal matrices B to zero and simplifying the equation (276) to the eigenvalue equation (279). As a consequence of neglecting the backward transitions, the Thomas-Reiche-Kuhn sum rule is violated in TDA

$$AX = \omega X \tag{279}$$

There are other approximations to the Casida equation, such as the small-matrix approximation (SMA), which ignores all the off-diagonal elements of both $A$ and $B$ matrices, and the single-pole approximation (SPA), which neglects the frequency-dependece of the exchange-correlation kernel.[289]

## 2.7 Statistical Thermodynamics

In previous sections, a variety of methods to obtain the electronic energy of a system have been presented, such as HF, CCSD, DFT .... However, specially when studying chemical reactions, it may be interesting to work with macroscopic thermodynamic properties. Statistical thermodynamics provides the tools to compute these properties, including entropy, enthalpy, and Gibbs free energy, through the calculation of the molecular partition function $q$.[290,291] First, it is important to remark that in all the equations non-interacting particles will be considered, so they can only be applied to an ideal gas. Within the canonical ensemble framework, the partition function depends on the temperature ($T$) and the volume ($V$). The definition of $q$ for a molecule is

$$q = \sum_i e^{-\epsilon_i / k_B T} \tag{280}$$

The sum runs over all the $i$ states of the molecule and depends on the temperature, which is multiplied by the Boltzmann constant, $k_B$. This equation can be written as a sum of energy levels instead of states, being $g_i$ the degeneracy of each level

$$q = \sum_i g_i e^{-\epsilon_i / k_B T} \tag{281}$$

For a system of $N$ indistinguishable molecules, the corresponding total partition function $Q$ is defined as,

$$Q = \frac{q^N}{N!} \tag{282}$$

which is the result of multiplying $N$ times the partition function (one for each molecule), and dividing by $N!$, to account for the indistinguishability of the molecules.

All the thermodynamic functions, like, for instance, the Helmholtz free energy ($A$) can be calculated from the partition function

$$A = -k_B T \ln Q \tag{283}$$

From this equation, and using the thermodynamic relations, several macroscopic properties, such as the pressure $p$, are computed

$$p = -\left(\frac{\partial A}{\partial V}\right)_{N,T} = k_B T \left(\frac{\partial \ln Q}{\partial V}\right)_{N,T} \tag{284}$$

It is also quite straightforward to calculate the other thermodynamic functions. In the case of the entropy $S$, the internal energy $U$, the enthalpy $H$, and the Gibbs free energy $G$, the following equations are obtained

$$S = -\left(\frac{\partial A}{\partial T}\right)_{N,V} = k_B T \left(\frac{\partial \ln Q}{\partial T}\right)_{N,V} + k_B \ln Q \tag{285}$$

$$U = A + TS = k_B T^2 \left(\frac{\partial \ln Q}{\partial T}\right)_{N,V} \tag{286}$$

$$H = U + pV = k_B T^2 \left(\frac{\partial \ln Q}{\partial T}\right)_{V} + k_B T V \left(\frac{\partial \ln Q}{\partial V}\right)_{T} \tag{287}$$

$$G = H - TS = k_B T V \left(\frac{\partial \ln Q}{\partial V}\right)_{T} - k_B T \ln Q \tag{288}$$

Hence, the partition function acts as the wave function of the system, in the sense that knowing the exact partition function, it is possible to obtain all the macroscopic properties of the system. However, as in the case of the wave function, it is not a simple task to obtain the exact partition function and, consequently, some approximations must be employed. As seen in equation (280), the partition function depends on all the states of the system, so it is generally assumed that the total energy of a molecule ($\epsilon$) can be split in translational, rotational, vibrational, and electronic ($\epsilon_{tran}$, $\epsilon_{rot}$, $\epsilon_{vib}$, $\epsilon_{elec}$, respectively) contributions. The energy levels associated with nuclear spins are usually ignored since the nuclear spins do not change during chemical reactions, so $\epsilon$ is given by

$$\epsilon \approx \epsilon_{elec} + \epsilon_{tran} + \epsilon_{rot} + \epsilon_{vib} \tag{289}$$

Consequently, the molecular partition function can be written as a product of contributions

$$q = \sum_i e^{-(\epsilon_{elec}+\epsilon_{tran}+\epsilon_{rot}+\epsilon_{vib})/k_B T} = q_{elec} q_{tran} q_{rot} q_{vib} \tag{290}$$

Now, the approximations and equations for each of the contributions to the molecular partition function will be presented, showing the calculation of the contributions to the internal energy and the entropy as an example.

In practice, a typical frequency calculation in a QM software package does these computations automatically, including all the contributions and the thermodynamic functions, such as the enthalpy and the Gibbs free energy, which are added to the electronic energy.

### 2.7.1 Electronic Contribution

In most cases, the difference in energy between the ground state and the first electronic excited state is large. Then, it can be assumed that only the ground state, whose energy is set to zero, is occupied. With this approximation, the electronic partition function is equal to the degeneracy of the ground state $g_{elec,0}$

$$q_{elec} = \sum_i g_{elec,i} e^{-\epsilon_{elec,i}/k_B T} \approx g_{elec,0} \tag{291}$$

The electronic contribution to the internal energy is obviously zero because there is no dependence on the temperature in equation (291). However, the electronic entropy will be greater than zero if $g_{elec,0} \neq 1$. From now on, the calculations of thermodynamic functions will be made for molar quantities ($Nk_B \equiv R$)[292]

$$U_{elec} = RT^2 \left( \frac{\partial \ln q_{elec}}{\partial T} \right)_V = 0 \tag{292}$$

$$S_{elec} = RT \left( \frac{\partial \ln q_{elec}}{\partial T} \right)_V + R \ln q_{elec} = R \ln g_{elec,0} \tag{293}$$

### 2.7.2 Translational Contribution

The translational partition function can be approximated considering that the molecule is free to move in a three-dimensional box of volume $V = a \cdot b \cdot c$, as in the 'particle in a box' model. The energy levels for this model are easily obtained by solving the corresponding Schrödinger equation,

$$\epsilon_{tran} = \frac{h^2}{8m} \left( \frac{n_1^2}{a^2} + \frac{n_2^2}{b^2} + \frac{n_3^2}{c^2} \right) \tag{294}$$

where $m$ is the mass of the molecule and $(n_1, n_2, n_3)$ are the quantum numbers for motion in the three directions $(x, y, z)$, respectively. Then, the translational partition function can be split into contributions for each of the directions

$$q_{tran} = \sum_{n_1,n_2,n_3} \exp\left[ -\frac{h^2}{8mk_BT} \left( \frac{n_1^2}{a^2} + \frac{n_2^2}{b^2} + \frac{n_3^2}{c^2} \right) \right] = q_{tran,x} q_{tran,y} q_{tran,z} \tag{295}$$

Keeping in mind that the translational energy levels are usually very close, the sum for each contribution can be converted into an integral,

$$\begin{aligned} q_{tran,x} &= \sum_{n_1} \exp\left( -\frac{h^2}{8mk_BT} \frac{n_1^2}{a^2} \right) = \int_0^\infty \exp\left( -\frac{h^2}{8mk_BT} \frac{n_1^2}{a^2} \right) dn_1 \\ &= \left( \frac{2\pi m k_B T}{h^2} \right)^{1/2} a \end{aligned} \tag{296}$$

The solution for the two other directions is similar, just replacing $a$ by $b$ or $c$. Substituting eq. (296) and the analogous ones for the other directions $(y, z)$, the total translational partition function is obtained

$$q_{tran} = \left(\frac{2\pi m k_B T}{h^2}\right)^{3/2} V = \frac{V}{\Lambda^3} \tag{297}$$

where $\Lambda = h/(2\pi m k_B T)^{1/2}$ is called thermal wavelength (or 'thermal de Broglie wavelength'). The volume $V$ is usually calculated with the equation for the ideal gas.

The indistinguishability $N!$ factor is included in the translational contribution when calculating the thermodynamic functions. Applying the Stirling approximation ($\ln N! \approx NlnN - N$) and taking into account that $N \equiv N_A$ (the Avogadro constant) when working with molar quantities

$$U_{tran} = k_B T^2 \left(\frac{\partial \ln(q_{tran}^{N_A}/N_A!)}{\partial T}\right)_V = RT^2 \left(\frac{\partial \ln q_{tran}}{\partial T}\right)_V = \frac{3}{2}RT \tag{298}$$

$$\begin{aligned} S_{tran} &= RT \left(\frac{\partial \ln q_{tran}}{\partial T}\right)_V + R \ln q_{tran} - k_B(N_A - N_A \ln N_A) \\ &= \frac{3}{2}R + R \ln q_{tran} - R(1 - \ln N_A) = R \ln \frac{q_{tran} e^{5/2}}{N_A} \end{aligned} \tag{299}$$

### 2.7.3 Rotational Contribution

In order to obtain the rotational partition function, the approximation known as 'rigid rotor' model is usually applied. The expression for the energy levels within this assumption varies depending on the symmetry of the molecule. In the simplest case of a linear molecule (a linear rotor),

$$\epsilon_J = \frac{h^2}{8\pi^2 I} J(J+1) = hcBJ(J+1) \tag{300}$$

where $I$ es the inertia moment of the molecule ($I = \sum_{i=1}^{N} m_i d_i^2$, where $d_i$ is the distance of atom $i$ to the center of mass), $B$ is the rotational spectroscopic constant, and $J$ is the quantum rotational number, which can have any integer positive value. The degeneracy of each rotational level, $g_{rot}$, is $(2J + 1)$.

The rotational partition function for a linear molecule at the high temperature limit, which allows the change of the sum by an integral, is therefore

$$q_{rot} \approx \frac{1}{\sigma_r} \int_0^\infty (2J+1) e^{-J(J+1)\theta_r/T} dJ = \frac{1}{\sigma_r} \frac{T}{\theta_r} \tag{301}$$

where $\sigma_r$ is the symmetry number, the number of indistinguishable orientations of the molecule, and the factor $hcB/k_B$ has been substituted by $\theta_r$, the characteristic rotational temperature.

So far, only the simplest scenario, a linear molecule, has been considered. However, the most common one is an asymmetric top molecule, which has three different moments of inertia ($I_A \neq I_B \neq I_C$). The partition function for this case has the following result (at the high temperature limit)

$$q_{rot} \approx \frac{\sqrt{\pi}}{\sigma_r} \frac{T^{3/2}}{(\theta_A \theta_B \theta_C)^{1/2}} \tag{302}$$

The rotational internal energy and entropy for this type of molecule are

$$U_{rot} = RT^2 \left( \frac{\partial \ln q_{rot}}{\partial T} \right)_V = \frac{3}{2} RT \tag{303}$$

$$S_{rot} = RT \left( \frac{\partial \ln q_{rot}}{\partial T} \right)_V + R \ln q_{rot} = \frac{3}{2} R + R \ln q_{rot} = R \ln(q_{rot} e^{3/2}) \tag{304}$$

### 2.7.4 Vibrational Contribution

For the vibrational energy of a polyatomic molecule, a sum of independent 'simple harmonic oscillators' (SHO) is normally employed

$$\epsilon_{vib} = \sum_{i=1}^{3N-6(5)} (v_i + 1/2) h\nu_i \tag{305}$$

the summation runs over all the vibrational degrees of freedom, which are $3N-5$ for linear molecules and $3N-6$ for non-linear molecules. Each vibration will have a vibrational quantum number $v_i$, which can take any integer positive value. The frequency of each mode of vibration $\nu_i$ is related to the force constant $k_i$ and the reduced mass $\mu_i$ by the following equation

$$\nu_i = \frac{1}{2\pi} \sqrt{\frac{k_i}{\mu_i}} \tag{306}$$

Substituting the expression for the energy in the partition function for a given vibrational mode $i$:

$$\begin{aligned} q_{vib,i} &= \sum_{v_i=0}^{\infty} e^{-(v_i+1/2)h\nu_i/k_B T} = e^{-\theta_{v,i}/2T} \sum_{v_i=0}^{\infty} e^{-v_i \theta_{v,i}/T} \\ &= \frac{e^{-\theta_{v,i}/2T}}{1 - e^{-\theta_{v,i}/T}} \end{aligned} \tag{307}$$

where $\theta_{v,i} = h\nu_i/k_B$ is the characteristic vibrational temperature for $i$. The vibrational partition function for all the modes is the product of their corresponding partition functions

$$q_{vib} = \prod_{i=1}^{3N-6(5)} \frac{e^{-\theta_{v,i}/2T}}{1 - e^{-\theta_{v,i}/T}} \tag{308}$$

If $\theta_{v,i}/2$ is taken as the zero energy, the last equation is transformed into

$$q_{vib} = \prod_{i=1}^{3N-6(5)} \frac{1}{1 - e^{-\theta_{v,i}/T}} \tag{309}$$

The expressions for the vibrational internal energy and the vibrational entropy are shown below

$$\begin{aligned} U_{vib} &= RT^2 \left[ \frac{\partial}{\partial T} \sum_{i=1}^{3N-6(5)} \left( -\frac{\theta_{v,i}}{2T} - \ln(1 - e^{-\theta_{v,i}/T}) \right) \right]_V \\ &= R \sum_{i=1}^{3N-6(5)} \theta_{v,i} \left( \frac{1}{2} + \frac{1}{e^{\theta_{v,i}/T} - 1} \right) \end{aligned} \tag{310}$$

$$S_{vib} = R \sum_{i=1}^{3N-6(5)} \left( \frac{\theta_{v,i}/T}{e^{\theta_{v,i}/T} - 1} - \ln(1 - e^{-\theta_{v,i}}) \right) \tag{311}$$

### 2.7.5 Transition State Theory

In a typical computational study about the reaction mechanism of a chemical reaction, the thermodynamic functions mentioned above are computed for all the stationary points, including the minima (reactants, intermediates, and products) and the first-order saddle points (transition states connecting minima). Comparing the difference in Gibbs energy between products and reactants at a given pressure and temperature, an idea about the relative stability of the products and the thermodynamic control of the reaction is obtained. However, a key factor for the viability in the formation of a specific product is the energy of the transition state, which marks the kinetic control of the reaction.

Transition State Theory (TST)[178,291] provides an equation to calculate the reaction rate constant from the difference in Gibbs free energy between the activated complex and the reactants, $\Delta G^{\ddagger}$.

Taking as an example the reaction

$$\mathrm{A} + \mathrm{B} \longrightarrow \mathrm{P} \tag{312}$$

The hypotheses of this model are that the reactant molecules (A and B) interact with each other to form a cluster of atoms, which rises in potential energy forming the so-called activated complex ($\mathrm{C}^{\ddagger}$). This activated complex is in equilibrium with the reactants, but if it acquires a critical configuration, known as transition state, the products will be formed. Hence, if the activated complex reaches the transition state, it can not return to the reactants and will always form the products

$$\mathrm{A} + \mathrm{B} \rightleftharpoons \mathrm{C}^{\ddagger} \tag{313}$$

$$\mathrm{C}^{\ddagger} \longrightarrow \mathrm{P} \tag{314}$$

From the equilibrium constant for the formation of the activated complex, an expression for its concentration can be derived

$$K^{\ddagger} = \frac{p_{\mathrm{C}^{\ddagger}} p^0}{p_A p_B} \rightarrow [\mathrm{C}]^{\ddagger} = \frac{RT}{p^0} K^{\ddagger} [\mathrm{A}]\,[\mathrm{B}] \tag{315}$$

being $p_i$, with $i$ = A, B, $\mathrm{C}^{\ddagger}$, the partial pressures, and $p^0$ the standard pressure. The rate for the formation of the product is therefore

$$r = \frac{d[P]}{dt} = k_2 [\mathrm{C}]^{\ddagger} = k_2 \frac{RT}{p^0} K^{\ddagger} [\mathrm{A}]\,[\mathrm{B}] = k[A][B] \tag{316}$$

where $k_2$ is the rate constant for the formation of the product from the activated complex, and $k = k_2 K^{\ddagger} RT/p^0$.

TST assumes that there is a particular frequency $\nu^{\ddagger}$ along the reaction coordinate that leads to the formation of the transition state. If this frequency always took the activated complex through the transition state, $k$ would be equal to $\nu^{\ddagger}$. Nevertheless, other effects, such as rotations, may play a key role. To account for this, a proportional constant $\kappa$ is included, known as the transmission coefficient

$$k_2 = \kappa \nu^{\ddagger} \tag{317}$$

$$k = \kappa \nu^{\ddagger} \frac{RT}{p^0} K^{\ddagger} \tag{318}$$

Some of these effects will slow down the formation of the transition state ($\kappa < 1$), but others will accelerate it ($\kappa > 1$). So, in most situations, $\kappa$ is assumed to be about 1.

As seen in equation (309), the partition function for the vibrational mode with frequency $\nu^{\ddagger}$ may be written as

$$q = \frac{1}{1 - e^{-h\nu^{\ddagger}/k_B T}} \tag{319}$$

The force constant for this frequency is normally very low, so the previous equation can be approximated to

$$q \approx \frac{k_B T}{h\nu^{\ddagger}} \tag{320}$$

The total molecular partition function of $\mathrm{C}^{\ddagger}$, $q_{\mathrm{C}^{\ddagger}}$, will be the result of multiplying $k_B T/h\nu^{\ddagger}$ by all the other contributions of the activated complex, which will be denoted as $\bar{q}_{\mathrm{C}^{\ddagger}}$

$$q_{\mathrm{C}^{\ddagger}} = \frac{k_B T}{h\nu^{\ddagger}} \bar{q}_{\mathrm{C}^{\ddagger}} \tag{321}$$

It is possible to express the equilibrium constant of a reaction in terms of the molecular partition functions of products and reactants,

$$K = \prod_i \left( \frac{p_i}{p^0} \right)^{\nu_i} = e^{-\Delta E_0 / RT} \prod_i \left( \frac{q^0_{m,i}}{N_A} \right)^{\nu_i} \tag{322}$$

where $q^0_{m,i}$ is the standard molar partition function of the species $i$ ($q_i(T, V^0 = nRT/p^0)/n$), whose stoichiometric coefficient is $\nu_i$, and $\Delta E_0$ is the difference in zero point energies of products and reactants. For the formation of the activated complex, the equilibrium constant is therefore

$$K^\ddagger = e^{-\Delta E_0/RT} N_A \frac{q^0_{\mathrm{C}^\ddagger}}{q^0_{\mathrm{A}} q^0_{\mathrm{B}}} \tag{323}$$

Discarding the $\nu^\ddagger$ vibrational mode of $\mathrm{C}^\ddagger$,

$$\bar{K}^\ddagger = e^{-\Delta E_0/RT} N_A \frac{\bar{q}^0_{\mathrm{C}^\ddagger}}{q^0_{\mathrm{A}} q^0_{\mathrm{B}}} \tag{324}$$

$$K^\ddagger = \frac{k_B T}{h\nu^\ddagger} \bar{K}^\ddagger \tag{325}$$

and substituting $\nu^\ddagger$ in equation (318), the Eyring equation is obtained

$$k = \kappa \frac{k_B T}{h} \frac{RT}{p^0} \bar{K}^\ddagger \tag{326}$$

An alternative version can be derived by expressing the equilibrium constant in terms of concentrations ($\bar{K}^\ddagger = \bar{K}^\ddagger_C p^0/RTc^0$, being $c_0$ the standard molar concentration)

$$k = \kappa \frac{k_B T}{c^0} \bar{K}^\ddagger_C \tag{327}$$

Taking $\bar{K}^\ddagger$ as the equilibrium constant, it can be related to $\Delta G^\ddagger$ by the thermodynamic relation $\Delta G^\ddagger = -RT \ln \bar{K}^\ddagger$. Inserting this expression in the Eyring equation (326), the following equation is obtained

$$k = \kappa \frac{k_B T}{h} \frac{RT}{p^0} e^{-\Delta G^\ddagger/RT} \tag{328}$$

## 2.8 Molecular Dynamics

Quantum chemistry packages calculate the electronic energy via *ab initio* methods and the thermodynamic properties via statistical thermodynamics, as described in the previous section. However, the computational cost of *ab initio* methods scales rapidly with the number of electrons. So, when working with large systems such as proteins or molecules linked to explicit solvents, they can not be applied efficiently. The best solution from a computational point of view is to calculate the properties of the system as ensemble averages[178]

$$\langle A \rangle = \iint A(r,p) P(r,p) dr dp \tag{329}$$

where $\langle A \rangle$ is the average of the property to be calculated, $A(r,q)$ is its value at a specific point in the phase space, and $P(r,q)$ is the probability of the system

to be at that particular point, which is related to the partition function of the system

$$P(r,p) = \frac{e^{-E(r,p)/k_B T}}{Q} \tag{330}$$

In practice, it is impossible to sample all phase space. Molecular Dynamics (MD) simulations are an useful tool to sample relevant phase points. This method consists of the numerical, step-by-step, solution of the classical equations of motion, forming a trajectory

$$F_i = m_i a_i \tag{331}$$

$$F_i = -\frac{\partial}{\partial r_i} U \tag{332}$$

In order to calculate the force acting upon every atom of the system $F_i$, the potential energy $U$ must be known, which takes into account all the bonded and non-bonded interactions. Normally, a method with low computational cost is applied to calculate this potential energy at every sampled phase point. The most common one for this type of simulations is Molecular Mechanics (MM). Although nowadays, with the boom of computational facilities, the *ab initio* MD, which aims for realistic simulations of complex systems, are growing in popularity.

In MD simulations the trajectory is completely determined by the initial phase points (initial coordinates and velocities). The initial coordinates are usually obtained from experimental sources, such as X-ray, or, alternatively, from QM calculations. In the case of the velocities, they are normally assigned in a random way such that they fulfill the Maxwell distribution at a given temperature. However, before starting the collection of relevant phase points to calculate properties of the system, the system must be equilibrated by carrying out a short MD simulation in the same conditions and with the same method as in the final stage.

### 2.8.1 Velocity Verlet Algorithm

There are many possible algorithms to perform numerical integration of the equations of motion. Note that the analytical solution of these equations can not be performed, since there are $N$ differential equations as equation (332) that are coupled with each other. Most algorithms employ a finite difference method, changing the differential of $t$ ($dt$) by a finite interval ($\Delta t$) and integrating after each time step $\Delta t$. Among them, the so-called 'velocity Verlet algorithm', similar to the 'leapfrog algorithm', is the most popular.[293] Starting from a phase point at time $t$, $(r_i(t), p_i(t))$, the potential energy is calculated and the forces $F_i(t)$ are obtained. Then, the next point after a time step $\Delta t$ is calculated as follows

$$p_i(t + \frac{1}{2}\Delta t) = p_i(t) + \frac{1}{2}\Delta t F_i(t) \tag{333}$$

$$r_i(t + \Delta t) = r_i(t) + \Delta t p_i(t + \frac{1}{2}\Delta t)/m_i \tag{334}$$

$$p_i(t + \Delta t) = p_i(t + \frac{1}{2}\Delta t) + \frac{1}{2}\Delta t F_i(t + \Delta t) \tag{335}$$

where the velocities are calculated after half the time step $p_i(t + \frac{1}{2}\Delta t)$, and are employed to move the system to the next point in space $r(t+\Delta t)$. This algorithm provides important advantages, including time-reversibility, low order in time, which permits long time steps, and calculation of the forces only once per step (much more computationally expensive than the calculation of velocities, which is straightforward).

### 2.8.2 Periodic Boundary Conditions

When simulating systems that are not periodic by nature, such as molecules or proteins in biological environments, one major concern is the presence of surface effects. If the simulation was restricted to just the system, it would be the same as surrounding it with vacuum, so surface effects may arise. In most cases, there is no interest in such effects, so a clever solution to avoid this problem is to surround entirely the system with copies of itself, in such a way that it can not 'see' vacuum at all.

Periodic Boundary Conditions (PBCs) consist of placing the system into the unit cell of an ideal crystal.[294] The unit cell must be of sufficient size to account for all the interactions but, combining PBCs with a cutoff distance for computing them, only one set of copies of the system is necessary (a total of 26 periodic images). In this way, if a molecule leaves the simulation box (the unit cell), a copy of it will automatically enter through the opposite side of the cell, keeping constant the mass, the number of particles, and the linear momentum.

Note that the length of the simulation box must be, at least, the double of the cutoff distance to avoid the double counting of the interactions. Ideally, the periodicity created in the system must not affect its physical properties. This can be corroborated by varying the size of the simulation box and checking that the results do not change.

## 2.9 Molecular Mechanics

As mentioned above, the calculation of the potential energy in MD simulations is usually carried out with MM. This method does not consider the electrons explicitly and calculates the energy taking into account only the different motions that disrupt the reference geometry of the molecule (stretching, bending, torsion, and cross-terms), and the non-bonded interactions, adding their contributions, which depend on the nuclear coordinates. In addition to its use in MD simulations, MM is also useful when treating large systems, where the number of basis sets makes the *ab initio* energy calculations computationally unfeasible.

It is worth mentioning that the absolute value for the energy obtained from a MM calculation does not have any real physical meaning. It is only useful when comparing it with the one computed at another point of the energy surface or the trajectory. Furthermore, since MM does not consider the electrons explicitly, this method can not be employed in processes where bonds are formed or broken.

There are many different options to compute every interaction, each one with its corresponding set of parameters. A collection of all the specific equations and parameters designed to calculate the potential energy is called Force Field (FF). Each FF is designed for a specific type of system, with some exceptions such as the Universal Force Field (UFF),[295] which aims for a general applicability. For instance, AMBER[296,297] and CHARMM[298] are conceived for organic molecules and biomolecules, SHAPES[299] and VALBOND[300] for transition metal compounds, PFF[301] for proteins, etc.

### 2.9.1 Non-bonded Interactions

Normally, in order to maintain the computational cost and the number of parameters as low as possible, the models used for the non-bonded potentials are quite simple. For example, the most commonly used model for van der Waals interactions is Lennard-Jones 12-6 potential[302]

$$U(r_{ij}) = 4\epsilon_{ij}\left[\left(\frac{\sigma_{ij}}{r_{ij}}\right)^{12} - \left(\frac{\sigma_{ij}}{r_{ij}}\right)^{6}\right] \tag{336}$$

This equation includes two parameters: $\sigma_{ij}$, the distance between the atoms $i$ and $j$ at which the potential is zero, and $\epsilon_{i,j}$, the maximum potential depth. Another example of a more complex model used for van der Waals interactions is the 'Hill' potential, usually employed when working with small molecules, which do not require much computational resources

$$U(r_{ij}) = \epsilon_{ij}\left[\frac{6}{\beta_{ij}-6}\exp\left(\beta_{ij}\frac{1-r_{ij}}{r^*_{ij}}\right) - \frac{\beta_{ij}}{\beta_{ij}-6}\left(\frac{r^*_{ij}}{r_{ij}}\right)^{6}\right] \tag{337}$$

where $\beta_{ij}$ is a parameter, $\epsilon_{ij}$ is defined as in equation (336), and $r^*_{ij}$ is the bond length at the minimum of energy. In the case of equation (336), $r^*_{ij} = 2^{1/6}\sigma_{ij}$.

The van der Waals interactions between atoms torsionally related (at a distance of three bonds) is normally reduced by a scaling factor.

The coulomb potential, which describes the electrostatic interaction between atomic charges, must also be added

$$U(r_{ij}) = \frac{q_i q_j}{4\pi\epsilon_0 r_{ij}} \tag{338}$$

$q_i$ and $q_j$ are the charges of atoms $i$ and $j$, respectively, and $\epsilon_0$ is the permitivity of free space.

The non-bonded contributions are present for every pair of atoms in the system. In practice, computing all of them would involve a very large number of pairwise calculations, which leads to a rise of the computational cost that is not always worthy, since the van der Waals interactions between atoms at long distances are negligible. The most popular solution to this problem is to set a cutoff distance in such a way that all the van der Waals interactions between atoms at a larger distance than the cutoff one are neglected. In MD, this is

usually combined with a 'list of neighbours' for each atom, which is updated at some points along the simulation, to avoid the calculation of the distances in every step.

### 2.9.2 Bonded Interactions

The simplest possible model to account for the stretching (equation (339)) and bending (equation (340)) potentials is the SHO. In addition to those potentials, the ones related to torsional motions are also important, but there are many other potentials that can be added to treat molecules accurately, such as cross-terms, which are included in many FFs

$$U(r_{ij}) = \frac{1}{2} k_{ij} \left(r_{ij} - r_{ij,eq}\right)^2 \tag{339}$$

$$U(\theta_{ijk}) = \frac{1}{2} k_{ijk} \left(\theta_{ijk} - \theta_{ijk,eq}\right)^2 \tag{340}$$

These equations work reasonably well in regions near the reference point, $r_{eq}$ and $\theta_{eq}$.

The most obvious improvement to the previous equations is to add higher order terms to the Taylor expansion of the potential, usually until the quartic term. Another option for the bond stretching potential is the Morse potential (equation (341)), which depends on the dissociation energy $D_{ij}$, and a fitting constant $\alpha_{ij}$, showing greater accuracy over a wider range of distances. This potential can also be used for the calculation of van der Waals interactions. Nevertheless, since it is more computationally expensive to evaluate the exponential, and most FFs are designed to study molecules close to their equilibrium values, the SHO and the quartic potentials remain as the most popular ones. This is also the case for angle bending

$$U(r_{ij}) = D_{ij} \left[1 - e^{-\alpha_{ij}(r_{ij} - r_{ij,eq}}\right]^2 \tag{341}$$

There is a torsion angle $\omega_{ijkl}$ between every four atoms connected in sequence. The most important characteristic of this angle is the periodicity, so any potential modelling torsions must also be periodic. The most common choice is an expansion of periodic functions,

$$U(\omega_{ijkl}) = \frac{1}{2} \sum_m k^m_{ijkl} \left[1 + cos\left(m\omega_{ijkl} - \gamma_m\right)\right] \tag{342}$$

where $k^m_{ijkl}$ are the amplitudes, $m$ is the multiplicity, and $\gamma_m$ is the phase factor.

### 2.9.3 Parameterization

As already mentioned, each FF employs a different set of equations with their own parameters. The process of obtaining these constants is known as parameterization. Usually, a large number of experimental measurements, including

structures and energies, are gathered, and the parameters are chosen in such a way that they minimize the errors with respect to this set of data, according to a penalty function that measures the deviation. Nowadays, the experimental data are normally complemented with information from high quality *ab initio* calculations.

The result is a set of parameters for each atom considered in the FF. However, the parameters for a specific atom may work extremely well in a molecule but don't work at all in another one. This is because two atoms with the same atomic number may have very different behaviours depending on their oxidation state, the hybridization, the atoms to which they are bonded, etc. As a consequence, FFs have parameters for 'atom types', which are atoms that are similar enough, so they can be treated in an identical way even if they are in different molecules. The number and definition of atom types depend on each FF.

As an example, the General AMBER FF (GAFF)[303] has five different 'atom types' for the carbon: 'c' for a $sp^2$ C bonded to O or S, 'c1' for a $sp^1$ hybridization, 'c2' for an aliphatic $sp^2$ C, 'c3' for a $sp^3$ C, and 'ca' for a $sp^2$ carbon in an aromatic ring, whereas AMBER[296,297] has more than 20 carbon types.

One of the disadvantages of the FFs is that, since they are designed for specific purposes, some atoms or bonds in the system at hand may not have available parameters. In this scenario, there are several alternatives: change to a FF where all the necessary parameters are included, parameterize the missing ones according to the procedure described above, or use a method, such as the Seminario method,[304] to obtain these parameters directly from the output of *ab initio* calculations.

The Seminario method is mainly used for metal-containing systems, and it allows the calculation of harmonic force constants involving the metal atom, which is not likely to be parameterized in the most popular FFs, from the Hessian matrix. The VFFDT software,[305] which offers parameters from the output of frequency calculations, has an algorithm based on the Seminario method.

## 2.10 Solvation Models

So far, only calculations in gas phase have been covered. However, many reactions occur in solution and the solvent may not have a key role in the reaction, but it always has some kind of influence and there are examples where its presence or absence can lead to different results (e.g., Menshutkin reaction[306]). Therefore, the effect of solvent in the treatment of reactions in solution should always be considered somehow.

### 2.10.1 Explicit Models

The most obvious and computationally expensive option to account for solvent effects is to include explicit solvent molecules in the system. In this sense, the solvent is treated with the same theory level as the rest of the system, most

likely with a QM method, providing the most accurate model for solvation when enough and properly located solvent molecules are considered.[307]

This treatment greatly limits the number of solvent molecules that can be included in the calculation, typically only few molecules that may have importance in the problem at hand, forming a solvent cluster. Along with the large computational cost, there is a huge number of degrees of freedom due to the different orientations of the solvent molecules, which raises the difficulty of finding relevant stationary points on the PES.[308] In addition, most of the solvent effects are missing with this treatment since only local or 'short-range' effects between the solvent molecules and the system will be present, contrary to the 'long-range' effects associated with the remaining solvation shells,[309] such as solvent polarization, which require a large number of solvent molecules.

Another option would be considering all the system (solute + solvent) with MM combined with a MD simulation. Although this treatment allows a large number of solvent molecules in the calculation, it is useless for studying chemical reactions since MM cannot describe the formation and breakage of chemical bonds. The low computational cost of this treatment also comes with a huge cut in the accuracy of the results, so normally, it is only employed as a preliminary method to prepare an input for higher level calculations or to study very large systems in solution, such as proteins. There are specific FFs designed to treat solvents. For example, the most popular models for water are called TIPXP, where X is an integer number (typically 3 or 4)[310] indicating the number of spots for the evaluation of the energy, which are parameterized accordingly. They also constrain the geometry of the solvent molecules to lower the number of degrees of freedom.

A solution to some of the problems of QM and MM treatments consists of combining them in a QM/MM calculation.[178] Typically, if the solute is not too big (like a protein or an enzyme), it can be entirely treated with a QM method. Even some solvent molecules or the first solvation shell may be also included in the QM calculation in the so-called QM region or 'layer' and the rest of the solvent is modelled with MM, normally with one of the FFs designed for that specific solvent in the MM region. This method provides accurate results, accounting for both the short-range and the long-range (through interaction between the QM and MM regions) effects. Nevertheless, the large number of molecules comes with a huge number of degrees of freedom, making the optimization calculations quite tedious, specially for the optimization of TSs. Indeed, the total Hamiltonian (solute + solvent) in a QM/MM calculation has three different terms,

$$\hat{H} = \hat{H}_{QM}^{solute} + \hat{H}_{MM}^{solvent} + \hat{H}_{QM/MM}^{int} \tag{343}$$

the first one is the Hamiltonian of the QM region, the second term is the MM Hamiltonian corresponding to the solvent (the MM region), and the last one is the Hamiltonian that accounts for the interaction between both regions. Each of them depends on their corresponding degrees of freedom, with the interaction term depending on the degrees of freedom of both types of molecules.

In practice, this treatment is employed for single-point calculations or in reactions with a defined reaction path where Free Energy Perturbation (FEP) calculations can be carried out in conjunction with MD or Monte Carlo simulations.[311]

Note that, although QM/MM is a hybrid model, it will not be included in the hybrid section of the solvation models since it accounts for all the solvent molecules, both in the QM and the MM regions, in a explicit and discrete manner.

### 2.10.2 Implicit Models

The most popular treatments to account for solvation effects are the so-called continuum solvation models. These methods provide the inclusion of the solvent in an implicit manner, i.e., the solvent molecules are modelled by a continuous medium to reproduce some of its macroscopic properties. In this way, the degrees of freedom of the solvent are greatly reduced by employing a distribution function to describe it, in a similar way to the use of the electron density instead of the wave function in DFT. Furthermore, the Hamiltonian term corresponding to the solvent is completely removed, leaving an effective Hamiltonian for the solute.[312] Hence, the distribution function should only give a good description of the interaction with the solute, not of the solvent itself

$$\hat{H}^{eff} = \hat{H}^{solute} + \hat{H}^{int} \tag{344}$$

$$\hat{H}^{eff}|\Psi\rangle = E|\Psi\rangle \tag{345}$$

Now, the interaction potential only depends on the degrees of freedom of the solute and the distribution function of the solvent, which will vary depending on the implicit model of choice, although most of the continuum solvation models describe the solvent as an isotropic dielectric continuum characterized by its permitivity $\epsilon$.

In order to get a good description of $\hat{H}^{int}$, the concept of free energy of solvation, $\Delta G_{solvation}$, is employed,[178] which is the most important quantity used to evaluate the solvent effects in a solute. It is defined as the change in free energy of the solute associated with moving it from the gas phase to the condensed phase. It can be negative or positive, depending on the specific interactions between the solvent and the solute. There are different contributions to $\Delta G_{solvation}$ in the continuum solvation models, such as cavitation, electrostatic, repulsion, and dispersion interactions.

$$\Delta G_{solvation} = \Delta G_{cav} + \Delta G_{el} + \Delta G_{dis} + \Delta G_{rep} \tag{346}$$

The cavitation term, $\Delta G_{cav}$, refers to the change in free energy associated with the creation of a cavity for the solute within the solvent continuum medium, characterized by a dielectric constant. This term is always positive. There are many different choices for the size and shape of the cavity depending on the model. Ideally, the cavity should have a physical meaning and contain all

the charge distribution of the solute, although, in practice, there will always be some overlap between this charge distribution and the one of the solvent, which is called, referring to the fraction of the charge distribution from the solute outside the cavity, 'escaped charge' or 'outlying charge'. For the sake of simplicity, that fraction of the charge distribution of the solute is usually ignored.

The choice for the shape and size of the cavity is a compromise between accuracy and computational cost. From a computational point of view, cavities with simple shapes, such as spheres or ellipsoids, are much easier to compute than cavities with complex shapes. On the other hand, a shape that is as similar as possible to the solute shape is the most accurate choice, although it is usually very different from a sphere or an ellipsoid. There is a wide variety of techniques for this purpose,[309] with a different range of accuracy and computational requirement.

An accurate choice, although not widely used, consists of defining the cavity with an isodensity surface.[313,314] With this technique, a density value is given and the cavity is derived from the electronic distribution.

A related technique calculates the interaction between the solute and an atomic probe (normally a rare gas atom) placed at different positions in the molecular space, obtaining a set of three-dimensional isoenergy surfaces. It employs an Atoms in Molecules analysis (see section 2.11.1) of the solute and the atomic probe to get the surface for the cavity. Both techniques provide a realistic definition of the cavity at the expense of being computationally demanding.

The most widely used cavitation methods, with a fairly low computational cost and unrealistic but not too simplistic results, are based on constructing the cavity using the van der Waals radii of the atoms of the molecule. First, a set of radii must be chosen. Some of the most popular tabulations are those proposed by Bondi,[315] Pauling,[316] and the set of radii from the UFF.[295] The latter is the one employed by default in many QM packages, including Gaussian.[184] Then, the surface of the cavity is obtained by superposing the vdW spheres of all the atoms. Sometimes the radii are scaled to change the cavity size, for instance, Gaussian 16 employes a scaling factor of 1.1. Other examples of cavitation techniques are GEPOL[317] and DefPol.[318]

The cavitation energy is usually calculated using Pierotti's model,[319–321] which is based on the scaled particle theory. It calculates $\Delta G_{cav}$ by dividing the process in two steps, each one with its corresponding contribution. First, the work for creating the cavity is calculated as the free energy required to introduce hard-sphere molecules of the appropriate radius into the solvent, so they produce the cavity. Then, the free energy for placing the solute molecule inside the cavity is computed as the work associated with giving the cavity the proper electronic distribution to mimic the actual solute. Within this model, $\Delta G_{cav}$ is calculated according to the following formula,[312]

$$\Delta G_{cav} = K_0 + K_1 R_{MS} + K_2 R_{MS}^2 + K_3 R_{MS}^3 \tag{347}$$

where $R_{MS}$ is the radius of the hard-sphere molecules used to create the cavity, which is the sum of the radius of the solvent and the solute molecules $R_{MS} =$

$R_M + R_S$. The cavity must exclude the center of the solvent molecules. The coefficients $K_i (i = 0, 1, 2, 3)$ depend on properties from the solvent.

The electrostatic interactions between the solute and the solvent can be calculated as $\Delta G_{el} = G_{el} - G_0$, being $G_0$ the *ab initio* energy of the isolated solute, and $G_{el}$ the analogous energy calculated in solution. Contrary to the cavitation energy, the electrostatic interactions are always attractive (unless there are no electrical moments in the solute, in which case they are null). These interactions are described in a self-consistent manner and are the most important contribution to $\Delta G_{solvation}$. The electronic distribution of the solute, described either with $\rho(r)$ or as discrete point charges, is located inside the cavity created in the dielectric continuum (normally called reaction field), where it polarizes the solvent. At the same time, the solvent also induces a change in the charge distribution of the solute. This change will polarize again the solvent, which in turn produces another polarization to the solute, and so on. The process continues until the polarization between both of them stops. This occurs when the energy gained from the polarization coincides with the energy required to achieve it. Numerically, it is solved by an iterative procedure. The result is a modified $\rho(r)$ of the solute, which should be the one used to calculate any property in solution, and an electrostatic interaction potential to insert into the effective Hamiltonian of the solute.

The basic model for calculating the electrostatic interactions between the solute, described as $\rho(r)$, and the dielectric continuum, characterized by a dielectric constant $\epsilon$, employs the Poisson equation, in conditions of zero ionic strength, it is expressed as,[178]

$$\nabla^2 \phi(r) = -\frac{4\pi\rho(r)}{\epsilon} \tag{348}$$

where $\phi(r)$ is the electrostatic potential at point $r$, the sum of the electrostatic potential from the solute's charge density in vacuum, $\phi_M(r)$, and the potential generated by the polarization of the dielectric medium. The latter is usually called reaction potential, $\phi_R(r)$. This equation is valid when the dielectric medium responds in a linear fashion to the charge density. However, there are two regions in the problem, inside and outside the cavity. So, the general Poisson equation

$$\nabla \left[\epsilon(r) \nabla \phi(r)\right] = -4\pi\rho(r) \tag{349}$$

can be simplified for each of the regions.[309] Inside the cavity, since the solute is in vacuum, $\epsilon(r) = 1$,

$$\nabla^2 \phi(r) = -4\pi\rho(r) \tag{350}$$

and outside the cavity, where $\rho(r) = 0$ and $\epsilon(r) = \epsilon$

$$-\epsilon \nabla^2 \phi(r) = 0 \tag{351}$$

Equations (350) and (351) are only valid if the escaped charge is neglected. The $\epsilon$ inside the cavity is not a function and there are no electrolytes within

the solvent. Furthermore, there are some conditions that these equations must fulfill. At infinite distance

$$\lim_{r\to\infty} r\phi(r) = \alpha \tag{352}$$

$$\lim_{r\to\infty} r^2\phi(r) = \beta \tag{353}$$

where $\alpha$ and $\beta$ are finite numbers. For the boundary of the cavity (the surface),

$$\phi_{in} = \phi_{out} \tag{354}$$

this means that the interaction potential in neighbouring points inside and outside the cavity must be identical. Another condition is

$$\frac{\partial\phi_{in}}{\partial n} = \epsilon\frac{\partial\phi_{out}}{\partial n} \tag{355}$$

where $n$ is the normal vector of the cavity surface pointing outwards.

All this set of equations is the basis of the continuum solvation models. However, there are many methods to solve them, which are normally grouped into six different categories: the apparent surface charge (ASC) methods, the multipole expansions (MPE) methods, the generalized Born approximation (GBA), the image charge (IMC) methods, the finite element methods (FEM), and the finite difference methods (FDM). The focus will be made into the ASC methods, which are implemented in most QM packages and will be frequently used throughout this thesis.

All the different ASC methods have in common the strategy to represent the reaction potential, $\phi_R(r)$: the use of an apparent surface charge (ASC) distribution $\sigma(s)$ spread on the cavity surface. Hence, the total electrostatic potential at any point $r$ inside the cavity is

$$\phi(r) = \phi_M(r) + \phi_R(r) = \int_C \frac{\rho(r)}{|r-r'|}dr' + \int_S \frac{\sigma(s)}{|r-s|}ds \tag{356}$$

The first term is the electrostatic potential generated by $\rho(r)$, which is calculated by integration over the whole volume of the cavity (neglecting the escaped charge). The second term is the reaction potential, caused by the ASC distribution, $\sigma(s)$, and it is obtained by integration on the cavity surface ($S$). With this formulation, the reaction potential is exact if $\sigma(s)$ is defined properly, although the integration over the cavity surface may be challenging if the shape is complex. In that case the integral is normally discretized with the technique known as boundary element method (BEM). Using this approach, the reaction potential is calculated as a finite sum

$$\phi_R(r) \approx \sum_k \frac{q_k}{|r-s|} \tag{357}$$

In addition, there are different formulations for computing $\sigma(s)$, all based on the dielectric constant of the medium, along with the shape and size of the cavity, and the electronic properties of the solute at $S$.

The oldest ASC method is called Polarizable Continuum Model (PCM).[322] Nowadays, the term PCM groups a variety of models based on the same assumptions, including the original method (now called DPCM)[323] and more recent formulations, such as CPCM and IEFPCM.

In DPCM,[312] the ASC distribution is expressed in terms of the polarization vectors $\vec{P}_i$ and $\vec{P}_j$ of each of the different regions (with different dielectric constants) that the surface separates

$$\sigma_{ij} = -\left(\vec{P}_j - \vec{P}_i\right) \cdot \vec{n}_{ij} \tag{358}$$

The polarization vectors are obtained from the gradient of the total potential and the dielectric constant at the corresponding region,

$$\vec{P}_i(r) = -\frac{\epsilon_i - 1}{4\pi} \nabla\phi(r) \tag{359}$$

in the considered case, where the dielectric function inside the cavity is always 1, the polarization vector in this region is null, $\vec{P}_i = 0$. Therefore, equation (358), in the boundary between the cavity and the solvent, is simplified to

$$\sigma_{ij} = \frac{\epsilon_j - 1}{4\pi} \nabla\phi_{out}(r) \cdot \vec{n}_{ij} = \frac{\epsilon_j - 1}{4\pi\epsilon_j} \nabla\phi_{in}(r) \cdot \vec{n}_{ij} = \frac{\epsilon_j - 1}{4\pi\epsilon_j} \frac{\partial \left(\phi_M + \phi_R\right)_{in}}{\partial \vec{n}} \tag{360}$$

where the relation between the gradient of the potential inside (region $i$) and outside (region $j$) the cavity, expressed in equation (355), has been employed. This method for calculating $\sigma$ is called exact dielectric boundary condition (EDBC).

The Conductor-like Screening Model (COSMO)[324] is another ASC method, but based on the idea of changing the finite value of the dielectric constant characteristic of the solvent by the one from a conductor, (i.e., $\epsilon = \infty$). This approximation simplifies the electrostatic equations for the reaction potential, since, if the solvent is an ideal conductor, the electric potential on the cavity surface vanishes and the ASC distribution is now defined by the local value of the potential instead of its normal component gradient as in equation (360). In this type of models, the charge density corresponding to the conductor, $\sigma^*$, must be scaled to account for the electronic properties of the actual solvent with a finite $\epsilon$. This is done with a function that depends on $\epsilon$

$$\sigma(s) = f(\epsilon)\sigma^*(s) \tag{361}$$

This scaling function has been determined empirically with the following formula

$$f(\epsilon) = \frac{\epsilon - 1}{\epsilon + k} \tag{362}$$

In the original COSMO model, $k$ was suggested to have a 0.5 value. Other conductor-like models, including CPCM,[325] which is another PCM model, developed to benefit from the conductor-like approach of the solvent, adopt $k = 0$ instead. Depending on the source, the preferable choice for $k$ varies from 0[326] to 0.5.[327]

In 1997, Cances *et al*[328–330] introduced a new ASC model, the so-called integral equation formalism (IEF). The original IEF method is more general than any of the continuum models mentioned before, as it can even be used for anisotropic solvents. A simplified modification of IEF, at the cost of being again restricted to isotropic media, was developed by Mennucci *et al.*,[331] and belongs to the PCM family of models, being known as IEFPCM. This is the default PCM model of many computational codes, including Gaussian,[184] and it is very similar[332] to the SS(V)PE model from Chipman,[333] who put the focus on correcting the polarization error from the charge density outside the cavity, which is not treated in any of the previous models.

In IEFPCM, the potentials are expressed in terms of Green's functions, and its equation to get the ASC is formulated using two integral operators $A$ and $g$

$$A\sigma = -g \tag{363}$$

This formulation provides several advantages. The most important is that it depends on the reaction potential, as the COSMO model, rather than in its normal component, like in DPCM. As a consequence, the calculation is much more numerically stable along with a lower computational cost. In addition, it provides a correction for the error induced by the escaped charge, similar to the SS(V)PE model.

It is also remarkable that both the DPCM and CPCM formulations are contained in the IEFPCM one as special subcases.

As stated before, all these models must be solved iteratively, since the ASC distribution depends on the charge distribution of the solute through the reaction potential, and vice versa. The steps for solving the equations wil be presented using the most simplistic model, DPCM with the BEM formulation.

Coming back to equation (344), the effective Hamiltonian is divided into the Hamiltonian of the solute and the Hamiltonian for the interaction between the solute and the solvent, which is calculated as the integral of the product between the charge distribution of the solute $\rho_M$ (with both its electronic and nuclear components) and the reaction potential, $\phi_R$, which depends on $\sigma$. Therefore, the calculation of the interaction potential requires $\rho_M$ and the discrete charges at the cavity surface, $\{q_k\}$, which are obtained according to equation (360) in the case of DPCM.

A typical iterative solution of DPCM with BEM[309] consists of starting with an initial guess for $\rho_M$, normally the charge distribution of the solute in vacuum is taken for this step, and $\phi_M$ is calculated as the integral of equation (356) over the cavity volume. Then, an initial set of charges, $\{q_k\}$, is derived from equation (360). Note that these charges are not correct, since the reaction potential $\phi_R$ has not been introduced yet. This initial guess for $\{q_k\}$ is used to get $\phi_R$, and another set of charges is calculated from equation (360). The iterative procedure is repeated again with fixed $\rho_M$, until convergence is achieved. From the final set of $\{q_k\}$, the effective Hamiltonian is defined and the Schrödinger equation (345) is solved, resulting in a new charge distribution for the solute. The iterative calculation of $\sigma$ described above is performed again using the new $\rho_M$, leading

to a different effective Hamiltonian, and so on. This process continues until self-consistency.

All the aforementioned models belong to the so-called self-consistent reaction field (SCRF) methods, since all of them are based on placing the solute inside a cavity (the reaction field) and their equations must be solved in a self-consistent manner, as described above.

Dispersion interactions are always present when two (or more) molecules are at a finite distance. They are always attractive and they are consequence of correlation effects, so they can not be treated with a HF description. Its origin relates directly to the correlated motions of the electrons between the corresponding systems. In the case of solvation, the positions of the solute electrons are affected by the ones of the solvent, and vice versa.

There are several options for calculating the dispersion energy, $\Delta G_{dis}$. They are grouped into the ones using a discrete (pair-potentials) or a continuum approximation,[312] although the latter would be more desirable for an implicit solvation model, which treats the solvent as a continuum.

On the other hand, the repulsion energy, consequence of the steric repulsion generated when the solute is introduced into the cavity, is also called exchange energy. The reason is that its main contribution in the perturbation theory of intermolecular interactions comes from the exchange operator between the electrons of the solute and the solvent.

The dispersion and repulsion interactions are usually grouped together into a dispersion-repulsion term, $\Delta G_{dis-rep}$, since they are calculated together to minimize the error from couplings. Normally, these contributions are obtained along with the electrostatic interactions, mainly for two reasons: to benefit from the equations and the discretization of the cavity surface necessary to compute those interactions, and to account for the change in $\rho_M$ due to the dispersion and repulsion potentials.

The most popular model used for obtaining the solute-solvent dispersion and repulsion interaction energies has been proposed by Floris and Tomasi,[334,335] and mixes a pair-potential approximation with the use of a continuum distribution.

### 2.10.3 Hybrid Models

In general, the use of implicit models provides good results in solution. However, they lack many important features that are present when studying systems in solution with explicit solvation models, such as solvent structure characteristics from the first shells of solvation. On the other hand, as already mentioned, the explicit treatment comes with a large computational cost.

The hybrid models try to put together the benefits of both approaches. The most simple examples of hybrid models consist of treating with a QM method the solute and some explicit molecules (a cluster or the first solvation shells), and using an implicit solvation model for the long-range effects of the solvent. This can also be done in a QM/MM method, where the implicit solvent may be considered as a third layer (QM/MM/Continuum).

Another approximation within the hybrid models relies on the use of correlation functions for the solvent. Instead of using a continuum solvation model or an explicit solvation model, the methods based on this technique employ a pair correlation function (PCF) or a radial distribution function (RDF) to determine the probabilistic structure of the solvent.[308]

The Reference Interaction Site Models (RISM),[336] such as 1D-RISM and 3D-RISM, are examples of these type of hybrids. They employ statistical mechanics along with solvent distributions to improve the description of solvation without a large raise in the computational cost. Other examples of hybrid models are those proposed by Zhu and Krilov,[337] whose model accounts for the short-range effects by decreasing the number of solvation shells and removing the PBC, or by Grid Cell Theory (GCT),[338] which employs a 3D grid around the solute to calculate the enthalpy and entropy contributions of the free energy of solvation.

## 2.11 Methods of Analysis

So far, many methods and approximations to solve the Schrödinger equation have been presented. They result in information about the geometry, the energy, and other observables of the wave function. However, in many instances, this does not help to clarify the problem at hand and tools to connect the results from the quantum chemistry calculations to the 'traditional' language of chemistry (e.g. charges, aromaticity, reactivity, etc) are interesting.

In this section, several methods to obtain chemical properties through the analysis of the wave function or the electron density will be covered.

### 2.11.1 The Theory of Atoms in Molecules

The distribution of the electron density in a system is directly related to its structure features, such as atoms, bonds, ... Hence, the idea behind Bader's theory of Atoms in Molecules (AIM)[339] is to use the topology of the electron density to extract chemical information from the wave function. This theory is based on the generalized action principle, which demonstrates that all matter is composed of interacting open systems, where the systems are defined by the topology of the density and each one can be identified as an atom in a molecule.

Thus, the distribution of the electron density $\rho(r)$ provides a useful tool for mapping all the structural and stability concepts of a molecule. All the maxima, minima, and saddle points of the electron density are critical points, whose position is denoted by $r_C$, where the gradient of the electron density is zero, $\nabla\rho(r_C) = 0$.

To analyse the nature of each critical point, one must consider the Hessian matrix of $\rho(r_C)$, formed by nine second derivatives $H_{ij} = (\partial^2\rho(r_C))/(\partial r_i \partial r_j)$ $(i, j = 1, 2, 3)$. This matrix is real and symmetric and hence it can be diagonalized to obtain a set of three eigenvalues and their associated eigenvectors. The sign of each eigenvalue corresponds to the curvature of the electron density in the direction defined by its eigenvector. The curvature is negative at a maximum, and positive at a minimum. Each critical point is labelled with the

notation $(\omega, \sigma)$, where $\omega$ is the rank of the critical point, the number of nonzero curvatures, and it is normally 3 for critical points of energetically stable configurations; $\sigma$ is its signature, the sum of the algebraic signs of the eigenvalues.

The critical points with $\omega < 3$ are said to be degenerate and are unstable. Thus, the elements of the molecular structure correspond to critical points of rank 3. There are four possible critical points of rank 3:

- (3,-3). All the curvatures of the electron density are negative in this critical point and is therefore a local maximum. The coordinates of this critical point are located at the position of a nucleus as a consequence of the dominance of the attractive force between electrons and nuclei, which leads to an accumulation of electron density at this position.

- (3,-1). Two curvatures are negative and hence, the electron density is a maximum in the plane defined by the two associated axes (eigenvectors). The third curvature is positive, corresponding to a minimum in the axis perpendicular to the plane. This type of critical point is always found between two nuclei that are considered to be 'bonded', as explained below.

- (3,+1). Two curvatures are positive, so the electron density is a minimum in the surface defined by the two corresponding eigenvectors. The third curvature is negative and thus, $\rho(r)$ is a maximum at the axis perpendicular to the surface.

- (3,+3). All the curvatures are positive and, therefore, the electron density is a local minimum at this critical point.

In addition to the critical points, it is possible to extract information of the molecular structure from the gradient paths. The gradient paths are trajectories of $\nabla\rho(r)$, which are constructed as follows: starting from a point in space $r$, the gradient of the density at $r$ is calculated, determining the direction of maximum increase in $\rho(r)$. Then, the gradient is calculated again after moving along that given direction. This procedure is repeated until the gradient path finishes at a critical point, which must be a maximum in that direction. Therefore, every gradient path starts and terminates at a critical point, although it can also originate from a point at infinite distance from the maximum, e.g., an isolated atom is a maximum where all the gradient paths conclude, but there are not any other critical points that act as origin of the paths. The two trajectories linking bonded nuclei through a common origin, which is located at a (3,-1) critical point, form a line of maximum charge density (all the points in this line, including the critical point, are maximum in the directions perpendicular to it) that is called bond path, and the critical point is thus referred as a bond critical point (BCP). In addition, when a set of bond paths form a ring, a (3,+1) critical point is always found in its interior, so it is called ring critical point (RCP). It happens the same for the (3,+3) critical points, they appear when the bond paths are arranged in such a way that they form a cage (enclosed by at least two ring surfaces), then it is called cage critical point (CPC).

Since the (3,-3) critical points, which have already been identified as nuclei, act as attractors where the gradient paths terminate but never originate, a molecular system can be divided into different regions, each one containing an attractor (3,-3) critical point. These regions are called basins and are defined by all the gradient paths that terminate at the nucleus. In that sense, an atom can be defined as the conjuction of the (3,-3) critical point and its basin, e.g., the basin of an isolated atom is the entire space. Hence, some portions of this boundary may be infinitely distant from the attractor, but others are common to other basins forming an interatomic surface $S_{AB}$ of 'zero-flux' (no trajectories cross this surface). This surface fulfills the mathematical condition $\nabla\rho(r) * \mathbf{n} = 0$, where $\mathbf{n}$ is the normal vector of the surface, and it implies the presence of a BCP between atoms A and B. In fact, the interatomic surface can also be defined as the surface formed by all the gradient paths whose termination is the BCP (note that the bond path originates at the BCP so this trajectory does not belong to the interatomic surface).

Although some chemical information can be directly extracted from the presence of critical points, e.g., a BCP is an indicator of a bond between two atoms. It is possible to get many more properties within this theory. For instance, once the basin of an atom is defined, the calculation of its charge is straightforward: substract the total number of electrons in its basin, i.e., the integral of the electron density in that space, $\Omega$, to the atomic number of the nucleus, $Z_k$

$$q_k = Z_k - \int_{\Omega_k} \rho(r)dr \tag{364}$$

The partial charges obtained from this method are not very good compared to other methods. The main reason is that, since the charge is calculated from the number of electrons at the whole basin, the density located close to the nucleus has the same weight as the density situated at the boundaries of the basin. For example, the AIM charges at a saturated hydrocarbon are positive for the carbons and negative for the hydrogens.[178]

In the same manner that the electron density can be used to define atoms in space, it is possible to employ the so-called electron pair density or two-particle density to 'locate' pairs of electrons and obtain localization and delocalization indexes. The electron pair density $\rho_2(r_1, r_2)$ is the diagonal of the second order reduced density matrix, defined as the probability of finding simultaneously two electrons in the volumes $dr_1$ and $dr_2$.[340] Note that if the electrons are not correlated, the electron pair density is the product of the probability of finding the first electron at $dr_1$ and the probability of finding the second electron at $dr_2$, $\rho_2(r_1, r_2) = \rho(r_1)\rho(r_2)$. However, a term accounting for the change in the probability of finding a second electron at $dr_2$ once the first electron is located at $dr_1$ must be added. This term is normally called exchange-correlation hole, $\rho_2^{xc}(r_1, r_2)$, and it is closely related to Pauli's exclusion principle, i.e., the probability of finding two electrons with the same spin close to each other decays to zero.

The localization ($\lambda$) and delocalization ($\delta$) indexes can be computed from $\rho_2^{xc}(r_1, r_2)$, integrating in the same atomic basin or in two atomic basins, re-

spectively,[341,342]

$$\lambda(A) = \int_{\Omega_A}\int_{\Omega_A} \rho_2^{xc}(r_1, r_2) dr_1 dr_2 \tag{365}$$

$$\delta(A, B) = 2\int_{\Omega_A}\int_{\Omega_B} \rho_2^{xc}(r_1, r_2) dr_1 dr_2 \tag{366}$$

$\lambda(A)$ can be interpreted as a measure of the number of electrons localized in the basin of atom A, and $\delta(A, B)$ as the number of electron pairs shared or delocalized between the atomic basins A and B, which resembles the classical Lewis picture. Therefore, if the two atoms are bonded to each other, the delocalization index (DI) can be interpreted as the bond order. For an atom A, it is possible to get its total number of electrons with these indexes and, consequently, the total number of electrons can be obtained as well

$$N(A) = \lambda(A) + 1/2 \sum_{B \neq A} \delta(A, B) \tag{367}$$

It is also remarkable that the DI is related to the covariance of the electronic population of atoms A and B. If there is a bond between these atoms, their populations are statistically correlated.[341]

### 2.11.2 Nucleus-Independent Chemical Shifts (NICS)

There are many ways of obtaining an estimation of the aromaticity in a system. One of the most popular methods consists in determining the chemical shifts in aromatic rings.[343] Originally some atoms, like H or Li, were used in bridging positions for a direct calculation of chemical shifts through $^1$H and $^7$Li NMR, respectively (either theoretically or experimentally). However, these atoms can perturb the wave functions of the system under consideration. Schleyer and coworkers proposed the Nucleus-Independent Chemical Shifts (NICS) method as solution.[344]

NICS indices correspond to the negative (change of sign) of the magnetic shielding computed usually at ring centres or points above (or below) the rings. On the one hand, negative values of NICS inside rings or cages indicate the presence of induced diatropic ring currents or 'aromaticity'. On the other hand, positive values denote paratropic ring currents and 'antiaromaticity', whereas the value of zero corresponds to 'nonaromaticity'.

However, chemical shifts in organic molecules are affected by the $\sigma$ framework. This leads, for example, to non-zero values of NICS in nonaromatic rings. The influence of the $\sigma$ contribution decreases as the ring size increases (the ring centre is further from the C-C and C-H bonds). For relatively small and planar rings, the best solution comes from evaluating the NICS in points 1 Å above the ring centre, NICS(1), where the electron density from the $\pi$ orbitals is maximum and the $\sigma$ contribution is minimum. Therefore, NICS(1) is the recommended measure of the $\pi$ electron delocalization rather than NICS(0), which computes NICS at the ring centre.[345]

NICS values can be computed in QM programs such as Gaussian[184] by carrying out NMR calculations (in optimized molecular structures) and using ghost atoms for designating the positions for the NICS evaluations. Experimentally, NICS can be approached using inert probe atoms at distant positions. For example, $^3$He NMR has been used to obtain NICS from fullerene centres,[346] in good agreement with theoretical results.

### 2.11.3 Natural Bond Orbital Analysis

The first order reduced density matrix (1-RDM) $\gamma_1(r'_1, r_1)$ has special importance in electronic structure theory. It differs from $\rho(r)$ since it is calculated with two sets of coordinates. However, its diagonal, $\gamma_1(r_1, r_1)$, corresponds to the electron density function $\rho(r_1)$, furthermore, its trace is the total number of electrons in the system, $N$. The 1-RDM thus lies between the electron density and the wave function. Some methods obtain the ground state properties of a system through functionals of the 1-RDM, such as the Reduced Density Matrix Functional Theory (RDMFT).[347] RDMFT benefits from the fact that the kinetic energy is an explicit functional of $\gamma_1$, so the introduction of a fictitous non-interacting system is no longer necessary.

Instead of deepening on the functionals of the 1-RDM, its use for connecting the results from a quantum chemical calculation to the classical Lewis picture of bonds and pairs of electrons will be presented[173]

$$\gamma_1(r'_1, r_1) = N \int \psi^*(r_1, r_2, \ldots, r_N)\psi(r'_1, r'_2, \ldots, r'_N)dr_2 \cdots dr_N \tag{368}$$

$$\mathrm{Tr}\gamma_1(r'_1, r_1) = \int \gamma_1(r_1, r_1)dr_1 = N \tag{369}$$

$$\gamma_1(r_1, r_1) = N \int \psi^*(r_1, r_2, \ldots, r_N)\psi(r_1, r_2, \ldots, r_N)dr_2 \cdots dr_N = \rho(r_1) \tag{370}$$

The 1-RDM is obviously symmetrical and, hence, it can be diagonalized, thus obtaining a set of eigenvalues $n_i$ and their associated orthonormal eigenvectors $\phi_i$. These are called Occupation Numbers and Natural Orbitals (NO), respectively. In the case of a single-determinant wave function from a HF or a DFT calculation, the initial matrix (if the overlap matrix is the identity) coincides with the density matrix $\mathbf{P}$, defined in equation (75). After the diagonalization, there will be $N/2$ eigenvectors with degenerate eigenvalue 2, and the rest will have an eigenvalue of 0. Each NO will be a specific linear combination of the canonical orbitals. For multi-determinant and UHF wave functions, the occupation numbers can have any value between 0 and 2 (including fractional values)

$$\gamma_1(r'_1, r_1)\phi_i = n_i\phi_i \tag{371}$$

The electron density can be easily represented using the set of $M$ NOs with occupancy different from 0 (with maximum occupancy)

$$\rho(r) = \sum_{i=1}^{M} n_i|\phi_i|^2 \tag{372}$$

The 1-RDM, being a Hermitian operator with a complete set of orthonormal eigenvectors $\{\phi_i\}$ , can also be expressed as

$$\gamma_1(r_1', r_1) = \sum_{i=1}^{M} n_i \phi^*(r_1')\phi(r_1) \tag{373}$$

The idea of Weinhold and co-workers[348] is to use the 1-RDM to carry out a Natural Atomic Orbital (NAO) and Natural Bond Orbital (NBO) analysis to define the shape of atomic orbitals and locate bonds from the electron density between atoms. Instead of diagonalizing the 1-RDM as described above to get the Natural Orbitals, they use a different scheme.

First, the basis functions are arranged in such a way that all orbitals located on atom A are before those on atom B and so on. The density matrix can be built in terms of blocks of basis functions belonging to a specific centre (with off-diagonal blocks that define the bonds between atoms). Note that an obvious requisite for this procedure is that the basis set is atom-centred. For example, for a two-atom system

$$\mathbf{D} = \begin{pmatrix} D_{AA} & D_{AB} \\ D_{BA} & D_{BB} \end{pmatrix} \tag{374}$$

Each block is a matrix that can be diagonalized. For instance, if atom A has two basis functions, $\mu$ and $\nu$

$$D_{AA} = \begin{pmatrix} C_{\mu A}^2 & C_{\mu A}C_{\nu A} \\ C_{\nu A}C_{\mu A} & C_{\nu A}^2 \end{pmatrix} \tag{375}$$

When this matrix is diagonalized, the eigenvectors obtained are the NAOs for atom A in the molecular environment. NAOs are analogous to the eigenvectors described before in the sense that they also satisfy the maximum-occupancy criteria. However, NAOs are localized and they are only orthogonal with the eigenvectors of the same block.

This set of non-orthogonal NAOs is often called 'pre-NAOs' $\{\tilde{\phi}_i^A\}$ and must be submitted to an orthogonalization procedure to obtain a new set of NAOs $\{\phi_i^A\}$. This is carried out with a procedure called occupancy-weighted symmetric orthogonalization (OWSO), which uses a transformation matrix $\mathbf{T}_{\text{OWSO}}$ that minimizes the deviation between the occupancy of the new set of orthogonal orbitals and the non-orthogonal ones. In this context, the orbitals with the highest occupancies are the ones that are mostly preserved, whereas the orbitals with low occupancies, such as Rydberg orbitals, are distorted freely to achieve orthogonality. Now, the addition of the diagonal elements of the density matrix in this basis are the orbital populations, and adding all the contributions for a specific centre, the atomic population is obtained. This is the essence of the so-called natural population analysis.

Once the new NAO basis is defined, the NAOs are analysed according to their occupancies to extract information about the lone pairs and the atomic bonds, and thus, derive an optimal natural Lewis structure. This procedure starts by removing the contributions to the density matrix of core orbitals $K_A$,

which are located as NAOs within an atomic block with occupation number very close to 2, normally greater than 1.999. Then, the lone pair eigenvectors $n_A$, defined as NAOs within an atomic block with a large occupation number, greater than 1.90, are identified and also removed from the density matrix. After that, each pair of atoms (in the example only AB) is considered and the two-by-two sub-blocks of the density matrix (equation (374) would correspond to the AB pair of atoms) are diagonalized. The natural bond orbitals (NBO) $\sigma_{AB}$ are the resulting eigenvectors with large eigenvalues (occupation numbers), for example, greater than 1.90. The sum of all occupation numbers from core orbitals, lone pairs, and bond orbitals provides a measure for the accuracy of the new Lewis structure. If the total occupancy is close to the total number of electrons, it is considered accurate and accepted. On the other hand, if there is a considerable discrepancy, the criteria for accepting a NBO can be gradually lowered until the sum of the occupation numbers covers a sufficiently large fraction of electrons.

Each NBO $\sigma_{AB}$ is associated with covalency effects, and can be decomposed into orthonormal hybrid contributions $h_A$ and $h_B$, which are called natural hydrid orbitals (NHOs) and are obtained as a combination of NAOs

$$\sigma_{AB} = c_A h_A + c_B h_B \tag{376}$$

From this set of NHOs, an antibond NBO $\sigma^*_{AB}$ is also obtained. It represents regions of the atomic valence shell that are not saturated by covalent bonds and hence, they are related with noncovalent interactions. Therefore, if these orbitals show some occupancy, it is an indicator of deviations from the Lewis picture, which only considers localized covalent bonds

$$\sigma^*_{AB} = c_B h_A - c_A h_B \tag{377}$$

The energy of the system can be decomposed into covalent, $E_{\sigma\sigma}$, and non-covalent, $E_{\sigma\sigma^*}$, components, being the later usually much smaller than the former. Therefore, the energy lowering associated with the interaction between the bonding NBO $\sigma$ and the antibonding NBO $\sigma^*$ can be approximated with second-order perturbative expressions

$$\Delta E^{(2)}_{\sigma\sigma^*} = -2\frac{\langle\sigma|\hat{F}|\sigma^*\rangle}{\epsilon_{\sigma^*} - \epsilon_\sigma} \tag{378}$$

where $\hat{F}$ is the Fock or Kohn-Sham operator.

### 2.11.4 Conceptual DFT

In parallel to the development of DFT as a tool for calculating the energy and observables of a system, as described in section 2.4, another branch, named as 'conceptual DFT' by his creator Robert G. Parr, has emerged.[349] As the previous methods described in this section, 'conceptual DFT' focuses on extracting chemical properties and concepts to understand and predict the reactivity of a molecule, thus connecting the electron density from DFT with the traditional 'language' of chemistry.[350]

As already shown, the electron density integrates to the total number of electrons $N$, and it is directly connected with the external potential, $V_{ext}(r) \equiv v(r)$. So, the energy (see eq. (143)) can be considered as a functional of them $E[N, v(r)]$. This field of DFT concentrates on studying the response of the energy to changes in $N$ and $v(r)$, which is related to reactivity indexes.

In 1983,[351] Parr defined the change of $E$ with the total number of electrons at a fixed external potential as $\mu$,

$$\mu = \left(\frac{\partial E}{\partial N}\right)_{v(r)} \tag{379}$$

which then identified as the chemical potential, describing the tendency of the system to exchange electrons with the environment. In this context, the negative of $\mu$ is a measure of the electronegativity, $\chi$, of the system, a classical concept of chemistry

$$\chi = -\mu = -\left(\frac{\partial E}{\partial N}\right)_{v(r)} \tag{380}$$

Both $\mu$ and $\chi$ are global quantities, in the sense that they do not depend on the position, they have a fixed value for the entire system. This idea may collide with the classic idea of electronegativity, where some atoms of a system are more electronegative than others. However, as Sanderson[352,353] stated: "when two or more atoms initially different in electronegativity combine chemically, their electronegativities become equalised in the molecule". Therefore, $\chi$ can be used to explain some polar reactions, where two molecules with different electronegativities approach but, once the reaction occurs, the product will have an unique equilibrium value of $\chi$, regardless of the ones from the fragments that formed it.

The values for the chemical potential and the electronegativity can be approximated with the first ionization energy ($I$) and electron affinity ($A$)

$$\chi = -\mu \approx \frac{1}{2}(I + A) \tag{381}$$

As stated in the final paragraph of section 2.4.4, Koopmans' theorem[354] defines $I$ as the negative value of the HOMO energy, $-E_{HOMO}$. Analogously, $A$ can be defined as the negative value of the LUMO energy, $-E_{LUMO}$. Consequently, $\chi$ can be computed from the energy of the frontier orbitals

$$\chi = -\mu \approx -\frac{1}{2}(E_{HOMO} + E_{LUMO}) \tag{382}$$

On the other hand, the function that results from the response of the energy to variations of the external potential, keeping constant the number of electrons, is just the electron density

$$\rho(r) = \left(\frac{\partial E}{\partial v(r)}\right)_{N} \tag{383}$$

The second derivatives of the energy with respect to $N$ and $v(r)$ are also a key aspect in 'conceptual DFT'.

First, the change of $\mu$ with respect to $N$ at a fixed external potential has been identified by Parr and Pearson[351] as a measure of the chemical hardness $\eta$

$$\eta = \left(\frac{\partial \mu}{\partial N}\right)_{v(r)} \tag{384}$$

The chemical hardness is a chemical property defined by Pearson in 1963 in his 'hard and soft acids and bases principle' (HSAB).[355–357] Pearson classified acids and bases into hard or soft and proposed that the reactions are more favorable between hard acids with hard bases, and soft acids with soft bases. The introduction of a method to calculate the chemical hardness is thus crucial, since, so far, it had been only a qualitative measure, with no clear definition.

This property is global, and it can also be approximated with the energies of the frontier orbitals,

$$\eta \approx \frac{1}{2}\left(E_{LUMO} - E_{HOMO}\right) \tag{385}$$

in which the 1/2 factor is usually neglected.

The chemical hardness is directly related to the chemical softness, $S$, which has been defined as the inverse of the former

$$S = \frac{1}{\eta} \tag{386}$$

Second, the change in electron density at a given position with respect to the number of electrons, which coincides with the variation in $\mu$ due to changes in the external potential, has been defined by Parr as the so-called Fukui function $f(r)$[358]

$$f(r) = \left(\frac{\partial \rho(r)}{\partial N}\right)_{v(r)} = \left(\frac{\partial \mu}{\partial v(r)}\right)_{N} \tag{387}$$

This function is usually split into two, depending on the sign of $dN$ (if the number of electrons grows or decreases).[359] In a nucleophilic attack, there is an increase in $N$, so $f^+(r)$ provides a local index for the electrophilicity

$$f^+(r) = \left(\frac{\partial \rho(r)}{\partial N}\right)^{+}_{v(r)} \tag{388}$$

On the other hand, $f^-(r)$ is related to the nucleophilicity

$$f^-(r) = \left(\frac{\partial \rho(r)}{\partial N}\right)^{-}_{v(r)} \tag{389}$$

In most studies, these functions are approximated by the so-called finite difference method, calculating the Fukui functions as the difference in electron

density at a point in space with different number of electrons in the system ($N$, $N+1$, $N-1$)[360]

$$f^+(r) \approx \rho(r)_{N+1} - \rho(r)_N \tag{390}$$

$$f^-(r) \approx \rho(r)_N - \rho(r)_{N-1} \tag{391}$$

In general, the larger the value of the Fukui function $f^+(r)/f^-(r)$ at that point, the greater the electrophilic/nucleophilic character, respectively.

To obtain a value for the Fukui functions at an atomic position $A$, Yang and Mortier[359] proposed a condensed form of them, integrating the Fukui functions at the atomic regions. Combining this idea with the previous equations

$$f_A^+ \approx q_A(N+1) - q_A(N) \tag{392}$$

$$f_A^- \approx q_A(N) - q_A(N-1) \tag{393}$$

where $q_A$ is the charge of atom $A$ for a given number of electrons in the system. Its value can be computed with any of the methods that allow the calculation of atomic charges (NBO, AIM ...). The condensed Fukui functions are sensitive to the chosen method.

In addition, a dual descriptor that is able to reveal both the electrophilic and nucleophilic sites of a molecule has been proposed by Morrell *et al.*[361,362] It is defined as the variation of the Fukui function with respect to the number of electrons

$$f^{(2)}(r) = \left(\frac{\partial f(r)}{\partial N}\right)_{v(r)} \tag{394}$$

It can be approximated as the difference between $f^+(r)$ and $f^-(r)$

$$f^{(2)}(r) \approx f^+(r) - f^-(r) \tag{395}$$

In this sense, a positive value of $f^{(2)}(r)$ means an electrophilic site, whereas a negative value will be present at a nucleophilic one, making it a more useful descriptor than the Fukui functions.[363]

There are other descriptors computed from the Fukui functions, for example, the electrophilic $s_A^+$ and nucleophilic $s_A^-$ local softness,

$$s_A^+ = S f_A^+ \tag{396}$$

$$s_A^- = S f_A^- \tag{397}$$

which are derived by the definition of local softness from Yang and Parr.[364]

$$s(r) = \left(\frac{\partial \rho(r)}{\partial \mu}\right)_{v(r)} \tag{398}$$

Some of the most popular theoretical reactivity indices from 'conceptual DFT' have been presented. In general, they are easy to compute and provide a powerful tool for analysing chemical reactivity.

# 3 Results and Discussion

## 3.1 Reactivity towards Activated Alkynes

Herein we will present and analyse the reaction of a series of Re(I) tricarbonyl complexes [ReX(CO)$_3$(bpy)] towards an activated alkyne (methyl propiolate, HMAD) with different nucleophilic ligands (X = $NH_2$, NHMe, NH*p*Tol, OH, OMe, OPh, $PH_2$, PHMe, $PMe_2$, PHPh, $PPh_2$, PMePh, SH, SMe, SPh) as well as the effect of replacing the bpy ligand by phen in [Re($PPh_2$)(CO)$_3$(N–N)].

### 3.1.1 Description of the PES

In this theoretical study the chosen level of theory is CPCM-DLPNO-CCSD(T)/ def2-TZVPP//PCM-B3LYP/6-31+G(d,p) (LANL2DZ for Re). Although the number of complexes here handled is quite large, we have been able to group their PES into four different patterns. All the different reactions have in common the initial attack (**TS1**) from the nucleophilic ligand to the non-substituted carbon of HMAD (C1). The subsequent steps for the formation of the three different products, which are those coming from the coupling of the other acetylene carbon to the external *ortho* carbon of the bidentate ligand (**P*ccb***), to one of the carbonyl ligands in *cis* disposition to X (**P*cco***), or to its insertion into the Re-X bond (**P*ins***), differ in each PES pattern. **P*ccoh*** is only a possible outcome of the reaction if the nucleophilic ligand contains a hydrogen atom, which has to migrate to the oxygen atom of the coupled carbonyl ligand of **P*cco***.

In what we call the type I PES (see Scheme 3.1) , which describes the reactions of the hydroxo and the phosphanido complexes (X = OH, $PH_2$, PHMe, $PMe_2$, PHPh, $PPh_2$, PMePh), the species from which the different products are formed is a zwitterionic intermediate (**I1′**) where the C2 carbon of the alkyne is readily oriented to yield any of them. This species is formed after an isomerization of the intermediate formed by the initial attack (**I1**) through **TS1′**. Hence, the formation of **P*cco***/**P*ccoh***, **P*ccb*** and **P*ins*** occurs from **I1′** via the corresponding TSs (**TS2*cco***, **TS2*ccb*** and **TS2*ins***, respectively).

The type II PES (see Scheme 3.2) only appears with the methoxo complex (X = OMe). In this case, **P*ccb*** and **P*ins*** derive from **P*cco*** instead of **I1′** through **TS2*ccb*** and **TS2*ins***, respectively. The formation of **P*cco*** is analogous to that of **I1′** in the type I PES, that is, the first intermediate **I1** transforms to **P*cco*** via **TS1′**. The geometry of the structures involved in this type of PES is similar to that of the analogous ones in the type I PES.

The type III PES (see Scheme 3.3) describes the reaction of the complexes with nitrogen and sulphur ligands (X = $NH_2$, NHMe, NH*p*Tol, SH, SMe, SPh). This PES pattern is characterized by two possible approaches between the initial complex and the activated alkyne. On the one hand, the reactants link following a similar reaction path to the one of the previous type. In this sense, an initial intermediate **I1** is formed, which evolves to **P*cco*** through **TS1′**. The products **P*ccoh*** (if X presents a hydrogen atom) and **P*ins*** may be obtained from **P*cco*** through an intermolecular hydrogen migration and **TS2*ins***, respectively. This

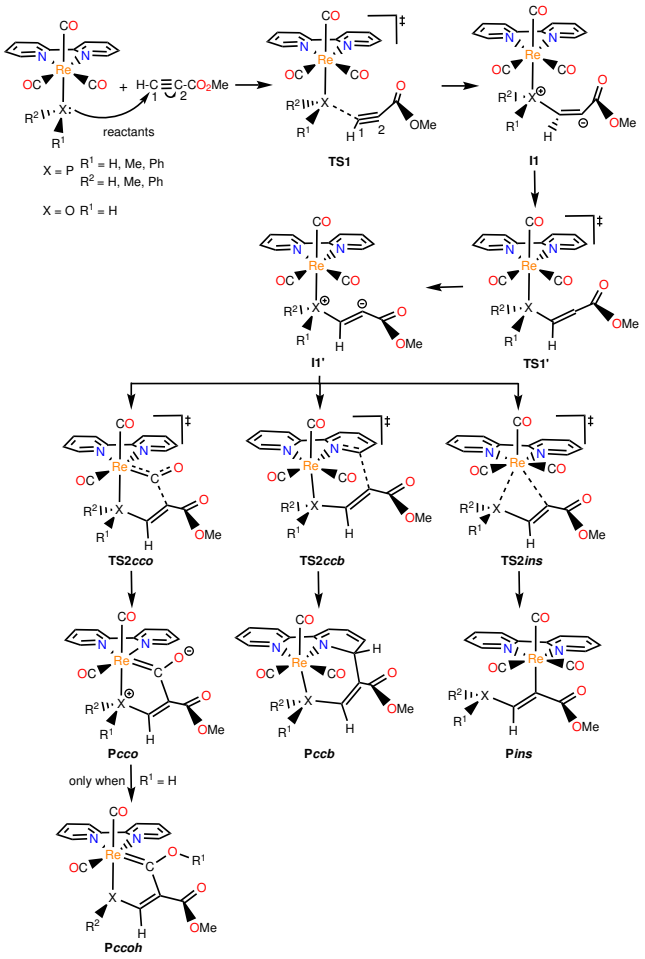


**Scheme 3.1.** Schematic geometries for the species located in the type I PES, which describes the reaction of $[ReX(CO)_3(bpy)]$ (X = OH, $PH_2$, PHMe, $PMe_2$, PHPh, $PPh_2$, PMePh) with HMAD .

is the case for NH*p*Tol, although with the other ligands the splitting point within this route varies. Thus, in the reaction with $NH_2$, NHMe, and SMe, the **I1′** species is formed, and **P*cco*** and **P*ins*** are obtained from it. Finally, for SH and SPh, the initial intermediate plays the same role as **I1′** in the previous ligands, connecting with **P*cco*** and **P*ins*** through **TS2*cco*** and **TS2*ins***, respectively. On the other hand, the formation of **P*ccb*** comes from a different route along the PES. For this route, the initial attack (**TS1b**) from the nucleophilic ligand to the C1 atom of HMAD to form the intermediate **I1b** occurs in the opposite orientation to that of **TS1**. This intermediate isomerizes to **I1b′** without any energy barrier. In this species the C2 carbon of the alkyne is closer to the

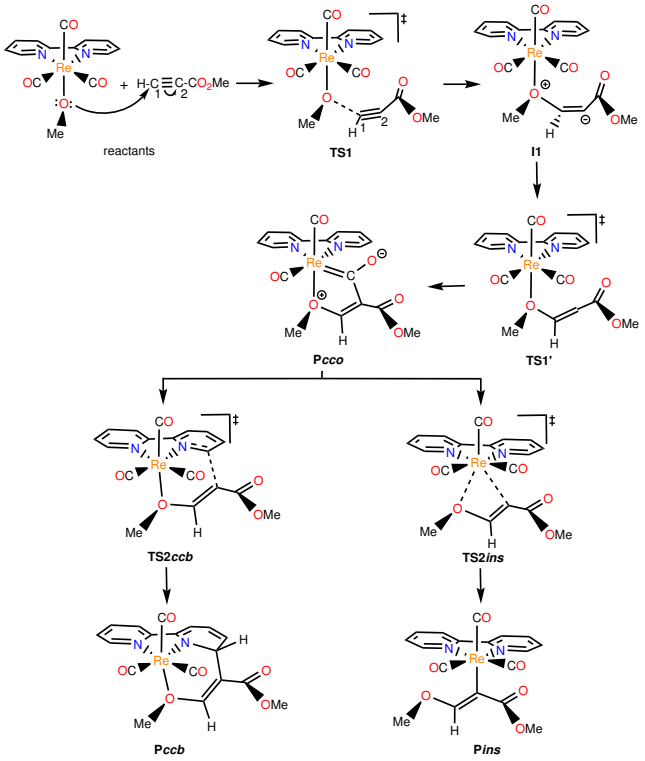


**Scheme 3.2.** Schematic structures for the species located for the reaction of [Re(OMe)(CO)$_3$(bpy)] with HMAD. This corresponds to the type II PES.

diimine ligand and it may form the **P*ccb*** product via **TS2*ccb***.

Another type of PES, the type IV, has only been found for the complex bearing the OPh ligand (see Scheme 3.4). Unlike in previously described PES, this one presents a splitting point in the first intermediate (**I1**). This species can either transform to **P*cco*** without any TS or to **P*ccb*** via **TS2*ccb***. The insertion product **P*ins*** results from the TS (**TS2*ins***) that connects it with **P*cco***, as in the type II and type III PES.

Note that there are some variations in the geometry of the different species involved in the reaction mechanisms between the various nucleophilic ligands, even if they belong to the same type of PES (e.g. the **I1** species when X = SH differs in the orientation of the C2 atom of HMAD when compared to X = SMe). However, this general picture and notation will help us to follow the discussion of the factors governing these reactions.

The formation of **P*ccoh*** from **P*cco*** when the nucleophilic ligand of the Re complex contains at least a H atom deserves special attention. **P*ccoh*** is the reported experimental product for the reactions with X = OH and NH*p*Tol, and the expected one for other ligands as we will cover below. There are many pos-

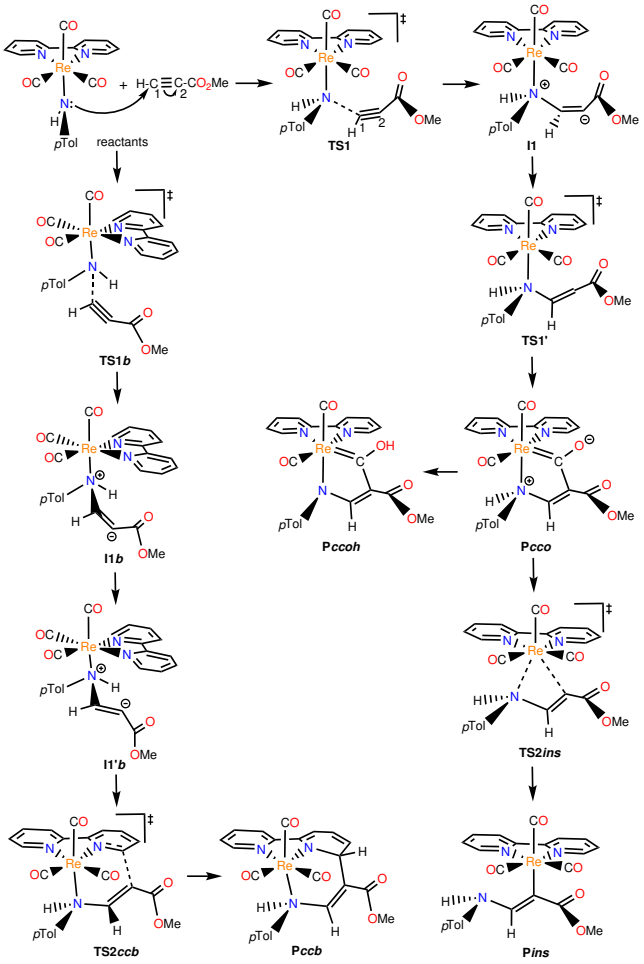


**Scheme 3.3.** Schematic representation of the species located for the reaction of [Re(NH*p*Tol)(CO)$_3$(bpy)] with HMAD. The presence of two possible initial routes, one that starts with **TS1** and another one with **TS1b**, is characteristic of the type III PES. The complexes with X = $NH_2$, NHMe, SH, SMe, and SPh also follow this type of PES, although the connectivity between the **P*cco***/**P*ccoh*** and **P*ins*** products with **I1** varies.

sible transformations that can lead to **P*ccoh*** from **P*cco***. First, we considered the possibility of an intramolecular migration of the ligand hydrogen atom to CO, but the barrier for that process is too large (greater than 50 kcal/mol). The explicit inclusion of solvent THF molecules does not affect this barrier. We have also wondered if the migration could take place after breaking the Re-X bond. The TS associated to that breaking is not too large, with a relative energy close to **TS2*ins***. Nevertheless, the barrier found for the subsequent intramolecular

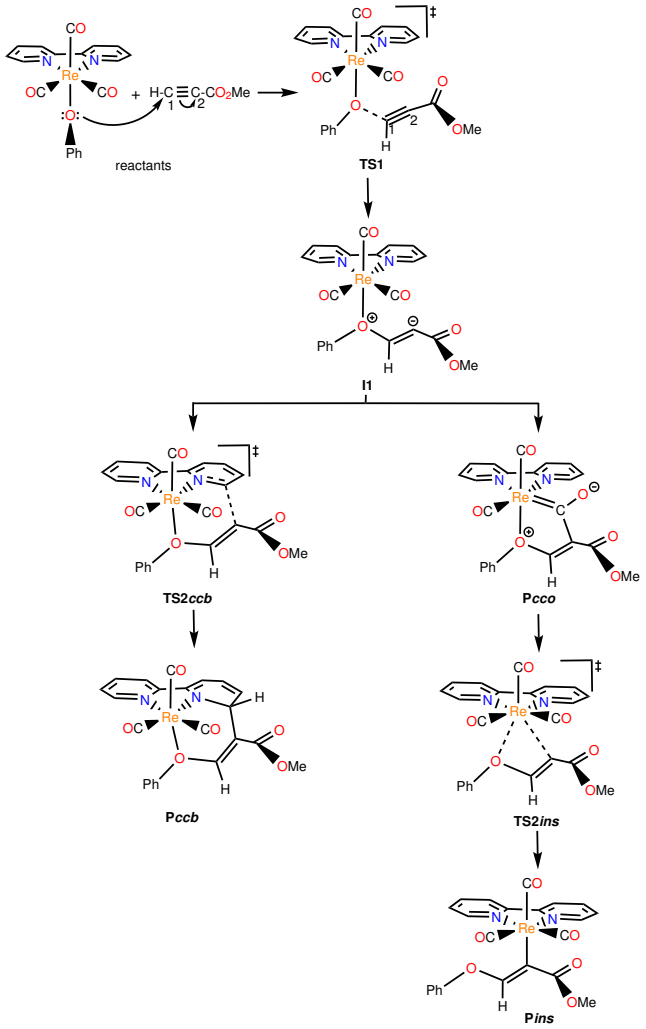


**Scheme 3.4.** Schematic picture of the species involved in the type IV PES. This type of PES has only been found for the reaction of the OPh complex with HMAD.

hydrogen migration is even higher than for the direct migration, so this route has also been discarded. Then, we tried the possibility of an intermolecular migration involving two **P*cco*** moities with X = OH (Figure 3.1). In this sense, a dimer where two **P*cco*** species interact through hydrogen bonds between the nucleophilic ligand and the carboxylate group of HMAD has been optimized (**P*cco*-dimer**). From this dimer, a TS for the simultaneous migration of both hydrogen atoms to the corresponding carboxylate groups (**TS-H1**) only raises 5.6 kcal/mol, forming an intermediate 5.2 kcal/mol above the dimer (**I0-H1**).

Hence, in **I0-H1** the hydrogen previously located in the nucleophilic ligand is bonded now to the carboxylic oxygen of the alkyne. Each of the monomers (**I-H1**) has a relative energy 12.0 kcal/mol above the reactants. As a consequence of the proximity between the oxygen from the carboxylic group and the oxygen at the carbonyl ligand (2.749 Å), the TS for the migration of the hydrogen atom between them (**TS-H2**) presents a barrier of only 14.5 kcal/mol. After **TS-H2**, the **P*ccoh*** product is already formed, which lies 12 kcal/mol below the reactants for X = OH. An analogous mechanism is assumed for the hydrogen migration between **P*cco*** and **P*ccoh*** for the other nucleophilic ligands.

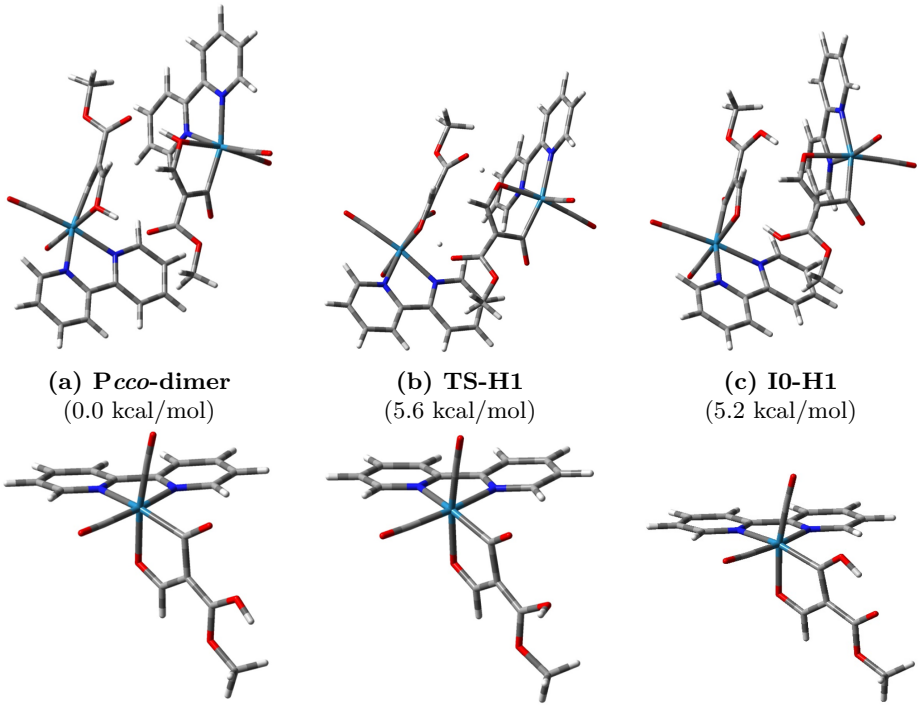

**(a) P*cco*-dimer** (0.0 kcal/mol)
**(b) TS-H1** (5.6 kcal/mol)
**(c) I0-H1** (5.2 kcal/mol)
**(d) I-H1** (12.0 kcal/mol)
**(e) TS-H2** (14.5 kcal/mol)
**(f) P*ccoh*** (-12.0 kcal/mol)

**Figure 3.1.** Optimized geometries with their corresponding CPCM-DLPNO-CCSD(T)/ def2-TZVPP//PCM-B3LYP/6-31+G (d,p) (LANL2DZ for Re) Gibbs relative energies of the species involved in the intermolecular hydrogen transfer between **P*cco*** and **P*ccoh*** for the hydroxo complex.

### 3.1.2 Effect of the Bidentate Ligand

Before deepening into the differences between the reactivity of the series of nucleophilic ligands investigated, it is interesting to clarify the effect of the bidentate ligand on the PES. There are experimental reports on the reaction

involving the complexes with X = $PPh_2$, NH*p*Tol, OH, and OMe,[31,45,53–57] but only the phosphanido complex was bearing a phen ligand, whereas the others presented a bpy ligand. Therefore, we have chosen this complex for studying the consequences of replacing phen by bpy. For this comparison, we will use PCM-B3LYP/6-311+G(2d,p) (LANL2TZ+*f* for Re)//PCM-B3LYP/6-31+G(d,p) (LANL2DZ for Re) Gibbs energies referred to the separate reactants. The species with a phen ligand will be denoted with the suffix '**_phen**'.

As already mentioned, the reaction between [Re($PPh_2$)$(CO)_3$(bpy)] and HMAD is described by a type I PES, with the zwitterionic intermediate **I1′** marking the splitting point for the formation of the three possible products (see Figure 3.2). This also holds for the reaction of the analogous complex with a phen ligand, with similar geometries in all the critical points of the PES.

The energetics for the first stages of the reaction, until the formation of **I1′**, are similar for both complexes, being the maximum difference between them 0.9 kcal/mol (in **TS1′**). In addition, the insertion route is always the most disfavoured one, since **TS2*ins*** relative energy is 21.6 and 22.8 kcal/mol for the phen and bpy complexes, respectively. This barrier is larger than the one that presents **TS1**, which is the rate-determining step for the formation of **P*ccb*** and **P*cco***, with a relative energy of 18.8 kcal/mol (**TS1_phen**) and 19.2 kcal/mol (**TS1**).

The difference in relative energy between the species involved in the formation of **P*cco*** is also subtle. The barrier is 9.7 and 11.0 kcal/mol for the phen and bpy complexes, respectively, and the relative energy of the product is, in both cases, close to -1 kcal/mol, with a difference of 0.4 kcal/mol between them.

However, there are important discrepancies in the route that leads to the formation of the coupling product with the bidentate ligand. In this route, **TS2*ccb*_phen** has a relative energy of 7.8 kcal/mol, and **P*ccb*_phen** of -11.1 kcal/mol. However, the barrier is 3.7 kcal/mol larger and the product 6.4 kcal/mol more unstable if the diimine ligand is bpy. As a consequence, the most favoured product with phen, from both a kinetic and a thermodynamic point of view, is **P*ccb*_phen**, since the barrier for its formation is the lowest one (7.8 kcal/mol) and it is the most stable product (-11.1 kcal/mol). This is in accordance with the experimental findings.[56,57] On the other hand, the formation of the **P*cco*** product has a lower barrier (11.0 kcal/mol) than the formation of **P*ccb*** (12.5 kcal/mol) with the bpy ligand. Hence, the coupling with the carbonyl ligands becomes the kinetically preferred route, although **P*ccb*** remains as the most stable product. The slight stability of **P*cco*** (-0.7 kcal/mol), which means that its reversion to **I1′** has a barrier of only 11.7 kcal/mol, along with the low relative energy of **P*ccb*** (-4.7 kcal/mol), implies that the thermodynamic control is expected to prevail. Therefore, the reaction of both complexes with HMAD would yield **P*ccb*** as the main product. Higher level energy computations for the bpy complex, with CPCM-DLPNO-CCSD(T)/def2-TZVPP, have confirmed our conclusions. With this level, **P*ccb*** remains as the most stable product (-20.0 kcal/mol), but **TS2*ccb*** now has a lower barrier (4.4 kcal/mol) than **TS2*cco*** (4.6 kcal/mol). Therefore, we have corroborated the coupling with the bidentate ligand as the most favoured route.

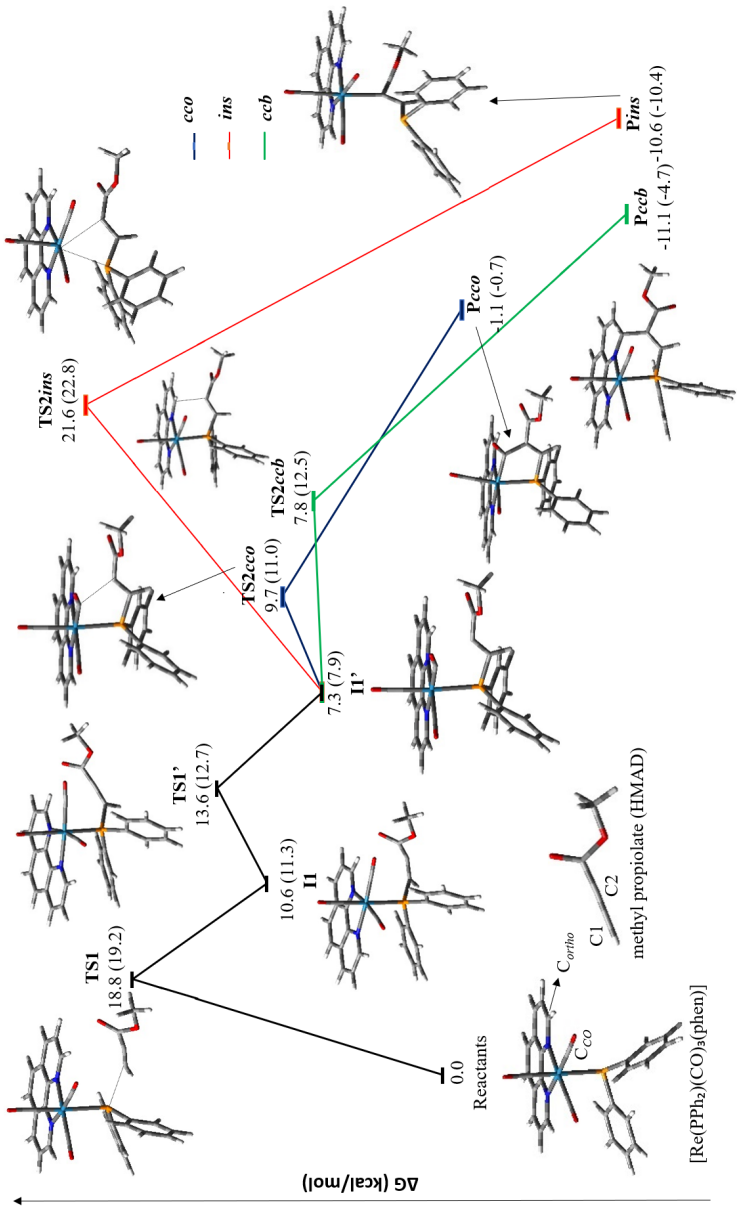


**Figure 3.2.** PCM-B3LYP/6-311+G(2d,p) (LANL2TZ+*f* for Re)//PCM-B3LYP/ 6-31+G(d,p) (LANL2DZ for Re) Gibbs energy profile in THF solution of the reaction between [Re($PPh_2$)$(CO)_3$(phen)] and HMAD. Gibbs energy values for the reaction between [Re($PPh_2$)$(CO)_3$(bipy)] and HMAD are also included between parentheses

Several theoretical analysis were performed to rationalize the differences in reactivity between the two complexes and the preference of coupling with the diimine ligand over the other routes. A NBO analysis of the reactive intermediate **I1′** (Figure 3.3) has confirmed that the carbon atom of the carbonyl ligand that is attacked in **TS2*cco*** presents the most positive charge (+0.76 *e*) in both complexes. This fact explains the low energy barrier for this coupling, which is electrostatically favoured. On the other hand, the external *ortho* carbon of the bidentate ligand has a charge of +0.08 *e* in bpy and +0.10 *e* in phen. In addition, the total charge of the pyridine ring where the coupling is produced is -0.76 *e* and -0.57 *e* for bpy and phen, respectively. Therefore, the nucleophilic attack from the C2 carbon of HMAD to the diimine ligand is less favoured with bpy than with phen, since it must overcome larger repulsive interactions.

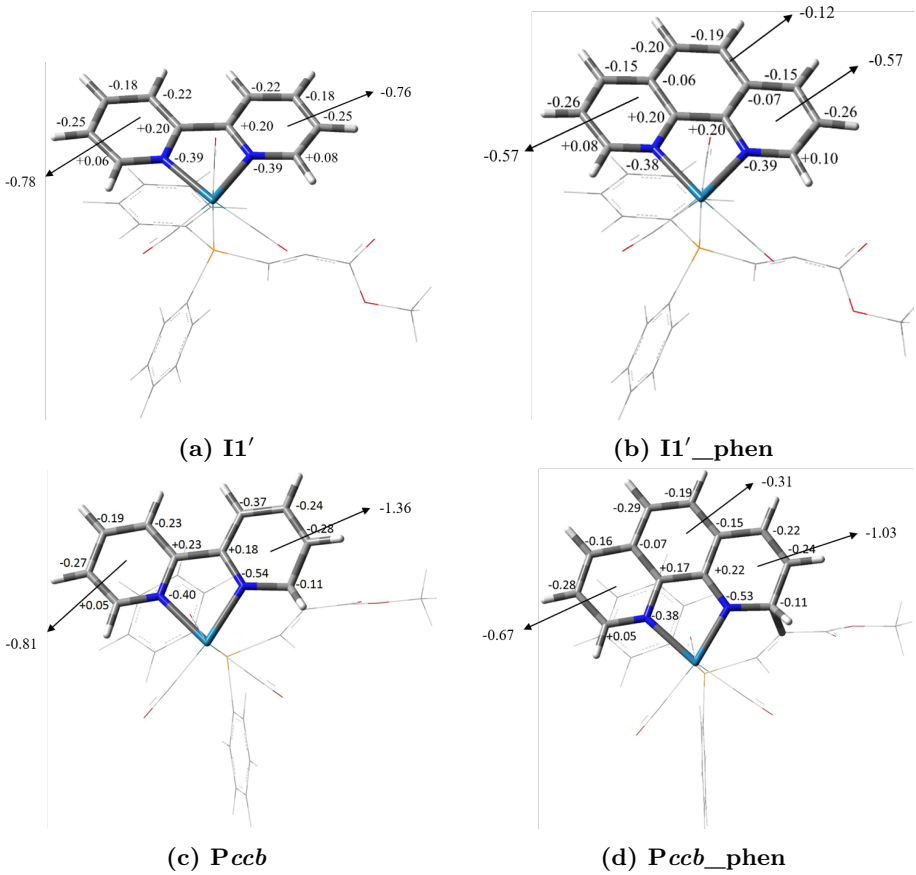


**(a) I1′** **(b) I1′_phen**

**(c) P*ccb*** **(d) P*ccb*_phen**

**Figure 3.3.** NBO charges of the non-hydrogen atoms of the diimine ligands at the **I1′** and **P*ccb*** species.

The comparison of NBO charges at the bidentate ligand on the **P*ccb*** species

(Figure 3.3) also helps to elucidate the reason for the greater stability of the phen product. In this sense, the nucleophilic attack to the diimine ligand induces a raise in the electron density at the ring that is attacked and the NBO analysis helps us to quantify these changes. In the case of the bpy ligand, the total charge at this ring increases from -0.76 $e$ to -1.36 $e$, whereas it changes from -0.57 $e$ to -1.03 $e$ in the phen ligand. In addition, the charge at the other pyridine ring of bpy remains practically the same, while the electron density at the other rings of phen suffer a slight increase. Hence, the negative charges at the phen ligand are more distributed than at the bpy one, which helps to stabilize the **P*ccb*** product.

The coupling to the diimine ligand also implies a loss of aromaticity on the attacked ring, as confirmed by NICS computations 1 Å above the RCP, which we will refer as NICS(1). The NICS(1) indexes at the intermediate **I1′**, previous to the bidentate ligand coupling step, show that all the bpy and phen rings are aromatic with strong $\pi$ electron delocalization, as the values range from -8.2 to -9.6 ppm. However, the NICS(1) values at the pyridine ring where the coupling is produced change to -1.7 and +1.7 for phen and bpy, respectively, once **P*ccb*** is formed, both values indicate that the ring is no longer aromatic. In the case of the other rings, the NICS(1) values demonstrate that their aromatic character is not affected, with a maximum change of 1.8 ppm. The extra fused aromatic ring of the phen ligand, which carries a greater $\pi$ electron delocalization, could explain the larger stability of **P*ccb*_phen** at the phen complex.

As a conclusion, the replacement of phen by bpy only induces significant changes in the route that involves the coupling to the bidentate ligand. In this sense, both the TS (**TS2*ccb*_phen**) and the product (**P*ccb*_phen**) are more stable with phen than with bpy. This is mainly due to the larger conjugation of the former, which makes the pyridine ring to be attacked more electrophilic and helps to stabilize the product. To study the effects of the nucleophilic ligands in the reactivity of the Re complexes towards HMAD we will only consider the bpy ligand, since most experimental reports deal with it and its smaller size provides a reduction in the computational cost of the theoretical study.

### 3.1.3 Effect of the Substituents of the Nucleophilic Ligand

Now, we will analyse the effect of the nucleophilic ligand in the reaction of the complexes [ReX(CO)$_3$(bpy)] (X = NH$_2$, NHMe, NH$p$Tol, OH, OMe, OPh, PH$_2$, PHMe, PMe$_2$, PHPh, PPh$_2$, PMePh, SH, SMe, SPh) with HMAD. Contrary to the replacement of the bidentate ligand, changes in X have a strong impact on the PES, since, for instance, the experimental product differs for X = PPh$_2$ (**P*ccb***), NH$p$Tol and OH (**P*ccoh***), and OMe (**P*ins***). First, we will study the influence of the substituents (H, Me, Ph/$p$Tol) on the nucleophilic ligands for each heteroatom (N, P, O, S).

In the case of the nitrogen ligands (NH$_2$, NHMe, NH$p$Tol), as already mentioned, all of them follow a type III PES, with two initial routes, one starting with **TS1** and ending up in the **P*cco*/P*ccoh*** or the **P*ins*** products, and another one where the initial nucleophilic attack is described by **TS1b** and leads

to the formation of **P*ccb***. Hence, the substituents on the nitrogen atom do not change the general mechanisms, although the splitting point of the former route differs from the NH*p*Tol ligand (**P*cco***) to the others (**I1′**). However, they do have a strong influence on the outcome of the reaction (see Table 3.1).

**Table 3.1.** CPCM-DLPNO-CCSD(T)/def2-TZVPP//PCM-B3LYP/6-31+G (d,p) (LANL2DZ for Re) Gibbs relative energies including thermal corrections in THF solution of the critical structures involved in the reaction between the complexes [Re(NHR)(CO)$_3$(bpy)] (R = H, Me, *p*Tol) and [Re(OR)(CO)$_3$(bpy)] (R = H, Me, Ph) with HMAD. All the values are given in kcal/mol.

| Species | $NH_2$ | NHMe | NH*p*Tol | OH | OMe | OPh |
|---|---|---|---|---|---|---|
| **TS1** | 18.5 | 17.2 | 22.4 | 27.0 | 25.9 | 33.5 |
| **I1** | 0.4 | 1.2 | 15.2 | 23.8 | 20.2 | 31.9 |
| **TS1′** | 8.5 | 4.3 | 17.0 | 28.0 | 24.8 | |
| **I1′** | 1.4 | -0.8 | | 23.9 | | |
| **TS2*cco*** | 4.3 | -0.1 | | 26.8 | | |
| **P*cco*** | -8.0 | -12.4 | -0.2 | 15.2 | 9.9 | 24.2 |
| **P*ccoh*** | -24.9 | -32.3 | -21.1 | 12.0 | | |
| **TS2*ins*** | 11.2 | 8.4 | 20.4 | 28.3 | 24.0 | 36.5 |
| **P*ins*** | -29.1 | -31.2 | -22.4 | -13.7 | -16.4 | -5.6 |
| **TS1b** | 19.3 | 14.0 | 21.4 | | | |
| **I1b** | -1.3 | -5.1 | 8.6 | | | |
| **I1′b** | -1.5 | -5.5 | 9.8 | | | |
| **TS2*ccb*** | 8.4 | 4.1 | 19.0 | 31.2 | 29.5 | 38.8 |
| **P*ccb*** | -15.1 | -19.3 | -5.1 | 8.1 | 4.9 | 16.2 |

From the comparison of the relative energies when one of the hydrogen atoms of $NH_2$ is replaced by Me (NHMe), a moderate relative stabilization of all the species except **I1** is produced. It is also remarkable that the expected product changes between these substituents. For $NH_2$, the route for the formation of **P*cco*** is kinetically favoured. From this species, the TS for the insertion product presents a larger energy barrier (19.2 kcal/mol) than the initial nucleophilic attack (18.5 kcal/mol), so the product resulting from the intermolecular migration of the hydrogen (**P*ccoh***) is favoured. On the other hand, the presence of a Me substituent makes the energy barrier of the route that starts with **TS1b** (14.0 kcal/mol) lower than the one of **TS1** (17.2 kcal/mol). Hence, according to the kinetic control, the **P*ccb*** species is formed. Since this product is very stable (-19.3 kcal/mol), and the barrier to return to **I1′b** is large (23.4 kcal/mol), **P*ccb*** is the expected product for the reaction with NHMe. On the contrary, the replacement of $NH_2$ by NH*p*Tol produces a relative destabilization of all the species. In this case, both reaction routes have similar energy barriers (22.4 kcal/mol, **TS1**, and 21.4 kcal/mol, **TS1b**), with a difference in relative Gibbs energy of only 1 kcal/mol. Therefore, the thermodynamic control dictates the outcome of the reaction. Given that **P*ccoh*** is the most stable species, this is the expected product in accordance to the experimental findings.[55]

Moving to the complexes with oxygen ligands (OH, OMe, OPh), the type of PES is largely influenced by the substituent, with a different type for each of the OR ligands. In addition, the reported experimental product with the hydroxo (**P*ccoh***)[45] and the methoxo (**P*ins***)[54] ligands differs.

The relative Gibbs free energies of all the species are collected in Table 3.1. Comparing the reaction of the hydroxo complex with that of the complexes bearing OMe and OPh, similar trends than those found for the nitrogen ligands are observed. Indeed, the replacement of H by Me produces a stabilization of all the species, whereas the aryl substituent induces a general destabilization. In all cases, both the **P*cco*** and the **P*ccb*** species are unstable, so the formation of those products is unlikely. Hence, the insertion product **P*ins*** is the most stable one for the three ligands and the expected one for X = OMe and OPh, in accordance with the experimental findings for the methoxo complex. However, the presence of a hydrogen atom in the hydroxo complex allows the formation of **P*ccoh***. Since the barrier for the insertion product (28.3 kcal/mol) is larger than the rate-determining step (**TS1′** with 28.0 kcal/mol), **P*ccoh*** is the expected product with OH, as experimentally reported. It is also noteworthy that the large energy barriers with the OPh ligand, 33.5 kcal/mol for the initial attack (**TS1**) and 36.5 kcal/mol for the formation of the insertion product (**TS2*ins***) make unlikely the reaction of the complex bearing this ligand with HMAD.

In the reaction of the phosphanido complexes (X = $PH_2$, PHMe, $PMe_2$, PHPh, $PPh_2$, PMePh) with HMAD, only the type I PES, where there is a common reactive intermediate (**I1′**) for all the different routes, is found. In this case there is only one reaction that has been reported experimentally, the one of the $PPh_2$ complex to yield **P*ccb***, although the complex had a phen ligand instead of bpy, as already covered.

The Gibbs relative energy of all the species involving the $PR^1R^2$ ligands is shown in Table 3.2. The reactions with all the phosphorous ligands have in common that the rate-determining step is the initial nucleophilic attack (**TS1**) and that the insertion route is the one with the largest barrier (**TS2*ins***). In addition, the TSs for the other routes, **TS2*cco*** and **TS2*ccb***, are close in relative energy, and **P*ccb*** is always more stable than **P*cco***. It is also remarkable that **P*ccoh***, when available, is more unstable than **P*cco***. Therefore, the expected product in all cases is the coupling with the diimine ligand, **P*ccb***. Comparing the relative energies of the species involved in the reaction of the complex bearing X = $PH_2$ with the ones bearing other phosphanido ligands, the substitution of the hydrogen atoms by Me and/or Ph induces stabilization in all of them, with the only exception of **TS1** with X = PHMe. Looking at the relative energies with PHMe and PHPh, the alkyl substituent seems to have a slightly larger stabilization effect than the aryl one, excluding **TS1** and **TS2*ins***. This effect is corroborated when comparing the reactions of the $PMe_2$ and $PPh_2$ complexes, given that all species are more stable with the former ligand. In addition, both ligands produce a larger stabilization effect than the analogous ones with a hydrogen atom. Finally, the PMePh ligand, with alkyl and aryl ligands, also lowers the energy of all the species, although the effect is not as large as the one with $PMe_2$. As a conclusion, the Me substituent has a similar effect than in the

**Table 3.2.** CPCM-DLPNO-CCSD(T)/def2-TZVPP//PCM-B3LYP/6-31+G (d,p) (LANL2DZ for Re) Gibbs relative energies including thermal corrections in THF solution of the critical structures involved in the reaction between the complexes [Re(PR$^1$R$^2$)(CO)$_3$(bpy)] (R$^1$R$^2$ = $H_2$, HMe, $Me_2$, HPh, $Ph_2$, MePh) and [Re(SR)(CO)$_3$(bpy)] (R = H, Me, Ph) with HMAD. All the values are given in kcal/mol.

| Species | $PH_2$ | PHMe | $PMe_2$ | PHPh | $PPh_2$ | PMePh | SH | SMe | SPh |
|---|---|---|---|---|---|---|---|---|---|
| **TS1** | 27.6 | 30.9 | 17.4 | 17.6 | 17.5 | 18.7 | 32.7 | 23.1 | 30.8 |
| **I1** | 10.3 | 0.9 | -5.5 | 5.6 | 2.2 | 0.1 | 29.9 | 21.9 | 26.1 |
| **TS1′** | 14.6 | 6.2 | -1.3 | 9.7 | 4.2 | 3.9 | | 26.1 | |
| **I1′** | 9.1 | 0.2 | -6.9 | 3.5 | -0.6 | -1.5 | | 20.3 | |
| **TS2*cco*** | 13.5 | 5.1 | -1.3 | 8.2 | 4.6 | 2.2 | 32.9 | 24.7 | 29.0 |
| **P*cco*** | 0.1 | -8.9 | -17.3 | -7.4 | -9.3 | -11.6 | 21.1 | 11.0 | 14.4 |
| **P*ccoh*** | 0.3 | -4.3 | | -4.2 | | | -2.6 | | |
| **TS2*ins*** | 34.2 | 21.1 | 13.4 | 17.5 | 20.0 | 17.2 | 39.1 | 32.1 | 34.8 |
| **P*ins*** | -13.1 | -18.3 | -24.1 | -17.5 | -16.8 | -21.1 | -2.4 | -9.1 | -5.7 |
| **TS1b** | | | | | | | 28.0 | 21.0 | 25.6 |
| **I1b** | | | | | | | 25.7 | 17.3 | 22.6 |
| **I1′b** | | | | | | | 28.6 | 18.8 | 25.0 |
| **TS2*ccb*** | 13.5 | 5.8 | -2.6 | 9.4 | 4.4 | 3.6 | 35.8 | 26.4 | 31.0 |
| **P*ccb*** | -9.5 | -16.3 | -25.5 | -12.8 | -20.0 | -20.0 | 13.7 | 3.1 | 8.9 |

ligands with nitrogen and oxygen. However, the replacement of hydrogen atoms by Ph has the opposite effect than in the previous cases, it produces stabilization instead of destabilization. The substitution of both hydrogen atoms by methyl and/or phenyl groups make the stabilization effects even larger.

To conclude, the reaction of the complexes with sulphur nucleophilic ligands (X = SH, SMe, SPh) with HMAD follows a type III PES. However, as already mentioned, the **P*cco*** and **P*ins*** products are directly formed from **I1** with SH and SPh, whereas they come from **I1′** with SMe. The relative Gibbs energies of all the species involved in these reactions are shown in Table 3.2.

As for the oxygen ligands, **P*cco*** and **P*ccb*** are always less stable than the corresponding reactants. However, the barrier for the insertion route is large in all cases (greater than 32 kcal/mol). Consequently, **P*ins*** seems to be the expected product for SMe and SPh. However, their large barriers make the reaction with HMAD quite unlikely. The same occurs for the SH complex, although the possibility of formation of **P*ccoh***, with a lower barrier (32.9 kcal/mol) than **TS2*ins*** (39.1 kcal/mol), favours that route over the insertion one. The influence of the alkyl and aryl substituents on the relative energies is similar to the one with the phosphorous ligands. Indeed, the replacement of the hydrogen atom of SH by either a methyl or a phenyl group lowers the relative energy of all the species. On top of that, the alkyl substituent has a larger stabilization effect than the aryl one.

To sum up this analysis, we have observed that the presence of a methyl

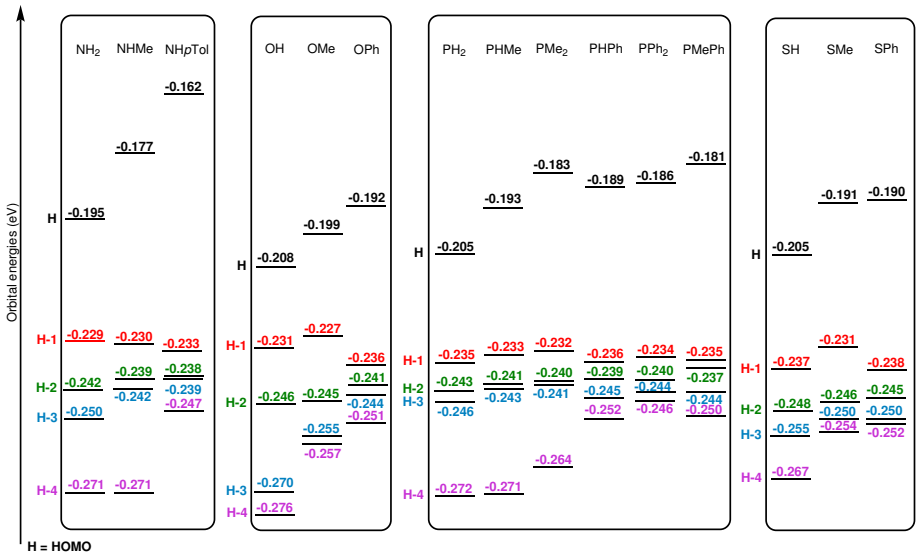


**Figure 3.4.** Orbital energies of the five highest occupied molecular orbitals of the reactant complexes [ReX(CO)$_3$(bpy)] (X = $NH_2$, NHMe, NH*p*Tol, OH, OMe, OPh, $PH_2$, PHMe, $PMe_2$, PHPh, $PPh_2$, PMePh, SH, SMe, SPh).

group in the nucleophilic ligand reduces all the energy barriers and stabilizes the corresponding products, sometimes changing the expected outcome of the reaction. This is likely due to a larger nucleophilic character of the ligand with an alkyl substituent, consequence of the electron-donating properties of the alkyl group. On the other hand, the replacement of hydrogen by an aryl group has opposite effects depending on the heteroatom. If the aryl substituent is bonded to N or O, the relative energy of the species involved in the reaction is destabilized, whereas they are stabilized if the aromatic ring is bonded to P or S. We will clarify these differences herein.

A comparison of the energy of the frontier occupied orbitals of all the complexes, as shown in Figure 3.4, can give us information about the changes in the overall nucleophilicity of the ligands. In general, higher energy HOMOs are related to a larger nucleophilic character.

Indeed, the energy of the HOMO of the initial complexes with ligands bearing hydrogen atoms is always raised when one of those is replaced by an alkyl or an aryl group. This explains the general stabilization effect that is observed with the inclusion of a methyl substituent, since it favours the reaction with HMAD. However, the orbital energies cannot be used to explain the effects of the aryl groups depending on the heteroatom. For that purpose, the composition of the HOMO for the different ligands may shed some light.

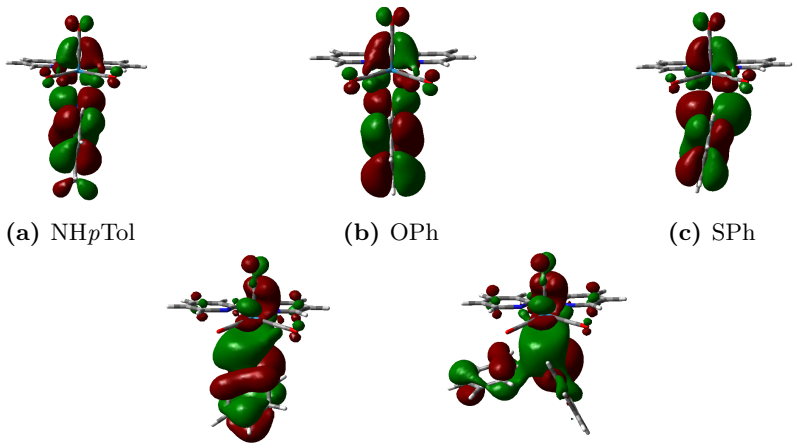

**(a)** NH*p*Tol **(b)** OPh **(c)** SPh

**(d)** PHPh **(e)** $PPh_2$

**Figure 3.5.** Pictures of the HOMO for the initial complexes containing nucleophilic ligands with aryl groups.

**Table 3.3.** Bond distances in Å between the heteroatom X of the nucleophilic ligand and the alkyl/aryl carbon atom bonded to it ($C_S$), DI at the BCP located between those atoms, and NAC in $e$ (computed with NBO) of the heteroatom for the reactant complexes [$ReX(CO)_3(bpy)$] (X = NHMe, NH*p*Tol, OMe, OPh, PHMe, PHPh, $PPh_2$, SMe, SPh).

| X | d(X-$C_S$) | DI(X-$C_S$) | NAC(X) |
|---|---|---|---|
| NHMe | 1.461 | 1.0399 | -0.799 |
| NH*p*Tol | 1.372 | 1.1322 | -0.790 |
| OMe | 1.400 | 0.9459 | -0.752 |
| OPh | 1.329 | 0.9925 | -0.678 |
| PHMe | 1.882 | 0.9166 | 0.180 |
| PHPh | 1.844 | 0.9337 | 0.232 |
| $PPh_2$ | 1.864 | 0.8793 | 0.519 |
| SMe | 1.841 | 1.1198 | -0.188 |
| SPh | 1.782 | 1.1956 | -0.085 |

As already mentioned, the aryl group has a destabilization effect on the N and O ligands, whereas the opposite effect was found on the P and S ones. Looking at Figure 3.5, it is clear that the addition of an aromatic ring produces some conjugation, this explains the changes in energy of the HOMO, which is destabilized. The computed Delocalization Indexes (DI), which are a measure of the number of covalent electrons shared between two atoms, at the Bond Critical Point (BCP) between the nucleophilic atom and the carbon of the alkyl/aryl group bonded to it ($C_S$) confirm this (see Table 3.3), with larger values for the

BCPs involving the aryl groups. This is also in accordance with a shortening in the bond distances between those atoms (see Table 3.3). Notably, the complex with the $PPh_2$ ligand, which does not present conjugation, has a lower DI than PHMe and the bond length only varies 0.018 Å (comparing PHMe and PHPh it shortens 0.038 Å). Nevertheless, we can see in Figure 3.5 that the conjugation is larger with N and O than with P and S. The main reason for that is the disposition of the ring, with N and O the dihedral angles Re-X-aryl (X is the heteroam, and aryl refers to the two carbon atoms of the ring closer to X) are 9° and 3°, respectively, whereas the analogous angles for P and S are 70° and 17° in PHPh and SPh, respectively. Therefore, the $\pi$ orbitals of the ring are more available for conjugation in the former group of ligands. As a consequence, despite the large destabilization of the HOMO energies due to this conjugation, it also has the effect of making the lone pair of the nucleophilic atom less available for the initial attack, which explains the lower reactivity of those ligands towards HMAD.

The net natural atomic charges (NAC) at the heteroatom of the nucleophilic ligand also confirms the depopulation effect that takes place when the alkyl group is replaced by the aryl one. Certainly, the NAC always becomes more positive when such replacement takes place, as displayed in Table 3.3, This is in accordance with the fact that the ligands with methyl groups are more nucleophilic.

### 3.1.4 Influence of the Heteroatom of the Nucleophilic Ligand

Once we have elucidated the effect of the different substituents in the nucleophilic ligand, we will now focus on the influence of the heteroatom in that ligand. First, we will analyse the replacement of N by P, both of them belonging to Group 15 of the periodic table, and then, the same for the ligands with heteroatoms from the Group 16, O and S. In order to compare the relative energies between them, we must choose nucleophilic ligands with analogous substituents (e.g., $NH_2$ and $PH_2$, NHMe and PHMe, NH*p*Tol and PHPh).

In the case of the ligands bearing only hydrogen atoms, the substitution of N by P causes a destabilization of all the species. In addition, the preferred product changes from **P*ccoh*** with $NH_2$ to **P*ccb*** with $PH_2$ as a consequence of the large destabilization of **P*ccoh*** (25.2 kcal/mol) with the $PH_2$ ligand. A similar effect is observed when comparing NHMe with PHMe, with the only exceptions of **I1**, which suffers a slight stabilization, and **TS2*ccb***, which is lowered 3.8 kcal/mol. Hence, the more accessible barrier for the coupling with the bidentate ligand, along with the destabilization of **TS2*cco*** and **P*ccoh***, favours the formation of **P*ccb*** as well. For the comparison between NH*p*Tol and PHPh we have to take into consideration that the aryl group produces destabilization for the nitrogen ligand, but stabilization for the phosphorous one. Therefore, there are two combined factors, the stabilization due to the lack of conjugation with the aryl group in PHPh, and the destabilization caused by changing N by P, as observed for the previous ligands. The overall effect is a relative stabilization of all the species, with the exception of **P*ins*** and **P*ccoh***, which are destabilized by 4.9

and 16.9 kcal/mol, respectively. These changes favour the formation of **P*ccb*** with the P ligand again.

Moving to the ligands with O and S atoms, the general trends are similar to those found for N and P. In this sense, the replacement of O by S in OH and OMe causes destabilization of all the species with only few exceptions, **TS1**, **TS2*ccb***, and **P*ccb*** with the alkyl substituent, whereas the same change in OPh causes a relative stabilization of all the species but **TS1**, **TS2*ccb***, and **TS2*ins***. As already discussed, only the **P*ccoh*** and the **P*ins*** products are more stable than the reactants for the oxygen and sulphur ligands. Hence, **P*ccoh*** is the expected product for OH and SH, and **P*ins*** for the remaining ligands. Therefore, in this case, the expected product does not depend on the heteroatom. However, the destabilization, consequence of the S atom, makes the reaction with HMAD quite unlikely.

As we have covered, the replacement of the heteroatom from the second period of the periodic table by the one belonging to the same group but the third period causes, in general, a destabilization. With respect to the first stage of the reaction, the differences in size between O and S, and N and P, are in accordance with this fact. Since S and P have larger molecular orbitals, more similar in size to the $d$ orbitals of Re, the overlap with those is more effective, and the attacking electron pair is less available. In addition, it is well known that, for instance, $OH^-$ is a stronger base than $SH^-$, due to their differences in size and electronegativity. The Fukui indexes $f_X^-$ computed at the heteroatom of the reactant complexes [ReX(CO)$_3$(bpy)] (X = OH, SH) can give us information about those differences in nucleophilicity (more negative $f_X^-$ means more nucleophilic atom) . Indeed, the value of this index is -0.881 $e$ with X = OH, and -0.564 $e$ with X = SH, confirming the more nucleophilic character of the OH ligand. The same reasoning applies for the comparison between N and P.

The more effective overlap of the Re orbitals with S and P also explains the larger kinetic penalization of the insertion route with those ligands. Hence, since the Re-X bond must be broken, it will require more energy if X is S or P. The computed DI at the BCP located between Re and X at the intermediate previous to the formation of **P*ins*** can be employed to check this hypothesis. Such values are 0.6687, 0.6145, 0.6736, and 0.6545 for X = $NH_2$, OH, $PH_2$, and SH, respectively. These indexes indicate that the Re-X bond becomes stronger when moving from the second to the third period of the periodic table along the same group. The differences in energy between **TS2*ins*** and the previous intermediates follow the same trend, since they are 19.2, 4.4, 25.1, and 18.0 kcal/mol for X = $NH_2$, OH, $PH_2$, and SH, respectively.

## 3.2 Reactivity of Molybdocenes towards Ethers

Now, we will present the results obtained for the theoretical study of the reaction mechanism of the hydrolysis of ethyl vinyl ether, diethyl ether, and divinyl ether catalyzed by $[Cp_2Mo(OH)(OH_2)]^+$ in water. The theory level employed for this computational investigation is PCM-B3LYP/aug-cc-pVTZ (aug-cc-pVTZ-PP for Mo)//PCM-B3LYP/aug-cc-pVDZ (aug-cc-pVDZ-PP for Mo). Our main goal is to elucidate the factors behind the divergent reactivity between ethyl vinyl ether and diethyl ether.

### 3.2.1 Reaction Mechanism

We will start covering the PES found for the hydrolysis of ethyl vinyl ether catalyzed by $[Cp_2Mo(OH)(OH_2)]^+$, since this compound contains both alkyl and alkenyl functional groups and this reaction has been experimentally reported,[52] yielding ethanol and acetaldehyde.

As found in previous theoretical studies,[43] $[Cp_2Mo(OH)(OH_2)]^+$ readily loses its aquo ligand to form $[Cp_2Mo(OH)]^+$, which is a stable but very reactive species due to the empty coordination site and the presence of the hydroxo ligand. In principle, the ethyl vinyl ether molecule has three potential coordination modes: through C1 (the vinyl group), O3 (the ether functionality) or C5 (the ethyl moiety). However, the last one has been discarded after being unable to find any intermediate or TS for that coordination, consequence of the saturated nature of the alkyl group. The other possible coordination modes lead to two different reaction profiles that we will cover separately, starting with the coordination via C1.

The numbering of the ether atoms and the Gibbs energy profile for the reaction that begins with the coordination of ethyl vinyl ether to the metal center through the vinyl moiety (C1) is shown in Figures 3.6 and 3.7. The first stages of the reaction are displayed in the former. The TS for that coordination mode (**TS0**) presents a barrier of 18.5 kcal/mol, forming the intermediate **I1** with a relative Gibbs energy of 6.2 kcal/mol with respect to the isolated reactants. In **I1**, the distance between the oxygen atom at the hydroxo ligand ($O_{hydroxo}$) and C2 is only 2.863 Å. In addition, the vinyl moiety is activated, as reflected by the the charge (computed with NBO) at that carbon, which varies from +0.147 *e* at the isolated organic substrate to +0.354 *e* at **I1**. Hence, the nucleophilic attack from $O_{hydroxo}$, which has a charge of -0.916 *e* at **I1**, to C2 is favorable, forming a more stable intermediate **I2** (5.0 kcal/mol) via **TS1** (12.2 kcal/mol). In **I2**, Mo, C1, C2, and $O_{hydroxo}$ form a four-membered metallacycle. As a consequence of the nucleophilic attack, the charge of $O_{hydroxo}$ decreases to -0.674 e, whereas the charges of C1 and C2 suffer only slight variations. On the other hand, the Mo charge varies from +0.391 *e* at **I1** to +0.236 *e* at **I2**, so the metal center receives most of the electron density from the nucleophilic attack. Then, the hydrogen atom bonded to $O_{hydroxo}$ migrates to O3, cleaving at the same time the C2-O3 bond to release ethanol and form a very stable intermediate **I3** (-9.5 kcal/mol), where Mo is interacting simultaneously with C1, C2 and $O_{hydroxo}$. At **I2**, the

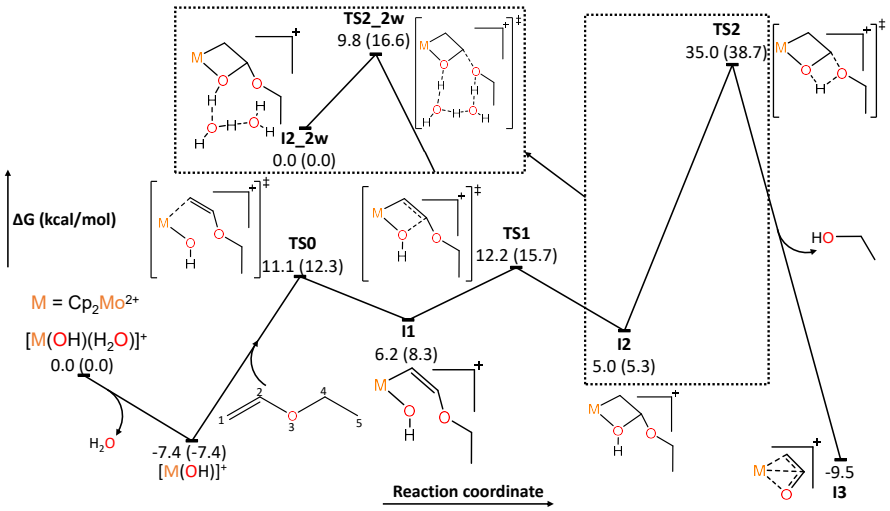


**Figure 3.6.** PCM-B3LYP/aug-cc-pVTZ (aug-cc-pVTZ-PP for Mo)//PCM-B3LYP/aug-cc-pVDZ (aug-cc-pVDZ-PP for Mo) Gibbs energy profile of the Mo-C1 coordination mechanism in water solution of the hydrolysis of ethyl vinyl ether catalyzed by $[Cp_2Mo(OH)(OH_2)]^+$ until the formation of **I3**. For comparison purposes, relative Gibbs energies for some relevant species in the hydrolysis of divinyl ether are also shown in parentheses.

distance between the hydrogen atom and O3 is large (2.839 Å), so the direct 1,3 migration implies a large barrier (**TS2**, 35.0 kcal/mol). Nevertheless, the presence of water molecules in the medium can stabilize this migration. In this sense, the explicit inclusion of two water molecules between the hydroxo ligand and O3 (**I2__2w**) lowers the barrier (**TS2__2w**) 20.2 kcal/mol.

The second part of the reaction, where **I3** evolves to the final products and the recovery of the catalyst, is included in Figure 3.7. At **I3**, either C1 or O3 may decoordinate from the metal center to form **I4-1** (-5.8 kcal/mol) or **I4-2** (1.4 kcal/mol), respectively, with an empty coordination site. Both the barrier and the corresponding intermediate are more stable for the breaking of the Mo-C1 bond than the Mo-O3 one. The vacant coordination site at the new intermediates is readily occupied by a water molecule from the medium. Then, one of the hydrogen atoms from that molecule migrates to O3 via **TS4-1** (5.1 kcal/mol) or **TS4-2** (6.5 kcal/mol) to yield **I6-1** (4.6 kcal/mol) and **I6-2** (7.5 kcal/mol), respectively. In those intermediates, the molybdenum center is coordinated to a vinyl alcohol moiety through O3 or C1, respectively. In the final step, the organic substrate is released by breaking the corresponding Mo-O3 (**TS5-1**, 11.9 kcal/mol) or Mo-C1 (**TS5-2**, 12.8 kcal/mol) bond. In the medium, vinyl alcohol tautomerizes to acetaldehyde, a more stable species. The

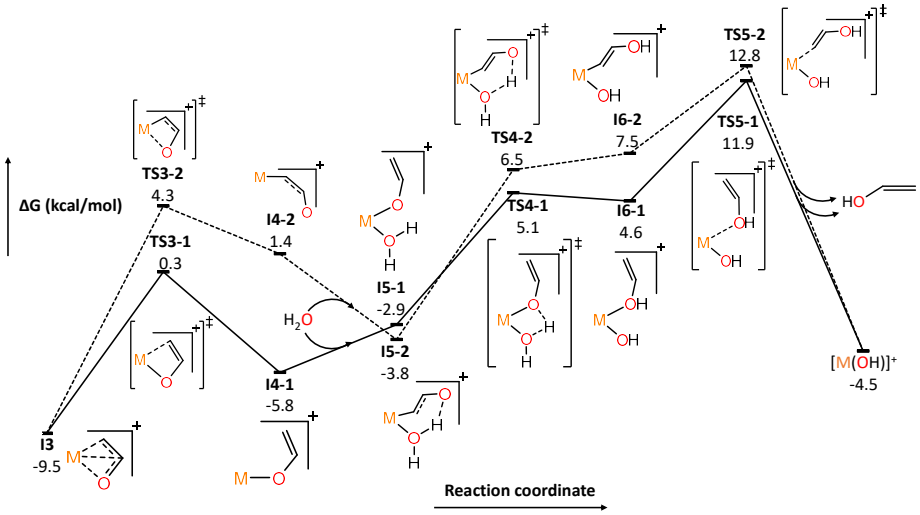


**Figure 3.7.** PCM-B3LYP/aug-cc-pVTZ (aug-cc-pVTZ-PP for Mo)//PCM-B3LYP/aug-cc-pVDZ (aug-cc-pVDZ-PP for Mo) Gibbs energy profile of the Mo-C1 coordination mechanism in water solution of the hydrolysis of ethyl vinyl ether catalyzed by $[Cp_2Mo(OH)(OH_2)]^+$, from **I3** to the recovery of the catalyst.

experimental barrier for such rearrangement is 15.2 kcal/mol, lower than the rate-determining step for the reaction, which is the migration of a hydrogen atom from $O_{hydroxo}$ to O3 (22.2 kcal/mol from the most stable previous intermediate).

Regarding the other coordination mode, there are two possible approaches for the coordination of ethyl vinyl ether through O3, one where the vinyl functionality is closer to the hydroxo ligand (denoted with the '**v_O**' label), and another one where the ethyl moiety is the one at a shorter distance of $O_{hydroxo}$ (denoted with '**e_O**'). The Gibbs energy profile for the former mechanism is displayed in Figure 3.8. The TS for that coordination mode (**TS0v_O**) has a similar relative energy (11.4 kcal/mol) to **TS0** (11.1 kcal/mol). Indeed, the charges of O3 and C1 at the isolated organic substrate only have a difference of 0.048 *e* (-0.608 *e* and -0.560 *e*, respectively). In the just formed intermediate, **I1v_O** (8.3 kcal/mol), the distance between $O_{hydroxo}$ and C2 is 2.850Å, close to the one found for **I1** (2.863 Å). Now, the nucleophilic attack from $O_{hydroxo}$ to C2 via **TS1v_O** (36.2 kcal/mol) to form **I2v_O** (5.9 kcal/mol) does not yield a four-membered metallacycle, since a simultaneous breaking of the C2-O3 bond occurs. In this way, as happened for **TS1**, the raise of electron density consequence of the nucleophilic attack lies as close as possible to the metal center. However, O3 is now the atom that suffers the biggest change in charge, varying from -0.503 *e* at **I1v_O** to -0.689 *e* at **I2v_O**. This can be attributed to the

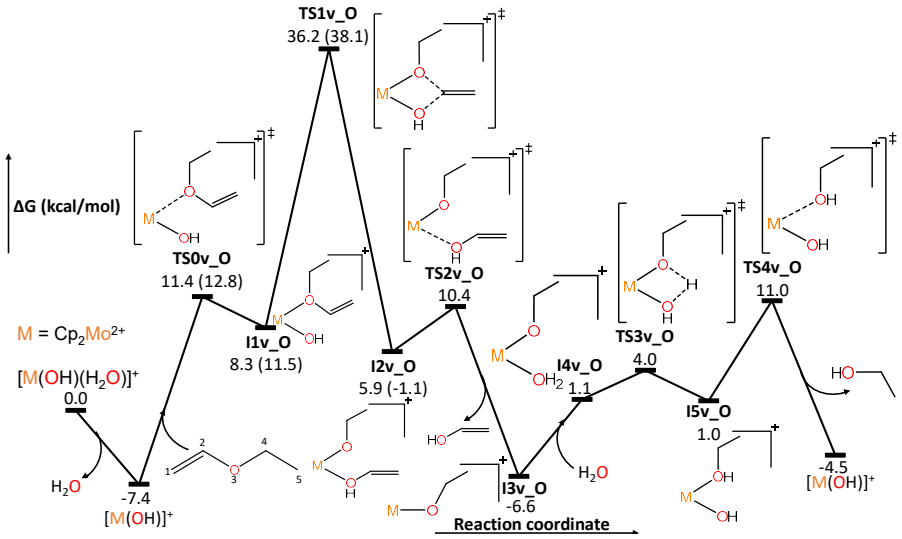


**Figure 3.8.** PCM-B3LYP/aug-cc-pVTZ (aug-cc-pVTZ-PP for Mo)//PCM-B3LYP/aug-cc-pVDZ (aug-cc-pVDZ-PP for Mo) Gibbs energy profile of the O3-Mo coordination mechanism in water solution of the hydrolysis of ethyl vinyl ether catalyzed by $[Cp_2Mo(OH)(OH_2)]^+$ where the vinyl moiety is closer to the hydroxo ligand than the ethyl one. Relative Gibbs energies for some relevant species in the hydrolysis of divinyl ether are shown in parentheses.

more electronegative character of oxygen compared to the carbon atom. Hence, if the C2-O3 bond was not broken, C1 would be the atom supporting the excess of electron density instead of O3. The breaking of the ether substrate into two moieties contributes to the high instability of **TS1v_O** compared to **TS1**. In the next step, vinyl alcohol is released through **TS2v_O** (10.4 kcal/mol), tautomerizing to acetaldehyde within the water medium. Consequently, the new intermediate **I3v_O** (-6.6 kcal/mol) has an empty coordination site, which is occupied by a water molecule from the solvent forming **I4v_O** (1.1 kcal/mol). In the final stage of the reaction, one of the water hydrogen atoms is transferred to O3 via **TS3v_O** (4.0 kcal/mol), yielding an intermediate **I5v_O** (1.0 kcal/mol) with an ethanol ligand that decoordinates through **TS4v_O** (11.0 kcal/mol), recovering the initial catalyst $[Mo(OH)]^+$ and giving the final ethanol product.

Finally, as displayed in Figure 3.9, ethyl vinyl ether may coordinate to Mo in a such a way that the ethyl moiety is closer to the hydroxo ligand than the vinyl one. Both the TS for the coordination, **TS0e_O** (11.1 kcal/mol), and the intermediate, **I1e_O** (8.1 kcal/mol) have similar relative energies than in the other mechanisms. Nevertheless, the nucleophilic attack from $O_{hydroxo}$ to C4, with the simultaneous breaking of the O3-C4 bond, via **TS1e_O** (39.5

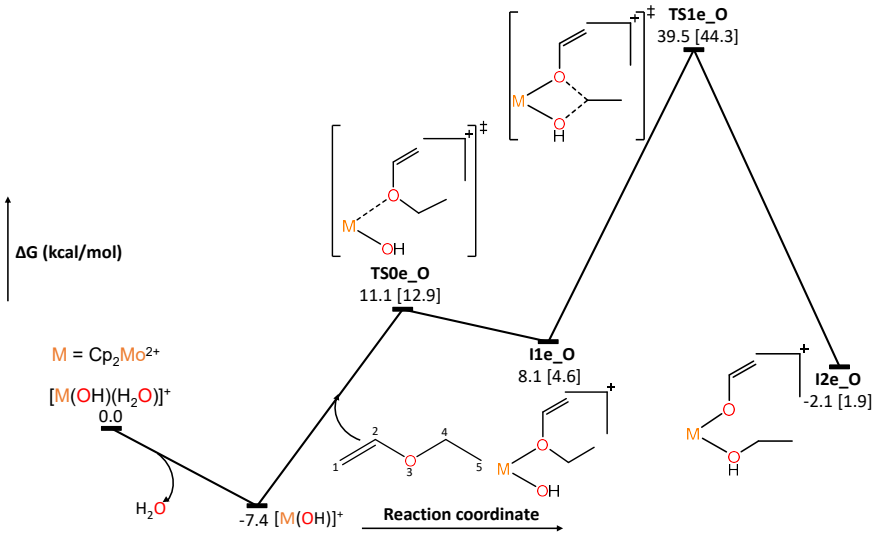


**Figure 3.9.** PCM-B3LYP/aug-cc-pVTZ (aug-cc-pVTZ-PP for Mo)//PCM-B3LYP/aug-cc-pVDZ (aug-cc-pVDZ-PP for Mo) Gibbs energy profile of the O3-Mo coordination mechanism in water solution of the hydrolysis of ethyl vinyl ether catalyzed by $[Cp_2Mo(OH)(OH_2)]^+$ where the ethyl moiety is closer to the hydroxo ligand than the vinyl one, until the formation of **I2e_O**. Relative Gibbs energies for the species involved the hydrolysis of diethyl ether are shown in square brackets.

kcal/mol) is penalized 3.3 and 27.3 kcal/mol with respect to **TS1v_O** and **TS1**, respectively. The reasons for that larger instability are the saturated nature of C4 and the very low change of electron density that this atom suffers after the coordination, which means that the vinyl moiety is not activated. The ethanol ligand coordinated to the metal center in **I2e_O** may then be released, yielding **I4-1**. The subsequent steps will be similar to those described for that intermediate (Figure 3.7).

### 3.2.2 Analysis of the Effects of the Ether Functionalities

So far, we have covered the three possible mechanisms found for the hydrolysis of ethyl vinyl ether catalyzed by $[Mo(OH)(H_2O)]^+$. Among them, the first mechanism, the one where the organic substrate is coordinated to Mo via C1, presents the lowest rate-determining step, **TS2_2w** with 22.2 kcal/mol from the most stable intermediate, compared to 43.6 and 46.9 kcal/mol for **TS1v_O** and **TS1e_O**, respectively, which are the highest barriers for the other mechanisms. Now, we will analyse the effect of replacing each of the functionalities of ethyl vinyl ether to obtain a monofunctional ether (divinyl and diethyl ether).

In the case of divinyl ether, denoted with the suffix '**__dv**', the mechanism with an initial coordination through the vinyl moiety is feasible. The relative Gibbs energies for the first stages of the hydrolysis of divinyl ether are shown in parentheses in Figure 3.6 for comparison purposes. We have focused on the species involved until the hydrogen migration, since we are mostly interested in analysing the differences in reactivity, which will be marked by either the intramolecular nucleophilic attack or the hydrogen transfer. The TS for the intramolecular hydrogen migration with the presence of two explicit water molecules (**TS2__2w__dv**) has a barrier of 29.3 kcal/mol, so it is again the rate-determining step. The main difference with **TS2__2w** is that now the hydrogen atom migrates to C5 instead of O3, releasing directly acetaldehyde. This divergent behaviour may arise from the significant negative charge of C5 at **I2__dv** (-0.526 e) and its geometrical disposition, favouring the migration to that atom.

This compound can also coordinate through O3, following a PES similar to that displayed in Figure 3.8, where the relative energies for the hydrolysis of divinyl ether are included in parentheses. The coordination proceeds through **TS0v__O__dv** (12.8 kcal/mol) to yield **I1v__O__dv** (11.5 kcal/mol). Then, the nucleophilic attack from $O_{hydroxo}$ to C2/C4 with the simultaneous breaking of the O3-C4/C2 bond takes place. The barrier for this step (**TS1v__O__dv**), as for ethyl vinyl ether, is very high (45.5 kcal/mol). Therefore, we can conclude that the hydrolysis of divinyl ether catalyzed by molybdocene follows a similar mechanism to that described for ethyl vinyl ether, with an initial Mo-C1/C5 coordination.

On the other hand, the mechanism where the ether coordinates to molybdenum through O3 with the alkyl moiety close to the hydroxo ligand is the only one that can describe the hydrolysis of diethyl ether catalyzed by $[Mo(OH)(H_2O)]^+$, denoted by the suffix '**__de**'. The relative Gibbs energies for the relevant species involved in that reaction are included in square brackets in Figure 3.9, for comparison purposes. The TS for the Mo-O3 coordination (**TS0e__O__de**) is only 1.8 kcal/mol less stable than **TS0e__O**. However, although the intermediate **I1e__O__de** is more stable than **I1e__O**, the barrier for the intramolecular nucleophilic attack remains too big (51.7 kcal/mol), even larger than for the hydrolysis of ethyl vinyl ether within that mechanism. As a consequence, we expect that this reaction is forbidden due to the vast energy barrier.

To sum up, we have found in this theoretical study that the hydrolysis of ethers bearing vinyl functionalities catalyzed by $[Mo(OH)(H_2O)]^+$ proceeds through the coordination of such functional group to Mo. The alternative mechanism where the ether oxygen coordinates to the metal center is disfavoured. This is not because the latter coordination mode is disfavoured, since the barriers for **TS0** and **TS0v__O** only differ by 0.3 kcal/mol, but because the intramolecular nucleophilic attack from the hydroxo ligand is a much more energy demanding step, with a difference of 24.0 kcal/mol between **TS1** and **TS1v__O**. The larger barrier for **TS1v__O** can be attributed to the fact that the vinyl group is only activated if it interacts with the metal center. In addition, the O3-C2 bond must be broken in **TS1v__O**, whereas **TS1** yields a four-membered metallacycle. The rate-determining step for both ethyl vinyl ether and divinyl ether

is the intramolecular hydrogen migration from the hydroxo ligand (**TS2__2w**), with a barrier of 22.2 and 29.3 kcal/mol, respectively. The reactivity and the released products from the hydrolysis of ethyl vinyl ether have been reported experimentally,[52] and they are in accordance with our results. For the hydrolysis of diethyl ether, where only the coordination via O3 may take place, the rate-determining step is the intramolecular nucleophilic attack (**TS1e__O__de**), with a barrier of 51.7 kcal/mol. Indeed, this barrier is in line with the results from the experimentalists,[52] who have found that $[Mo(OH)(H_2O)]^+$ is unable to catalyze the hydrolysis of such compound.

## 3.3 Reactivity of Re(I) and Mo(II) *N*-alkylimidazole Complexes towards Bases

The reaction of Re(I) and Mo(II) carbonyl *N*-alkylimidazole complexes bearing bpy or phen ligands with different substituents towards strong bases, such as $KN(SiMe_3)_2$, always starts with the deprotonation of the imidazole ring (RIm) and, afterwards, may evolve to different products depending on the nature of the metal center, and the substituents at the imidazole (R) and at the bidentate (R′) ligands. In this section of the Thesis we firstly study the reaction mechanism of the [Re(CO)$_3$(4,4′−*t*Bu$_2$bpy)(MeIm)]OTf complex, and then analyze the changes produced when the substituents at the bpy and the imidazole ligands are replaced by $NMe_2$ and Mes, respectively.[95] Furthermore, based on the trends found, we present our theoretical predictions for the same reaction when R′ = Br, as well as for the reaction of [Mo($\eta^3$−$C_4H_7$)(CO)$_2$(4,7−Cl$_2$phen)(RIm)]OTf (R= Me, Mes) complexes towards the same base. These theoretical predictions have been later confirmed experimentally.

The level of theory used in this work is PCM-B97D/6-31+G(d) (LANL2DZ for Br, LANL2DZ + *f* for Re and Mo). We start showing the reaction mechanism for the formation of the possible products from the intermediate formed after the deprotonation of the RIm ligand. The species involved in the different reaction pathways are similar to those described in previous studies for the transformation of Mn(I) imidazole complexes into NHC species[365] and for the reaction of analogous Re(I) and Mo(II) complexes bearing different bidentate ligands carried out in our group before the completion of this Thesis.[94,97]

### 3.3.1 General Reaction Mechanism

In all the reactions between the complexes [Re(CO)$_3$(4,4′−R′$_2$bpy)(RIm)]OTf and [Mo($\eta^3$−$C_4H_7$)(CO)$_2$(4,7−R′$_2$phen)(RIm)]OTf and $KN(SiMe_3)_2$ we have taken as the initial species for the study of the corresponding PES the neutral complex (**M**) that results from the deprotonation of the CH group located between the two N atoms in the RIm ligand ($C_{im}$). The relative energies of all species will be referred to the one of the corresponding **M** intermediate. As a representative model of all the species involved in the different outcomes of the reactions, we will consider first the deprotonation and subsequent evolution of the [Re(CO)$_3$(4,4′−*t*Bu$_2$bpy)(MeIm)]OTf complex. To differentiate the structures of this complex from the others studied in this work we will denote them with '**-*t*Bu**'.

From the deprotonated complex, **M-*t*Bu** (see Figure 3.10a), $C_{im}$ can either couple to the diimine ligand or form a C-bonded imidazol-2-yl product (a NHC-type of product). These two pathways are denoted as A and B, respectively. In the former case, there are two possible couplings, one with the external *ortho* carbon (C6 in bpy), in what we call the A1 route, and another with the internal *ortho* carbon (C2 in bpy), denoted as A2.

Both the A1 and the A2 routes consist in a single step. In the former (structures 3.10b and 3.10c in Figure 3.10), the barrier comes from the Gibbs energy

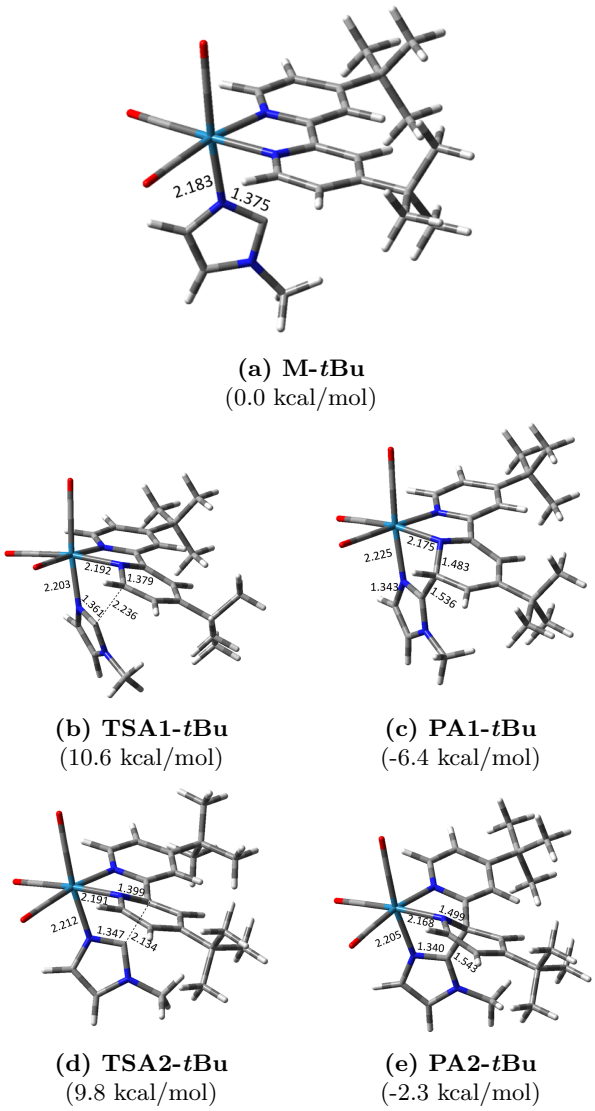


**(a) M-*t*Bu**
(0.0 kcal/mol)

**(b) TSA1-*t*Bu**
(10.6 kcal/mol)

**(c) PA1-*t*Bu**
(-6.4 kcal/mol)

**(d) TSA2-*t*Bu**
(9.8 kcal/mol)

**(e) PA2-*t*Bu**
(-2.3 kcal/mol)

**Figure 3.10.** PCM-B97D/6-31+G(d) (LANL2DZ + $f$ for Re) optimized geometries and Gibbs energies relative to the initial deprotonated complex of the species involved in the intramolecular coupling with the bpy ligand bearing tBu substituents. Relevant distances in Å are also included.

of **TSA1-*t*Bu** (10.6 kcal/mol), where $C_{im}$ is at 2.236 Å from C6. In the product, **PA1-*t*Bu** (-6.4 kcal/mol), there is a new bond between those two carbon atoms, as the distance $C_{im}$-C6 has changed to 1.536 Å. Moving to the A2 route (structures 3.10d and 3.10e in Figure 3.10), the nucleophilic attack from $C_{im}$ is

now aimed at the C2 atom of the bpy ligand passing through **TSA2-*t*Bu** (9.8 kcal/mol), and forming a bond between them, **PA2-*t*Bu** (-2.3 kcal/mol). The length of the new bond is close to the analogous one in the previous pathway (1.543 Å). Both *ortho* carbons of the diimine ligand are potential electrophilic sites, as reflected by their NBO charges: +0.078 e at C6, and +0.220 e at C2. The nucleophilic attack to those carbons causes a dearomatization in the pyridine ring where the attack is produced and a significant distortion of its geometry. In this sense, the dihedral angle between the C3-C2-N1-C6 atoms changes from 1.569° at **M-*t*Bu**, to 27.170° at **PA1-*t*Bu** and 33.240° at **PA2-*t*Bu**, also confirming that the coupling to C2 induces a larger loss of planarity than the one to C6. These facts are in accordance with kinetic and thermodynamic features observed in the PES of the reaction. Thus, the lower barrier of **TSA2-*t*Bu** is due to the fact that C2 is a more electrophilic center, and the greater stability of **PA1-*t*Bu** results from the diimine smaller geometry distortion in the ring affected by the nucleophilic attack.

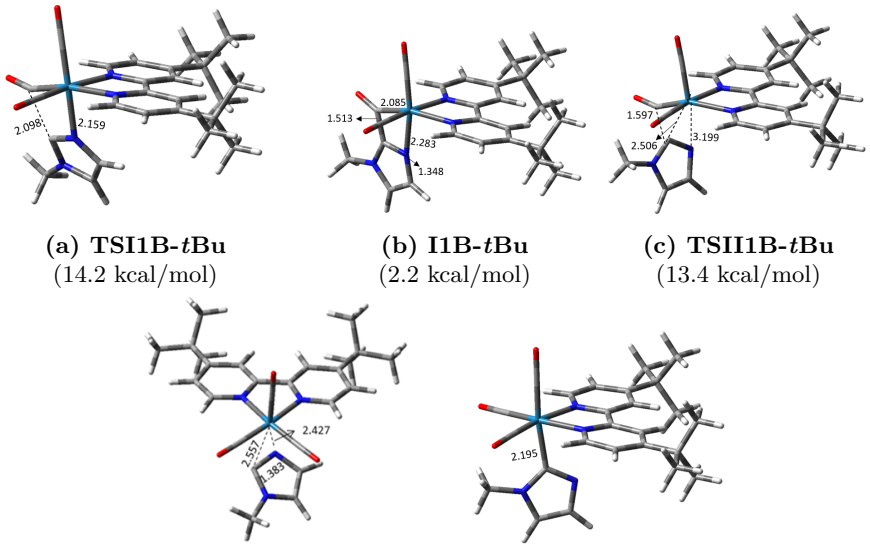


**(a) TSI1B-*t*Bu** (14.2 kcal/mol)

**(b) I1B-*t*Bu** (2.2 kcal/mol)

**(c) TSII1B-*t*Bu** (13.4 kcal/mol)

**(d) TS2B-*t*Bu** (16.4 kcal/mol)

**(e) PB-*t*Bu** (-18.9 kcal/mol)

**Figure 3.11.** PCM-B97D/6-31+G(d) (LANL2DZ + *f* for Re) optimized geometries, and Gibbs energies relative to the initial deprotonated complex of the species involved in the formation of a imidazol-2-yl complex with the bpy ligand bearing tBu substituents. Relevant distances in Å are also included.

Regarding the B route, which ends up in the formation of an imidazol-2-yl product, there are two possible mechanisms for that transformation. One of them, denoted by 1B, is a two-step route where $C_{im}$ couples to a CO ligand in *cis* disposition before its bonding to the metal center, and in the other one (2B) the

bond between the metal center and the deprotonated carbon is formed in a single step. The species involved in the 1B mechanism are shown in Figure 3.11. As just mentioned, this mechanism starts with a nucleophilic attack to a carbonyl ligand via **TSI1B-*t*Bu** (14.2 kcal/mol), forming the intermediate **I1B-*t*Bu** (2.2 kcal/mol) with a four-membered metallacycle. Then, **I1B-*t*Bu** evolves through a three-center TS, **TSII1B-*t*Bu** (13.4 kcal/mol), to form the very stable imidazol-2-yl product, **PB-*t*Bu** (-18.9 kcal/mol), where the bond with the CO ligand has been broken and the RIm ligand is now coordinated to the metal through $C_{im}$. On the other hand, the 2B reaction pathway is characterized by a unique $\kappa^2$ (C,N)-imidazolyl TS, **TS2B-*t*Bu** (16.4 kcal/mol), where the Re-$N_{im}$ bond breaks and the Re-$C_{im}$ bond forms simultaneously (Structure 3.11d in Figure 3.11). The barrier for the direct arrangement to **PB-*t*Bu** is 2.2 kcal/mol higher than for the 1B case, so this mechanism can be discarded. The preference for the 1B route is consequence of a weakening of the Re-$N_{im}$ bond upon formation of **I1B-*t*Bu**, where it is elongated 0.1 Å, due to the loss of electron density in the RIm ligand after the coupling to the carbonyl ligand. This hypothesis can be tested by computing the DI values at the BCP located between Re and $N_{im}$ at **M-*t*Bu** and **I1B-*t*Bu**, which are 0.573 and 0.412, respectively. These numbers confirm the loss of strength of the Re-$N_{im}$ bond in the intermediate **I1B-*t*Bu**, favouring the formation of **PB-*t*Bu**.

Comparing the stability of the different products, **PB-*t*Bu** is clearly the most stable one, but the rate-determining step for its formation (14.2 kcal/mol) is larger than the ones of the A route, which avoids its formation. With respect to the formation of **PA1-*t*Bu** and **PA2-*t*Bu**, as already discussed, the barrier is 0.8 kcal/mol higher for the former, but it leads to a much more stable product (4.1 kcal/mol lower in energy). The narrow difference between both barriers, along with the greater stability of the **PA1-*t*Bu** product, points to the formation of that species, as experimentally confirmed.

### 3.3.2 Effect of the Imidazole and the Bidentate Ligands

Having presented the mechanism for the reaction of the complex with *t*Bu substituents on the bpy ligand and a MeIm monodentate ligand, we will analyse the effect of replacing MeIm by MesIm, as well as of varying the substituents at the diimine ligand. The experimentalists have reported that the **PA1** product is also formed in the reaction of the [Re(CO)$_3$(4,4′−R′$_2$bpy)(MesIm)]OTf (R = *t*Bu, $NMe_2$) complexes. However, they have found that the deprotonation of the [Re(CO)$_3$(4,4′−($NMe_2$)$_2$bpy)(MeIm)]OTf complex yields a **PB** product. Therefore, we wish to rationalize those remarkable differences. The relative energies of all the species involved in the intramolecular transformations of these complexes are shown in Table 3.4.

The replacement of the *t*Bu substituents by the more electron-donating group $NMe_2$ in [Re(CO)$_3$(4,4′−*t*Bu$_2$bpy)(MeIm)]OTf should, in principle, disfavour the coupling of the imidazole ring with the bidentate ligand, since the bpy ligand will have less electrophilic character due to the increase in its electron density. The molecular electrostatic potential (MEP) maps at **M-*t*Bu** and

**Table 3.4.** PCM-B97D/6-31+G(d) (LANL2DZ + *f* for Re) Gibbs relative energies in kcal/mol referred to the corresponding **M** complex of the species involved in the four possible reaction pathways for the reaction of [Re(CO)$_3$(4,4′−R′$_2$bpy)(RIm)]OTf (R′ = *t*Bu, NMe$_2$; R = Me, Mes) with KN(SiMe$_3$)$_2$ in THF solution.

| R | R′ | **TSA1** | **PA1** | **TSA2** | **PA2** | **TSI1B** | **I1B** | **TSII1B** | **PB** | **TS2B** |
|---|---|---|---|---|---|---|---|---|---|---|
| *t*Bu | Me | 10.6 | -6.4 | 9.8 | -2.3 | 14.2 | 2.2 | 13.4 | -18.9 | 16.4 |
| *t*Bu | Mes | 7.5 | -11.4 | 5.3 | -7.8 | 8.4 | 1.2 | 9.5 | -21.5 | 14.4 |
| NMe$_2$ | Me | 14.9 | 0.8 | 12.9 | 3.0 | 13.1 | 3.3 | 14.7 | -17.0 | 18.9 |
| NMe$_2$ | Mes | 9.1 | -6.5 | 5.7 | -3.3 | 11.4 | 4.6 | 9.3 | -23.0 | 13.8 |

**M-NMe$_2$** (Figure 3.12), which show the charge distribution of the deprotonated complexes in three dimensions, illustrate the fact that the bpy ligand is more electrophilic (more blue) with the *t*Bu substituents than with the NMe$_2$ ones. Besides, both the **PA1-NMe$_2$** (0.8 kcal/mol) and the **PA2-NMe$_2$** (3.0 kcal/mol) products are now less stable than the deprotonated initial complex, and the barriers for their formation are also higher than in the *t*Bu substituted system. Therefore, the **PB-NMe$_2$** species, with a relative energy of -17.0 kcal/mol and a rate-determining step close to the ones of the A routes, is the expected product, as found by the experimentalists.

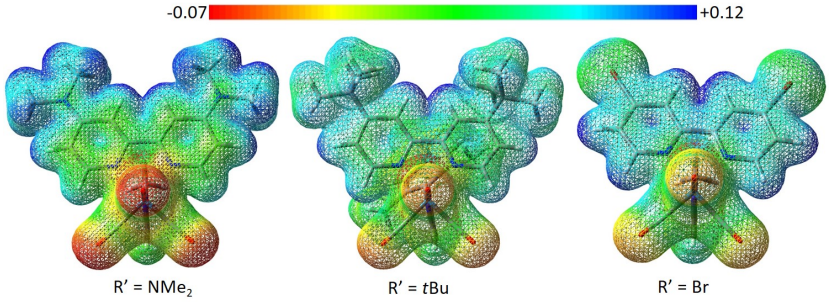


**Figure 3.12.** Molecular electrostatic potential (MEP) map of the deprotonated initial complexes **M-NMe$_2$**, **M-*t*Bu** and **M-Br** with a MeIm ligand, illustrating the change in electron density of the bpy ligand depending on its substituents.

On the other hand, the main effect of exchanging MeIm by MesIm in the *t*Bu complex is a relative stabilization of all the species. This is specially important in the A1 and A2 routes, whose corresponding products are stabilized 5.0 and 5.5 kcal/mol, respectively. The low barrier of **TSA1-*t*Bu** (7.5 kcal/mol), and the stability of **PA1-*t*Bu** (-11.4 kcal/mol) explain the formation of such a coupling with the bpy ligand, as experimentally reported. The same trend is found for the NMe$_2$ complexes. Contrary to the reaction with the MeIm ligand, with the MesIm one both the **PA1-NMe$_2$** (-6.5 kcal/mol) and the **PA2-NMe$_2$**

(-3.3 kcal/mol) products are more stable than **M-NMe$_2$**. The lower barrier for the A1 route (9.1 kcal/mol) than the one for the formation of **PB-NMe$_2$** (11.4 kcal/mol) leads to the formation of the experimentally observed product **PA1-NMe$_2$**. As a conclusion, the larger electron density of the MeIm ligand, as displayed in Figure 3.13, makes the coupling to the bidentate ligand less favourable. The main reason is that it yields an excess of electron density at the bidentate ligand, due to the presence of electron-donating groups (*t*Bu and $NMe_2$). This effect is more pronounced with the $NMe_2$ more electron-rich bpy.

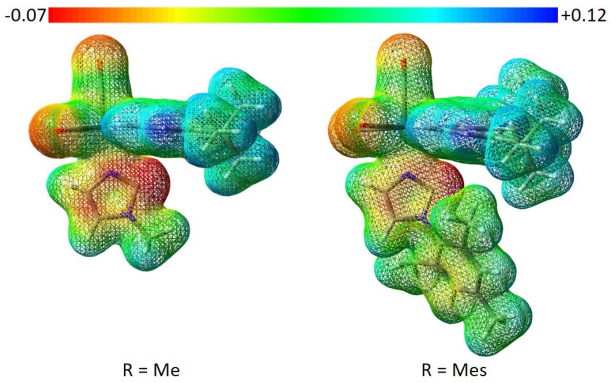


**Figure 3.13.** Molecular electrostatic potential (MEP) map of the deprotonated complex **M-*t*Bu** with a MeIm and a MesIm ligand, showing the change in nucleophilic character of such a ligand.

Our analysis has shown the effects of adding electron-donating groups to the bidentate ligand as well as those related to the nature of the imidazole ligand. However, the effect of adding electron-withdrawing substituents on the bpy had not been experimentally tested when we finished the previous study. According to our theoretical analysis, the electron-withdrawing substituents on the bpy should produce the opposite effect, that is the preference for the A routes. To confirm this point, we decided to extend our analysis to a complex bearing electron-withdrawing substituents, such as Br, on the bpy: $[Re(CO)_3(4,4'-Br_2bpy)(RIm)]OTf$. In fact, the MEP map of **M-Br** (Figure 3.12) shows a much more electrophilic bpy than the one at the complexes bearing electron-donating substituents.

As seen in Table 3.5, the barriers and the products for the A routes are much more lower in energy with the Br substituent than with the electron-donating ones. With respect to the B route, the rate-determining barrier remains higher than for the A pathways, so the formation of **PB-Br** is discarded. It is remarkable that the A2 route still presents the lowest barriers, but now the stability of **PA2-Br** is large, so it seems to be the most possible outcome for the reaction. Given the fact that such a product had not been reported yet for a Re(I) complex (analogous couplings have been reported for Mo(II) complexes with Cl and Br substituents on the bpy ligand), we suggested the experimentalists

**Table 3.5.** PCM-B97D/6-31+G(d) (LANL2DZ for Br, LANL2DZ + $f$ for Re) Gibbs relative energies in kcal/mol referred to **M-Br** of the species involved in the four possible reaction pathways for the reaction of [Re(CO)$_3$(4,4′−Br$_2$bpy)(RIm)]OTf (R = Me, Mes) with KN(SiMe$_3$)$_2$ in THF solution.

| R | R′ | **TSA1** | **PA1** | **TSA2** | **PA2** | **TSI1B** | **I1B** | **TSII1B** | **PB** | **TS2B** |
|---|---|---|---|---|---|---|---|---|---|---|
| Br | Me | 5.4 | -12.6 | 3.4 | -9.8 | 10.4 | -0.4 | 10.8 | -20.3 | 13.9 |
| Br | Mes | 6.4 | -15.9 | 3.6 | -11.7 | 11.3 | 0.4 | 9.6 | -21.8 | 15.1 |

to carry out the reaction of [Re(CO)$_3$(4,4′−Br$_2$bpy)(RIm)]OTf (R = Me, Mes) with KN(SiMe$_3$)$_2$. As expected, they were able to isolate a complex with a C$_{im}$-C2 bond with the bpy ligand.

As already mentioned, the [Mo($\eta^3$−C$_4$H$_7$)(CO)$_2$(4,4′−R′$_2$bpy)(RIm)]OTf (R′ = Cl, Br; R = Me, Mes) complexes react with KN(SiMe$_3$)$_2$ to also yield a coupling with the internal *ortho* carbon of the bidentate ligand. Then, we have wondered if replacing bpy by a more rigid phen ligand would avoid the formation of such a product. For that purpose, we have also studied the deprotonation reaction of [Mo($\eta^3$−C$_4$H$_7$)(CO)$_2$(4,7−Cl$_2$phen)(RIm)]OTf (R = Me, Mes), starting from the deprotonated complex **M-Cl**. The relative energies for the species involved in that reaction are shown in Table 3.6.

**Table 3.6.** PCM-B97D/6-31+G(d) (LANL2DZ + $f$ for Mo) Gibbs relative energies in kcal/mol referred to **M-Cl** of the species involved in the three possible reaction pathways for the reaction of complexes [Mo($\eta^3$−C$_4$H$_7$)(CO)$_2$(4,7−Cl$_2$phen)(RIm)]OTf (R = Me, Mes) with KN(SiMe$_3$)$_2$ in THF solution.

| R | R′ | **TSA1** | **PA1** | **TSA2** | **PA2** | **TSI1B** | **I1B** | **TSII1B** | **PB** |
|---|---|---|---|---|---|---|---|---|---|
| Cl | Me | 7.9 | -13.9 | 7.7 | -6.5 | 8.6 | -3.4 | 4.0 | -15.5 |
| Cl | Mes | 5.1 | -16.5 | 6.3 | -10.3 | 6.9 | -3.4 | 6.1 | -16.9 |

The geometries of the species found for this reaction are analogous to the ones of the Re(I) tricarbonyl complexes (see Figure 3.14), with the only exception that we have not been able to locate **TSB2**. If we compare the relative energies of the A1 and A2 routes, **TSA2-Cl** is similar (with MeIm) or even more unstable (with MesIm) than the corresponding **TSA1-Cl**. In addition, the **PA1-Cl** products are always much more stable than the **PA2-Cl** ones. Therefore, it is clear that the coupling with the external *ortho* carbon is now more favoured than with the internal one, as we expected for the phen ligand. Hence, the product of the reaction is either **PA1-Cl** or **PB-Cl**. In the case of the MesIm complex, the rate-determining barrier for the B route is 4.4 kcal/mol more unstable than **TSA1-Cl**, so the formation of **PB-Cl** is prevented and we would expect a **PA1-Cl** product from the reaction. However, the barrier for the B pathway is only 0.7 kcal/mol higher than **TSA1-Cl** with a MeIm ligand, and both the

**PA1-Cl** (-13.9 kcal/mol) and the **PB-Cl** (-15.5 kcal/mol) products are very stable. As a consequence, either of them, or a mixture of both species, will be formed in the reaction of the MeIm complex. Since we predict different types of products with the phen ligand than with the bpy one, we have prompted the experimentalists to carry out these reactions. As a result, and in agreement with our predictions, they have obtained **PA1-Cl** for the complex with MesIm, and a mixture of **PA1-Cl** and **PB-Cl** for the MeIm complex.

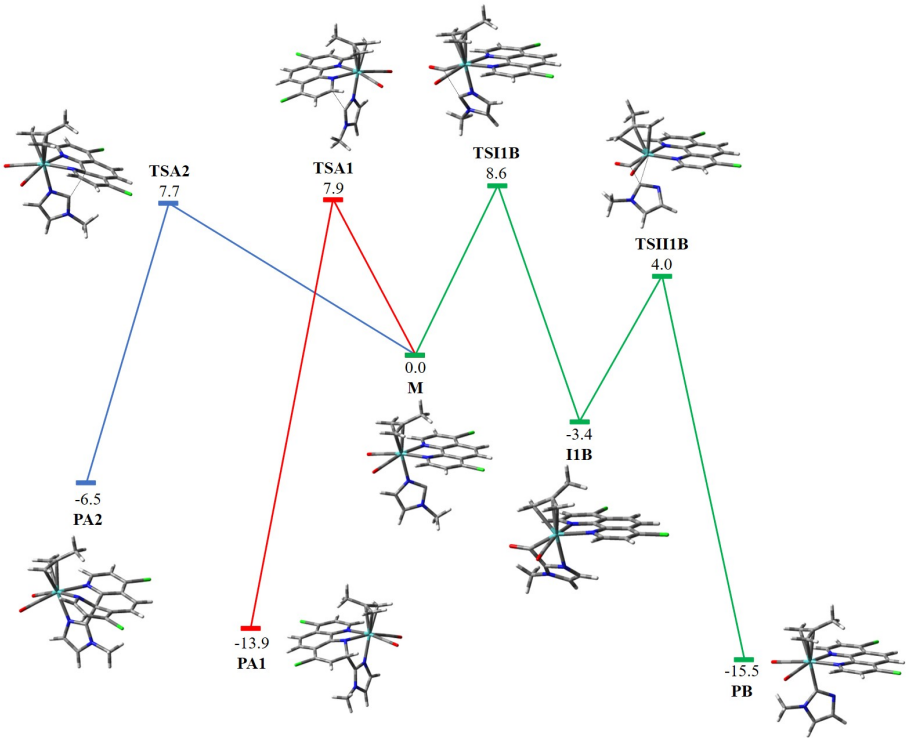


**Figure 3.14.** PCM-B97D/6-31+G(d) (LANL2DZ + $f$ for Mo) optimized geometries of all the species for the reaction between $KN(SiMe_3)_2$ and the complex $[Mo(\eta^3-C_4H_7)(CO)_2(4,7-Cl_2phen)(MeIm)]OTf$ in THF solution. Relative Gibbs energies in kcal/mol referred to the deprotonated **M-Cl** complex are also included.

## 3.4 Reactivity of a Re(I) Tricarbonyl Aquo Complex towards Biological Targets

It has been reported that the Re(I) complex $[Re(CO)_3(dmphen)(OH_2)]^+$ (dmphen = 2,9-dimethyl-1,10-phenantroline), **1** in Scheme 3.5, is able to inhibit tumor growth both *in vitro* and *in vivo*,[118,119] showing higher activity than cisplatin in some cancer cell lines and being able to overcome cisplatin resistance. It has been suggested that complex **1** and derivatives can bind covalently to N-donor ligands found in DNA or proteins via substitution of the labile ligand aquo.[29,366] Among the possible targets in DNA, the N7 atom of guanine and the N1 and N7 atoms of adenine are the most nucleophilic ones (see Scheme 3.5), although, to the best of our knowledge, only several covalent adducts between Re(I) tricarbonyl complexes and guanine nucleobases have been reported.[34–37] On the other hand, histidine residues are the prime amino acid targets (see Scheme 3.5), as suggested by the crystallization of several proteins containing Re(I) centers covalently linked to the N1 atom of histidine residues.[29,367–374] Based on these two facts, the reactivity of complex **1** towards 9-ethylguanine and *N*-acetylhistidine was investigated experimentally, finding that the first reaction is faster than the other one.[118] It has been proposed that this complex must act in a different way than cisplatin, but the mechanism of action is still unknown. Therefore, we decided to undertake a theoretical study on the reactivity of complex **1** in water solution towards 9-ethylguanine (**G**) and a derivative of *N*-acetylhistidine where the carboxylic termination has been substituted by a *N*-methyl amide group to reproduce more accurately the actual protein environment (**H** in Scheme 3.6). Apart from this issue, we also focused on analyzing the influence of the bidentate ligand on the cytotoxic activity.

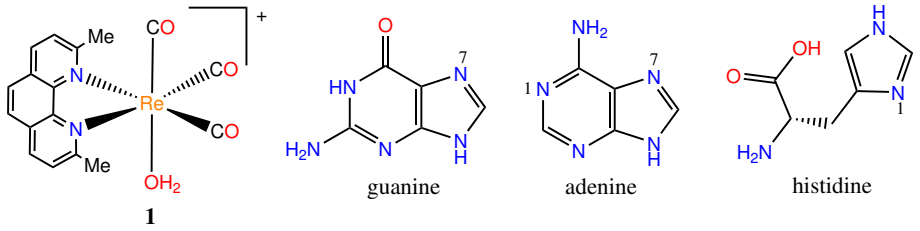


**Scheme 3.5.** Structure of complex $[Re(CO)_3(dmphen)(OH_2)]^+$ (**1**), nucleobases guanine and adenine, and the histidine amino acid. Atom numbering of the most nucleophilic atoms of the nucleobases and amino acid is also given.

### 3.4.1 Mechanism of Action

Since there are many possible orientations for the biological targets, and the water molecules in the cell environment could play a significant role in the reaction, the mechanism of action of complex **1** towards **G** and **H** was investigated in several steps by performing QM calculations and MD simulations as explained

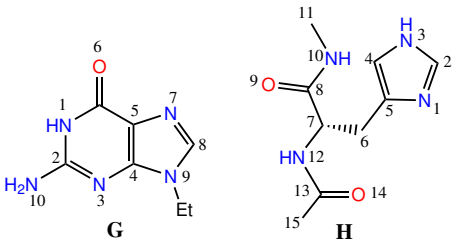


**Scheme 3.6.** Structure of **G** and **H**. Atom numbering of the non-hydrogen atoms is also given.

below.

First, we optimized an initial geometry for the dimers resulting from the interaction between the complex **1** and **G** and **H** (**1-G** and **1-H**, respectively) with the MN15 functional and the basis set 6-31+G(d,p) for the non-metal atoms and LANL2DZ for Re. MN15 was selected among a series of functionals (B3LYP, D3-B3LYP, MN15, PBE, M06, M06-L) by comparing the optimized geometry of **1** to the experimental X-ray structure. In the initial optimized structure of the dimer **1-G**, the aquo ligand of **1** forms hydrogen bonds with the O6 and N7 atoms of **G**, whereas in **1-H** the aquo ligand is interacting with the N1 atom of the amino acid.

Second, the optimized structures obtained for **1-G** and **1-H** were used to perform MD simulations in a water box aiming at getting a more realistic description of these dimers in the cell environment. To accomplish this task, we used the General Amber Force Field (GAFF) for non-water molecules,[303] whereas TIP3P was employed to modeling water molecules.[310] However, due to the lack of parameters for metal atoms in GAFF, those for the bond stretching and the bond bending terms concerning the Re atom were obtained from a QM frequency calculation through the VFFDT software,[305] the dihedral parameters involving the metal center have been set to zero, and the Re Lennard-Jones parameters have been acquired from the literature.[375–377] All the partial charges have been computed using the Restrained Electrostatic Potential (RESP) method. The dimers **1-G** and **1-H** were introduced into a square water box of approximately 20 Å in each side along with a chloride ion to neutralize the positive charge of the complex. Then, MD simulations were carried out using the NAMD program. We started with a (N, V, T) minimization of 200 ps to follow with a (N, P, T) simulation at 310 K and 1 atm of 120 ns, where we took snapshots from the simulation only after the first 20 ns. Then, we clustered the structures obtained from the simulation using the GROMACS software with the Gromos algorithm and a cutoff distance of 0.15 Å.

Third, in order to handle an adequate number of atoms to carry out a QM study on the evolution of the dimers **1-G** and **1-H** obtained in the water box, the number of explicit water molecules was drastically reduced. Hence, only the most relevant water molecules for the reaction investigated, which are

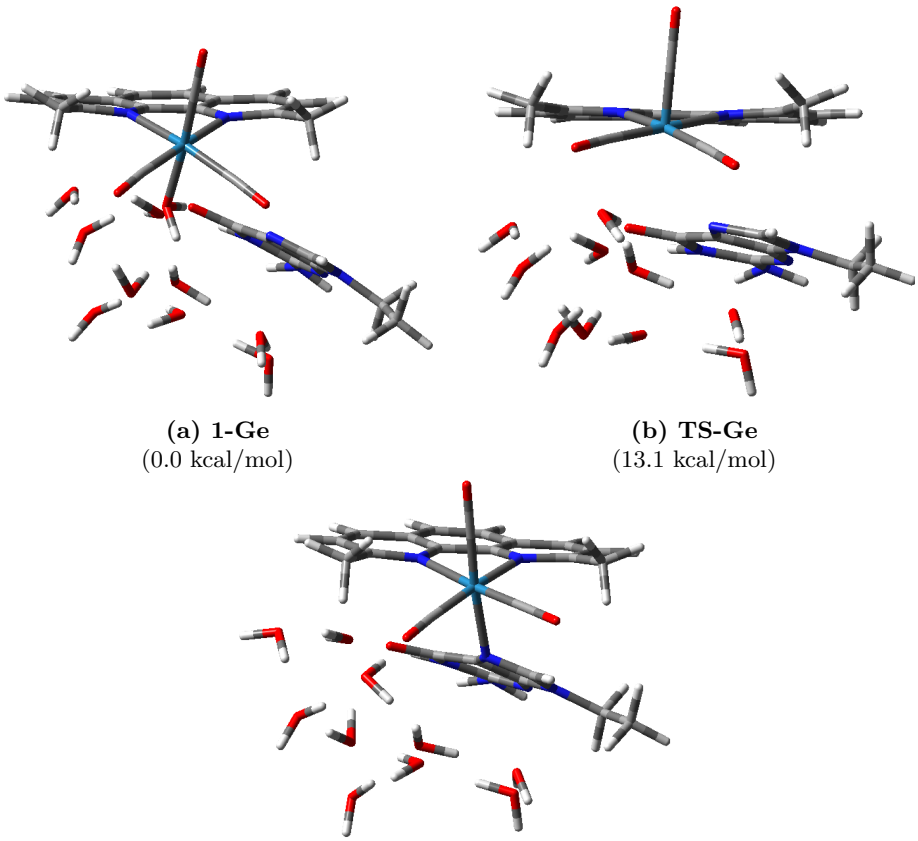

**(a) 1-Ge**
(0.0 kcal/mol)

**(b) TS-Ge**
(13.1 kcal/mol)

**(c) P-Ge**
(-5.4 kcal/mol)

**Figure 3.15.** MN15/6-31+G(d,p) (LANL2DZ for Re) optimized geometries obtained for **1-Ge** and its posterior species when considering explicit solvent water molecules. CPCM-DLPNO-CCSD(T)/def2-TZVPP//MN15/6-31+G(d,p) (LANL2DZ for Re) relative Gibbs energies are also included in parenthesis.

those closer to the reaction center (the aquo ligand), were considered. Thus, we took the water molecules within 4.0 Å of the oxygen at the aquo ligand (Ow), which are 8 molecules in the case of **1-G** and 7 for **1-H**. We will denote the structures with explicit water molecules by adding the suffix '**e**' to the previous notation. Figures 3.15 and 3.16 display the corresponding optimized structures at the MN15/6-31+G(d,p) (LANL2DZ for Re) level, respectively. In addition, to get more accurate energies, the MN15/6-31+G(d,p) (LANL2DZ for Re) energies were refined using the highly sophisticated level CPCM-DLPNO-CCSD(T)/def2-TZVPP, relative Gibbs energies computed at that level are also included in Figures 3.15 and 3.16. The main difference between the initial dimer and the optimized structure with explicit water molecules is found for **1-He**,

where the conformation of the histidine moiety has significantly changed as the aquo ligand is now interacting with O9 instead of N1 (see Figure 3.16). The lability of the aquo ligand favors the cleavage of the Re-$OH_2$ bond in both **1-Ge** and **1-He** with the simultaneous formation of the new bonds Re-**G** and Re-**H** to give the products **P-Ge** and **P-He** through the TSs **TS-Ge** and **TS-He**, respectively.

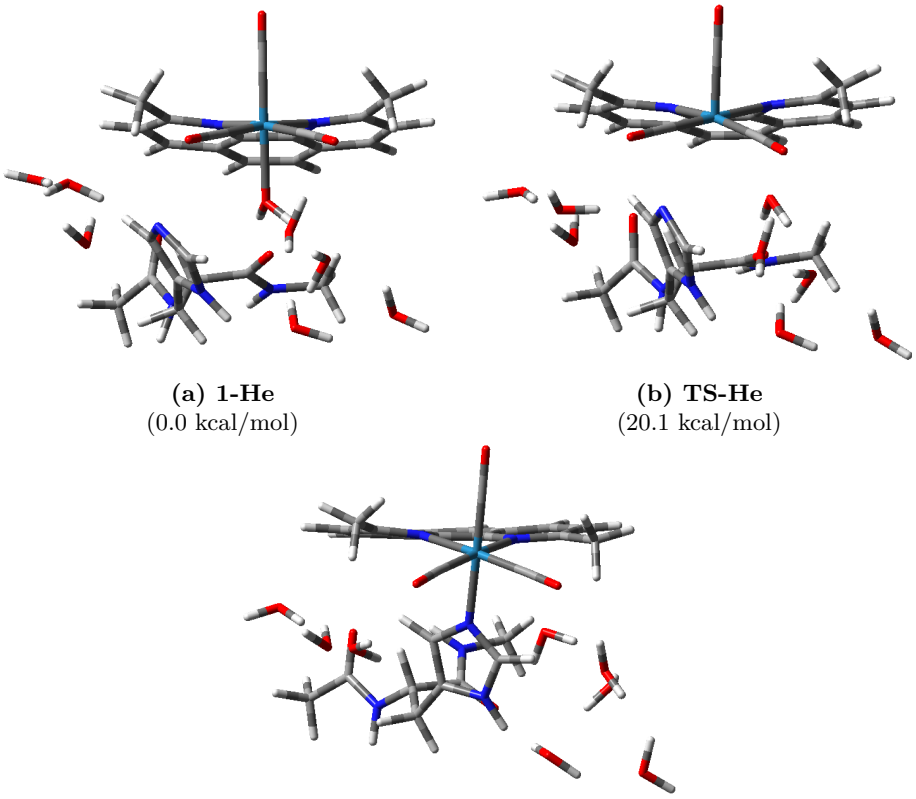

**(a) 1-He**
(0.0 kcal/mol)

**(b) TS-He**
(20.1 kcal/mol)

**(c) P-He**
(-6.6 kcal/mol)

**Figure 3.16.** MN15/6-31+G(d,p) (LANL2DZ for Re) optimized geometries obtained for **1-He** and its posterior species when considering explicit solvent water molecules. CPCM-DLPNO-CCSD(T)/def2-TZVPP//MN15/6-31+G(d,p) (LANL2DZ for Re) relative Gibbs energies are also included in parenthesis.

The associative displacement mechanism of the aquo ligand and coordination to Re of the biomolecules **G** and **H** found is in accordance to previous theoretical studies in the reaction mechanism of an Ir complex with **G**.[378] According to our CPCM-DLPNO-CCSD(T)/def2-TZVPP//MN15/6-31+G(d,p) (LANL2DZ for Re) Gibbs energy results, **1-Ge** proceeds through **TS-Ge** (13.1 kcal/mol) where the distance between the N7 atom of the guanine moiety and Re is 2.891

Å and the one between the oxygen from the aquo ligand (Ow) and Re is 2.831 Å (see Figure 3.15). In the product formed, **P-Ge** (-5.4 kcal/mol), there is a new bond between Re and N7 with a distance of 2.301 Å, whereas the water molecule that has been released forms hydrogen bonds with N7, O6, and another water molecule, which helps to stabilize the product (see Figure 3.15). On the other hand, **1-He** surpasses an energy barrier of 20.1 kcal/mol (**TS-He**) to give the product **P-He** (-6.6 kcal/mol). At **TS-He** the distances between Re and the N1 atom of the **H** moiety and Ow are 2.891 Å and 2.831 Å, respectively (see Figure 3.16). The comparison of both reactive processes shows that **TS-He** is 7.0 kcal/mol more unstable than **TS-Ge**, which is in line with the higher reactivity of complex **1** towards 9-ethylguanine over *N*-acetylhistidine.[118] However, **P-He** is 1.2 kcal/mol more stable than **P-Ge**. Therefore, the reaction with the amino acid residue histidine is kinetically more penalized than with the DNA nucleobase guanine, but more thermodynamically favored. The inclusion of some relevant explicit water molecules is key for a proper description of the mechanism of action of complex **1**, as the study of the reactions without those molecules did not reproduce the experimental trend for the reaction rates.

### 3.4.2 Influence of the Bidentate Ligand

In their original paper, Wilson and co-workers selected complex **1** from a series of Re(I) tricarbonyl aquo complexes bearing different substituted bidentate ligands (see Scheme 1.14).[118] Among all of them, the complexes that showed the highest cytotoxic activity are those with electron-donating substituents at the diimine ligand (dmphen, 4,4′−$Me_2$bpy, 4,4′$(OMe)_2$bpy), whereas the complex with electron-withdrawing groups attached to the bpy ligand (4,4′−$(COOMe)_2$bpy) display, by far, the lowest activity.[118] In addition, the complexes with phen ligands were more cytotoxic than their bpy counterparts. Thus, since they only took into account three phen ligands (phen, dmphen, and 4,7-diphenylphen) without considering stronger electron-donating substituents, we were motivated by exploring the effect of adding this type of substituents to the phen ligand. For that purpose, we have investigated the reaction of the Re(I) complexes $[Re(CO)_3(4,7-R_2phen)(OH_2)]^+$ (R = OMe (**2**), $NMe_2$ (**3**)) towards **H**. The theory level used is the same as for the reaction of **1** with **H** in the presence of explicit water molecules, that is, CPCM-DLPNO-CCSD(T)/def2-TZVPP//MN15/6-31+G(d,p) (LANL2DZ for Re).

The optimized structures obtained for all the species with their relative Gibbs energies referred to the corresponding dimer (**2-He** or **3-He**) are displayed in Figures 3.17 and 3.18.

As expected, both TSs (**2-TS-He** and **3-TS-He**) and products (**2-P-He** and **3-P-He**) stabilize when each of these OMe and $NMe_2$ substituents are present in both 2- and 9- positions of the phen ligand. In the case of the complex with OMe groups, **2-TS-He** is 1.8 kcal/mol more stable than **TS-He**, whereas **2-P-He** is 6.0 kcal/mol lower in relative energy than **P-He**. The stabilizing effect of the stronger electron-donating group $NMe_2$ is more moderate than the one of OMe, stabilizing **3-TS-He** and **3-P-He** 0.5 and 1.4 kcal/mol, respectively. The

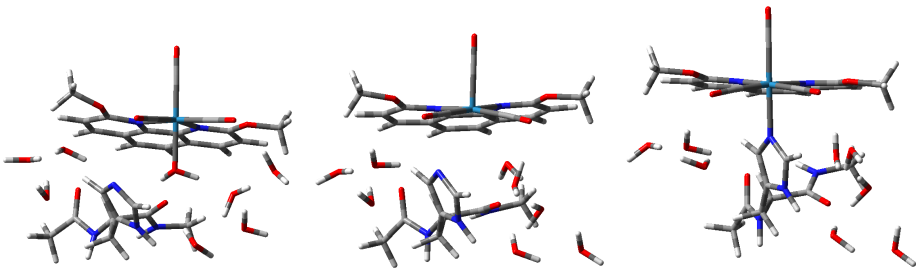

**(a) 2-He** (0.0 kcal/mol) **(b) 2-TS-He** (18.3 kcal/mol) **(c) 2-P-He** (-12.6 kcal/mol)

**Figure 3.17.** MN15/6-31+G(d,p) (LANL2DZ for Re) optimized geometries obtained for **2-He** and its posterior species when considering explicit solvent water molecules. CPCM-DLPNO-CCSD(T)/def2-TZVPP//MN15/6-31+G(d,p) (LANL2DZ for Re) relative Gibbs energies are also included in parenthesis.

substituted bidentate ligands do not produce significant modifications on the geometry of the species. For example, we have compared the optimized geometry of **TS-He** with that of **2-TS-He** and **3-TS-He** (see Figure 3.19). The RMSD of **2-TS-He**, and **3-TS-He** with respect to **TS-He** (excluding the substituents at the phen ligand) is 0.211 and 0.199 Å, respectively, which reflects the similarity between the three species. The largest differences are found within the diimine ligand, where its orientation slightly varies to minimize the repulsion between the carbonyl ligands and the methyl groups of the substituents. Therefore, the differences in energy are due to electronic effects rather than structural ones.

The aquo ligand, which is released in the TS, is a labile ligand due to its poor overlap with the Re *d* orbitals. As a consequence, if the metal center is more electron-rich, as in **2-He** and **3-He**, its displacement should be favoured. Indeed, the bond length between Re and Ow increases from 2.189 Å in **1-He** to 2.200 and 2.239 Å in **2-He** and **3-He**, respectively. This is also related to the larger stability of the products in the sense that, since we are comparing relative Gibbs energies referred to the initial complexes, if **2-He** and **3-He** are more unstable, the difference in energy with their corresponding product also increases.

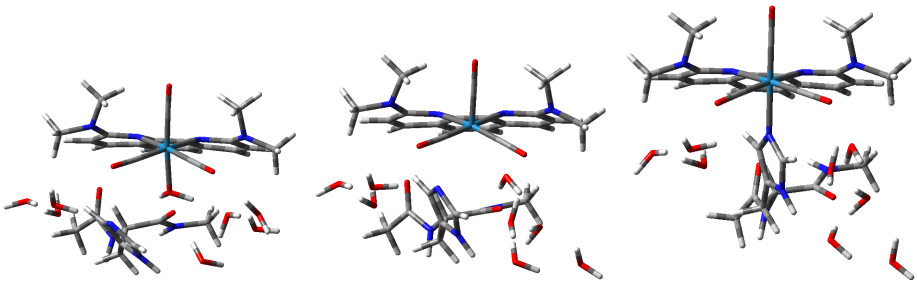

**(a) 3-He** (0.0 kcal/mol) **(b) 3-TS-He** (19.6 kcal/mol) **(c) 3-P-He** (-8.0 kcal/mol)

**Figure 3.18.** MN15/6-31+G(d,p) (LANL2DZ for Re) optimized geometries obtained for **3-He** and its posterior species when considering explicit solvent water molecules. CPCM-DLPNO-CCSD(T)/def2-TZVPP//MN15/6-31+G(d,p) (LANL2DZ for Re) relative Gibbs energies are also included in parenthesis.

## 3.5 Computational Design of Re(I) Carbonyl Complexes for their Use in Photodynamic Therapy

The spectroscopic properties of a series of Re(I) carbonyl complexes bearing pyridocarbazole and pyridine ligands with potential application as PSs in PDT have been investigated. To that end, we have designed some derivatives of the complexes synthesized by Megger's group[139,140] (see Scheme 1.18), which are the Re(I) carbonyl complexes with photocytotoxicity activated at the longest wavelength among all the examples in the literature. We were interested in analysing the effect of increasing the conjugation of the pyridocarbazole ligand as well as of adding certain electron-donating and withdrawing groups to that ligand. Finally, inspired by the work of Kurtz *et al.*,[147] we have also explored the influence of replacing the carbonyl ligand in *cis* disposition to the diimine ligand by phosphine groups.

The electronic absorption spectra of all the species have been computed at the level of theory PCM-TD-M06/6-31+G(d) (LANL2DZ for Re)//B3LYP-D3/6-31+G(d) (LANL2DZ for Re) in DMSO solvent. Validation calculations have been carried out to select the functionals used both in the TD-DFT computations and in the geometry optimizations. Only the first 10 transitions between singlet states have been computed. In this work, we will focus mostly on the lowest-lying absorption band, which is the most interesting one for exploring the potential use of the complexes as PSs in PDT.

### 3.5.1 Influence of the Conjugation at the Bidentate Ligand

To analyse the effect of the degree of conjugation at the bidentate ligand on the absorption properties, we have selected three complexes with a stepwise expansion of the pyridocarbazole ligand from complex **3** to **1**, similar to those synthesized by Meggers and co-workers.[139] The optimized structures of the complexes

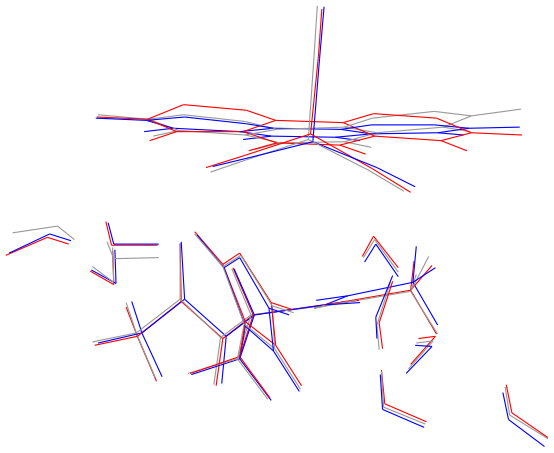

**Figure 3.19.** Comparison of the optimized geometries of **TS-He** (grey), **2-TS-He** (blue), and **3-TS-He** (red), excluding the electron-donating groups at the phen ligand.

are displayed in Figure 3.20. Hence, complex **1** presents the highest conjugation at the bidentate ligand, with a pyridocarbazole ligand containing carbazole, pyridine, and 1H-pyrrole-2,5-dione heterocycles. In complex **2**, the 1H-pyrrole-2,5-dione moiety is not present, whereas complex **3** has a 2-(2′-pyridyl)indolato ligand.

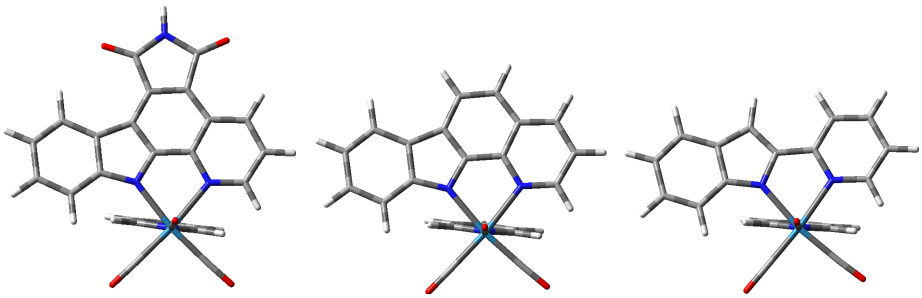

**(a) 1** **(b) 2** **(c) 3**

**Figure 3.20.** B3LYP-D3/6-31+G(d) (LANL2DZ for Re) optimized structures for complexes **1-3**.

The computed electronic absorption spectra of those complexes, which are in good agreement with the experimental ones, are shown in Figure 3.21. Complex **1**, with the longest $\lambda_{max}$ at 521 nm, is the one with the most red-shifted absorption band, compared to the analogous $\lambda_{max}$ values of 446 nm and 373 nm for complexes **2** and **3**, respectively. Therefore, the degree of conjugation seems to be directly correlated to $\lambda_{max}$, red-shifting the absorption bands as the

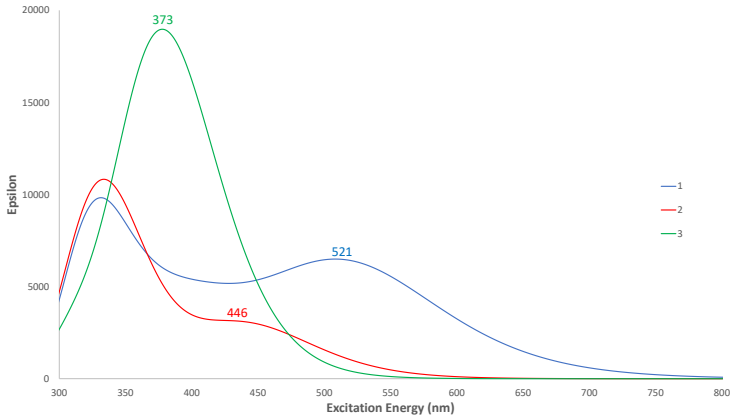


**Figure 3.21.** Computed electronic absorption spectra of complexes **1** (blue), **2** (red), and **3** (green). The longest $\lambda_{max}$ in nm for each complex is also displayed.

conjugation increases from **3** to **1**. The Kohn-Sham orbitals (KSOs) involved in that band for each complex give us information about the influence of the conjugation. For both **1** and **2** complexes, that band is mainly described as a HOMO $\rightarrow$ LUMO transition, whereas the main contribution is a HOMO-1 $\rightarrow$ LUMO transition in the case of complex **3**, with a minor participation of the HOMO $\rightarrow$ LUMO transition. Those KSOs, along with their energies in eV, are displayed in Figure 3.22.

In complexes **1** and **2** the HOMO is quite similar, both in composition and in energy, with a difference of 0.34 eV between them. Thus, it is mainly composed of a Re $d$ orbital combined with the $\pi^*$ orbitals of two of the CO ligands, and a $\pi$ orbital located in the pyridocarbazole ligand, with a larger contribution of the indole moiety than the pyridyl one. Since the pyridocarbazole $\pi$ orbital at complex **1** involves the 1H-pyrrole-2,5-dione heterocycle, which is not present in **2**, the HOMO is more stable in **1**. The composition of the HOMO-1 in complex **3**, which lies 0.11 eV below the HOMO of complex **1**, resembles to the one of the HOMO at the previous complexes, with participation of the Re $d$ orbital combined with the two CO $\pi^*$ orbitals and the $\pi$ orbital at the pyridocarbazole ligand. Regarding the HOMO of complex **3**, its energy is 0.36 eV higher than the HOMO-1, in between the one of the other two complexes. On the other hand, the LUMO is formed by a $\pi^*$ pyridocarbazole orbital in the three complexes, with more contribution of the pyridyl ring than the indole moiety. As a consequence, the energy of the LUMO is greatly affected by the number of rings at the bidentate ligand. Hence, the LUMO at complex **1** is the most stable one, with an energy of -2.82 eV, and this energy increases 0.84 and 0.94 eV when moving to complexes **2** and **3**, respectively. Therefore, comparing complexes **2** and **3**, it is clear that the effect of the conjugation at the bidentate ligand is to reduce the HOMO-LUMO gap by destabilization of the HOMO and stabilization of the LUMO. This fact, along with the larger contribution of

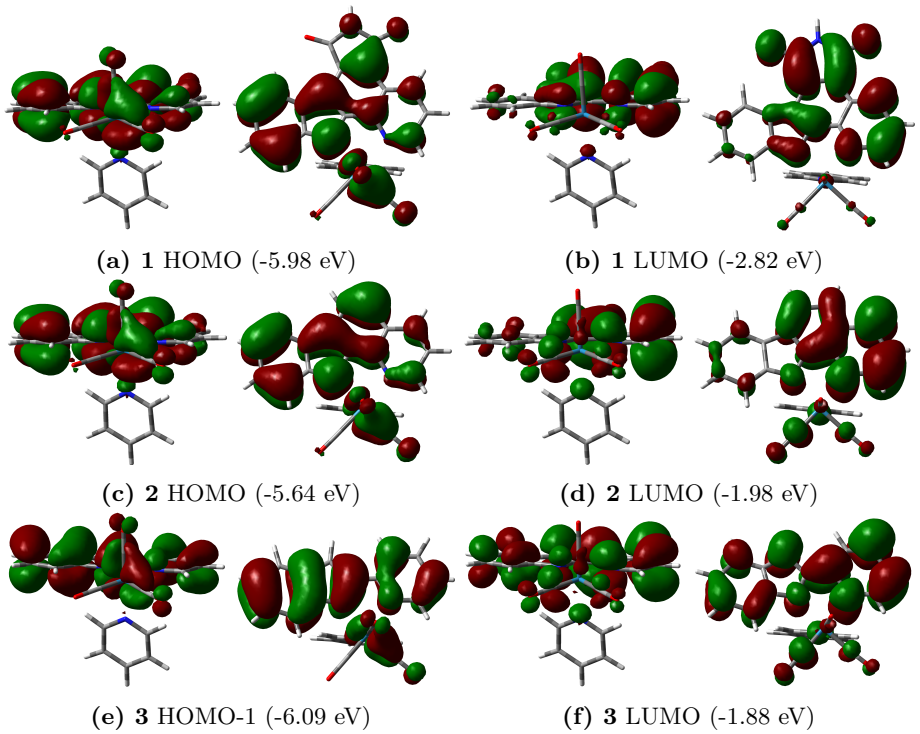

**(a)** **1** HOMO (-5.98 eV) **(b)** **1** LUMO (-2.82 eV)

**(c)** **2** HOMO (-5.64 eV) **(d)** **2** LUMO (-1.98 eV)

**(e)** **3** HOMO-1 (-6.09 eV) **(f)** **3** LUMO (-1.88 eV)

**Figure 3.22.** Contour maps of the Kohn-Sham orbitals involved in the main transition of the lowest-lying absorption band found for complexes **1-3**.

the HOMO-1 than the HOMO to the lowest-lying absorption band of complex **3**, explains the observed bathochromic shift at complex **2**. Finally, the 1H-pyrrole-2,5-dione heterocycle at complex **1** adds an extra ring to the bidentate ligand, but it also has the effect of decreasing its electron density. Consequently, both the HOMO and the LUMO suffer a stabilizing effect, which is much more pronounced in the LUMO, and the gap between the HOMO and the LUMO decreases compared to the other compounds, leading, in turn, to the longest $\lambda_{max}$ among the three complexes.

Although these complexes do not present absorption bands within the therapeutic window, limiting their use as PSs in PDT, Meggers and co-workers have found that they are able to produce singlet oxygen upon irradiation of light with the proper wavelength.[139] Hence, only complex **1** is able to produce $^1O_2$ after irradiation with $\lambda \geq 505$ nm, due to the lack of absorption of the other two complexes in this region of the spectrum, whereas all of them produced singlet oxygen upon irradiation with $\lambda \geq 330$ nm. To examine their ability of photosensitizing singlet oxygen, we have optimized their structures in the first triplet excited state ($T_1$) and computed the energy gap between $T_1$ and the singlet ground state ($S_0$). It has been reported that the difference in energy must

be at least 22.5 kcal/mol in order to transform $^3O_2$ into $^1O_2$.[126,135] Indeed, the $S_0$-$T_1$ energy gap ($\Delta E_{ST}$) is 38.7, 47.1, and 49.1 kcal/mol for complexes **1**, **2**, and **3**, respectively, in accordance with their production of singlet oxygen experimentally found.[139]

### 3.5.2 Effect of the Substituents at the Bidentate Ligand

Motivated by the interesting photoproperties of a series of Re(I) substituted pyridocarbazole complexes synthesized by Meggers' group,[140] which displayed photocytotoxicity upon irradiation of light with $\lambda = 620$ nm, we have investigated the influence of adding certain electron-donating and -withdrawing groups to the bidendate ligand of **1** in eight Re(I) substituted pyridocarbazole complexes (see Scheme 3.7).

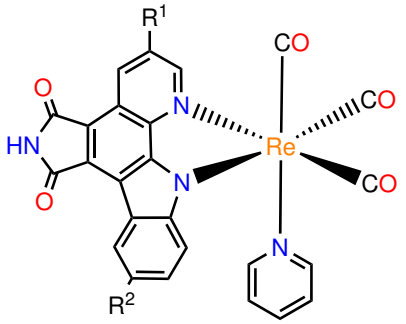


**1a** $R^1 = CO_2Et$, $R^2 = H$
**1b** $R^1 = F$, $R^2 = H$
**1c** $R^1 = H$, $R^2 = OMe$
**1d** $R^1 = H$, $R^2 = NMe_2$
**1e** $R^1 = CO_2Et$, $R^2 = OMe$
**1f** $R^1 = CO_2Et$, $R^2 = NMe_2$
**1g** $R^1 = CO_2Et$, $R^2 = CO_2Et$
**1h** $R^1 = F$, $R^2 = OMe$

**Scheme 3.7.** Structure of the eight Re(I) tricarbonyl pyridine complexes bearing different substituted pyridocarbazole ligands investigated.

In this sense, we have explored the effect of adding the $\sigma$-accepting $CO_2Et$ (**1a**) and F (**1b**) substituents in the C3 atom of the pyridine ring of the pyridocarbazole ligand, as well as of introducing $\pi$-donating OMe (**1c**) and $NMe_2$ (**1d**) groups to the C5 atom of the indole moiety. Finally, we have also considered complexes where both types of substituents are present simultaneously in the diimine ligand (**1e-1h**), with the exception of complex **1g**, which has $CO_2Et$ groups at both the indole and the pyridine moieties of the pyridocarbazole ligand.

The electronic absorption spectra of the complexes **1a-1d**, which have only one substituent at the pyridocarbazole ligand, are shown in Figure 3.23. The complexes bearing an electron-withdrawing group present a similar absorption band, with a $\lambda_{max}$ value of 532 and 534 nm for complexes **1a** and **1b**, respectively. Thus, the bathochromic shift when comparing to complex **1** is slightly more pronounced if such a group is $CO_2Et$. On the other hand, the introduction of electron-donating substituents, as in **1c** and **1d**, has a greater effect on $\lambda_{max}$, shifting to 565 and 659 nm, respectively. It is noteworthy that the stronger $\pi$-donating effect of $NMe_2$ induces a red-shift which is 94 nm longer than the one produced by OMe.

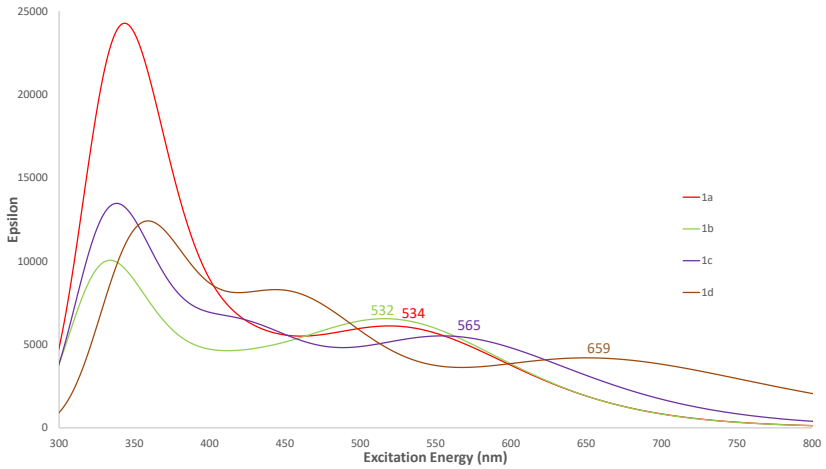


**Figure 3.23.** Computed electronic absorption spectra of complexes **1a** (red), **1b** (green), **1c** (purple), and **1d** (brown). The longest $\lambda_{max}$ in nm for each complex is also displayed.

Then, we decided to investigate the effect of combining the slightly better $\sigma$-accepting group $CO_2Et$ at the pyridine ring of the pyridocarbazole ligand with the OMe (**1e**) and $NMe_2$ (**1f**) substituents at the indole moiety, as well as of an extra $CO_2Et$ group (**1g**) to explore the effect of adding another electron-withdrawing substituent to the bidentate ligand. A complex with OMe and a F group instead of $CO_2Et$ (**1h**) has also been considered for comparison purposes. The electronic absorption spectra of those complexes are displayed in Figure 3.24.

Comparing complexes **1e** and **1f** with the corresponding ones containing only one of the substituents at the diimine ligand, it is clear that the combination of a $\sigma$-accepting group at the pyridine ring with a $\pi$-donating one at the indole moiety provokes a stronger bathochromic shift of the lowest-lying absorption band. Hence, the band at **1c** (565 nm) is shifted to 579 nm when the $CO_2Et$ group is introduced. That lengthening of $\lambda_{max}$ (14 nm) is very similar to the one produced in complex **1** when the same electron-withdrawing group is added (13 nm). This is also the case of the complex with the other $\sigma$-accepting substituent (**1h**), where the longest $\lambda_{max}$ increases 13 nm when compared to **1c**. The larger effect of the $NMe_2$ substituent is also reflected in complex **1f** (678 nm), displaying the strongest absorption at the visible region of all the complexes so far considered. Finally, regarding complex **1g**, a hypsochromic shift of the absorption band is observed, with a $\lambda_{max}$ of 517 nm. This indicates that the introduction of $\sigma$-accepting groups at the pyridine ring of the pyridocarbazole ligand provokes the opposite effect to the $\pi$-donating ones.

To gain insights on the effect of the substituents in $\lambda_{max}$, Table 3.7 reflects the energy of the HOMO and LUMO orbitals in complexes **1a-h**. In all cases,

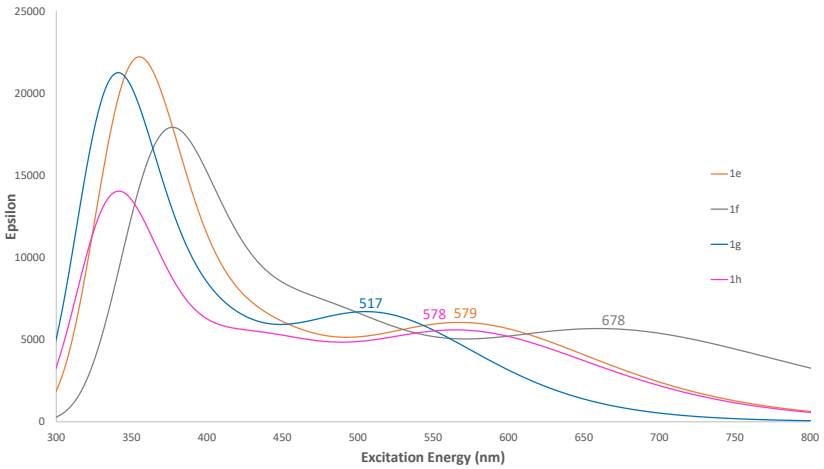


**Figure 3.24.** Computed electronic absorption spectra of complexes **1e** (orange), **1f** (grey), **1g** (blue), and **1h** (pink). The longest $\lambda_{max}$ in nm for each complex is also displayed.

the lowest-lying absorption band is mainly described by a HOMO → LUMO transition, so the energy gap between those orbitals ($\Delta E_{H\rightarrow L}$) and $\lambda_{max}$ are also included.

**Table 3.7.** HOMO and LUMO energies, HOMO-LUMO ($\Delta E_{H\rightarrow L}$) energy gap and the maximum wavelength ($\lambda_{max}$) of the lowest-lying absorption band for complexes **1a-1h** computed at the theory level PCM-M06/6-31+G(d) (LANL2DZ for Re).

| Species | HOMO (eV) | LUMO (eV) | $\Delta E_{H\rightarrow L}$ (eV) | $\lambda_{max}$ (nm) |
|---|---|---|---|---|
| **1a** | -6.04 | -2.96 | 3.08 | 534 |
| **1b** | -6.04 | -2.93 | 3.11 | 532 |
| **1c** | -5.75 | -2.80 | 2.95 | 565 |
| **1d** | -5.35 | -2.77 | 2.58 | 659 |
| **1e** | -5.81 | -2.94 | 2.87 | 579 |
| **1f** | -5.40 | -2.91 | 2.49 | 678 |
| **1g** | -6.21 | -3.04 | 3.17 | 517 |
| **1h** | -5.80 | -2.91 | 2.89 | 578 |

According to our results, the relation between $\lambda_{max}$ and $\Delta E_{H\rightarrow L}$ is confirmed, as larger energy gaps are always reflected by lower $\lambda_{max}$ values. In this sense, the energy of the HOMO is mostly affected by the introduction of substituents in the indole moiety of the bidentate ligand. Thus, the energy of the HOMO in **1a** and **1b** (-6.04 eV) is very close to that of complex **1** (-5.98 eV), whereas this energy increases to, approximately, -5.8 eV with the OMe group (**1c**, **1e**, and **1h**), and to -5.4 eV with $NMe_2$ (**1d** and **1f**), demonstrat-

ing again the stronger electron-donating effect of this group. In the case of complex **1g**, where the substituent at the indole has an electron-withdrawing effect, the HOMO is stabilized to -6.21 eV. Therefore, a more electron-rich indole moiety induces a bathochromic shift on the longest absorption band through a destabilization of the HOMO. This is consequence of the $\pi$ orbital with a large contribution from the indole in the HOMO. On the other hand, the energy of the LUMO mainly varies when adding substituents at the pyridine ring of the pyridocarbazole ligand. Since all the groups introduced in that ring are $\sigma$-acceptors, the LUMO always undergoes a stabilization effect to, approximately, -2.9 eV, whereas it remains close to the -2.82 eV value of complex **1** in the complexes without such substituents (**1c** and **1d**). Compared to the variations in energy of the HOMO, which are as large as 0.63 eV (comparing **1** and **1d**), the energy of the LUMO is much less affected by the substituents, with a maximum variation from **1** to **1g** of 0.22 eV. This is in accordance with the larger bathochromic shifts observed when adding electron-donating groups.

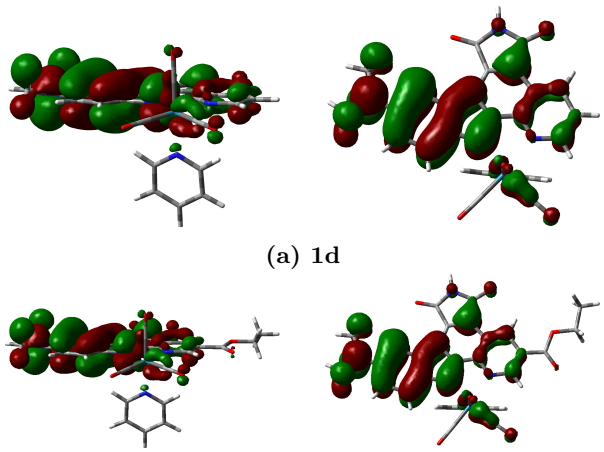

**(a) 1d**

**(b) 1f**

**Figure 3.25.** Contour maps of the Kohn-Sham HOMO of the complexes bearing a $NMe_2$ group (**1d** and **1f**).

Concerning the capacity of generating singlet oxygen of these complexes, we have computed $\Delta E_{ST}$ energy gaps. All of them have a value greater than 22.5 kcal/mol, ranging from 26.8 in complex **1f** to 39.6 kcal/mol in complex **1g**. Therefore, they should be able to produce singlet oxygen. However, it has been experimentally reported that the formation of singlet oxygen is suppressed by the strong $\pi$-donating group $NMe_2$ in the indole moiety. The reason for that is related to the nature of the HOMO in those complexes (**1d** and **1f**), which are displayed in Figure 3.25. Hence, the contribution of the Re *d* orbitals to that KSO is practically negligible, changing the nature of the first singlet excited state from a mixture of metal-to-ligand ($^1$MLCT) and intra-ligand ($^1$ILCT) charge transfers, to just $^1$ILCT. It has been reported that the intersystem conversion to

the triplet state of the PS, which is the one that reacts with $^3O_2$, is enhanced if the singlet excited state has a significant contribution from the metal center, due to the heavy atom effect.[379,380] This is not the case of the **1f** and **1g** complexes. From this point, due the lack of capacity for producing $^1O_2$ of the complexes with $NMe_2$ groups, we will not consider complexes with that substituent.

### 3.5.3 Effect of Replacing the Carbonyl Ligand

Aiming at shifting $\lambda_{max}$ to even longer values than those for the previous complexes, and following the work of Kurtz *et al.*,[147] we decided to replace the CO ligand in *cis* disposition to the diimine ligand by the phosphines $PMe_3$ and CAP (complexes **1i-1r** in Scheme 3.8). The CAP ligand has been chosen for its strong $\sigma$-donating character and its water solubility. First, we have replaced the CO ligand of complex **1** by $PMe_3$ (**1i**) and CAP (**1j**). Then, we have introduced substituents in the pyridocarbazole ligand of those complexes as in the previous section (complexes **1k-1r**).

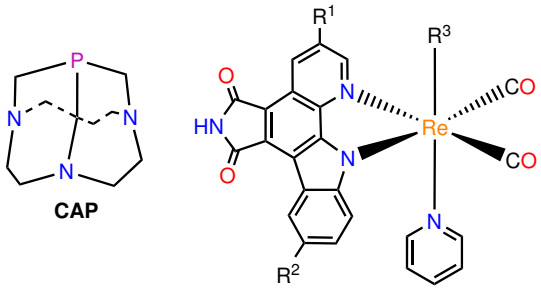


**1i** $R^1$ = H, $R^2$ = H, $R^3$ = $PMe_3$
**1j** $R^1$ = H, $R^2$ = H, $R^3$ = CAP
**1k** $R^1$ = $CO_2Et$, $R^2$ = H, $R^3$ = $PMe_3$
**1l** $R^1$ = $CO_2Et$, $R^2$ = OMe, $R^3$ = $PMe_3$
**1m** $R^1$ = $CO_2Et$, $R^2$ = H, $R^3$ = CAP
**1n** $R^1$ = $CO_2Et$, $R^2$ = OMe, $R^3$ = CAP
**1o** $R^1$ = F, $R^2$ = H, $R^3$ = $PMe_3$
**1p** $R^1$ = F, $R^2$ = OMe, $R^3$ = $PMe_3$
**1q** $R^1$ = F, $R^2$ = H, $R^3$ = CAP
**1r** $R^1$ = F, $R^2$ = OMe, $R^3$ = CAP

**Scheme 3.8.** Structure of CAP and complexes **1i-r**, where the carbonyl ligand has been replaced by either $PMe_3$ or CAP.

The computed absorption spectra of complexes **1i** and **1j** along that of complex **1**, for comparison purposes, are displayed in Figure 3.26. As expected, the absorption band suffers a significant bathochromic shift when compared to **1**, shifting to 584 and 611 nm for complexes **1i** and **1j**, respectively. It is remarkable that these values are even larger than the best ones obtained from the modifications in the pyridocarbazole ligand (excluding the $NMe_2$ substituents).

To illustrate the effect of the replacement of the carbonyl ligand by $PMe_3$ and CAP in the lowest energy band, which is mainly described as a HOMO $\rightarrow$ LUMO transition in both complexes, although the HOMO-1 $\rightarrow$ LUMO transition also contributes in the complex with a CAP ligand, the frontier KSOs of **1i** and **1j** with their corresponding energies are shown in Figure 3.27. On the one hand, the energy and composition of the LUMO in both complexes is very similar to that in complex **1**. Therefore, the effect of the phosphine ligand in that orbital is minimum, as it is mainly described by the $\pi^*$ orbital of the pyridocarbazole ligand. On the other hand, the HOMO suffers notable changes. In the case of

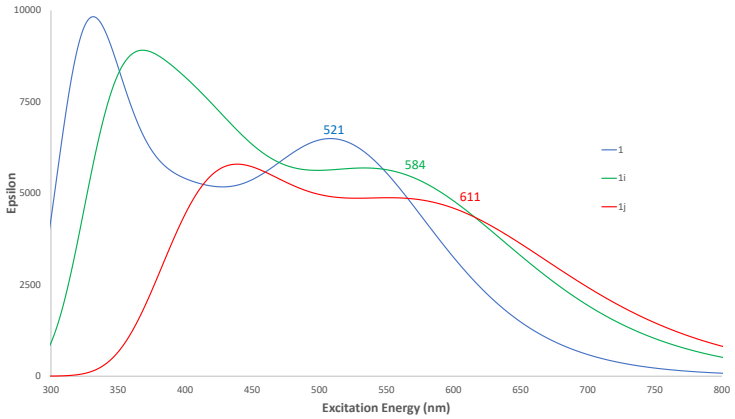


**Figure 3.26.** Computed electronic absorption spectra of complexes **1** (blue), **1i** (green), and **1j** (red). The longest $\lambda_{max}$ in nm for each complex is also displayed.

complex **1i**, it is described as a combination of a Re *d* orbital with the $\pi^*$ orbital of one of the equatorial CO ligands, and a $\pi$ orbital belonging to the bidentate ligand, mainly centered on the indole moiety. The loss of the $\pi^*$ orbital of the CO ligand, which has a stabilizing effect, raises the energy of the HOMO 0.37 eV when compared to complex **1**. Finally, in complex **1j**, the HOMO is now composed by the combination of a Re *d* orbital with the $\pi^*$ orbital of the CO ligand, a very small contribution from the $\pi$ orbital of the pyridocarbazole, and an orbital centered on the CAP ligand. Thus, the energy of the HOMO is destabilized to -5.45 eV (a variation of 0.53 eV with respect to complex **1**), and the character of the first singlet excited state is now mainly described as a mixture of $^1$MLCT and ligand-to-ligand charge transfer ($^1$LLCT).

**Table 3.8.** HOMO and LUMO energies, HOMO-LUMO ($\Delta E_{H\rightarrow L}$) energy gap and the maximum wavelength ($\lambda_{max}$) of the lowest-lying absorption band for complexes **1a-1h** computed at the theory level PCM-M06/6-31+G(d) (LANL2DZ for Re).

| Species | HOMO (eV) | LUMO (eV) | $\Delta E_{H\rightarrow L}$ (eV) | $\lambda_{max}$ (nm) |
|---|---|---|---|---|
| **1k** | -5.66 | -2.88 | 2.78 | 608 |
| **1l** | -5.54 | -2.86 | 2.68 | 631 |
| **1m** | -5.47 | -2.89 | 2.58 | 644 |
| **1n** | -5.44 | -2.86 | 2.58 | 653 |
| **1o** | -5.67 | -2.84 | 2.83 | 601 |
| **1p** | -5.54 | -2.81 | 2.73 | 627 |
| **1q** | -5.48 | -2.85 | 2.64 | 632 |
| **1r** | -5.45 | -2.82 | 2.63 | 645 |

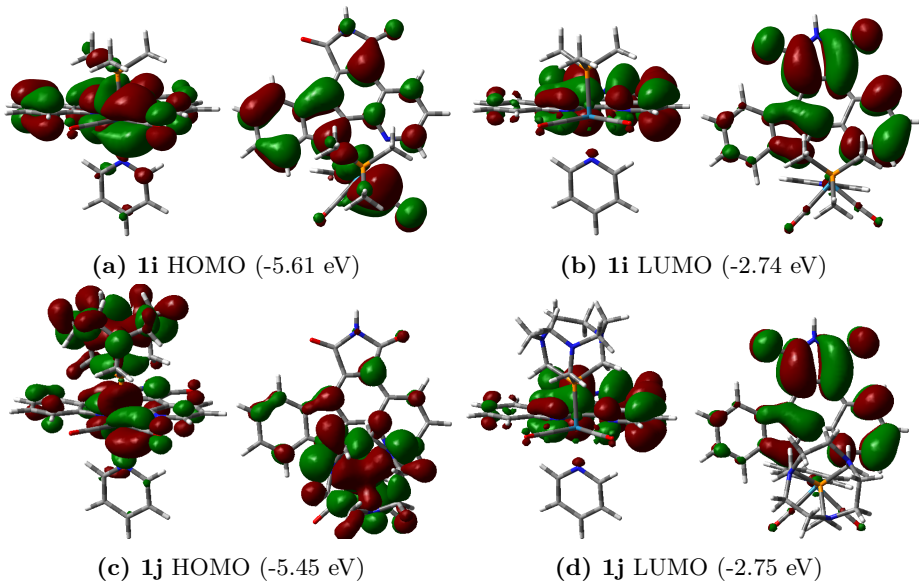

**(a) 1i** HOMO (-5.61 eV) **(b) 1i** LUMO (-2.74 eV)

**(c) 1j** HOMO (-5.45 eV) **(d) 1j** LUMO (-2.75 eV)

**Figure 3.27.** Contour maps of the frontier Kohn-Sham orbitals for the Re(I) pyridocarbazole complexes containing the phosphine ligands $PMe_3$ or CAP (**1i** and **1j**, respectively).

Then, with the goal of combining the effect of replacing the carbonyl ligand in *cis* disposition to the diimine ligand by either $PMe_3$ or CAP with the one resulting from modifications in the electron density of the pyridocarbazole ligand, we investigated the spectroscopic properties of a series of complexes (**1k-1r** in Scheme 3.8) where we introduced substituents at the pyridine and the indole moieties of **1i** and **1j**. In all cases, the main transition of the lowest-lying absorption band is HOMO $\rightarrow$ LUMO, so we will pay special attention to those orbitals, although the HOMO-1 $\rightarrow$ LUMO transition has a moderate contribution in the complexes bearing the CAP ligand (**1m**, **1n**, **1q**, and **1r**). The energy of those orbitals, as well as the HOMO-LUMO energy gap and the $\lambda_{max}$ for each complex are collected in Table 3.8.

First of all, it can be observed that the trend for the complexes bearing the $\sigma$-accepting substituent $CO_2Et$ (**1k-1n**) is the same as for the ones with a F group (**1o-1r**), although the effect of the former substituent on $\lambda_{max}$ is slightly larger due to a higher stabilization of the LUMOs, in accordance with the results from the previous section. Therefore, we will focus on complexes **1k-1n**, as the discussion for the remaining ones is analogous. Regarding the complexes with the $PMe_3$ ligand (**1k** and **1n**), the effect of adding the $CO_2Et$ group to the pyridine ring of the pyridocarbazole ligand is, as expected, a stabilization of the LUMO of around 0.14 eV, similar to the one observed when comparing complex **1** with **1a** and **1e** (the corresponding complexes with a CO ligand instead of $PMe_3$). However, the raise in energy of the HOMO when introducing the OMe $\pi$-

donating ligand in the indole moiety is only 0.07 eV when comparing complexes **1i** and **1l**, quite smaller than the difference between complexes **1** and **1e** (0.17 eV). This is mainly due to the lower contribution of the $\pi$ pyridocarbazole orbital to the HOMO. Nevertheless, the red-shift induced to the absorption band in both complexes is significant, reaching $\lambda_{max}$ values greater than 600 nm. On the other hand, the energy of the LUMO of the complexes bearing the CAP ligand (**1m** and **1n**) is identical to the one of the $PMe_3$ complexes, as the composition of the LUMO in all of them is the same, but the energy of the HOMO does not suffer variations of more than 0.02 eV when comparing complex **1j** with **1m** and **1n**. The reason for that is the almost negligible contribution of the pyridocarbazole ligand to the HOMO. Therefore, the main reason for the 20 and 33 nm lengthening of the longest $\lambda_{max}$, with respect to **1j**, in complexes **1m** and **1n**, respectively, is the stabilization of the LUMO caused by the $CO_2Et$ group, although the minor effect of the OMe group on the HOMO (and the HOMO-1) also contributes to make the red-shift even larger.

Concerning some of the requirements for a good PS in PDT: $\Delta E_{ST} > 22.5$ kcal/mol and absorption at the therapeutic window (around 620-850 nm). All the complexes considered in this study fulfill the first one, as the minimum $\Delta E_{ST}$ found, in complex **1n**, is 30.3 kcal/mol (excluding **1d** (28.0 kcal/mol) and **1f** (26.8 kcal/mol)). With respect to the other requirement, the complexes with stronger absorption at that region, as shown in Figure 3.28, are **1l**, **1m**, **1n**, **1p**, **1q**, and **1r**, so they are potential candidates for their use in PDT.

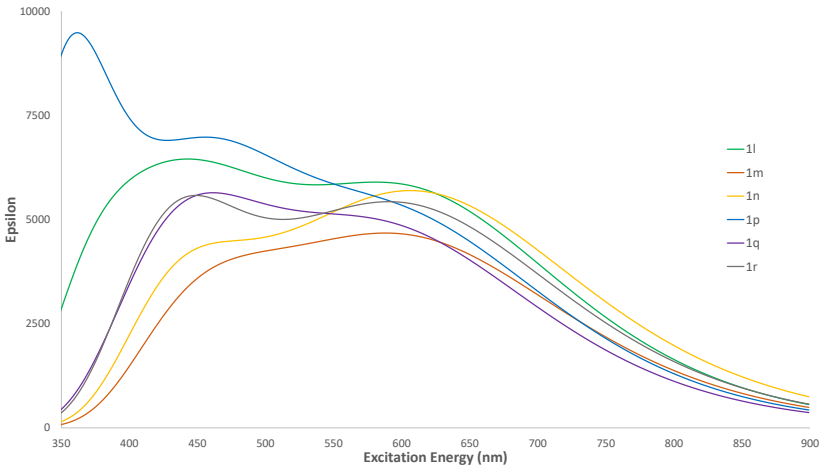


**Figure 3.28.** Computed electronic absorption spectra of complexes **1l** (green), **1m** (orange), **1n** (yellow), **1p** (blue), **1q** (purple), and **1r** (grey). The longest $\lambda_{max}$ in nm for each complex is also displayed.

## 3.6 Assessment of BODIPY-Oxasmaragdyrin Dyads for Dye-Sensitized Solar Cells

A series of dyads of potential interest for DSSC formed by a porphyrin-like compound (oxasmaragdyrin) and a BODIPY, linked by different bridges, have been analysed. The oxasmaragdyrin is chosen because of its $\pi$-extended system, which produces a red-shift in the absorption bands compared to regular porphyrins, with strong absorption in the visible region. The selected oxasmaragdyrin (S1 in Scheme 3.9) has 2,6-dimethoxyphenyl and methylamine groups in two of its meso carbons to enhance the push-up effect towards the BODIPY. The BODIPY, on the other hand, is able to capture light in the UV region of the spectrum, as well as in a narrow band in the visible region. In this study, the BODIPY (B in Scheme 3.9) is similar to a commercial BODIPY 650/660-succinimidyl ester with a decrease in the size of its side chain. It has two substituents, a pyrrole ring, and an unsaturated chain containing a phenyl, ether and carboxylic functionalities. These modifications extend the $\pi$ conjugation of the BODIPY and ensure adsorption to the semiconductor through the carboxylic group. The bridges of the dyads (D2-D11 in Scheme 3.9) have different functionalities, including alkyl, phenyl, and alkynyl groups. The notation S2-S11 will be employed for the dyads without BODIPY (the oxasmaragdyrin-bridge fragments). We will examine the molecular structure, aromaticity and spectroscopic properties of the dyads, paying special attention to the influence of the bridges and to the fulfillment of the criteria for a good dye in a DSSC.

### 3.6.1 Molecular Structure

First, we will analyse the molecular structure starting with the isolated oxasmaragdyrin (S1) and the S2-S11 fragments, and then, the dyads (D1-D11). For that purpose, the planarity of the oxasmaragdyrin macrocycle (R7 in Scheme 3.9), and the disposition of B with respect to S1 in the dyads will be examined.

The theory level used for the optimization of all the structures is B3LYP/6-311G(d,p), also including the dispersion interactions during the B3LYP energy computations through calculation of the atom-pairwise DFT-D3 dispersion developed by Grimme and co-workers. The planarity of the oxasmaragdyrin ring (R7) has been analysed by obtaining through least-squares fitting the best plane defined by the non-hydrogen atoms of the ring (without the substituents) and calculating the root mean square deviation (RMSD) of the distance from all those atoms to the plane.

In the case of S1 (see Figure 3.29), it presents a significant deviation from planarity, with a RMSD of 0.31 Å. This is mainly consequence of the R2 and R5 rings, which locate out of the plane to minimize the steric repulsion with the 2,6-dimethoxyphenyl and methylamine groups, respectively.

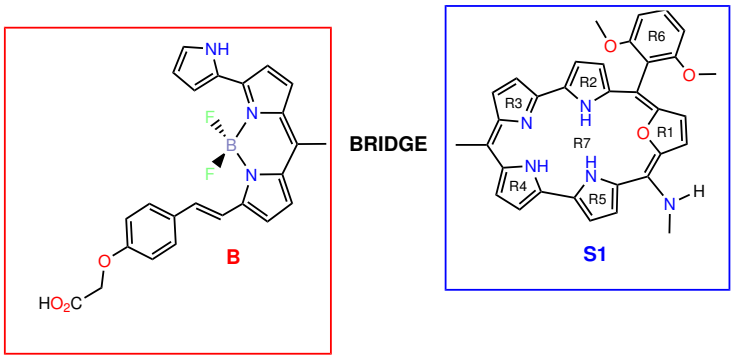


| Notation | Dyad |
|---|---|
| D1 | B—S1 |
| D2 | B—$CH_2$—$CH_2$—$CH_2$—S1 |
| D3 | B—C≡C—S1 |
| D4 | B—$CH_2$—C≡C—S1 |
| D5 | B—C≡C—C≡C—S1 |
| D6 | B—C≡C—C≡C—C≡C—S1 |
| D7 | B—C≡C— 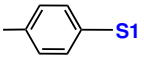 —S1 |
| D8 | B— 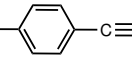 —C≡C—S1 |
| D9 | B—C≡C— 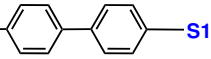 —S1 |
| D10 | B—C≡C— 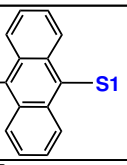 —S1 |
| D11 | B—C≡C— 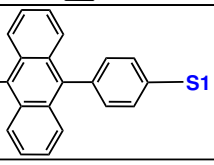 —S1 |

**Scheme 3.9.** Molecular structure of the BODIPY (B) and the oxasmaragdyrin (S1) molecules and notation of the dyads.

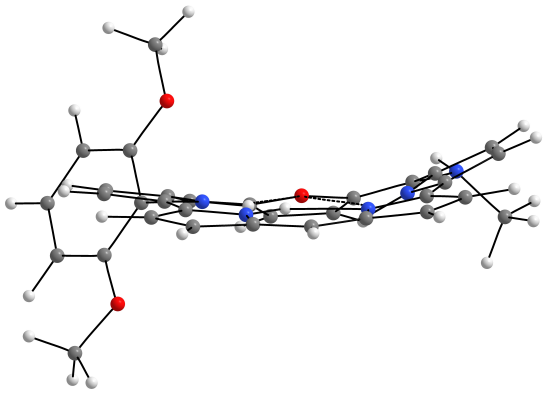

**Figure 3.29.** Optimized geometry of S1, showing the deviation of planarity due to the repulsions between R2 and R5 rings and the substituents of the macrocycle.

Interestingly, the planarity of R7 when the bridges are connected to S1 (S2-S11) largely increases in all cases (see Table 3.9). In those fragments, the RMSD varies from a maximum of 0.13 Å in S5 to a minimum of 0.05 Å in S9. The bridges where the S1 moiety is bonded to an alkynyl group present the highest RMSD values (0.11-0.13 Å), whereas the ones connected to a phenyl group range between 0.05 and 0.07 Å, with the only exception of S11.

**Table 3.9.** RMSD in Å of the non-hydrogen atoms of R7 to the plane obtained through a least squares method for the different oxasmaragdyrin fragments (S1-S11) and the corresponding dyads (D1-D11).

| Species | RMSD | Species | RMSD |
|---|---|---|---|
| S1 | 0.31 | D1 | 0.11 |
| S2 | 0.09 | D2 | 0.15 |
| S3 | 0.12 | D3 | 0.14 |
| S4 | 0.12 | D4 | 0.13 |
| S5 | 0.13 | D5 | 0.11 |
| S6 | 0.12 | D6 | 0.11 |
| S7 | 0.08 | D7 | 0.11 |
| S8 | 0.11 | D8 | 0.14 |
| S9 | 0.05 | D9 | 0.13 |
| S10 | 0.06 | D10 | 0.13 |
| S11 | 0.11 | D11 | 0.11 |

On the other hand, when B is linked to the oxasmaragdyrin fragments, the RMSD hardly varies, with a maximum change of 0.08 Å when going from S9 to D9. Therefore, we can conclude that the presence of the BODIPY moiety does not affect the planarity of S1. Note that this is not the case for S1 and D1,

since the direct linkage of B to S1 has a similar effect on the planarity than the bridges, thus decreasing the RMSD from 0.31 to 0.11 Å.

Regarding the relative orientation of B with respect to S1, there are large variations depending on the bridge. For instance, they lay in almost perpendicular planes in the dyads D1, D2, D4, D7, D8, and D10, whereas they are nearly coplanar in the remaining ones (see Figure 3.30 for the comparison between a dyad with each orientation). The presence of bridges with only alkynyl groups (D3, D5, and D6) or with two sets of aryl functionalities (D9 and D11) seems to enhance the coplanarity.

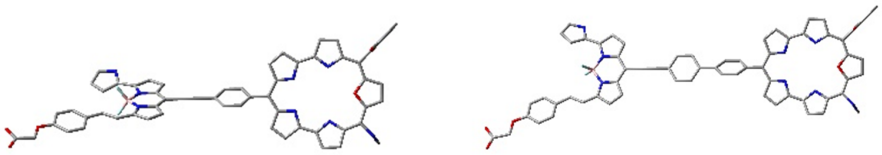

**(a)** D7 **(b)** D9

**Figure 3.30.** Optimized geometry of the dyads D7 and D9, illustrating the perpendicular orientation of B with respect to S1 in the former, and the coplanarity in the latter.

### 3.6.2 Aromaticity

Now, we will investigate the aromaticity at the oxasmaragdyrin ring (R7) in all the species, along with its relationship to the planarity of S1 and the HOMO-LUMO energy gap. To get a quantitative value of the aromaticity, we have performed NICS calculations at the ring critical point (RCP) located inside R7. In addition, we have also analysed the ring current densities 1 Å above the plane to show the aromatic pathways at the oxasmaragdyrin fragment.

The NICS values, collected in Table 3.10, reflect the aromatic character of the oxasmaragdyrin ring in all the compounds. The lowest aromaticity (-10.7 ppm) is found for S1, in consonance with the large deviation from planarity in this fragment. In all the other species the NICS index hardly varies as ranging from -11.2 to -12.4 ppm. The correlation between planarity and aromaticity cannot be properly tested with such small variations in the NICS values. However, it is remarkable that the largest aromaticity indexes in the oxasmaragdyrin fragments are found for S3 (-12.1 ppm), S5 (-12.3 ppm), and S6 (-12.4 ppm), which are the ones with alkynyl bridges containing an increasing number of triple bonds. In addition, the other species where S1 is connected to an alkynyl functionality (S4 and S8) present the largest aromaticities (-11.8 ppm) among the remaining fragments. Hence, the presence of a triple bond directly attached to S1 promote the electron delocalization inside the oxasmaragdyrin ring. On the other hand, the bridge consisting in an alkyl chain (S2) gives the lowest rise in aromaticity (-11.2 ppm) compared to S1. Finally, when the BODIPY moiety

**Table 3.10.** NICS values in ppm computed at the R7 RCP for the different oxasmaragdyrin fragments (S1-S11) and the corresponding dyads (D1-D11).

| Species | NICS | Species | NICS |
|---|---|---|---|
| S1 | -10.7 | D1 | -12.0 |
| S2 | -11.2 | D2 | -11.2 |
| S3 | -12.1 | D3 | -12.1 |
| S4 | -11.8 | D4 | -12.0 |
| S5 | -12.3 | D5 | -12.3 |
| S6 | -12.4 | D6 | -12.3 |
| S7 | -11.6 | D7 | -11.6 |
| S8 | -11.8 | D8 | -12.0 |
| S9 | -11.7 | D9 | -11.4 |
| S10 | -11.6 | D10 | -11.5 |
| S11 | -11.6 | D11 | -11.4 |

is attached to the bridge (D2-D11) the aromaticity does not suffer any changes, with a maximum deviation of 0.3 ppm when comparing S9 with D9. Therefore, as happened with the planarity, the linkage of B does not affect the aromaticity at the oxasmaragdyrin macrocycle.

To get a more detailed picture of the aromatic pathways in the dyads investigated, magnetically current densities were also evaluated at the B3LYP/6-311G(d,p) level. The magnetically induced current density vectors are associated with the aromatic character. When a magnetic field is applied along the +Z axis (perpendicular to the ring plane) to an aromatic system, a diatropic ring current involving the delocalized $\pi$ electrons of the ring is induced, following a clockwise direction. On the other hand, if the system is antiaromatic, the ring current is paratropic and follow an anticlockwise direction. In between, if the system does not present $\pi$ electron delocalization, there will not be ring current. To visualize the ring current involving the $\pi$ electrons of the oxasmaragdyrin, we have computed the current density maps of S1-S11 along a plane located 1 Å above the oxasmaragdyrin plane (the one used in the analysis of the planarity). Since the differences in aromaticity between the oxasmaragdyrin fragments are small, we will compare the ring current density maps between the ones with the lowest (S1 and S2) and the largest (S6 and S5) NICS values.

As depicted in Figures 3.31 and 3.32, the four oxasmaragdyrin fragments present ring current. The current density always follows a clockwise direction, reflecting the aromatic character, and it passes over all the non-hydrogen atoms of the macrocycle. The intensity of the current density vectors is related to their colour, being red the lowest intensity and blue the highest. Hence, we can see that the ring current at S5 and S6 is much more intense than at S1 and S2, confirming their larger aromatic character.

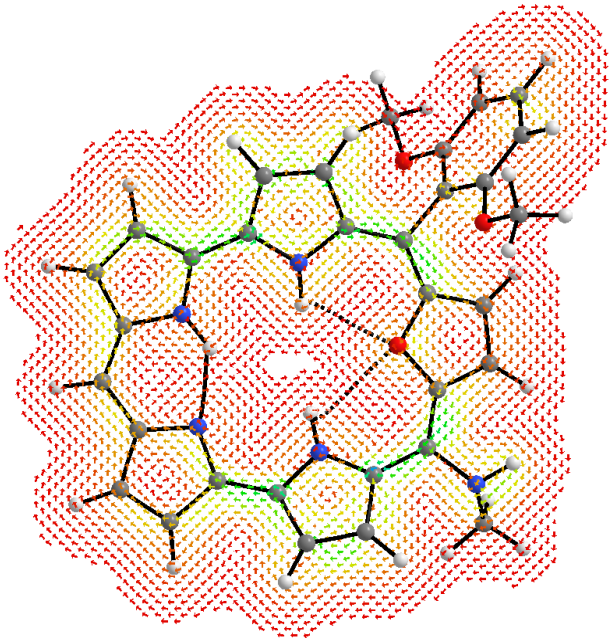

**(a)** S1

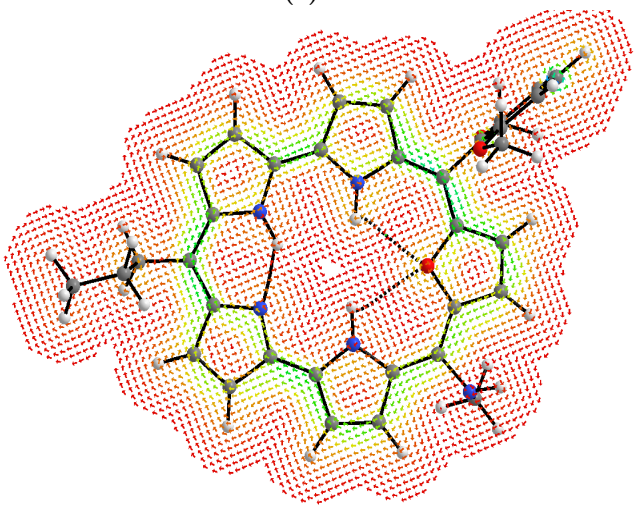

**(b)** S2

**Figure 3.31.** Ring current density maps at 1 Å above the plane of the oxasmaragdyrin macrocycle of S1 and S2 induced by a magnetic field applied along the normal vector of the plane.

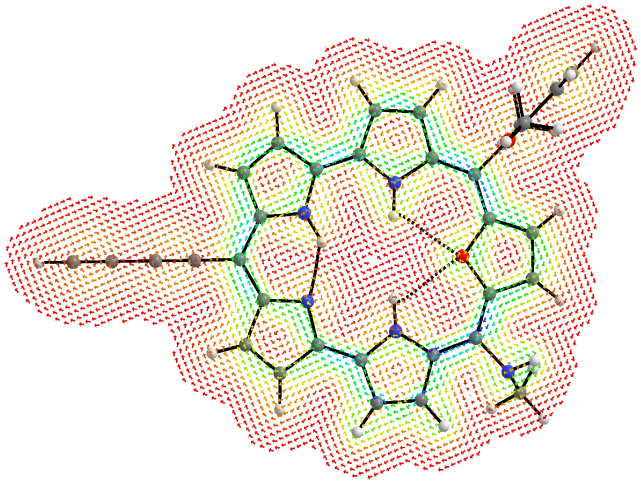

**(a)** S5

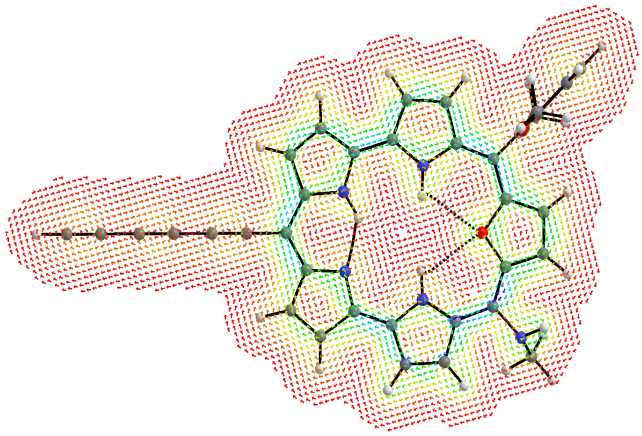

**(b)** S6

**Figure 3.32.** Ring current density maps at 1 Å above the plane of the oxasmaragdyrin macrocycle of S5 and S6 induced by a magnetic field applied along the normal vector of the plane.

To test the potential use as dyes in DSSCs of the dyads here considered, we need to evaluate the energy of their frontier orbitals. In this sense, the HOMO energy must be lower than the redox potential of the mediator to permit the recovery of the dye. One of the most popular redox mediators is $I^-/I_3{}^-$, with a redox potential of -4.8 eV. In addition, the LUMO energy must be higher than the conduction band of the semiconductor, which is -4.3 eV in the case of $TiO_2$, for an efficient electron injection. The energy of the HOMO, the LUMO and the HOMO-LUMO energy gap ($\Delta E_{H\rightarrow L}$) are shown in Table 3.11.

**Table 3.11.** HOMO, LUMO and difference in energy between them ($\Delta E_{H\rightarrow L}$) in eV for all the species, computed a the theory level B3LYP/6-311G(d,p).

| Species | HOMO (eV) | LUMO (eV) | $\Delta E_{H\rightarrow L}$ (eV) |
|---|---|---|---|
| S1 | -4.43 | -2.02 | 2.41 |
| S2 | -4.45 | -2.00 | 2.45 |
| S3 | -4.57 | -2.29 | 2.28 |
| S4 | -4.48 | -2.17 | 2.31 |
| S5 | -4.63 | -2.47 | 2.16 |
| S6 | -4.68 | -2.62 | 2.06 |
| S7 | -4.54 | -2.17 | 2.37 |
| S8 | -4.52 | -2.35 | 2.17 |
| S9 | -4.54 | -2.15 | 2.39 |
| S10 | -4.57 | -2.14 | 2.43 |
| S11 | -4.57 | -2.16 | 2.41 |
| D1 | -4.70 | -2.82 | 1.88 |
| D2 | -4.57 | -2.86 | 1.71 |
| D3 | -4.80 | -3.13 | 1.67 |
| D4 | -4.56 | -2.92 | 1.64 |
| D5 | -4.81 | -3.19 | 1.62 |
| D6 | -4.82 | -3.26 | 1.56 |
| D7 | -4.66 | -3.12 | 1.54 |
| D8 | -4.65 | -2.95 | 1.70 |
| D9 | -4.60 | -3.16 | 1.44 |
| D10 | -4.68 | -3.14 | 1.54 |
| D11 | -4.62 | -3.18 | 1.44 |

Starting with the oxasmaragdyrin fragments (S1-S11), none of the species meet the first criteria for the HOMO energy, being the lowest HOMO energies those of S6 (-4.68 eV) and S5 (-4.63 eV). On the other hand, the LUMO energy is always above the conduction band of $TiO_2$. With respect to the HOMO-LUMO energy gap, conjugation has the effect of reducing that gap if the frontier orbitals involve the $\pi$ orbitals where the electrons are delocalized. This is mainly due to a large stabilization of the LUMO. Indeed, the lowest energy gaps are found for S6 (2.06 eV) and S5 (2.16 eV), followed by S8, S3, and S4, which are also the species that showed the largest aromatic character (the ones where S1 is bonded to an alkynyl group). So, again, the acetylene bridge seems to enhance the conjugation.

In the dyads, the LUMO energy requirement is always fulfilled as well. However, there are only three dyads with energy lower (or equal) than -4.8 eV: D6 (-4.82 eV), D5 (-4.81 eV), and D3 (-4.80 eV). It is noteworthy that the LUMO is largely stabilized when the BODIPY moiety is linked, reducing the HOMO-LUMO energy gap in all the dyads. Now, $\Delta E_{H\rightarrow L}$ does not match the previous trends in aromaticity, this is because the LUMO is no longer centered on S1 but on the BODIPY fragment, as shown in Figure 3.33. This fact also explains

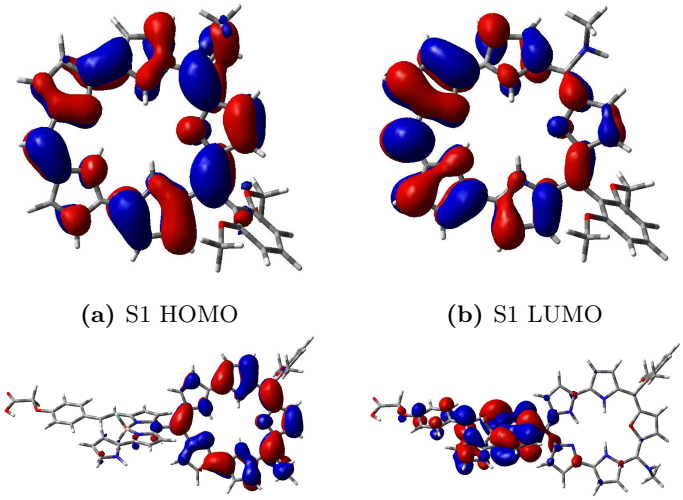

**(a)** S1 HOMO **(b)** S1 LUMO

**(c)** D1 HOMO **(d)** D1 LUMO

**Figure 3.33.** Representation of the HOMO and the LUMO of S1 and D1.

why the HOMO energy only changes slightly when the BODIPY is attached (a maximum of -0.27 eV when comparing D1 with S1), whereas the LUMO energy suffers variations up to -1.02 eV (from S11 to D11).

### 3.6.3 Spectroscopic Properties

Having analysed the geometry, aromaticity, and orbital energies of both the oxasmaragdyrin fragments and the dyads, we will now focus on their spectroscopic properties. To that end, we have employed TD-DFT methodology to obtain the absorption spectrum of all the compounds. The TPSSh functional has been chosen after testing several DFT functionals against the experimental absorption bands of the commercial BODIPY-650/660 succinimidyl ester ($B_{ref}$), a oxasmaragdyrin with phenyl substituents on the three meso carbons ($S_{ref}$), and the dyad synthesized by Kalita *et al.* ($D_{ref}$). Hence, the level of theory for the TD-DFT calculations is TPSSh/6-311G(d,p)//B3LYP/6-311G(d,p). Solvent effects have been taken into account by means of CPCM, with a dielectric constant of 8.93 to simulate $CH_2Cl_2$. The maximum error of this level of theory when comparing the TD-DFT bands and the experimental ones is 0.07 eV.

The absorption spectrum of the isolated oxasmaragdyrin (S1) presents three main bands: two weak Q bands located in the visible region, with the maximum wavelength at 636 and 588 nm, and an intense Soret band in the visible zone although close to the UV region (437 nm). Similar bands were observed in the experimental spectrum of $S_{ref}$ (633, 591, and 443 nm, respectively). When the bridges are connected to S1 (S2-S11), the three bands are preserved (see Table 3.12). However, in all species but S2, their excitation wavelengths increase. We

**Table 3.12.** CPCM-TPSSh/6-311G(d,p) excitation wavelength ($\lambda$) and assignment of the main absorption bands of all the species.

| Species | $\lambda$ (nm) | Band | Species | $\lambda$ (nm) | Band |
|---|---|---|---|---|---|
| S1 | | | D1 | 640 | BODIPY |
| | 636 | Q | | 635 | Q |
| | 588 | Q | | 599 | Q |
| | 437 | Soret | | 438 | Soret |
| S2 | | | D2 | 629 | BODIPY |
| | 615 | Q | | 626 | Q |
| | 583 | Q | | 587 | Q |
| | 431 | Soret | | 437 | Soret |
| S3 | | | D3 | 555 | BODIPY |
| | 660 | Q | | 622 | Q |
| | 610 | Q | | 582 | Q |
| | 452 | Soret | | 459 | Soret |
| S4 | | | D4 | 639 | BODIPY |
| | 653 | Q | | 662 | Q |
| | 608 | Q | | 610 | Q |
| | 452 | Soret | | 453 | Soret |
| S5 | | | D5 | 569 | BODIPY |
| | 690 | Q | | 659 | Q |
| | 629 | Q | | 581 | Q |
| | 459 | Soret | | 459 | Soret |
| S6 | | | D6 | 585 | BODIPY |
| | 719 | Q | | 688 | Q |
| | 650 | Q | | 605 | Q |
| | 472 | Soret | | 479 | Soret |
| S7 | | | D7 | 707 | BODIPY |
| | 643 | Q | | 642 | Q |
| | 596 | Q | | 594 | Q |
| | 458 | Soret | | 448 | Soret |
| S8 | | | D8 | 667 | BODIPY |
| | 691 | Q | | 689 | Q |
| | 628 | Q | | 624 | Q |
| | 470 | Soret | | 471 | Soret |
| S9 | | | D9 | 705 | BODIPY |
| | 640 | Q | | 645 | Q |
| | 595 | Q | | 596 | Q |
| | 442 | Soret | | 448 | Soret |
| S10 | | | D10 | 697 | BODIPY |
| | 687 | Q | | 675 | Q |
| | 625 | Q | | 630 | Q |
| | 453 | Soret | | 453 | Soret |
| S11 | | | D11 | 694 | BODIPY |
| | 669 | Q | | 633 | Q |
| | 620 | Q | | 596 | Q |
| | 449 | Soret | | 452 | Soret |

will limit now our discussion to the lowest energy band, which is the one that suffers the largest shifts, although the other bands undergo similar changes. This band is mostly described by a transition from the HOMO to the LUMO, with some contribution from a HOMO-1 $\rightarrow$ LUMO+1 transition. The maximum displacement of that band, compared to S1, is produced in S6 (83 nm), S8 (55 nm), and S5 (54 nm), which are the oxasmaragdyrin fragments where $\Delta E_{H\rightarrow L}$

was minimum. Therefore, the presence of an alkynyl group bonded to S1 seems to promote a bathochromic shift. In accordance, S3 has a significant red-shift as well (24 nm). Although the red-shift of the band at S10 and S11 (51 and 33 nm, respectively) is also remarkable, their oscillator strengths are very low compared to the other species. This is because the lowest unoccupied molecular orbitals of those compounds have strong contributions from the bridge (see Figure 3.34), so new transitions from the oxasmaragdyrin to the bridge appear. On the other hand, S7 and S9, where S1 is directly linked to a phenyl group, have the lowest shifts in their absorption band (7 and 4 nm, respectively).

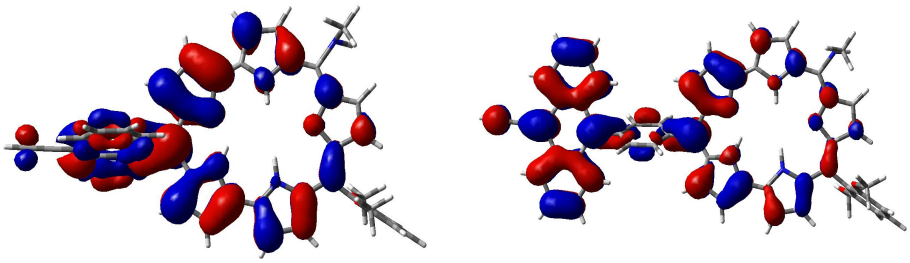

**(a)** S10 LUMO **(b)** S11 LUMO

**Figure 3.34.** Representation of the LUMO of S10 and S11.

In the case of $B_{ref}$, its experimental absorption spectrum is characterized by a narrow absorption band at the visible region, with a maximum absorption wavelength of 646 nm, and two bands located in the UV region (at 351 and 288 nm). In the dyads (D1-D11), the bands coming from the isolated oxasmaragdyrin and BODIPY moieties still appear, although they suffer some shifts (see Table 3.12). The Soret band, which always involve only the oxasmaragdyrin macrocycle, does not undergo significant changes due to the presence of the BODIPY. Regarding the Q bands, they are not displaced more than 12 nm in D1, D2, D4, D7, D8, D9, and D10, whereas in D3, D5, and D6 the minimum decrease of the Q bands maximum wavelength is 31 nm. This divergent behaviour of the Q bands depending on the bridge is mainly due to the orientation of B with respect to S1 and the bridge. Hence, the dyads with the largest shifts are those in which the BODIPY moiety is oriented almost coplanar to the oxasmaragdyrin, with an alkynyl linkage between them. This disposition permits some conjugation between B and the bridge, causing the large blue-shifts at the Q bands due to the stabilization of the HOMO (as seen in Table 3.11). On the other hand, the perpendicular orientation of B with respect to S1 in the other group of dyads does not alter the composition of the orbitals centered on the oxasmaragdyrin. D9 is the only exception to that, its low displacement of the Q bands despite the coplanarity between the two moieties is due to the perpendicular orientation of the phenyl groups in the bridge, thus, the conjugation with the bridge is not affected by the presence of the BODIPY, so the composition of the molec-

ular orbitals involved in the transitions, which are mainly the HOMO and the LUMO in S9 and the HOMO and the LUMO+1 in D9, are essentially the same (see Figure 3.35). In the case of D11, the large hypsochromic shift of the Q bands (36 and 24 nm) are due to the lack of contribution from the bridge in the unoccupied orbitals that receive the transition when the BODIPY is linked, which is mainly the LUMO in S11 and the LUMO+2 in D11 (see Figure 3.36). Finally, the band centered on the BODIPY suffers large changes depending on the bridge. In the dyads, this band is mostly described by transitions from the HOMO-2/-3 to the LUMO. Compared to D1, this band is blue-shifted in the dyads D2-D6, although D2 and D4 are hardly affected. The hypsochromic shifts at D3, D5, and D6 can be attributed to the large stabilities of their occupied orbitals. Contrarily, the BODIPY band undergoes a large bathochromic shift at D7-D11 due to the stabilization of the LUMO.

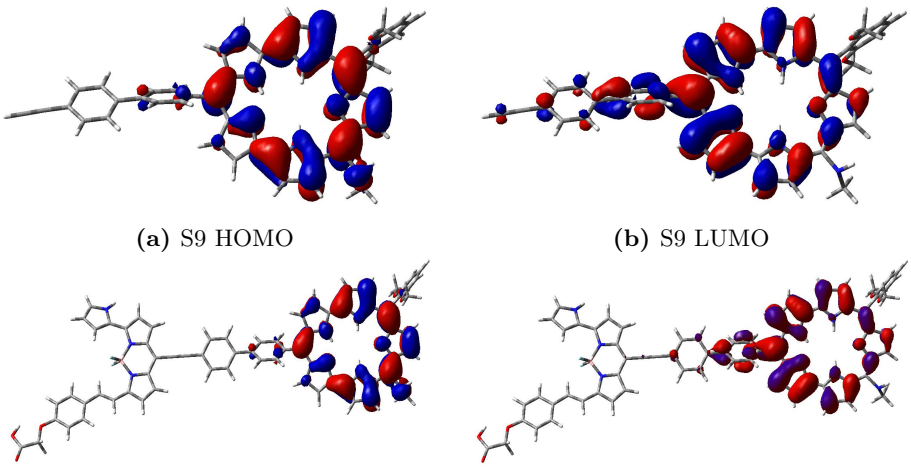

**(a)** S9 HOMO **(b)** S9 LUMO

**(c)** D9 HOMO **(d)** D9 LUMO+1

**Figure 3.35.** Molecular orbitals with the largest contributions in the Q bands of S9 and D9.

Interestingly, apart from the bands centered at S1 and B described above, there is another broad and intense band, located at around 1000 nm, that appears only in the D3 (975 nm), D5 (1031 nm), and D6 (1095 nm) dyads. Analysing the natural transition orbitals (NTO) that describe that band (see Figure 3.37), it is clear that a charge transfer (CT) transition from S1 to B through the alkynyl bridge occurs. Hence, the use of alkynyl functionalities to link both moieties enhance the CT between them, this is in accordance with our analysis of the geometry, aromaticity, and molecular orbitals of those dyads, which showed the largest coplanarity, aromatic character at the oxasmaragdyrin macrocycle, and conjugation with the bridge among all the species.

As already mentioned, the absorption spectrum of an ideal dye in DSSCs should be panchromatic, with strong absorption bands on the visible and the

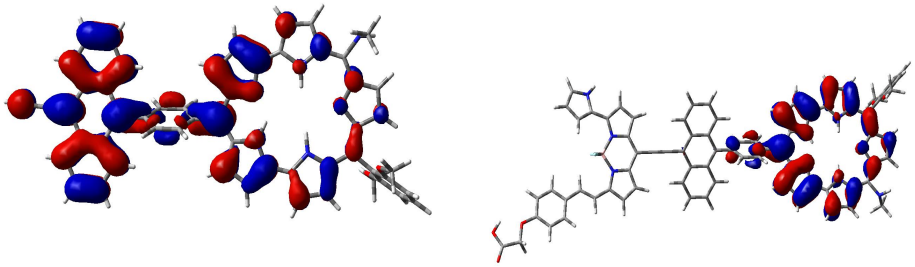

**(a)** S11 LUMO **(b)** D11 LUMO+2

**Figure 3.36.** LUMO of S11 and LUMO+2 of D11, which are the main electron-receiving orbitals of their corresponding Q bands.

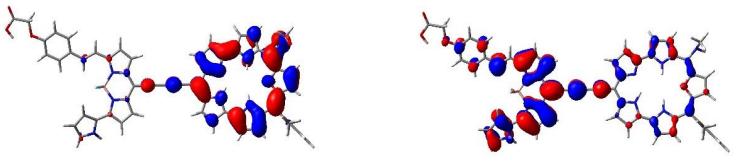

**(a)** D5 Occupied NTO **(b)** D5 Unoccupied NTO

**Figure 3.37.** Natural transition orbitals (NTO) of the separate charge excited state of dyad D5.

near-infrared regions. The computed spectrum of all the dyads is shown in Figure 3.38. It can be seen that the absorption at wavelengths longer than 750 nm is very low in all the species but D3, D5, and D6, where the CT transition presents a broad and intense band. These dyads show lower absorption at shorter wavelengths, however, their panchromatism makes them good sunlight harvesting compounds. It is remarkable that their absorption profiles have been improved compared to $D_{ref}$. In addition, these are also the only compounds that fulfilled the energy requirement for the HOMO (lower than -4.8 eV). As a conclusion, the dyads D3, D5, and D6, with bridges containing only alkynyl functionalities, are the most promising candidates for their use as dyes in DSSCs.

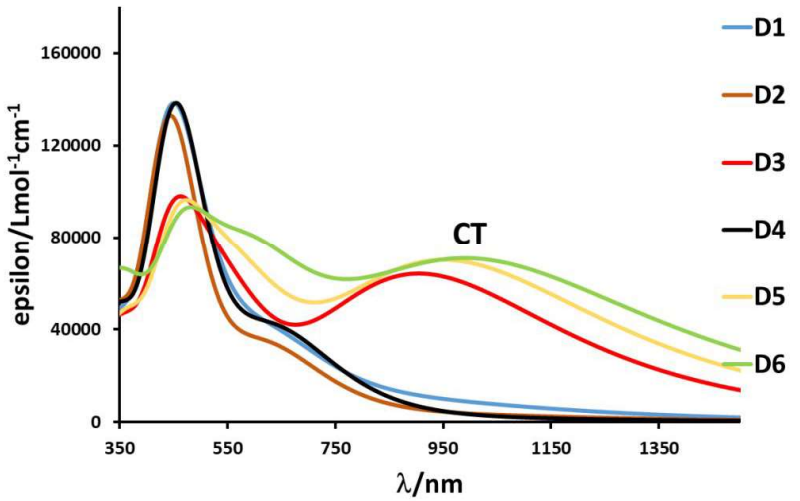


**(a)** Absorption Spectra of D1-D6

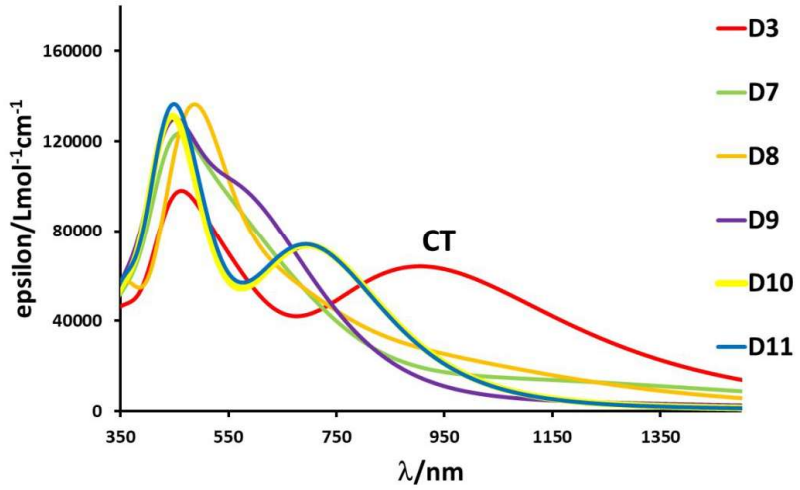


**(b)** Absorption Spectra of D7-D11 and D3

**Figure 3.38.** CPCM-TPSSh/6-311G(d,p) electronic absorption spectra of all the dyads. D3 has been included in both profiles for comparison purposes.

## 3.7 Photophysical Properties of Modified BODIPY Units and their Combination with Re(I) Tricarbonyl Complexes: Utility in Dye-Sensitized Solar Cells and Photodynamic Therapy

Inspired by the work of Rosenthal *et al.* on a series of isomeric [ReCl(CO)3(bpy)] complexes bearing pendant BODIPYs,[20] we have theoretically investigated the capability as PS for dye-sensitized solar cells (DSSCs) and photodynamic therapy (PDT) of such a Re(I) complex with a modified BODIPY. The selected BODIPY is the same as the one employed in the previous section (B in Scheme 3.9), which is similar to the commercial BODIPY 650/660-succinimidyl ester but with a decrease in the size of its side chain. We have analysed the spectroscopic and electronic properties of three complexes bearing two pendant B moieties attached to the x,x′ (x = 4, 5, 6) positions of the bpy ligand, $[ReCl(CO)_3(x,x'-B_2bpy)]$ (x = 4, 5, 6). For simplicity, hereinafter, the notation x,x′-$B_2$bpy will be referred to as BBbxx. In addition, to fully understand all the aspects affecting the behaviour of the combined systems, we initially analysed the photophysical properties of the isolated B, as well as of the 1:1 and 2:1 adducts formed by one B unit linked to bpy (Bbx; x = 4, 5, 6) and those resulting from two B moieties attached to bpy (Bbxx; x = 4, 5, 6), respectively.

The electronic absorption spectra of all the species have been computed at the level of theory PCM-TD-M06/6-31+G(d) (LANL2DZ for Re)//PCM-B3LYP/6-31G(d) (LANL2DZ for Re). The M06 functional has been chosen after testing the two functionals (TPSSh and M06) employed in our previous works against the experimental spectra of the commercial BODIPY 650/660-succinimidyl ester, and the complexes reported by Rosenthal *et al.*[20] Although both functionals rendered small errors for the isolated B, M06 showed much more accurate results for all the Re complexes, with a maximum error of 0.08 eV (a value of 0.34 was obtained with TPSSh).

### 3.7.1 Isolated BODIPY

First, we have optimized and analysed a series of conformers of the isolated BODIPY due to its flexibility in two substituents: the pyrrole ring, and the unsaturated chain with phenyl, ether, and carboxylic functionalities (see Scheme 3.9). On the one hand, the pyrrole nitrogen atom can be oriented close to the $BF_2$ unit ('ni') or pointing to the opposite direction to this unit ('no'). By varying the dihedral angles between the pyrrole and the benzene rings with the central rings of the BODIPY we have optimized four structures with each pyrrole orientation, finding that 'ni' isomers are always, approximately, 4 kcal/mol more stable than 'no' ones. The energy differences resulting from changes in the pyrrole and benzene arms orientation are minimal, with a maximum variation of 0.3 kcal/mol. The optimized structure of the most stable conformation, which has a 'ni' orientation and almost parallel pyrrole and benzene rings, is displayed in Figure 3.39. From this point, we will denote this conformer as **B**.

Since the Gibbs energy barrier found for the rotation of the pyrrole-arm is

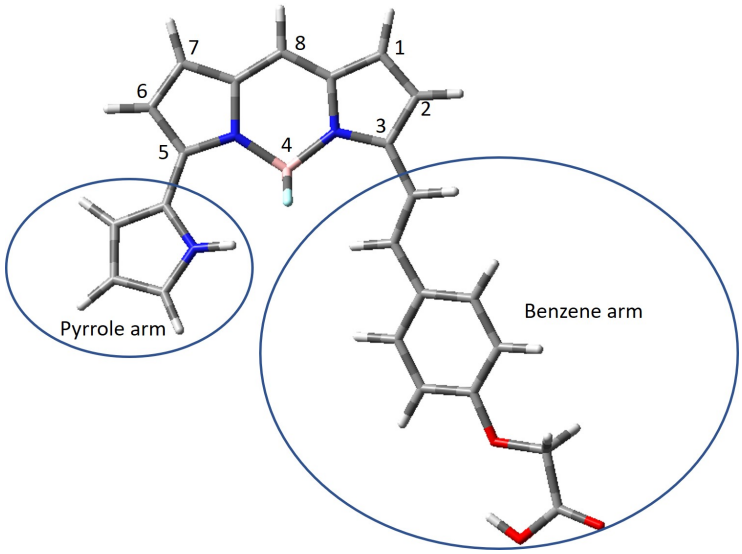


**Figure 3.39.** PCM-B3LYP/6-31G(d) optimized structure of the most stable conformer of the isolated BODIPY (**B**).

only 10.2 kcal/mol measured with respect to the energy of B, we have computed the electronic absorption spectra of three different isomers to analyse the effect of the arms conformation on the absorption bands. The electronic absorption spectrum of conformer **B**, shown in Figure 3.40, displays two main absorption bands, one of them in the visible region ($\lambda_{max}$ = 627 nm) and another one centered at the UV region ($\lambda_{max}$ = 348 nm), although a transition with moderate intensity also appears at 415 nm. Note that the other UV band characteristic of B has not been computed due to the limited number of transitions included in the calculations. The same absorption bands have been found for the other two conformers, with a maximum variation in $\lambda_{max}$ of 4 nm. Therefore, the conformation of the substituents at the BODIPY has a negligible effect on the absorption bands, so we will only consider the most stable isomer. With respect to the nature of each absorption band, the one at the visible region corresponds to a HOMO $\rightarrow$ LUMO transition, whereas the peak located at 415 nm is a HOMO-1 $\rightarrow$ LUMO transition. The HOMO-1, HOMO, and LUMO orbitals are displayed in Figure 3.41, the band at the UV region is consequence of several transitions between different molecular orbitals.

Regarding the application of B as PS for DSSCs, as already mentioned in the previous section, it presents bands in a wide range of wavelengths, but these bands are narrow and it lacks strong absorption at many regions of the spectrum. Hence, it does not have a proper light harvesting capacity for its use in DSSCs. Despite this, both the energy of the HOMO (-5.5 eV) and the LUMO (-3.0 eV) fulfill the requirements for the dyes, as the HOMO below -4.8 eV assures the recovery of the compound from the redox couple (such as $I^-/I_3^-$),

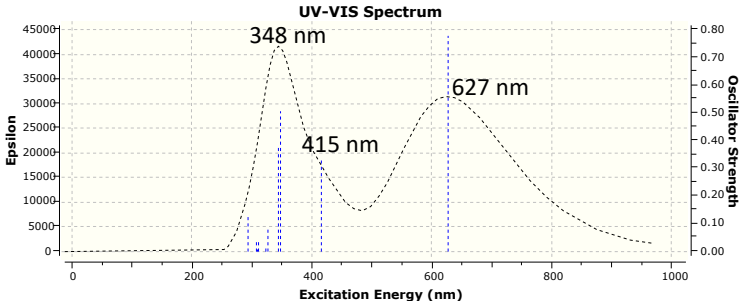


**Figure 3.40.** Computed electronic absorption spectra of the isolated **B** moiety at the PCM-TD-M06/6-31+G(d)//PCM-B3LYP/6-31G(d) level.

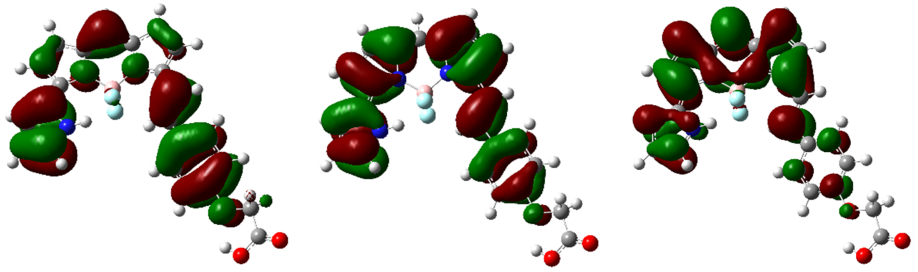

**(a)** HOMO -1 (-6.56 eV) **(b)** HOMO (-5.51 eV) **(c)** LUMO (-3.01 eV)

**Figure 3.41.** Contour maps of the HOMO-1, HOMO, and LUMO orbitals of **B**. The energy of each orbital is also included in parenthesis.

and the LUMO energy above the conduction band of $TiO_2$ (-4.3 eV) enhances the electron injection after the excitation.

Finally, concerning the potential use of **B** as a PS in PDT, although the absorption band at 627 nm is within the therapeutic window (620-850 nm), the difference in energy between the singlet ground state and its first triplet excited state ($\Delta E_{ST}$) is only 22.2 kcal/mol. As a consequence, this compound has a poor capacity for producing singlet oxygen, since the minimum $\Delta E_{ST}$ for transforming $^3O_2$ into $^1O_2$ is 22.5 kcal/mol.

### 3.7.2 1:1 Adducts of BODIPY with 2,2′-Bipyridine

In a first step towards the investigation of the Re(I) complex with BODIPY moieties attached to the bpy ligand, we have analysed the photophysical properties of the isolated bpy linked to **B** through its C8 atom at different bpy positions (Bb4, Bb5, and Bb6). Due to the absence of substituents at the C1 and C7 atoms of **B**, we could optimize four different conformers in each case, which differ in the relative orientation between the bpy and the **B** core planes. Nevertheless, the relative energy of the 12 isomers is similar, with differences

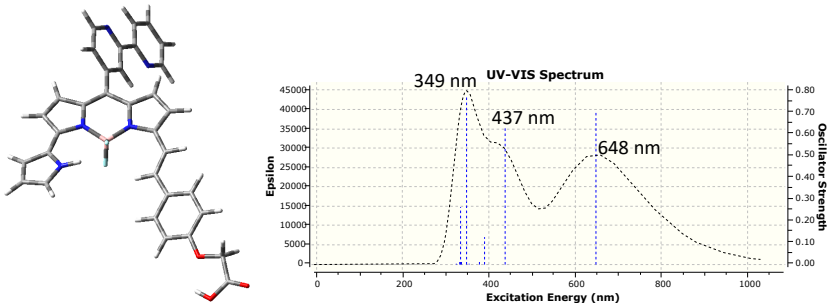


**(a) Bb4**

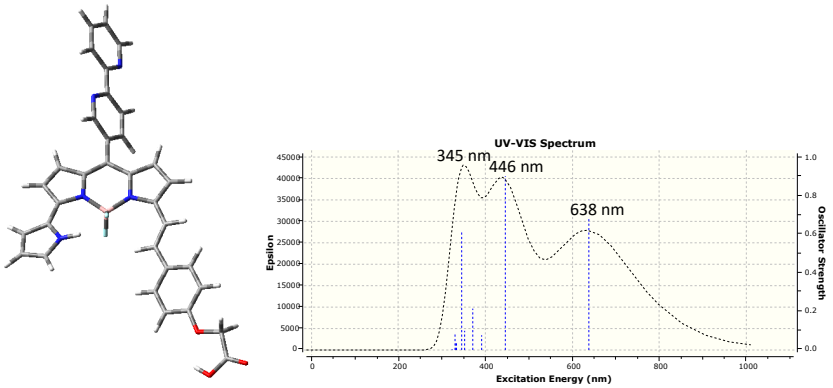


**(b) Bb5**

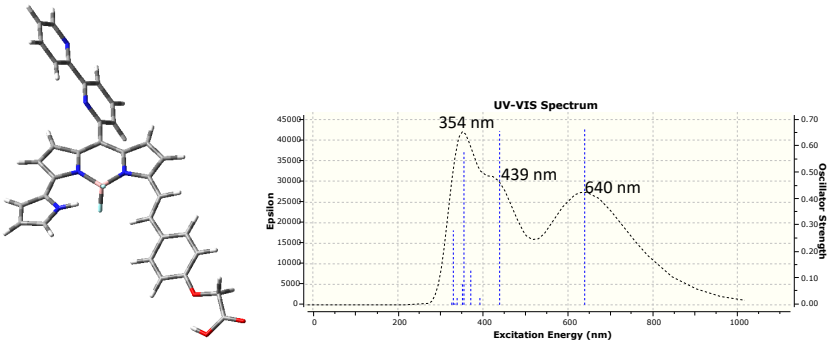


**(c) Bb6**

**Figure 3.42.** PCM-B3LYP/6-31G(d) optimized structures of **Bb4**, **Bb5**, and **Bb6**, along with their corresponding PCM-TD-M06/6-31+G(d)//PCM-B3LYP/6-31G(d) electronic absorption spectra.

of less than 1 kcal/mol. In addition, after computing the electronic absorption spectra for each set of four Bbx conformers, we have found that the variation in the absorption wavelengths is never larger than 4 nm, so it is reasonable to assume that all spectra are practically coincident in a given substitution pattern,

regardless the relative tilting of the two moieties. Then, to analyse the effect of the bpy substitution pattern on the absorption spectra, we compare those isomers with the same relative orientation between **B** and the bpy moieties. The optimized structures along with their corresponding electronic absorption spectra are displayed in Figure 3.42. Each 1:1 adduct between **B** and bpy has been identified as **BBx** with **x** = **4**, **5**, and **6**.

The same bands as in the isolated BODIPY are found for the **Bbx** species, although the peak just above 400 nm is much more intense, forming now a separate band. Looking at the $\lambda_{max}$ values for the three bands, there are not significant differences between the three isomers, with a maximum variation of 10 nm. We will denote the three bands in order of increasing energy as band-1, band-2, and band-3. Thus, the longest $\lambda_{max}$ corresponding to band-1 ranges from 638 nm in **Bb5** to 648 nm in **Bb4**, the next one, band-2, from 437 nm in **Bb4** to 446 nm in **Bb5**, and the $\lambda_{max}$ of band-3 from 349 nm in **Bb4** to 354 nm in **Bb6**. It is noteworthy that band-2 is considerably more intense for **Bb5** than for the other compounds. Comparing the absorption bands at the **Bbx** species with those at the isolated **B**, there are no relevant differences in the band-3, but the band-1 suffers red-shifts of 10-21 nm. Band-2, apart from largely increasing its intensity, is also displaced 18-31 nm.

To understand the main features of the **Bbx** absorption spectra, we inspect the frontier Kohn-Sham orbitals involved in the shifted absorption bands of the three isomers (see Figure 3.43). In the case of band-1, it is always described as a HOMO $\rightarrow$ LUMO transition. The HOMO of all the species is described as a $\pi$ orbital involving the two arms of the BODIPY, as in the isolated **B**, whereas the LUMO is a $\pi^*$ orbital with almost negligible contribution from the benzene arm and some contribution from the C8 atom and the bpy ring connected to it. The extra conjugation over the bpy ring at the LUMO of **Bbx** compared to **B** is related to the bathochromic shift of band-1, since the HOMO-LUMO energy gap is lower because of the larger stability of the LUMO. On the other hand, band-2 is mainly due to a HOMO-1 $\rightarrow$ LUMO transition. The HOMO-1 has now large a contribution from a $\pi$ orbital at the bpy in **Bb5** and **Bb6**, which explains the destabilization of 0.09 and 0.08 eV of that orbital, respectively. The significant raise in the energy of the HOMO-1 at **Bb5**, along with the 0.10 eV stabilization of the LUMO previously mentioned when compared to **B**, explains the 31 nm bathochromic shift at band-2 in this species.

According to their electronic absorption spectra, the **Bbx** adducts can be considered more panchromatic than the isolated **B**, since the range of absorption clearly enlarge towards the infrarred region of the spectrum, and the absorption between 400 and 600 nm is enhanced due to the appearance of band-2. The energy of the HOMO and LUMO of all the **Bbx** species fulfills the requirements for the dyes in DSSCs, as the HOMO ranges from -5.51 to -5.56 eV (below -4.8 eV), and the LUMO from -3.08 to -3.14 eV (above -4.3 eV). Therefore, the properties of **Bbx** for their use as dyes in DSSCs have been improved with respect to **B**. On the contrary, the gap between the ground singlet and the first excited triplet states is even lower than for the isolated **B**, with values between 21.4 and 21.7 kcal/mol for the three **Bbx** isomers. As a consequence, these

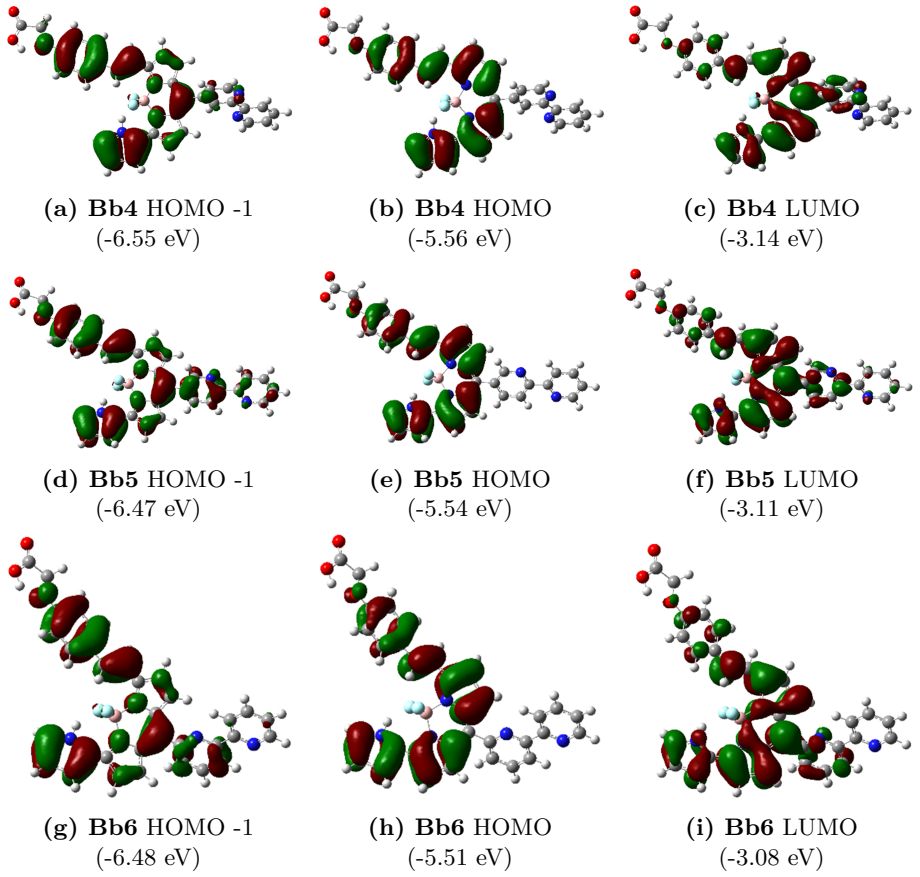

**(a) Bb4** HOMO -1 (-6.55 eV) **(b) Bb4** HOMO (-5.56 eV) **(c) Bb4** LUMO (-3.14 eV)

**(d) Bb5** HOMO -1 (-6.47 eV) **(e) Bb5** HOMO (-5.54 eV) **(f) Bb5** LUMO (-3.11 eV)

**(g) Bb6** HOMO -1 (-6.48 eV) **(h) Bb6** HOMO (-5.51 eV) **(i) Bb6** LUMO (-3.08 eV)

**Figure 3.43.** Contour maps of the HOMO-1, HOMO, and LUMO orbitals for **Bbx** (**x** = **4**, **5**, **6**). The energy of each orbital is also included in parenthesis.

compounds are not suitable for being employed as PSs in PDT.

### 3.7.3 2:1 Adducts of BODIDY with 2,2′-Bipyridine

Then, we have explored the photophysical properties of the **Bbx** species after appending another **B** moiety on the analogous position at the other bpy ring (BBbxx; x = 4, 5, 6). We have optimized two isomers for each BBbxx system, one of which with the same arms of the **B** units above and below the bpy plane (*cis* isomers), and another one with different arms in each **B** moiety above and below the bpy plane (*trans* isomers). Our calculations indicate that the six considered isomers present very similar energies, being the *trans* conformers slightly more stable than their *cis* counterparts, with a maximum deviation of 3.6 kcal/mol when comparing the *trans* isomer of BBb55 with the *cis* isomer of BBb44. The comparison of the electronic absorption spectra between two two

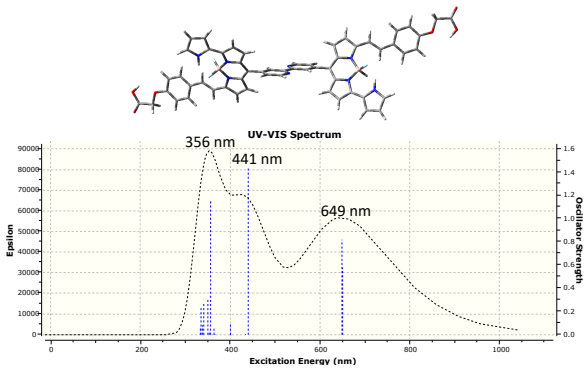


**(a) BBb44**

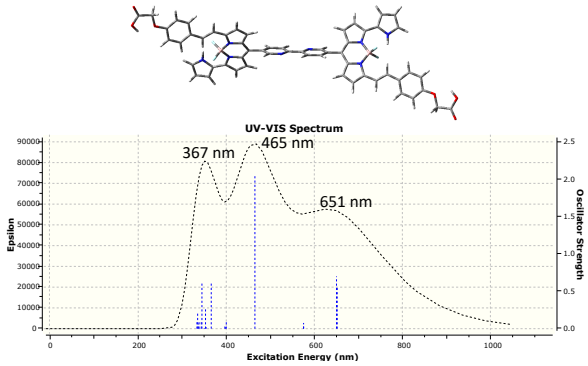


**(b) BBb55**

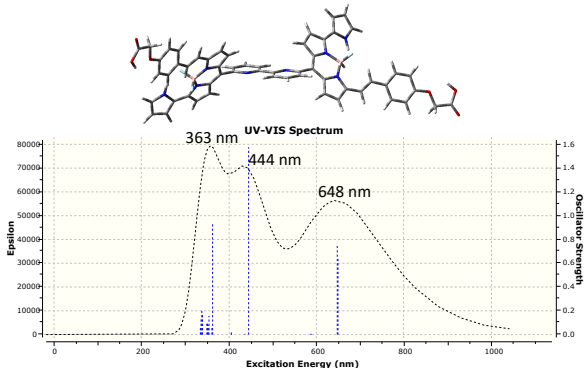


**(c) BBb66**

**Figure 3.44.** PCM-B3LYP/6-31G(d) optimized structures of **BBb44**, **BBb55**, and **BBb66**, along with their corresponding PCM-TD-M06/6-31+G(d)//PCM-B3LYP/6-31G(d) electronic absorption spectra.

types of conformers reveals differences of less than 2 nm in the main absorption bands. Therefore, we will focus our discussion on the most stable *trans* isomers,

which will be denoted as '**BBbxx**' adducts.

Figure 3.44 collects the absorption spectra for the three **BBbxx** isomers. The same bands as in the **Bbx** species appear, although it is remarkable that their intensity doubles when introducing the extra **B** moiety. The bands are slightly red-shifted when compared to those of **Bbx** isomers, except for **BBb55**, where the shift is larger than 13 nm for all the absorption bands. Besides, band-2 in **BBb55** is much more intense than the other bands.

Regarding band-1, it presents two excitation energies corresponding to transitions from HOMO-1/HOMO to LUMO/LUMO+1, with a difference of less than 2 nm between them. The HOMO and the HOMO-1 orbitals, with no participation from the bpy, become degenerate in each **BBbxx** system (see Table 3.13). Meanwhile, LUMO and LUMO+1 are also degenerate for **BBb44** and **BBb66**, whereas the LUMO is 0.14 eV more stable than the LUMO+1 in **BBb55**. In addition, the difference in energy between the HOMO-1/HOMO orbitals of **BBbxx** and the HOMO of **Bbx** is always less 0.04 eV, very close to the difference between the LUMO/LUMO+1 orbitals of **BBb44** and **BBb66** and the LUMO orbital of the corresponding **Bbx** species. However, the energy of the LUMO in **BBb55** is 0.11 eV more stable than the one at **Bb5** due to the conjugation involving the two **B** moieties and the bpy ligand, which only appears at this compound. This explains the larger bathochromic shift observed at this system. A similar picture is found for band-2, which is described as HOMO-3/HOMO-2 transitions to LUMO/LUMO+1. In this sense, all those orbitals are also degenerated for **BBb44** and **BBb66**, but at **BBb55**, apart from the more stable LUMO, the HOMO-2 is higher in energy due to a relevant contribution from the bpy moiety. Consequently, band-2 for **BBb44** and **BBb66** is very similar to that of **Bb4** and **Bb6**, but it increases in intensity and appears at longer wavelengths when comparing **BBb55** and **Bb5**.

**Table 3.13.** PCM-M06/6-31+G(d) energies of some relevant frontier Kohn-Sham orbitals in eV for adducts **BBbxx** (**x** = **4**, **5**, **6**).

| Species | HOMO-3 | HOMO-2 | HOMO-1 | HOMO | LUMO | LUMO+1 |
|---|---|---|---|---|---|---|
| **BBb44** | -6.57 | -6.56 | -5.57 | -5.57 | -3.16 | -3.15 |
| **BBb55** | -6.55 | -6.46 | -5.57 | -5.56 | -3.22 | -3.08 |
| **BBb66** | -6.53 | -6.50 | -5.54 | -5.53 | -3.13 | -3.11 |

Although the addition of an extra **B** moiety in **BBb44** and **BBb66** does not produce significant shifts at the absorption bands, they do increase their intensity, so they are more suitable for their use as dyes in DSSCs. On the other hand, in addition to the stronger absorption, the **BBb55** species displays a significant red-shift for bands 1 and 2, so it presents the best panchromatic features. The energy of the frontier orbitals at the **BBbxx** compounds, as shown in Table 3.13, fulfills the requirements for the dyes.

Interestingly, the $\Delta E_{ST}$ value of **BBb55** is now larger than 22.5 kcal/mol (23.2 kcal/mol), so its triplet state could react with $^3O_2$ to yield $^1O_2$. On the

contrary, **BBb44** and **BBb66** yield triplet states about 20 kcal/mol above their corresponding singlet ground states.

### 3.7.4 Re(I) Tricarbonyl Complexes Bearing 2:1 Adducts of BODIPY with 2,2′-Bipyridine

Now, we will present the results of appending the **BBbxx** (**x** = **4**, **5**, **6**) to a Re(I) tricarbonyl complex ([ReCl(CO)$_3$(BBbxx)]), which will be denoted as **BBbxx-Re**, comparing their photophysical properties with those of the reference [ReCl(CO)$_3$(bpy)] complex. The electronic absorption spectra of this isolated complex, which is displayed in Figure 3.45 along with its optimized structure, presents two absorption bands, one with large intensity centered at 291 nm, and another one with low intensity at 405 nm, which corresponds to a HOMO-1 → LUMO transition from a Re *d* orbital to a $\pi^*$ orbital centered at the bpy ligand ($^1$MLCT). The other band is a mixture of $^1$MLCT and $^1$ILCT transfers.

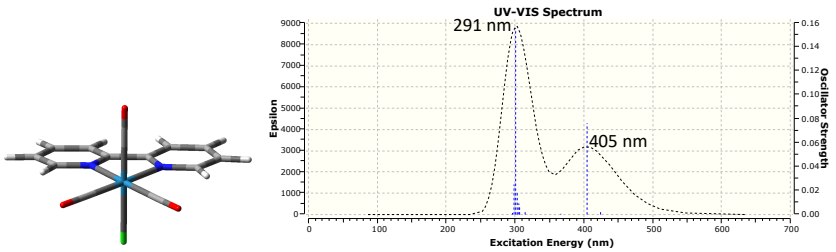


**Figure 3.45.** PCM-B3LYP/6-31G(d) (LANL2DZ for Re) optimized structure of [ReCl(CO)$_3$(bpy)], along with its PCM-TD-M06/6-31+G(d) (LANL2DZ for Re)//PCM-B3LYP/6-31G(d) (LANL2DZ for Re) electronic absorption spectra.

Once we have covered the spectroscopic features of the reference complex, we will turn our attention to the **BBbxx-Re** complexes. Note that **BBbxx** adducts had to be twisted around the C2-C2′ atoms of the bpy in order to face both N atoms to the metal. We have optimized four different conformers for each **BBbxx** (**x** = **4**, **5**), all of them with similar energy, resulting from locating the same or different arms of the **B** moieties above and below the bpy plane and from varying the **B**-bpy dihedrals angles. As a consequence of the proximity between the **B** units and the monodentate Re ligands for the **BBb66-Re** conformations, only two conformers with nearly the same energy are possible. These last isomers are less stable than the previous ones by about 16 kcal/mol. Since the electronic absorption spectra of all the isomers for a given substitution pattern are very similar, we will only consider one of them for each **BBbxx-Re** complex. The optimized structures of the selected (most stable) isomers are shown in Figure 3.46, along with their electronic absorption spectra.

There are significant differences in the absorption bands of the **BBbxx-Re** complexes. The spectrum of the **BBb44-Re** complex displays two bands, one

centered close to an intense transition at 689 nm, with a difference of 40 nm with band-1 of **BBb44**, and another one at 472 nm. In the case of **BBb55-Re**, the lowest-lying absorption band, at 703 nm, is less intense compared to the other one, which appears at 474 nm. Another transition at 611 nm contributes to its panchromatic character. Finally, the spectrum of **BBb66-Re** only contains a wide absorption band, due to a very intense transition at 637 nm. We note however the possibility of a band at around 400 nm should not be ruled out due to the number of transitions considered in the TD-DFT computations.

As for **BBbxx**, the lowest-lying absorption band (band-1) for the **BBbxx-Re** (**x** = **4**, **5**) complexes involve the HOMO-1, HOMO, LUMO, and LUMO+1 orbitals, and corresponds to a $^1$ILCT within the **BBbxx** fragment (see Figure 3.47). The comparison of those orbitals with the ones at the **BBbxx** (**x** = **4**, **5**) moieties indicates that, despite the lack of direct contribution from the metal in that band, it promotes a large participation of the bpy orbitals at the LUMO, thus increasing the conjugation and stabilizing this orbital by more than 0.2 eV, yielding the observed bathochromic shift. On the other hand, the energy of the HOMO and the HOMO-1 hardly varies. Unlike band-1, the other band (band-2) at the **BBbxx-Re** (**x** = **4**, **5**) complexes changes its character to $^1$MLCT, with orbitals involving the Re center. For **BBb66-Re**, the main absorption involves the HOMO-1, HOMO, LUMO, and LUMO+1 orbitals and presents a $^1$ILCT character (see Figure 3.47). However, the bpy moiety does not participate in the LUMO, that is, the electron conjugation is reduced and the maximum wavelength is shorter with respect to the previous Re complexes. The nearly perpendicular disposition of the B moieties with respect to bpy avoids this electron delocalization along the bpy fragment.

Concerning the potential use of these complexes as dyes in DSSCs. The requirement for the energy of the frontier orbitals is still fulfilled, as the HOMO and the LUMO are centered at the **BBbxx** moieties, suffering slight variations of energy. On top of that, the complexes display strong absorption at both the visible and the UV regions of the spectrum.

The $\Delta E_{ST}$ values for the complexes are again below the 22.5 kcal/mol threshold, so we conclude that they are not adequate for PDT.

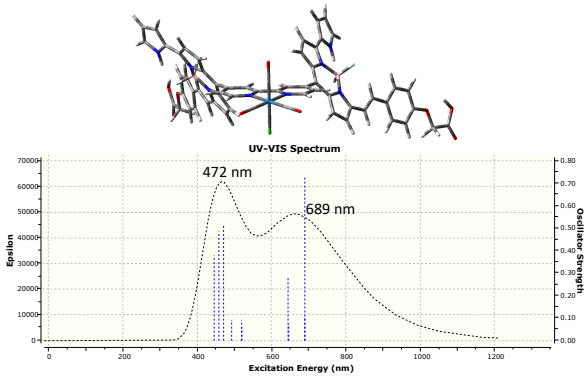


**(a) BBb44-Re**

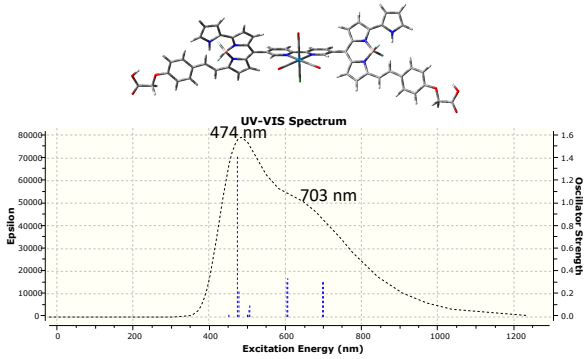


**(b) BBb55-Re**

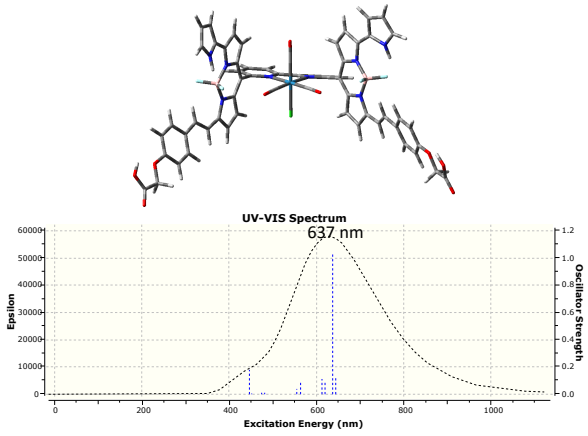


**(c) BBb66-Re**

**Figure 3.46.** PCM-B3LYP/6-31G(d) (LANL2DZ for Re) optimized structures of **BBb44-Re**, **BBb55-Re**, and **BBb66-Re**, along with their corresponding PCM-TD-M06/6-31+G(d) (LANL2DZ for Re)// PCM-B3LYP/6-31G(d) (LANL2DZ for Re) electronic absorption spectra.

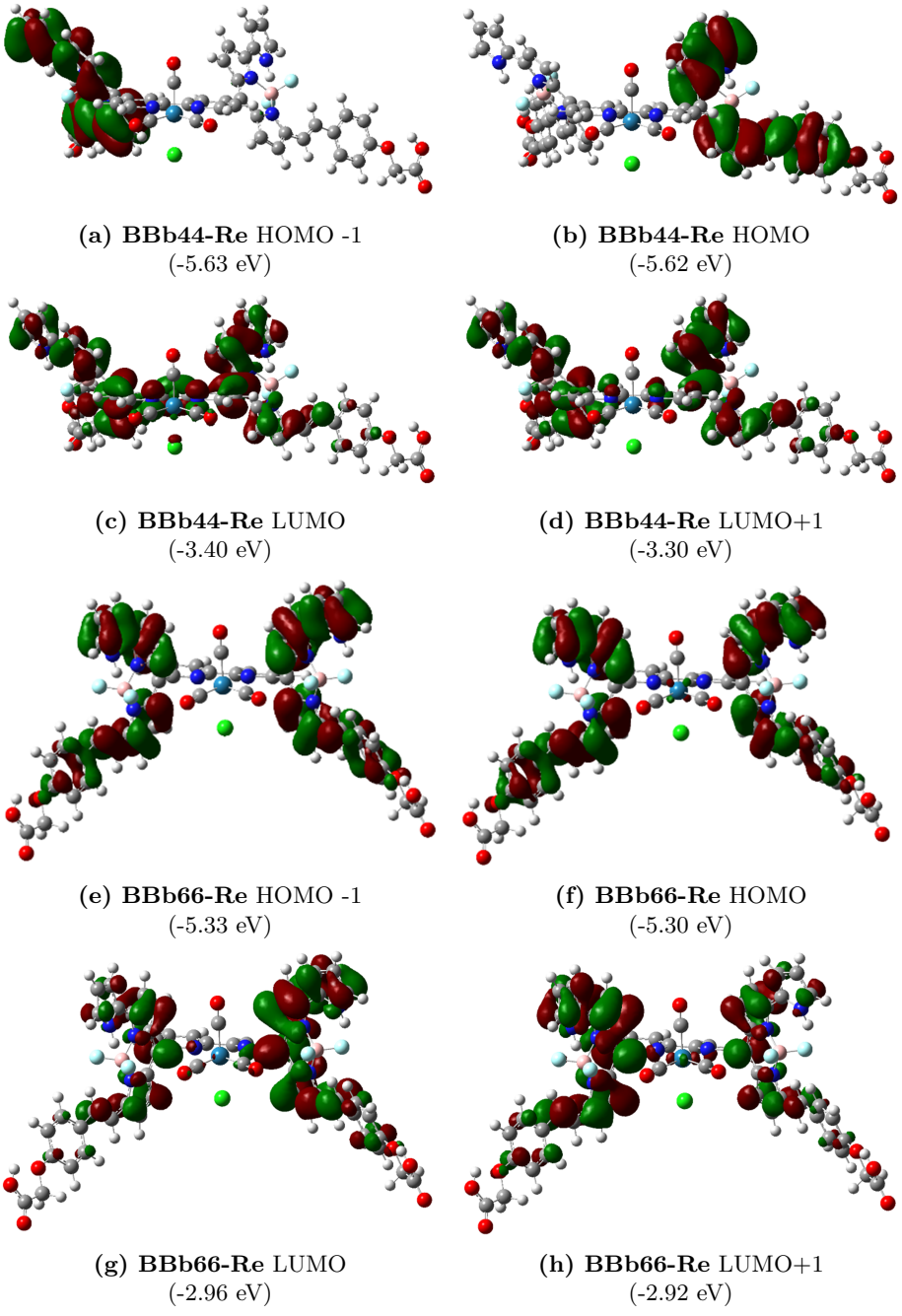

**(a) BBb44-Re** HOMO -1 (-5.63 eV)

**(b) BBb44-Re** HOMO (-5.62 eV)

**(c) BBb44-Re** LUMO (-3.40 eV)

**(d) BBb44-Re** LUMO+1 (-3.30 eV)

**(e) BBb66-Re** HOMO -1 (-5.33 eV)

**(f) BBb66-Re** HOMO (-5.30 eV)

**(g) BBb66-Re** LUMO (-2.96 eV)

**(h) BBb66-Re** LUMO+1 (-2.92 eV)

**Figure 3.47.** Contour maps of the HOMO-1, HOMO, LUMO, and LUMO+1 orbitals for **BBbxx-Re** (**x** = **4**, **6**). The energy of each orbital is also included in parenthesis.

# 4 Conclusions

In this PhD Thesis, the following conclusions have been reached:

1. The theoretical study on the reaction between [Re($PPh_2$)$(CO)_3$(N–N)] (N–N = bpy, phen) complexes towards the activated alkyne methyl propiolate (HMAD) has revealed the role of the bidentate ligand in the mechanism for the formation of the different types of products. In this sense, the energetics for the coupling with the carbonyl ligand as well as for the insertion of the non-attacked acetylene carbon into the Re-P bond are not affected by the exchange between bpy and phen. However, the presence of a phen ligand makes the reaction pathway leading to the coupling with the diimine ligand more favorable by stabilizing both the transition state and the product. Hence, the pyridine ring where the coupling is produced is more electrophilic due to the larger conjugation of the phen ligand, lowering the corresponding energy barrier. In addition, the extra conjugation alleviates the excess of electron density at the diimine ligand once the coupling takes place, stabilizing the product. This is in accordance with the experimental product found for the reaction of the complex with the phen ligand.

2. The results from the investigation of the reaction between complexes [ReX$(CO)_3$(bpy)] (X = $NH_2$, NHMe, NH*p*Tol, OH, OMe, OPh, $PH_2$, PHMe, $PMe_2$, PHPh, $PPh_2$, PMePh, SH, SMe, SPh) and HMAD have clarified the influence of the nucleophilic ligand, X. First, from the comparison of the reaction profile in complexes with the same nucleophilic atom directly linked to Re, we have concluded that the Me substituent at the nucleophilic ligand makes the complex more reactive towards HMAD due to its electron-donating effect, whereas the influence of the aryl groups depends on the nature of the nucleophilic atom. On the one hand, if the nucleophilic ligand has an atom from the second period (N or O), the presence of the aryl ligand makes the reaction more unfavorable, as aryl orbitals interact strongly with those from the heteroatom, making them less available for the initial nucleophilic attack. On the other hand, the phenyl groups attached to an atom from the third period (P or S) make the reaction between the Re(I) complex and HMAD more favorable, although their stabilizing effect is not as strong as the one caused by the alkyl groups. Finally, regarding the influence of the nature of the heteroatom at the nucleophilic ligand, we have found that the larger size of the heteroatoms from the third period (P and S) makes the overlap with the Re *d* orbitals more effective and, thus, a general destabilizing effect in all the species is observed, which is especially relevant for the insertion route.

3. Apart from rationalizing the experimental products found for the reaction of complexes [ReX$(CO)_3$(N–N)] (X = NH*p*Tol, OH, OMe, $PPh_2$; N–N = bpy, phen), we have made a series of predictions for the reaction of the

Re(I) complexes bearing nucleophilic ligands that have not been tested experimentally. The product resulting from the coupling to the carbonyl ligand and the subsequent hydrogen migration from the nucleophilic ligand to the oxygen of the carbonyl is the expected one for the N and O ligands that contain a H atom ($NH_2$, NHMe, NH*p*Tol, OH), due to the low barrier characteristic of that coupling and the large stability of the product. This is also the case for the SH ligand, but its large initial energy barrier could avoid the formation of such a product. On the other hand, given the unstability of the other types of products, the insertion into the Re-X bond is the most likely outcome for the reaction of the complexes with OMe, OPh, SMe, and SPh ligands, although the high energy barriers for all of them but OMe make the reactions less accessible. Finally, we predict the coupling to the bidentate ligand for the complexes with nucleophilic ligands containing P, as the insertion route is greatly penalized due to the strong bond formed between P and Re, and the barriers for the other types of couplings are similar, but the product coupled to the bpy ligand is always more stable.

4. The computational modelling on the hydrolysis of a series of ether substrates (diethyl ether, divinyl ether, and ethyl vinyl ether) catalyzed by the aqueous molybdocene $[Cp_2Mo(OH)(H_2O)]^+$ has led to the following conclusions. To begin with, we have demonstrated that the ether functionality (i.e., the ether oxygen) is not active in the catalysis of ethers by molybdocenes. The reason for that is not related to an unfavorable coordination to Mo through that atom, as the largest barrier found for that step is 20.3 kcal/mol, but to the activation of the other functionalities. Accordingly, the intramolecular nucleophilic attack from the hydroxo ligand of the molybdocene to either the ethyl or the vinyl functionalities is always the rate-determining step if the ether coordinates via the oxygen atom, being the lowest barrier for such attack 43.6 kcal/mol (to the vinyl group of ethyl vinyl ether). However, the intramolecular nucleophilic attack to the ethyl vinyl and divinyl ethers is much more feasible if they coordinate to the metal through the vinyl functionality. Thus, the largest energy barrier for that mechanism is 22.2 and 29.3 kcal/mol for ethyl vinyl ether and divinyl ether, respectively, in both cases corresponding to the transition state for the intramolecular hydrogen migration. On the contrary, diethyl ether can not coordinate to the metal center through a different functionality than the ether one, so $[Cp_2Mo(OH)(H_2O)]^+$ is not able to catalyze the hydrolysis of this compound, as experimentally reported.

5. In the computational study of the reaction of Re(I) tricarbonyl complexes bearing *N*-alkylimidazoles (RIm, R = Me, Mes) and 4,4′-disubstituted 2,2′-bipyridines (4,4′-R2′bpy, R′ = *t*Bu, $NMe_2$) towards the strong base $KN(SiMe_3)_2$, we have been able to clarify the effect of both the bidentate and the imidazole ligands. Regarding the complexes bearing *t*Bu substituents at the bpy ligand, the low energy barrier and stability for the

coupling of the deprotonated carbon of the imidazole to the external *ortho* carbon of the diimine ligand favour that product over the other ones. However, the replacement of the *t*Bu groups by the more electron-donating $NMe_2$ makes the coupling with the bpy ligand less accessible due to its raise of electron density. In the case of the $NMe_2$ complex with a MesIm ligand, the destabilization for that coupling is moderate, so the product, as experimentally found, is the same as for the *t*Bu complexes. On the other hand, the deprotonation of $[Re(CO)_3(4,4'-(NMe_2)_2bpy)(MeIm)]OTf$ forms an imidazo-2-yl product instead. This is a consequence of the larger nucleophilic character of the MeIm ligand, which would yield an excess of electron density at the bpy ligand and, therefore, both the coupling to the external and the internal *ortho* carbon atoms of that ligand is heavily penalized.

6. On the basis of the results obtained for the deprotonation reaction of complexes $[Re(CO)_3(4,4'-R'_2bpy)(RIm)]OTf$ ($R' = t$Bu, $NMe_2$; R = Me, Mes), we reasoned that the replacement of the electron-donating *t*Bu and $NMe_2$ substituents by electron-withdrawing ones would favour the coupling products to the bpy ligand. In this respect, the theoretical study of the reaction with $R' = Br$, which had not been tested experimentally, revealed that the product resulting from the coupling of the deprotonated carbon of the imidazole ligand to the internal *ortho* carbon of the bpy ligand was the most likely outcome for the reaction, with both the MeIm and MesIm ligands. These theoretical predictions were subsequently corroborated experimentally.

7. The analysis of the reaction between $KN(SiMe_3)_2$ and the Mo(II) complexes $[Mo(\eta^3-C_4H_7)(CO)_2(4,7-Cl_2phen)(RIm)]OTf$ (R = Me, Mes) has confirmed that the presence of the more rigid phen ligand instead of the bpy one makes the coupling to the internal *ortho* carbon, which is the experimental product for the latter ligand, more energy-demanding. Thus, we have predicted that the complex with MesIm would yield a coupling to the external *ortho* carbon of the phen ligand, whereas the complex with MeIm would form a mixture of that type of product and an imidazo-2-yl product. Both predictions have been confirmed by experimental findings.

8. The comparison of the computational results obtained for the interaction of the complex $[Re(CO)_3(dmphen)(H_2O)]^+$ (dmphen = 2,9-dimethylphen) with a model of the DNA nucleobase guanine and with a derivative of the histidine amino acid has shed light on the cytotoxic mechanism of action of this complex. Hence, despite the slightly lower energy barriers found for the reaction with the nucleobase, in agreement with the experimental results, the reaction with the amino acid is more favorable thermodynamically. In this sense, the inclusion of some explicit water molecules in the model used to elucidate the mechanism has been crucial for a proper description of the reaction. Therefore, as suggested by the experimental evidence of a mechanism of action different from that

of cisplatin, our results indicate that the cytotoxicity of the Re(I) aquo complex is a consequence of its reaction with proteins within the cell rather than with DNA. In addition, the exploration of the reaction of two new $[Re(CO)_3(2,9–R_2phen)(H_2O)]^+$ (R = OMe, $NMe_2$) complexes towards the derivative of histidine has proven that the presence of more electron-donating substituents on the bidentate ligand enhances the cytotoxic activity of the complex.

9. In the theoretical investigation on the spectroscopic properties of a series of Re(I) carbonyl pyridyl complexes with pyridocarbazole ligands we have rationalized the effect on the lowest-lying absorption band of changing the conjugation and the electron density at the bidentate ligand, as well as of replacing the carbonyl ligand in *cis* disposition to the bidentate ligand by different phosphines. First of all, we have found that the expansion of the diimine ligand lowers the HOMO-LUMO energy gap, inducing a red-shift to the longest $\lambda_{max}$. Secondly, the addition of $\sigma$-accepting substituents, such as $CO_2Et$ and F, to the pyridine ring of the pyridocarbazole ligand produces a stabilizing effect on the LUMO, whereas the energy of the HOMO raises as $\pi$-donating groups, like OMe and $NMe_2$, are introduced into the indole moiety. Both types of substituents result in a bathochromic shift of the lowest-lying absorption band, which is even larger if they are combined in the same complex. Finally, the removal of the carbonyl ligand (with its $\pi^*$ orbital) when replaced by a phosphine group, e.g. $PMe_3$ and CAP, causes an extra bathochromic shift due to the destabilization of the HOMO, which is especially large with the CAP ligand. Through the combination of the $PMe_3$ or CAP ligands with the adequate substituents at the pyridocarbazole ligand, we have designed several complexes with significant absorption at the therapeutic window. These complexes are potential candidates for their use as PSs in PDT.

10. The computational analysis of eleven different BODIPY-oxasmaragdyrin dyads designed for their use as dyes in DSSCs has shown the influence of the bridge that links the two moieties in a series of structural, electronic, and spectroscopic properties. To begin with, we have found that the coplanarity between the two moieties is promoted if the bridge is formed by alkynyl groups or two sets of aryl functionalities. In addition, the presence of a bridge containing an alkynyl group bonded to the oxasmaragdyrin also enhances the aromaticity at the oxasmaragdyrin macrocycle, as confirmed by the computation of NICS and ring current density maps. Regarding the electronic and spectroscopic properties, which are key for evaluating the potential of the dyes, only the three dyads containing alkynyl bridges fulfill the requirement for the energy of the HOMO. On top of that, the electronic absorption spectra of those dyads present a charge transfer from the oxasmaragdyrin to the BODIPY that largely enhances the light harvesting capacity of the compounds. Therefore, we have concluded that the alkynyl bridges are the most suitable choice for improving the properties of the dyads as dyes in DSSCs.

11. The photophysical properties of the BODIPY for its use as dye in DSSCs have also been improved by attaching one or two BODIPY moieties to a 2,2′-bipyridine, either as part of a Re(I) tricarbonyl complex or as isolated adducts. In this sense, the BODIPY is known for its strong absorption but in a narrow range of wavelengths. After appending a BODIPY unit to a 2,2′-bipyridine, we have found that the panchromatic character is enhanced, as the bands undergo bathochromic shifts and new ones also appear. This effect is even stronger if two BODIPY moieties are attached, forming 2:1 adducts. If those adducts are coordinated to the metal center of a Re(I) tricarbonyl complex, the absorption bands are displaced to even longer wavelengths, although their intensity of absorption is lower. Nevertheless, the design of Re(I) complexes with absorption bands at the red region of the electromagnetic spectrum is remarkable. All the species considered in this study fulfill the energy requirements for the frontier orbitals (energy of the HOMO below the potential of the redox couple, and energy of the LUMO above the conduction band of the semiconductor).

# Conclusiones

Los estudios realizados en esta Tesis han llevado a las siguientes conclusiones:

1. El estudio teórico sobre la reacción del complejo $[Re(PPh_2)(CO)_3(N{-}N)]$ (N−N = bpy, phen) frente a propiolato de metilo (HMAD) ha servido para esclarecer el papel que juega el ligando bidentado en el mecanismo de formación de los diferentes tipos de productos. De esta forma, las energías tanto para el acoplamiento con el ligando carbonilo como para la inserción del carbono no atacado en el enlace Re-P no se ven afectadas por el intercambio entre la bpy y la phen. Sin embargo, la presencia de un ligando phen hace que el camino de reacción para el acoplamiento con el ligando diimina sea más favorable debido a la estabilización del estado de transición y del producto correspondiente. Así, el anillo piridínico donde el acoplamiento tiene lugar es más electrofílico debido al mayor grado de conjugación del ligando phen, lo que hace que disminuya la barrera energética de ese acoplamiento. Además, ese mayor grado de conjugación también alivia el exceso de densidad electrónica que se produce en el ligando bidentado una vez tiene lugar el acoplamiento, lo que favorece un aumento de la estabilidad relativa del producto. Estos resultados concuerdan con el producto encontrado experimentalmente para la reacción del complejo con el ligando phen.

2. Los resultados alcanzados en la investigación sobre la reacción entre los complejos $[ReX(CO)_3(bpy)]$ (X = $NH_2$, NHMe, NH*p*Tol, OH, OMe, OPh, $PH_2$, PHMe, $PMe_2$, PHPh, $PPh_2$, PMePh, SH, SMe, SPh) y HMAD han revelado qué influencia tiene el ligando nucleofílico, X. En primer lugar, mediante la comparación de los perfiles de reacción en complejos con el mismo átomo nucleofílico unido directamente al Re, hemos concluido que, mientras que el sustituyente Me en el ligando nucleofílico hace que el complejo sea más reactivo frente a HMAD debido a su carácter dador de electrones, el efecto de los grupos arilo varía con la naturaleza del átomo nucleofílico. Por un lado, si este átomo pertenece al segundo período (N u O), la presencia del ligando arilo hace que la reacción sea más desfavorable, ya que los orbitales del arilo interaccionan fuertemente con los del heteroátomo, haciendo que los de dicho heteroátomo estén menos disponibles para el ataque nucleofílico inicial. Por otro lado, los grupos fenilo unidos a un átomo del tercer período (P o S) hacen que la reacción entre el complejo de Re(I) y HMAD sea más favorable, aunque su efecto estabilizador es menor que el causado por los grupos metilo. Por último, respecto al papel del heteroátomo del ligando nucleofílico, hemos descubierto que el mayor tamaño de los heteroátomos del tercer período (P y S) produce un mayor solapamiento con los orbitales *d* del Re y, por tanto, se observa una estabilización relativa de todas las especies, particularmente de las implicadas en la ruta de inserción.

3. Además de racionalizar los productos encontrados experimentalmente para

la reacción de los complejos [ReX(CO)$_3$(N−N)] (X = NH*p*Tol, OH, OMe, PPh$_2$; N−N = bpy, phen), también hemos realizado una serie de predicciones para las reacciones de los complejos de Re(I) con ligandos nucleofílicos que no han sido testeados experimentalmente. El producto resultante del acoplamiento con el ligando carbonilo y la posterior migración del hidrógeno desde el ligando nucleofílico hacia el oxígeno del carbonilo, es el esperado para la reacción de complejos con ligandos N y O que contengan H (NH$_2$, NHMe, NH*p*Tol, OH), debido a la baja barrera característica de ese acoplamiento y a la gran estabilidad del producto. Este también es el caso para el ligando SH, pero la gran barrera energética inicial de la reacción con este ligando podría evitar la formación de dicho producto. Por otro lado, dada la inestabilidad de los otros tipos de productos, la inserción en el enlace Re-X es el resultado más probable para la reacción de los complejos con ligandos OMe, OPh, SMe y SPh, aunque las grandes barreras encontradas para todos ellos menos para OMe hacen que las reacciones correspondientes sean menos accesibles. Finalmente, proponemos que el producto de reacción que se formaría en el caso de complejos con ligandos nucleofílicos que contienen P sería el del acoplamiento con el ligando bidentado, dado que la ruta de inserción está muy penalizada por el fuerte enlace Re-P y las barreras para la formación de los otros dos tipos de acoplamiento son similares, pero el producto de acoplamiento con la bpy es siempre más estable.

4. El estudio computacional sobre la hidrólisis de una serie de éteres (dietil éter, divinil éter y etil vinil éter) catalizada por el molibdoceno acuoso [Cp$_2$Mo(OH)(H$_2$O)]$^+$ ha dado lugar a las siguientes conclusiones. Para empezar, hemos demostrado que la funcionalidad éter (el oxígeno) no es activa frente a la catálisis de éteres por molibdocenos. La razón no está relacionada con una coordinación desfavorable de ese oxígeno al Mo, ya que la barrera más alta para dicho proceso es 20.3 kcal/mol, sino con la activación de las otras funcionalidades del sustrato. De esta forma, el ataque nucleofílico intramolecular del ligando hidroxo del molibdoceno a las funcionalidades etilo o vinilo es siempre la etapa determinante de la reacción si el éter se coordina por el átomo de oxígeno, siendo la barrera más baja para dicho ataque con un valor de 43.6 kcal/mol (al grupo vinilo del etil vinil éter). No obstante, el ataque nucleofílico intramolecular al etil vinil y al divinil éter es mucho más favorable si se coordinan a través de la funcionalidad vinilo. Siendo así, la barrera energética más alta es 22.2 y 29.3 kcal/mol para el etil vinil y el divinil éter, respectivamente, siendo en ambos casos la correspondiente al estado de transición para la migración de hidrógeno intramolecular. Por otra parte, el dietil éter no se puede coordinar al metal a través de un átomo diferente del oxígeno, por lo que, de acuerdo con las evidencias experimentales, [Cp$_2$Mo(OH)(H$_2$O)]$^+$ no es capaz de catalizar la hidrólisis de dicho compuesto.

5. Mediante la investigación computacional sobre la reacción de complejos tricarbonílicos de Re(I) con ligandos *N*-alquilimidazol (RIm, R = Me,

Mes) y 2,2′-bipiridinas 4,4′-disustituidas (4,4′-R2′bpy, R′ = *t*Bu, $NMe_2$) frente a la base fuerte $KN(SiMe_3)_2$, hemos sido capaces de esclarecer el efecto tanto del ligando bidentado como del ligando imidazol. Respecto a los complejos con sustituyentes *t*Bu en el ligando bpy, la baja barrera energética y la estabilidad del producto de acoplamiento entre el carbono desprotonado del imidazol y el carbono *orto* externo del ligando diimina favorece dicho producto sobre los demás. Sin embargo, si los grupos *t*Bu son reemplazados por $NMe_2$, que es un dador de electrones más fuerte, el acoplamiento con el ligando bpy se vuelve más desfavorable debido al aumento de densidad electrónica en ese ligando bidentado. En el caso del complejo con grupos $NMe_2$ y un ligando MesIm, la desestabilización de dicho acoplamiento es moderada, por lo que el producto, como se encontró experimentalmente, es el mismo que para los complejos con sustituyentes *t*Bu. Por el contrario, la desprotonación del complejo $[Re(CO)_3(4,4'-(NMe_2)_2bpy)(MeIm)]OTf$ conduce a la formación de un producto de tipo imidazol-2-ilideno porque el mayor carácter nucleofílico del ligando MeIm provocaría un exceso de densidad electrónica en el ligando bpy y, por ende, penaliza los posibles acoplamientos con dicho ligando.

6. En base a los resultados alcanzados para las reacciones de desprotonación de los complejos $[Re(CO)_3(4,4'-R'_2bpy)(RIm)]OTf$ (R′ = *t*Bu, $NMe_2$; R = Me, Mes), hemos deducido que la sustitución de los grupos dadores de electrones *t*Bu y $NMe_2$ por aceptores de electrones favorecería los productos de acoplamiento con el ligando bpy. A este respecto, el estudio teórico sobre la reacción con R′ = Br, que no había sido llevada a cabo experimentalmente, puso de manifiesto que el acoplamiento del carbono desprotonado del ligando imidazol con el carbono *orto* interno de la bpy es el producto más probable de la reacción, tanto con MeIm como MesIm. Estas predicciones teóricas fueron posterioremente confirmadas de forma experimental.

7. El análisis de la reacción entre $KN(SiMe_3)_2$ y los complejos de Mo(II) $[Mo(\eta^3-C_4H_7)(CO)_2(4,7-Cl_2phen)(RIm)]OTf$ (R = Me, Mes) ha confirmado que la presencia de un ligando phen, más rígido que la bpy, hace que el acoplamiento con el carbono *orto* interno, que es el producto experimental con bpy, esté más desfavorecido energéticamente. En este caso, sugerimos que el complejo con un ligando MesIm daría un producto de acoplamiento con el carbono *orto* externo del ligando phen, mientras que el complejo con MeIm formaría una mezcla de ese producto y un producto de tipo imidazol-2-ilideno. Ambas predicciones han sido confirmadas experimentalmente.

8. La comparación de los resultados obtenidos para la interacción del complejo de Re(I) $[Re(CO)_3(dmphen)(H_2O)]^+$ (dmphen = 2,9-dimetilphen) con un derivado del aminoácido histidina y un modelo de la nucleobase guanina ha ayudado a desvelar el mecanismo de acción citotóxico de este

complejo. En este sentido, a pesar de las barreras más bajas encontradas para la reacción con la nucleobase, lo que está en acuerdo con las evidencias experimentales, la reacción con el aminoácido es más favorable termodinámicamente. La inclusión de moléculas de agua explícitas en el estudio teórico realizado ha sido crucial para conseguir una descripción más realista de las reacciones investigadas. Por lo tanto, como sugiere la evidencia experimental de un mecanismo de acción diferente al del cisplatino, nuestros resultados indican que la citotoxicidad del complejo aquo de Re(I) es debida a su reacción con proteínas dentro de la célula, en vez de con el ADN. Además, la exploración de la reacción con dos nuevos complejos $[Re(CO)_3(2,9\text{–}R_2phen)(H_2O)]^+$ (R = OMe, $NMe_2$) frente al derivado de histidina ha demostrado que la presencia de sustituyentes con mayor capacidad dadora de electrones en el ligando bidentado aumenta la actividad citotóxica del complejo.

9. La investigación teórica sobre las propiedades espectroscópicas de una serie de complejos carbonílicos de Re(I) con un ligando monodentado piridínico y otro bidentado de tipo piridocarbazol ha servido para descubrir los efectos de alterar la conjugación y la densidad electrónica del ligando bidentado y de sustituir el ligando carbonilo en posición *cis* respecto al piridocarbazol por diferentes fosfinas en la banda de absorción de menor energía. Primero, hemos encontrado que la expansión del ligando diimina provoca una disminución en la diferencia de energía HOMO-LUMO, lo que produce un desplazamiento hacia el rojo de la $\lambda_{max}$ más larga. Después, los resultados obtenidos tras añadir sustituyentes $\sigma$-aceptores, tales como $CO_2Et$ y F, al anillo piridínico del ligando piridocarbazol muestran que se produce un efecto de estabilización en el LUMO, mientras que la energía del HOMO aumenta al introducir sustituyentes $\pi$-dadores, como OMe y $NMe_2$, en el indol. Ambos tipos de sustituyentes dan lugar a un desplazamiento batocrómico de la banda de absorción de menos energía, que es incluso mayor si los dos tipos de sustituyentes se combinan en el mismo complejo. Por último, la sustitución del ligando carbonilo (con su orbital $\pi^*$) por una fosfina, como por ejemplo $PMe_3$ y CAP, causa otro desplazamiento batocrómico debido a la desestabilización del HOMO, que es especialmente importante con el ligando CAP. A través de la combinación de los ligandos $PMe_3$ o CAP con los sustituyentes adecuados en el ligando piridocarbazol, hemos diseñado varios complejos con una absorción notable en la ventana terapeútica. Estos complejos son candidatos potenciales para su uso como fotosensibilizadores en terapia fotodinámica.

10. El análisis computacional de once díadas BODIPY-oxasmaragdirina diseñadas para su uso como colorantes en celdas solares sensibilizadas con colorantes (DSSCs) ha servido para mostrar la influencia del puente que une las dos moléculas en una serie de propiedades estructurales, electrónicas y espectroscópicas. Hemos descubierto que la disposición coplanaria entre las dos especies que componen la díada se ve favorecida si el puente

está formado o bien por grupos alquino, o bien por dos grupos de funcionalidades de tipo arilo. Además, la presencia de un puente con un grupo alquino unido a la oxasmaragdirina, también aumenta la aromaticidad en el macrociclo de esta molécula, como hemos confirmado mediante la computación de NICS y de mapas de densidad de corriente. Con respecto a las propiedades electrónicas y espectroscópicas, que son claves para evaluar el potencial de los colorantes, solo las tres díadas con puentes alquino cumplen el requisito para la energía del HOMO. Además, el espectro de absorción de esas díadas presenta una transferencia de carga desde la oxasmaragdirina hacia la BODIPY que da lugar a una capacidad de absorción de luz mucho mejor. Por lo tanto, concluimos que los puentes alquino son la mejor opción para mejorar las propiedades de las díadas como colorantes en DSSCs.

11. Las propiedades fotofísicas de la BODIPY para su uso en DSSCs han sido también mejoradas mediante la unión de una o dos BODIPYs a una 2,2′-bipiridina, tanto formando aductos aislados, como parte de un complejo tricarbonílico de Re(I). En este sentido, la BODIPY es conocida por su gran capacidad de absorción pero en un rango estrecho de longitudes de onda. Tras enlazar una BODIPY a una 2,2′-bipiridina, hemos descubierto que el carácter pancromático mejora, ya que las bandas de absorción sufren un desplazamiento batocrómico y aparecen otras nuevas bandas de absorción. Este efecto se acentúa si se unen dos BODIPYs en vez de una, formando aductos 2:1. Si esos aductos se coordinan al centro metálico de un complejo tricarbonílico de Re(I), las bandas de absorción se desplazan a longitudes de onda todavía más largas, aunque la intensidad de absorción disminuye. No obstante, el diseño de complejos de Re(I) con bandas de absorción en la región del color rojo del espectro electromagnético es destacable. Además, todas las especies consideradas en este estudio cumplen los criterios para la energía de los orbitales frontera (energía del HOMO por debajo del potencial de la pareja redox y energía del LUMO por encima de la banda de conducción del semiconductor).

# 5 Publications and Manuscripts

## 5.1 Insights on the Reactivity of Terminal Phosphanido Metal Complexes toward Activated Alkynes from Theoretical Computations

Daniel Álvarez, Raúl Mera-Adasme, Lucía Riera, Gloria I. Cárdenas Jirón, Julio Pérez, Jesús Díaz, M. Isabel Menéndez, and Ramón López
*Inorg. Chem.* **2017**, *56*, 6652-6661

Inorganic Chemistry

Article

pubs.acs.org/IC

# Insights on the Reactivity of Terminal Phosphanido Metal Complexes toward Activated Alkynes from Theoretical Computations

Daniel Álvarez,[†] Raúl Mera-Adasme,[‡] Lucía Riera,[§] Gloria I. Cárdenas-Jirón,[‡] Julio Pérez,[§,∥] Jesús Díaz,[⊥] M. Isabel Menéndez,[†] and Ramón López*[,†]

[†]Departamento de Química Física y Analítica, Facultad de Química and [∥]Departamento de Química Orgánica e Inorgánica, Facultad de Química, Universidad de Oviedo, C/Julián Clavería 8, 33006 Oviedo, Spain

[‡]Laboratorio de Química Teórica, Facultad de Química y Biología, Universidad de Santiago de Chile, Casilla 40, Correo 33, Santiago, Chile

[§]Centro de Investigación en Nanomateriales y Nanotecnología, CSIC-Universidad de Oviedo-Principado de Asturias, Avenida de la Vega 4-6, 33940 El Entrego, Spain

[⊥]Departamento de Química Orgánica e Inorgánica, Universidad de Extremadura, Avenida de la Universidad s/n, 10071 Cáceres, Spain

Supporting Information

**ABSTRACT:** Herein we present a theoretical study on the reaction of [Re(PPh$_2$) (CO)$_3$(phen)] (phen = 1,10-phenanthroline) and [Re(PPh$_2$) (CO)$_3$(bipy)] (bipy = 2,2′-bipyridine) toward methyl propiolate. In agreement with experimental results for the phen ligand, the coupling of the substituted acetylenic carbon with the nonsubstituted *ortho* carbon of the phen ligand is the preferred route from both kinetic and thermodynamic viewpoints with a Gibbs energy barrier of 18.8 kcal/mol and an exoergicity of 11.1 kcal/mol. There are other two routes, the insertion of the acetylenic fragment into the P−Re bond and the coupling between the substituted acetylenic carbon and a carbonyl ligand in *cis* disposition, which are kinetically less favorable than the preferred route (by 2.8 and 1.9 kcal/mol, respectively). Compared with phen, the bipy ligand shows less electrophilic character and also less $\pi$ electron delocalization due to the absence of the fused ring between the two pyridine rings. As a consequence, the route involving the coupling with a carbonyl ligand starts to be kinetically competitive, whereas the product of the attack to bipy is still the most stable and would be the one mainly obtained after spending enough time to reach thermal equilibrium.

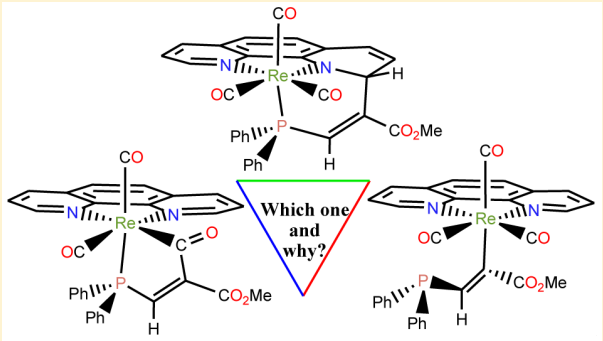


## INTRODUCTION

The chemistry of metal complexes holding terminal phosphanido ligands [M(PR$_2$)L$_n$] (M = metal, L = ancillary ligands) is a matter that attracts considerable attention, partly on account of the participation of such complexes as intermediates in organic synthesis and catalytic processes.[1] Particularly, the reactivity of carbonyl complexes with terminal phosphanido functionalities toward activated alkynes has been investigated and has yielded diverse results (see Scheme 1). Thus, the reaction of [Re(PPh$_2$) (CO)$_3$(phen)] (phen = 1,10-phenanthroline) (**1**) with methyl propiolate (HMAD, HC≡CCO$_2$Me) and dimethyl acetylenedicarboxylate (DMAD, MeO$_2$CC≡CCO$_2$Me) leads to the formation of a C−C coupling product between the acetylenic fragment and the phen ligand (see P1 in Scheme 1).[2,3] This kind of product stands in contrast with other experimental results.[4−10] On the one hand, the reaction of [CpFe(CO)$_2$(PR$_2$)] (Cp = $\eta^5$-C$_5$H$_5$; R = Ph, C$_6$F$_5$) (**2** and **3**, respectively),[4] [CpM(CO)$_3$(PPh$_2$)] (Cp = $\eta^5$-C$_5$H$_5$; M = Mo, W) (**4** and **5**, respectively),[5] and [Ir(ABPN$_2$) (CO)(H) (PPh$_2$)] (ABPN$_2$ = (allyl)B(Pz)$_2$(CH$_2$PPh$_2$); Pz = pyrazolate) (**6**)[6] with HMAD and/or DMAD gives rise to the formation of metallacyclic complexes, which contain a five-membered chelate ring formed by the linkage of the phosphanido group, the alkyne, and the CO ligand (see P2 in Scheme 1). Analogous five-membered metallacyclic products were also reported both when replacing carbonyls by other ancillary ligands like alkyl or aryl isocyanides in certain Nb complexes[7] and when using iron carbonyl complexes containing acetyl and deprotonated phosphanido ligands.[8] On the other hand, the reaction of [Nb($\eta^5$-C$_5$H$_4$SiMe$_3$)$_2$(CO) (PPh$_2$)] (**7**) with HMAD and methyl 2-butynoate (MeC≡CCO$_2$Me) affords another type of product, which results from the insertion of the acetylene into the $\sigma$ Nb−P bond (see P3 in Scheme 1).[9] Furthermore, it is believed that the reaction of a stannylphosphole complex with DMAD evolves through an intermediate resulting from the alkyne insertion into

**Received:** March 24, 2017
**Published:** May 18, 2017




DOI: 10.1021/acs.inorgchem.7b00767
*Inorg. Chem.* 2017, 56, 6652−6661

**Scheme 1. Types of Products Obtained from the Reaction of Terminal Diphenylphosphanido Metal Complexes with Electron-Poor Acetylenes**

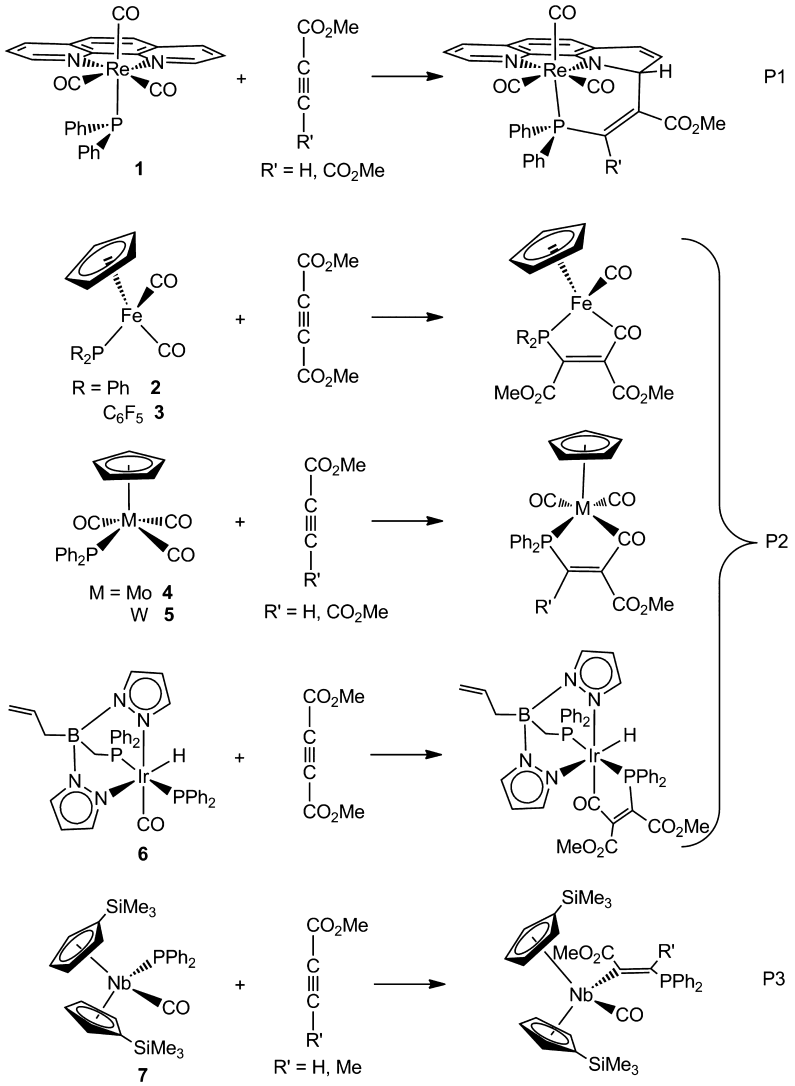


the P−Sn bond.[10] The last two types of products were also found when replacing the phosphanido ligand at Re carbonyl complexes analogous to **1** by OH,[11] OMe,[12] and NH*p*Tol.[13] Specifically, the reaction of the methoxo complex [Re(OMe)$(CO)_3$(bipy)] (bipy = 2,2′-bipyridine) with DMAD leads to the formation of a P3-type complex while those of [Re(OH)$(CO)_3$(bipy)] and [Re(NH*p*Tol)$(CO)_3$(bipy)] with the same acetylene afford P2-type products.

Concerning the mechanism of the reactions of terminal phosphanido metal complexes with electron-poor alkynes, a concerted process, on the one hand, has been invoked to explain the formation of P2-type products when using the **2** and **3** complexes[4] and of P3-type products with the **7** complex.[9] On the other hand, a nonconcerted process has been suggested for the formation of P1-type product from the **1** complex[2,3] and of P2-type products when using the **4**, **5**, and **6** complexes.[6,8] As seen in Scheme 2, the first step would imply the attack of the nucleophilic phosphanido ligand on one of the acetylenic carbon atoms to form a zwitterionic intermediate. In this species, the other carbon of the initially acetylenic moiety would present a negative charge. In the second step, this last atom could attack on either one of the *ortho* carbon atoms ($C_{ortho}$) of a bipy or phen bidentate ligand, *ccb* route, or the carbon atom of a carbonyl ligand ($C_{CO}$) in *cis* disposition, *cco* route, to give C−$C_{ortho}$ and C−$C_{CO}$ coupling products, respectively (P1- and P2-type products, respectively). For the [Re(OH)$(CO)_3$(bipy)] and [Re(NH*p*Tol)$(CO)_3$(bipy)] complexes, we note that the final P2-type products obtained present a hydrogen atom bound to the oxygen atom of the attacked carbonyl ligand due to H migration from the OH and NH*p*Tol ligands once the C−$C_{CO}$ bond is formed.[11,13] As the nucleophilic carbon of the acetylenic moiety in the zwitterion could also attack the metal center and produce an alkyne insertion into the M−$PR_2$ bond (*ins* route), this kind of intermediate has also been invoked to explain the formation of P3-type products when a rhenium carbonyl complex containing a methoxo ligand reacts with electron-deficient alkynes.[12]

Theoretical studies on the reaction mechanism of terminal phosphanido metal complexes toward electron-poor acetylenes are scarce and limited in focus.[6,9] To gain a deeper knowledge about these interesting processes, wider theoretical investigations considering all the plausible reaction mechanisms leading



DOI: 10.1021/acs.inorgchem.7b00767
*Inorg. Chem.* 2017, 56, 6652−6661

**Scheme 2. Stepwise Reaction Mechanisms Suggested for the Reaction of Rhenium Carbonyl Complexes Containing a Nucleophilic Ligand (XR) with Electron-Poor Acetylenes**

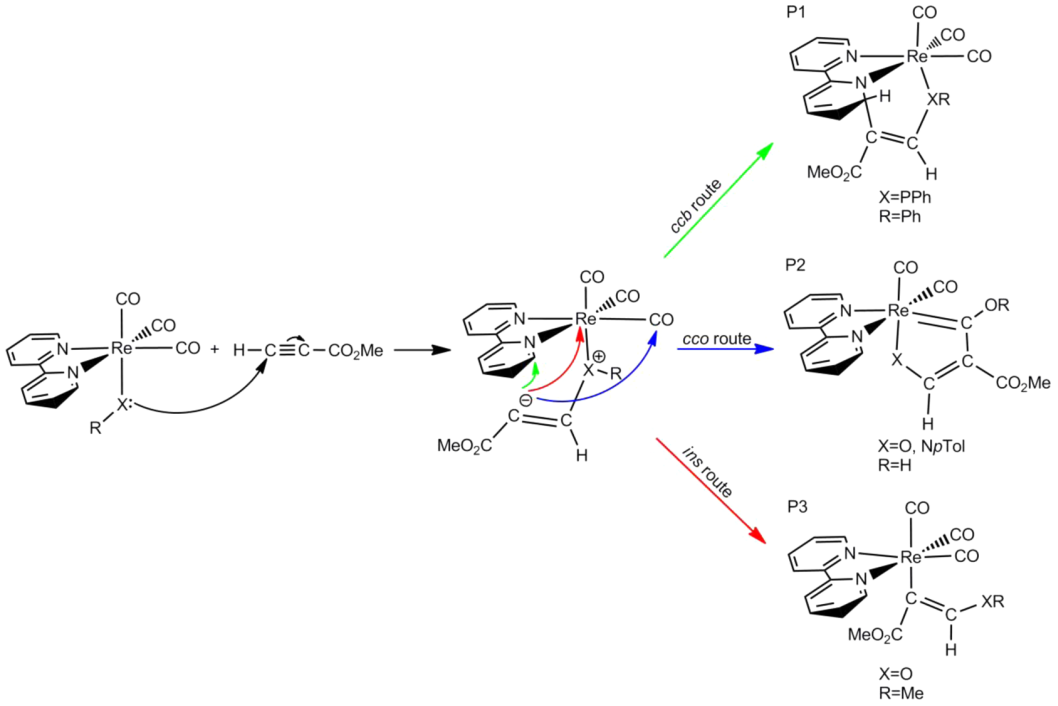


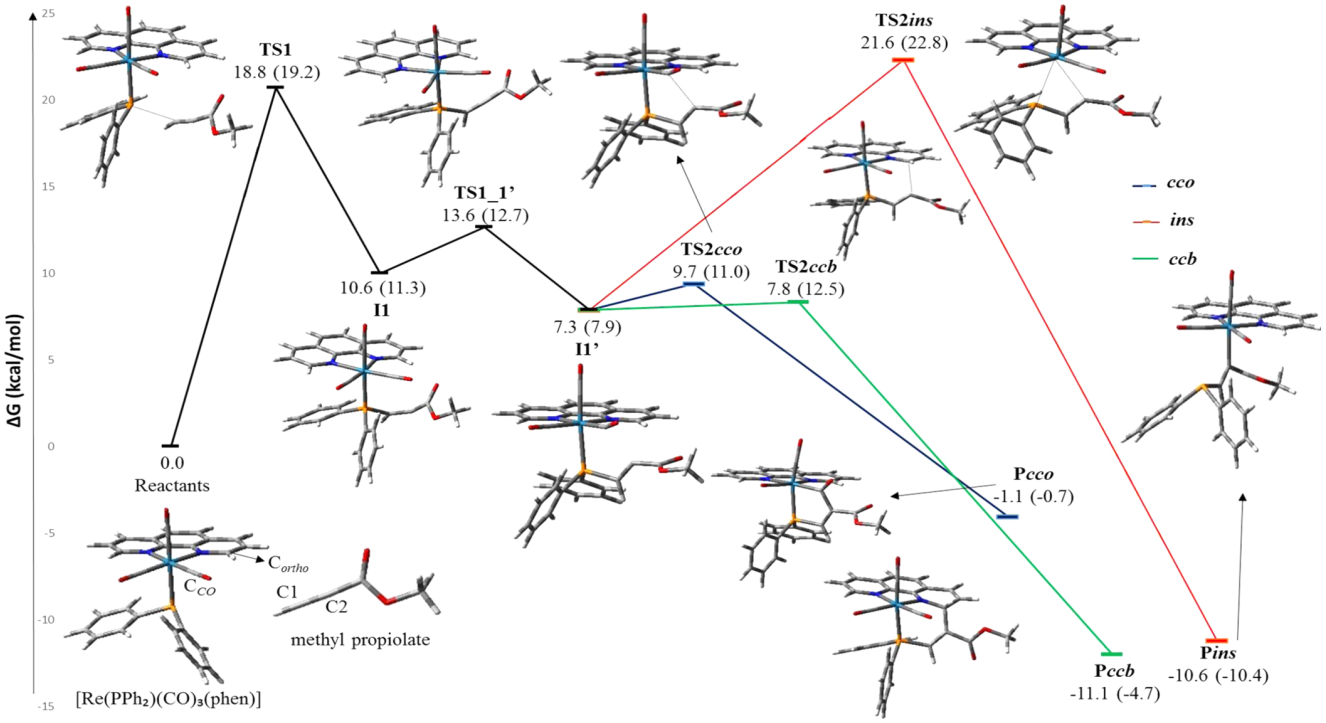


**Figure 1.** PCM-B3LYP/6-311+G(2d,p) (LANL2TZ+*f* for Re)//PCM-B3LYP/6-31+G(d,p) (LANL2DZ for Re) Gibbs energy profile in THF solution of the reaction pathways obtained for the reaction between [Re(PPh$_2$) (CO)$_3$(phen)] and methyl propiolate. Gibbs energy values for the reaction between [Re(PPh$_2$) (CO)$_3$(bipy)] and methyl propiolate are also included in parentheses.

to one or different products are needed. To that end, as a first step and aiming at understanding the different reactivity patterns experimentally found for the reaction of terminal phosphanido metal complexes with electron-poor acetylenes, a computational chemistry study was undertaken on the reaction mechanism of [Re(PPh$_2$) (CO)$_3$(phen)] with HMAD. No experimental information has been reported for the analogous reaction where phen is replaced by bipy. In this work we analyze the differences between these two bidentate ligands that are able to affect their reactivity hoping that the chemical trends found may



DOI: 10.1021/acs.inorgchem.7b00767
*Inorg. Chem.* 2017, 56, 6652−6661

be helpful for designing new synthetic and catalytic processes using these or related complexes.

## RESULTS AND DISCUSSION

The analysis of our results will be done as follows. First, we will report the best computational-chemistry data obtained for the reaction between the [Re($PPh_2$) $(CO)_3$(phen)] complex and the acetylenic system HC≡C−$CO_2$Me (HMAD) in tetrahydrofuran (THF) solution. Second, we will analyze the effect of replacing the phen ligand by bipy in the Re complex on the reaction mechanism. Finally, we will provide a general discussion by comparing the results obtained with the available experimental data and propose the expected products for the reaction with the bipy ligand.

**Elucidating the Reaction Mechanism.** The most plausible nonconcerted mechanisms shown in Scheme 2, identified as the *ccb* route for the coupling of the acetylene moiety with the bidentate ligand, the *cco* route for analogous coupling with a CO ligand in *cis* disposition to the nucleophilic ligand, and the *ins* route for the insertion of the acetylene moiety between the Re−P bond, were investigated. The species involved in these routes will be denoted with an acronym containing the suffixes *ccb*, *cco*, and *ins*, respectively. Figure 1 collects the Gibbs energy profiles obtained in THF solution along with the optimized structures of the species involved (more detailed information is collected in Tables S1−S4 and Figure S1 in the Supporting Information). We also considered the possibility of concerted mechanisms, but all the attempts to locate the corresponding transition state (TS) failed after an extensive search. A similar result was found in theoretical explorations involving Ir and Nb complexes with terminal phosphanido and activated alkynes.[6,9] The hexacoordination of Re is likely to prevent a concerted interaction between the two reactants due to steric repulsions. Hereafter, unless otherwise stated, PCM-B3LYP/6-311+G(2d,p) (LANL2TZ+*f* for Re)//PCM-B3LYP/6-31+G(d,p) (LANL2DZ for Re) Gibbs energies referred to the separate reactants are given in the text. A detailed description of this theory level is given in the Computational Details section (see below), in which we also reason its adequacy based on the validation and rate constant calculations collected in the Supporting Information.

According to our results, the three nonconcerted mechanisms start with the attack of the lone pair on the phosphorus atom of the Re-bonded phosphanido ligand on the nonsubstituted acetylenic carbon atom (C1, see Figure 1 for atom numbering) of HMAD via the TS **TS1** (18.8 kcal/mol) to form the intermediate **I1** (10.6 kcal/mol). In agreement with previous proposals,[2,3,6,8] a natural population analysis[14] on the isolated acetylenic system confirms that C1 (−0.12 e) is slightly preferred for a nucleophilic attack over the acetylenic carbon atom bearing the methoxycarbonyl substituent (C2, −0.18 e). **TS1** is an early TS, where the P···C1 distance is 2.646 Å, so the carbon backbone of the acetylenic moiety practically keeps intact the triple C1−C2 bond (d(C1−C2) = 1.236 Å, quite close to 1.209 Å at HMAD). **I1** evolves to its more stable isomer **I1′** (7.3 kcal/mol) via **TS1_1′** (13.6 kcal/mol). At **I1** and **I1′** the P−C1 bond is clearly formed (d(P−C1) = 1.869 and 1.823 Å, respectively) and, consequently, the C1−C2 bond of the HMAD moiety has practically become a double bond (d(C1−C2) = 1.324 and 1.336 Å, respectively). As a result, the carbon backbone of the HMAD moiety has lost its linearity (C1−C2−C($O_2$Me) bond angles of ∼141° and 126° at **I1** and **I1′**, respectively). As expected, the natural bond order (NBO)[14] charge of C2 increases from −0.18 e at the isolated reactant to −0.29 e at **I1′** passing through a value of −0.25 e at **I1**. Both **I1** and **I1′** can be considered the zwitterions suggested in previous stepwise mechanistic proposals,[2,3,6,8] and the present theoretical characterization allows seeing that they both exist and differ from each other in the orientation of the lone pair at C2. At **I1** the lone pair points opposite the phen plane, whereas at **I1′** it points toward phen plane. Although a weak hydrogen bond interaction between the alkyne carbonyl oxygen and one *ortho* H atom at phen exists at **I1** (d(O···H−C) = 2.074 Å),[15] the evolution to **I1′** is needed to predispose the lone electron pair at C2 toward electrophilic sites of the metal complex. The most plausible and close ones are the *ortho* carbon atom of the phen ligand ($C_{ortho}$), the carbon atom of a CO ligand in *cis* disposition to the nucleophilic ligand ($C_{CO}$), and the metal center. The first option, green line in Figure 1, proceeds through **TS2*ccb*** (7.8 kcal/mol, d(C2···$C_{ortho}$) = 2.451 Å) to give the product **P*ccb*** (−11.1 kcal/mol), which presents a new C−C bond (d(C2−$C_{ortho}$) = 1.543 Å) and consequently a new six-membered metallacycle. Besides, this ring shows a notable strengthening of the bond between Re and the N atom of the attacked pyridine ring as the Re−N distance shortens 0.045 Å from **I1′** to **P*ccb***. The large stability of **P*ccb*** compared to **I1′** (18.4 kcal/mol) suggests that the formation of the C2−$C_{ortho}$ bond and its consequences overcompensate the energy cost associated with the loss of planarity/aromaticity of the affected ring of the bidentate ligand. The second option, blue line in Figure 1, gives rise to the C−C coupling product **P*cco*** (−1.1 kcal/mol) with a C−$C_{CO}$ bond distance of 1.557 Å via **TS2*cco*** (9.7 kcal/mol). An NBO analysis at **I1′** shows that $C_{CO}$ (0.76 e) presents larger positive charge than $C_{ortho}$ (0.10 e) at phen. However, steric and electronic repulsions between the $CO_2$Me group of the alkyne moiety and the phen ligand are stronger at **TS2*cco*** than at **TS2*ccb***. For our chemical system, the balance between charge attraction and steric repulsion makes **TS2*ccb*** preferred. The transformation of **I1′** into **P*cco*** leads to the formation of a five-membered metallacycle, a more strained ring than that formed when going from **I1′** to **P*ccb***, and a significant weakening of the Re−$C_{CO}$ bond implied in such a metallacycle (an elongation of 0.173 Å was found from **I1′** to **P*cco***). The latter, however, is partly compensated by the strengthening of the remaining Re−CO bonds, whose distances vary from 1.920 and 1.943 Å to 1.894 and 1.915 Å when going from **I1′** to **P*cco***, respectively. These facts explain why **P*cco*** is clearly less stable than **P*ccb*** but lower in energy than **I1′**. The third way, red line in Figure 1, proceeds via **TS2*ins*** (21.6 kcal/mol), wherein the metal center is simultaneously interacting with the phosphorus atom and C2 at distances of 3.034 and 2.980 Å, respectively. This species evolves to the product **P*ins*** (−10.6 kcal/mol), in which a new Re−C bond is formed (d(Re−C) = 2.256 Å), while the original Re−P is clearly cleaved. The relative stability of **P*ins*** in electronic energy terms, −25.3 kcal/mol, is comparable to that found, −22.1 kcal/mol, for the analogous product resulting from the insertion of HMAD into the Nb−P bond of the [Nb($\eta^5$-$C_5H_5$)$_2$(CO) ($PH_2$)] complex.[9]

According to our results, **TS1** is the rate-determining step for the C−C coupling routes (*ccb* and *cco*) with a Gibbs energy barrier of 18.8 kcal/mol. This value is 2.8 kcal/mol lower than that determined by **TS2*ins***, the rate-determining TS for the *ins* route. As **TS2*ccb*** is 1.9 kcal/mol more favored than **TS2*cco***, and the C−$C_{ortho}$ coupling product (**P*ccb***) is 10.0 kcal/mol more favored than the C−$C_{CO}$ coupling product (**P*cco***), theoretical predictions agree with the formation of the product experimentally detected, **P*ccb***,[2] according to both kinetic and thermodynamic data.



DOI: 10.1021/acs.inorgchem.7b00767
*Inorg. Chem.* 2017, 56, 6652−6661

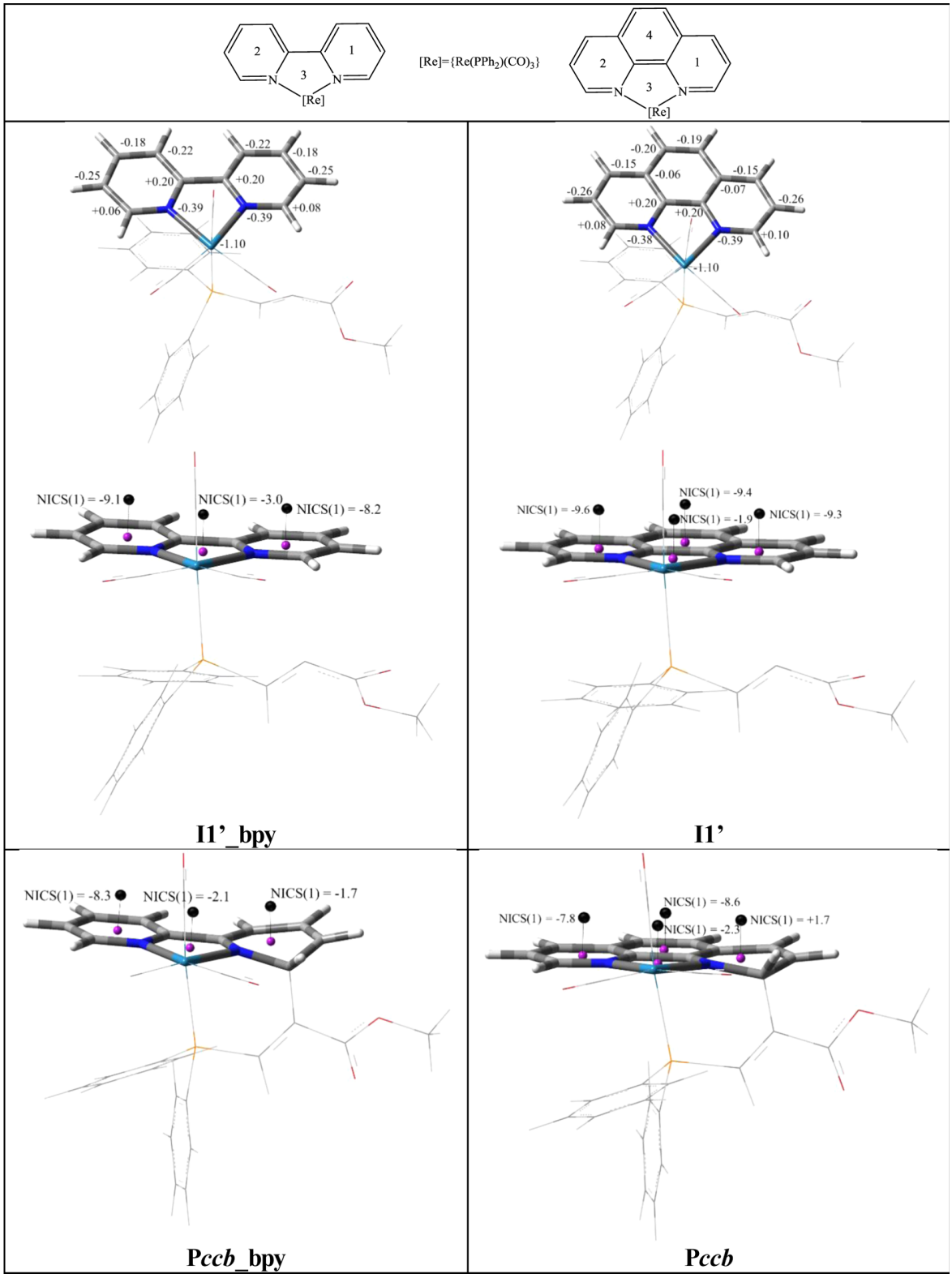


**Figure 2.** Some relevant NBO charges and NICS(1) values (in ppm) related to the bidentate ligands at **I1′_bpy**, **I1′**, **P*ccb*_bpy**, and **P*ccb***.

**Effect of the bipy Ligand.** In spite of some chemical differences, the similarities between phen and bipy as bidentate ligands make that both of them are frequently tested in Re and other metal complexes to be used in analogous reactions.[11,12,16−19] However, as already said, there are no reported results for the reaction between [Re(PPh$_2$) (CO)$_3$(bipy)] and HMAD, and we think it may be interesting to theoretically compare the reaction mechanisms for the reaction of both complexes with HMAD and even to predict the expected products. Tables S5−S8 and Figure S2 in the Supporting



DOI: 10.1021/acs.inorgchem.7b00767
*Inorg. Chem.* 2017, 56, 6652−6661

Information collect the geometry and energy obtained for all the located species for the reaction involving [Re($PPh_2$) ($CO)_3$(bipy)] and HMAD. By analogy, all the structures are denoted with the same acronym as in the phen case followed by the suffix bpy. Figure 1 shows in parentheses the Gibbs energies of the bipy-containing system referred to the corresponding separate reactants.

The presence of the bipy ligand at the Re complex leads to the same reaction pathways found for [Re($PPh_2$) ($CO)_3$(phen)]. Again, the *ins* route is clearly disfavored, with a Gibbs energy barrier of 22.8 kcal/mol controlled by **TS2*ins*_bpy**. For *ccb* and *cco* routes the rate-determining step continues to be the nucleophilic attack of the phosphorus atom on C1, **TS1_bpy** (19.2 kcal/mol). The relative energy of all intermediates, products, and TSs obtained with the bipy ligand are higher than the corresponding ones for the phen case, except for **TS1_1′_bpy**, whose relative Gibbs energy becomes 0.9 kcal/mol lower than that of **TS1_1′**. Particularly, species involved in the *ccb* route, for the coupling of the alkyne moiety with bipy, undergo the largest destabilization (**TS2*ccb*_bpy** and **P*ccb*_bpy** are 4.7 and 6.4 kcal/mol less stable than the analogous phen structures, respectively). As a consequence, the addition of the alkyne moiety to one carbonyl ligand in *cis* disposition to the nucleophilic ligand becomes kinetically preferred over the addition to the bidentate ligand by 1.5 kcal/mol. On the one hand, at **TS2*ccb*_bpy**, a shortening of the C2···$C_{ortho}$ distance by ∼0.18 Å in comparison with that at **TS2*ccb*** indicates a later TS and, consequently, yields a rise of its Gibbs energy barrier. On the other hand, **P*ccb*_bpy** remains more stable (now by 4 kcal/mol) than **P*cco*_bpy**, which means that thermodynamic stabilities favor the formation of the product derived from the coupling with the bidentate ligand.

**Discussion and Comparison with Experiment.** The theoretical investigation on the reaction toward HMAD of the [Re($PPh_2$) ($CO)_3$(phen)] and [Re($PPh_2$) ($CO)_3$(bipy)] complexes indicates that the *ccb* and *cco* routes have in common the same rate-determining TS, namely, **TS1** (phen) and **TS1_bpy** (bipy). These species are 2.8 and 3.6 kcal/mol lower in Gibbs energy than the rate-determining TS of the *ins* route, **TS2*ins*** (phen) and **TS2*ins*_bpy** (bipy), respectively, which means that the insertion product is not formed. We have also seen that kinetic and thermodynamic data confirm the experimental preference for the formation of the **P*ccb*** product in the case of Re complexes with phen ligand,[2,3] whereas both kinds of arguments point to different coupling products in the case of bipy ligand.

The destabilization of 4.7 kcal/mol undergone by **TS2*ccb*_bpy** in comparison with **TS2*ccb*** indicates that the nucleophilic attack of the HMAD C2 atom at **I1′_bpy** is less favored than in the phen case. A natural population analysis of **I1′** and **I1′_bpy** shows that the sum of the NBO charges for the non-hydrogen atoms of the pyridine ring 1, the heterocycle that is going to be attacked, is −0.57 e at **I1′**, while a notably greater value, −0.76 e, was obtained for **I1′_bpy** (see Figure 2 for NBO charges and ring numbering). In addition, the NBO charge of the nonsubstituted *ortho* carbon atom ($C_{ortho}$) of ring 1 is 0.10 and 0.08 e at **I1′** and **I1′_bpy**, respectively. Thus, the area of the bipy ligand faced to the nucleophilic attack is more electronically dense than the corresponding area at phen; therefore, the nucleophile atom, C2, must overcome larger repulsive interactions. However, the change of phen by bipy hardly affects the NBO population at the attacked carbonyl carbon, $C_{CO}$, so the relative Gibbs energy of **TS2*cco***-type TSs undergoes a small variation.

Thermodynamic arguments for the preference of one route over the other rest on the relative stability of the products each one can render. Figure 1 shows that the replacement of phen by bipy yields a coupling product with the bidentate ligand, **P*ccb*_bpy**, less stable than the corresponding one for phen, **P*ccb***, by 6.4 kcal/mol. Bader analysis[20] does not provide significant discrepancies between the electron density at the ring critical points (RCP, purple dots in Figure 2) located at the center of the rings 1−4 for [Re($PPh_2$) ($CO)_3$(bipy)] versus [Re($PPh_2$) ($CO)_3$(phen)], **I1′_bpy** versus **I1′**, and **P*ccb*_bpy** versus **P*ccb*** (see Table S9). Among other criteria, it is known that nucleus-independent chemical shift values calculated 1 Å above the corresponding RCPs (NICS(1)), black dots in Figure 2, provide a good measure of the aromaticity/$\pi$ electron delocalization along a ring.[21,22] Typical NICS(1) values, in parts per million, are ca. −10.2 for benzene, the paradigm of an aromatic ring,[23,24] −10.1 for pyridine,[25,26] and −10.8 (rings 1 and 2) and −8.4 (ring 4) for isolated phen.[23] In this work, NICS(1) values for phen at [Re($PPh_2$) ($CO)_3$(phen)] (−10.1, −10.3, and −8.7 ppm for rings 1, 2, and 4 in Table S10, respectively) are similar to those mentioned above for the isolated ligand. The replacement of phen by bipy at the Re complex causes a small rise of the NICS(1) values of the comparable rings 1 and 2 between 1.9 and 1.2 ppm (see Table S10), which is in good agreement with the well-known greater $\pi$ electron delocalization of phen over bipy due to the extra fused ring. An increase of 0.5 ppm, for instance, was obtained when going from naphthalene to benzene owing to the loss of an aromatic ring.[23] In keeping with the foregoing, NICS(1) values of the rings 1 and 2 for **I1′_bpy** are 1.1 and 0.6 ppm higher than those analogous ones for **I1′**, respectively (see Figure 2). All these rings show aromatic character and strong $\pi$ electron delocalization as NICS(1) ranges from −8.2 to −9.6 ppm. However, the comparison of NICS(1) values for the rings of **P*ccb*_bpy** versus **P*ccb*** ones in Figure 2 indicates that strong $\pi$ electron delocalization still remains in the rings of the rigid phen ligand that are nonaffected by the nucleophilic attack, rings 2 and 4, (NICS(1) of −7.8 and −8.6 ppm for rings 2 and 4, respectively), whereas only ring 2 at the bipy ligand remains aromatic (NICS(1) of −8.3 ppm). We attribute the notably greater stability of **P*ccb*** compared to **P*ccb*_bpy** to the greater $\pi$ electron delocalization of the phen ligand due to the extra fused ring.

Considering all previous arguments and taking into account the relative Gibbs energies collected in Figure 1, the reaction of [Re($PPh_2$) ($CO)_3$(bipy)] with HMAD is expected to yield a mixture of both **P*cco*_bpy** and **P*ccb*_bpy**. At the beginning of the reaction kinetic control would prevail thus rendering **P*cco*_bpy**. However, this is a very slightly stable product (−0.5 kcal/mol) whose reversion to the previous intermediate, **I1′_bpy**, would imply the surmounting of an accessible energy barrier (11.7 kcal/mol). Besides, the energy barrier associated with **TS2*ccb*_bpy** is only 1.5 kcal/mol higher than that of **TS2*cco*_bpy** but **P*ccb*_bpy** is 4 kcal/mol more stable than **P*cco*_bpy**, so, after some time, the thermodynamic control would operate, and the product corresponding to the bidentate coupling would form. When the phen ligand is present, a different scenario was found. **TS2*ccb*** is only 0.5 kcal/mol less stable than the previous intermediate **I1′** (4.4 kcal/mol in the bipy case) and 1.9 kcal/mol more stable than **TS2*cco***. Besides, **P*ccb*** is now much more stable than **P*cco*** (10.0 kcal/mol). Therefore, the reaction of [Re($PPh_2$) ($CO)_3$(phen)] with HMAD only leads to **P*ccb*** in good agreement with the high yield experimentally found for this species.[2]



DOI: 10.1021/acs.inorgchem.7b00767
*Inorg. Chem.* 2017, 56, 6652−6661

It is interesting to remark how a change in the bidentate ligand of the phosphanido carbonyl Re complexes has altered the mechanistic evolution of their reaction with HMAD. Since the difference between the barriers of the rate-determining steps of the three mechanisms studied (displayed at Scheme 2) is small (close to 3 kcal/mol) it is reasonable to think that these three may be involved in the reaction of other phosphanido metal complexes with similar activated alkynes. Arguments here pointed out together with the analysis of the effect of the metal, could be useful to understand why one particular route becomes favorable giving rise to different products in each situation.

## CONCLUSIONS

The reaction mechanism of the reactive process between [Re($PPh_2$) $(CO)_3$(phen)] and methyl propiolate (HMAD) was investigated at the PCM-B3LYP/6-311+G(2d,p) (LANL2TZ+*f* for Re)//PCM-B3LYP/6-31+G(d,p) (LANL2DZ for Re) level. The *ccb* route leading to the coupling between the substituted carbon of HMAD (C2) and the nonsubstituted *ortho* carbon of the phen ligand ($C_{ortho}$) is the preferred one according to kinetic and thermodynamic data, thus confirming the product experimentally reported. However, the other two routes investigated by us, the insertion of the acetylenic fragment into the P−Re bond (*ins*) and the coupling between C2 and a carbonyl carbon ligand in *cis* disposition to the nucleophilic phosphanido ligand (*cco*), are kinetically less favorable than the *ccb* route (by 2.8 and 1.9 kcal/mol, respectively). Analogous reaction mechanisms were found when investigating the title process using the bipy ligand instead of phen. However, bipy presents less electrophile character and also less $\pi$ electron delocalization than phen; therefore, the coupling with bipy is now kinetically disfavored. Although bipy loses $\pi$ electron delocalization in the product of the *ccb* route, the formation of a less strained metallacyclic ring together with the strengthening of one Re−N bond makes it even more stable than the *cco* route product. This thermodynamic preference is expected to determine the formation of the *ccb* route product once the reaction equilibrium is reached. Therefore, the set of results obtained in this work provides a deeper understanding of the reactions between terminal phosphanido Re complexes and electron-deficient acetylenes and related reactions that may have some practical applications in the design of new synthetic and catalytic processes.

## COMPUTATIONAL DETAILS

For the theoretical investigation on the reactivity of [Re($PPh_2$) $(CO)_3$(phen)] and [Re($PPh_2$) $(CO)_3$(bipy)] toward HMAD, the geometry and energy of stable species (reactants, intermediates, and products) and TS were optimized without any constraints in THF solution from the outset with the Polarizable Continuum Model[27] (PCM) and the Universal Force Field[28] (UFF) radii in conjunction with the hybrid density functional B3LYP[29] and the 6-31+G(d,p) basis set for nonmetal atoms[30] together with the valence double-$\zeta$ basis set LANL2DZ plus the effective core potential of Hay and Wadt for the Re atom,[31] and by using a modified Schlegel[32] algorithm. The relatively large ("Ultrafine") integration grid with 99 radial shells and 590 angular points was used in these computations. Electrostatic, cavitation, dispersion, and repulsion terms[33] were considered in the PCM computations, wherein a relative permittivity of 7.58 was assumed to simulate THF as the solvent experimentally used.[2,3] The nature of the stationary points was confirmed by analytical computations of harmonic vibrational frequencies. Normal-mode analysis corresponding to the imaginary frequency in the TS and intrinsic reaction coordinate (IRC) calculations with the Gonzalez and Schlegel method[34] were performed to check the two minimum-energy structures connecting each TS. Thermodynamic magnitudes ($\Delta H$, $\Delta S$, and $\Delta G$) were also calculated within the ideal gas, rigid rotor, and harmonic oscillator approximations at a pressure of 1 atm and a temperature of 298.15 K.[35] The calculation of thermodynamic magnitudes in solution starting with molecular partition functions developed for computing gas-phase thermodynamics properties is a standard procedure that has proven to be a correct and useful approach.[36]

For interpretation purposes a natural bond order (NBO) analysis[14,37] in conjunction with a topological analysis of the electron density based on the Atoms-in-Molecules (AIM) theory of Bader[20,38] were performed. Besides, using the Gauge-including atomic orbital (GIAO) method at the above-mentioned theory level, nucleus-independent chemical shifts (NICS)[23,39] were also calculated at the ring critical point (RCP) located at the center of relevant rings, NICS(0), as well as 1.0 Å above these RCP, NICS(1), as aromaticity indexes. The latter, NICS(1), were recommended as a better measure of the $\pi$ electron delocalization as compared to the former, NICS(0).[21,22] Thus, in the present work, we only discuss NICS(1) values.

Although the PCM-B3LYP/6-31+G(d,p) (LANL2DZ for Re) level selected is in the line of previous investigations involving rhenium complexes,[40] we decide to compare its performance against other computational chemistry protocols to ensure its adequacy to the present research (see the Validating the Computational Protocol section in the Supporting Information). On the one hand, for the Re complex containing the bipy ligand, we reoptimized the species involved in the rate-determining step covering a variety of different density functional methodologies like the generalized gradient approximation, GGA (BP86,[29a,41] PBE[42]), meta-GGA (TPSS[43]), hybrid-GGA (PBE0,[44] B3P86,[29a,45] BHandHLYP[29b,46]), hybrid-meta-GGA (TPSSh[43,47]), and range-separate (CAM-B3LYP,[48] LC-wPBE,[49] wB97x,[50] wB97xD[51]). On the other hand, we performed single-point energy calculations at the PCM-B3LYP/6-311+G(2d,p) (LANL2TZ+*f* for Re) level on the PCM-B3LYP/6-31+G(d,p) (LANL2DZ for Re) optimized geometries with both the phen and bipy ligands. At this large basis set, the nonmetal atoms are described by the triple-$\zeta$ basis set 6-311+G(2d,p),[52] while the valence triple-$\zeta$ basis set LANL2TZ[31,53] augmented with an *f* function[54] of exponent 0.869 plus an effective core potential is used for Re.

On the basis of the density functional theory (DFT) computations (see the Validating the Computational Protocol section in the Supporting Information), we corroborate the adequacy of using the B3LYP method to investigate the present processes, as all the functionals checked give a rate-determining Gibbs energy barrier higher than that found with B3LYP. In addition, using the thermodynamic formulation of the transition state theory (TST),[55] B3LYP predicts reaction rate constants of $\sim 2.51 \times 10^{-3}$ $s^{-1}$ at room temperature ($4.15 \times 10^{-3}$ $s^{-1}$ for the phen case), while a value of $6.11 \times 10^{-5}$ $s^{-1}$ was found with wB97xD, which among the checked functionals is the one that gives the lowest rate-determining Gibbs energy barrier. The rate constants obtained for the reactions of [Re($PPh_2$) $(CO)_3$(bipy)] and [Re($PPh_2$) $(CO)_3$(phen)] toward HMAD imply fast reactive processes, as they would take ∼7 and 4 min, respectively. The use of a more flexible basis set in the B3LYP computations favors a slight decrease of such a barrier for the reaction of [Re($PPh_2$) $(CO)_3$(phen)] and [Re($PPh_2$) $(CO)_3$(bipy)] with HMAD and makes it possible to clarify the factors governing the formation of the product experimentally obtained in the case of the phen ligand. Particularly, that reduction in the rate-determining Gibbs energy barrier confirms the experimental fact that the reaction between [Re($PPh_2$) $(CO)_3$(phen)] and HMAD is instantaneous,[2,3] as it would take place in ∼10 s (rate constant of $\sim 1.03 \times 10^{-3}$ $s^{-1}$) on the basis of the thermodynamic formulation of TST. Therefore, the PCM-B3LYP/6-311+G(2d,p) (LANL2TZ+*f* for Re)//PCM-B3LYP/6-31+G(d,p) (LANL2DZ for Re) results are those considered in this research.

All the quantum chemical calculations were performed with the Gaussian 09 (G09) suite of programs.[56]



DOI: 10.1021/acs.inorgchem.7b00767
*Inorg. Chem.* 2017, 56, 6652−6661

## ■ ASSOCIATED CONTENT

### Supporting Information

The Supporting Information is available free of charge on the ACS Publications website at DOI: 10.1021/acs.inorgchem.7b00767.

Full DFT details and discussion on the validation of the computational protocol used in this work (PDF)

## ■ AUTHOR INFORMATION


### Corresponding Author

*E-mail: rlopez@uniovi.es.

### ORCID

Gloria I. Cárdenas-Jirón: 0000-0003-4305-8088
Julio Pérez: 0000-0002-4788-2296
M. Isabel Menéndez: 0000-0002-5062-4319
Ramón López: 0000-0001-8899-705X


### Notes

The authors declare no competing financial interest.

## ■ ACKNOWLEDGMENTS

The authors thank Ministerio de Economía y Competitividad (Grant No. CTQ2015-70231-P) and Principado de Asturias (Grant No. FC-15-GRUPIN14-103) for financial support. We also acknowledge financial support from CONICYT/CHILE under the Project PAI No. 79150043 (G.I.C.-J. and R.M.-A.) and computing resources from the Fundación Computación y Tecnologías Avanzadas de Extremadura (J.D.).

## ■ REFERENCES


(1) (a) Mastrorilli, P. Bridging and terminal (phosphanido)platinum complexes. *Eur. J. Inorg. Chem.* **2008**, *2008*, 4835−4850. (b) Glueck, D. S. Recent advances in metal-catalyzed C-P bond formation. *Top. Organomet. Chem.* **2010**, *31*, 65−100. (c) Waterman, R. Mechanisms of metal-catalyzed dehydrocoupling reactions. *Chem. Soc. Rev.* **2013**, *42*, 5629−5641. (d) Rosenberg, L. Mechanisms of metal-catalyzed hydrophosphination of alkenes and alkynes. *ACS Catal.* **2013**, *3*, 2845−2855. (d1) Latronico, M.; Todisco, S.; Gallo, V.; Englert, U.; Mastrorilli, P. Synthesis of heterodimetallic complexes by reaction of a terminal phosphido Pt complex with metal-based nucleophiles and electrophiles. *Eur. J. Inorg. Chem.* **2014**, *2014*, 1669−1678. (e) Leitao, E. M.; Jurca, T.; Manners, I. Catalysis in service of main group chemistry offers a versatile approach to p-block molecules and materials. *Nat. Chem.* **2013**, *5*, 817−829. (f) Koshti, V.; Gaikwad, S.; Chikkali, S. H. Contemporary avenues in catalytic P-H bond addition reaction: A case study of hydrophosphination. *Coord. Chem. Rev.* **2014**, *265*, 52−73. (g) Sues, P. E.; Lough, A. J.; Morris, R. H. Reactivity of ruthenium phosphido species generated through the deprotonation of a tripodal phosphine ligand and implications for hydrophosphination. *J. Am. Chem. Soc.* **2014**, *136*, 4746−4760. (h) Geer, A. M.; Serrano, A. L.; de Bruin, B.; Ciriano, M. A.; Tejel, C. Terminal phosphanido rhodium complexes mediating catalytic P-P and P-C bond formation. *Angew. Chem.* **2015**, *127*, 482−485. (i) Belli, R. G.; Burton, K. M. E.; Rufh, S. A.; McDonald, R.; Rosenberg, L. Inner- and outer-sphere roles of ruthenium phosphido complexes in the hydrophosphination of alkenes. *Organometallics* **2015**, *34*, 5637−5646. (j) Latypov, S. K.; Polyancev, F. M.; Ganushevich, Y. S.; Miluykov, V. A.; Sinyashin, O. G. Mechanism of intramolecular transformations of nickel phosphanido hydride complexes. *Dalton Trans.* **2016**, *45*, 2053−2059. (k) Arévalo, R.; Espinal-Viguri, M.; Huertos, M. A.; Pérez, J.; Riera, L. Dearomatization of transition metal-coordinated *N*-heterocyclic ligands and related chemistry. *Adv. Organomet. Chem.* **2016**, *65*, 47−114. (l) Bange, C. A.; Waterman, R. Challenges in catalytic hydrophosphination. *Chem. - Eur. J.* **2016**, *22*, 12598−12605.

(2) Cuesta, L.; Hevia, E.; Morales, D.; Pérez, J.; Riera, V.; Rodríguez, E.; Miguel, D. Activation of a 1,10-phenanthroline ligand on a rhenium tricarbonyl complex. *Chem. Commun.* **2005**, 116−117.

(3) Cuesta, L.; Hevia, E.; Morales, D.; Pérez, J.; Riera, V.; Seitz, M.; Miguel, D. Activation of ancillary ligands in the reactions of DMAD with phosphido and alkylideneamido rhenium complexes. *Organometallics* **2005**, *24*, 1772−1775.

(4) Ashby, M. T.; Enemark, J. H. Cycloaddition of alkenes and alkynes to $CpFe(CO)_2PR_2$ to give [cyclic]$Cp(CO)FePR_2C$:CC:O heterometallacycles. *Organometallics* **1987**, *6*, 1323−1327.

(5) Adams, H.; Bailey, N. A.; Day, A. N.; Morris, M. J.; Harrison, M. M. Reactivity of the metallophosphines [$CpM(CO)_3PPh2$] (Cp = $\eta$-$C_5H_5$), M = Mo, W) towards alkynes. X-ray crystal structure of [$CpMo(CO)_2${$Ph_2PCH$ = C(Ph)CO}]. *J. Organomet. Chem.* **1991**, *407*, 247−258.

(6) Serrano, A. L.; Casado, M. A.; Ciriano, M. A.; de Bruin, B.; López, J. A.; Tejel, C. Nucleophilicity and P-C bond formation reactions of a terminal phosphanido iridium complex. *Inorg. Chem.* **2016**, *55*, 828−839.

(7) Antiñolo, A.; García-Yuste, S.; Lopez-Solera, M. I.; Otero, A.; Pérez-Flores, J. C.; Reguillo-Carmona, R.; Villaseñor, E. Activation of a CNXylyl ancillary ligand in the reaction of electron-deficient alkynes with a phosphido niobocene complex. *Dalton Trans.* **2006**, 1495−1496.

(8) Adams, H.; Bailey, N. A.; Blenkiron, P.; Morris, M. J. Metallacycle formation through the linking of an alkyne with phosphide and acetyl groups at an iron centre: X-Ray Structure of [$CpFe(CO)${$Ph_2PCH$-$(CO_2Me)C(CO_2Me)$=C(Me)O}] (Cp = $\eta^5$-$C_5H_5$). *J. Organomet. Chem.* **1993**, *460*, 73−81.

(9) Antiñolo, A.; García-Yuste, S.; Lopez-Solera, I.; Otero, A.; Pérez-Flores, J. C.; Reguillo-Carmona, R.; Villaseñor, E.; Santos, E.; Zuidema, E.; Bo, C. Reactions of alkynes with phosphido niobocenes: a combined experimental and theoretical study. *Dalton Trans.* **2010**, *39*, 1962−1971.

(10) Huang, C.; Liu, H.; Zhang, J.; Duan, Z.; Mathey, F. Dimethyl acetylenedicarboxylate and phospholes: A variety of reaction pathways. *Eur. J. Inorg. Chem.* **2010**, *2010*, 5498−5502.

(11) Cuesta, L.; Gerbino, D. C.; Hevia, E.; Morales, D.; Navarro-Clemente, M. E.; Pérez, J.; Riera, L.; Riera, V.; Miguel, D.; del Río, I.; García-Granda, S. Reactivity of molybdenum and rhenium hydroxo-carbonyl complexes toward organic electrophiles. *Chem. - Eur. J.* **2004**, *10*, 1765−1777.

(12) Hevia, E.; Pérez, J.; Riera, L.; Riera, V.; et al. Reactive alkoxide complexes of groups 6 and 7 metals. *Organometallics* **2002**, *21*, 1750−1752.

(13) Hevia, E.; Pérez, J.; Riera, V.; Miguel, D. Reactivity of the amido complex [Re(NH*p*Tol) $(CO)_3$(bipy)] toward neutral organic electrophiles. *Organometallics* **2003**, *22*, 257−263.

(14) Weinhold, F.; Landis, C. R. *Valency and Bonding: A Natural Bond Orbital Donor-Acceptor Perspective;* Cambridge University Press: Cambridge, England, 2005.

(15) The weak O···H-C interaction has been confirmed by the existence of donor−acceptor (bond-antibond) interactions between the lone pairs of the O atom and the antibonding $\sigma^*$(C−H) with second-order perturbation energies of 0.99, 0.50, and 0.77 kcal/mol. In consonance with this, a Bader analysis also shows an electron density of 0.0219 e Å$^{-3}$ and positive values for the laplacian of the electron density and the total electron density ($\nabla^2\rho(r)$ = 0.0615 e Å$^{-5}$ and $H(r)$ = 0.0004 e$^2$ Å$^{-4}$, respectively) at the O···H−C hydrogen bond critical point located.

(16) Hevia, E.; Pérez, J.; Riera, L.; Riera, V.; del Río, I.; García-Granda, S.; Miguel, D. Insertion of unsaturated organic electrophiles into molybdenum-alkoxide and rhenium-alkoxide bonds of neutral, stable carbonyl complexes. *Chem. - Eur. J.* **2002**, *8*, 4510−4521.

(17) Butschke, B.; Schlangen, M.; Schwarz, H.; Schröder, D. C−H bond activation of methane with gaseous [$(CH_3)$Pt(L)]$^+$ complexes (L = pyridine, bipyridine, and phenanthroline). *Z. Naturforsch., B: J. Chem. Sci.* **2007**, *62*, 309−313.

(18) Kiran, R. V.; Zammit, E. M.; Hogan, C. F.; James, B. D.; Barnett, N. W.; Francis, P. S. Chemiluminescence from reactions with *bis*-




DOI: 10.1021/acs.inorgchem.7b00767
*Inorg. Chem.* 2017, 56, 6652−6661

cyclometalated iridium complexes in acidic aqueous solution. *Analyst* **2009**, *134*, 1297−1298.
(19) Boltz, M.; Blanc, A.; Laugel, G.; Pale, P.; Louis, B. Heterogenization of [Cu(2,2′-bpy)$Cl_2$] and [Cu(1,10-phen)$Cl_2$] on polyoxometalates: New catalysts for the selective oxidation of tetralin. *Chin. J. Catal.* **2011**, *32*, 807−811.
(20) Bader, R. F. W. *Atoms in Molecules. A Quantum Theory;* University Press: Oxford, England, 1990.
(21) Schleyer, P. v. R.; Jiao, H.; Hommes, N. J. R. v. E.; Malkin, V. G.; Malkina, O. An evaluation of the aromaticity of inorganic rings: Refined evidence from magnetic properties. *J. Am. Chem. Soc.* **1997**, *119*, 12669−12670.
(22) von Rague Schleyer, P.; Manoharan, M.; Wang, Z. X.; Kiran, B.; Jiao, H.; Puchta, R.; van Eikema Hommes, N. J. R. Dissected nucleus-independent chemical shift analysis of $\pi$-aromaticity and antiaromaticity. *Org. Lett.* **2001**, *3*, 2465−2468.
(23) Chen, Z.; Wannere, C. S.; Corminboeuf, C.; Puchta, R.; Schleyer, P. v. R. Nucleus-independent chemical shifts (NICS) as an aromaticity criterion. *Chem. Rev.* **2005**, *105*, 3842−3888.
(24) Andjelkovic, L.; Peric, M.; Zlatar, M.; Grubišic, S.; Gruden-Pavlovic, M. Magnetic criteria of aromaticity in a benzene cation and anion: how does the Jahn−Teller effect influence the aromaticity? *Tetrahedron Lett.* **2012**, *53*, 794−799.
(25) Shobe, D. S. Calculations on the Group 15 intraring substituted benzenes (pyridine to bismin series) and their datively bonded oxides and sulfides. *J. Phys. Chem. A* **2005**, *109*, 9118−9122.
(26) Pausescu, I.; Medeleanu, M.; Stefanescu, M.; Peter, F.; Pop, R. A DFT study on the stability and aromaticity of heterobenzenes containing Group 15 elements. *Heteroat. Chem.* **2015**, *26*, 206−214.
(27) (a) Mennucci, B.; Tomasi, J. Continuum solvation models: A new approach to the problem of solute's charge distribution and cavity boundaries. *J. Chem. Phys.* **1997**, *106*, 5151−5158. (b) Barone, V.; Cossi, M.; Tomasi, J. A new definition of cavities for the computation of solvation free energies by the polarizable continuum model. *J. Chem. Phys.* **1997**, *107*, 3210−3221. (c) Cancès, M. T.; Mennucci, B.; Tomasi, J. A new integral equation formalism for the polarizable continuum model: Theoretical background and applications to isotropic and anisotropic dielectrics. *J. Chem. Phys.* **1997**, *107*, 3032−3041. (d) Barone, V.; Cossi, M.; Tomasi, J. Geometry optimization of molecular structures in solution by the polarizable continuum model. *J. Comput. Chem.* **1998**, *19*, 404−417. (e) Tomasi, J.; Mennucci, B.; Cancès, M. T. The IEF version of the PCM solvation method: an overview of a new method addressed to study molecular solutes at the QM ab initio level. *J. Mol. Struct.: THEOCHEM* **1999**, *464*, 211−226. (f) Scalmani, G.; Frisch, M. J. Continuous surface charge polarizable continuum models of solvation. I. General formalism. *J. Chem. Phys.* **2010**, *132*, 114110.
(28) Rappé, A. K.; Casewit, C. J.; Colwell, K. S.; Goddard, W. A., III; Skiff, W. M. UFF, a full periodic table force field for molecular mechanics and molecular dynamics simulations. *J. Am. Chem. Soc.* **1992**, *114*, 10024−10039.
(29) (a) Becke, A. D. Density-functional exchange-energy approximation with correct asymptotic behavior. *Phys. Rev. A: At., Mol., Opt. Phys.* **1988**, *38*, 3098−3100. (b) Lee, C.; Yang, W.; Parr, R. G. Development of the Colle-Salvetti correlation-energy formula into a functional of the electron density. *Phys. Rev. B: Condens. Matter Mater. Phys.* **1988**, *37*, 785−789. (c) Becke, A. D. Density-functional thermochemistry. III. The role of exact exchange. *J. Chem. Phys.* **1993**, *98*, 5648−5652.
(30) Hehre, W. J.; Radom, L.; Pople, J. A.; Schleyer, P. v. R. *Ab Initio Molecular Orbital Theory;* Wiley: New York, 1986.
(31) Hay, P. J.; Wadt, W. R. Ab initio effective core potentials for molecular calculations. Potentials for the transition metal atoms Sc to Hg. *J. Chem. Phys.* **1985**, *82*, 270−283.
(32) (a) Schlegel, H. B. Optimization of equilibrium geometries and transition structures. *J. Comput. Chem.* **1982**, *3*, 214−218. (b) Schlegel, H. B. Estimating the hessian for gradient-type geometry optimizations. *Theor. Chem. Acc.* **1984**, *66*, 333−340. (c) Li, X.; Frisch, M. J. Energy-represented direct inversion in the iterative subspace within a hybrid geometry optimization method. *J. Chem. Theory Comput.* **2006**, *2*, 835−839.
(33) Tomasi, J.; Persico, M. Molecular interactions in solution: An overview of methods based on continuous distributions of the solvent. *Chem. Rev.* **1994**, *94*, 2027−2094.
(34) (a) Gonzalez, C.; Schlegel, H. B. An improved algorithm for reaction path following. *J. Chem. Phys.* **1989**, *90*, 2154−2161. (b) Gonzalez, C.; Schlegel, H. B. Reaction path following in mass-weighted internal coordinates. *J. Phys. Chem.* **1990**, *94*, 5523−5527.
(35) McQuarrie, D. A. *Statistical Mechanics;* Harper and Row: New York, 1976.
(36) Ribeiro, R. F.; Marenich, A. V.; Cramer, C. J.; Truhlar, D. G. Use of solution-phase vibrational frequencies in continuum models for the free energy of solvation. *J. Phys. Chem. B* **2011**, *115*, 14556−14562.
(37) Glendening, E. D.; Reed, A. E.; Carpenter, J. E.; Weinhold, F. *NBO,* Version 3.1; University of Wisconsin: Madison, WI, 2012
(38) (a) Biegler-Konig, F. W.; Bader, R. F. W.; Tang, T.-H. Calculation of the average properties of atoms in molecules. II. *J. Comput. Chem.* **1982**, *3*, 317−328. (b) Bader, R. F. W.; Popelier, P. L. A.; Keith, T. A. Theoretical definition of a functional group and the molecular orbital paradigm. *Angew. Chem., Int. Ed. Engl.* **1994**, *33*, 620−631.
(39) Schleyer, P. v. R.; Maerker, C.; Dransfeld, A.; Jiao, H. J.; Hommes, N. J. R. V. Nucleus-independent chemical shifts: A simple and efficient aromaticity probe. *J. Am. Chem. Soc.* **1996**, *118*, 6317−6318.
(40) (a) Yeguas, V.; Campomanes, P.; López, R. A theoretical study on the reactivity of a rhenium hydroxo-carbonyl complex towards $\beta$-lactams. *Eur. J. Inorg. Chem.* **2008**, *2008*, 4547−4554. (b) Yeguas, V.; Campomanes, P.; López, R. Reactivity of a rhenium hydroxo-carbonyl complex toward carbon disulfide: insights from theory. *Dalton Trans.* **2010**, *39*, 874−882. (c) Fombona, S.; Espinal-Viguri, M.; Huertos, M. A.; Díaz, J.; López, R.; Menéndez, M. I.; Pérez, J.; Riera, L. Activation of aromatic C-C bonds of 2,2′-bipyridine ligands. *Chem. - Eur. J.* **2016**, *22*, 17160−17164.
(41) Perdew, J. P. Density-functional approximation for the correlation energy of the inhomogeneous electron gas. *Phys. Rev. B: Condens. Matter Mater. Phys.* **1986**, *33*, 8822−8824.
(42) (a) Perdew, J. P.; Burke, K.; Ernzerhof, M. Generalized gradient approximation made simple. *Phys. Rev. Lett.* **1996**, *77*, 3865−3868. (b) Perdew, J. P.; Burke, K.; Ernzerhof, M. Errata: Generalized gradient approximation made simple. *Phys. Rev. Lett.* **1997**, *78*, 1396−1399.
(43) Tao, J.; Perdew, J. P.; Staroverov, V. N.; Scuseria, G. E. Climbing the density functional ladder: Nonempirical meta-generalized gradient approximation designed for molecules and solids. *Phys. Rev. Lett.* **2003**, *91*, 146401−146405.
(44) (a) Adamo, C.; Barone, V. Toward reliable density functional methods without adjustable parameters: The PBE0 model. *J. Chem. Phys.* **1999**, *110*, 6158−6169. (b) Ernzerhof, M.; Scuseria, G. E. Assessment of the Perdew-Burke-Ernzerhof exchange-correlation functional. *J. Chem. Phys.* **1999**, *110*, 5029−5036.
(45) Becke, A. D. Density-functional thermochemistry. IV. A new dynamical correlation functional and implications for exact-exchange mixing. *J. Chem. Phys.* **1996**, *104*, 1040−1046.
(46) Becke, A. D. A new mixing of Hartree-Fock and local density-functional theories. *J. Chem. Phys.* **1993**, *98*, 1372−1377.
(47) Staroverov, V. N.; Scuseria, G. E.; Tao, J.; Perdew, J. P. Comparative assessment of a new nonempirical density functional: Molecules and hydrogen-bonded complexes. *J. Chem. Phys.* **2003**, *119*, 12129−12137.
(48) Yanai, T.; Tew, D.; Handy, N. A new hybrid exchange-correlation functional using the Coulomb-attenuating method (CAM-B3LYP). *Chem. Phys. Lett.* **2004**, *393*, 51−57.
(49) (a) Vydrov, O. A.; Scuseria, G. E. Assessment of a long range corrected hybrid functional. *J. Chem. Phys.* **2006**, *125*, 234109. (b) Vydrov, O. A.; Heyd, J.; Krukau, A.; Scuseria, G. E. Importance of short-range versus long-range Hartree-Fock exchange for the performance of hybrid density functional. *J. Chem. Phys.* **2006**, *125*, 074106. (c) Vydrov, O. A.; Scuseria, G. E.; Perdew, J. P. Tests of functionals for systems with fractional electron number. *J. Chem. Phys.* **2007**, *126*, 154109.


DOI: 10.1021/acs.inorgchem.7b00767
*Inorg. Chem.* 2017, 56, 6652−6661

(50) Chai, J. D.; Head-Gordon, M. Systematic optimization of long-range corrected hybrid density functional. *J. Chem. Phys.* **2008**, *128*, 084106.
(51) Chai, J. D.; Head-Gordon, M. Long-range corrected hybrid density functionals with damped atom-atom dispersion corrections. *Phys. Chem. Chem. Phys.* **2008**, *10*, 6615−6620.
(52) (a) Krishnan, R.; Binkley, J. S.; Seeger, R.; Pople, J. A. Self-consistent molecular orbital methods. XX. A basis set for correlated wave functions. *J. Chem. Phys.* **1980**, *72*, 650−654. (b) McLean, A. D.; Chandler, G. S. Contracted Gaussian basis sets for molecular calculations. I. Second row atoms, Z = 11−18. *J. Chem. Phys.* **1980**, *72*, 5639−5648. (c) Clark, T.; Chandrasekhar, J.; Spitznagel, G. W.; Schleyer, P. v. R. Efficient diffuse function-augmented basis sets for anion calculations. III. The 3-21+ G basis set for first-row elements, Li−F. *J. Comput. Chem.* **1983**, *4*, 294−301. (d) Frisch, M. J.; Pople, J. A.; Binkley, J. S. Self-consistent molecular orbital methods 25. Supplementary functions for Gaussian basis sets. *J. Chem. Phys.* **1984**, *80*, 3265−3269.
(53) (a) Wadt, W. R.; Hay, P. J. Ab initio effective core potentials for molecular calculations. Potentials for main group elements Na to Bi. *J. Chem. Phys.* **1985**, *82*, 284−298. (b) Hay, P. J.; Wadt, W. R. Ab initio effective core potentials for molecular calculations. Potentials for K to Au including the outermost core orbitals. *J. Chem. Phys.* **1985**, *82*, 299−305. (c) Roy, L. E.; Hay, P. J.; Martin, R. L. Revised basis sets for the LANL effective core potentials. *J. Chem. Theory Comput.* **2008**, *4*, 1029−1031.
(54) Ehlers, A. W.; Böhme, M.; Dapprich, S.; Gobbi, A.; Höllwarth, A.; Jonas, V.; Köhler, K. F.; Stegmann, R.; Veldkamp, A.; Frenking, G. A set of *f*-polarization functions for pseudo-potential basis sets of the transition metals Sc-Cu, Y-Ag and La-Au. *Chem. Phys. Lett.* **1993**, *208*, 111−114.
(55) (a) Steinfeld, J. I.; Francisco, J. S.; Hase, W. L.*Chemical Kinetics and Dynamics,* 2nd ed.; Prentice Hall: Upper Saddle River, New Jersey, 1999. (b) The inverse of the rate constant determined in accordance with the thermodynamic formulation of TST gives an estimate of how long a given reaction takes.
(56) Frisch, M. J.; Trucks, G. W.; Schlegel, H. B.; Scuseria, G. E.; Robb, M. A.; Cheeseman, J. R.; Scalmani, G.; Barone, V.; Mennucci, B.; Petersson, G. A.; Nakatsuji, H.; Caricato, M.; Li, X.; Hratchian, H. P.; Izmaylov, A. F.; Bloino, J.; Zheng, G.; Sonnenberg, J. L.; Hada, M.; Ehara, M.; Toyota, K.; Fukuda, R.; Hasegawa, J.; Ishida, M.; Nakajima, T.; Honda, Y.; Kitao, O.; Nakai, H.; Vreven, T.; Montgomery, J. A., Jr.; Peralta, J. E.; Ogliaro, F.; Bearpark, M.; Heyd, J. J.; Brothers, E.; Kudin, K. N.; Staroverov, V. N.; Kobayashi, R.; Normand, J.; Raghavachari, K.; Rendell, A.; Burant, J. C.; Iyengar, S. S.; Tomasi, J.; Cossi, M.; Rega, N.; Millam, J. M.; Klene, M.; Knox, J. E.; Cross, J. B.; Bakken, V.; Adamo, C.; Jaramillo, J.; Gomperts, R.; Stratmann, R. E.; Yazyev, O.; Austin, A. J.; Cammi, R.; Pomelli, C.; Ochterski, J. W.; Martin, R. L.; Morokuma, K.; Zakrzewski, V. G.; Voth, G. A.; Salvador, P.; Dannenberg, J. J.; Dapprich, S.; Daniels, A. D.; Farkas, O.; Foresman, J. B.; Ortiz, J. V.; Cioslowski, J.; Fox, D. J. *Gaussian 09,* Revision A.1; Gaussian, Inc.: Wallingford, CT, 2009.



DOI: 10.1021/acs.inorgchem.7b00767
*Inorg. Chem.* 2017, 56, 6652−6661

## 5.2 Addition of Re-Bonded Nucleophilic Ligands to Activated Alkynes: A Theoretical Rationalization

Daniel Álvarez, Jesús Díaz, M. Isabel Menéndez, and Ramón López
*Eur. J. Inorg. Chem.* **2020**, 269-280

ChemPubSoc Europe

DOI: 10.1002/ejic.201901196

EurJIC European Journal of Inorganic Chemistry

Full Paper

Coordination Chemistry

# Addition of Re-Bonded Nucleophilic Ligands to Activated Alkynes: A Theoretical Rationalization

Daniel Álvarez,[a] Jesús Díaz,[b] M. Isabel Menéndez,[a] and Ramón López*[a]

**Abstract:** Reactions between $[Re(X)(CO)_3(bipy)]$ (X = OH, OMe, NH*p*Tol, $PPh_2$; bipy = 2,2′-bipyridine) complexes and methyl propiolate (HMAD) are studied to rationalize the different products experimentally obtained. Three reaction patterns were found with a common and limiting initial attack of X to HMAD. Thus, the experimental selectivity depends on the kinetics and/or thermodynamics of the last reaction stages. For X = OH and NH*p*Tol an easy intramolecular attack of the X-linked HMAD to a highly electrophilic CO ligand is followed by a hydrogen transposition to this CO, yielding very stable species (*C*-$C_{COH}$ products). When X = OMe, the insertion of the X-attached HMAD into the Re–OMe bond (*ins* product) takes place due to the smallest barrier and the largest stability of the *ins* route. Finally, when X = $PPh_2$ the *ins* route becomes restricted and the route for the coupling of the X-attached HMAD with bipy (*C*-$C_{bipy}$ product) wins over the one for the coupling with CO (*C*-$C_{CO}$ product) only due to the larger stability of the *C*-$C_{bipy}$ product.

## Introduction

Rhenium(I) tricarbonyl complexes of the general formula *fac*-$[Re(CO)_3(N–N)L]^n$, where N–N is a 2,2′-bipyridine or 1,10-phenanthroline-based diimine ligand and L is neutral ($n$ = +1) or anionic ($n$ = 0) monodentate ligand, are involved in numerous, diverse, and important applications. Among others, that kind of Re compounds has been investigated as photocatalysts and/or electrocatalysts for reducing $CO_2$ and $H^+$ (**1–16** in Scheme 1),[1–18] molecular sensors or photoswitches (**16–20** in Scheme 1),[19–26] emitting centers in organic light-emitting diodes (**1**, **11**, **12**, **17**, **18**, and **21–23** in Scheme 1),[27] anticancer agents (**15** and **24–34** in Scheme 1),[28–34] cellular and biomolecular imaging agents (**1**, **2**, and **35–39** in Scheme 1),[35–46] or reagents for synthesizing new organometallic compounds (**3**, **4**, and **40–44** in Scheme 1).[47–54] These applications can be adjusted by choosing the diimine ligand N–N or the monodentate ligand L with the appropriate substituents. Besides this, the changes in the non-carbonyl ligands of the $Re^I$ complexes can also drastically modify their reactivity towards other molecular systems. Particularly, several experimental findings have shown that the reaction between the complexes $[Re(X)(CO)_3(N–N)]$ {X = OH (hydroxo), OMe (methoxo), NH*p*Tol (*para*-tolylamido), $PPh_2$ (diphenylphosphanido); N–N = 2,2′-bipyridine (bipy); 1,10-phenanthroline (phen)} and activated alkynes like methyl propiolate (HMAD) or dimethylacetylenedicarboxylate (DMAD) gives rise to the formation of different reaction products.[47,49–52] The

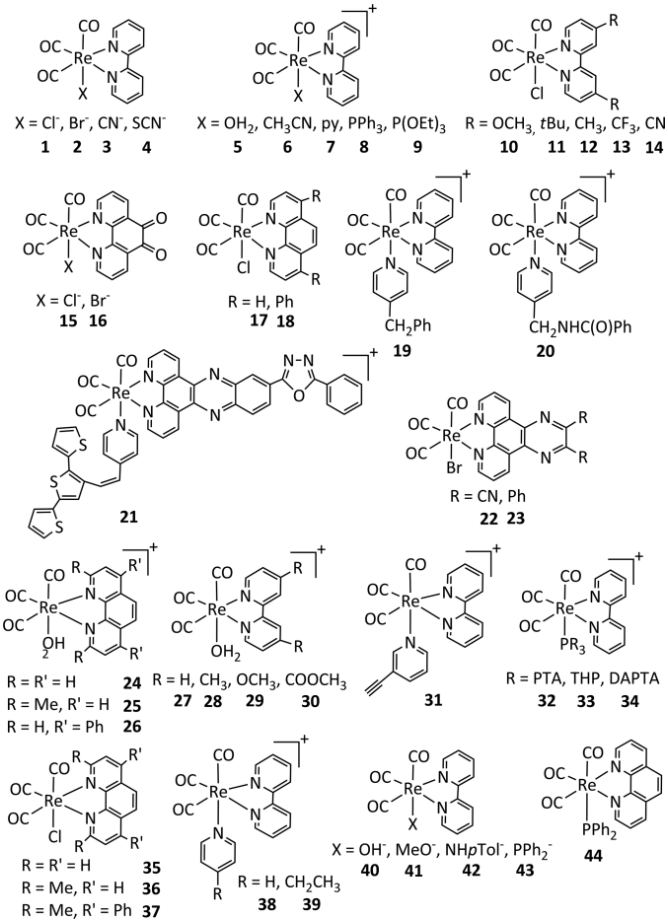


Scheme 1. Basic structures of rhenium(I) tricarbonyldiimine complexes containing neutral or anionic monodentate ligands involved in diverse applications.

[a] *Departamento de Química Física y Analítica, Universidad de Oviedo, C/ Julián Clavería 8, 33006 Oviedo, Asturias, Spain*
*E-mail: rlopez@uniovi.es*
[b] *Departamento de Química Orgánica e Inorgánica, Universidad de Extremadura, Avenida de la Universidad s/n, 110071 Cáceres, Extremadura, Spain*
*Supporting information and ORCID(s) from the author(s) for this article are available on the WWW under https://doi.org/10.1002/ejic.201901196.*

product formed depends on the nucleophilic ligand (X) used, rather than the bidentate ligand of the metal complex (see below). Molybdenum(II) complexes of type [Mo($\eta^3$-allyl)(X)(CO)$_2$-(N–N)] (X = OH, OMe, NH*p*Tol; N–N = bipy, phen) have also shown the same reactivity patterns against activated alkynes as their Re$^I$ analogues.[47–52]

According to experimental findings, it has been suggested that all reactions between [Re(X)(CO)$_3$(N–N)] and activated alkynes start with an initial attack of the nucleophilic ligand X to one of the acetylenic carbon atoms to form a zwitterionic intermediate (I in Scheme 2).[51,52] In this scheme X was replaced by YR to better follow the formation of the different types of reaction products. In the amido and hydroxo complexes the just added alkyne binds to a CO ligand in *cis* disposition (*see* P*cco* species in Scheme 2) and transposition of a proton from the nucleophilic ligand to the attacked CO takes place (*C*-$C_{CO}$ route and P*ccoh* product in Scheme 2).[49,50] Alternatively, in the alkoxo complex the alkyne inserts into the Re–OMe bond (*ins* route and P*ins* product in Scheme 2).[47] Finally, the phosphanido complex leads to the formation of a different kind of product coming from the addition of the alkyne to the bidentate ligand (*C*-$C_{bipy}$ route and P*ccb* product in Scheme 2).[51,52] This last reaction is remarkable because of the inertness of coordinated bipy and phen. Furthermore, this result stands in contrast with the P*cco*-type products reported for the reaction towards activated alkynes of Fe, Mo, W, and Ir complexes containing the same $PPh_2$ phosphanido ligand[55–57] and with P*ins*-type product detected in case of a Nb complex.[58] It is also believed that the reaction of a stannylphosphole complex with DMAD evolves through an intermediate resulting from the alkyne insertion into the P–Sn bond.[59]

Within this framework, we wondered about the aspects of the nucleophile ligand that are key to obtaining a given product in the reaction of Re$^I$ complexes and activated alkynes. This is particularly important to get a better understanding of such chemistry, but above all to gather information that could guide a strategy to tune those complexes in order to get new or improved technological, biomedical or chemical synthesis applications. For instance, a systematic modification of the axial ligands to a substituted bipy ligand has allowed for red-shifted absorbance features in Re$^I$ carbonyl complexes.[60] Computations have been crucial to show that the aforementioned result is a consequence of destabilization of the Re *d*-orbitals. Therefore, we undertook a comparative theoretical study on the reactivity of [Re(X)(CO)$_3$(bipy)] (X = OH, OMe, NH*p*Tol, $PPh_2$) complexes and HMAD. The choice of the simplest bidentate ligand bipy and activated alkyne HMAD in this investigation does not imply a loss of generality of the results obtained, although there is indeed a significant improvement in the computational cost-efficiency ratio. The reactive process involving the $PPh_2$ ligand had been previously investigated from a theoretical point of view.[61] The reaction mechanism found is closely related to that shown in Scheme 2 (see below) and confirms the product experimentally found. However, the results of this single study are not enough to rationalize the formation of different products when $PPh_2$ is replaced by OH, OMe or NH*p*Tol. The type of atom directly linked to Re (O, N or P) and/or its substituents (H, Me, H*p*Tol or $Ph_2$) seem to be responsible for the selectivity of the

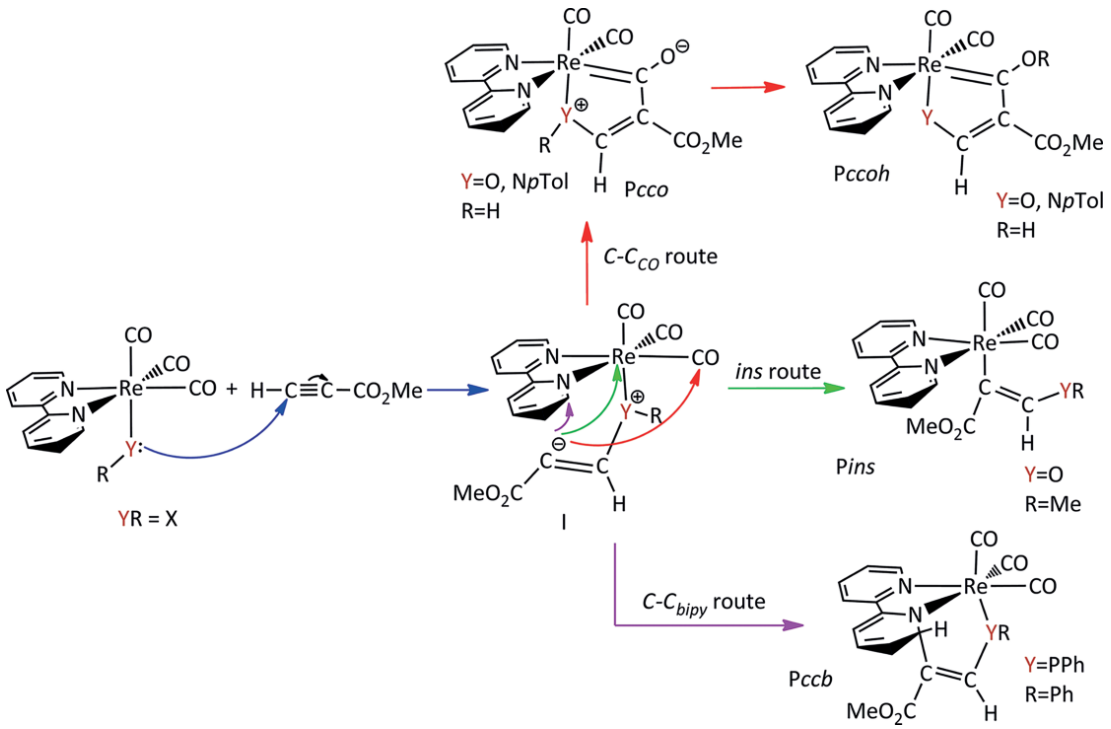


Scheme 2. Reaction mechanisms suggested for the reaction of rhenium(I) tricarbonyl complexes containing a nucleophilic ligand (X) with methyl propiolate (HMAD). For clarity, the YR label for X was used here.

reaction and, consequently, the present research is needed to clarify their particular effects.

## Computational Chemistry Details

Full geometry optimizations of the species involved in the reactive processes between [Re(X)(CO)$_3$(bipy)] (X = OH, OMe, NH*p*Tol) and HMAD were carried out in tetrahydrofuran (THF, $\varepsilon$ = 7.58) solution at the PCM-B3LYP/6-31G+(d,p) (LANL2DZ for Re) level. The nature of the critical structures located on the different potential energy surfaces (PES) investigated was verified by means of harmonic vibrational frequency computations. Normal-mode analysis of the imaginary frequency in the transition states (TS) and intrinsic reaction coordinate (IRC) calculations with the second order Gonzalez-Schlegel integration method[62] were carried out in order to connect each TS to the two associated minima of the proposed mechanism. To get more accurate energies (particularly energy barriers), single-point energy calculations on the PCM-B3LYP/6-31G+(d,p) (LANL2DZ for Re) geometries were performed using the domain localized pair natural orbital-coupled cluster approach with single, double, and perturbative triple excitations [DLPNO-CCSD(T)].[63] The balanced Karlsruhe triple-zeta basis set def2-TZVPP[64] and the conductor-like polarizable continuum model (CPCM)[65] were used in the DLPNO-CCSD(T) computations. All organometallic systems investigated showed T1 diagnostic values less than 0.02,[66] suggesting that a multi-reference treatment is not necessary. In general, DLPNO-CCSD(T) energies are more accurate than B3LYP ones using at least a triple-zeta quality basis set.[67] For comparison purposes, the single-point energy of the species containing the $PPh_2$ ligand, previously investigated at the PCM-B3LYP/6-311+G(2d,p) (LANL2TZ+*f* for Re)//PCM-B3LYP/6-31+G(d,p) (LANL2DZ for Re) level,[61] was also recomputed at the CPCM-DLPNO-CCSD(T)/def2-TZVPP//PCM-B3LYP/6-31+G(d,p) (LANL2DZ for Re) one (Tables S1–S4 in the Supporting Information). For brevity, henceforth in this work, the levels of theory PCM-B3LYP/6-31+G(d,p) (LANL2DZ for Re) and CPCM-DLPNO-CCSD(T)/def2-TZVPP//PCM-B3LYP/6-31+G(d,p) (LANL2DZ for Re) will be denoted as B3LYP and DLPNO-CCSD(T), respectively.

Thermal free energy corrections in THF solution ($G_{therm}$) were calculated at the B3LYP level starting with molecular partition functions developed for computing gas-phase thermodynamics properties within the ideal gas, rigid rotor, and harmonic oscillator approximations at a pressure of 1 atm and a temperature of 298.15 K.[68] This is a standard procedure that has proven to be a correct and useful approach.[69] For each species, Gibbs free energy in solution was determined by adding $G_{therm}$ to the highly accurate DLPNO-CCSD(T) energy. Unless stated otherwise, for each reactive process investigated, energies discussed in the following sections are all Gibbs free energies in THF solution referred to the corresponding separate reactants.

In order to shed light on the factors governing the formation of the different products experimentally detected depending on the nucleophilic ligand of the Re complex, we carried out different theoretical analyses on the B3LYP electron density of some of the relevant species. The natural bond orbital (NBO)[70] method was used to obtain net atomic charges (NAC) as implemented in the Gaussian 09 suite of programs.[71] Electron delocalization indexes between two atoms *A* and *B* in a molecule, $\delta(A,B)$ = DI,[72] were computed using AIMAll program[73] within the framework of Bader's Atoms in Molecules (AIM) theory.[74] The DI is a measure of the number of electrons shared between two atoms and therefore, of the covalency of the bond between them.

All B3LYP computations were carried out with the Gaussian 09 suite of programs,[71] while DLPNO-CCSD(T) calculations employed the ORCA program version 4.0.1[75] and the frozen-core approximation. More technical details on the computational chemistry tools mentioned above as well as a justification for the choice of the DLPNO-CCSD(T) method are included in the Supporting Information.

## Results and Discussion

Figure 1 displays the DLPNO-CCSD(T) Gibbs energy profiles obtained for the reaction of [Re(X)(CO)$_3$(bipy)] complexes (X = OH, OMe, NH*p*Tol, $PPh_2$) towards HMAD (more energy details in Tables S1–S13 in the Supporting Information). The labeling of the theoretically located species is in line with the acronyms used in Scheme 2. So, **I1** identifies the zwitterionic intermediate formed in the initial attack of the nucleophile ligand on the HMAD acetylenic carbon bearing the H atom (C1). **I1′** corresponds to an isomer of **I1** wherein the electron lone pair of the acetylenic carbon bearing the $CO_2$Me group (C2) is oriented towards the plane defined by Re and the bipy ligand. **Pcco**, ***Pins***, and ***Pccb*** are possible products generated through the addition of C2 to a CO ligand, the Re atom, and the bipy ligand, respectively. ***Pccoh*** is another possible product, only present for X = OH and NH*p*Tol, which is similar to **Pcco** wherein a H atom of the nucleophile ligand has migrated to the attacked carbonyl ligand. As seen in Figure 1, three different reaction patterns are found. First, for the OH and $PPh_2$ ligands initial reactive approaches between reactants converge to **I1′** after passing through **I1** via the corresponding TSs **TS1** and **TS1_1′**. From **I1′** the reaction path splits into three routes giving rise to **Pcco**, ***Pins***, and ***Pccb*** via the TS **TS2*cco***, **TS2*ins***, and **TS2*ccb***, respectively. For X = OH, **Pcco** undergoes a posterior rearrangement to finally give ***Pccoh***. Second, for X = OMe the initial nucleophilic attack also leads to **I1** via **TS1** and then transforms into **Pcco** passing through **TS1_1′**. **Pcco** is the splitting structure towards ***Pins*** and ***Pccb*** now. Third, NH*p*Tol ligand yields a different surface where two approaching orientations of the reactants render separate routes starting both with the attack of the nucleophile ligand on C1 at HMAD to give the corresponding zwitterions **I1** and **I1b**. At **I1** the C1-bonded H atom is oriented to the same side of the complex as the *p*Tol substituent whereas the opposite orientation is found at **I1b** (see below). On the one hand, **I1** directly becomes **Pcco**, which in turn can evolve to either ***Pins*** or ***Pccoh***. On the other hand, **I1b** gives rise to ***Pccb*** after a certain rearrangement.

Let us focus in a comparative way on the formation and rearrangement steps of **I1** (blue line in Figure 1), first, and then on the subsequent routes leading to the addition of the alkyne moiety to CO (red line in Figure 1), the Re ion in an insertion

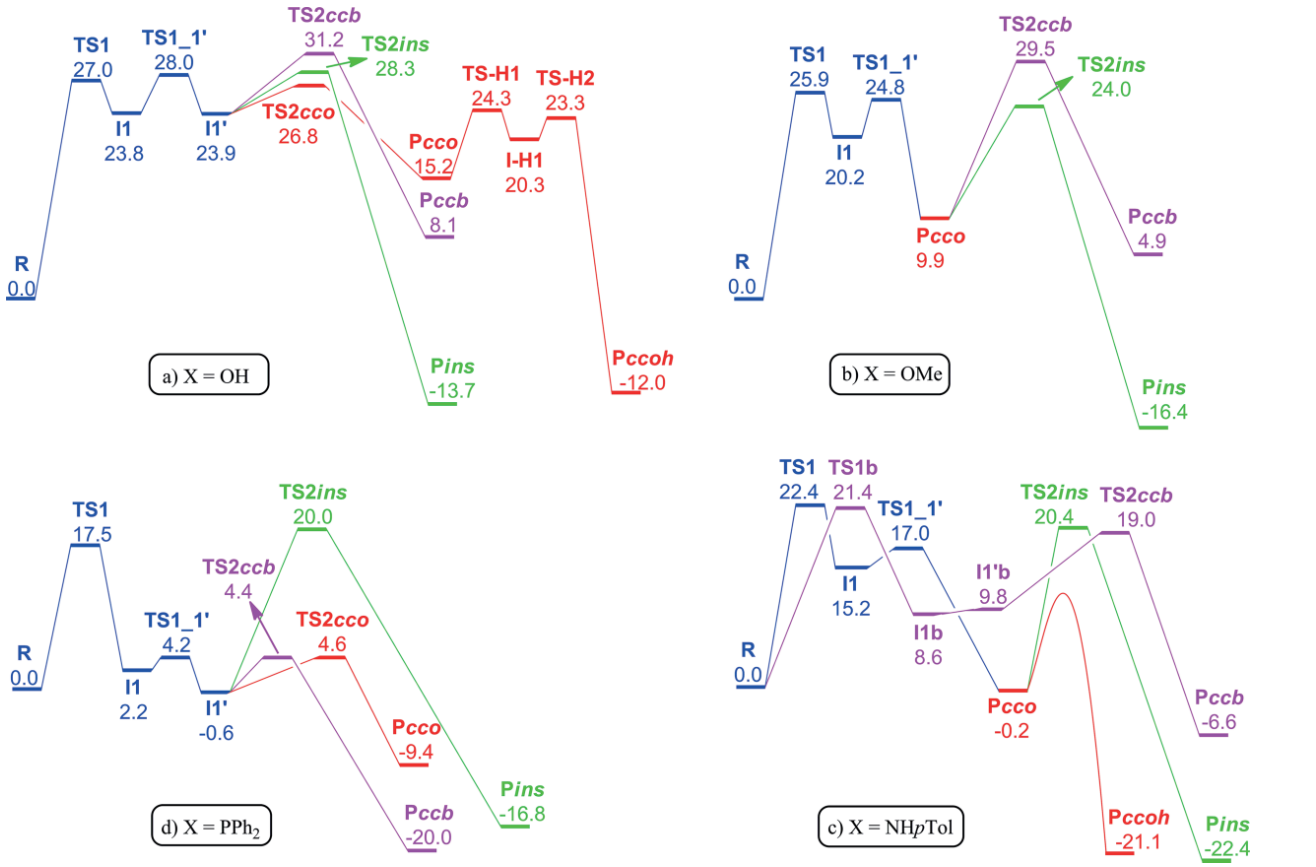


Figure 1. DLPNO-CCSD(T) Gibbs energy profiles in kcal/mol for the reaction of $[Re(X)(CO)_3(bipy)]$ with HMAD, being X = a) OH, b) OMe, c) NH*p*Tol, and d) $PPh_2$. For **Pcco** and **Pccoh** species with X = NH*p*Tol, an approximate connectivity is shown (see text)

process (green line in Figure 1), and the bidentate ligand bipy (purple line in Figure 1).

### a) Formation and Rearrangement of the Initial Intermediate

According to Figure 1, for the reaction of the complexes with X = OH and OMe, the TS for the attack of the X ligand to C1, **TS1**, leading to **I1** competes with the TS for the rearrangement of this intermediate, **TS1_1′**, for being the rate-limiting step. In the case of the complexes containing X = NH*p*Tol and $PPh_2$, **TS1** is clearly less stable than **TS1_1′** and ends up being the rate limiting TS. As mentioned above, the complex with NH*p*Tol, presents an alternative reactive approach of the reactants, which is controlled by **TS1b**, a TS analogous to **TS1**. Both TSs present similar relative energies, but the **TS1**-controlled route leads to the very stable product **Pccoh**, the one detected experimentally, while the **TS1b**-controlled route gives rise to **Pccb**, which is 14.5 kcal/mol less stable than **Pccoh**. Therefore, in this scenario, we focus on conducting a detailed comparative analysis of the **TS1** species found for the four complexes (see optimized geometries at Figure 2). The route leading to **Pccb** when X = NH*p*Tol will be described afterwards.

The energy barrier determined by **TS1** increases from $PPh_2$ (17.5 kcal/mol) to NH*p*Tol (22.4 kcal/mol), OMe (25.9 kcal/mol), and OH (27.0 kcal/mol), in good agreement with the well-known observation that large atoms are more easily polarizable, and by extension more nucleophilic than small ones. However, the size of the attacking atom is not the only feature affecting the barrier of the nucleophilic attack. The energy of the HOMO of a nucleophile is directly related to its nucleophilicity, being better nucleophiles those with the largest energy HOMOs (considering the sign). For the initial $[Re(X)(CO)_3(bipy)]$ complexes (X = OH, OMe, NH*p*Tol, $PPh_2$), **C** in Figure 2, HOMO energies are –0.162 (NH*p*Tol), –0.186 ($PPh_2$), –0.199 (OMe), and –0.208 (OH), all in eV. As seen in Figure 3, the greater stability of the HOMO of the complexes containing OH and OMe can be ascribed to the presence of a notable stabilizing interaction found between a *d*-type orbital of Re and one of the π* antibonding orbitals of the CO ligand *trans* to nucleophile ligand. This kind of interaction is notably reduced for complexes containing NH*p*Tol and $PPh_2$. More interestingly, the HOMO energy sequence aforementioned matches the trend in the barriers computationally obtained except when comparing NH*p*Tol and $PPh_2$ with each other. HOMO energies can be understood as a measurement of the general nucleophilicity of the whole complex, where X is one of the ligands. However, electron donation takes place from a particular atom, so the availability of the electron density at this atom is a matter of concern. For the Re complex with X = NH*p*Tol the sum of the three angles centered on N is 359.5°, representative of a planar distribution of groups around N, in

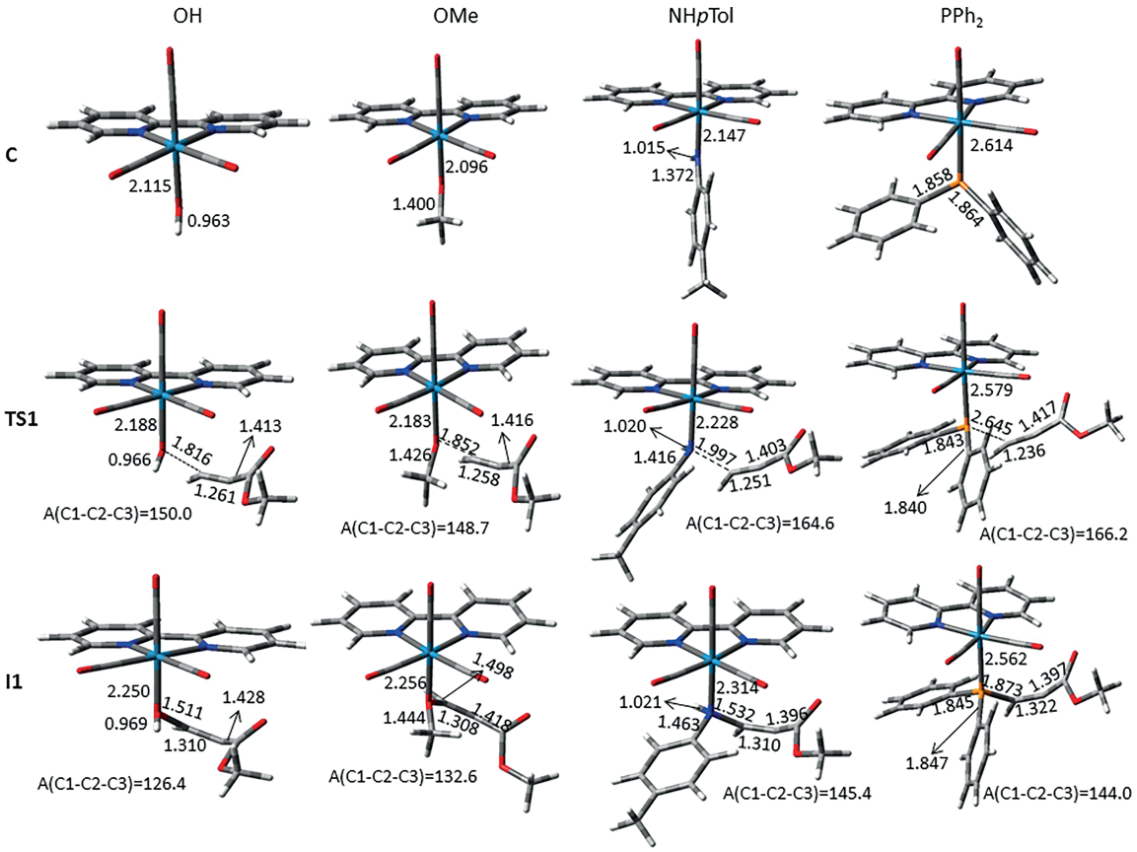


Figure 2. B3LYP optimized structures of the initial [Re(X)(CO)$_3$(bipy)] complexes (X = OH, OMe, NH*p*Tol, PPh$_2$), **C**, and the species involved in their nucleophilic attack to HMAD. Relevant bond lengths in angstroms and bond angles involving the carbon skeleton of the HMAD moiety, A(HC(1)≡C(2)-C(3)OOCH$_3$) = A(C1-C2-C3), in degrees are given.

good agreement with the value of 359.8° obtained from X-ray data.[49] The same sum of angles for the complex with X = PPh$_2$ amounts to 319.3°, far from a planar coordination around P (see Figure 2). Both N and P ligands have at least one aromatic group bonded to them. Thanks to the planar coordination and the similar atomic size, the lone pair of the N atom is conjugated with the *p*Tol group, so it is less available for a nucleophilic attack than in the case of the P ligand, where no conjugation between the electron density of the large P atom and any of the Ph groups is present. Actually, the resonance electronic structures where the aromaticity of the *p*Tol ligand is lost contribute to the energy destabilization of the HOMO of the NH*p*Tol ligand. The shape of the HOMO of these two complexes shows the availability of the lone pair of the nucleophile ligand in agreement with previous discussion. As seen in Figure 3, for the complex with PPh$_2$, HOMO is mainly described by the *p* orbital of the P atom while the one containing NH*p*Tol, the *p* orbital of the N atom is combined with one of the π bonding orbitals of the *p*Tol substituent.

The stability of **I1** with respect to **TS1** amounts to 3.2, 5.7, 7.2, and 15.3 kcal/mol for [Re(X)(CO)$_3$(bipy)] complexes with X = OH, OMe, NH*p*Tol, and PPh$_2$, respectively. In this intermediate some electron density has been transferred from the nucleophilic atom of the X ligand to the alkyne [0.275 *e* from O in the OH complex, 0.184 *e* from O in the OMe complex, 0.137 *e* from N, and 0.654 *e* from P, according to NBO population (see Figure S1 in the Supporting Information)] in such a way that a concentration of electron density at C2 has taken place [NAC(C2) = –0.404 *e* for OH complex, –0.388 *e* for OMe complex, –0.317 *e* for NH*p*Tol complex, and –0.245 *e* for PPh$_2$ complex]. At **I1** the incipient lone pair at C2 is in *trans* disposition with respect to the attacking nucleophilic atom and needs to be reoriented towards the equatorial plane of the Re complex where electrophilic positions are placed (see Figure 2). This is done through **TS1_1′**, a broad allene-like TS in the corresponding PES that is 4.2, 4.6, 1.8, and 2.0 kcal/mol larger in energy than **I1** (see Figure 1 and Figure 4) for X = OH, OMe, NH*p*Tol, and PPh$_2$, respec-

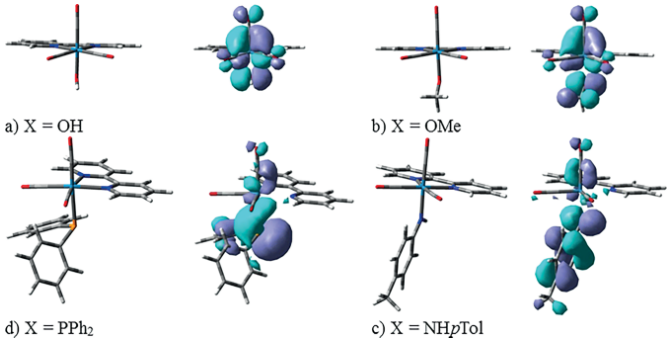


Figure 3. Shape of the HOMOs for [Re(X)(CO)$_3$(bipy)] complexes with X = a) OH, b) OMe, c) NH*p*Tol, and d) PPh$_2$.

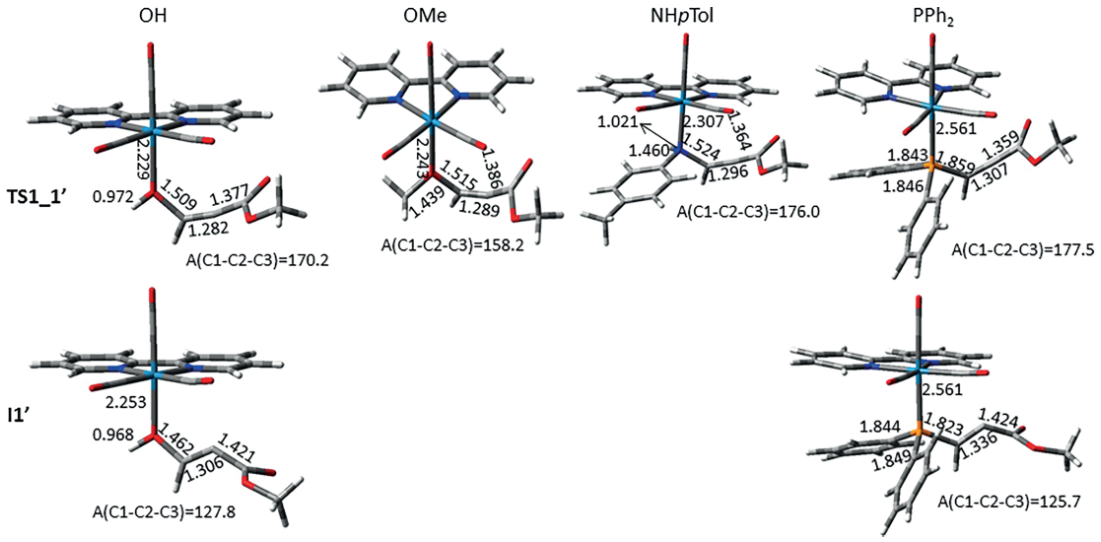


Figure 4. B3LYP optimized structures of **TS1_1′** and **I1′** (when present) for the reaction of $[Re(X)(CO)_3(bipy)]$ (X = OH, OMe, NH*p*Tol, and $PPh_2$) towards HMAD. Relevant bond lengths in angstroms and bond angles involving the carbon skeleton of the HMAD moiety, A(HC(1)≡C(2)-C(3)$OOCH_3$) = A(C1-C2-C3), in degrees are given.

tively. As already said, complexes with OH and $PPh_2$ ligands present **I1′** corresponding to a kind of zwitterion stereoisomer of **I1** with the lone pair at C2 in *cis* position with respect to the attacking nucleophilic atom (see Figure 4). NBO charges indicate that both N and P lose electron density when evolving from the initial complexes to **I1** and then to **I1′**, when present. At **I1** with $PPh_2$ the charge mainly concentrates at C1 of HMAD [NAC(C1) = –0.637 *e*, NAC(C2) = –0.245 *e*], whereas with OH [NAC(C1) = –0.059 *e*, NAC(C2) = –0.404 *e*], OMe [NAC(C1) = –0.047 *e*, NAC(C2) = –0.388 *e*], and NH*p*Tol [NAC(C1) = –0.154 *e*, NAC(C2) = –0.317 *e*] the electron density is pushed towards C2. However, we note that for the latter the charge concentration at C1 is notably greater than that for the O ligands. For the OMe and NH*p*Tol ligands an exhaustive search through IRC calculations from **TS1_1′** failed to find a similar **I1′** intermediate but led the system to **Pcco**. This particular region of PES seems to be very sensitive to the X ligand.

### b) Addition of the Alkyne Moiety to a CO Ligand

As displayed in Figure 1, **I1′** becomes **Pcco** through the TS **TS2*cco*** for the OH and $PPh_2$ ligands. However, **Pcco** is obtained from **I1** via **TS1_1′** for OMe and NH*p*Tol. Moreover, for these ligands, **I1′** and **TS2*cco*** could not be detected after an extensive search.

**TS2*cco*** is for the C–C coupling between C2 and a CO ligand in *cis* with respect to the attacking nucleophilic ligand, which leads to the formation of a five-membered ring in a new bidentate ligand. It presents a low barrier of 2.9 kcal/mol (OH) and 5.2 kcal/mol ($PPh_2$), when measured from **I1′**. According to NBO charges, the CO ligand in *cis* disposition with respect to the alkyne moiety is a strong electrophile due to the large positive charge on its C atom (0.730 and 0.756 *e* for OH and $PPh_2$ ligands at **I1′**, respectively). As seen in Figure 5, both of them are early TSs where the new C2–CO bond is still long (2.406 and 2.439 Å for OH and $PPh_2$, respectively) and the triple C1–C2 bond still short (1.308 and 1.331 Å for OH and $PPh_2$, respectively). Geometrically, CO is close to the attacking C2 atom, so both electronic and steric factors point to a small barrier, as it is indeed.

At **Pcco** the alkyne moiety has been fully incorporated to the Re complex through its C1–C2 bond yielding the new five-membered metallacycle (see Figure 5). The Gibbs energy of **Pcco** is larger than that of isolated reactants for OH (15.2 kcal/mol) and OMe (9.9 kcal/mol) complexes, but smaller for NH*p*Tol (–0.2 kcal/mol) and $PPh_2$ (–9.4 kcal/mol) complexes. It is interesting to note that the Re–X distance at **Pcco** is about 8.5 % longer than in isolated reactants for OH, OMe, and NH*p*Tol ligands, whereas it becomes reduced by about 4 % at **Pcco** for the $PPh_2$ complex. The strengthening of the Re–P bond seems to provide extra stability to this last **Pcco** product. In the case of $Re^{I}$ complexes with the OH and NH*p*Tol ligands, both containing a H atom bonded to a nucleophilic atom, **Pcco** evolves to a new product where that H atom has migrated to the O atom of the attacked CO ligand (see **Pccoh** in Figure 5). The transformation **Pcco** → **Pccoh** could occur via an intramolecular hydrogen shift. Several options were considered, but none of them proved feasible (see discussion and Figure S2 in the Supporting Information), so, we figured it could take place through an intermolecular hydrogen shift. Figure 6 displays the main structures located for the OH ligand and Tables S5–S7 collect their energy data. The process starts with the species **Pcco_dimer** where two **Pcco** moieties oriented themselves with the H atoms of the OH ligands heading to the carbonyl oxygen atoms of the ester groups of the opposite molecule. Then, **TS-H1** performs the simultaneous transfer of both H atoms with a Gibbs energy barrier of 9.1 kcal/mol from **Pcco_dimer** to give rise to intermediate **I0-H1**, where the carboxylate groups hold the travelling hydrogen atoms at a distance of 1.010 Å. From **I0-H1** several low energy demanding rearrangements place the transferred H atom closer to the attacked carbonyl ligand, as shown in the monomer species **I-H1**. Finally, the last step in the H migration occurs through **TS-H2** where the migrated

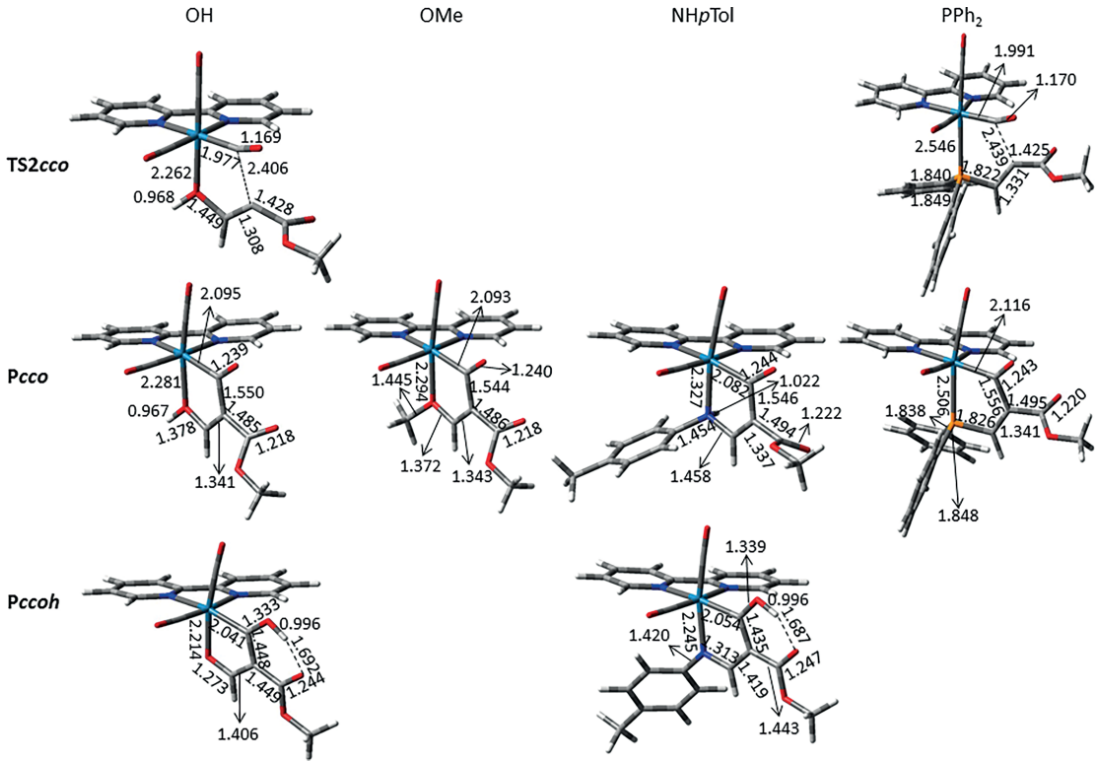


Figure 5. B3LYP optimized structures of **TS2*cco***, **Pcco**, and **Pccoh** (when present) for the reaction of [Re(X)(CO)$_3$(bipy)] (X = OH, OMe, NH*p*Tol, and PPh$_2$) towards HMAD. Relevant bond lengths in angstroms are displayed.

hydrogen rotates and transfers to the target CO, leading to a new stabilizing H-bond with the ester group. Geometrically, the metallacyle at **Pccoh** products is tighter than that at the corresponding **Pcco** previous species (see Figure 5). Only the C1–C2 bond slightly elongates. These issues, along with the absence of charges of **Pccoh** products, make them the second most stable ones (after ***Pins***) for the reaction of these complexes (–12.0 and –21.1 kcal/mol for OH and NH*p*Tol ligands, respectively).

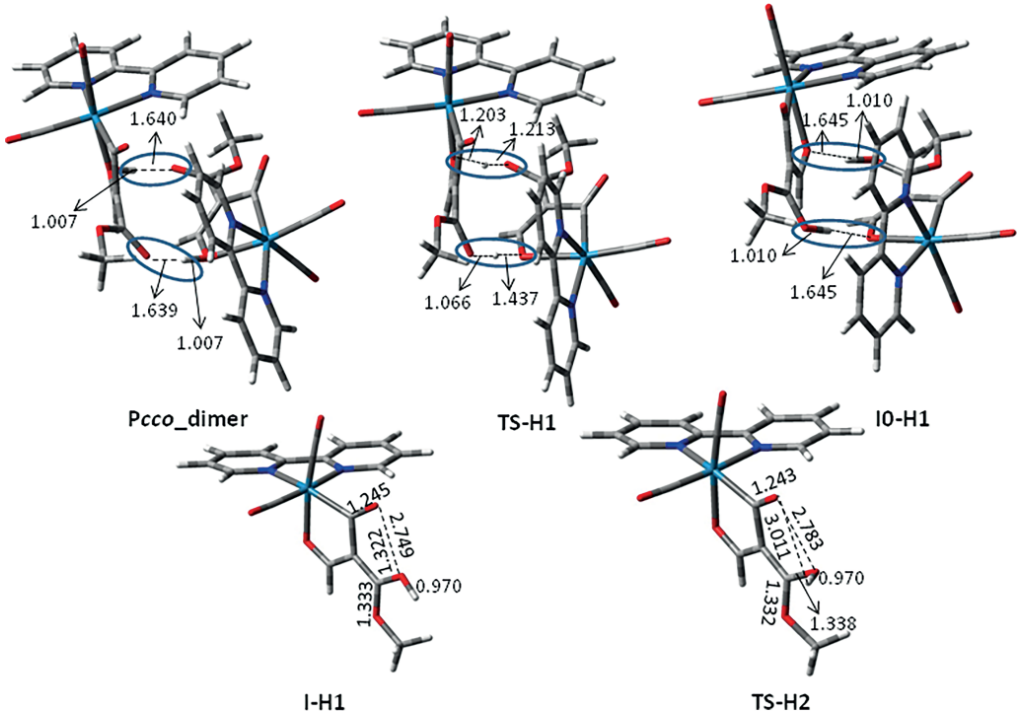


Figure 6. B3LYP optimized structures for the H transpositions from the OH ligands to the carbonyl oxygen atoms in the **Pcco** structures. Relevant bond lengths in angstroms are displayed.

Analogous dimer intermediates and reaction path are assumed to describe the H transfer between **Pcco** and **Pccoh** for the complex with NH*p*Tol. Although the notable size of the dimer systems containing this ligand prevents the performance of the very demanding DLPNO-CCSD(T) calculations, the similarity of the species found for the intramolecular hydrogen migration to those for the OH ligand seems to validate our assumption (see Supporting Information).

### c) Addition of the Alkyne Moiety to the Re Atom: the *ins* Route

The C2 atom of either **I1′** or **Pcco** species could also bond to the Re metal evolving through **TS2*ins*** (see Figure 7). At the intermediates previous to **TS2*ins*** the corresponding Re–X bond is strong and starts weakening when the new C2–Re bond begins to form during the concerted synchronous process characterized by **TS2*ins***. For the complex with X = OH, the barrier for **TS2*ins*** is just 4.4 kcal/mol, from **I1′**. Such a small value indicates that the energy released from the partial formation of the new C2–Re bond nearly compensates for the cost of breaking the Re–O bond. A different situation appears for the complex with X = $PPh_2$, where the barrier for **TS2*ins*** raises to 20.6 kcal/mol from its previous intermediate, **I1′**. This means that the Re–P bond is much stronger than the bond formed between Re and O in the X = OH complex considered here. Actually, the DI shows a value of 0.614 for the Re–P bond, notably larger than that found for the Re–O one (0.374). The *d* orbitals in a third-row atom, like phosphorus, are better sized to largely overlap with Re ones than second-row atoms. This makes the insertion path very unlikely for the complex with the $PPh_2$ ligand. On the other hand, in complexes with X = OMe and NH*p*Tol IRC calculations clearly demonstrate that **Pcco** is the structure preceding **TS2*ins***, with a barrier of 14.1 and 20.6 kcal/mol respectively, measured from it. These large values come from the fact that two bond breakages are needed to accomplish the insertion, the Re–O or Re–N and the C2–CO ones. The products formed at the end of this reaction path are *Z*-alkenyl complexes with no charge separation. This explains why this type of products is more stable than reactants (between 13 and 17 kcal/mol for OH, OMe, and $PPh_2$ systems and 22.4 kcal/mol for NH*p*Tol). In the case of NH*p*Tol the aromatic ring bonded to the N atom is placed far away from the complex equatorial ligands, thus avoiding repulsive interactions present in the remaining structures of its reaction profile. It has been reported that, when the insertion product is the main one, addition of an acid like HTOf in $CDCl_3$ allows the release of the corresponding *Z*-alkenyl complex with H replacing the metal.[47]

### d) Addition of the Alkyne Moiety to the *bipy* Ligand

Although hardly electrophilic, one of the *ortho* C atoms bearing a hydrogen at the bipy ligand, C6, could also be attacked by the C2 alkyne atom, as it was experimentally observed for the complex with $PPh_2$ ligand.[51,52] **TS2*ccb*** represents this addition and has been theoretically characterized for the four complexes here considered (see Figure 8 and Figure 9). However, three different reaction paths are computationally observed for the formation of **Pccb**. As for **TS2*ins***, **TS2*ccb*** may come from **I1′** (complexes with X = OH and $PPh_2$) or **Pcco** (complex with X = OMe). However, for the complex with X = NH*p*Tol IRC calculations indicate that a slightly different zwitterion, **I1′b**, is preceding **TS2*ccb***. At **I1′b** the C1-bonded hydrogen atom of the alkyne moiety (H1) is placed *outwards* with respect to the bidentate ligand (see Figure 8), which suggests an approach of the reactants different from that considered so far. Actually, leaving

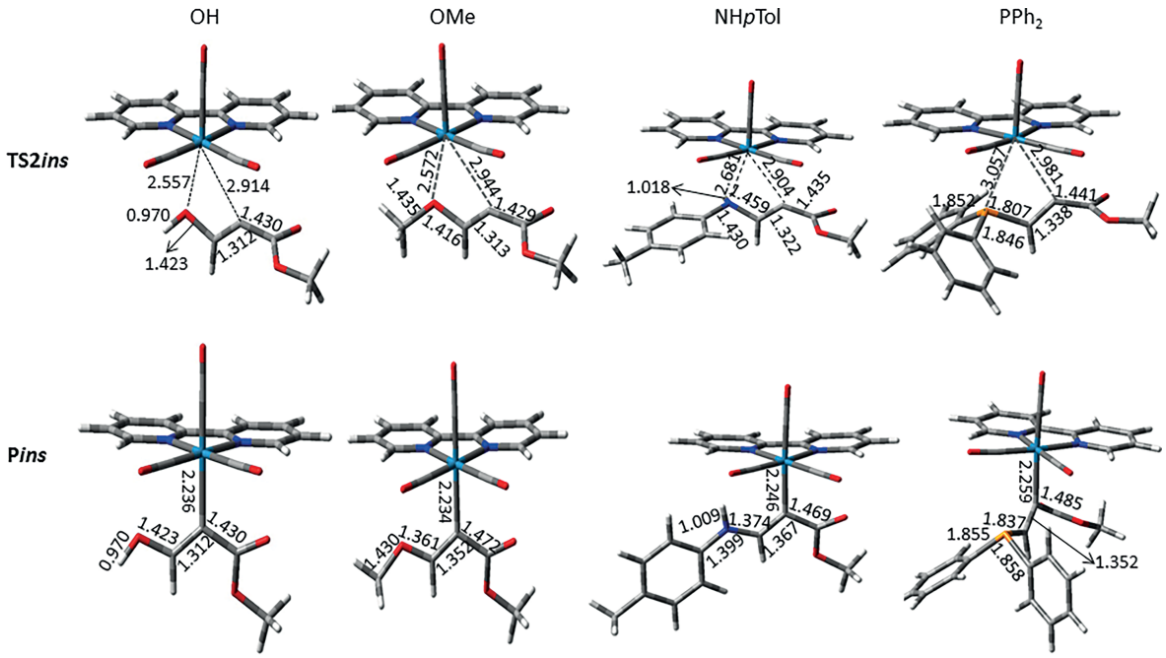


Figure 7. B3LYP optimized structures of the species involved in the addition step to the Re atom for the reaction of [Re(X)(CO)$_3$(bipy)] (X = OH, OMe, NH*p*Tol, and $PPh_2$) towards HMAD. Relevant bond lengths in angstroms are shown.

H1 *outwards* at the initial interaction between reactants leads to a TS, **TS1b**, with nearly the same energy as **TS1** that evolves to **I1b** (see Figure 8). This intermediate resembles **I1** in the sense that the lone pair that starts forming at C2 is in *trans* disposition with respect to the attacking N atom, but **I1b** is 6.6 kcal/mol more stable than **I1**. No TS but a steadily decreasing energy path joins **I1b** with **I1′b**, where the lone pair at C2 is in *cis* orientation with respect to the nucleophilic N atom. **I1′b** resembles intermediates **I1′** found for the rest of complexes in the sense that some electron density concentrates on the C2 atom of the alkyne (–0.422 e) and faces towards the electron poor area of the equatorial ligands. However, C2 electron charge is pointing to bipy in a more tilted way than in the remaining **I1′** intermediates. **I1′b**, with a relative Gibbs energy of 9.8 kcal/mol, evolves to **TS2*ccb*** and finally to **P*ccb***. The approach of HMAD to H1 in the *outward* orientation was also found for the rest of the complexes, but did not link to the routes leading to the experimentally observed products.

For complexes with NH*p*Tol and mainly for those with OH and OMe ligands, the barrier of **TS2*ccb*** is large when measured from the reactants (31.2, 29.5, and 19.0 kcal/mol for OH, OMe, and NH*p*Tol systems, respectively) and the **P*ccb*** products present no or low positive Gibbs energy stabilization (8.1, 4.9, and –6.6 kcal/mol for X = OH, OMe, and NH*p*Tol, respectively). Several reasons explain the high instability of **TS2*ccb*** and **P*ccb*** structures for X ligands with a second row element (N or O). First, as seen in Figure S1, the C6 atom of bipy shows a small positive charge at the intermediates preceding **TS2*ccb***, which

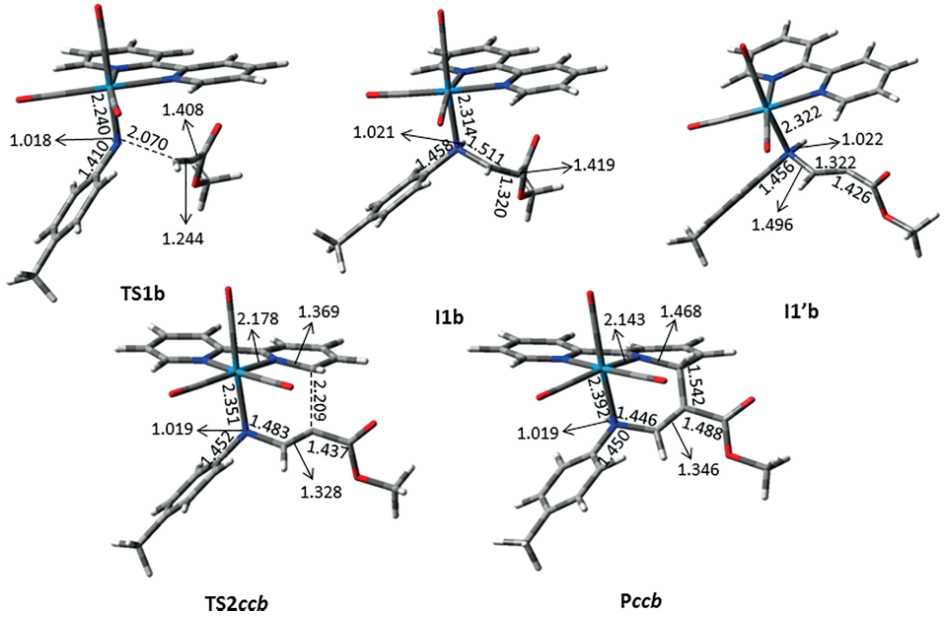


Figure 8. B3LYP optimized structures for the reaction of [Re(NH*p*Tol)(CO)$_3$(bipy)] with HMAD to yield **P*ccb***. Some relevant distances in angstroms are given.

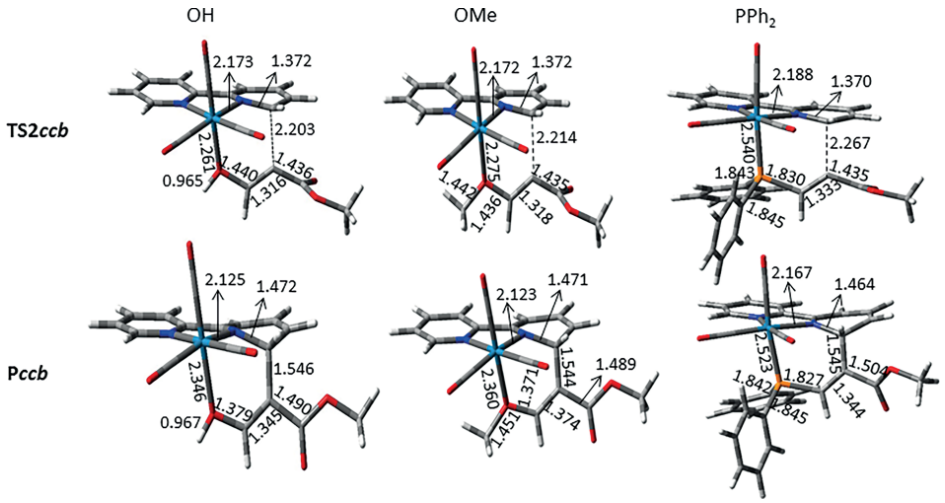


Figure 9. B3LYP optimized structures of the species implied in the addition step of the alkyne moiety to the bipy ligand for the reaction of [Re(X)(CO)$_3$(bipy)] (X = OH, OMe, and PPh$_2$) towards HMAD. Relevant bond lengths in angstroms are shown.

means that it is a poor electrophile. Second, as it can be seen in Figure 8 and Figure 9, at **TS2*ccb*** a six-membered non-planar metallacycle is starting to form and, as a consequence, the aromaticity in the attacked bipy ring becomes reduced, losing its planarity. When X ligand contains an O atom the C2–C6 bond is shorter, the aromatic ring is more distorted, that is, largest barriers correlate with larger aromaticity reductions. For the **TS2*ccb*** and **P*ccb*** structures when X = OH, OMe, and NH*p*Tol the Re–X bond is considerably longer than in the corresponding reactant complex (see Figure 9). The weakening of the bond with the metal may also contribute to the instability of these structures. When X = $PPh_2$, **TS2*ccb*** presents a barrier of only 4.4 kcal/mol, similar to that of **TS2*cco*** (4.6 kcal/mol) and much smaller than that of the other **TS2*ccb***-type species. The loss of bipy aromaticity seems to be compensated by the formation of a loose six-membered metallacycle where the Re–P bond becomes stronger than in the initial reactant (with a shorter distance), which makes it particularly stable.

### e) General Discussion of the Theoretical Results and Comparison with the Experiment

In spite of the apparent similarity of [Re(X)$(CO)_3$(bipy)] (X = OH, OMe, NH*p*Tol, and $PPh_2$) complexes, it has been experimentally found that the nature of the X ligand determines the formation of different products in their reactivity towards activated alkynes, such as HMAD. The detailed analyses previously done for these reactions confirm experimental observations and shed some light on the reasons under this behavior. Actually, it is shown that the prevalence of one of the three possible products, **P*cco*** (**P*ccoh***, when present), **P*ins*** or **P*ccb***, depends on a subtle balance between the kinetic barriers of the final step of their formation, since the initial nucleophilic approach of the X ligand to the alkyne is common for routes leading to all of the products (see Figure 1), and their associated thermodynamic stability. These facts are not expected to change in the event that HMAD was computationally replaced by symmetric activated acetylenes like DMAD, since this substitution did not modify the kind of reaction product obtained experimentally.[49,51,52] The presence of DMAD will lower the energy barrier of the initial nucleophilic approach to afford **I1** as the acetylenic carbons (C1 and C2) for the isolated DMAD are less electronically populated (≈ 0.12 *e*) than the analogous ones for HMAD and also the LUMO of DMAD is lower in energy (0.008 eV) than the analogous one of HMAD (see Table S17). By contrast, a slight increase in energy barriers for the formation of the different reaction products from **I1** is expected, taking into account that C2 in **I1** with DMAD is less electronically populated than that one with HMAD (see **I1** for the NH*p*Tol case in Figure S1 and Table S17). Nonetheless, this will not affect the selectivity of these reactive processes because the NBO charges of the three atoms attacked by C2 (*Re*, $C_{CO}$, and $C_{bipy}$) are very similar to those found at **I1** with HMAD (compare **I1** in Figure S1 and Table S17).

For X = OH and NH*p*Tol the experimentally observed product is **P*ccoh***.[49,50] The intramolecular addition to an equatorial CO ligand is an easy process for all four $Re^I$ complexes, to the point that it may not require surpassing a Gibbs energy barrier when X = OMe and NH*p*Tol [**TS2*cco*** was not found for these ligands and instead it is the TS for **I1** rearrangement (**TS1_1′**) that ends up giving rise **P*cco***]. However, only **P*cco***-type products are clearly more stable than the separate reactants for the $PPh_2$ ligand and are always less stable than the corresponding **P*ccb*** and **P*ins***-type products. Only when X contains a nucleophilic atom bonded to a H atom (X = OH and NH*p*Tol), the addition to CO is followed by an accessible H transposition that yields the very stable species **P*ccoh*** as the preferred product in accordance with experimental findings.[45,50] For the case of the [Re(NH*p*Tol)$(CO)_3$(bipy)] complex the PES has two different reaction channels from the beginning of the reaction. The channel leading to **P*ccb*** is not competitive with that for the formation of **P*ccoh*** due to the large stabilization of this last product.

For X = OMe the experimentally observed product is **P*ins***.[47] The *ins* route is the most kinetically unfavorable for X = $PPh_2$ due to the strong bond between Re and the third period element, phosphorus, that has to be broken at **TS2*ins***; is kinetically unfavorable for X = OMe and NH*p*Tol due to fact that the structure previous to **TS2*ins***, **P*cco***, needs to break two bonds (Re–O/N and C2–CO) to yield the corresponding **P*ins***; and becomes more favorable for X = OH from **I1′** intermediate, where only the Re–O bond has to be broken. Thermodynamically, the *ins* route is favorable, since it yields very stable products with no charge separation for all complexes. For the particular case of the reaction of [Re(OMe)$(CO)_3$(bipy)] with HMAD, the lower Gibbs energy barrier of **TS2*ins*** compared to its potential competitor **TS2*ccb*** determines, according to experimental evidences,[47] the formation of **P*ins*** as the main reaction product (besides the large thermodynamic stability of the insertion product **P*ins***).

Eventually, for the complex with the $PPh_2$ ligand, intermediate **I1′** exists and is the separation point for the independent routes leading to each of the products (**P*cco***, **P*ins*** or **P*ccb***) via the corresponding TS (**TS2*cco***, **TS2*ins*** or **TS2*ccb***). Compared to X = OH, OMe, NH*p*Tol, the presence of a larger nucleophilic atom at the X ligand like phosphorus relieves the ring strain of the four, five, and six-member metallacycles at **TS2*ins***, **TS2*cco***, and **TS2*ccb***, respectively. This causes an important stabilization of **TS2*cco*** and **TS2*ccb***, and to a much lesser extent **TS2*ins*** due to the strength of the Re–P bond. As a result, the addition routes to CO and bipy, kinetically similar, are much more favorable than the insertion one. The largest stability of the **P*ccb*** product determines a preference for the formation of **P*ccb***, as experimentally observed.[51,52] Except for the complex with X = $PPh_2$, the route for the coupling with the bipy ligand ($C$-$C_{bipy}$) is quite unfavorable both kinetically and thermodynamically.

As just said, the formation of the products experimentally detected, **P*ccoh*** ($C$-$C_{COH}$ coupling product) for OH and NH*p*Tol, **P*ins*** (insertion product) for OMe, and **P*ccb*** ($C$-$C_{bipy}$ coupling product) for $PPh_2$, could be rationalized in this work and some reactivity guidelines seem to be emerging. The understanding of the independent or combined effects of the heteroatoms and their substituents at the X ligand on this reactivity will benefit from a systematic study involving complexes not yet experimentally tested that is under way in our laboratory.

## Conclusions

A comparative mechanistic study on the reactions of [Re(X)(CO)$_3$(bipy)] (X = OH, OMe, NH*p*Tol, PPh$_2$; bipy = 2,2′-bipyridine) towards methyl propiolate (HMAD) was carried out at the CPCM-DLPNO-CCSD(T)/def2-TZVPP//PCM-B3LYP/6-31+G(d,p)-LANL2DZ level of theory to understand the effect of ligand X on the selectivity of the reaction. Three different reaction patterns were found having in common the initial nucleophilic attack of the X ligand on the terminal acetylenic carbon of HMAD. First, for OH and PPh$_2$ initial reactive approaches lead to the formation of a zwitterionic intermediate that subsequently becomes an isomeric zwitterion. This species is the splitting point for the reaction paths leading to three possible products: the addition of the X-bonded acetylene to one of the CO ligands in *trans* disposition to the bipy one (*C*-$C_{CO}$ coupling product), the Re atom in an insertion process (*ins* product) or the bipy ligand (*C*-$C_{bipy}$ coupling product). Second, for OMe, the zwitterion formed at the first step evolves directly to the *C*-$C_{CO}$ coupling species, which is the splitting structure towards the *ins* and *C*-$C_{bipy}$ products. Third, for NH*p*Tol two approaching orientations of the reactants render separate routes, one leading to the *C*-$C_{bipy}$ product and the other to the *C*-$C_{CO}$ product to which, the *ins* product is linked. In addition, for X ligands containing a hydrogen atom bonded to the nucleophilic atom, OH and NH*p*Tol, we have found an intermolecular mechanism for the evolution of *C*-$C_{CO}$ species evolves to a more stable one, *C*-$C_{COH}$ product, where that H atom has shifted to the oxygen atom of the attacked carbonyl ligand. According to our computations, the ester group in HMAD plays a two-fold role by activating the alkyne for the initial nucleophilic addition and by assisting an intermolecular hydrogen migration from *C*-$C_{CO}$ to *C*-$C_{COH}$ species in these complexes.

The reaction rate of the reactive processes investigated is determined by the initial nucleophilic attack step. Since this step is common for all the reactions, the preferred product depends on the kinetics and/or thermodynamics ascribed to the last part of the corresponding reaction profile. The formation of *C*-$C_{CO}$ species is kinetically more favored than that of *C*-$C_{bipy}$ and *ins* ones, except for X = PPh$_2$ where the energy barriers for the generation of *C*-$C_{CO}$ and *C*-$C_{bipy}$ species compete with each other. By contrast, thermodynamics always favors the formation of *ins*, *C*-$C_{bipy}$ or, when present, *C*-$C_{COH}$ species over the *C*-$C_{CO}$ one. Specifically, when X = OH and NH*p*Tol, an easy intramolecular attack of the HMAD that was just linked to a highly electrophilic CO equatorial ligand is followed by the formation of the very stable *C*-$C_{COH}$ products. When X = OMe, the *ins* product forms thanks to the smaller barrier and the larger stability of the *ins* route compared to that of its potential competitor, the *C*-$C_{bipy}$ product. Finally, when X = PPh$_2$ the *ins* route becomes restricted and, therefore the *C*-$C_{bipy}$ coupling wins over the *C*-$C_{CO}$ one, but only for the largest stability of the *C*-$C_{bipy}$ product. Based on this, the products experimentally detected, *C*-$C_{COH}$ for OH and NH*p*Tol, *ins* for OMe, and *C*-$C_{bipy}$ for PPh$_2$, could be rationalized and some general reactivity trends have been unveiled. Therefore, the information collected can help design new rhenium carbonyl complexes and other related systems with improved technological, biomedical or chemical synthesis applications.

## *Acknowledgments*

The authors thank the governments of Spain (grants CTQ2015-70231-P and PG2018-100013-B-I00) and Principado de Asturias (grant FC-15-GRUPIN14-103) for financial support. We also acknowledge computing resources from the Fundación Computación y Tecnologías Avanzadas de Extremadura (COMPUTAEX) (JD). We are grateful to both D. Suárez and J. Pérez, from the University of Oviedo (Spain), and R. Mera-Adasme, from the University of Santiago de Chile (USACH), for useful suggestions to the manuscript and calculations.

**Keywords:** Rhenium · Nucleophilic addition · Ligand effects · Reaction mechanisms · Computational chemistry

[1] J. Hawecker, J. M. Lehn, R. Ziessel, *J. Chem. Soc., Chem. Commun.* **1983**, 536–538.
[2] J. Hawecker, J. M. Lehn, R. Ziessel, *J. Chem. Soc., Chem. Commun.* **1984**, 328–330.
[3] B. P. Sullivan, C. M. Bolinger, D. Conrad, W. J. Vining, T. J. Meyer, *J. Chem. Soc., Chem. Commun.* **1985**, 1414–1416.
[4] J. Hawecker, J. M. Lehn, R. Ziessel, *Helv. Chim. Acta* **1986**, *69*, 1990–2012.
[5] Y. Hayashi, S. Kita, B. S. Brunschwig, E. Fujita, *J. Am. Chem. Soc.* **2003**, *125*, 11976–11987.
[6] P. Kurz, B. Probst, B. Spingler, R. Alberto, *Eur. J. Inorg. Chem.* **2006**, 2966–2974.
[7] H. Takeda, K. Koike, H. Inoue, O. Ishitani, *J. Am. Chem. Soc.* **2008**, *130*, 2023–2031.
[8] B. Probst, A. Rodenberg, M. Guttentag, P. Hamm, R. Alberto, *Inorg. Chem.* **2010**, *49*, 6453–6460.
[9] J. M. Smieja, C. P. Kubiak, *Inorg. Chem.* **2010**, *49*, 9283–9289.
[10] H. Takeda, O. Ishitani, *Coord. Chem. Rev.* **2010**, *254*, 346–354.
[11] B. Probst, M. Guttentag, A. Rodenberg, P. Hamm, R. Alberto, *Inorg. Chem.* **2011**, *50*, 3404–3412.
[12] K. A. Grice, C. P. Kubiak, A. Michele, E. van Rudi, *Adv. Inorg. Chem.* **2014**, *66*, 163–188.
[13] J. J. Teesdale, A. J. Pistner, G. P. A. Yap, Y. Z. Ma, D. A. Lutterman, J. Rosenthal, *Catal. Today* **2014**, *225*, 149–157.
[14] C. Matlachowski, B. Braun, S. Tschierlei, M. Schwalbe, *Inorg. Chem.* **2015**, *54*, 10351–10360.
[15] T. W. Schneider, M. Z. Ertem, J. T. Muckerman, A. M. Angeles-Boza, *ACS Catal.* **2016**, *6*, 5473–5481.
[16] C. Kefalidi, E. Koutsouri, L. Marchiò, A. Zarkadoulas, S. Efstathiadou, C. A. Mitsopoulou, *Polyhedron* **2016**, *110*, 157–164.
[17] E. Koutsouri, C. A. Mitsopoulou, *Open Chem.* **2016**, *14*, 393–403.
[18] M. L. Clark, P. L. Cheung, M. Lessio, E. A. Carter, C. P. Kubiak, *ACS Catal.* **2018**, *8*, 2021–2019.
[19] D. B. MacQueen, K. S. Schanze, *J. Am. Chem. Soc.* **1991**, *113*, 6108–6110.
[20] K. S. Schanze, D. B. MacQueen, T. A. Perkins, L. A. Cabana, *Coord. Chem. Rev.* **1993**, *122*, 63–89.
[21] S. S. Sun, A. J. Lees, *J. Am. Chem. Soc.* **2000**, *122*, 8956–8967.
[22] M. Bakir, *Acta Crystallogr., Sect. C: Struct. Chem.* **2001**, *57*, 1371–1373.
[23] A. S. Polo, M. K. Itokazu, K. M. Frin, A. O. de T. Patrocínio, N. Y. M. Iha, *Coord. Chem. Rev.* **2006**, *250*, 1669–1680.
[24] D. Pelleteret, N. C. Fletcher, A. P. Doherty, *Inorg. Chem.* **2007**, *46*, 4386–4388.
[25] M. C. L. Yeung, V. W. W. Yam, *Chem. Soc. Rev.* **2015**, *44*, 4192–4202.
[26] A. Zarkadoulas, E. Koutsouri, C. Kefalidi, C. A. Mitsopoulou, *Coord. Chem. Rev.* **2015**, *304–305*, 55–72.
[27] a) N. J. Lundin, A. G. Blackman, K. C. Gordon, D. L. Officer, *Angew. Chem. Int. Ed.* **2006**, *45*, 2582–2584; *Angew. Chem.* **2006**, *118*, 2644; b) G. W. Zhaoa, J. H. Zhaoa, Y. X. Hua, D. Y. Zhangb, X. Lia, *Synth. Met.* **2016**, *212*, 131–141.
[28] G. Gasser, I. Ott, N. Metzler-Nolte, *J. Med. Chem.* **2011**, *54*, 3–25.
[29] A. Leonidova, V. Pierroz, L. A. Adams, N. Barlow, S. Ferrari, B. Graham, G. Gasser, *ACS Med. Chem. Lett.* **2014**, *5*, 809–814.
[30] A. Leonidova, G. Gasser, *ACS Chem. Biol.* **2014**, *9*, 2180–2193.

[31] M. Kaplanis, G. Stamatakis, V. D. Papakonstantinou, M. Paravatou-Petsotas, C. A. Demopoulos, C. A. Mitsopoulou, *J. Inorg. Biochem.* **2014**, *135*, 1–9.
[32] R. R. Ye, C. P. Tan, M. H. Chen, L. Hao, L. N. Ji, Z. W. Mao, *Chem. Eur. J.* **2016**, *22*, 7800–7809.
[33] K. M. Knopf, B. L. Murphy, S. N. MacMillan, J. M. Baskin, M. P. Barr, E. Boros, J. J. Wilson, *J. Am. Chem. Soc.* **2017**, *139*, 14302–14314.
[34] S. C. Marker, S. N. MacMillan, W. R. Zipfel, Z. Li, P. C. Ford, J. J. Wilson, *Inorg. Chem.* **2018**, *57*, 1311–1331.
[35] M. Salmain, M. Gunn, A. Gorfti, S. Top, G. Jaouen, *Bioconjugate Chem.* **1993**, *4*, 425–433.
[36] W. B. Connick, A. J. DiBilio, M. G. Hill, J. R. Winkler, H. B. Gray, *Inorg. Chim. Acta* **1995**, *240*, 169–173.
[37] T. A. Oriskovich, P. S. White, H. H. Thorp, *Inorg. Chem.* **1995**, *34*, 1629–1631.
[38] K. K.-W. Lo, W.-K. Hui, C.-K. Chung, K. H.-K. Tsang, T. K.-W. Lee, C.-K. Li, J. S.-Y. Lau, D. C.-M. Ng, *Coord. Chem. Rev.* **2006**, *250*, 1724–1736.
[39] C. Beck, J. Brewer, J. Lee, D. McGraw, B. A. DeGraff, J. N. Demas, *Coord. Chem. Rev.* **2007**, *251*, 546–553.
[40] K. K.-W. Lo, M.-W. Louie, K.-S. Sze, J. S.-Y. Lau, *Inorg. Chem.* **2008**, *47*, 602–611.
[41] V. Fernández-Moreira, F. L. Thorp-Greenwood, M. P. Coogan, *Chem. Commun.* **2010**, *46*, 186–202.
[42] K. K.-W. Lo, M.-W. Louie, K. Y. Zhang, *Coord. Chem. Rev.* **2010**, *254*, 2603–2622.
[43] K. K.-W. Lo, K. Y. Zhang, S. P.-Y. Li, *Eur. J. Inorg. Chem.* **2011**, 3551–3568.
[44] R. Balasingham, M. P. Coogan, F. L. Thorp-Greenwood, *Dalton Trans.* **2011**, *40*, 11663–11674.
[45] K. K.-W. Lo, A. W.-T. Choi, W. H.-T. Law, *Dalton Trans.* **2012**, *41*, 6021–6047.
[46] J. Skiba, T. Bernas, D. Trzybinski, K. Wozniak, G. Ferraro, D. Marasco, A. Merlino, M. Z. Shafikov, R. Czerwieniec, K. Kowalski, *Molecules* **2017**, *22*, 809–820.
[47] E. Hevia, J. Pérez, L. Riera, V. Riera, *Organometallics* **2002**, *21*, 1750–1752.
[48] E. Hevia, J. Pérez, L. Riera, V. Riera, I. del Río, S. García-Granda, D. Miguel, *Chem. Eur. J.* **2002**, *8*, 4510–4521.
[49] E. Hevia, J. Pérez, V. Riera, D. Miguel, *Organometallics* **2003**, *22*, 257–263.
[50] L. Cuesta, D. C. Gerbino, E. Hevia, D. Morales, M. E. Navarro-Clemente, J. Pérez, L. Riera, V. Riera, D. Miguel, I. del Río, S. García-Granda, *Chem. Eur. J.* **2004**, *10*, 1765–1777.
[51] L. Cuesta, E. Hevia, D. Morales, J. Pérez, V. Riera, E. Rodríguez, D. Miguel, *Chem. Commun.* **2005**, 116–117.
[52] L. Cuesta, E. Hevia, D. Morales, J. Pérez, V. Riera, M. Seitz, D. Miguel, *Organometallics* **2005**, *24*, 1772–1775.
[53] R. Arévalo, M. Espinal-Viguri, M. A. Huertos, J. Pérez, L. Riera, *Adv. Organomet. Chem.* **2016**, *65*, 47–114.
[54] F. Villafañe, *Coord. Chem. Rev.* **2017**, *339*, 128–137.
[55] M. T. Ashby, J. H. Enemark, *Organometallics* **1987**, *6*, 1323–1327.
[56] H. Adams, N. A. Bailey, A. N. Day, M. J. Morris, M. M. Harrison, *J. Organomet. Chem.* **1991**, *407*, 247–258.
[57] A. L. Serrano, M. A. Casado, M. A. Ciriano, B. de Bruin, J. A. López, C. Tejel, *Inorg. Chem.* **2016**, *55*, 828–839.
[58] A. Antiñolo, S. García-Yuste, I. Lopez-Solera, A. Otero, J. C. Pérez-Flores, R. Reguillo-Carmona, E. Villaseñor, E. Santos, E. Zuidema, C. Bo, *Dalton Trans.* **2010**, *39*, 1962–1971.
[59] C. Huang, H. Liu, J. Zhang, Z. Duan, F. Mathey, *Eur. J. Inorg. Chem.* **2010**, 5498–5502.
[60] D. A. M. Kurtz, K. R. Brereton, K. P. Ruoff, H. M. Tang, G. A. N. Felton, A. J. M. Miller, J. L. Dempsey, *Inorg. Chem.* **2018**, *57*, 5389–5399.
[61] D. Álvarez, R. Mera-Adasme, L. Riera, G. I. Cárdenas-Jirón, J. Pérez, J. Díaz, M. I. Menéndez, R. López, *Inorg. Chem.* **2017**, *56*, 6652–6661.
[62] a) C. Gonzalez, H. B. Schlegel, *J. Chem. Phys.* **1989**, *90*, 2154–2161; b) C. Gonzalez, H. B. Schlegel, *J. Phys. Chem.* **1990**, *94*, 5523–5527.
[63] a) C. Riplinger, F. Neese, *J. Chem. Phys.* **2013**, *138*, 034106–18; b) C. Riplinger, B. Sandhoefer, A. Hansen, F. Neese, *J. Chem. Phys.* **2013**, *139*, 134101–13.
[64] a) F. Weigend, R. Ahlrichs, *Phys. Chem. Chem. Phys.* **2005**, *7*, 3297–3305; b) D. Andrae, U. Haeussermann, M. Dolg, H. Stoll, H. Preuss, *Theor. Chim. Acta* **1990**, *77*, 123–141.
[65] a) V. Barone, M. Cossi, *J. Phys. Chem. A* **1998**, *102*, 1995–2001; b) J. L. Pascual-Ahuir, E. Silla, *J. Comput. Chem.* **1990**, *11*, 1047–1060; c) J. L. Pascual-Ahuir, E. Silla, I. Tuñón, *J. Comput. Chem.* **1991**, *12*, 1077–1088; d) J. L. Pascual-Ahuir, E. Silla, I. Tunón, *J. Comput. Chem.* **1994**, *15*, 1127–1138; e) T. N. Truong, E. V. Stefanovich, *Chem. Phys. Lett.* **1995**, *240*, 253–260.
[66] T. J. Lee, P. R. Taylor, *Int. J. Quantum Chem.* **1989**, *36*, 199–207.
[67] D. G. Liakos, F. Neese, *J. Chem. Theory Comput.* **2015**, *11*, 4054–4063.
[68] D. A. McQuarrie, *Statistical Mechanics*, Harper and Row: New York, **1976**.
[69] R. F. Ribeiro, A. V. Marenich, C. J. Cramer, D. G. Truhlar, *J. Phys. Chem. B* **2011**, *115*, 14556–14562.
[70] a) E. D. Glendening, A. E. Reed, J. E. Carpenter, F. Weinhold, *NBO Version 3.1.*; University of Wisconsin: Madison, WI, **2012**; b) F. Weinhold, C. R. Landis, *Valency and Bonding: A Natural Bond Orbital Donor-Acceptor Perspective*; Cambridge University Press: Cambridge, **2005**.
[71] M. J. Frisch, G. W. Trucks, H. B. Schlegel, G. E. Scuseria, M. A. Robb, J. R. Cheeseman, G. Scalmani, V. Barone, B. Mennucci, G. A. Petersson, H. Nakatsuji, M. Caricato, X. Li, H. P. Hratchian, A. F. Izmaylov, J. Bloino, G. Zheng, J. L. Sonnenberg, M. Hada, M. Ehara, K. Toyota, R. Fukuda, J. Hasegawa, M. Ishida, T. Nakajima, Y. Honda, O. Kitao, H. Nakai, T. Vreven, J. A. Montgomery Jr., J. E. Peralta, F. Ogliaro, M. Bearpark, J. J. Heyd, E. Brothers, K. N. Kudin, V. N. Staroverov, R. Kobayashi, J. Normand, K. Raghavachari, A. Rendell, J. C. Burant, S. S. Iyengar, J. Tomasi, M. Cossi, N. Rega, J. M. Millam, M. Klene, J. E. Knox, J. B. Cross, V. Bakken, C. Adamo, J. Jaramillo, R. Gomperts, R. E. Stratmann, O. Yazyev, A. J. Austin, R. Cammi, C. Pomelli, J. W. Ochterski, R. L. Martin, K. Morokuma, V. G. Zakrzewski, G. A. Voth, P. Salvador, J. J. Dannenberg, S. Dapprich, A. D. Daniels, Ö. Farkas, J. B. Foresman, J. V. Ortiz, J. Cioslowski, D. J. Fox, Gaussian 09, Revision A.1, Gaussian, Inc., Wallingford CT, **2009**.
[72] a) X. Fradera, M. A. Austen, R. F. W. Bader, *J. Phys. Chem. A* **1999**, *103*, 304–314; b) X. Fradera, J. Poater, S. Simon, M. Durán, M. Solá, *Theor. Chem. Acc.* **2002**, *108*, 214–224.
[73] T. A. Keith, *AIMAll program*, Version 10.12.11, **2010**.
[74] a) R. F. W. Bader, *Atoms in Molecules. A Quantum Theory*; University Press: Oxford, **1990**; b) R. F. W. Bader, *Chem. Rev.* **1991**, *91*, 893–928.
[75] F. Neese, Software Update: The ORCA Program System, Version 4.0.1, *WIREs Comput. Mol. Sci.* **2018**, *8*: e1327. DOI: https://doi.org/10.1002/wcms.1327.

Received: November 7, 2019

## 5.3 Influence of the Nucleophilic Ligand on the Reactivity of Carbonyl Rhenium(I) Complexes towards Methyl Propiolate: A Computational Chemistry Perspective

Daniel Álvarez , Elena López-Castro, Arturo Guerrero, Lucía Riera, Julio Pérez, Jesús Díaz, M. Isabel Menéndez, and Ramón López

*Molecules* **2020**, *25*, 4134-4153

molecules

MDPI

Article

# Influence of the Nucleophilic Ligand on the Reactivity of Carbonyl Rhenium(I) Complexes towards Methyl Propiolate: A Computational Chemistry Perspective

**Daniel Álvarez [1], Elena López-Castro [1], Arturo Guerrero [1], Lucía Riera [2], Julio Pérez [2,3], Jesús Díaz [4], M. Isabel Menéndez [1] and Ramón López [1,*]**

1 Departamento de Química Física y Analítica, Universidad de Oviedo, C/Julián Clavería 8, 33006 Oviedo, Asturias, Spain; alvarezldaniel@uniovi.es (D.Á.); elena.castro.lpz@gmail.com (E.L.-C.); uo244375@uniovi.es (A.G.); isabel@uniovi.es (M.I.M.)

2 Centro de Investigación en Nanomateriales y Nanotecnología (CINN), CSIC-Universidad de Oviedo-Principado de Asturias, Avenida de la Vega 4-6, 33940 El Entrego, Spain; l.riera@cinn.es (L.R.); japm@uniovi.es (J.P.)

3 Departamento de Química Orgánica e Inorgánica, Facultad de Química, Universidad de Oviedo, C/ Julián Clavería 8, 33006 Oviedo, Spain

4 Departamento de Química Orgánica e Inorgánica, Universidad de Extremadura, Avenida de la Universidad s/n, 10071 Cáceres, Extremadura, Spain; jdal@unex.es

* Correspondence: rlopez@uniovi.es; Tel.: +34-985-102-967

Academic Editor: Athanassios C Tsipis

Received: 11 August 2020; Accepted: 7 September 2020; Published: 10 September 2020


**Abstract:** A comparative theoretical study on the reactivity of the complexes [ReY(CO)$_3$(bipy)] (Y = NH$_2$, NHMe, NH*p*Tol, OH, OMe, OPh, PH$_2$, PHMe, PMe$_2$, PHPh, PPh$_2$, PMePh, SH, SMe, SPh; bipy = 2,2′-bipyridine) towards methyl propiolate was carried out to analyze the influence of both the heteroatom (N, O, P, S) and the alkyl and/or aryl substituents of the Y ligand on the nature of the product obtained. The methyl substituent tends to accelerate the reactions. However, an aromatic ring bonded to N and O makes the reaction more difficult, whereas its linkage to P and S favour it. On the whole, ligands with O and S heteroatoms seem to disfavour these processes more than ligands with N and P heteroatoms, respectively. Phosphido and thiolato ligands tend to yield a coupling product with the bipy ligand, which is not the general case for hydroxo, alcoxo or amido ligands. When the Y ligand has an O/N and an H atom the most likely product is the one containing a coupling with the carbonyl ligand, which is not always obtained when Y contains P/S. Only for OMe and OPh, the product resulting from formal insertion into the Re-Y bond is the preferred.

**Keywords:** organometallic chemistry; rhenium complexes; activated alkynes; computational chemistry; reaction mechanisms

## 1. Introduction

Rhenium(I) *fac*-tricarbonyl complexes bearing conjugated diimine bidentate ligands (i.e., bipyridines, phenanthrolines, etc.) and neutral or anionic monodentate ligands (e.g., halides, pyridines, aqua, phosphines, alkyls, etc.) are functional molecules with applications in several important areas, such as catalytic reduction of $CO_2$ [1–16], luminescence [17–30], medicinal chemistry [31–46], supramolecular chemistry [47], etc. We reported, among others, the synthesis of the complexes [ReY(CO)$_3$(N-N)] (Y = alkoxo [48,49], amido [50,51], hydroxo [52], phosphido [53,54], thiolato [55]; N-N = 2,2′-bipyridine (bipy) and/or 1,10 phenanthroline (phen)). The Y ligand in these complexes bears one or more lone electron pairs. Due to their filled $d^6$ electron configuration, the Y ligands cannot act as π-donors in these complexes (see Supporting Information for more details). On the other hand, the kinetically

inert character of these $d^6$ third row complexes prevents the formation of Y-bridged polynuclear species. These new compounds showed different reactivity patterns when reacting towards activated alkynes such as methyl propiolate ($HC{\equiv}CCO_2Me$ = HMAD) and/or dimethylacetylenedicarboxylate ($MeO_2CC{\equiv}CCO_2Me$ = DMAD). The first step is common and consists in a nucleophilic attack from the heteroatom (O, N, P) of the Y ligand onto an acetylene carbon atom, generating a zwitteronic species, which evolves to afford different types of products [56]. Specifically, the Re complexes with Y = NH*p*Tol (*para*-tolylamido) and OH (hydroxo) led to the formation of a coupling product with one of the carbonyl ligands in *cis* disposition to Y. This carbonyl oxygen is protonated while the N and O atoms of the Y ligand have lost their respective hydrogen atoms (see **A** in Scheme 1, **P*ccoh*** products). It is thought that there is another stable species prior to the formation of **P*ccoh***, denoted as **P*cco***, where the carbonyl oxygen is not protonated while the N and O atoms of the Y ligand still display the hydrogen atom [51,52]. A coupling product with one of the non-subtituted *ortho* carbons of the bidentate ligand was obtained for the Re complex containing the diphenylphosphanido ($PPh_2$) ligand (see **B** in Scheme 1, **P*ccb*** products) [53,54]. Finally, for the Re methoxo (OMe) complex, the product obtained corresponds to the alkyne insertion into the Re-OMe bond (see **C** in Scheme 1, **P*ins*** products) [48].

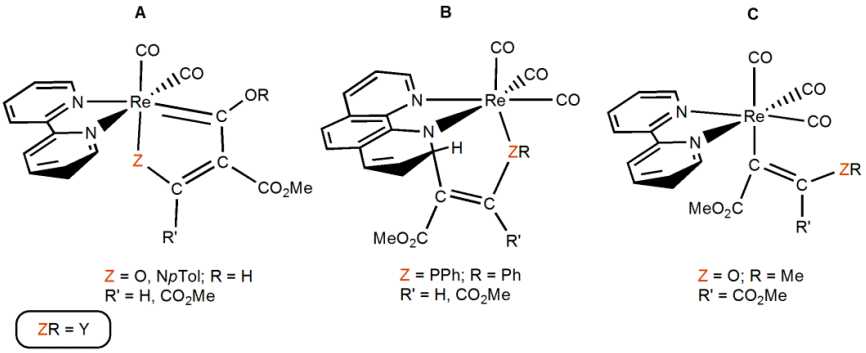


**Scheme 1.** Types of products experimentally obtained in the reaction of $[ReY(CO)_3(N\text{-}N)]$ (Y = NH*p*Tol, OH, OMe, $PPh_2$; N-N = bipy and/or phen) with activated alkynes and herein denoted as **A** (**P*ccoh***), **B** (**P*ccb***), and **C** (**P*ins***).

Our theoretical investigations on the reaction between the complexes $[ReY(CO)_3(bipy)]$ (Y = NH*p*Tol, OH, OMe, $PPh_2$) and HMAD uncovered that the reaction rate is, on the whole, controlled by the first stage of the reaction mechanism, that is, the nucleophilic attack of the Y ligand on the non-substituted alkyne carbon [57,58]. Nonetheless, the subtle balance between kinetics and thermodynamics of the formation step of the plausible products determines the type of product formed. While this detailed investigation was relevant to understand these processes, an overlap of different factors in the nucleophilic Y ligand complicates a clear rationalization of the reactivity trends and therefore hinders the attempts to obtain the relevant information for developing new rhenium complexes. Two simultaneous factors are present in the Y ligand of the Re complex, namely the donor atom directly linked to Re (O, N, P) and the nature of its substituents (one or two hydrogen, alkyl, aryl groups). For instance, we noted that the results obtained for the Re hydroxo and methoxo complexes allow us to understand the effect of an alkyl substituent, but not the effect of an aryl one. By contrast, the comparison between the NH*p*Tol and $PPh_2$ cases is not reliable to rationalize either the effect of an aryl group or the effect of the donor atom directly linked to Re. The situation is even worse if we wanted to extract chemical trends when comparing the four cases mentioned above at the same time. The results obtained for the reactivity of the $[Re(PPh_2)(CO)_3(bipy)]$ complex are not comparable with those found for $[ReY(CO)_3(bipy)]$ (Y = OH, OMe) because there are different substituents and donor atoms belonging to different groups of the Periodic System.

Therefore, to get more general conclusions about these processes, ultimately aiming at tuning the Re complexes in order to obtain more interesting synthetic, industrial or biochemical applications [59,60], a more systematic computational investigation is needed. To accomplish this task, we undertook a

theoretical study on the reaction mechanism of the reactivity towards the substrate HMAD of the complexes [ReY(CO)$_3$(bipy)] (Y = $NH_2$, NHMe, OPh, $PH_2$, PHMe, $PMe_2$, PHPh, PMePh, SH, SMe, SPh). The theoretical results obtained on these hypothetical reactions along with those previously found for the reactivity between the complexes [ReY(CO)$_3$(bipy)] (Y = NH*p*Tol, OH, OMe, $PPh_2$) and HMAD may be beneficial in gaining a broader understanding of the effect of Y ligand focusing on the alkyl and aryl substituents and the heteroatom directly bonded to Re.

## 2. Results

The presentation and analysis of the results obtained for the reaction between the 15 complexes [ReY(CO)$_3$(bipy)] (Y = $NH_2$, NHMe, NH*p*Tol, OH, OMe, OPh, $PH_2$, PHMe, $PMe_2$, PHPh, $PPh_2$, PMePh, SH, SMe, SPh) and HMAD will be done as follows. First, we will report a general description of the types of potential energy surfaces found taking into consideration our DLPNO-CCSD(T) data. Second, we will analyze the effect of alkyl and aryl substituents at the nucleophilic ligand Y on the energetics of the reactive processes investigated. The same objective will be pursued when analyzing the influence of replacing, within Groups 15 and 16, the heteroatom of the second period by its counterpart of the third period (i.e., P instead of N). Finally, we will provide a general discussion by considering all the results mentioned in the previous subsections.

### *2.1. General Description of the Potential Energy Surfaces*

As just mentioned in the Introduction section, experimental studies on the reactivity of the complexes [ReY(CO)$_3$(N-N)] (Y = NH*p*Tol, OH, OMe, $PPh_2$; N-N = bipy and/or phen) towards activated alkynes (HMAD and/or DMAD) have shown the formation of three types of products (see Scheme 1) [48,51–54]. Theoretical investigations using the bipy ligand and the HMAD activated alkyne have not only corroborated the formation of such products, but also shown all the species involved in the reaction mechanisms leading to the **P*cco*/P*ccoh***, **P*ccb***, and **P*ins*** products [57,58]. Looking at the reaction mechanisms involved, three different patterns of potential energy surfaces (PES) were found [58]. The type-I PES found for Y = OH and $PPh_2$ starts with the nucleophilic attack of the Y ligand on the non-substituted acetylenic carbon of HMAD (C1) through the TS **TS1** to give a zwitterionic intermediate (**I1**), in which a new HO/$Ph_2$P-C1 bond is formed and, consequently, the original triple bond between C1 and the substituted acetylenic carbon of the HMAD fragment (C2) presents now a double bond character (see Scheme 2). Evolving via **TS1′**, **I1** isomerizes into another intermediate (**I1′**) wherein C2 is readily oriented to yield any of the products. **I1′** is the common precursor species of **P*cco*/P*ccoh***, **P*ccb***, and **P*ins*** via the TS **TS2*cco***, **TS2*ccb***, and **TS2*ins***, respectively (see Scheme 2). For OH, **P*cco*** evolves to **P*ccoh*** through an intermolecular transformation with a Gibbs energy barrier lower than that found for the nucleophilic attack step [58]. This fact along with the greater stability of **P*ccoh*** over **P*cco*** explains the formation of the former product as experimentally observed [52]. A different PES named as type II was found for OMe (see Scheme 3). Reactants evolve to **I1** via **TS1**, which in turn directly transforms into **P*cco*** via **TS1′**. **P*cco*** is now the species from which the products **P*ccb*** and **P*ins*** are formed via **TS2*ccb*** and **TS2*ins***, respectively. All these species show structures analogous to those identified with the same acronyms on the type-I PES. The type-III PES was obtained for the NH*p*Tol case wherein two splitting species were found, the first one being the reactants (see Scheme 4). On the one hand, reactants may become **I1**, first, and then **P*cco*** passing through **TS1** and **TS1′**, respectively. **P*cco*** can lead to either **P*ccoh*** as in the OH case [58] or **P*ins*** via **TS2*ins***. On the other hand, reactants may proceed through **TS1*b*** for the attack of the NH*p*Tol ligand on the C1 atom of the alkyne fragment, which is oriented in the opposite direction to that presented at **TS1** or **TS1′** (see Scheme 4 and Figure 1). **TS1*b*** evolves to the corresponding intermediate **I1*b***, in which the new H*p*TolN-C1 bond is just established. **I1*b*** becomes an isomer **I1′*b*** without any TS to finally give **P*ccb*** via **TS2*ccb***. **I1′*b*** mainly differs from **I1*b*** in the orientation of the C2-bonded $CO_2$Me group of the alkyne moiety. This group and the C1-bonded H atom are on opposite sides of the C1=C2 double bond at **I1*b***, while at **I1′b** they are on the same side to favour the attack of C2 on the bipy ligand

(see Scheme 4 and Figure 1). All the species implied in the reaction mechanism for the formation of **P*ccoh*** and **P*ins*** display structures analogous to those denoted with the same acronyms on the type-I and II PES. However, for the reaction mechanism leading to **P*ccb***, the geometry discrepancy mentioned above between **TS1*b*** and **TS1** or **TS1′** is also present when comparing **I1*b*** and **I1′*b*** with **I1** and **I1′** (when located for OH and $PPh_2$), respectively (see Figure 1). In addition, we also note that the plane defined by the heteroatom of the NH*p*Tol ligand, C1, and C2 is practically perpendicular to the plane defined by Re and the bipy ligand at **I1′**, while an almost parallel disposition between these planes was located at **I1′*b***. A similar geometry difference was detected when comparing the TS **TS2*ccb*** located for OH and $PPh_2$ with the one found for NH*p*Tol (see, for instance, **TS2*ccb*** for $PPh_2$ and NH*p*Tol in Figure 1). Intermediates analogous to **I1*b*** and/or **I1′*b*** were also located when Y = OH, OMe, and $PPh_2$, but **TS2*ccb*** connects **P*ccb*** with **I1′** (**P*cco*** for the OMe case) instead of **I1*b*** and/or **I1′*b*** [58].

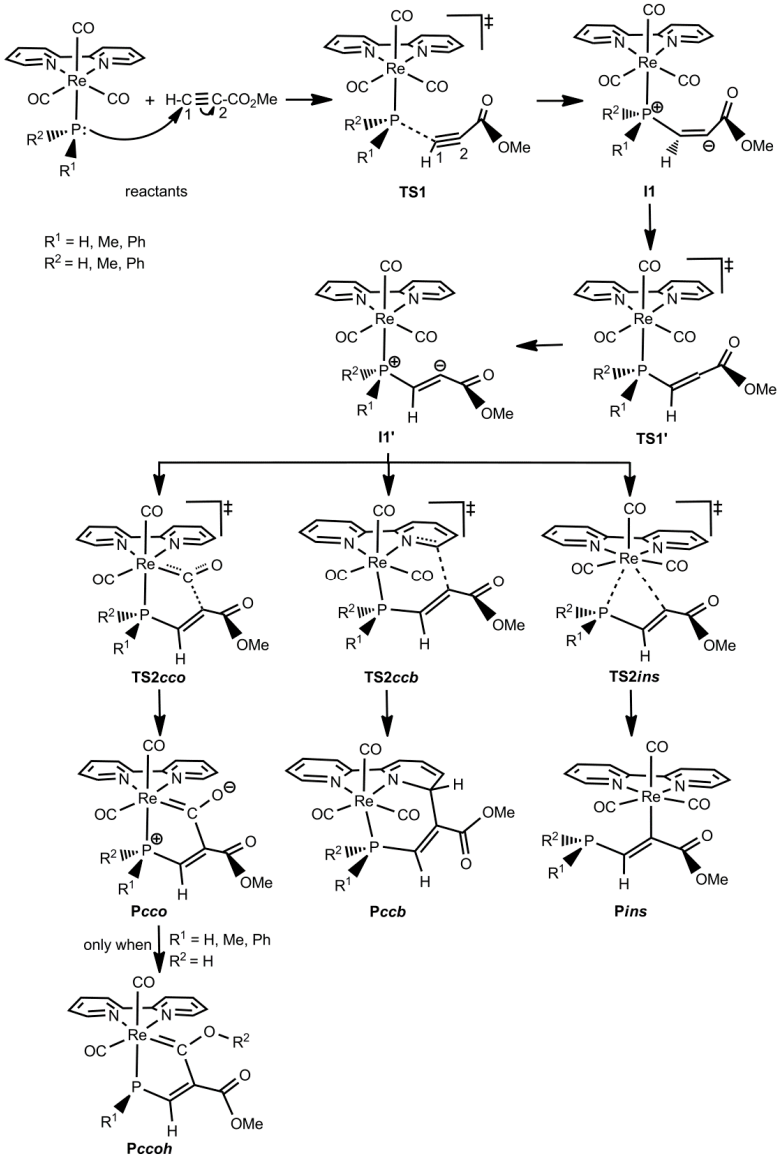


**Scheme 2.** Schematic structures of the species located on the type-I potential energy surfaces (PES) found for the reaction of the complexes $[ReY(CO)_3(bipy)]$ (Y = $PR^1R^2$ with $R^1$ = $R^2$ = H, Me, Ph) towards HMAD. The connectivities among these species are also shown with arrows. Acetylenic carbon atoms of HMAD are numbered both in the isolated reactant and in **TS1**. Analogous structures were found for the Re complex with Y = OH.

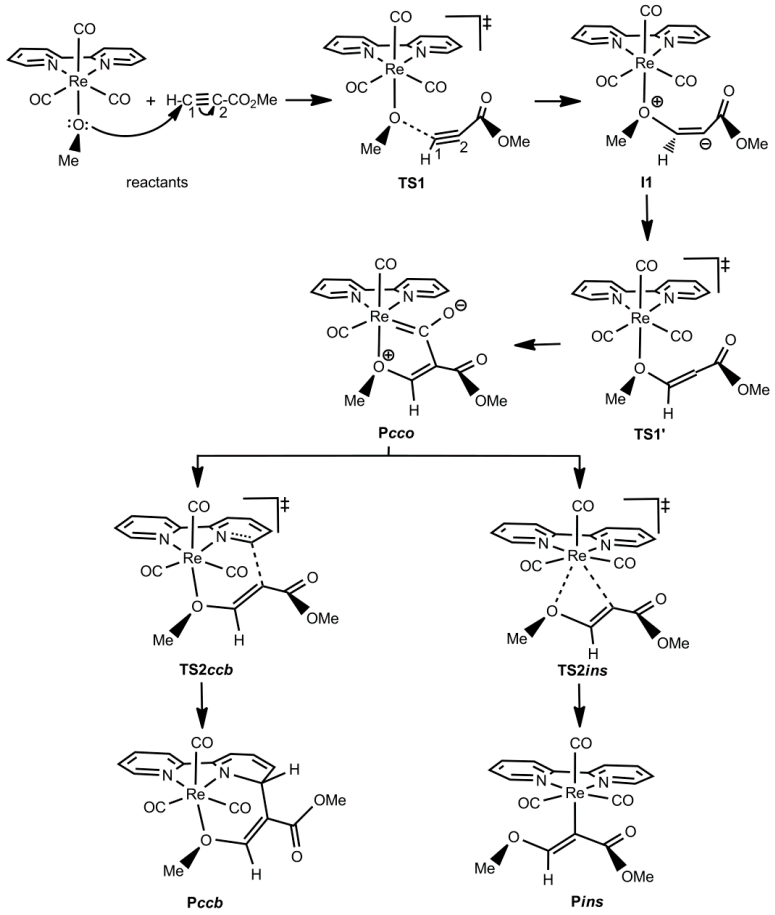


**Scheme 3.** Schematic structures of the species located on the type-II PES found for the reaction of the complex [Re(OMe)(CO)$_3$(bipy)] towards HMAD. The connectivities among these species are also shown with arrows. Acetylenic carbon atoms of HMAD are numbered both in the isolated reactant and in **TS1**.

With all of this in mind, we extended our theoretical mechanistic investigation by considering the new nucleophilic ligands $NH_2$, NHMe, OPh, $PH_2$, PHMe, $PMe_2$, PHPh, PMePh, SH, SMe, and SPh. All the geometry and energy data of the species located are collected in the Supporting Information (Figures S1–S11 and Tables S1–S33). For comparison purposes, data previously reported for the analogous Re complexes with Y = NH*p*Tol, OH, OMe, and $PPh_2$ have also been included in the Supporting Information (Figures S12–S15 and Tables S34–S45). All the PES found can be grouped according to the number of splitting species and the type of the first splitting species. First, all the Re complexes with a nucleophilic ligand containing a phosphorus atom directly linked to the metal center present the type-I PES as **I1′** is the only splitting species (see Scheme 2). All the optimized structures for the five ligands with P and denoted with the same acronyms as in Scheme 2 are analogous to those previously reported for the $PPh_2$ case [58]. The PES obtained for the nucleophilic ligands $NH_2$, NHMe, SH, SMe, and SPh resemble the type III (see Scheme 4), since a separate channel to **P*ccb*** is found from the reactants, although with some differences among them. Particularly, for SH and SPh **I1** (instead of **P*cco***) is the second splitting species that connects reactants with **P*cco*** (**P*ccoh*** for SH) and **P*ins***. The transformations reactants → **I1**, **I1** → **P*cco***/**P*ccoh***, and **I1** → **P*ins*** are controlled by **TS1**, **TS2*cco***, and **TS2*ins***, respectively. For $NH_2$, NHMe, and SMe **I1′** (instead of **P*cco***) is the second splitting species, which in turn may transform into **P*cco*** (**P*ccoh*** for $NH_2$ and NHMe) and **P*ins***. The evolution to these products from the reactants is the same as that found for the generation of **P*cco***/**P*ccoh*** and **P*ins*** with the OH and $PR^1R^2$ ($R^1$ = $R^2$ = H, Me, Ph) ligands (see Scheme 2). Despite these differences in the type-III PES obtained, all the species implied in the reaction mechanism leading

to **P*cco*/P*ccoh*** and **P*ins*** with Y = $NH_2$, NHMe, SH, SMe, and SPh show optimized structures similar to those identified with the same acronyms for NH*p*Tol, OH, OMe, and $PPh_2$ (see Schemes 2–4), except **I1** when Y = SH and SPh, whose respective optimized structures are analogous to those found for the type-**I1′** species (see Figure 1). For the reaction mechanism leading to **P*ccb*** when Y = $NH_2$, NHMe, SH, SMe, and SPh, the optimized structures of all the species found (**TS1*b***, **I1*b***, **I1′*b***, **TS2*ccb***, and **P*ccb***) are similar to those of their analogues when Y = NH*p*Tol (see Scheme 4 and Figure 1). Finally, the OPh case uncovers a new mode of PES, type IV, where reactants proceed through **TS1** to **I1** (see Scheme 5). This intermediate resulting from the attack of the nucleophilic ligand on the HMAD non-substituted carbon is the splitting species now and can evolve either to **P*cco*** without any barrier to subsequently transform into **P*ins*** via **TS2*ins*** or to **P*ccb*** via **TS2*ccb***. As for SH and SPh, the optimized structure of **I1** resembles that of **I1′** when Y = $NH_2$, NHMe, OH, $PR^1R^2$, and SMe. The remaining species found on the type-IV PES display structures similar to those denoted with the same acronyms in Schemes 2–4.

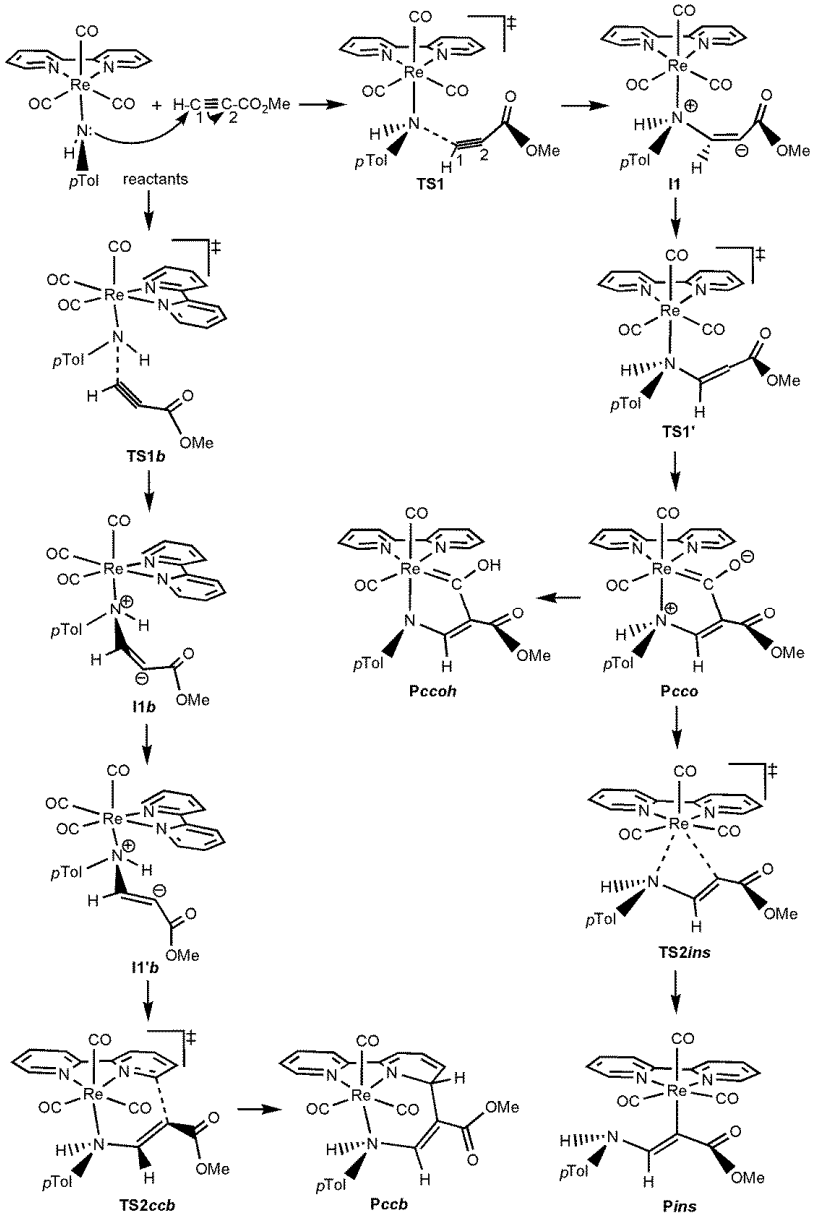


**Scheme 4.** Schematic structures of the species located on the type-III PES found for the reaction of the complex [Re(NH*p*Tol)$(CO)_3$(bipy)] towards HMAD. The connectivities among these species are also shown with arrows. Acetylenic carbon atoms of HMAD are numbered both in the isolated reactant and in **TS1**.

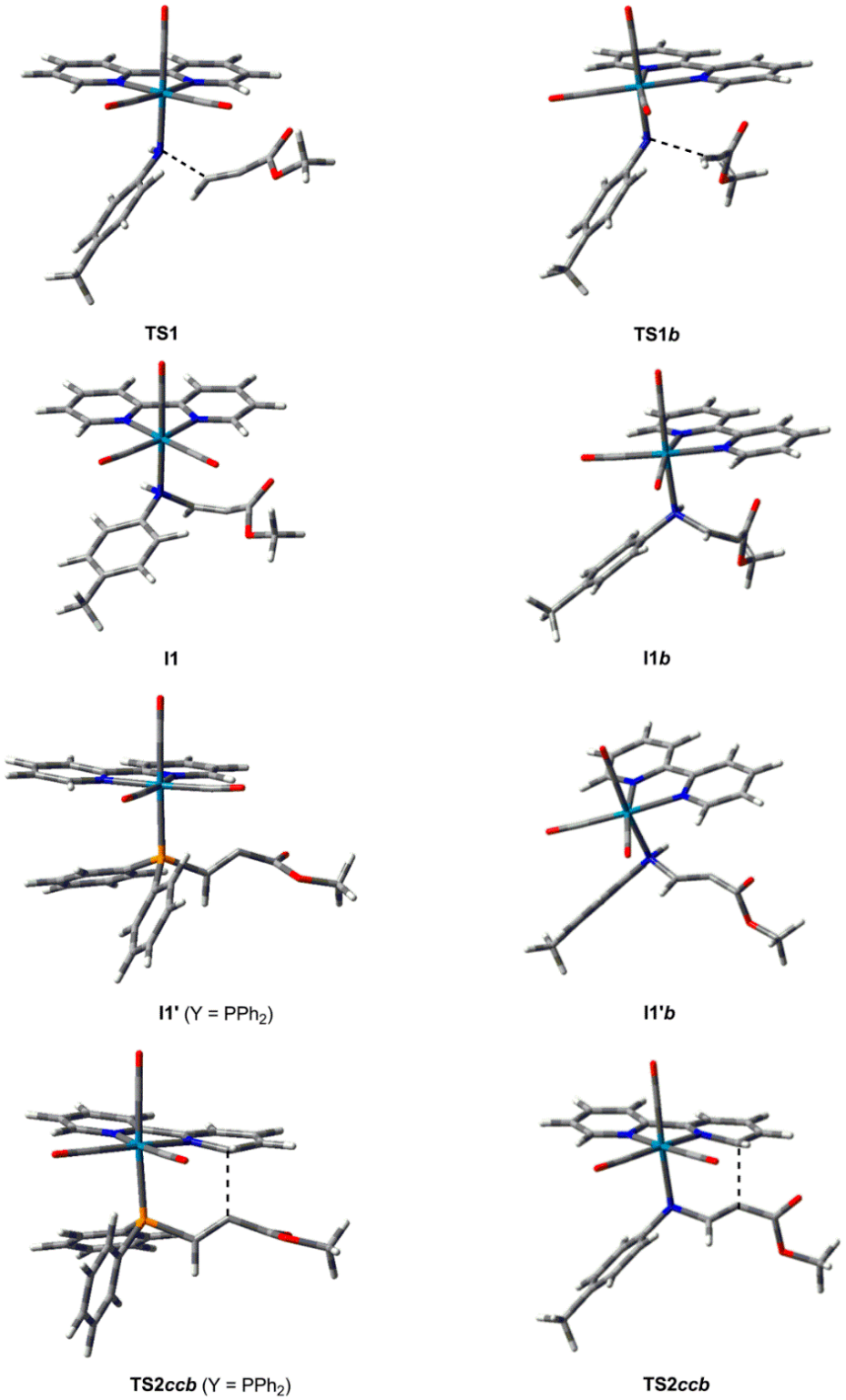


**Figure 1.** B3LYP optimized structures of some species located for the reaction of the complex [Re(NH*p*Tol)(CO)$_3$(bipy)] towards HMAD. B3LYP optimized structures of **I1′** and **TS2*ccb*** for Y = PPh$_2$ are also given for comparison purposes.

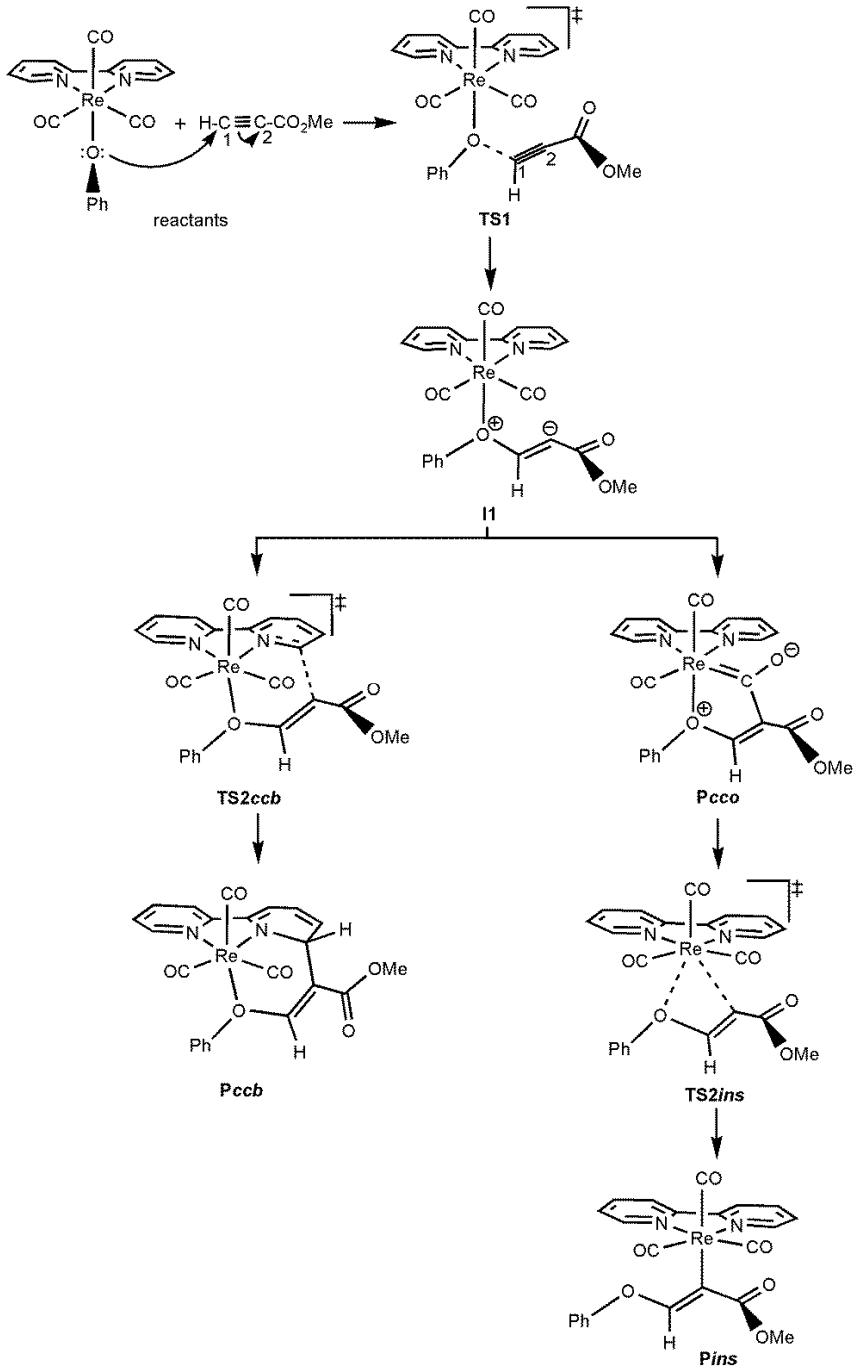


**Scheme 5.** Schematic structures of the species located on the type-IV PES found for the reaction of the complex [Re(OPh)(CO)$_3$(bipy)] towards HMAD. The connectivities among these species are also shown with arrows. Acetylenic carbon atoms of HMAD are numbered both in the isolated reactant and in **TS1**.

A general view of Schemes 2–5 shows that only those Y ligands with N and S atoms display the alternative route reactants → **TS1*b*** → **I1*b*** → **I1′*b*** → **TS2*ccb*** → **P*ccb***. While **I1*b*** and/or **I1′*b*** are expected to exist for $PH_2$, PHMe, $PMe_2$, PHPh, PMePh, and OPh, computations show that **TS2*ccb*** connects **P*ccb*** with **I1′** for the five ligands containing the phosphorus atom as for the OH and $PPh_2$ (see Scheme 2) and with **I1** when Y = OPh (see Scheme 5). Besides, OMe and OPh ligands are the only ones whose PES do not present intermediate **I1′**. This is a consequence of the geometry of their **I1** intermediates, whose lone pair at the C2 atom of HMAD is quite close to the electrophilic positions in the equatorial ligands, which avoid the existence of an intermediate such as **I1′** with that lone pair ready but not reacting with these positions.

### 2.2. *Effect of the Alkyl and Aryl Substituents of the Nucleophilic Ligand*

The substitution of one of the hydrogen atoms in the $NH_2$ ligand by a methyl group causes a relative stabilization of all the species between 1.3 and 7.4 kcal/mol, except **I1**, which slightly destabilizes by 0.8 kcal/mol (see Table S46). It is interesting to note that such a replacement relatively stabilizes **TS1*b*** from 19.3 to 14.0 kcal/mol whereas **TS1** only changes from 18.5 kcal/mol to 17.2 kcal/mol when going from $NH_2$ to NHMe (see Table 1). Since **TS1** and **TS1*b*** are the rate limiting steps for both alternative routes, the presence of the methyl substituent would change the preferred product from **P*ccoh*** (−24.9 kcal/mol) for $NH_2$ to **P*ccb*** (−19.3 kcal/mol) for NHMe without changing the kind of PES (type-III). The replacement of one of the hydrogen atoms in the $NH_2$ ligand by an aryl substituent (pTol), as in NHpTol, shows the opposite effect since all the species relatively destabilize between 2.1 and 14.8 kcal/mol (see Table S46). As seen in Table 1, the reaction channel controlled by **TS1** leading to **P*cco***/**P*ccoh*** and **P*ins*** is only 1.0 kcal/mol larger in Gibbs energy than that controlled by **TS1*b*** leading to **P*ccb***. The small difference between these determining Gibbs energy barriers and the large stability of **P*ccoh*** (−21.1 kcal/mol) points to **P*ccoh*** as the expected product, as experimentally observed [51].

**Table 1.** Gibbs energy barriers, in kcal/mol, determined by the TS located along the reaction mechanisms found for the reaction between the complexes $[ReY(CO)_3(bipy)]$ (Y = $NH_2$, NHMe, NH*p*Tol, OH, OMe, OPh, $PH_2$, PHMe, $PMe_2$, PHPh, $PPh_2$, PMePh, SH, SMe, SPh) and HMAD at the DLPNO-CCSD(T) level. [1,2] Gibbs energy, in kcal/mol, of the plausible products referred to that of the respective separate reactants at the same level of theory and type of PES found for each Y ligand are also given.

| Y | TS1 | TS1′ | TS1*b* | TS2*cco* | TS2*ccb* | TS2*ins* | P*cco* (P*ccoh*) | P*ccb* | P*ins* | PES |
|---|---|---|---|---|---|---|---|---|---|---|
| $NH_2$ | **18.5** | **8.5** | 19.3 | **4.3** | 9.9 | 11.2 | −8.0 (**−24.9**) | −15.1 | −29.1 | III |
| NHMe | 17.2 | 4.3 | **14.0** | 0.7 | **9.6** | 9.2 | −12.4 (−32.3) | **−19.3** | −31.2 | III |
| NH*p*Tol | **22.4** | **17.0** | 21.4 | | 19.0 | 20.6 | −0.2 (**−21.1** [3]) | −5.1 | −22.4 | III |
| OH | **27.0** | **28.0** | | **26.8** | 31.2 | 28.3 | 15.2 (**−12.0** [3]) | 8.1 | −13.7 | I |
| OMe | **25.9** | **24.8** | | | 29.5 | **24.0** | **9.9** | 4.9 | **−16.4** [3] | II |
| OPh | **33.5** | | | | 38.8 | **36.5** | 24.2 | 16.2 | **−5.6** | IV |
| $PH_2$ | **27.6** | **14.6** | | 13.5 | **13.5** | 34.2 | 0.1 (0.3) | **−9.5** | −13.1 | I |
| PHMe | **30.9** | **6.2** | | 5.1 | **5.8** | 21.1 | −8.9 (−4.3) | **−16.3** | −18.3 | I |
| $PMe_2$ | **17.4** | **4.2** | | 5.6 | **4.3** | 20.3 | −17.3 | **−25.5** | −24.1 | I |
| PHPh | **17.6** | **9.7** | | 8.2 | **9.4** | 17.5 | −7.4 (−4.2) | **−12.8** | −17.5 | I |
| $PPh_2$ | **17.5** | **4.2** | | 5.2 | **5.0** | 20.6 | −9.3 | **−20.0** [3] | −16.8 | I |
| PMePh | **18.7** | **3.9** | | 3.7 | **5.1** | 18.7 | −11.6 | **−20.0** | −21.1 | I |
| SH | **32.7** | | 28.0 | **32.9** | 35.8 | 39.1 | 21.1 (**−2.6**) | 13.7 | −2.4 | III |
| SMe | 23.1 | 26.1 | **21.0** | 24.7 | **26.4** | 32.1 | 11.0 | **3.1** | −9.1 | III |
| SPh | 30.8 | | **25.6** | 29.0 | **31.0** | 34.8 | 14.4 | **8.9** | −5.7 | III |

[1] All the Gibbs energy barriers are determined with respect to the sum of the Gibbs energies of the respective separate reactants or with respect to the Gibbs energy of the immediately preceding intermediate when this species is more stable than the corresponding separate reactants. [2] Bold data show the most preferred reaction route. [3] The product theoretically preferred is consistent with available experimental data (see Scheme 1).

Let us now consider the case of the OR ligands (R = H, Me, OPh). Taking as reference the relative Gibbs energies of the species found for the OH case and comparing them with those for OMe and OPh (see Table S47), similar trends to those of the NHR′ (R′ = H, Me, pTol) ligands are found. Thus, all the species stabilize between 1.1 and 5.3 kcal/mol and destabilize between 6.5 and 9.0 kcal/mol when replacing OH by OMe and OPh, respectively. The presence of the alkyl substituent provokes a modification of the PES from type-I for OH to type-II for OMe (see Schemes 2 and 3). Besides, the product observed changes from **P*ccoh*** for OH ligand to **P*ins*** for OMe ligand in good agreement with experimental findings [48,52]. With both OH and OMe ligands **TS1** and **TS1′** compete against each other to be the rate-determining TS of the overall process; **TS1** is 1.0 kcal/mol more stable than **TS1′** for OH, while the reverse situation was found for OMe as **TS1** is 1.1 less stable than **TS1′** (see Table 1). A different situation was found for the OPh ligand. As collected in Table 1, contrary to the case with the OH ligand (yielding the **P*ccoh*** product), the expected product for the OPh ligand would be **P*ins***, since this product is the most stable structure (−5.6 kcal/mol) and the Gibbs energy barrier for its formation

($\Delta G^{\neq}$(**TS2*ins***) = 36.5 kcal/mol) is lower than that for the formation of the alternative product **P*ccb*** ($\Delta G^{\neq}$(**TS2*ccb***) = 38.8 kcal/mol). It has to be noted that the large values of both **TS1** (33.5 kcal/mol) and **TS2ins** make the reaction of OPh complex quite unlikely. In addition, the replacement of OH by OPh changes the PES from type-I to type-IV (see Schemes 2 and 5).

How are the trends described above when the alkyl and aryl substituents are bonded to phosphorus and sulfur atoms instead of nitrogen and oxygen, respectively? We start with ligands containing P and take $PH_2$ as the initial reference. As previously noted, all these ligands render the type-I PES (see Scheme 2); in all cases **TS1** is the rate-determining TS and the insertion route is highly penalized due to the large barrier of **TS2*ins*** ranging from 17.5 kcal/mol for Y = PHPh to 34.2 kcal/mol for Y = $PH_2$ (see Table 1). **TS2*cco*** and **TS2*ccb***, notably less unstable than **TS2*ins***, have similar Gibbs energy barriers, but **P*ccb*** is always much more stable than **P*cco***/**P*ccoh*** (see Table 1). Despite these similarities, particular features of each substituent deserve some comments. The substitution of the $PH_2$ ligand by the PHMe one relatively stabilizes all the structures between 4.6 and 13.1 kcal/mol, except **TS1**, which destabilizes by 3.3 kcal/mol (see Table S48). The alkyl substituent does not change the fact that **TS1** remains the rate-determining TS and **P*ccb*** is the expected product for both ligands (see Table 1). For the case of $PMe_2$ the presence of a second methyl group further stabilizes all the species, including **TS1 (**except **TS2*cco*** that is 0.5 kcal/mol larger for $PMe_2$ than for PHMe) making this ligand specially adequate to yield **P*ccb***. On the other hand, the substitution of $PH_2$ by PHPh also produces a relative stabilization of all the species, including **TS1**, between 3.3 and 16.7 kcal/mol (see Table S48). This trend is contrary to that found for the substitution of one H atom by an aromatic group in the Y ligands containing the N and O donor atoms. The presence of two Ph groups at $PPh_2$ futher stabilizes all the species between 0.1 and 7.2 kcal/mol with respect to PHPh, except **TS2*ins*** (17.5 kcal/mol for PHPh and 20.6 kcal/mol for $PPh_2$) and **P*ins*** (−17.5 kcal/mol for PHPh and −16.8 kcal/mol for $PPh_2$). As for the alkyl substitution cases, the presence of one or two aryl groups bonded to P also points to the formation of **P*ccb*** products due to their large stability (−12.8 and −20.0 kcal/mol for PHPh and $PPh_2$, respectively) and the accessible and competitive barriers for their generation (9.4 and 5.0 kcal/mol for PHPh and $PPh_2$, respectively). Whithin the accuracy of the computational level used, as seen in Table 1, $PMe_2$ and $PPh_2$ present very similar Gibbs energies for the TSs for all the reaction routes, being the largest difference that for **TS2*ccb***, which is lower for $PMe_2$ (4.3 kcalmol) than for $PPh_2$ (5.0 kcal/mol). Besides, all kinds of products are considerably more stable with the $PMe_2$ substituent. On the other hand, comparing the PHMe and PHPh cases, we see that the substitution of Me by Ph produces a destabilization of all the species between 0.1 and 4.7 kcal/mol except **TS1** and **TS2*ins***, which stabilize 13.3 and 3.6 kcal/mol, respectively (see Table S48). We have also considered the hybrid ligand PMePh, whose barriers parallel those of $PPh_2$ and slightly favour the coupling route with a carbonyl ligand but not as much as to change the preference for the formation of **P*ccb*** (see Table 1).

The three ligands SH, SMe, and SPh have in common the presence of **TS1*b*** (typical of the type-III PES collected in Scheme 4) leading to **P*ccb*** and the fact that the route to **P*ins*** has the largest barrier to yield the most stable product (see Table 1). The energy trends obtained for the SR ligands (R = H, Me, Ph) resemble those found for the $PR^1R^2$ ligands. Indeed, both the alkyl and aryl substituents give rise to a stabilization of all the species, mainly with the Me replacement in SH. In particular, the methyl substitution relatively stabilizes all the species in the gap 6.7−10.6 kcal/mol, whereas a relative stabilization range between 1.9 and 6.7 kcal/mol was obtained for the phenyl substitution (see Table S49). On the whole, the degree of stabilization due to SMe is less than when replacing OH by OMe. For SH, as seen in Table 1, the formation of **P*ccoh*** is preferred, since it has the smallest limiting barrier (32.9 kcal/mol for **TS2*cco***) and shows the largest stability (−2.6 kcal/mol). This image changes when replacing SH by SMe. Now, the barrier for **P*cco*** is still the smallest one (24.7 kcal/mol for **TS2*cco***) followed by the barrier to **P*ccb*** (26.4 kcal/mol for **TS2*ccb***), but **Pcco** is less stable (11.0 kcal/mol) than **P*ccb*** (3.1 kcal/mol), although both products are less stable than their isolated reactants (see Table 1). These reasons make difficult to suggest the preferred product for the SMe case. A similar picture was found for the SPh case in which **TS1** (30.8 kcal/mol) competes with **TS2*ccb*** (31.0 kcal/mol) and

both **P*cco*** (14.4 kcal/mol) and **P*ccb*** (8.9 kcal/mol) are higher in energy than their reactants. Actually, the barriers found the SH (~33 kcal/mol) and SPh (~31 kcal/mol) ligands indicate a low reaction probability with these ligands (see Table 1).

The previous analysis shows that ligands $NH_2$, OH, $PH_2$, and SH are bad nucleophiles (worsening from $NH_2$ to SH in the previous list) for the reaction between the corresponding Re complex and HMAD. On the one hand, a methyl group replacing one of the H atoms in these ligands enhances the process, since it reduces the barriers involved. In some cases, this substitution determines a change in the nature of the most favourable product. On the other hand, an aromatic ring bonded to N and O impairs the reaction, whereas when it is a substituent bonded to P and S the reverse effect is observed. Since the $\pi$ electrons in the aromatic ring are able to conjugate with the lone pair at N atom in the NH*p*Tol ligand this lone pair becomes less available for the nucleophilic attack on the HMAD molecule. The larger size of P prevents this conjugation, which explains the higher reactivity of PHPh compared to that of NH*p*Tol.

### *2.3. Effect of the Heteroatom of the Nucleophilic Ligand*

We now focus on the replacement of the heteroatom of the Y ligand when going from the second period to the third one along Groups 15 and 16 of the periodic table. The substitution of the nitrogen atom of $NH_2$ by phosphorus in $PH_2$ leads to an important relative destabilization of all the species between 5.1 and 25.2 kcal/mol (see Table S50). The rate-determining Gibbs energy barrier determined by **TS1**, goes from 18.5 kcal/mol for $NH_2$ to 27.6 kcal/mol for $PH_2$ (see Table 1). From $NH_2$ to $PH_2$, **TS2*cco***, **TS2*ccb***, and **TS2*ins***, increase by 9.2, 3.6, and 23.0 kcal/mol, respectively, being **P*ins*** remarkably kinetically penalized (see Table 1). Besides, the expected product changes from **P*ccoh*** for $NH_2$ to **P*ccb*** for $PH_2$. When comparing the NHMe and PHMe cases (see Table S50), all the species destabilize between 1.0 and 28.0 kcal/mol, except **I1**, which only stabilizes 0.3 kcal/mol and **TS2ccb** whose relative Gibbs energy changes from 9.6 kcal/mol for NHMe to 5.8 kcal/mol for PHMe (see Table 1). The Gibbs energy barriers for **P*cco***/**P*ccoh*** and **P*ins*** increase by 4.4 and 11.9 kcal/mol, respectively. When Y = NHMe there is a kinetics competition between **P*ccb*** and **P*cco***/**P*ccoh*** formation, as previously explained, whereas for PHMe, **P*ccb*** is clearly the preferred product (see Table 1). By contrast, the comparison of the results for the NHpTol and PHPh cases reflects that all the species stabilize when replacing N by P between 2.9 and 9.6 kcal/mol, except **Pccoh** and **Pins**, which destabilize 16.9 and 4.9 kcal/mol, respectively (see Table S50). Even **TS2*ins*** lowers its barrier, although it is still one of the largest. **P*ccoh*** is the product formed for NHpTol, in good agreement with experimental evidences [51], while **P*ccb*** is expected to be formed when [Re(PHPh)$(CO)_3$(bipy)] reacts with HMAD. In the presence of an aromatic ring, its available conjugation with the N atom, which does not occur with the P atom, overcomes the destabilization observed in the two previous cases (see below).

On the other hand, for Group 16, the substitution of OH by SH relatively destabilizes all the species between 4.6 and 11.3 kcal/mol as it was found when replacing $NH_2$ by $PH_2$ (see Table S51). Again, **TS2*ins*** is the most penalized TS and, in this case, **P*ccoh*** remains as the preferred product for both ligands. On the whole, the replacement of OMe by SMe show trends similar to those found when replacing NHMe by PHMe. Most of the species destabilize between 1.1 and 8.1 kcal/mol, whereas **TS1**, **TS2*ccb***, and **P*ccb***, stabilize by 2.8, 3.1, and 1.8 kcal/mol, respectively (see Table S51). As deduced from Table 1, **P*ins*** becomes again the most kinetically penalized product as found for the PHR (R = H, Me, Ph) ligands. **P*cco*** and **P*ccb*** compete with each other to be the preferred product for SMe while **P*ins*** is the most stable one. In contrast, when replacing OPh by SPh, all the species stabilize between 0.1 and 9.8 kcal/mol. **TS1**, **TS2*ccb***, and **TS2*ins*** (**TS2*cco*** was not located for OPh) become 2.7, 7.8, and 1.7 kcal/mol more stable when going from OPh to SPh, with **TS2*ins*** again the highest in energy (see Table 1 and Table S51). As previously said, for OPh **P*ins*** is the expected product, which changes to a competition between **P*cco*** and **P*ccb*** for SPh, although both OPh and SPh ligands are quite unreactive towards HMAD.

With respect to the heteroatom of the Y ligand directly linked to Re, it is clear that the insertion route is greatly penalized for P and S ligands, although **P*ins*** is very stable. This fact can be atributed to the strong bond formed between these large atoms and Re, which is weaker in the case of N and O atoms, as later explained. This bond needs to be broken for the insertion of the HMAD fragment in the Re-Y bond. Besides, P and S ligands tend to yield **P*ccb*** as the main product, which is not the general case for O and N ones. On the other hand, when the Y ligand has an O/N heteroatom bonded to an H atom the most probable product is **P*ccoh***, which is not always obtained when Y contains P/S.

### *2.4. General Discussion*

The investigation on the reaction mechanism of the reactivity of the 15 Re complexes [ReY(CO)$_3$(bipy)] (Y = NH$_2$, NHMe, NHpTol, OH, OMe, OPh, PH$_2$, PHMe, PMe$_2$, PHPh, PPh$_2$, PMePh, SH, SMe, SPh) towards HMAD displayed a variety of PES. However, all of them can be grouped into four different types on the basis of the number and the first splitting species as collected in Scheme 2, Schemes 3–5. Whereas all ligands of the PR$^1$R$^2$ family always present the type-I PES the three ligands of the OR family (R = H, Me, Ph) show three different types of PES named as I, II, and IV, respectively. The remaining Y ligands (NH$_2$, NHMe, NHpTol, SH, SMe, SPh), which present two splitting species, have been grouped within the type-III PES.

On the whole, the overall reaction rate is determined by the first stage of the reaction mechanism, that is, the TS for the attack of the nucleophilic Y ligand of the Re complex on HMAD (**TS1** or **TS1*b***, when present). For the sake of generality, we also consider **TS1** as the determinant step for complexes with OH, OPh, and SH ligands, although their **TS1'**, **TS2*ins***, and **TS2*cco*** are only 1.0, 3.0, and 0.2 kcal/mol higher in energy than their **TS1**, respectively (see Table 1).

As seen in Table 1 the replacement of a hydrogen atom by a methyl substituent at the NH$_2$, OH, and SH as well as the change from the PH$_2$ to the PMe$_2$ ligands reduces the Gibbs energy barrier controlled by **TS1** by 1.3, 1.1, 9.6, and 10.2 kcal/mol, respectively. It is well-known that the higher the Y-centered HOMO energy of the Re complex, the greater the nucleophilic character of the ligand and, consequently, the lowest Gibbs energy barrier for **TS1**. Accordingly, as seen in Figure 2, the energies of the HOMOs of the complexes with methyl substituents are always higher than those unsubstituted ones. Figure 3 shows how the presence of a methyl substituent adds an extra antibonding $\pi$ interaction in the Y ligand environment, which explains the instability of the HOMO of these methyl substituted complexes.

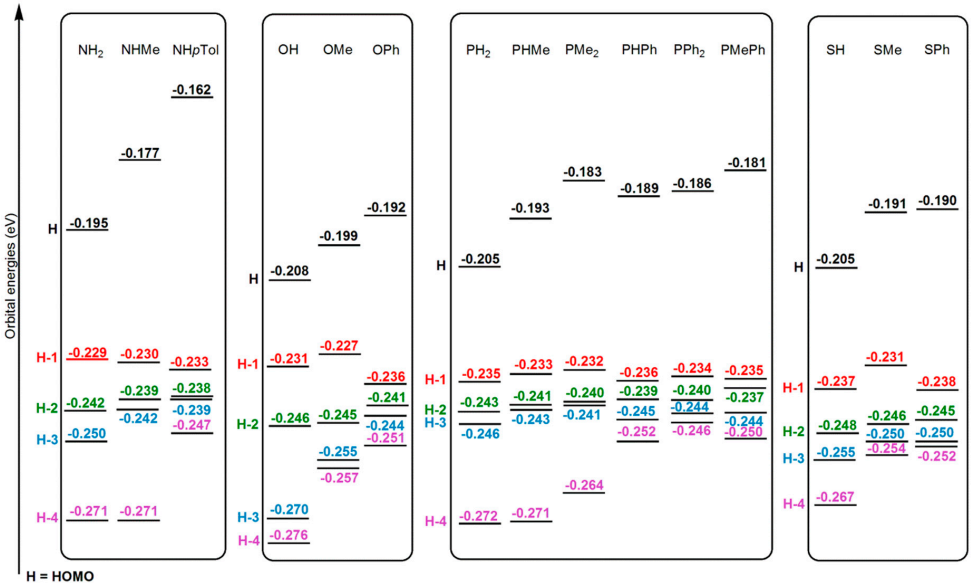


**Figure 2.** Energies (in eV) of the five highest occupied orbitals in the reactant complexes [ReY(CO)$_3$(bipy)] (Y = NH$_2$, NHMe, NH*p*Tol, OH, OMe, OPh, PH$_2$, PHMe, PMe$_2$, PHPh, PPh$_2$, PMePh, SH, SMe, SPh).

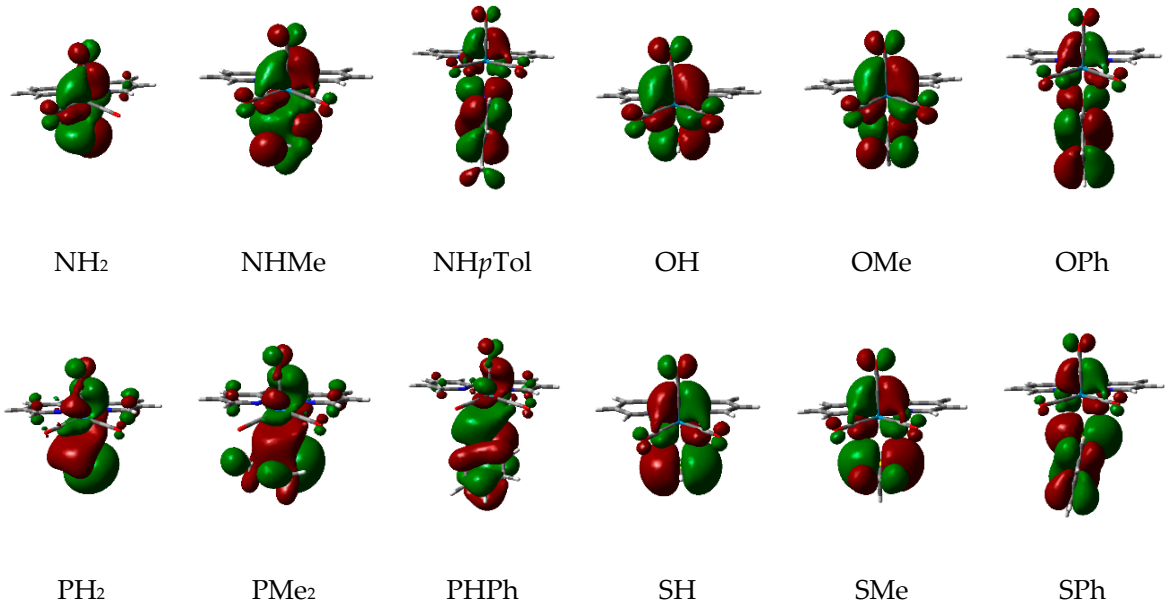


**Figure 3.** Pictures of the computed HOMO of the reactant complexes [ReY(CO)$_3$(bipy)] (Y = $NH_2$, NHMe, NH*p*Tol, OH, OMe, OPh, $PH_2$, $PMe_2$, PHPh, SH, SMe, SPh).

For the aryl substitution at the Y ligand the HOMOs of the complexes with Y = NHpTol, OPh, PHPh, and SPh are 0.015, 0.007, 0.004, and 0.001 eV higher in energy than those with Y = NHMe, OMe, PHMe, and SMe, respectively (see Figure 2). The presence of an aromatic ring bonded to the nucleophilic atom increases even more the antibonding interactions above mentioned (see Figure 3). However, a reduction in the Gibbs energy barrier of **TS1** only happens for PHPh and SPh but not for NHpTol and OPh (see Table 1). As previously reported [58], apart from the HOMO energy of the reactant complex, other factors must be considered to rationalize this unexpected trend, so we now focus on the availability of the attacking electron lone pair of the nucleophilic atom at the Y ligand. Firstly, the N atom of the NHpTol ligand presents a $sp^2$ hybridization, whereas a $sp^3$ one happens for the NHMe ligand. As seen in Figure 3, $sp^2$ hybridization reduces the availability of the electron lone pair of the nitrogen atom due to its conjugation with the aromatic ring, which provokes a rise of the Gibbs energy barrier for the nucleophilic addition. To confirm this point, the electron delocalization indexes (DI) of the bonds between the N atom at NHMe and NHpTol and the carbon atom ($C_S$) of the alkyl or aryl substituent directly linked to it have been calculated, obtaining the values 1.0399 and 1.1322, respectively (see Table 2). The increase in DI agrees with the 0.089 Å shortening of the N-$C_S$ bond distance when replacing NHMe by NHpTol. Similar but less accentuated trends were found when comparing the DI of the O-Me (0.9459) and S-Ph (1.1956) bonds at the corresponding reactant complexes. This bodes well with the fact that the O-Me bond distance is 0.071 Å longer than the O-Ph one. In addition, when analyzing the reactant Re complexes, we note that the net natural atomic charge (NAC) of the donor atoms N, O, P, and S reflects an electron depopulation of 0.009, 0.074, 0.048, and 0.294 e when going from NHMe, OMe, PHMe, and SMe to NHpTol, OPh, PHPh, and SPh, respectively (see Table 2).

In summary, for complexes wherein the aryl group is electronically conjugated with a lone pair at the donor atom, as for NHpTol and OPh, the negative effect of the unavailability of the electron lone pair prevails over the positive effect of the increase in the HOMO energy and, consequently, the instability of **TS1** increases. By contrast, when the aryl group is not strongly conjugated with the nucleophilic atom, as for PHPh (see Figure 3), the availability of the electron lone pair further favours the positive effect of the rise in the HOMO energy, thus provoking a notable stabilization of **TS1** (see Table 1).

**Table 2.** Bond distances between Re and the heteroatom of the Y ligand and between the heteroatom and the carbon of the alkyl or aryl substituent directly linked to it (d(Re-Y) and d(Y-$C_S$) in Å, respectively), electron delocalization indexes at the bond critical points located between each of the two pairs of atoms mentioned above (DI(Re-Y) and DI(Y-$C_S$), respectively), and net natural atomic charges of the nucleophilic atom of the Y ligand, the attacked carbon of the carbonyl ligand in *cis* disposition to the Y ligand, and the attacked non-substituted *ortho* carbon of the bipy ligand (NAC(Y), NAC($C_{CO}$), and NAC($C_{bipy}$) in *e*, respectively) of the reactant complexes [ReY$(CO)_3$(bipy)] (Y = $NH_2$, NHMe, NH*p*Tol, OH, OMe, OPh, $PH_2$, PHMe, $PMe_2$, PHPh, $PPh_2$, PMePh, SH, SMe, SPh) at the B3LYP level.

| Y | d(Re-Y) | d(Y-$C_S$) | DI(Re-Y) | DI(Y-$C_S$) | NAC(Y) | NAC($C_{CO}$) | NAC($C_{bipy}$) |
|---|---|---|---|---|---|---|---|
| $NH_2$ | 2.174 | | 0.6687 | | −1.164 | 0.734 | 0.063 |
| NHMe | 2.156 | 1.461 | 0.6689 | 1.0399 | −0.799 | 0.733 | 0.066 |
| NH*p*Tol | 2.147 | 1.372 | 0.6218 | 1.1322 | −0.790 | 0.734 | 0.068 |
| OH | 2.115 | | 0.6145 | | −1.016 | 0.724 | 0.069 |
| OMe | 2.096 | 1.400 | 0.5998 | 0.9459 | −0.752 | 0.724 | 0.067 |
| OPh | 2.134 | 1.329 | 0.5231 | 0.9925 | −0.678 | 0.728 | 0.069 |
| $PH_2$ | 2.586 | | 0.6736 | | −0.128 | 0.739 | 0.056 |
| PHMe | 2.582 | 1.882 | 0.6803 | 0.9166 | 0.180 | 0.737 | 0.059 |
| $PMe_2$ | 2.602 | 1.876 | 0.6661 | 0.8962 | 0.462 | 0.734 | 0.058 |
| PHPh | 2.591 | 1.844 | 0.6525 | 0.9337 | 0.232 | 0.735 | 0.062 |
| $PPh_2$ | 2.614 | 1.864 | 0.6352 | 0.8793 | 0.519 | 0.739 | 0.060 |
| PMePh | 2.615 | 1.847 | 0.6341 | 0.9256 | 0.510 | 0.735 | 0.058 |
| SH | 2.551 | | 0.6541 | | −0.482 | 0.747 | 0.068 |
| SMe | 2.535 | 1.841 | 0.6758 | 1.1198 | −0.188 | 0.745 | 0.066 |
| SPh | 2.545 | 1.782 | 0.6427 | 1.1956 | −0.085 | 0.740 | 0.068 |

The replacement of the N- and P-containing Y ligands by the O- and S-containing analogues disfavours their reactivity with HMAD (see Table 1). As displayed in Figure 2, the HOMO of the reactant complexes with $NH_2$, NHMe, and NHpTol are 0.013, 0.022, and 0.020 eV higher in energy than those with OH, OMe, and OPh, thus yielding an increase in the Gibbs energy barrier of 8.5, 8.7, and 11.1 kcal/mol when going from NHR to OR (R = H, Me, *p*Tol/Ph), respectively. In consonance with this, the HOMO of the OH and OMe reactant complexes shows a simultaneous bonding overlap of a Re *d* orbital with three CO antibonding π orbitals, whereas only two CO antibonding π orbitals interact with a Re *d* orbital for the $NH_2$ and NHMe cases (see Figure 3). For both NH*p*Tol and OPh the HOMO display a bonding overlap similar to that mentioned for the OH and OMe cases, but the greater antibonding nature of the π orbital of the NH*p*Tol that interacts with the Re *d* orbitals explains the greater stability of the HOMO of the OPh reactant complex. The same reasoning cannot be used to explain the instability rise of **TS1,** between 5.1 and 13.2 kcal/mol, when replacing ligands with P by the ones with S since the HOMO energy is practically the same when comparing analogous complexes (see Figure 2). Looking at the pictures of the HOMO of the reactant complexes with P ligands in Figure 3 and Figure S16, we note that such orbitals are mainly composed of a P-centered π orbital, whereas for the SR (R = H, Me, Ph) complexes the HOMO shows a notable antibonding π overlap between a Re *d* orbital and a π orbital of the SR ligand (see Figure 3). Therefore, the attacking electron lone pair of the S atom is less available to attack the activated alkyne than that of the P atom, thus involving a more energy-demanding step as mentioned above.

On the other hand, as previously mentioned, the regioselectivity of these processes is controlled by the Gibbs energy barriers for the formation of the possible products (**P*cco*/P*ccoh***, **P*ccb***, **P*ins***) and their relative stability. As seen in Table 1, despite the remarkable relative stability of **P*ins***, this product is the most kinetically penalized except for the OR ligands. This fact is related to the strength in the Re-Y bond that can be quantified by the variation of the DI values of the Re-Y bond when going from reactants to **I1'**, the intermediate immediately prior to the formation of **P*ins*** in most cases. Tables 2 and 3 show that all DIs reduce, but mainly those for N and O-containing ligands. The important weakening of the Re-O bond at **I1'** (or **I1**) explains why **TS2*ins*** competes with **TS2*ccb*** and **TS2*cco*** (when located), and **P*ins*** is

the detected product for OMe, as experimentally found [48], and the suggested one for OPh. On the other hand, ligands with P and S display the smallest weakening of the R-Y bond (the DI reduction is 0.0046 and 0.0307 for the PMePh and PHMe cases, respectively). The similar size of the atomic orbitals of the P and Re atoms promotes a large overlap between them that makes their bond strong, so difficult to break in the insertion process. Concerning the Gibbs energy barriers for the formation of **P*cco*/P*ccoh*** and **P*ccb***, **TS2*cco*** is, on the whole, less energy-demanding than **TS2*ccb*** as the attacked carbon of the carbonyl ligand in cis disposition to Y is less electronically populated than the attacked non-substituted carbon of the bipy ligand. Only for $PPh_2$ **TS2*cco*** is 0.2 kcal/mol larger in energy than **TS2*ccb*** while for $PH_2$ **TS2*cco*** and **TS2*ccb*** show the same relative instability. This explains why **P*cco*** (or **P*ccoh*** when present) is the preferred kinetic product. Nonetheless, when those TSs compete each other, **P*ccb*** is the predominat product as these products are always notably more stable than **P*cco***.

**Table 3.** Bond distances between Re and the heteroatom of the Y ligand (d(Re-Y) in Å), electron delocalization indexes at the bond critical points located between Re and Y (DI(Re-Y)), and net natural atomic charges of the nucleophilic atom of the Y ligand, the attacked carbon of the carbonyl ligand in *cis* disposition to the Y ligand, the attacked non-substituted *ortho* carbon of the bipy ligand, the non-substituted acetylenic carbon, and the substituted acetylenic carbon (NAC(Y), NAC($C_{CO}$), NAC($C_{bipy}$), NAC(C1), and NAC(C2) in *e*, respectively) at the intermediate **I1'** when Y = $NH_2$, NHMe, NH*p*Tol, OH, OMe, OPh, $PH_2$, PHMe, $PMe_2$, PHPh, $PPh_2$, PMePh, SH, SMe, SPh) at the B3LYP level.

| Y | d(Re-Y) | DI(Re-Y) | NAC(Y) | NAC($C_{CO}$) | NAC($C_{bipy}$) | NAC(C1) | NAC(C2) |
|---|---|---|---|---|---|---|---|
| $NH_2$ | 2.271 | 0.4893 | −0.825 | 0.740 | 0.081 | −0.155 | −0.348 |
| NHMe | 2.292 | 0.4650 | −0.646 | 0.727 | 0.080 | −0.139 | −0.336 |
| NH*p*Tol [1] | 2.314 | 0.4594 | −0.652 | 0.737 | 0.078 | −0.154 | −0.317 |
| OH | 2.253 | 0.3747 | −0.706 | 0.730 | 0.082 | −0.004 | −0.392 |
| OMe [1] | 2.256 | 0.3930 | −0.568 | 0.725 | 0.089 | −0.047 | −0.388 |
| OPh [1] | 2.316 | 0.3269 | −0.544 | 0.726 | 0.087 | 0.003 | −0.370 |
| $PH_2$ | 2.514 | 0.6458 | 0.686 | 0.762 | 0.079 | −0.671 | −0.298 |
| PHMe | 2.518 | 0.6496 | 0.956 | 0.763 | 0.081 | −0.681 | −0.295 |
| $PMe_2$ | 2.534 | 0.6412 | 1.199 | 0.761 | 0.080 | −0.679 | −0.290 |
| PHPh | 2.525 | 0.6389 | 0.970 | 0.762 | 0.081 | −0.669 | −0.290 |
| $PPh_2$ | 2.561 | 0.6135 | 1.225 | 0.756 | 0.078 | −0.671 | −0.293 |
| PMePh | 2.544 | 0.6295 | 1.215 | 0.756 | 0.080 | −0.672 | −0.288 |
| SH [1] | 2.572 | 0.5528 | 0.199 | 0.756 | 0.083 | −0.456 | −0.333 |
| SMe | 2.565 | 0.5593 | 0.444 | 0.756 | 0.084 | −0.479 | −0.319 |
| SPh [1] | 2.582 | 0.5372 | 0.470 | 0.750 | 0.085 | −0.464 | −0.311 |

[1] For the sake of some degree of comparison, the non-appearance of **I1'** led us to analyze **I1** instead.

## 3. Computational Methods

Based on our previous theoretical studies on the reactions of [ReY$(CO)_3$(bipy)] (Y = NH*p*Tol, OH, OMe, $PPh_2$) complexes towards HMAD [57,58] and for comparison purposes, the present research was carried out using the levels of theory PCM-B3LYP/6-31+G(d, p)-LANL2DZ and CPCM-DLPNO-CCSD(T)/def2-TZVPP//PCM-B3LYP/6-31+G(d, p)-LANL2DZ for obtaining molecular geometries and energies, respectively (see Computational Chemistry Details in the Supporting Information for a more detailed description). For brevity, the levels of theory PCM-B3LYP/6-31+G(d, p)-LANL2DZ and CPCM-DLPNO-CCSD(T)/def2-TZVPP//PCM-B3LYP/6-31+G(d, p)-LANL2DZ have been denoted as B3LYP and DLPNO-CCSD(T), respectively. A relative permittivity of 7.58 was assumed in these calculations to simulate THF as the solvent experimentally used when investigating the reactivity of [ReY$(CO)_3$(N-N)] (Y = NH*p*Tol, OH, OMe, $PPh_2$; N-N = bipy and/or phen) towards activated alkynes [48,51–54]. All the B3LYP species located present singlet electronic state without spin contamination. Similarly, all the DLPNO-CCSD(T) species investigated showed T1 diagnostic values less than 0.02 [61], suggesting that a multi-reference treatment is not necessary.

Thermal free energy corrections in THF solution ($G_{therm}$) were calculated at the B3LYP level using the standard procedure starting from the molecular partition functions developed for computing gas-phase thermodynamics properties within the ideal gas, rigid rotor, and harmonic oscillator approximations at a pressure of 1 atm and a temperature of 298.15 K [62,63]. For each species, Gibbs free energy in solution was determined by adding $G_{therm}$ to the highly accurate DLPNO-CCSD(T) energy. Unless stated otherwise, for each reactive process investigated, energies discussed in the following sections are all Gibbs free energies in THF solution referred to the corresponding separate reactants.

For interpretation purposes, the electronic structure of some relevant critical structures along the reaction mechanisms found was analyzed using the natural bond orbital (NBO) method [64] and the Bader's Quantum Theory of Atoms in Molecules [65–67] to get, among other electron properties, net atomic charges (NAC) and electron delocalization indexes (DI) [68,69], respectively. The DI is a measure of the number of electrons shared between two atoms in a molecular system and therefore, of the covalency of the bond between them.

All B3LYP computations were carried out with the Gaussian 09 suite of programs [70], while DLPNO-CCSD(T) calculations employed the ORCA (version 4.0.1) program [71] and the frozen-core approximation. NAC and DI were computed with the NBO (version 3.1) and AIMAll (version 10.12.11) programs, respectively [72,73].

## 4. Conclusions

The systematic study of the reaction of [ReY(CO)$_3$(bipy)] complexes (with Y being 15 different ligands of general formula NHR, OR, PR$^1$R$^2$, or SR; R$^1$ = R$^2$ = R = H, Me, Ph or *p*Tol) with HMDA gave rise to several potential energy surfaces, all of them with an initial large energy TS for the nucleophilic attack of Y to HMAD followed by diverse reaction channels towards three kinds of products, **P*cco*/P*ccoh***, **P*ccb***, and **P*ins***. Ligands with N and S show an alternative approach of the reactants leading to **P*ccb***. The particular features of each ligand cause slight differences that determine the resulting product. Thus, ligands $NH_2$, OH, $PH_2$, and SH are poorer nucleophiles for the reaction with HMAD, whereas the presence of a moderate electron-donating substituent like a methyl group replacing one of the H atoms in these ligands favours the processes. The energy destabilization of the HOMO of the reactant complexes seems to be responsible for the diminution of the Gibbs energy barrier corresponding to the nucleophilic attack step. The presence of an aryl substituent replacing one of the H atoms in these ligands increases even more the energy destabilization of the HOMO of the reactant complexes, but this does not always imply an easier process as factors other than the HOMO energy may be predominant. Particularly, an aromatic ring bonded to N and O makes the reaction more difficult, whereas its linkage to P and S favours it. Since the π electrons in the aromatic ring conjugate with the lone pair at N atom in NH*p*Tol, this pair becomes less available for the nucleophilic attack on the HMAD molecule. The larger size of P prevents this conjugation, which explains the easier reactivity of PHPh compared to that of NH*p*Tol. It is also interesting to note that a more contracted donor atom at the Y ligand tends to disfavour the reactivity of these Re complexes towards HMAD. On the whole, ligands with N and P atoms show lower rate-determining Gibbs energy barriers than ligands with O and S atoms, respectively. This trend is ascribed to the stability of the HOMO of the reactant complexes and the availability of the attacking electron lone pair of the donor atom of the Y ligand.

Concerning the reaction products, the insertion route is greatly penalized for P and S ligands (although **P*ins*** is very stable) due to the strong bond formed between these large atoms and Re, which is weaker in the case of N and O atoms. P and S ligands tend to yield **P*ccb*** as the main product, which is not the general case for O and N ones. When the Y ligand has an O/N and an H atom the most likely product is **P*ccoh***, which is not always obtained when Y contains P/S. For OMe and OPh, the weakness of the Re-O bonds together with the instability of **P*cco*** and the absence of an O-bonded hydrogen atom explain why **P*ins*** is the preferred product only for these two situations.

**Supplementary Materials:** The following are available online, Explanation about the $d^6$ electron configuration on these Re complexes, Computational Chemistry Details, Figures S1–S15: B3LYP optimized geometries of the species involved in the reaction between [ReY(CO)$_3$(bipy)] (Y = $NH_2$, NHMe, OPh, $PH_2$, PHMe, $PMe_2$, PHPh, PMePh, SH, SMe, SPh, NH*p*Tol, OH, OMe, and $PPh_2$) towards HMAD, Tables S1–S45: B3LYP and DLPNO-CCSD(T) absolute and relative energies and entropies as well as Cartesian coordinates of the key species implied in the reaction of [ReY(CO)$_3$(bipy)] (Y = $NH_2$, NHMe, OPh, $PH_2$, PHMe, $PMe_2$, PHPh, PMePh, SH, SMe, SPh, NH*p*Tol, OH, OMe, and $PPh_2$) towards HMAD, Figure S16: Pictures of the HOMO of the reactant complexes [ReY(CO)$_3$(bipy)] (Y = PHMe, $PPh_2$, PMePh), Table S46: Variation of the DLPNO-CCSD(T) relative Gibbs energies for all the analogous species when going from $NH_2$ to NHMe and NH*p*Tol, Table S47: Variation of the DLPNO-CCSD(T) relative Gibbs energies for all the analogous species when going from OH to OMe and OPh, Table S48: Variation of the DLPNO-CCSD(T) relative Gibbs energies for all the analogous species when going from $PH_2$ to PHMe, $PMe_2$, PHPh, $PPh_2$, and PMePh, Table S49: Variation of the DLPNO-CCSD(T) relative Gibbs energies for all the analogous species when going from SH to SMe and SPh, Table S50: Variation of the DLPNO-CCSD(T) relative Gibbs energies for all the analogous species when going from $NH_2$, NHMe, and NH*p*Tol to $PH_2$, PHMe, and PHPh, respectively, Table S51: Variation of the DLPNO-CCSD(T) relative Gibbs energies for all the analogous species when going from OH, OMe, and OPh to SH, SMe, and SPh, respectively.

**Author Contributions:** Research concept, R.L., M.I.M., J.P., L.R. and J.D.; methodology, R.L. and M.I.M.; software, D.Á., E.L.-C. and A.G.; B3LYP and DLPNO-CCSD(T) computations, D.Á., E.L.-C., A.G. and J.D.; writing and discussions, R.L., M.I.M., D.Á., L.R. and J.P.; project administration, R.L.; funding acquisition, J.P., L.R., M.I.M. and R.L. All authors have read and agreed to the published version of the manuscript.

**Funding:** This research was funded by the Ministerio de Ciencia, Innovación y Universidades (MCIU) of Spain, grant number PGC2018-100013-B-I00.

**Acknowledgments:** J.D. acknowledges computing resources from the Fundación Computación y Tecnologías Avanzadas de Extremadura (COMPUTAEX).

**Conflicts of Interest:** The authors declare no conflict of interest.

## References

1. Takeada, H.; Koike, K.; Inoue, H.; Ishitani, O. Development of an efficient photocatalytic system for $CO_2$ reduction using Rhenium(I) complexes based on mechanistic studies. *J. Am. Chem. Soc.* **2008**, *130*, 2023–2031. [CrossRef] [PubMed]
2. Morris, A.J.; Meyer, G.J.; Fujita, E. Molecular approaches to the photocatalytic reduction of carbon dioxide for solar fuels. *Acc. Chem. Res.* **2009**, *42*, 1983–1994. [CrossRef] [PubMed]
3. Takeda, H.; Ishitani, O. Development of efficient photocatalytic systems for $CO_2$ reduction using mononuclear and multinuclear metal complexes based on mechanistic studies. *Coord. Chem. Rev.* **2010**, *254*, 346–354. [CrossRef]
4. Kou, Y.; Nabetani, Y.; Masui, D.; Shimada, T.; Takagi, S.; Tachibana, H.; Inoue, H. Direct detection of key reaction intermediates in photochemical $CO_2$ reduction sensitized by a rhenium bipyridine complex. *J. Am. Chem. Soc.* **2014**, *136*, 6021–6030. [CrossRef]
5. Machan, C.W.; Chabolla, S.A.; Yin, J.; Gilson, M.K.; Tezcan, F.A.; Kubiak, C.P. Supramolecular assembly promotes the electrocatalytic reduction of carbon dioxide by Re(I) bipyridine catalysts at a lower overpotential. *J. Am. Chem. Soc.* **2014**, *136*, 14598–14607. [CrossRef]
6. Teesdale, J.J.; Pistner, A.J.; Yap, G.P.; Ma, Y.Z.; Lutterman, D.A.; Rosenthal, J. Reduction of $CO_2$ using a rhenium bipyridine complex containing ancillary BODIPY moieties. *Catal. Today* **2014**, *225*, 149–157. [CrossRef]
7. Windle, C.D.; George, M.W.; Perutz, R.N.; Summers, P.A.; Sun, X.Z.; Whitwood, A.C. Comparison of rhenium–porphyrin dyads for $CO_2$ photoreduction: Photocatalytic studies and charge separation dynamics studied by time-resolved IR spectroscopy. *Chem. Sci.* **2015**, *6*, 6847–6864. [CrossRef]
8. Oh, S.; Gallagher, J.R.; Miller, J.T.; Surendranath, Y. Graphite-conjugated rhenium catalysts for carbon dioxide reduction. *J. Am. Chem. Soc.* **2016**, *138*, 1820–1823. [CrossRef]
9. Ci, C.; Carbó, J.J.; Neumann, R.; de Graaf, C.; Poblet, J.M. Photoreduction mechanism of $CO_2$ to CO catalyzed by a rhenium(I)–polyoxometalate hybrid compound. *ACS Catal.* **2016**, *6*, 6422–6428. [CrossRef]
10. Rohacova, J.; Ishitani, O. Rhenium(I) trinuclear rings as highly efficient redox photosensitizers for photocatalytic $CO_2$ reduction. *Chem. Sci.* **2016**, *7*, 6728–6739. [CrossRef]
11. Clark, M.L.; Cheung, P.L.; Lessio, M.; Carter, E.A.; Kubik, C.P. Kinetic and mechanistic effects of bipyridine (bpy) substituent, labile ligand, and Brønsted acid on electrocatalytic $CO_2$ reduction by Re(bpy) complexes. *ACS Catal.* **2018**, *8*, 2021–2029. [CrossRef]

12. Zhanaidarova, A.; Jones, S.C.; Despagnet-Ayoub, E.; Pimentel, B.R.; Kubiak, C.P. Re(*t*Bu-bpy)$(CO)_3$Cl supported on multi-walled carbon nanotubes selectively reduces $CO_2$ in water. *J. Am. Chem. Soc.* **2019**, *141*, 17270–17277. [CrossRef] [PubMed]
13. Zhanaidarova, A.; Ostericher, A.L.; Miller, C.J.; Jones, S.C.; Kubiak, C.P. Selective reduction of $CO_2$ to CO by a molecular Re(ethynyl-bpy)$(CO)_3$Cl catalyst and attachment to carbon electrode surfaces. *Organometallics* **2019**, *38*, 1204–1207. [CrossRef]
14. Willkomm, J.; Bertin, E.; Atwa, M.; Lin, J.-B.; Birss, V.; Piers, W.E. Grafting of a molecular rhenium $CO_2$ reduction catalyst onto colloid-imprinted carbon. *ACS Appl. Energy Mater.* **2019**, *2*, 2414–2418. [CrossRef]
15. Sato, S.; McNicholas, B.J.; Grubbs, R.H. Aqueous electrocatalytic $CO_2$ reduction using metal complexes dispersed in polymer ion gels. *Chem. Commun.* **2020**, *56*, 4440–4443. [CrossRef]
16. Yu, H.; Haviv, E.; Neumann, R. Visible-light photochemical reduction of $CO_2$ to CO coupled to hydrocarbon dehydrogenation. *Angew. Chem. Int. Ed.* **2020**, *59*, 6219–6223. [CrossRef]
17. Cannizzo, A.; Blanco-Rodríguez, A.M.; El Nahhas, A.; Sebera, J.; Zális, S.; Vlcek, A., Jr.; Chergui, M. Femtosecond fluorescence and intersystem crossing in rhenium(I) carbonyl−bipyridine complexes. *J. Am. Chem. Soc.* **2008**, *130*, 8967–8974. [CrossRef]
18. Ng, C.-O.; Lai, S.-W.; Feng, H.; Yiu, S.-M.; Ko, C.-C. Luminescent rhenium(I) complexes with acetylamino- and trifluoroacetylamino-containing phenanthrolineligands: Anion-sensing study. *Dalton Trans.* **2011**, *40*, 10020–10028. [CrossRef]
19. Yu, T.; Tsand, D.P.-K.; Au, V.K.-M.; Lam, W.H.; Chan, M.-Y.; Yam, V.W.-W. Deep red to near-infrared emitting rhenium(I) complexes: Synthesis, characterization, electrochemistry, photophysics, and electroluminescence studies. *Chem. Eur. J.* **2013**, *19*, 13418–13427. [CrossRef]
20. Chu, W.-K.; Ko, C.-C.; Chan, K.-C.; Yiu, S.-M.; Wong, F.-L.; Lee, C.-S.; Roy, V.A.L. A simple design for strongly emissive sky-blue phosphorescent neutral rhenium complexes: Synthesis, photophysics, and electroluminescent devices. *Chem. Mater.* **2014**, *26*, 2544–2550. [CrossRef]
21. Xu, G.; Lu, M.; Huang, C.; Wang, Y.; Ge, S. Study on an oxygen sensing rhenium(I) complex with enlarged sensing/active area: Fabrication, photophysical parameters and molecular oxygen sensing performance. *Spectrochim. Acta A Mol. Biomol. Spectrosc.* **2014**, *123*, 369–375. [CrossRef] [PubMed]
22. Choi, A.W.-T.; Tso, K.K.-S.; Yim, V.M.-W.; Liu, H.-W.; Lo, K.K.-W. Modification of 1,2,4,5-tetrazine with cationic rhenium(I) polypyridine units to afford phosphorogenic bioorthogonal probes with enhanced reaction kinetics. *Chem. Commun.* **2015**, *51*, 3442–3445. [CrossRef]
23. Lo, K.K.-W. Luminescent Rhenium(I) and iridium(III) polypyridine complexes as biological probes, imaging reagents, and photocytotoxic agents. *Acc. Chem. Res.* **2015**, *48*, 2985–2995. [CrossRef] [PubMed]
24. Chu, W.-K.; Wei, X.-G.; Yiu, S.-M.; Ko, C.-C.; Lau, K.-C. Strongly phosphorescent neutral rhenium(I) isocyanoborato complexes: Synthesis, characterization, and photophysical, electrochemical, and computational studies. *Chem. Eur. J.* **2015**, *21*, 2603–2612. [CrossRef] [PubMed]
25. Zhao, G.-W.; Zhao, J.-H.; Hu, Y.-X.; Zhang, D.-Y.; Li, X. Recent advances of neutral rhenium(I) tricarbonyl complexes for application in organic light-emitting diodes. *Synth. Met.* **2016**, *212*, 131–141. [CrossRef]
26. Lee, L.C.; Leung, K.K.; Lo, K.K. Recent development of luminescent rhenium(I) tricarbonyl polypyridine complexes as cellular imaging reagents, anticancer drugs, and antibacterial agents. *Dalton Trans.* **2017**, *46*, 16357–16380. [CrossRef] [PubMed]
27. Raszeja, L.J.; Siegmund, D.; Cordes, A.L.; Gueldenhaupt, J.; Gerwert, K.; Hahn, S.; Metzler-Nolte, N. Asymmetric rhenium tricarbonyl complexes show superior luminescence properties in live cell imaging. *Chem. Commun.* **2017**, *53*, 905–908. [CrossRef]
28. Hu, Y.-X.; Zhao, G.-W.; Dong, Y.; Lu, Y.-L.; Li, X.; Zhang, D.-Y. New rhenium(I) complex with thiadiazole-annelated 1,10-phenanthroline for highly efficient phosphorescent OLEDs. *Dyes Pigments* **2017**, *137*, 569–575. [CrossRef]
29. Skiba, J.; Bernás, T.; Trzybinski, D.; Wozniak, K.; Ferraro, G.; Marasco, D.; Merlino, A.; Shafikov, M.Z.; Czerwieniec, R.; Kowalski, K. Mitochondria targeting with luminescent rhenium(I) complexes. *Molecules* **2017**, *22*, 809. [CrossRef]
30. Yip, A.M.-H.; Shum, J.; Liu, H.-W.; Zhou, H.; Jia, M.; Niu, N.; Li, Y.; Yu, C.; Lo, K.K.-W. Luminescent rhenium(I)–polypyridine complexes appended with a perylene diimide or benzoperylene monoimide moiety: Photophysics, intracellular sensing, and photocytotoxic activity. *Chem. Eur. J.* **2019**, *25*, 8970–8974. [CrossRef]

31. Gasser, G.; Ott, I.; Metzler-Nolte, N. Organometallic anticancer compounds. *J. Med. Chem.* **2011**, *54*, 3–25. [CrossRef] [PubMed]
32. Pierri, A.E.; Pallaoro, A.; Wien, G.; Ford, P.C. A luminescent and biocompatible PhotoCORM. *J. Am. Chem. Soc.* **2012**, *134*, 18197–18200. [CrossRef] [PubMed]
33. Kastl, A.; Dieckmann, S.; Wähler, K.; Völker, T.; Kastl, L.; Merkel, A.L.; Vultur, A.; Shanna, B.; Harms, K.; Ocker, M.; et al. Rhenium Complexes with Visible-Light-Induced Anticancer Activity. *ChemMedChem* **2013**, *8*, 924–927. [CrossRef] [PubMed]
34. Leonidova, A.; Pierroz, V.; Adams, L.A.; Barlow, N.; Ferrari, S.; Graham, B.; Gasser, G. Enhanced cytotoxicity through conjugation of a "clickable" luminescent Re(I) complex to a cell-penetrating lipopeptide. *ACS Med. Chem. Lett.* **2014**, *5*, 809–814. [CrossRef] [PubMed]
35. Kaplanis, M.; Stamatakis, G.; Papakonstantinou, V.D.; Paravatou-Petsotas, M.; Demopoulos, C.A.; Mitsopoulou, C.A. Re(I) tricarbonyl complex of 1,10-phenanthroline-5,6-dione: DNA binding, cytotoxicity, anti-inflammatory and anti-coagulant effects towards platelet activating factor. *J. Inorg. Biochem.* **2014**, *135*, 1–9. [CrossRef]
36. Leonidova, A.; Gasser, G. Underestimated potential of organometallic rhenium complexes as anticancer agents. *ACS Chem. Biol.* **2014**, *9*, 2180–2193. [CrossRef]
37. Ye, R.R.; Tan, C.P.; Chen, M.H.; Hao, L.; Ji, L.N.; Mao, Z.W. Mono- and dinuclear phosphorescent rhenium(I) complexes: Impact of subcellular localization on anticancer mechanisms. *Chem. Eur. J.* **2016**, *22*, 7800–7809. [CrossRef]
38. Knopf, K.M.; Murphy, B.L.; MacMillan, S.N.; Baskin, J.M.; Barr, M.P.; Boros, E.; Wilson, J.J. In Vitro anticancer activity and in vivo biodistribution of rhenium(I) tricarbonyl aqua complexes. *J. Am. Chem. Soc.* **2017**, *139*, 14302–14314. [CrossRef]
39. Marker, S.C.; MacMillan, S.N.; Zipfel, W.R.; Li, Z.; Ford, P.C.; Wilson, J.J. Photoactivated in vitro anticancer activity of rhenium(I) tricarbonyl complexes bearing water-soluble phosphines. *Inorg Chem.* **2018**, *57*, 1311–1331. [CrossRef]
40. King, A.P.; Marker, S.C.; Swanda, R.V.; Woods, J.J.; Qian, S.B.; Wilson, J.J. A rhenium isonitrile complex induces unfolded protein response-mediated apoptosis in cancer cells. *Chemistry* **2019**, *25*, 9206–9210. [CrossRef]
41. Collery, P.; Desmaele, D.; Vijaykumar, V. Design of Rhenium compounds in targeted anticancer therapeutics. *Curr. Pharm. Des.* **2019**, *25*, 3306–3322. [CrossRef] [PubMed]
42. Konkankit, C.C.; Vaughn, B.A.; MacMillan, S.N.; Boros, E.; Wilson, J.J. Combinatorial synthesis to identify a potent, necrosis-inducing rhenium anticancer agent. *Inorg. Chem.* **2019**, *58*, 3895–3909. [CrossRef] [PubMed]
43. Bauer, E.B.; Haase, A.A.; Reich, R.M.; Crans, D.C.; Kuehn, F.E. Organometallic and coordination rhenium compounds and their potential in cancer therapy. *Coord. Chem. Rev.* **2019**, *393*, 79–117. [CrossRef]
44. Luengo, A.; Redrado, M.; Marzo, I.; Fernandez-Moreira, V.; Gimeno, M.C. Luminescent Re(I)/Au(I) species as selective anticancer agents for HeLa cells. *Inorg. Chem.* **2020**, *59*, 8960–8970. [CrossRef] [PubMed]
45. Capper, M.S.; Packman, H.; Rehkaemper, M. Rhenium-based complexes and in vivo testing: A brief history. *ChemBioChem* **2020**. [CrossRef]
46. Marker, S.C.; King, A.P.; Swanda, R.V.; Vaughn, B.; Boros, E.; Qian, S.-B.; Wilson, J.J. Exploring ovarian cancer cell resistance to rhenium anticancer complexes. *Angew. Chem. Int. Ed.* **2020**. [CrossRef]
47. Gupta, G.; Sathiyendiran, M. Rhenium-carbonyl-based supramolecular coordination complexes: Synthesis, structure and properties. *ChemistrySelect* **2018**, *3*, 7439–7458. [CrossRef]
48. Hevia, E.; Pérez, J.; Riera, L.; Riera, V. Reactive alkoxide complexes of groups 6 and 7 metals. *Organometallics* **2002**, *21*, 1750–1752. [CrossRef]
49. Hevia, E.; Pérez, J.; Riera, L.; Riera, V.; del Río, I.; García-Granda, S.; Miguel, D. Insertion of unsaturated organic electrophiles into molybdenum-alkoxide and rhenium-alkoxide bonds of neutral, stable carbonyl complexes. *Chem. Eur. J.* **2002**, *8*, 4510–4521. [CrossRef]
50. Hevia, E.; Pérez, J.; Riera, V.; Miguel, D. New octahedral rhenium(I) tricarbonyl amido complexes. *Organometallics* **2002**, *21*, 1966–1974. [CrossRef]
51. Hevia, E.; Pérez, J.; Riera, V.; Miguel, D. Reactivity of the amido complex [Re(NH*p*Tol)$(CO)_3$(bipy)] toward neutral organic electrophiles. *Organometallics* **2003**, *22*, 257–263. [CrossRef]

52. Cuesta, L.; Gerbino, D.C.; Hevia, E.; Morales, D.; Navarro-Clemente, M.E.; Pérez, J.; Riera, L.; Riera, V.; Miguel, D.; del Río, I.; et al. Reactivity of molybdenum and rhenium hydroxo-carbonyl complexes toward organic electrophiles. *Chem. Eur. J.* **2004**, *10*, 1765–1777. [CrossRef]
53. Cuesta, L.; Hevia, E.; Morales, D.; Pérez, J.; Riera, V.; Rodríguez, E.; Miguel, D. Activation of a 1,10-phenanthroline ligand on a rhenium tricarbonyl complex. *Chem. Commun.* **2005**, 116–117. [CrossRef] [PubMed]
54. Cuesta, L.; Hevia, E.; Morales, D.; Pérez, J.; Riera, V.; Seitz, M.; Miguel, D. Activation of ancillary ligands in the reactions of DMAD with phosphido and alkylideneamido rhenium complexes. *Organometallics* **2005**, *24*, 1772–1775. [CrossRef]
55. Cañadas, P.; Ziegler, S.; Fombona, S.; Hevia, E.; Miguel, D.; Pérez, J.; Riera, L. Molybdenum and rhenium carbonyl complexes containing thiolato ligands. *J. Organomet. Chem.* **2019**, *896*, 113–119. [CrossRef]
56. Arévalo, R.; Espinal-Viguri, M.; Huertos, M.A.; Pérez, J.; Riera, L. Dearomatization of transition metal-coordinated N-heterocyclic ligands and related chemistry. *Adv. Organomet. Chem.* **2016**, *65*, 47–114.
57. Álvarez, D.; Mera-Adasme, R.; Riera, L.; Cárdenas-Jirón, G.I.; Pérez, J.; Díaz, J.; Menéndez, M.I.; López, R. Insights on the reactivity of terminal phosphanido metal complexes toward activated alkynes from theoretical computations. *Inorg. Chem.* **2017**, *56*, 6652–6661. [CrossRef]
58. Álvarez, D.; Díaz, J.; Menéndez, M.I.; López, R. Addition of Re-bonded nucleophilic ligands to activated alkynes: A theoretical rationalization. *Eur. J. Inorg. Chem.* **2020**, 269–280. [CrossRef]
59. Villafañe, F. $Re^{I}(CO)_3$ complexes with diimine ligands synthesized in situ. *Coord. Chem. Rev.* **2017**, *339*, 128–137. [CrossRef]
60. Kurtz, D.A.; Brereton, K.R.; Ruoff, K.P.; Tang, H.M.; Felton, G.A.N.; Miller, A.J.M.; Dempsey, J.L. Bathochromic shifts in rhenium carbonyl dyes induced through destabilization of occupied orbitals. *Inorg. Chem.* **2018**, *57*, 5389–5399. [CrossRef]
61. Lee, T.J.; Taylor, P.R. A diagnostic for determining the quality of single-reference electron correlation methods. *Int. J. Quantum Chem.* **1989**, *36*, 199–207. [CrossRef]
62. McQuarrie, D.A. *Statistical Mechanics*; Harper and Row: New York, NY, USA, 1976.
63. Ribeiro, R.F.; Marenich, A.V.; Cramer, C.J.; Truhlar, D.G. Use of solution-phase vibrational frequencies in continuum models for the free energy of solvation. *J. Phys. Chem. B* **2011**, *115*, 14556–14562. [CrossRef]
64. Weinhold, F.; Landis, C.R. *Valency and Bonding: A Natural Bond Orbital Donor-Acceptor Perspective*; Cambridge University Press: Cambridge, UK, 2005.
65. Biegler-Konig, F.W.; Bader, R.F.W.; Hua-Tang, T. Calculation of the average properties of atoms in molecules. II. *J. Comput. Chem.* **1982**, *3*, 317–328. [CrossRef]
66. Bader, R.F.W. *Atoms in Molecules. A Quantum Theory*; University Press: Oxford, UK, 1990.
67. Bader, R.F.W.; Popelier, P.L.A.; Keith, T.A. Theoretical definition of a functional group and the molecular orbital paradigm. *Angew. Chem. Int. Ed.* **1994**, *33*, 620–631. [CrossRef]
68. Fradera, X.; Austen, M.A.; Bader, R.F.W. The Lewis model and beyond. *J. Phys. Chem. A* **1999**, *103*, 304–314. [CrossRef]
69. Fradera, X.; Poater, J.; Simon, S.; Durán, M.; Solá, M. Electron-pairing analysis from localization and delocalization indices in the framework of the atoms-in-molecules theory. *Theor. Chem. Acc.* **2002**, *108*, 214–224. [CrossRef]
70. Frisch, M.J.; Trucks, G.W.; Schlegel, H.B.; Scuseria, G.E.; Robb, M.A.; Cheeseman, J.R.; Scalmani, G.; Barone, V.; Mennucci, B.; Petersson, G.A.; et al. *Gaussian 09*; revision A.1; Gaussian, Inc.: Wallingford, CT, USA, 2009.
71. Neese, F. Software Update: The ORCA Program System, Version 4.0.1. *WIREs Comput. Mol. Sci.* **2018**, *8*, e1327. [CrossRef]
72. Glendening, E.D.; Reed, A.E.; Carpenter, J.E.; Weinhold, F. *NBO*, version 3.1; University of Wisconsin: Madison, WI, USA, 2003.
73. Keith, T.A. *AIMAll Program*, version 10.12.11; TK Gristmill Software: Overland Park, KS, USA, 2010.


**Sample Availability:** Not available.

## 5.4 $[Cp_2Mo(OH)(OH_2)]^+$ - Catalyzed Hydrolysis of Mono- and Difunctional Ethers: Theoretical Understanding of Their Divergent Reactivity

Daniel Álvarez, Elena Castro-López, Yoana Fernández-Pulido, M. Isabel Menéndez, and Ramón López

*Eur. J. Inorg. Chem.* **2019**, 2924-2932

ChemPubSoc Europe

DOI: 10.1002/ejic.201900513

EurJIC European Journal of Inorganic Chemistry

Full Paper

Sustainable Chemistry | *Very Important Paper* |

VIP

# $[Cp_2Mo(OH)(OH_2)]^+$-Catalyzed Hydrolysis of Mono- and Difunctional Ethers: Theoretical Understanding of Their Divergent Reactivity

Daniel Álvarez,[a] Elena Castro-López,[a] Yoana Fernández-Pulido,[b] M. Isabel Menéndez,[a] and Ramón López*[a]

**Abstract:** The reaction mechanism of $[Cp_2Mo(OH)(OH_2)]^+$-catalyzed hydrolysis of ethyl vinyl, divinyl, and diethyl ethers was theoretically investigated. The reaction pathway evolving through the coordination of the ether oxygen to Mo is notably disfavored, as experimentally suggested. This is the only operative coordination mode for diethyl ether and explains why this monofunctional ether is not hydrolyzed by molybdocenes. However, difunctional ethers containing a functionality susceptible to activation like the vinyl group present an alternative reaction pathway proceeding through the coordination of the vinyl terminal carbon to Mo with accessible rate-determining Gibbs energy barriers of 29.3 kcal/mol (divinyl ether) and 22.2 kcal/mol (ethyl vinyl ether). In these cases, the catalyst withdraws electron density from the unsaturated bonds and prepares the group for an easy OH-nucleophilic attack. This explains the molybdocene-catalyzed hydrolysis of ethyl vinyl ether experimentally observed and, more interestingly, reveals what the crucial role of the functional groups linked to the ether oxygen really is in the viability of these reactive processes.

## Introduction

The interest in designing compounds and chemical processes that reduce or eliminate the presence of chemical substances dangerous to human health and the environment comes from the last decade of the twentieth century.[1] One way to make chemistry less polluting is to find alternatives to the organic solvents frequently used.[2–7] Several research lines are underway today: reactive systems "without solvent",[8–15] immobilization of solvents,[7] ionic liquids,[16–19] biphasic solvents,[20] and harmless and renewable solvents like $CO_2$ and $H_2O$.[21–26] The aqueous reaction medium is the classic alternative to organic solvents because water is cheap, abundant, and harmless, but also has many unique physical and chemical properties: wide range of temperatures for liquid state, high dielectric constant, extensive hydrogen bonds, high heat capacity, and optimal oxygen solubility to maintain aquatic life forms. Numerous chemical transformations such as oxidations, reductions, formation and breakage of carbon–carbon and carbon–heteroatom bonds, etc. successfully proceed in water owing to the presence of transition metals.[26,27] Nowadays, it is known that many organometallic compounds of transition metals are perfectly compatible with aqueous environments since the hydrolysis of their metal-carbon bonds is kinetically disadvantaged. Besides, owing to their accessible *d* orbitals, the transition metals can interact selectively with soft nucleophilic and electrophilic orbitals ($\pi$ and $\pi^*$, respectively) of alkynes, olefins, and arenes, but not with hard nucleophilic groups that can be present in any concentration in aqueous solution.[28]

Molybdocenes ($Cp_2MoX_2$; Cp = cyclopentadienyl or $\eta^5$-$C_5H_5$ and derivatives, X = halide or pseudo halide) are water-soluble $Mo^{IV}$ complexes whose aqueous chemistry has received much attention in order to investigate their possible use as an antitumor agent[29–35] as well as their catalytic properties in organic synthesis and polymerization processes.[36–39] Experimental studies on the coordination chemistry between $Cp_2MoCl_2$ and different DNA (deoxyribonucleic acid) models allowed to propose that $[Cp_2Mo(OH)(OH_2)]^+$ is the dominant species at physiological pH and, therefore, the active species in chemical transformations catalyzed or mediated by $Cp_2MoCl_2$ in water.[29] A theoretical study carried out in our laboratory has confirmed this fact, but it has also revealed the reactive role of the species $[Cp_2Mo(OH)]^+$.[40] The presence of an open coordination site and an internal hydroxo ligand in these hydroxo complexes significantly enhances the catalytic effectiveness of aqueous molybdocenes. Specifically, they have proven to be efficient when catalyzing a variety of organic reactions: H/D exchange in alcohols,[41–43] hydrogenation of olefins,[36] nitrile hydration,[37–39,44–46] carbon monoxide oxidation,[45] and hydrolysis of ethers,[45] esters of carboxylic acids,[36,37,45] and various organophosphates.[37,45–51]

Recent in-depth theoretical studies on the hydrolysis of ethyl acetate,[52] the acrylonitrile hydration,[53] and the carbon monoxide oxidation[54] catalyzed by $[Cp_2Mo(OH)(OH_2)]^+$ have been

[a] *Departamento de Química Física y Analítica, Universidad de Oviedo, C/ Julián Clavería 8, 33006 Oviedo, Asturias, Spain*
*E-mail: rlopez@uniovi.es*
[b] *Departamento de Ingeniería Eléctrica, Universidad de Oviedo, Campus de Gijón, 33203 Gijón, Asturias, Spain*
*Supporting information and ORCID(s) from the author(s) for this article are available on the WWW under https://doi.org/10.1002/ejic.201900513.*

valuable to corroborate and rationalize the experimental belief that the intramolecular nucleophilic attack of the hydroxo ligand on the Mo-coordinated substrate is the operative mechanism (see Scheme 1).[36,44,45] In accordance with experimental suggestions,[44,45] this mechanism begins with the replacement of the aqua ligand of the catalytically active complex $[Cp_2Mo(OH)(OH_2)]^+$ by the substrate (XY in Scheme 1). The next step implies the attack of the hydroxo ligand to the substrate coordinated to the molybdocene metal center resulting in the formation of a metallacyclic intermediate. Then, this metallacycle opens by the addition of water from the reaction medium followed by the formation of the corresponding product with the subsequent recovery of the catalyst. More interestingly, those theoretical results have also shown that the rate-determining step of this kind of organometallic processes depends on the organic substrate considered. Specifically, the attack of the hydroxo ligand is the most energy-demanding step for the substrates acrylonitrile and carbon monoxide.[53,54] Kinetic trends found experimentally for the hydration of several nitriles could be satisfactorily rationalized from that theoretical fact.[53] However, in case of the hydrolysis of the ethyl acetate substrate,[52] the ethanol release from the metallacycle intermediate formed just after the attack of the hydroxo ligand competes with the acetic acid formation to be the rate-determining step.

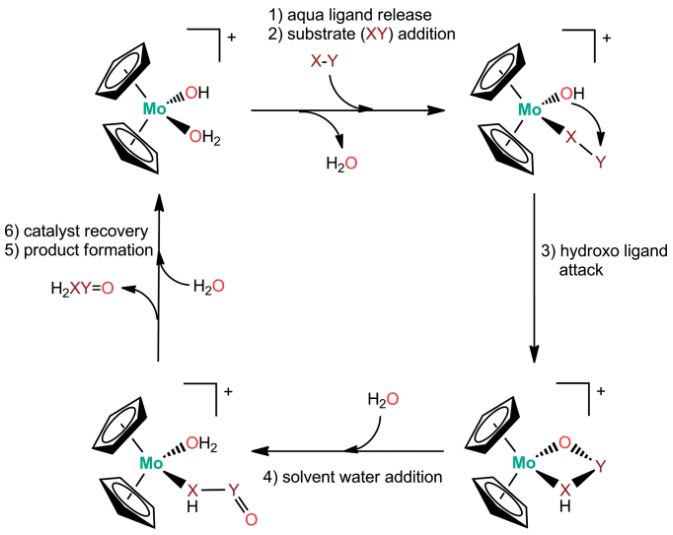


Scheme 1. General mechanism found for the intramolecular nucleophilic attack of the hydroxo ligand in the catalysis by molybdocenes {e.g., $[Cp_2Mo(OH)(OH_2)]^+$} of different organic substrates (XY).

Taking into consideration the rich information provided by Computational Chemistry in the aforementioned studies, we extended our theoretical research on the reactivity of molybdocenes to the hydrolysis of ethers containing vinyl and/or ethyl groups. Metal-catalyzed hydrolysis of vinyl (alkenyl) ethers is relevant in asymmetric synthesis owing to the high availability and low preparation cost of such substrates.[55] Investigating the catalytic cleavage of C–O bonds in alkenyl and aliphatic ethers by hydrolysis is also interesting because it provides insight on the decomposition pathways of biomass into fuels and chemicals.[56] Experimentally, it has been found that difunctional ethers like ethyl vinyl ether and 2-methoxyacetonitrile hydrolyze in aqueous solution with $[Cp'_2Mo(OH)(OH_2)]^+$ (Cp′ = $\eta^5$-$C_5H_4CH_3$), but monofunctional ethers like diethyl ether do not.[45] The reasons for these behaviors have not been fully elucidated. It has been reasoned that the coordination of the ether to the catalyst via the oxygen atom is prevented because the ether functionality is a weak ligand and is sterically hindered. As only the difunctional ethers previously mentioned hydrolyze, it has been suggested that their hydrolysis occurs after precoordination of one of the ether substituents to the catalyst. Particularly, we wonder if it is the mono/difunctional character of an ether or the presence of a vinyl moiety the determinant feature for its hydrolysis catalyzed by molybdocenes, so we undertake a density functional theory (DFT) study on the reaction mechanism of this kind of organometallic reactions. To accomplish this task, we selected $[Cp_2Mo(OH)(OH_2)]^+$ as a very good model of the catalyst used experimentally, $[Cp'_2Mo(OH)(OH_2)]^+$, as well as the real organic substrates ethyl vinyl ether and diethyl ether. To go further in the analysis of the influence of the ether functional groups, we also considered in the computations the equally substituted divinyl ether case.

## Methodology

Based on previous computational investigations on the reactivity of molybdocenes towards organic substrates other than ethers[52–54] and for comparison purposes, the reaction mechanism of the hydrolysis of mono- and difunctional ethers catalyzed by $[Cp_2Mo(OH)(OH_2)]^+$ was carried out at the level of theory PCM-B3LYP/aug-cc-pVTZ (aug-cc-pVTZ-PP for Mo)//PCM-B3LYP/aug-cc-pVDZ (aug-cc-pVDZ-PP for Mo). That is, full geometry optimizations of stable species (reactants, intermediates, and products) and transition states (TS) were carried out from the outset in water solution at the PCM-B3LYP/aug-cc-pVDZ (aug-cc-pVDZ-PP for Mo) level using a modified version of the Schlegel's algorithm.[57] Polarizable Continuum Model (PCM) approach of Tomasi and co-workers[58] together with the Bondi radii[59] were used to take into account solvent effects on both geometry and energy. Electrostatic contributions to the solvation energy[60] and a relative permittivity of 78.39 to simulate the water solvent used in the experiments on the ether hydrolysis catalyzed by molybdocenes[45] were considered in the PCM computations. B3LYP is the popular three-parameter hybrid DFT functional that combines the Becke's nonlocal exchange functional, the Hartree–Fock exchange energy, the nonlocal correlation functional of Lee, Yang, and Parr (LYP), and the Vosko–Wilk–Nusair (VWN) fitting to the correlation energy derived from the local spin density approximation.[61] The nonmetal atoms are described by the correlation consistent double-ζ basis set augmented by diffuse functions aug-cc-pVDZ,[62] while for Mo the valence electrons are represented explicitly by aug-cc-pVDZ and the core electrons are modelled by the corresponding double-ζ Stuttgart–Koln energy-consistent relativistic pseudopotential.[63] The character of all critical points located on the potential energy surface (PES) was confirmed by means of analytical calculations of harmonic vibrational frequencies. Normal-mode analysis corresponding to the imaginary frequency in the TS was used to verify the expected con-

nections between the first-order saddle points and local minima on the PES. However, in some doubtful cases, the connectivity was also checked through intrinsic reaction coordinate (IRC) computations with the second order Gonzalez-Schlegel integration method.[64]

Electronic energies were refined by carrying out PCM-B3LYP/aug-cc-pVTZ (aug-cc-pVTZ-PP for Mo) single-point energy calculations on the PCM-B3LYP/aug-cc-pVDZ (aug-cc-pVDZ-PP for Mo) optimized geometries. In these computations, the non-metal atoms are described with the consistent correlation triple-ζ basis set augmented by diffuse functions aug-cc-pVTZ,[62] while Mo is represented by the basis set aug-cc-pVTZ-PP,[63] in which the valence electrons are considered explicitly by the consistent correlation triple-ζ basis set cc-pVTZ augmented by diffuse functions while the core electrons are modelled by the corresponding triple-ζ Stuttgart–Koln energy-consistent relativistic pseudopotential. In these calculations, both electrostatic and non-electrostatic (cavitation, dispersion, and repulsion) terms were considered.[60] Dispersion interactions in the B3LYP energy calculations were assessed by computing the atom-pair wise DFT-D3 dispersion correction ($E_{disp}$) developed by Grimme and co-workers.[65] The single-point DFT-D3 calculations were done on the PCM-B3LYP/aug-cc-pVDZ (aug-cc-pVDZ-PP for Mo) geometries using the Becke–Johnson damping function[66] as in the previous study on the $[Cp_2Mo(OH)(OH_2)]^+$-catalyzed hydrolysis of ethyl acetate.[52] Hereafter, unless otherwise stated, the computational level PCM-B3LYP/aug-cc-pVTZ (aug-cc-pVTZ-PP for Mo)//PCM-B3LYP/aug-cc-pVDZ (aug-cc-pVDZ-PP) including the energy dispersion correction will be identified in the text as PCM-B3LYP-D3/VTZ//PCM-B3LYP/VDZ.

Thermodynamics magnitudes ($\Delta H$, $\Delta S$, and $\Delta G$) were calculated in water solution at the PCM-B3LYP/VDZ theory level starting with molecular partition functions developed for computing gas-phase thermodynamics properties within the ideal gas, rigid rotor, and harmonic oscillator approximations at a temperature of 298.15 K and a pressure of 1 atm.[67] This is a standard procedure that has proven to be a correct and useful approach.[68]

Electronic structure of some relevant critical structures obtained for $[Cp_2Mo(OH)(OH_2)]^+$-catalyzed hydrolysis of the ethers investigated in this work was analyzed by the natural bond orbital (NBO) method.[69]

All the quantum-chemical computations mentioned above were carried out with the Gaussian 09 series of programs.[70]

## Results and Discussion

This section is organized in three subsections. First one is devoted to the description of the intramolecular reaction mechanism found for the hydrolysis of ethyl vinyl ether catalyzed by $[Cp_2Mo(OH)(OH_2)]^+$ to give ethanol and acetaldehyde. In the second subsection the variations of this mechanism for the hydrolysis of diethyl and divinyl ethers are analyzed. Finally, a general discussion of the results is performed aiming at understanding experimental findings and uncovering relevant trends.

### a) Overview of the Intramolecular Mechanism of Ethyl Vinyl Ether Hydrolysis

Figure 1, Figure 2, and Figure 3 display a schematic view of all the structures located in the PCM-B3LYP-D3/VTZ//PCM-B3LYP/VDZ investigation on the intramolecular mechanism of the $[Cp_2Mo(OH)(OH_2)]^+$-catalyzed hydrolysis of ethyl vinyl ether (see Figure S1 and Tables S1 and S2 for optimized geometry and energy data of the implied species, respectively). Hereafter, unless otherwise stated, the Gibbs energy of all those species will be referred to that of the separate reactants, $[Cp_2Mo(OH)(OH_2)]^+$ + ethyl vinyl ether. As seen in Figure 1, the typical initial step of the intramolecular mechanism is the de-coordination of the aqua ligand from the starting complex $[Cp_2Mo(OH)(OH_2)]^+$, without energy barrier, to form a more stable species $[Cp_2Mo(OH)]^+$ (–7.4 kcal/mol). A NBO analysis of the $[Cp_2Mo(OH)(OH_2)]^+$ and $[Cp_2Mo(OH)]^+$ complexes reflects that Mo presents a positive net atomic charge of +0.45 and +0.57 *e*, respectively. For the case of isolated ethyl vinyl ether, the NBO charges at the terminal carbon atom of the vinyl group (C1), the oxygen atom (O3), and the terminal carbon atom of the ethyl group (C5) amount to –0.56, –0.61, and –0.66 *e*, respectively (see Figure 1 for atom numbering), which suggest that, from the electronic charge point of view, any of these atoms could coordinate to Mo. Next, we describe the reaction mechanisms found for these coordination modes, starting with the most favorable ones.

Figure 1 and Figure 2 display the Gibbs energy profiles obtained for the mechanism proceeding through the vinyl coordination to Mo. As displayed at Figure 1, C1 coordinates to Mo through **TS0** (11.1 kcal/mol) for the formation of intermediate **I1** (6.2 kcal/mol). At **TS0** the Mo···C1 distance is 3.049 Å while a value of 2.472 Å was found at **I1**, clearly indicating the formation of the Mo–C1 bond and, consequently, a certain loss of the double bond character of the C1–C2 bond, whose bond length varies from 1.340 Å at the isolated ether to 1.380 Å at **I1**. Then, the oxygen atom of the hydroxo ligand ($O_{hydroxo}$) attacks C2, activated by the C1–Mo linkage, to give the four-membered metallacycle **I2** (5.0 kcal/mol) via **TS1** (12.2 kcal/mol). The $O_{hydroxo}$···C2 distance notably shortens from 2.119 Å at **TS1** to 1.502 Å at **I2** wherein the $O_{hydroxo}$–C2 bond has already been formed. Besides, the C1–C2 bond length of the vinyl moiety lengthens from 1.434 to 1.508 Å when going from **TS1** to **I2**, thus becoming a single C–C bond. **I2** undergoes a 1,3-hydrogen shift from $O_{hydroxo}$ to O3 with simultaneous cleavage of the C2–O3 bond of the ether moiety through **TS2** (35.0 kcal/mol) to release ethanol, a very stable molecule and one of the reaction products, and the corresponding intermediate **I3** (–9.5 kcal/mol). As in previous theoretical investigations on the reactivity of $[Cp_2Mo(OH)(OH_2)]^+$ towards different organic substrates,[52–54] a more realistic simulation of this type of H-shift was obtained by using a discrete-continuum solvation model that allows the description of the essential role of some water molecules in this step. The inclusion of two explicit water molecules in the computations on **TS2** (**TS2_2w**) and **I2** (**I2_2w**), see Figure 1, reduces the energy difference between them from 30.0 kcal/mol, G(**TS2**)-G(**I2**), to 9.8 kcal/mol, G(**TS2_2w**)-G(**I2_2w**), and, therefore, the Gibbs energy of **TS2** becomes now

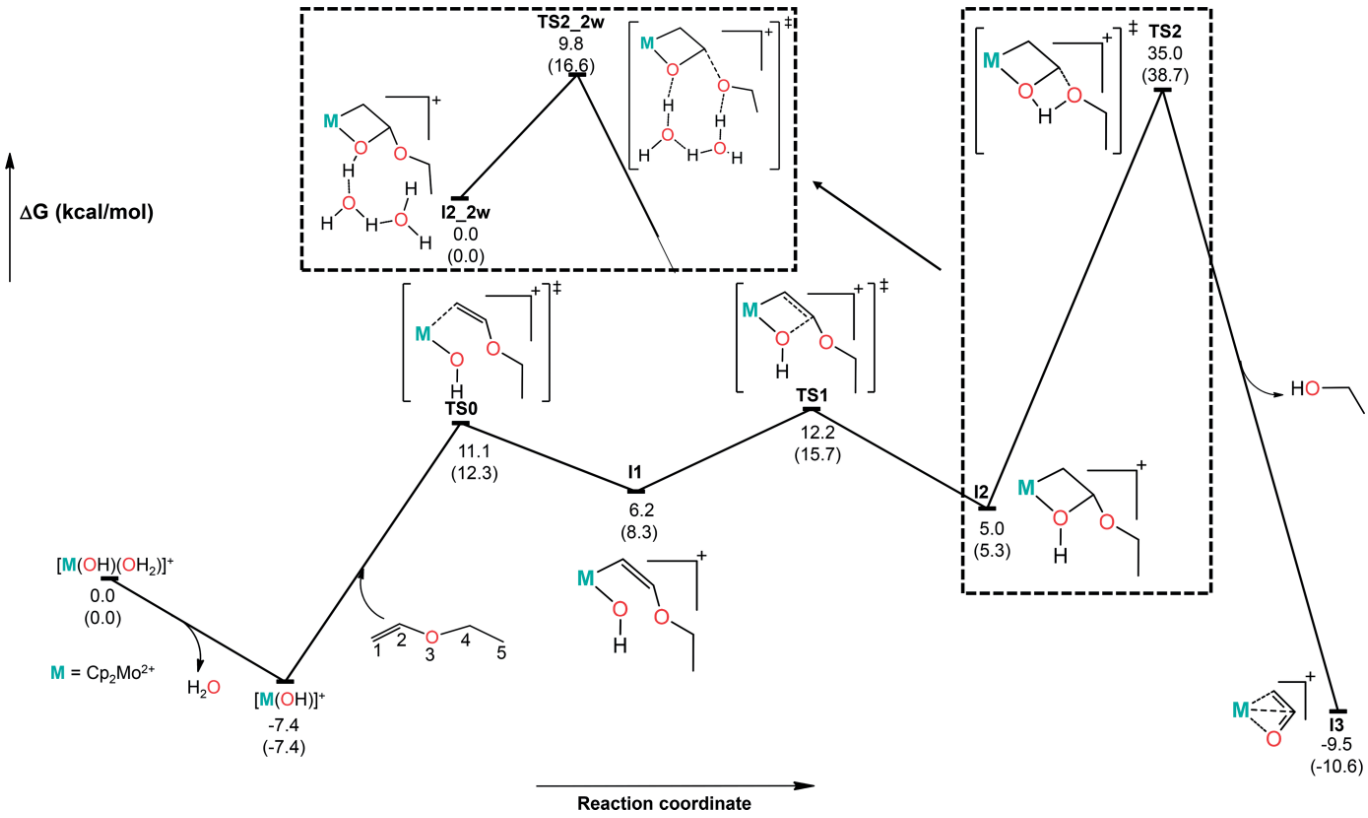


Figure 1. PCM-B3LYP-D3/VTZ//PCM-B3LYP/VDZ Gibbs energy profile of the steps leading to the formation of a $\eta^3$-vinyloxyl Mo complex (**I3**) along the C1–Mo coordination mechanism for the $[Cp_2Mo(OH)(OH_2)]^+$-catalyzed hydrolysis of ethyl vinyl ether. For comparison purposes, relative Gibbs energy values in parenthesis have also been included for some relevant analogous species implied in the $[Cp_2Mo(OH)(OH_2)]^+$-catalyzed hydrolysis of divinyl ether.

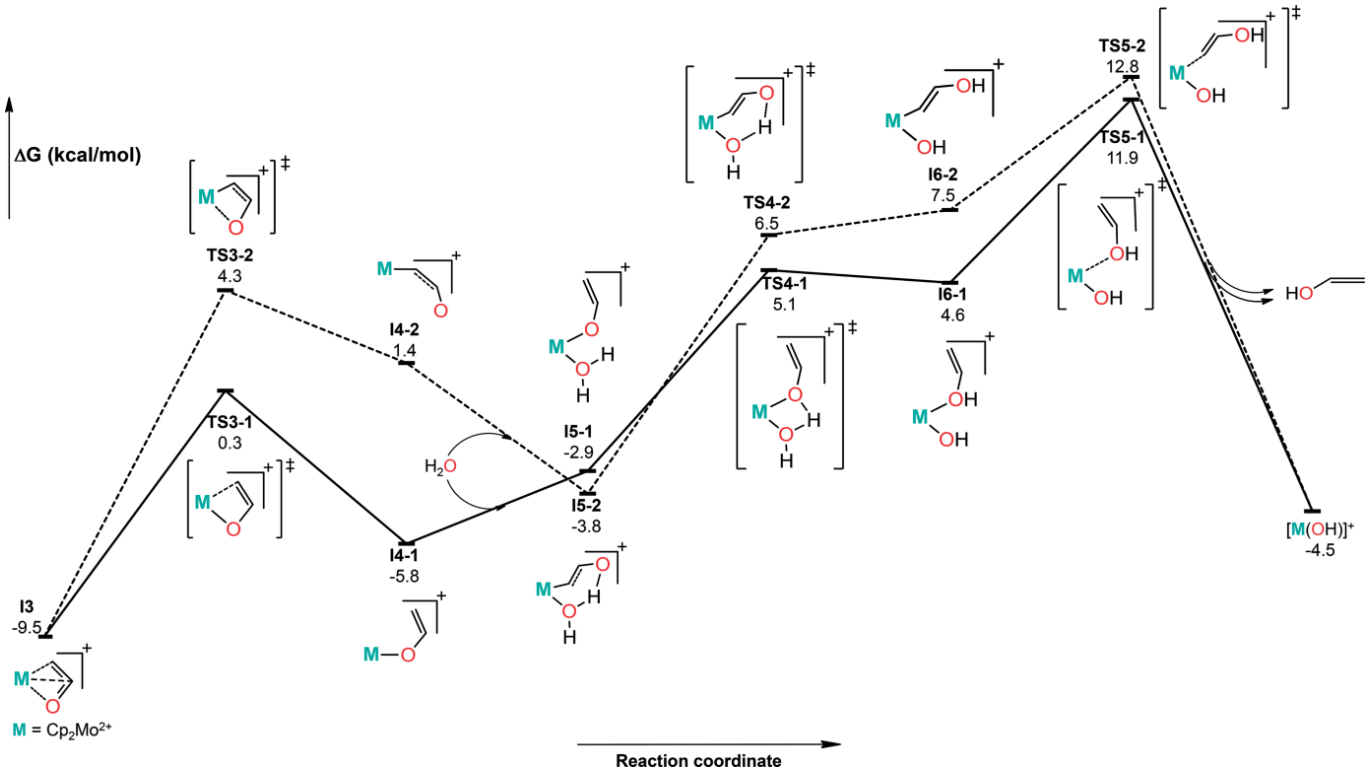


Figure 2. PCM-B3LYP-D3/VTZ//PCM-B3LYP/VDZ Gibbs energy profiles of the steps going from the $\eta^3$-vinyloxyl Mo complex **I3** to the separate products along the C1–Mo coordination mechanism for the $[Cp_2Mo(OH)(OH_2)]^+$-catalyzed hydrolysis of ethyl vinyl ether.

14.8 kcal/mol with respect to the separate reactants. The resultant energy reduction, 20.2 kcal/mol, is in consonance with values close to 16 kcal/mol obtained for analogous migrations in the case of ethyl acetate hydrolysis[52] and acetonitrile hydration[53] catalyzed by $[Cp_2Mo(OH)(OH_2)]^+$. At **I3** Mo is simultaneously interacting with $O_{hydroxo}$ and the C1 and C2 atoms of the original vinyl group of the ether at distances of 2.130, 2.355, and 2.350 Å, respectively. This coordination resembles the typical $\eta^3$-allyl–metal interaction found in pseudo-octahedral Mo complexes and other related ones.[71] As seen in Figure 2, **I3** can evolve through the cleavage of either the Mo–C1 or Mo-$O_{hydroxo}$ bond to give the open intermediates **I4-1** (–5.8 kcal/mol) or **I4-2** (1.4 kcal/mol) via **TS3-1** (0.3 kcal/mol) or **TS3-2** (4.3 kcal/mol), respectively. At both intermediates Mo presents a vacant coordination site, which is immediately occupied by one water molecule from the aqueous reaction medium without any TS. Thus, **I4-1** and **I4-2** become **I5-1** (–2.9 kcal/mol) and **I5-2** (–3.8 kcal/mol) after forming a new bond between Mo and the oxygen atom of the aqua ligand ($O_{water}$) at distances of 2.217 and 2.199 Å, respectively. Besides this, **I5-2** is stabilized by a six-membered ring consequence of a hydrogen bonding interaction between one hydrogen atom of the water ligand ($H_{water}$) and the terminal $O_{hydroxo}$ atom with a bond length of 1.647 Å and $O_{water}$–$H_{water}$···O3 bond angle of 158.1°. At **I5-1**, however, such an interaction is not present [distance($H_{water}$···$O_{hydroxo}$) = 2.086 Å, angle($O_{water}$–$H_{water}$···$O_{hydroxo}$) = 101.4°] because its existence would imply the formation of a very strained four-membered ring ($O_{water}$–$H_{water}$···$O_{hydroxo}$–Mo). Therefore, the transformation **I4-2** + $H_2O$ → **I5-2**, energetically disfavored by the entropy, is partly overcompensated by the energy stabilization caused by the establishment of a hydrogen bond at **I5-2**, but this does not happen in the **I4-1** + $H_2O$ → **I5-1** transformation. **I5-1** and **I5-2** proceed through **TS4-1** (5.1 kcal/mol) and **TS4-2** (6.5 kcal/mol) for another hydrogen migration from $O_{water}$ to $O_{hydroxo}$, directly or non-directly linked to Mo, leading to the intermediates **I6-1** (4.6 kcal/mol) and **I6-2** (7.5 kcal/mol), respectively. The vinyl alcohol moiety present at both intermediates is released in the next step by means of the cleavage of the Mo-$O_{hydroxo}$ (**TS5-1**, 11.9 kcal/mol) and Mo–C1 bonds (**TS5-2**, 12.8 kcal/mol), respectively, thus recovering the active catalyst $[Cp_2Mo(OH)]^+$. We clarify that **I6-2** is 1.0 kcal/mol larger in Gibbs energy than the previous **TS4-2**, but in terms of electronic energy is 0.2 kcal/mol lower than it. Finally, vinyl alcohol would tautomerize into acetaldehyde, the other product experimentally observed, through a H migration from $O_{hydroxo}$ to C1. The experimental activation energy reported for this intramolecular rearrangement (15.2 kcal/mol)[72] is lower than the Gibbs energy barriers found for previous steps.

The reaction mechanism evolving through the coordination of O3 to Mo allows two mechanistic routes depending on whether the vinyl or the ethyl group is the one closest to the hydroxo ligand. For the first option whose PCM-B3LYP-D3/VTZ//PCM-B3LYP/VDZ Gibbs energy profile is collected in Figure 3 (species denoted with the **v_O** label), O3 coordinates to the metal center of $[Cp_2Mo(OH)]^+$ via **TS0v_O** (11.4 kcal/mol) to yield intermediate **I1v_O** (8.3 kcal/mol), in which the newly formed Mo–O3 bond has a distance of 2.375 Å. Then, the nucleophilic attack of $O_{hydroxo}$ on C2, the vinyl carbon directly bonded to O3, occurs with simultaneous cleavage of the C2–O3 bond through **TS1v_O** (36.2 kcal/mol). Afterwards, intermediate **I2v_O** (5.9 kcal/mol), wherein the $\{Cp_2Mo^{2+}\}$ fragment is attached to the ethoxo and vinyl alcohol monodentate ligands via O3 and $O_{hydroxo}$, respectively, forms. The notable diminution of the NBO charge of $O_{hydroxo}$ from –0.90 *e* at **I1v_O** to –0.63 *e* at **I2v_O** is due to the formation of the $O_{hydroxo}$–C2 bond, with the concomitant lengthening of the Mo-$O_{hydroxo}$ bond length, 0.270 Å, when going from **I1v_O** to **I2v_O**. On the other hand, the shortening of the Mo–O3 bond length, 0.365 Å, along with the cleavage of the O3–C2 bond is in consonance with the moderate increase of the NBO charge of O3 from –0.503 *e* at **I1v_O** to –0.689 *e* at **I2v_O**. In addition, that nucleophilic attack at **TS1v_O** involves a very strained four-membered metallacycle (Mo-$O_{hydroxo}$–C2–O3) with an $O_{hydroxo}$–Mo–O3 bond angle of 62.0°, which also contributes to the high instability of **TS1v_O**. Analogous four-membered interactions were found in the nucleophilic attack of the hydroxo ligand on $[Cp_2Mo(OH)]^+$-coordinated ethyl acetate, acetonitrile, and even ether with C1–Mo coordination, but those TSs are between 10 and 25 kcal/mol more stable than **TS1v_O** with respect to their corresponding reactants. In the easiest cases, the OH nucleophilic attack partially breaks an activated double or triple bond, but a simple one, together with the bond in the vinyl fragment, are affected in the ether case with O3–Mo coordination, becoming the substrate split in two moieties.[52,53] Next, the vinyl alcohol ligand at **I2v_O** de-coordinates through **TS2v_O** (10.4 kcal/mol) and, then, would tautomerize to acetaldehyde in water solution. The new complex formed $[Cp_2Mo(OEt)]^+$ (**I3v_O**, –6.6 kcal/mol) has a vacant coordination site, which is immediately occupied by one water molecule without any TS to render the corresponding complex $[Cp_2Mo(OEt)(OH_2)]^+$ (**I4v_O**, 1.1 kcal/mol). The entropic factor is mainly responsible for the energy destabilization in the **I3v_O** + $H_2O$ → **I4v_O** transformation. The Mo-coordinated water molecule transfers one of its hydrogen atoms to O3 through **TS3v_O** (4.0 kcal/mol), thus yielding intermediate **I5v_O** (1.0 kcal/mol). This species has an ethanol ligand that de-coordinates via **TS4v_O** (11.0 kcal/mol) to finally give the ethanol product and the recovery of the $[Cp_2Mo(OH)]^+$ catalyst.

The second orientation of the ethyl vinyl ether for the O3–Mo coordination is even less favored for the ether hydrolysis than the previous one (species are now identified with the **e_O** label). The coordination of the substrate with the ethyl group close to the OH ligand has an energy barrier of 18.5 kcal/mol, **TS0e_O**, with respect to the most stable previous species, $[Cp_2Mo(OH)]^+$, similar to those above described for the different coordination modes of this ether (18.5 kcal/mol, **TS0**, and 18.8 kcal/mol, **TS0v_O**). Now, at **I1e_O** $O_{hydroxo}$ points to C4, a carbon atom with all its valences saturated and whose electron density has hardly reduced, which makes the TS for the nucleophilic attack, **TS1e_O**, 3.3 and 27.3 kcal/mol less stable than **TS1v_O** and **TS1**, respectively. As **TS1v_O**, **TS1e_O** brings about the ether cleavage into two fragments anchored to Mo through O3 (O3–CH=$CH_2$) and $O_{hydroxo}$ ($O_{hydroxo}$–$CH_2$–$CH_3$), as evidenced by intermediate **I2e_O** (–2.1 kcal/mol). After releasing the ethanol ligand, **I2e_O** will evolve to products following

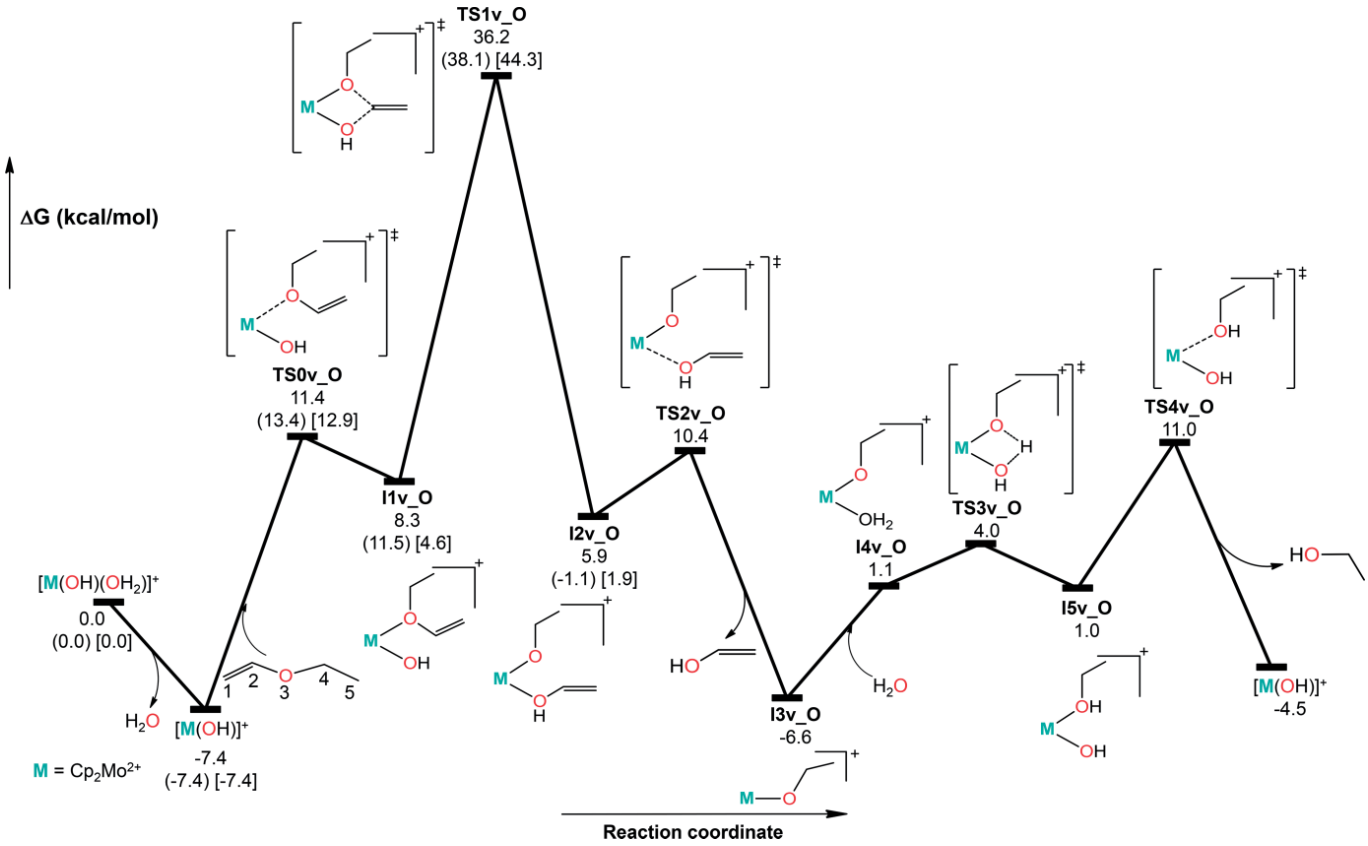


Figure 3. PCM-B3LYP-D3/VTZ//PCM-B3LYP/VDZ Gibbs energy profile of the most favored O3–Mo coordination mechanism for the $[Cp_2Mo(OH)(OH_2)]^+$-catalyzed hydrolysis of ethyl vinyl ether. For comparison purposes, relative Gibbs energy values in parenthesis and square brackets have also been included for some relevant analogous species implied in the $[Cp_2Mo(OH)(OH_2)]^+$-catalyzed hydrolysis of divinyl and diethyl ethers, respectively.

the sequence **I4-1** → **I5-1** → **TS4-1** → **I6-1** → **TS5-1** displayed in Figure 2.

Finally, the coordination of the ethyl vinyl ether to Mo via C5 has been discarded as neither TS nor intermediate were found as a consequence of the saturated nature of the carbon atoms of the ethyl functionality.

The comparison of the most favorable hydrolysis mechanisms of ethyl vinyl ether, displayed in Figure 1, Figure 2, and Figure 3, shows that the ones with vinyl coordination to the catalyst (C1–Mo) are clearly preferred over those with O3–Mo coordination. The most favored C1–Mo route proceeds through the breakage of the C1–Mo bond at **I3** and comprises six steps (initial coordination of the ether; intramolecular nucleophilic OH attack; 1,3-H transfer with elimination of the first alcohol; recovering of a three coordination of Mo; H transfer from just linked water; and elimination of the second alcohol), being the 1,3-H transfer, assisted by two water molecules, the rate-limiting step with an energy barrier of 22.2 kcal/mol measured from its most stable previous species, $[Cp_2Mo(OH)]^+$. Along this route the number of ligands coordinated to Mo varies from 3 {at $[Cp_2Mo(OH)]^+$, **I2**, **I3**, and **I4-1**} to 4 {at $[Cp_2Mo(OH)(OH_2)]^+$, **I1**, **I5-1**, and **I6-1**}. Besides, for the former case, the hapticity displayed by the non-Cp ligand can be 1 {at $[Cp_2Mo(OH)]^+$ and **I4-1**}, 2 (at **I2**), or even 3 (at **I3**). This coordination versatility involves an easy deformation capability of the $Cp_2Mo$ part of the catalyst and is one of its relevant features. As a consequence, it is noteworthy that the energy barrier for the initial coordination of ethyl vinyl ether to the catalyst has always a value between 18 and 19 kcal/mol, irrespective of the ether atom, C1 or O3, which links to Mo or even the ether orientation in the O3–Mo coordination. It is the intramolecular OH nucleophilic attack that makes the difference between the possible routes. Thus, for the C1–Mo coordination the vinyl moiety is activated by the bonding of C1 to the molybdocene and the attack of OH to C2 is quite easy (**TS1**, with an energy barrier of 19.6 kcal/mol), whereas for the O3–Mo coordination no activation of the C atoms singly bonded to O3 (no matter whether they are part of a double or simple C–C bond) is achieved and this step becomes the rate limiting one (**TS1v_O**, with an energy barrier of 43.6 kcal/mol). Actually, C2 is greatly affected by the C1–Mo coordination since at **I1** the C1–C2 bond length increases in 0.040 Å relative to that at the isolated ether and C2 acquires a positive NBO charge of +0.35 *e* at **I1**. The elongations in C2–O3 and O3–C4 bond lengths are much smoother at **I1v_O** (0.024 and 0.020 Å, respectively) and the electron density reduction at O3 neighbor atoms is also much smaller (NBO charges of +0.14 *e* and –0.07 *e* for C2 and C4, respectively).

### b) Influence of Replacing Functionalities at the Ethyl Vinyl Ether to Obtain Equally Substituted Ethers

To gain a deeper insight into ether hydrolysis catalyzed by molybdocenes, we investigated the influence of replacing both the ethyl group by a vinyl one (to yield divinyl ether) and the

vinyl group by an ethyl one (to obtain diethyl ether) on the intramolecular attack mechanisms described in the previous subsection. Given the chemical resemblance, it is reasonable to assume that analogous reaction paths happen for the difunctional and the equally substituted ethers, so we focus on their most relevant steps, i.e., the coordination of the ether to Mo, the nucleophilic attack of the hydroxo ligand to the Mo-coordinated ether, and 1,3-hydrogen migration from the hydroxo ligand to the Mo-coordinated ether (which only happens in the C1–Mo coordination). To denote the species involved in the hydrolysis of the equally substituted ethers, we will use the same acronyms as in the case of ethyl vinyl ether plus the suffixes **dv** or **de** for divinyl or diethyl ether, respectively. For the O3–Mo coordination mechanism, we note however that letters **v** and **e**, used in the ethyl vinyl ether, have been removed in the equally substituted ones for obvious reasons. Figure S2 and Figure S3 collect the optimized geometry of the involved species, while the corresponding energy data are shown in Tables S3–S6. For comparison purposes, relative Gibbs energies of the relevant species involved in the $[Cp_2Mo(OH)(OH_2)]^+$-catalyzed hydrolysis of divinyl ether are displayed in parenthesis in Figure 1 and Figure 3, whereas those of diethyl ether are collected in square brackets in Figure 3.

As for ethyl vinyl case, divinyl ether can coordinate to Mo through either one terminal carbon atom of the vinyl functionality (C1) or the oxygen atom (O3). Again, the first coordination mode is more favorable than the second one (see relative Gibbs energy values in parenthesis in Figure 1 and Figure 3). As seen in Figure 1, all the species involved in the relevant steps of the C1–Mo coordination mechanism are less stable than the analogous ones for the difunctional ether between 0.3 kcal/mol (**I2_dv**) and 3.5 kcal/mol (**TS1**). The C1 atom of divinyl ether coordinates to Mo via **TS0_dv** (12.3 kcal/mol above reactants) to give rise to intermediate **I1_dv** (8.3 kcal/mol), in which the distance of the formed Mo–C1 bond is 2.517 Å (2.925 Å at **TS0_dv**). The next step implies the nucleophilic attack of the hydroxo ligand to C2 via **TS1_dv** (15.7 kcal/mol) to render the four-membered metallacyle **I2_dv** (5.3 kcal/mol). At **TS1_dv** the distance between $O_{hydroxo}$ and C2 is 2.118 Å, which is similar to that in **TS1** (2.119 Å). One may then wonder why the presence of a second vinyl group in the ether makes the barrier for the OH attack slightly larger (by 1.4 kcal/mol) than that for ethyl vinyl ether. The comparison of the geometries of **I1** and **I1_dv** reflects that a second vinyl fragment makes the interaction between the ether and the catalyst slightly weaker, with the C1–Mo bond length a bit larger (by 0.045 Å) and the C1–C2 bond a bit shorter (by 0.011 Å) than in **I1**. As a consequence, the C1–C2 bond is less activated and C2 presents smaller electrophilic character (NBO charge of 0.02 *e* lower in **I1_dv** than in **I1**). At **I2_dv** one hydrogen migrates to the ether oxygen atom from the hydroxo one through **TS2_dv** (38.7 kcal/mol) to provoke the release of the vinyl alcohol with a simultaneous formation of **I3** (–10.6 kcal/mol), the same species as in the analogous H-shift step when ethyl vinyl ether is coordinated to Mo via C1. Again, to get a better modelling of such a H-migration in water solution, we re-compute **I2_dv** and **TS2_dv** including two explicit water molecules, and the difference in Gibbs energy between the corresponding species **I2_2w_dv** and **TS2_2w_dv** amounts to 16.6 kcal/mol (see Figure 1 and Figure S2), 6.8 kcal/mol more than in the analogous assisted step for the ethyl vinyl ether. In this case, unlike in **TS2_2w**, at **TS2_2w_dv** water transfers a proton to C5, the terminal C atom of the non-interacting vinyl group, thus rendering directly acetaldehyde instead the vinyl alcohol. Actually, C5 in the divinyl ether has a significant negative charge and geometrical disposition ready for a proton acceptance. All the attempts to locate a TS analogous to **TS2_2w** failed.

On the other hand, the alternative coordination of divinyl ether to Mo could take place via **TS0_O_dv** (13.4 kcal/mol), in which the Mo···O3 distance is 2.686 Å. This TS evolves to intermediate **I1_O_dv** (11.5 kcal/mol) wherein the Mo–O3 bond is clearly formed with a bond length of 2.433 Å. The next step corresponds to the nucleophilic attack of the hydroxo ligand to the C4 atom through **TS1_O_dv** (38.1 kcal/mol) to split the ether into two moieties. One of them remains linked to Mo via the ether oxygen ($O–CH=CH_2$), while the other one is now linked to the hydroxo oxygen ($HO–CH=CH_2$). Considering both possible reaction routes, it can be seen that the hydrolysis of divinyl ether catalyzed by molybdocene follows the same mechanism as that found for the hydrolysis of ethyl vinyl ether, that is, through C1–Mo coordination.

Regarding the monofunctional diethyl ether, the oxygen atom (O3) is the only one able to coordinate to Mo since the coordination by a saturated terminal carbon of one ethyl functionality is not viable, as previously checked. Relative Gibbs energy values in square brackets in Figure 3 show that the energy barrier for the coordination of diethyl ether to Mo slightly increases by 1.5 kcal/mol compared to that of ethyl vinyl ether. In consonance with this similarity, the Mo···O3 distance at **TS0_O_de** (2.828 Å) is close to the analogous one at **TS0_0** (2.801 Å). As for all routes involving O3–Mo coordination, the nucleophilic attack of OH to one of the saturated C atoms bonded to O3 (C2/C4) is the rate-limiting step with a very large energy relative to isolated reactants (44.3 kcal/mol, 8.1 kcal/mol larger than the corresponding energy barrier for ethyl vinyl ether). Such an energy demanding step means that the hydrolysis of this ether catalyzed by molybdocenes will be much slower (or even forbidden) than that of any ether containing at least one vinyl group linked to the ether O atom.

### c) Comparison with Experimental Findings

Our theoretical investigation on the intramolecular nucleophilic attack mechanism for the hydrolysis of ethyl vinyl ether catalyzed by $[Cp_2Mo(OH)(OH_2)]^+$ shows that the coordination of the end vinyl carbon atom of this difunctional ether to Mo is by far more favorable than routes involving ether oxygen coordination to Mo. Hydrogen migration from OH catalyst ligand to ether oxygen already bonded to the catalyst is the most energy demanding step with a Gibbs energy barrier of 22.2 kcal/mol. This barrier is consistent with the experimental suggestion that the precoordination of the second functional group (i.e., the ether vinyl group) is essential for the ethyl vinyl ether to be hydrolyzed under mild conditions by the Mo catalyst.[45] On

the other hand, a barrier of 22.2 kcal/mol fits well with the experimental activation Gibbs energy found for the same chemical process catalyzed by perchloric acid in water solution (17.1 kcal/mol at 299.85 K)[73] as well as with the Gibbs energy barrier (ca. 23–26 kcal/mol at 313.15 K)[55b] derived from the experimental reaction time using the thermodynamic formulation of the transition state theory[67] for the hydrolysis of benzyl vinyl ether catalyzed by various metal complexes [$PdCl_2$-$(MeCN)_2$, $PtCl_2(MeCN)_2$, $HgSO_4$, $Sc(OTf)_3$, $CuCl_2$, etc.] in water/acetonitrile solution. Regarding the monofunctional diethyl ether, it can only coordinate to Mo via the ether oxygen, so the rate-determining step is now the intramolecular nucleophilic OH attack on an internal ethyl C atom with a large energy barrier of 51.7 kcal/mol. Consequently, such an ether does not hydrolyze in the presence of molybdocenes as experimentally observed.[45]

In addition, the results obtained for the mechanistic investigation on the hydrolysis of the equally substituted divinyl ether are similar to those found for ethyl vinyl ether. The coordination of one of the two terminal carbon atoms of divinyl ether to Mo is again the most favored mechanism with a rate determining Gibbs energy barrier of 29.3 kcal/mol controlled by the same hydrogen transposition. The comparison of the Gibbs energy barriers for the $[Cp_2Mo(OH)(OH_2)]^+$-catalyzed hydrolysis of the three ethers investigated in this work is in good agreement with the experimental fact that ethyl vinyl ether is more reactive than divinyl one, which in turn is more reactive than diethyl ether, for the molybdocene[45] and the acid-catalyzed hydrolysis process.[74]

## Conclusions

The theoretical study (PCM-B3LYP-D3/VTZ//PCM-B3LYP/VDZ level) of the hydrolysis of one difunctional, ethyl vinyl, and two equally substituted, divinyl and diethyl, ethers catalyzed by $[Cp_2Mo(OH)(OH_2)]^+$ leads to the following conclusions.

The ether functionality by itself is not active for the hydrolysis of ethers catalyzed by molybdocenes, as experimentally observed. Our investigation shows that all reaction routes with ether oxygen coordination to Mo produce very large energy barriers (43.6 and 46.9 kcal/mol for ethyl vinyl ether when the catalyst OH attacks a vinyl and an ethyl carbon, respectively, and 45.5 and 51.7 kcal/mol for divinyl and diethyl ethers, respectively). As a consequence, the second functionality (i.e., the ether non-alkane substituent) is crucial for the viability of the ether hydrolysis in the presence of molybdocenes. Only if the second functionality has a double or triple bond this will coordinate to Mo and start an accessible hydrolysis process. Thus, ethyl vinyl and divinyl ethers hydrolyze through the coordination of the vinyl group to the metal with Gibbs energy barriers of 22.2 and 29.3 kcal/mol, respectively. The barriers found in our study agree with the experimental reactivity trend observed for hydrolysis of the ethers here considered. In this sense, we have seen that a second vinyl substituent does not reduce the barrier for the hydrolysis, but the opposite; it renders a weaker coordination of the ether with the catalyst and a costlier nucleophilic OH addition.

The preference for a terminal vinyl coordination over the ether oxygen one could be thought to depend on the steric hindrance produced by the ramification in the ether oxygen atom. However, all the energy barriers for the initial Mo coordination of the three ethers here handled present similar values, in the range of 18.5–21.8 kcal/mol. This fact goes against that reasoning and can be explained on the basis of observed flexibility of the $Cp_2Mo$ fragment at the catalyst. The comparison of our reaction mechanisms shows that the main effect of the kind of ether coordination relates to the energy cost of the second reaction step, the intramolecular OH nucleophilic attack on the atoms directly bonded to the one linked to Mo. For a vinyl coordination (or for the coordination of any unsaturated functionality like carbonyl or nitrile ones) the catalyst withdraws electron density from the functionality, which activates the group for an easy nucleophilic attack. Such an activation is not possible for an $O_{ether}$–Mo coordination, so the nucleophilic attack, which is the rate-limiting step, is energetically very expensive in these cases.

## Acknowledgments

The authors thank Ministerio de Economía y Competitividad (Grant No. CTQ2015-70231-P) and Universidad de Oviedo (Grant No. PAPI-18-PF-05) of Spain for financial support.

**Keywords:** Sustainable chemistry · Molybdenum · Ether hydrolysis · Divergent reactivity · Density functional calculations

[1] P. T. Anastas, J. C. Warner, *Green Chemistry: Theory and Practice*, Oxford University Press, London, **1998**.
[2] A. S. Matlack, *Introduction to Green Chemistry*, Marcel Dekker Inc., New York, **2001**.
[3] J. H. Clark, D. J. Macquarrie, *Handbook of Green Chemistry and Technology*, Blackwell Publishers, Oxford, **2002**.
[4] V. K. Ahluwalia, M. Kidwai, *New Trends in Green Chemistry*, Springer Netherlands, Dordrecht, **2004**.
[5] R. Mestres, *Env. Sci. Pollut. Res.* **2005**, *12*, 128–132.
[6] I. T. Horváth, P. T. Anastas, *Chem. Rev.* **2007**, *107*, 2169–2173.
[7] P. T. Anastas, J. B. Zimmerman (Eds.), *Innovations in Green Chemistry and Green Engineering*, Springer, New York, **2013**.
[8] K. Tanaka, F. Toda, *Chem. Rev.* **2000**, *100*, 1025–1074.
[9] P. J. Walsh, H. Li, C. A. Anaya de Parrodi, *Chem. Rev.* **2007**, *107*, 2503–2545.
[10] K. Tanaka, *Solvent-Free Organic Synthesis*, 2nd Ed. Wiley-VCH, Weinheim, **2009**.
[11] M. A. P. Martins, C. P. Frizzo, D. N. Moreira, L. Buriol, P. Machado, *Chem. Rev.* **2009**, *109*, 4140–4182.
[12] T. Ema, Y. Miyazaki, S. Koyama, Y. Yano, T. Sakai, *Chem. Commun.* **2012**, *48*, 4489–4491.
[13] T. Ema, Y. Miyazaki, J. Shimonishi, C. Maeda, J. Hasegawa, *J. Am. Chem. Soc.* **2014**, *136*, 15270–15279.
[14] C. Maeda, T. Taniguchi, K. Ogawa, T. Ema, *Angew. Chem. Int. Ed.* **2015**, *54*, 134–138; *Angew. Chem.* **2015**, *127*, 136.
[15] C. Maeda, J. Shimonishi, R. Miyazaki, J. Hasegawa, T. Ema, *Chem. Eur. J.* **2016**, *22*, 6556–6563.
[16] J. Ranke, S. Stolte, R. Störmann, J. Aming, B. Jastorff, *Chem. Rev.* **2007**, *107*, 2183–2206.
[17] C. D. Hubbard, P. Illner, R. van Eldik, *Chem. Soc. Rev.* **2011**, *40*, 272–290.
[18] T. Itoh, *Chem. Rev.* **2017**, *117*, 10567–10607.
[19] Z. Radai, N. Z. Kiss, G. Keglevich, *Curr. Org. Chem.* **2018**, *22*, 533–556.

[20] Y. Medina-Gonzalez, S. Camy, J. S. Condoret, *ACS Sustainable Chem. Eng.* **2014**, *2*, 2623–2636.
[21] P. Licence, J. Ke, M. Sokolova, S. K. Ross, M. Poliakoff, *Green Chem.* **2003**, *5*, 99–104.
[22] S. Campestrini, U. Tonellato, *Curr. Org. Chem.* **2005**, *9*, 31–47.
[23] T. Kitanosono, K. Masuda, P. Xu, S. Kobayashi, *Chem. Rev.* **2018**, *118*, 679–746.
[24] W. Wang, L. Cui, P. Sun, L. Shi, C. Yue, F. Li, *Chem. Rev.* **2018**, *118*, 9843–9929.
[25] F. Joó, *Aqueous Organometallic Catalysis*, *Vol. 23*, Kluwer Academic Publishers, Dordrecht, **2001**.
[26] P. H. Dixneuf, V. Cadierno (Eds.), *Metal-Catalyzed Reactions in Water*, Wiley-VCH, Weinheim, **2013**.
[27] B. Cornils, W. A. Herrmann (Eds.), *Applied Homogeneous Catalysis with Organometallic Compounds: A Comprehensive Handbook in Three Volumes*, Wiley-VCH, Weinheim, **2002**.
[28] A. Chanda, V. V. Fokin, *Chem. Rev.* **2009**, *109*, 725–748.
[29] L. Y. Kuo, M. G. Kanatzidis, M. Sabat, A. L. Tipton, T. J. Marks, *J. Am. Chem. Soc.* **1991**, *113*, 9027–9045.
[30] M. M. Harding, G. Mokdsi, J. P. Mackay, M. Prodigalidad, S. W. Lucas, *Inorg. Chem.* **1998**, *37*, 2432–2437.
[31] J. B. Waern, M. M. Harding, *J. Organomet. Chem.* **2004**, *689*, 4655–4668.
[32] J. B. Waern, M. M. Harding, *Inorg. Chem.* **2004**, *43*, 206–213.
[33] A. Erxleben, *Inorg. Chem.* **2005**, *44*, 1082–1094.
[34] A. Erxleben, J. Kottmann, *Inorg. Chim. Acta* **2006**, *359*, 13–24.
[35] E. Meléndez, *J. Organomet. Chem.* **2012**, *706–707*, 4–12.
[36] K. L. Breno, T. J. Ahmed, M. D. Pluth, C. Balzarek, D. R. Tyler, *Coord. Chem. Rev.* **2006**, *250*, 1141–1151.
[37] T. J. Ahmed, L. N. Zakharov, D. R. Tyler, *Organometallics* **2007**, *26*, 5179–5187.
[38] T. J. Ahmed, B. R. Fox, S. M. M. Knapp, R. B. Yelle, J. J. Juliette, D. R. Tyler, *Inorg. Chem.* **2009**, *48*, 7828–7837.
[39] T. J. Ahmed, S. M. M. Knapp, D. R. Tyler, *Coord. Chem. Rev.* **2011**, *255*, 949–974.
[40] D. Suárez, M. Zakarianezhad, R. López, *Theor. Chem. Acc.* **2013**, *132*, 1409–1419.
[41] C. Balzarek, D. R. Tyler, *Angew. Chem. Int. Ed.* **1999**, *38*, 2406–2408; *Angew. Chem.* **1999**, *111*, 2563.
[42] C. Balzarek, T. J. R. Weakley, D. R. Tyler, *J. Am. Chem. Soc.* **2000**, *122*, 9427–9434.
[43] K. L. Breno, D. R. Tyler, *Organometallics* **2001**, *20*, 3864–3868.
[44] K. L. Breno, M. D. Pluth, D. R. Tyler, *Organometallics* **2003**, *22*, 1203–1211.
[45] K. L. Breno, M. D. Pluth, C. W. Landorf, D. R. Tyler, *Organometallics* **2004**, *23*, 1738–1746.
[46] T. J. Ahmed, D. R. Tyler, *Organometallics* **2008**, *27*, 2608–2613.
[47] L. Y. Kuo, S. Kuhn, D. Ly, *Inorg. Chem.* **1995**, *34*, 5341–5345.
[48] L. Y. Kuo, L. A. Barnes, *Inorg. Chem.* **1999**, *38*, 814–817.
[49] L. Y. Kuo, N. M. Perera, *Inorg. Chem.* **2000**, *39*, 2103–2106.
[50] L. Y. Kuo, A. P. Blum, M. Sabat, *Inorg. Chem.* **2005**, *44*, 5537–5541.
[51] L. Y. Kuo, A. K. Bentley, Y. A. Shari'ati, C. P. Smith, *Organometallics* **2012**, *31*, 5294–5301.
[52] E. Tílvez, G. I. Cárdenas-Jirón, M. I. Menéndez, R. López, *Inorg. Chem.* **2015**, *54*, 1223–1231.
[53] E. Tílvez, M. I. Menéndez, R. López, *Organometallics* **2012**, *31*, 1618–1626.
[54] E. Tílvez, M. I. Menéndez, R. López, *Eur. J. Inorg. Chem.* **2012**, 4445–4453.
[55] a) Y. Okimoto, S. Sakaguchi, Y. Ishii, *J. Am. Chem. Soc.* **2002**, *124*, 1590–1591 and references cited therein; b) H. Aoyama, M. Tokunaga, S. Hiraiwa, Y. Shirogane, Y. Obora, Y. Tsuji, *Org. Lett.* **2004**, *6*, 509–512.
[56] a) G. H. Huber, S. Iborra, A. Corma, *Chem. Rev.* **2006**, *106*, 4044–4098; b) A. G. Sergeev, J. F. Hartwig, *Science* **2011**, *332*, 439–443; c) X. Liang, A. Montoya, B. S. Haynes, *J. Phys. Chem. B* **2011**, *115*, 8199–8206; d) J. Cornella, C. Zaratea, R. Martin, *Chem. Soc. Rev.* **2014**, *43*, 8081–8097; e) C. Li, X. Zhao, A. Wang, G. W. Huber, T. Zhang, *Chem. Rev.* **2015**, *115*, 11559–11624.
[57] a) H. B. Schlegel, *J. Comput. Chem.* **1982**, *3*, 214–218; b) H. B. Schlegel, *Theor. Chim. Acta* **1984**, *66*, 333–340; c) X. Li, M. J. Frisch, *J. Chem. Theory Comput.* **2006**, *2*, 835–839.
[58] a) B. Mennucci, J. Tomasi, *J. Chem. Phys.* **1997**, *106*, 5151–5158; b) V. Barone, M. Cossi, J. Tomasi, *J. Chem. Phys.* **1997**, *107*, 3210–3221; c) E. Cancès, B. Mennucci, J. Tomasi, *J. Chem. Phys.* **1997**, *107*, 3032–3041; d) V. Barone, M. Cossi, J. Tomasi, *J. Comput. Chem.* **1998**, *19*, 404–417; e) J. Tomasi, B. Mennucci, E. Cancès, *THEOCHEM* **1999**, *464*, 211–226; f) G. Scalmani, M. J. Frisch, *J. Chem. Phys.* **2010**, *132*, 114110/1–5.
[59] A. Bondi, *J. Phys. Chem.* **1964**, *68*, 441–445.
[60] J. Tomasi, M. Persico, *Chem. Rev.* **1994**, *94*, 2027–2094.
[61] a) A. D. Becke, *Phys. Rev. A* **1988**, *38*, 3098–3100; b) C. Lee, W. Yang, R. G. Parr, *Phys. Rev. B* **1988**, *37*, 785–789; c) P. J. Stephens, F. J. Devlin, C. F. Chabalowski, M. J. Frisch, *J. Phys. Chem.* **1994**, *98*, 11623–11627; d) A. D. Becke, *J. Chem. Phys.* **1993**, *98*, 5648–5652.
[62] a) T. H. Dunning, *J. Chem. Phys.* **1989**, *90*, 1007–1023; b) R. A. Kendall, T. H. Dunning, R. J. Harrison, *J. Chem. Phys.* **1992**, *96*, 6796–6806.
[63] K. A. Peterson, D. Figgen, M. Dolg, H. Stoll, *J. Chem. Phys.* **2007**, *126*, 124101/1–12.
[64] a) C. Gonzalez, H. B. Schlegel, *J. Chem. Phys.* **1989**, *90*, 2154–2161; b) C. Gonzalez, H. B. Schlegel, *J. Phys. Chem.* **1990**, *94*, 5523–5527.
[65] S. Grimme, J. Antony, S. Ehrlich, H. A. Krieg, *J. Chem. Phys.* **2010**, *132*, 154104/1–19.
[66] a) E. R. Johnson, A. D. Becke, *J. Chem. Phys.* **2006**, *124*, 174104/1–9; b) S. Grimme, S. Ehrlich, L. Goerigk, *J. Comput. Chem.* **2011**, *32*, 1456–1465.
[67] D. A. McQuarrie, *Statistical Mechanics*, Harper & Row, New York, **1976**.
[68] R. F. Ribeiro, A. V. Marenich, C. J. Cramer, D. G. Truhlar, *J. Phys. Chem. B* **2011**, *115*, 14556–14562.
[69] a) E. D. Glendening, A. E. Reed, J. E. Carpenter, F. Weinhold, *NBO Program, Version 3.1*, University of Wisconsin, Madison, **1998**; b) F. Weinhold, C. R. Landis, *Valency and Bonding: A Natural Bond Orbital Donor-Acceptor Perspective*, Cambridge University Press, Cambridge, **2005**.
[70] M. J. Frisch, G. W. Trucks, H. B. Schlegel, G. E. Scuseria, M. A. Robb, J. R. Cheeseman, G. Scalmani, V. Barone, B. Mennucci, G. A. Petersson, H. Nakatsuji, M. Caricato, X. Li, H. P. Hratchian, A. F. Izmaylov, J. Bloino, G. Zheng, J. L. Sonnenberg, M. Hada, M. Ehara, K. Toyota, R. Fukuda, J. Hasegawa, M. Ishida, T. Nakajima, Y. Honda, O. Kitao, H. Nakai, T. Vreven, J. A. Montgomery Jr., J. E. Peralta, F. Ogliaro, M. Bearpark, J. J. Heyd, E. Brothers, K. N. Kudin, V. N. Staroverov, R. Kobayashi, J. Normand, K. Raghavachari, A. Rendell, J. C. Burant, S. S. Iyengar, J. Tomasi, M. Cossi, N. Rega, J. M. Millam, M. Klene, J. E. Knox, J. B. Cross, V. Bakken, C. Adamo, J. Jaramillo, R. Gomperts, R. E. Stratmann, O. Yazyev, A. J. Austin, R. Cammi, C. Pomelli, J. W. Ochterski, R. L. Martin, K. Morokuma, V. G. Zakrzewski, G. A. Voth, P. Salvador, J. J. Dannenberg, S. Dapprich, A. D. Daniels, Ö. Farkas, J. B. Foresman, J. V. Ortiz, J. Cioslowski, D. J. Fox, *Gaussian 09*, *Revision B.01*, Gaussian, Inc., Wallingford CT, **2009**.
[71] a) J. Pérez, V. Riera, A. Rodríguez, R. López, T. L. Sordo, S. García-Granda, E. García-Rodríguez, A. Galindo, *Organometallics* **2003**, *22*, 1540–1545; b) M. Brill, J. Díaz, M. A. Huertos, R. López, J. Pérez, L. Riera, *Chem. Eur. J.* **2011**, *17*, 8584–8595; c) A. Cebollada, M. E. Viguri, J. Pérez, J. Díaz, R. López, L. Riera, *Inorg. Chem.* **2015**, *54*, 2580–2590; d) S. Fombona, M. Espinal-Viguri, M. A. Huertos, J. Díaz, R. López, M. I. Menéndez, J. Pérez, L. Riera, *Chem. Eur. J.* **2016**, *22*, 17160–17164.
[72] B. Capon, C. Zucco, *J. Am. Chem. Soc.* **1982**, *104*, 7567–7572.
[73] A. J. Kresge, Y. Chiang, *J. Chem. Soc. B* **1967**, 58–61.
[74] A. J. Kresge, Y. Chiang, *J. Chem. Soc. B* **1967**, 53–57. See also references 2 and 5 therein.

Received: May 8, 2019

## 5.5 Regiochemistry control by Bipy substituents in the deprotonation of Re(I) and Mo(II) N-alkylimidazole complexes

Maialen Espinal-Viguri, Sergio Fombona, Daniel Álvarez, Jesús Díaz, M. Isabel Menéndez, Ramón López, Julio Pérez, and Lucía Riera
*Chem. Eur. J.* **2019**, *25*, 9253-9265

Organometallic Chemistry |*Hot Paper*|

# Regiochemistry Control by Bipyridine Substituents in the Deprotonation of $Re^{I}$ and $Mo^{II}$ *N*-Alkylimidazole Complexes

Maialen Espinal-Viguri,[b] Sergio Fombona,[b] Daniel Álvarez,[d] Jesús Díaz,*[c] M. Isabel Menéndez,[d] Ramón López,*[d] Julio Pérez,[a, b] and Lucía Riera*[a]

**Abstract:** Compounds containing *N*-alkylimidazoles (*N*-RIm) and 4,4′-disubstituted 2,2′-bipyridines (4,4′-$R'_2$bipy) coordinated to cationic $\{Mo(\eta^3\text{-}C_4H_7)(CO)_2\}$ and $\{Re(CO)_3\}$ fragments undergo deprotonation of the C2-H group of the *N*-RIm ligands in their reactions with $KN(SiMe_3)_2$. The resulting internal nucleophile adds either to one pyridyl ring, which becomes dearomatized and can undergo ring opening in the subsequent reaction with excess MeOTf, or to the metal center, yielding imidazol-2-yl complexes, which in turn add HOTf or MeOTf, affording N-heterocyclic carbene complexes. Which pathway is followed is dictated by the metal and the nature of the imidazole (R) and bipyridine (R′) substituents. For $Re^{I}$ compounds, addition to pyridine is found with R′ = *t*Bu and OMe, whereas for R = Me and R′ = $NMe_2$, imidazolyl formation is preferred. Coordination of 4,7-$Cl_2$-1,10-phenanthroline to $Mo^{II}$ favors C–C coupling, in contrast to the analogous parent bipy or phenanthroline complexes, for which formation of the imidazol-2-yl complexes had been found. DFT calculations showed the theoretically expected products in each case, and following their predictions new types of products were obtained experimentally.

## Introduction

The study of the dearomatization of pyridines mediated by transition metal complexes is expected to provide homogeneous models for the industrially relevant, yet poorly understood, hydrodenitrogenation process.[1] The first examples of pyridine ring opening, reported by Wolczanski et al.[2] and Wigley et al.,[3] involved strongly reducing early transition metal complexes capable of binding pyridines in the very rare $\kappa^2$-*C*,*N* mode. In such compounds, the strong backdonation from the metal fragment weakens the metal-coordinated C–N bond so much that the complex can be regarded as a metallaaziridine. As a consequence, the electrophilic character of its α-carbon atom increases. Mindiola and co-workers effected pyridine ring opening by a completely different approach, namely, cycloaddition between the pyridine C=N bond and a highly reactive titanium alkylidine intermediate.[4] Diaconescu et al.[5] achieved the ring opening of substituted imidazoles by group 3 metals Sc and Y[6] as well as by U alkyl complexes. More recently, Luo and Hou reported the extrusion of a nitrogen atom from a pyridine or quinoline ring at a trinuclear titanium polyhydride complex through reduction of a HC=N unit followed by cleavage of the two C–N bonds.[7]

In the chemistry of main group metals, several reagents are known to dearomatize pyridine rings.[8] In the cases in which mechanistic information is available, the initial formation of a metal pyridine complex is followed by intramolecular metal-to-pyridine group transfer of $NH_2$, R, H, or F.[9] Formally related are alkyl transfers from f-block metals to pyridines. In the overwhelmingly large majority of their transition metal complexes, pyridine donors are $\kappa^1$-*N* coordinated.[1a,10] Outer-sphere nucleophilic attack on coordinated pyridines in these species has been proposed long ago by Gillard and Lyons,[11,12] but the few uncontroversial examples required hydrothermal conditions.[13]

We have demonstrated several examples of pyridyl ring dearomatization by intramolecular nucleophilic attack of a deprotonated *N*-alkyimidazole (*N*-RIm) ligand on coordinated 2,2′-bipyridine (bipy) and 1,10-phenanthroline (phen).[14] In the products of these reactions one of the C–N bonds has been activated and transformed into a single bond. Bipy and phen have been widely employed in all areas of coordination chemistry;[15] however, prior to our work, examples of dearomatization of transition-metal-coordinated bipy and phen under mild conditions were hardly known.[16,17] In one instance,

[a] *Dr. J. Pérez, Dr. L. Riera*
*Centro de Investigación en Nanomateriales y Nanotecnología-CINN*
*CSIC-Universidad de Oviedo-Principado de Asturias*
*Avda. de la Vega 4–6, 33940 El Entrego (Spain)*
*E-mail: l.riera@cinn.es*

[b] *Dr. M. Espinal-Viguri, S. Fombona, Dr. J. Pérez*
*Departamento de Química Orgánica e Inorgánica*
*Universidad de Oviedo, C/ Julián Clavería, 8. 33006 Oviedo (Spain)*

[c] *Dr. J. Díaz*
*Departamento de Química Orgánica e Inorgánica*
*Universidad de Extremadura, Avda. de la Universidad s/n.*
*10071 Cáceres (Spain)*
*E-mail: jdal@unex.es*

[d] *D. Álvarez, Dr. M. I. Menéndez, Dr. R. López*
*Departamento de Química Física y Analítica*
*Universidad de Oviedo, C/ Julián Clavería, 8. 33006 Oviedo (Spain)*
*E-mail: rlopez@uniovi.es*

*Supporting information and the ORCID identification number(s) for the author(s) of this article can be found under: https://doi.org/10.1002/chem.201901060.*

we found that two successive methylations of the dearomatized pyridyl moiety cleave a C–N bond with formation of a pyridyl ring-opening product.[14g] Herein, we report a study on the effect of the nature of bipy or phen backbone substituents on the deprotonation outcome of $Mo^{II}$ and $Re^{I}$ imidazole complexes.[18] The electronic properties of these substituents determine the type of product obtained, and allow one to favor either intramolecular C–C coupling products (involving bipy C2 or C6, depending on the nature of the substituent) or formation of imidazol-2-yl products. Some of the substituents employed herein promote the pyridyl ring-opening reaction, of which a single example was previously known.

## Results and Discussion

We started our study on the effect of the nature of the groups at the 4- and 4′-positions of 2,2′-bipyridine ligands by employing *tert*-butyl groups as substituents. The addition of equimolar amounts of $KN(SiMe_3)_2$ to THF solutions of [Mo($\eta^3$-$C_4H_7$)$(CO)_2$(4,4′-*t*$Bu_2$bipy)(*N*-RIm)]OTf (R = Mes (2,4,6-trimethylphenyl), **1a**; Me, **1b**)[19–21] at −78 °C resulted in a color change from orange to brown, and in a shift to lower wavenumbers of the IR $\nu_{CO}$ bands consistent with the formation of neutral products (e.g., from 1950, 1868 to 1930, 1848 $cm^{-1}$ for **1a**). The stability of these species was not high enough to allow their isolation, so electrophilic interception was performed by addition of an equimolar amount, in each case, of HOTf or MeOTf to afford **2a**,**b** or **3a**,**b**, respectively (see Scheme 1).

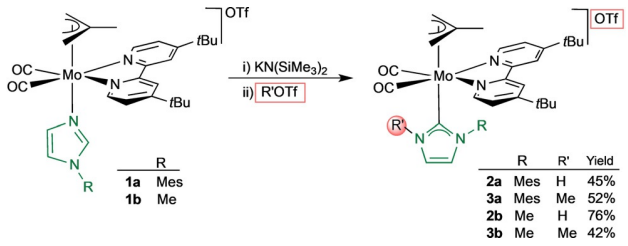


**Scheme 1.** Reactivity of [Mo($\eta^3$-$C_4H_7$)$(CO)_2$(4,4′-*t*$Bu_2$bipy)(*N*-RIm)]OTf (**1a**,**b**). Synthesis of $Mo^{II}$ NHC complexes.

Similar spectroscopic key features were found for all of the new compounds, indicating that the same type of product was formed. The IR $\nu_{CO}$ bands indicate retention of the *cis*-{$Mo(CO)_2$} unit, shifted to higher wavenumbers compared to the neutral intermediates as a consequence of the reaction with the electrophilic reagents (e.g., 1946, 1865 $cm^{-1}$ for **2a**). NMR spectra clearly showed the presence of a molecular mirror plane, so formation of the corresponding *N*-heterocyclic carbene (NHC) complexes can be proposed, via the *C*-bonded imidazol-2-yl neutral species, which are subsequently protonated or methylated on the nonsubstituted nitrogen atom. Accordingly, $^1$H NMR spectra of **2a**,**b** and **3a**,**b** showed only the signals for two imidazole CH groups, and the low-intensity signal corresponding to the Mo-$C_{carbene}$ atom in the $^{13}$C NMR spectra, in the range 185.2–186.8 ppm, is good evidence of the formation of NHC complexes. The solid-state structure determi-

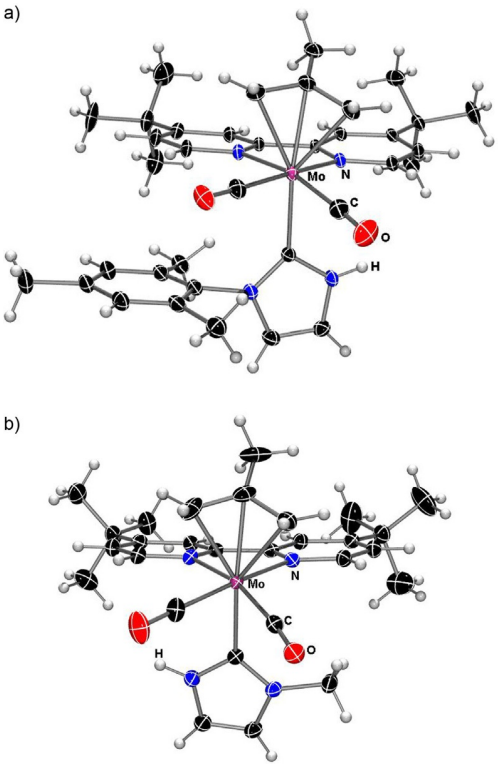


**Figure 1.** Molecular structure of the cations of: a) **2a**, and b) **2b** with thermal ellipsoids at 30% probability.

nation by X-ray diffraction of compounds **2a** and **2b** confirmed the formation of $Mo^{II}$ NHC complexes (Figure 1).[22]

In both structures the NH-NHC ligand is in *trans* disposition to the $\eta^3$-methallyl ligand, whereas the bipy and the two carbonyl ligands define the meridional plane of the pseudooctahedral molybdenum coordination environment. The Mo–$C_{carbene}$ bond lengths of 2.247(4) and 2.228(4) Å for compounds **2a** and **2b** are in the range from 2.143(2) to 2.285(9) Å established for $Mo^{II}$ NHC complexes.[23]

This behavior is reminiscent of that previously found for the nonsubstituted $Mo^{II}$ bipy complexes,[24,25] whereas for 4,4′-$X_2$bipy (X = Cl, Br) derivatives products of C–C coupling between imidazole C2 and bipy C2 were observed.[14d]

To carry out similar studies on $Re^{I}$ compounds, cationic *fac*-{$Re(CO)_3$} *N*-alkylimidazole complexes were prepared by simple substitution of the triflate anion by the *N*-RIm ligand in [Re(OTf)$(CO)_3$(4,4′-R′$_2$bipy)] (R′ = *t*Bu, OMe, $NMe_2$) complexes.[19] We had previously found that for the nonsubstituted bipy complexes [$Re(CO)_3$(bipy)(*N*-RIm)]OTf, deprotonation of the central CH group of the imidazole ligand triggered nucleophilic attack on the C6 atom of bipy, which became dearomatized.[14g] This reaction can be regarded as a C–C coupling reaction in which a nucleophile generated in situ (the deprotonated imidazole carbon atom) attacks an electrophile (the bipy ligand). Therefore, for $Re^{I}$ *N*-alkylimidazole species, electron-donating substituents were chosen in an attempt to increase the electron density of the aromatic diimine ligand, diminish its electrophilic character, and hence discourage the C–C coupling reaction

and encourage the reaction to follow a different pathway. The reaction of the *tert*-butyl derivatives [Re(CO)$_3$(4,4′-*t*Bu$_2$bipy)(*N*-RIm)]OTf (R = Mes, **4a**; Me **4b**) with an equimolar amount of KN(SiMe$_3$)$_2$ afforded immediately, as indicated by the IR $\nu_{CO}$ values, neutral species, which in the case of **5b** could be characterized in solution by means of $^1$H NMR spectroscopy. The $^1$H NMR spectrum showed distinct signals for each nucleus of the bipy moiety and strongly upfield shifted signals of one ring (at 5.70, 5.54, and 4.92 ppm). These features indicate that the reaction involved a transformation of the bipy ligand, so we can propose that complex **5b** results from the intramolecular nucleophilic attack at a bipy C6 atom by the deprotonated imidazole, which generates a new C–C bond with consequent dearomatization of the involved pyridyl ring (Scheme 2), in a similar reaction pathway to that found for the nonsubstituted bipy *N*-RIm complexes.[14g]

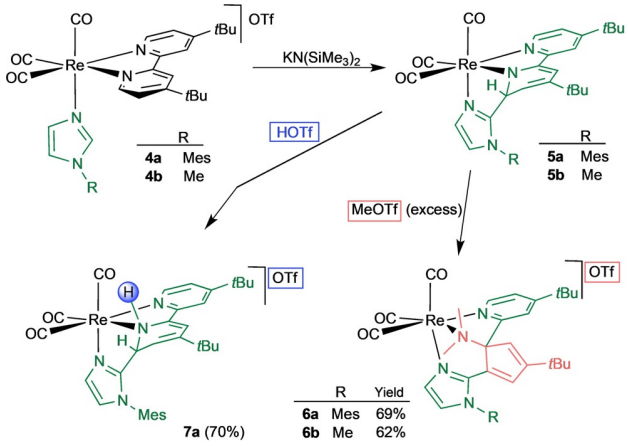


**Scheme 2.** Reactivity of [Re(CO)$_3$(4,4′-*t*Bu$_2$bipy)(*N*-RIm)]OTf towards the strong base KN(SiMe$_3$)$_2$, and afterwards towards an electrophile (HOTf or MeOTf).

The addition of excess MeOTf in $CH_2Cl_2$ to neutral intermediates **5a**,**b** led to two successive methylations and cleavage of the C–N bond of the dearomatized ring, resulting in formation of ring-opening products **6a**,**b** (Scheme 2). The new compounds were spectroscopically characterized in solution, and, for **6a**, also by X-ray diffraction in the solid state (Figure 2a).[22]

The most striking feature of these new complexes is the fact that, in the overall reaction, one of the pyridine rings of the bipy chelate underwent nitrogen extrusion to afford an N-bonded cyclopentadienyldimethylamino group. Activation of bipy ligands is very rare, as they form very stable five-membered chelate rings with transition metals,[26] and cleavage of their pyridine C–N bonds remains unknown, apart from our previous example with the parent bipy [Re(CO)$_3$(bipy)(*N*-MeIm)]OTf complex.[14g] Even when an excess of MeOTf was used with the analogous *N*-mesitylimidazole derivative, [Re(CO)$_3$(bipy)(*N*-MesIm)]OTf, pyridine ring opening did not take place; instead, only the product of C–C coupling and monomethylation was obtained. A product of this latter type, namely **7a**, was obtained from the reaction of **5a** with HOTf

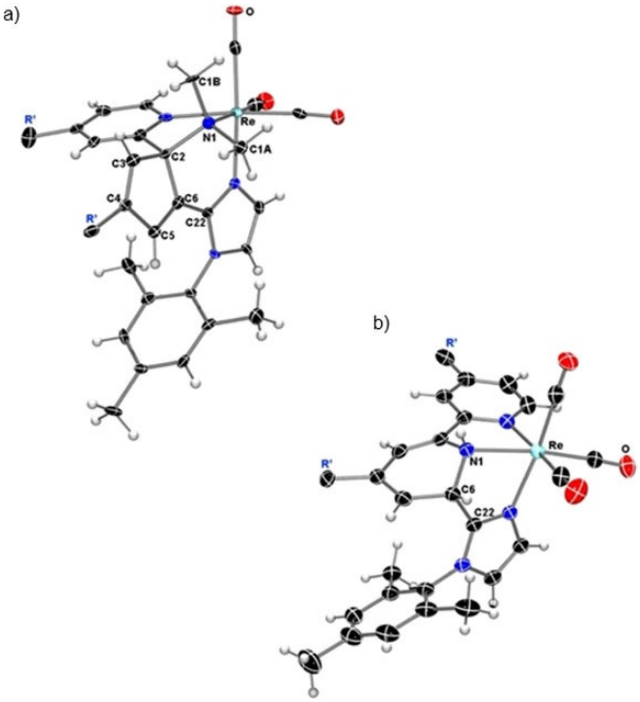


**Figure 2.** Molecular structure of the cation of compounds: a) **6a**, and b) **7a** with thermal ellipsoids at the 30% probability (R′ = *t*Bu).

(Scheme 2) and was fully characterized. As shown in Figure 2b, the central imidazole C atom (C22) is bonded to an *ortho* bipy C atom (C6), dearomatization of that pyridyl ring is maintained, and protonation has occurred on the nitrogen atom of the dearomatized ring (N1), transforming it from an amido nitrogen atom, in **5a**, to an amino-like nitrogen atom in **7a**.

It is remarkable that the strongly electron releasing *tert*-butyl substituents not only do not prevent nucleophilic attack on the bipy ligand by the N-bonded 2-imidazolyl group formed in the deprotonation reaction, but also in fact enhance the reactivity of the complexes, as for the 4,4′-*t*Bu$_2$bipy derivatives the less nucleophilic *N*-MesIm ligand is able to cause the ring-opening process, too. Presumably, the remote 4,4′-location of the *tert*-butyl substituents deprives them of steric influence on the attack at bipy C$_{ortho}$, while their electron-releasing character makes the C–C coupling product more reactive towards the MeOTf electrophile.

Similar results have been found for the methylation reaction (excess of MeOTf) of the 4,4′-dimethoxy-2,2′-bipy rhenium complexes once deprotonated.[27] For both *N*-alkylimidazole ligands, *N*-MesIm and *N*-MeIm, C–C coupling and pyridyl ring-opening products were obtained (species **8a** and **8b**, respectively). The solid-state structure of *N*-methylimidazole derivative **8b** was determined by X-ray diffraction (Figure 3).[22] These results highlight the generality of this new type of ring-opening process, which takes place under very mild condition, and starts from stable and easily available metal complexes.

In an attempt to block the nucleophilic attack at the *ortho* C6 atom of the diimine ligand (C2 for phen), 2,9-dimethyl-1,10-phenanthroline (2,9-Me$_2$phen) was used instead. The reaction

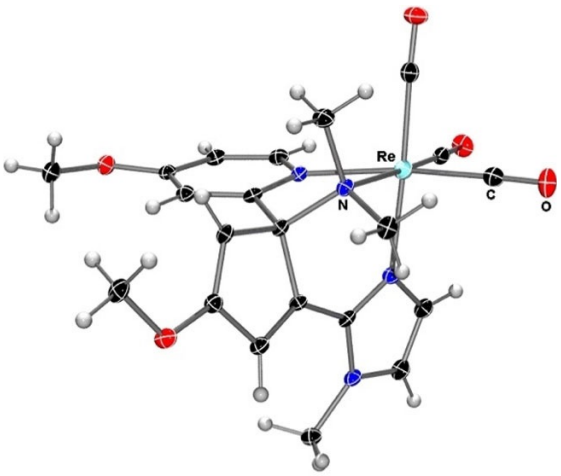


**Figure 3.** Molecular structure of the cation of compound **8b** with thermal ellipsoids at 30% probability.

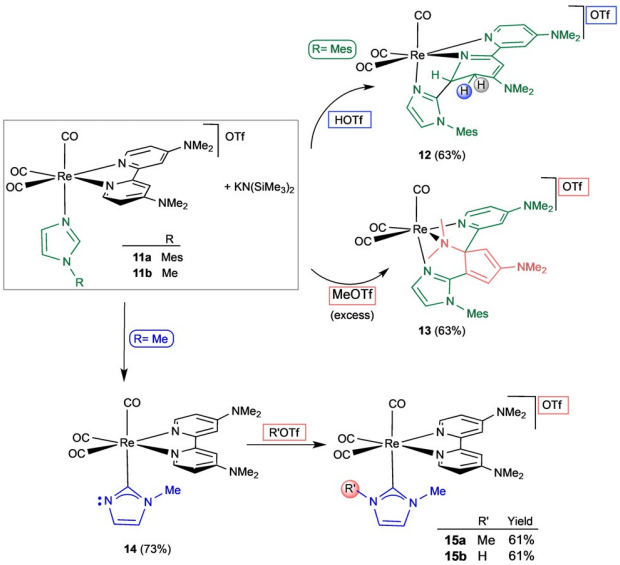


**Scheme 3.** Different reactivity pathways found for $[Re(CO)_3(4,4'\text{-}(NMe_2)_2bipy)(N\text{-}Rlm)]OTf$ (**11a,b**) depending on the nature of the imidazole substituent (Me vs. Mes).

of $[Re(CO)_3(2,9\text{-}Me_2phen)(N\text{-}MesIm)]OTf$ (**9**) with the strong base $KN(SiMe_3)_2$ and then MeOTf led to deprotonation and methylation of an α-methyl group, affording an asymmetric 2-ethyl-9-methyl-1,10-phenanthroline ligand coordinated to the $\{Re(CO)_3(N\text{-}MesIm)\}$ fragment, as was evidenced spectroscopically in solution and by X-ray diffraction in the solid state (compound **10**, see Supporting Information for further experimental details).

When the even more electron-donating dimethylamino groups were used as substituents at 4- and 4′-positions of the bipy ligand in *fac*-$\{Re(CO)_3(N\text{-}Rlm)\}$ fragments, a different reactivity pattern was found for methyl- and mesitylimidazole complexes. The reactivity pattern found for the latter was reminiscent of that described above, that is, C–C coupling between the deprotonated imidazole central carbon atom and C6 of the bipy ligand, affording a dearomatized neutral product that is too unstable to be characterized. Subsequent addition of an equimolar amount of HOTf led to formation of cationic rhenium complex **12** bearing a methylenic group at the 5-position of the dearomatized pyridyl ring as a consequence of the protonation reaction (Scheme 3). This fact was evidenced by $^1H$ NMR spectroscopy in solution. The $^1H$ NMR spectrum showed signals corresponding to a nonsymmetric dearomatized bipy ligand, and a 2D $^1H$–$^1H$ COSY study clearly established that the two 1H multiplets at 2.33 and 2.89 ppm corresponded to the $CH_2$ moiety. A 2D HSQC study showed that these signals correspond to a peak at 27.1 ppm in the $^{13}C$ NMR spectrum, and a DEPT-135 experiment confirmed that it corresponds to a $CH_2$ group.

The solid-state structure of **12**, determined by X-ray diffraction (Figure 4),[22] confirmed the presence of a tridentate ligand formed by coupling between the deprotonated imidazole C2 atom and the C6 carbon of the bipy ligand. The bond lengths around C5 (C5–C6 1.513(4), C5–C4 1.498(4) Å), which are indicative of single C–C bonds, are good evidence for the formation of the $CH_2$ unit at this position, in accordance with the NMR data in solution.[28]

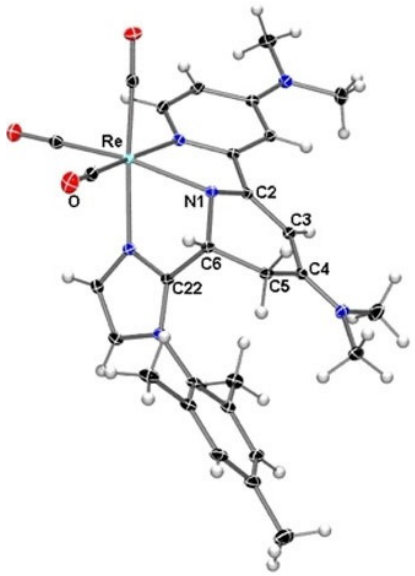


**Figure 4.** Molecular structure of the cation of compound **12** with thermal ellipsoids at 30% probability.

As shown in Scheme 3, the reaction of the *N*-MesIm complex **11a** with $KN(SiMe_3)_2$ and MeOTf in excess afforded another example of a C–C coupling and ring-opening product, namely, compound **13**, as those described above for 4,4′-di-*tert*-butyl- and 4,4′-dimethoxy-2,2′-bipy rhenium compounds (see Supporting Information for full spectroscopic characterization and X-ray structure in the solid state).

A different reactivity pattern was found, in contrast, for *N*-methylimidazole complex **11b**. Deprotonation of $[Re(CO)_3(4,4'\text{-}(NMe_2)_2bipy)(N\text{-}MeIm)]OTf$ (**11b**) in THF at low temperature (−78 °C) led to the formation of neutral complex **14**, as indicated by its $\nu_{CO}$ IR bands (at 2000, 1884, and 1878 $cm^{-1}$). The

$^1$H NMR spectrum of **14** in $CD_2Cl_2$ clearly showed that the outcome of this reaction was different from those described above, since no features of dearomatization were observed. Instead, a symmetric 4,4′-$(NMe_2)_2$-2,2′-bipy ligand was detected, and, in agreement with the deprotonation of the imidazole central CH group, only two signals at 6.90 and 6.86 ppm for this ligand could be found. Furthermore, the $^{13}$C NMR spectrum of **14** showed a low-intensity signal at 178.5 ppm attributable to a Re-bonded C atom. Thus, it seems that the dimethylamino substituents at the 4- and 4′-positions make the bipy ligand so electron rich that the nucleophilic attack by the carbeniate generated in situ, which is also very rich in electron density, as it results from the deprotonation of *N*-MeIm, is directed to the rhenium atom instead, affording an imidazol-2-yl complex (Scheme 3). Complexes featuring *C*-bonded imidazol-2-yl ligands with a nonsubstituted N atom are very rare and have been proposed as intermediates in the tautomerization of *N*-alkylimidazoles to NHC ligands.[29] Addition of the equimolar amount of MeOTf to a solution of imidazol-2-yl complex **14** in $CH_2Cl_2$ led to methylation of the non-substituted nitrogen atom, and corresponding NHC compound **15a** was obtained. Figure 5 shows the molecular structure of the cation of **15a** confirming its carbenic nature.[22] The Re—C(22) distance of 2.192(8) Å is similar to those of other NHC complexes with an $\{Re^{I}(CO)_3\}$ fragment.[30]

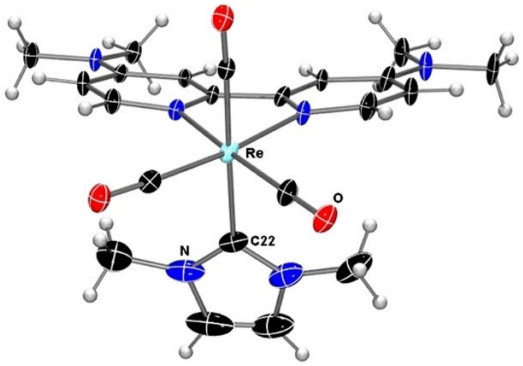


**Figure 5.** Molecular structure of the cation of compound **15a** with thermal ellipsoids at the 30% probability level.

The spectroscopic data of **15a** in solution are in agreement with the formation of the *N*,*N*′-dimethylimidazol-2-ylidene ligand. The $^1$H NMR spectrum of **15a** in $CD_2Cl_2$ shows the presence of an intact 4,4′-$(NMe_2)_2$-2,2′-bipy ligand and the signals of a symmetric $Me_2$-NHC ligand: one singlet at 6.80 ppm for the two equivalent C—H groups, and other at 3.53 ppm that integrates for 6H, attributable to the two methyl substituents. The $^{13}$C NMR spectrum of **15a** is consistent with the formulation given above and the presence of a mirror plane. It shows two signals, one of double intensity compared with the other, for the three carbonyl ligands, and a low-intensity signal at 177.1 ppm, characteristic of the carbene carbon atom of the NHC ligand.

The analogous reaction of imidazol-2-yl complex **14** with HOTf instead of MeOTf afforded, in a similar way, the corresponding NH-NHC compound **15b** (see Scheme 3). Complexes containing NH-NHC ligands are less common, as their synthesis is more difficult because the most common preparation method of deprotonation of *N*,*N*′-dialkylimidazolium salts cannot be used.[29a,31] The spectroscopic data in solution (IR, $^1$H and $^{13}$C NMR) of **15b** are similar to those found for compound **15a**. The characteristic signal of the carbene C atom is observed in the $^{13}$C NMR spectrum as a low-intensity peak at 177.0 ppm. The NH group is clearly observed in the $^1$H NMR spectrum as a broad singlet at 9.54 ppm, and the IR $\nu_{CO}$ bands of compound **15b** in $CH_2Cl_2$ solution at 2022, 1909 cm$^{-1}$ are indicative of a cationic *fac*-$\{Re(CO)_3\}$ fragment ($\nu_{CO}$ bands of neutral imidazol-2-yl complex **14** are observed at 2000, 1884, and 1878 cm$^{-1}$). On the other hand, the solid-state structure of compound **15b** was determined by X-ray diffraction and, although the data were very poor because of twinning, confirmed the connectivity of the cationic complex and formation of the NHC ligand (see Supporting Information). Although the study of transition metal NHC complexes is an ongoing, prominent field of organometallic chemistry, the chemistry of rhenium(I) NHC complexes has been little explored, and in the vast majority of the reported complexes the NHC moiety is part of a bidentate ligand.[32] The incorporation of strong donor substituents into the bipy skeleton can be an alternative for the preparation of NHC complexes with the $\{Re(CO)_3(bipy)\}$ fragment, which is widely employed in several areas of chemical research.[33]

A DFT study was carried out with the aim of understanding the different behaviors experimentally observed for the deprotonation of $[Re(CO)_3(4,4'\text{-}R'_2bipy)(N\text{-}RIm)]OTf$ (R′ = *t*Bu, $NMe_2$; R = Me, Mes) compounds in THF solution (see Computational Details and Supporting Information for a discussion about the chosen computational protocol). The starting structures to develop the potential-energy surface for the four mechanisms studied (**M** in Scheme 4) are the neutral species resulting from the deprotonation of the central CH group of the *N*-RIm ligand of $[Re(CO)_3(4,4'\text{-}R'_2bipy)(N\text{-}RIm)]OTf$ compounds. These possible reaction pathways have been already considered in our previous studies[14d,24,34] and comprise: 1) C—C coupling reactions between the deprotonated imidazole C atom ($C_{Im}$) and an *ortho* pyridyl C atom of the bipy ligand, that is, bipy C6 or C2 (pathway A1 or A2, respectively, in Scheme 4) to afford the corresponding dearomatized products $\mathbf{P_{A1}}$ and $\mathbf{P_{A2}}$, respectively, and 2) formation of *C*-bonded imidazol-2-yl product $\mathbf{P_B}$ by a two-step mechanism starting with nucleophilic attack at a *cis*-CO ligand (pathway 1B in Scheme 4) or by formation of a $\kappa^2$-*C*,*N*-imidazolyl transition state (pathway 2B in Scheme 4). Table 1 lists the Gibbs energy of each species (transition states, intermediates, and products) relative to the corresponding **M** of each reactive process. The optimized structures and energies of all the species located are shown in Figures S1–S4 and Tables S1 and S2, respectively (see Supporting Information).

As shown in Table 1, for the *t*Bu substituent the formation of $C_{Im}$—C6 ($\mathbf{P_{A1}}$-***t*Bu**) and $C_{Im}$—C2 ($\mathbf{P_{A2}}$-***t*Bu**) coupling products is favored over the reaction to yield the imidazol-2-yl product ($\mathbf{P_B}$-***t*Bu**). The formation of $\mathbf{P_{A1}}$-***t*Bu** and $\mathbf{P_{A2}}$-***t*Bu**, controlled by their respective transition states $\mathbf{TS_{A1}}$-***t*Bu** and $\mathbf{TS_{A2}}$-***t*Bu**, has lower

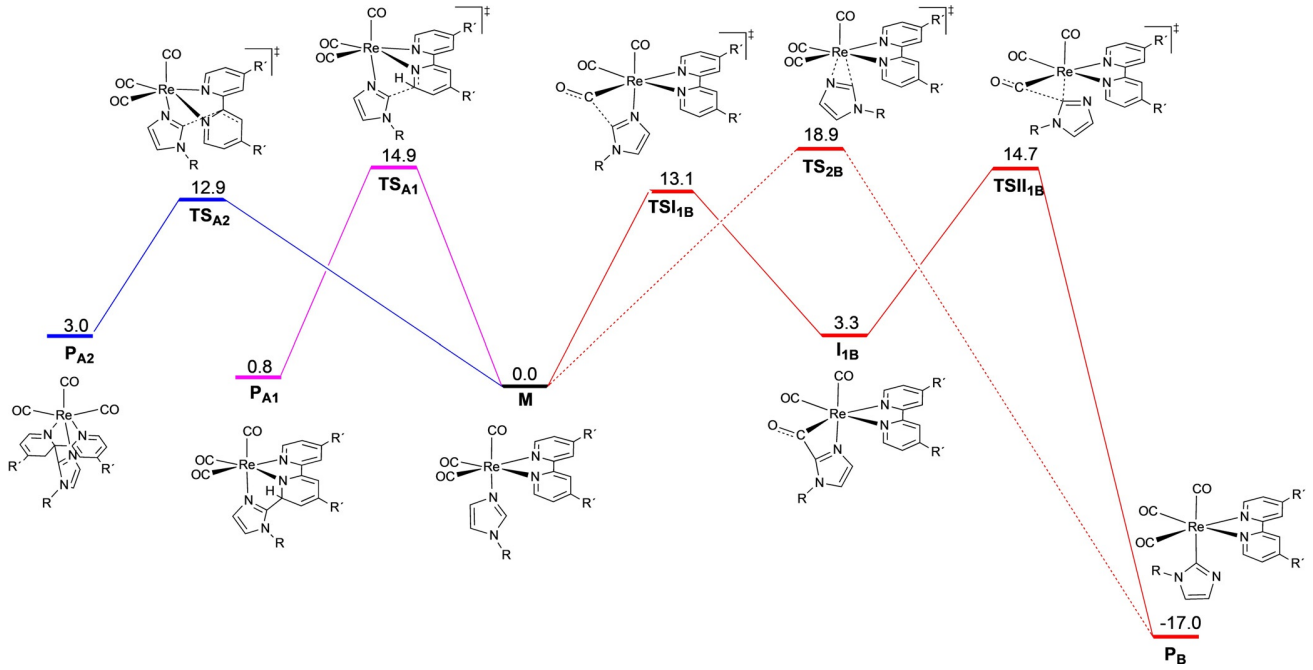


**Scheme 4.** Schematic view of the DFT structures involved in the formation of the $C_{Im}$–C6 ($\mathbf{P_{A1}}$, blue) and $C_{Im}$–C2 ($\mathbf{P_{A2}}$, purple) coupling products, and those involved in the formation of the imidazol-2-yl product ($\mathbf{P_B}$, red) starting from [Re(CO)$_3$(4,4′-R′$_2$bipy)(*N*-RIm)] (**M**) complexes. Relative Gibbs energies [kcal mol$^{-1}$] depicted in the figure are those corresponding to the deprotonation of [Re(CO)$_3$(4,4′-NMe$_2$bipy)(*N*-MeIm)]$^+$; for the full energy values, see Table 1.

**Table 1.** Gibbs energies [kcal mol$^{-1}$] of all the TSs, intermediates, and product types relative to the corresponding starting complex **M**[a] for the four different reaction pathways depicted in Scheme 4.

| M | R′ | R | $TS_{A1}$ | $P_{A1}$ | $TS_{A2}$ | $P_{A2}$ | $TSI_{1B}$ | $I_{1B}$ | $TSII_{1B}$ | $P_B$ | $TS_{2B}$ |
|---|---|---|---|---|---|---|---|---|---|---|---|
| [Re] | *t*Bu | Me | 10.6 | −6.4 | 9.8 | −2.3 | 14.2 | 2.2 | 13.4 | −18.9 | 16.4 |
| [Re] | *t*Bu | Mes | 7.5 | −11.4 | 5.3 | −7.8 | 8.4 | 1.2 | 9.5 | −21.5 | 14.4 |
| [Re] | $NMe_2$ | Me | 14.9 | 0.8 | 12.9 | 3.0 | 13.1 | 3.3 | 14.7 | −17.0 | 18.9 |
| [Re] | $NMe_2$ | Mes | 9.1 | −6.5 | 5.7 | −3.3 | 11.4 | 4.6 | 9.3 | −23.0 | 13.8 |
| [Re] | Br | Me | 5.4 | −12.6 | 3.4 | −9.8 | 10.4 | −0.4 | 10.8 | −20.3 | 13.9 |
| [Re] | Br | Mes | 6.4 | −15.9 | 3.6 | −11.7 | 11.3 | 0.4 | 9.6 | −21.8 | 15.1 |
| [Mo] | Cl | Me | 7.9 | −13.9 | 7.7 | −6.5 | 8.6 | −3.4 | 4.0 | −15.5 | –[b] |
| [Mo] | Cl | Mes | 5.1 | −16.5 | 6.3 | −10.3 | 6.9 | −3.4 | 6.1 | −16.9 | –[b] |

[a] [Re] = [Re(CO)$_3$(4,4′-R′$_2$bipy)(*N*-RIm)]; [Mo] = [Mo($\eta^3$-$C_4H_7$)(CO)$_2$(4,7-Cl$_2$phen)(*N*-RIm)]. [b] Non-located TS.[37]

energy barriers than those for the formation of $\mathbf{P_B}$-***t*Bu**.[35] $\mathbf{TS_{A1}}$-***t*Bu** has a higher energy barrier than $\mathbf{TS_{A2}}$-***t*Bu**, as C6 (net atomic charge, NAC, of +0.078 e) is less electrophilic than C2 (NAC of +0.220 e). However, $\mathbf{P_{A1}}$-***t*Bu** is more stable than $\mathbf{P_{A2}}$-***t*Bu**, as the $C_{Im}$-C2 coupling significantly disrupts the π-electron delocalization between the two pyridyl rings. The proximity of the energy barriers for $\mathbf{P_{A1}}$-***t*Bu** and $\mathbf{P_{A2}}$-***t*Bu** formation, along with the greater stability of $\mathbf{P_{A1}}$-***t*Bu** compared to $\mathbf{P_{A2}}$-***t*Bu**, allow the formation of $\mathbf{P_{A1}}$-***t*Bu**, as experimentally observed (complexes **5a**,**b**, see above).

When a more electron donating group, such as $NMe_2$, is attached to the bipy ligand at the 4- and 4′-positions, a different picture is found. As shown in Figure 6a, the molecular electrostatic potential (MEP) map for **M** species shows a notable increase of the electron density at the bipy core atoms (more pronounced green color compared to the MEP map of the 4,4′-*t*Bu$_2$bipy ligand).[36] As a consequence, the nucleophilic attack at the 4,4′-bis(dimethylamino)bipy ligand is more energy demanding than that at 4,4′-*t*Bu$_2$bipy.

On the other hand, the MEP map of **M** complexes clearly shows higher electron density of the deprotonated central C atom of *N*-MeIm compared to that of *N*-MesIm (see Figure 6b). For the *N*-MesIm species the attack at the 4,4′-(NMe$_2$)$_2$bipy ligand is energetically favored over formation of the imidazol-2-yl complex (see Table 1), a fact that jointly with the stabilities of the dearomatized products $\mathbf{P_{A1}}$-$\mathbf{NMe_2}$ (−6.5 kcal mol$^{-1}$) and $\mathbf{P_{A2}}$-$\mathbf{NMe_2}$ (−3.3 kcal mol$^{-1}$) explains the formation of the former. In contrast, the higher electron density of the *N*-MeIm ligand makes the attack at the electronically enriched 4,4′-bis(dimethylamino)bipy ligand similar in energy cost to that found for imidazol-2-yl formation via pathway 1B.[38] The high stability of the imidazol-2-yl species ($\mathbf{P_B}$-$\mathbf{NMe_2}$), along with the instability of the dearomatized C–C coupling products, determines the formation of the former (complex **14**).

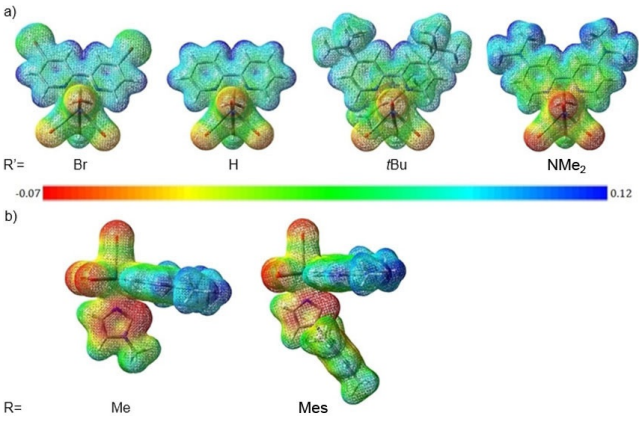


**Figure 6.** MEP map for the starting deprotonated complexes [Re(CO)$_3$(4,4′-R′$_2$bipy)(*N*-Rlm)] (**M**) showing visually the change of the electron density of: a) the bipy ligand depending on the electronic nature of the substituents at the 4- and 4′-positions (R = Me; R′ = Br, H, *t*Bu or NMe$_2$), and b) the substituent of the *N*-alkylimidazole ligand (R = Me or Mes; R′ = NMe$_2$).

The electron-rich 4,4′-bis(dimethylamino)bipy ligand is on the edge of deciding the reactivity towards C–C coupling or formation of an imidazol-2-yl complex, depending on the nature of *N*-alkylimidazole co-ligand. We then explored, by means of DFT calculations, the reactivity of analogous Re$^{I}$(CO)$_3$ compounds bearing bipy ligands with electron-withdrawing groups, such as bromo substituents, at the 4- and 4′-positions. The presence of these substituents would make the bipy ligand more electrophilic, and therefore should favor the dearomatization and C–C coupling reactions (see Scheme S1, Figures S5 and S6, and Table S3 in the Supporting Information). Indeed, the MEP analysis for **M** species containing a 4,4′-dibromobipy ligand shows a notable loss of electron density at the bipy backbone (less pronounced green color) compared to those bearing *t*Bu and NMe$_2$ (see Figure 6a, wherein the non-substituted 2,2′-bipyridine **M** complex has been included for comparison purposes).

Table 1 shows that for 4,4′-dibromobipy complexes the lowest Gibbs energy barrier is that corresponding to C$_{Im}$–C2 coupling via **TS$_{A2}$-Br** to yield **P$_{A2}$-Br** products, notably more stable than the analogous ones with *t*Bu and NMe$_2$ substituents. Therefore, in this case, kinetic control prevails, and **P$_{A2}$-Br** are the theoretically expected products for both *N*-MeIm and *N*-MesIm ligands.

In the case of {Mo$^{II}$(η$^3$-allyl)} complexes, the coordination of 4,7-dichloro-1,10-phenanthroline was included in the present work. DFT computations performed at the same level of theory as those for Re complexes highlighted that the greater rigidity of phen compared to bipy particularly disfavors the attack on the fused *ortho* C atoms, that is, C11 or C13,[39] namely, C$_{bridge}$ herein (see Figures S7 and S8 and Table S4 in the Supporting Information). For the *N*-MesIm complex, the Gibbs energy barrier for the formation of the imidazol-2-yl product (**P$_B$-ClPhen**) is notably higher than those for the formation of C–C coupling products, precluding the formation of this product (see Table 1). These data together with the enhanced stability of the C$_{Im}$–C2 coupling product compared with the C$_{Im}$–C$_{bridge}$ product, allow us to predict the formation of the former, **P$_{A1}$-ClPhen** product. For the *N*-MeIm ligand, the Gibbs energy barriers corresponding to the formation of the three types of products are very similar (Table 1). Therefore, the higher stability of the C$_{Im}$–C2 coupling product (**P$_{A1}$-ClPhen**) and imidazol-2-yl (**P$_B$-ClPhen**) would be responsible for the formation of a mixture of these two types of products.

The results of the computational calculations prompted us to study experimentally the deprotonation of *fac*-{Re(CO)$_3$} imidazole complexes bearing a 4,4′-dibromo-2,2′-bipyridine ligand. The addition of an equimolar amount of KN(SiMe$_3$)$_2$ to a low-temperature solution of [Re(CO)$_3$(4,4′-Br$_2$bipy)(*N*-MeIm)]-OTf (**16b**) afforded a neutral complex (**17b**, as judged by the lower-frequency IR ν$_{CO}$ bands, at 2012, 1908, 1895 cm$^{-1}$ in THF), which was spectroscopically characterized in solution at low temperature (253 K).[19] The $^1$H NMR spectrum showed that the bipy ligand was no longer symmetrical, and signals at 5.77 and 4.32 ppm were clearly indicative of dearomatization of one of the pyridyl rings. In the same way, in the $^{13}$C NMR spectrum three signals of the bipy ligand were remarkably upfield shifted at 95.3, 91.8, and 78.9 ppm. A 2D HMBC NMR spectrum of **17b** showed a two-bond correlation between the bipy hydrogen atom at 5.77 ppm and the $^{13}$C NMR signal at 78.9 ppm, assigned to a bipy quaternary carbon atom (DEPT-135), demonstrating that the attack occurred at C2 of the bipy ligand, as predicted by DFT calculations (Scheme 5). Analogous nucleophilic attack at quaternary C2 atoms of 4,4′-dihalobipyridines upon deprotonation of *N*-alkylimidazole ligands had been previously found by us at {Mo(η$^3$-allyl)(CO)$_2$} fragments, with similar spectroscopic features.[14d]

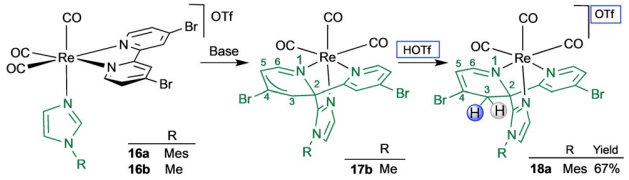


**Scheme 5.** Reactivity of [Re(CO)$_3$(4,4′-Br$_2$bipy)(*N*-Rlm)]OTf compounds towards the strong base KN(SiMe$_3$)$_2$, and afterwards towards HOTf.

Deprotonation and subsequent protonation of *N*-MesIm complex **16a** afforded a new species **18a** resulting from the formation of a dihydropyridyl group (see Scheme 5). The $^1$H NMR spectrum of **18a** shows, therefore, an asymmetric dearomatized 4,4′-dibromo-2,2′-bipyridine ligand, and a 2D $^1$H–$^1$H COSY study clearly established that the 2H multiplet at 3.58 ppm corresponds to the methylenic unit. Accordingly, a 2D HSQC study showed that this signal correlates with a peak at 38.4 ppm in the $^{13}$C NMR spectrum, the CH$_2$ nature of which was confirmed by a DEPT-135 experiment. DFT calculations showed that the C3-protonated complex bearing the *N*-MesIm and 4,4′-Br$_2$-2,2′-bipy ligands is 2.2 kcal mol$^{-1}$ more favorable than that protonated at C5-, which is the most likely alternative carbon atom for protonation in this type of complexes (see Figure S9 in the Supporting Information).

Finally, to ascertain whether a different kind of products could be obtained by deprotonation of *N*-RIm complexes of the {Mo($\eta^3$-allyl)$(CO)_2$} fragment, we used the 4,7-dichloro-1,10-phenanthroline ligand, as suggested by the theoretical calculations. Thus, addition of an equimolar amount of $KN(SiMe_3)_2$ to a THF solution of [Mo($\eta^3$-$C_4H_7$)$(CO)_2$(4,7-$Cl_2$phen)(*N*-MesIm)]OTf (**19a**) at −78 °C resulted in formation of neutral product **20a** (IR $\nu_{CO}$ bands in THF at 1931 and 1847 $cm^{-1}$).

The $^1H$ and $^{13}C$ NMR spectra of **20a** featured distinct signals for every nucleus of the phen and allyl moieties, as well as for each of the three methyl groups of the mesityl substituent. The two carbonyl ligands appeared also as two singlets in the $^{13}C$ NMR spectrum. These features reflect the asymmetry of the molecule of **20a**, and therefore indicate that the reaction involved a transformation of the phen ligand. The subsequent addition of an equimolar amount of HOTf in $CH_2Cl_2$ afforded a more stable cationic product, namely, **21a**, which showed in the NMR spectrum the formation of a product of C–C coupling between the deprotonated central carbon atom imidazole and the C2 carbon atom of the phen ligand (see Scheme 6).

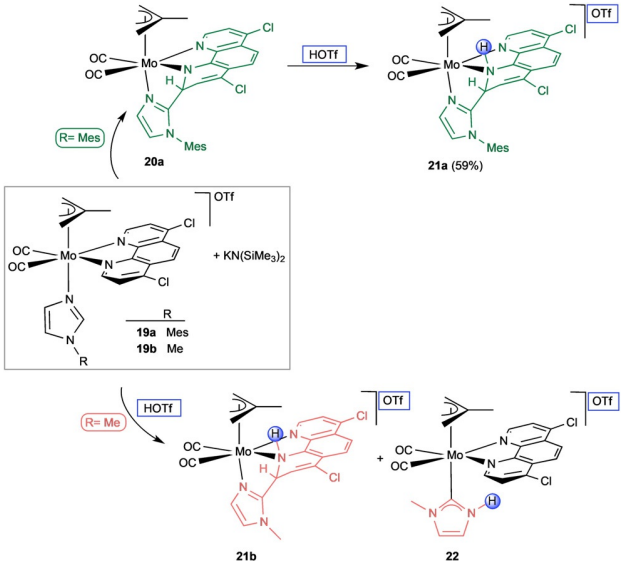


**Scheme 6.** Different reactivity pathways found for [Mo($\eta^3$-$C_4H_7$)$(CO)_2$(4,7-$Cl_2$phen)(*N*-RIm)]OTf (**19a**,**b**) compounds depending on the nature of the imidazole substituent (Me vs. Mes).

The *N*-methylimidazole compound **19b** afforded, upon a deprotonation–protonation sequence, an analogous dearomatized species, namely, **21b**, which could be structurally characterized in the solid state by X-ray diffraction (Figure 7a).[22]

The cationic complex contains a new tridentate N-donor ligand formed by C–C coupling between the central imidazole C atom (C22) and the C2 carbon atom of the phen ligand. As a consequence of the formation of this new single C21–C2 bond, the pyridyl group is dearomatized, as evidenced by the bond lengths (C2–C3 1.50(2), C2–N1 1.52 (1), and N1–C11 1.46(1) Å), which are clearly longer than those expected for an aromatic ring. The C2 atom is, therefore, $sp^3$-hybridized and shows angles consistent with an approximately tetrahedral geometry [C3-C2-N1 111.9(8), C3-C2-C22 117.7(8), C22-C2-N1 102.5(8)°]. A similar situation is encountered for the angles around N1 of 107.8(6), 110.1(6), and 110.6(9)°, in agreement with a pyramidal geometry of this atom (the sum of the angles around N1 is 330.6°), which has been protonated. However, as already evidenced by the DFT calculations (see above), for the *N*-methylimidazole derivative **19b**, another protonation product was obtained along with **21b** that was found to be the NH-NHC species **22** (Scheme 6). It seems, therefore, that in the case of *N*-MeIm, the higher electron density of this ligand does not preclude the formation of the imidazol-2-yl complex, as found for the [Mo($\eta^3$-$C_4H_7$)$(CO)_2$(N-N)(*N*-RIm)]OTf complexes with nonsubstituted bipy and phen,[24] and a mixture of both kind of compounds, C–C-coupled and imidazol-2-yl, are obtained. Compound **22** was also characterized by X-ray diffraction in the solid state (Figure 7b).[22] The cationic complex of **22** shows a pseudooctahedral geometry around the metal center. The intact 4,7-dichlorophen ligand is coplanar with the two CO ligands, and the carbene moiety is *trans* to the $\eta^3$-methallyl ligand. The Mo–C22 bond distance of 2.242(3) Å is in good agreement with reported $Mo^{II}$–$C_{NHC}$ bond lengths (see above).

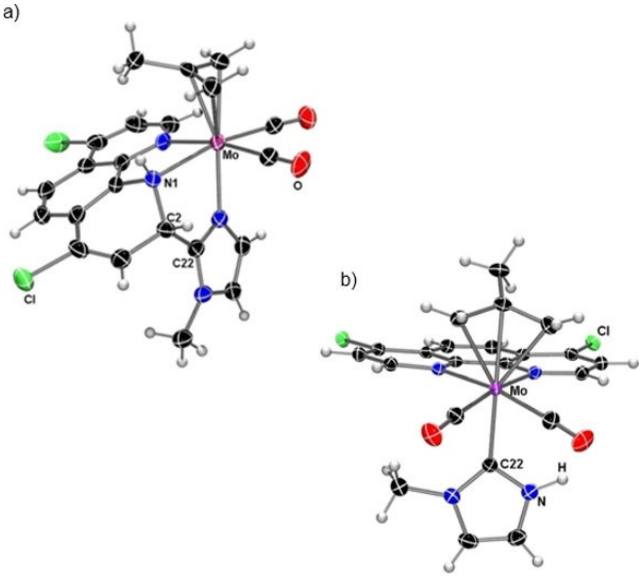


**Figure 7.** Molecular structures of the cations of: a) **21b**, and b) **22** with thermal ellipsoids at 30% probability.

## Conclusions

Two families of cationic complexes bearing mutually *cis* 4,4′-disubstituted-2,2′-bipyridine and *N*-alkylimidazole ligands were synthesized, and it was shown that the combination of imidazole and bipy substituents at the same metal fragment determines the type of product obtained on deprotonation. Two kinds of products were obtained: 1) complexes in which a new C–C bond between the central carbon atom of the imidazole ligand and one *ortho* carbon atom of the bipyridine ligand (C2 or C6) was formed, and in which the involved pyridine ring

became dearomatized, and 2) imidazol-2-yl complexes. Both are consistent with initial deprotonation of the imidazole central CH group and subsequent intramolecular addition of the thus-generated nucleophile to the bipy ligand or to the metal center. Which type of compound is formed was found to depend on the metal, the nature of the substituent at the imidazole ring, and the nature of the substituents of the bipy backbone (see Figure 8).

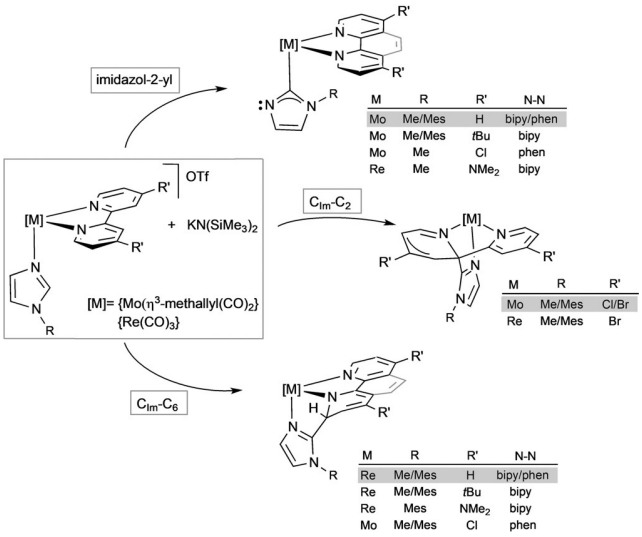


**Figure 8.** Summary schematic view of the types of compounds obtained depending on the metal and the nature of the substituents at imidazole ring or of the bipy/phen backbone. Shaded compounds have been previously reported.[14d,g,24]

For the {Mo($\eta^3$-methallyl)$(CO)_2$} fragment formation of imidazol-2-yl products is preferred over C–C coupling and dearomatization, unless dihalo-substituted $\alpha$-diimines are used to favor the C–C coupling products (with C2 of 4,4′-$Cl_2$bipy, as reported in the preliminary communication,[14d] and with C2, i.e., analogous to bipy C6, of 4,7-$Cl_2$phen reported herein).

For $\{Re(CO)_3\}$ derivatives, formation of dearomatized C–C coupling products is preferred over the formation of imidazol-2-yl complexes, which can be attributed to the lower lability of the imidazole ligand compared to the $Mo^{II}$ fragment. The use of strongly electron releasing substituents (R′ = *t*Bu, OMe, $NMe_2$) does not prevent nucleophilic attack at the 4,4′-R′$_2$bipy ligand. Rather, it enhances the reactivity of the C–C coupling complexes towards MeOTf affording new pyridine ring-opening products. Only in the case of the combination of the most electron-rich ligands tested herein (4,4′-$(NMe_2)_2$bipy and *N*-MeIm) formation of the rhenium imidazol-2-yl complex was observed.

DFT calculations have shown that the reactivity patterns found depend on a delicate balance between kinetic and thermodynamic factors. In general, energy barriers for the formation of C–C coupling products are lower than those for the formation of the imidazol-2-yl product. Furthermore, the barrier for nucleophilic attack on the C2 atom of the bipy ligand is lower than that for the bipy C6 carbon atom, but the stability of the $C_{Im}$–C2 coupling product is lower than that of the $C_{Im}$–C6 coupling product. Therefore, $C_{Im}$–C6 coupling products are formed when the difference in energy barriers for such attacks is small. Thermodynamically, the imidazol-2-yl product is always the most stable species. For the $\{Re(CO)_3\}$ species, the presence of electron-donor groups such as *t*Bu, OMe, and $NMe_2$ at the 4,4′-positions of the bipy ligand increases the electron density of this ligand and thus disfavors the formation of $C_{Im}$–$C_{bipy}$ coupling products. However, this does not overcome the energy cost required for the formation of the imidazol-2-yl product, except for [$Re(CO)_3$(4,4′-$(NMe_2)_2$bipy)(*N*-MeIm)]OTf. On the other hand, DFT calculations also predicted that the presence of an electron-withdrawing group, such as bromo, at the 4- and 4′-positions of the bipy ligand would produce a remarkable decrease of the energy barrier for the formation of the $C_{Im}$–C2 coupling product, along with notable stabilization of such C–C coupling product, which indeed has been experimentally obtained.

## Experimental Section

### General

All manipulations were carried out under a nitrogen atmosphere by using Schlenk techniques. Solvents were distilled from Na (toluene and hexanes), Na/benzophenone (THF), and $CaH_2$ ($CH_2Cl_2$). Deuterated dichloromethane (Cambridge Isotope Laboratories, Inc.) was stored under nitrogen in a Young's tube and used without further purification. $^1$H NMR and $^{13}$C NMR spectra were recorded on a Bruker Avance 300, DPX-300, or Avance 400 spectrometer. NMR spectra were references to the internal residual solvent peak for $^1$H and $^{13}C\{^1H\}$ NMR spectroscopy. Solution IR spectra were obtained with a PerkinElmer FT 1720-X spectrometer by using 0.2 mm $CaF_2$ cells. NMR samples were prepared under nitrogen by using Kontes manifolds purchased from Aldrich. Full experimental details of all compounds are given in the Supporting Information, whereas herein only representative compounds are included. Labeling scheme for bipy and phen derivatives:

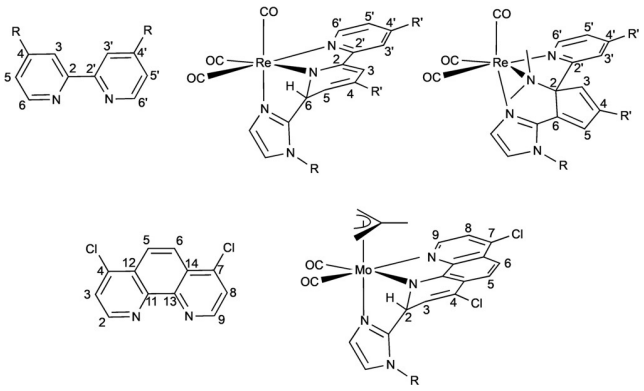

### Crystal structure determination

For compounds **2a**, **2b**, **7a**, **8b**, **21b**, and **22**, crystal data were collected with an Oxford Diffraction Xcalibur Nova single-crystal diffractometer by using $Cu_{K\alpha}$ radiation ($\lambda = 1.5418$ Å) at 100(2) K. Images were collected at a 65 mm fixed crystal–detector distance, by using the oscillation method, with 1° oscillation and variable ex-

posure time per image (4–16 s). Data collection strategy was calculated with the program CrysAlis$^{Pro}$ CCD.[40] Data reduction and cell refinement was performed with the program CrysAlis$^{Pro}$ RED.[40] An empirical absorption correction was applied by using SCALE3 ABSPACK.[40] For compounds **6a**, **12**, and **15a**, data collection was performed with a Bruker APPEX II diffractometer by using graphite-monochromated $Mo_{K\alpha}$ radiation ($\lambda = 0.71073$ Å) from a fine-focus sealed-tube source at 100 K. Data Computing and reduction were done with the APPEX II software.[41] In all cases empirical absorption corrections were applied by using SADABS.[42] In all cases the structures were solved with SIR92[43] or SIR97[44] and finally refined by full-matrix, least-squares based on $F^2$ by SHELXL.[45] Molecular graphics were made with ORTEP 3.[46]

### Computational details

Quantum chemical computations at the PCM-B97D/6–31+G(d) (LANL2DZ for Br, LANL2DZ+f for Re and Mo) level of theory were carried out with the Gaussian 09 series of programs.[47] The updated version of Schlegel's algorithm[48] was used from the outset to fully optimize the geometry of stable species (reactants, intermediates, and products) and transition states (TSs) in THF solution with the polarizable continuum model (PCM)[49] and the universal force field (UFF) radii[50] in conjunction with the dispersion-corrected generalized gradient approximation (GGA) density functional B97D[51] and the 6-31+G(d)[52] basis set for H, C, N, O, and Cl combined with the LANL2DZ[53] basis set for the remaining atoms without (Br) and with f polarization functions[54] of exponents 1.043 (Mo) and 0.869 (Re). B97D is a reparametrized version of the original B97 functional including Grimme's second generation dispersion correction (D2). A relative permittivity of 7.43 was assumed in the calculations to simulate THF as the solvent experimentally used. The nature of the stationary points was verified by analytical computations of harmonic vibrational frequencies. The analysis of the normal mode corresponding to the imaginary frequency in the TS was carried out to check that the two minimum-energy structures connecting each TS. Thermodynamic quantities ($\Delta H$, $\Delta S$, and $\Delta G$) were also calculated within the ideal gas, rigid rotor, and harmonic oscillator approximations at a pressure of 1 atm and a temperature of 298.15 K.[55] The calculation of thermodynamic quantities in solution starting with molecular partition functions developed for computing gas-phase thermodynamics properties is a standard procedure that has proven to be a correct and useful approach.[56] The electronic structure of some relevant species was analyzed in terms of the natural bond orbital (NBO) method of Weinhold et al.[57] and the molecular electrostatic potential (MEP).[58]

### Synthesis of 2a

$KN(SiMe_3)_2$ (0.20 mL of a 0.7 M solution in toluene, 0.140 mmol) was added to a solution of [Mo($\eta^3$-$C_4H_7$)(CO)$_2$(4,4′-*t*Bu$_2$bipy)(*N*-MesIm)]OTf (**1a**, 0.100 g, 0.123 mmol) in THF (20 mL) previously cooled to −78 °C. The solvent was evaporated to dryness under reduced pressure, a solution of HOTf (12 μL, 0.136 mmol) in $CH_2Cl_2$ (20 mL) was then added, and the reaction mixture was stirred for 10 min. The reaction mixture was filtered through a cannula and evaporated to a volume of 5 mL. The addition of hexane (20 mL) caused the precipitation of an orange solid, which was washed with hexane (1×15 mL) and diethyl ether (1×15 mL) and dried in vacuo. Yield: 45 mg (45%). IR ($CH_2Cl_2$): 1946, 1865 cm$^{-1}$ ($\nu_{CO}$). $^1$H NMR ($CD_2Cl_2$): $\delta = 10.71$ ($s_{br}$, 1H, N*H*), 8.38 (d, $J = 5.8$ Hz, 2H, $H_{6,6'}$), 8.07 (d, $J = 1.7$ Hz, 2H, $H_{3,3'}$), 8.07 (dd, $J = 5.8$, 1.7 Hz, 2H, $H_{5,5'}$), 7.37 (m, 1H, C*H* *N*-MesIm), 6.86 (s, 2H, Mes), 6.71 (m, 1H, C*H* *N*-MesIm), 2.91 (s, 2H, $H_{syn}$ $\eta^3$-$C_4H_7$), 2.41 (s, 3H, C$H_3$ *N*-MesIm), 1.61 (m, 8H, $H_{anti}$ $\eta^3$-$C_4H_7$ and C$H_3$ *N*-MesIm), 1.46 (s, 18H, C$H_3$ *t*Bu), 0.71 (s, 3H, C$H_3$ $\eta^3$-$C_4H_7$). $^{13}$C{$^1$H} NMR ($CD_2Cl_2$): $\delta = 225.3$ (*C*O), 186.1 (Mo-*C*), 164.0, 153.8, 153.2, 125.2, 119.6 (4,4′-*t*Bu$_2$bipy), 139.7, 136.7, 135.9, 129.3 (Mes), 123.5, 121.8 (*C*H *N*-MesIm), 87.5 ($C_2$ $\eta^3$-$C_4H_7$), 59.4 ($C_1$ and $C_3$ $\eta^3$-$C_4H_7$), 36.0 (*C*(CH$_3$)$_3$), 30.5 (6*C*H$_3$ *t*Bu), 21.4 (*C*H$_3$ *N*-MesIm), 19.1 (*C*H$_3$ $\eta^3$-$C_4H_7$ and 2*C*H$_3$ *N*-MesIm). Elemental analysis (%) calcd for $C_{37}H_{45}F_3MoN_4O_5S$: C 54.81, H 5.59, N 6.91; found: C 55.22, H 5.31, N 7.25.

### Synthesis of 3b

Compound **3b** was prepared as described above for the synthesis of **2a** starting from [Mo($\eta^3$-$C_4H_7$)(CO)$_2$(4,4′-*t*Bu$_2$bipy)(*N*-MeIm)]OTf (**1b**, 0.100 g, 0.141 mmol) $KN(SiMe_3)_2$ (0.25 mL of a 0.7 M solution in toluene, 0.175 mmol) and MeOTf (17 μL, 0.155 mmol). Compound **3b** was obtained as an orange microcrystalline solid. Yield: 0.43 g (42%). IR ($CH_2Cl_2$): 1945, 1862 cm$^{-1}$ ($\nu_{CO}$). $^1$H NMR ($CD_2Cl_2$): $\delta = 8.86$ (d, $J = 5.9$ Hz, 2H, $H_{6,6'}$), 8.07 (d, $J = 1.7$ Hz, 2H, $H_{3,3'}$), 7.61 (dd, $J = 5.9$, 1.7 Hz, 2H, $H_{5,5'}$), 6.87 (m, 2H, C*H* *N*-MeIm), 3.42 (s, 6H, *N*-C$H_3$), 3.33 (s, 2H, $H_{syn}$ $\eta^3$-$C_4H_7$), 1.88 (s, 2H, $H_{anti}$ $\eta^3$-$C_4H_7$), 1.41 (s, 18H, C$H_3$ *t*Bu), 0.89 (s, 3H, C$H_3$ $\eta^3$-$C_4H_7$). $^{13}$C{$^1$H} NMR ($CD_2Cl_2$): $\delta =$ 226.1 (*C*O), 186.8 (Mo-*C*), 165.5, 154.7, 153.5, 124.0 120.6 (4,4′-*t*Bu$_2$bipy), 125.0 (*C*H *N*-MeIm), 89.0 ($C_2$ $\eta^3$-$C_4H_7$), 60.1 ($C_1$ and $C_3$ $\eta^3$-$C_4H_7$), 39.6 (2CH$_3$ *N*-*C*H$_3$), 36.2 (*C*(CH$_3$)$_3$), 30.5 (6*C*H$_3$ *t*Bu), 17.8 (*C*H$_3$ $\eta^3$-$C_4H_7$). Elemental analysis (%) calcd for $C_{30}H_{39}F_3MoN_4O_5S$: C 50.00, H 5.45, N 7.77; found: C 49.68, H 5.59, N 8.01.

### Synthesis of 6a

$KN(SiMe_3)_2$ (0.13 mL of a 0.7 M solution in toluene, 0.091 mmol) was added to a solution of [Re(CO)$_3$(*N*-MesIm)(4,4′-*t*Bu$_2$bipy)]OTf (**4a**, 75 mg, 0.086 mmol) in THF (20 mL) previously cooled to −78 °C. The solvent was evaporated to dryness under reduced pressure, the residue dissolved in $CH_2Cl_2$ (20 mL), and MeOTf (21 μL, 0.189 mmol) added. The mixture was stirred at room temperature for 30 min., filtered through a cannula, and evaporated to dryness. The resulting yellow solid was washed with hexane (3×15 mL) and dried in vacuo. Yield: 54 mg (69%). IR ($CH_2Cl_2$): 2033, 1928, 1922 cm$^{-1}$ ($\nu_{CO}$). $^1$H NMR ($CD_2Cl_2$): $\delta = 8.78$ (d, $J = 5.9$ Hz, 1H, $H_{6'}$), 7.69 (d, $J = 1.5$ Hz, 1H, C*H* *N*-MesIm), 7.51 (dd, $J = 6.0$, 2.0 Hz, 1H, $H_{5'}$), 7.25 (d, $J = 2.0$ Hz, 1H, $H_{3'}$), 7.21 ($s_{br}$, 1H, *N*-MesIm), 7.15 (d, $J =$ 1.5 Hz, 1H, C*H* *N*-MesIm), 7.04 ($s_{br}$, 1H, *N*-MesIm), 6.51, 6.48 (d, $J =$ 1.6 Hz, 1H each, $H_3$ and $H_5$), 3.44, 2.80 (s, 3H each, *N*-C$H_3$), 2.42, 2.07 (s, 3H each, C$H_3$ *N*-MesIm), 1.28 (s, 9H, C$H_3$ *t*Bu), 1.24 (s, 3H, C$H_3$ *N*-MesIm), 1.13 (s, 9H, C$H_3$ *t*Bu). $^{13}$C{$^1$H} NMR ($CD_2Cl_2$): $\delta = 195.9$, 195.0, 194.3 (*C*O), 166.8, 166.1, 158.4 ($C_4$, $C_{4'}$ and $C_{2'}$), 153.6 ($C_{6'}$), 141.8, 139.4, 135.3, 134.7, 133.9, 132.0, 130.2, 130.1 (4,4′-*t*Bu$_2$bipy and *N*-MesIm), 134.8, 124.6 (*C*H *N*-MesIm), 131.8, 123.4 ($C_3$ and $C_5$), 124.3 ($C_{5'}$), 119.4 ($C_{3'}$), 88.0 ($C_6$), 57.2, 47.4 (*N*-*C*H$_3$), 35.7, 33.1 (*C*(CH$_3$)$_3$), 29.7, 28.3 (3CH$_3$ *t*Bu), 20.9, 17.4, 16.1 (*C*H$_3$ *N*-MesIm). Elemental analysis (%) calcd for $C_{36}H_{43}F_3N_4O_6ReS$: C 47.88, H 4.80, N 6.20; found: C 47.52, H 4.75, N 6.57.

### Synthesis of 7a

$KN(SiMe_3)_2$ (0.13 mL of a 0.7 M solution in toluene, 0.094 mmol) was added to a solution of [Re(CO)$_3$(*N*-MesIm)(4,4′-*t*Bu$_2$bipy)] (**4a**, 75 mg, 0.086 mmol) in THF (20 mL) previously cooled to −78 °C. The solvent was evaporated to dryness under reduced pressure, the residue dissolved in $CH_2Cl_2$ (20 mL), and HOTf (9 μL, 0.095 mmol) was then added. The mixture was stirred at room temperature for 10 min, filtered through a cannula, and evaporated to dryness. The resulting yellow solid was washed with hexane (3×

15 mL) and dried in vacuo. Yield: 54 mg (70%). IR ($CH_2Cl_2$): 2032, 1928, 1916 $cm^{-1}$ ($\nu_{CO}$). $^1H$ NMR ($CD_2Cl_2$): $\delta = 8.87$ (d, $J = 6.0$ Hz, 1H, $H_{6'}$), 8.11 ($s_{br}$, 1H, N*H*), 7.67 (d, $J = 1.4$ Hz, 1H, $H_{3'}$), 7.40 (dd, $J = 6.0$, 1.4 Hz, 1H, $H_{5'}$), 7.29 (d, $J = 1.4$ Hz, 1H, C*H* *N*-MesIm), 7.13, 6.98 ($s_{br}$, 1H each, *N*-MesIm), 6.96 (d, $J = 1.4$ Hz, 1H, C*H* *N*-MesIm), 6.86 ($s_{br}$, 1H, $H_3$), 5.29 (m, 1H, $H_6$), 5.12 (m, 1H, $H_5$), 2.40, 2.04, 1.75 (s, 3H each, C$H_3$ *N*-MesIm), 1.40, 0.95 (s, 9H, C$H_3$ *t*Bu). $^{13}C\{^1H\}$ NMR ($CD_2Cl_2$): $\delta = 196.5$, 194.9, 194.4 (*CO*), 164.7, 157.0 (4,4′-*t*Bu$_2$bipy), 152.9 ($C_{6'}$), 149.5, 145.3, 141.3, 139.6, 135.3, 134.8, 131.6, 130.0, 129.8 (4,4′-*t*Bu$_2$bipy and *N*-MesIm), 130.2, 124.4 (*CH* *N*-MesIm), 124.3 ($C_{3'}$), 123.4 ($C_{5'}$), 118.9 ($C_5$), 118.1 ($C_3$), 58.1 ($C_6$), 35.9, 34.3 ($C(CH_3)_3$), 30.2, 28.3 (3*CH*$_3$ *t*Bu), 21.1, 18.5, 17.2 (*CH*$_3$ *N*-MesIm). Elemental analysis (%) calcd for $C_{34}H_{38}F_3N_4O_6ReS$: C 46.73, H 4.38, N 6.41; found: C 46.98, H 4.44, N 6.07.

### Synthesis of 14

$KN(SiMe_3)_2$ (0.14 mL of a 0.7 M solution in toluene, 0.096 mmol) was added to a solution of [Re(*N*-MeIm)(CO)$_3$(4,4′-(NMe$_2$)$_2$bipy)] (**11b**, 65 mg, 0.087 mmol) in THF (20 mL) previously cooled to −78 °C. The color of the solution changed from yellow to red, and the solvent was evaporated to dryness under reduced pressure. The residue was redissolved in toluene (20 mL), filtered through a cannula, and evaporated to dryness. The resulting red solid was washed with hexane (3×15 mL) and dried in vacuo. Yield: 47 mg (73%). IR (THF): 2000, 1884, 1878 $cm^{-1}$ ($\nu_{CO}$). $^1H$ NMR ($CD_2Cl_2$): $\delta = 8.35$ (d, $J =$ 6.6 Hz, 2H, $H_{6,6'}$), 7.27 (d, $J = 2.5$ Hz, 2H, $H_{3,3'}$), 6.72 (s, 1H, C*H* *N*-MeIm), 6.48 (dd, $J = 6.6$, 2.5 Hz, 2H, $H_{5,5'}$), 6.45 (s, 1H, C*H* *N*-MeIm), 3.79 (s, 3H, C$H_3$ *N*-MeIm), 3.14 (s, 12H, C$H_3$ NMe$_2$). $^{13}C\{^1H\}$ NMR ($CD_2Cl_2$): $\delta = 202.4$ (2*CO*), 196.1 (*CO*), 178.5 (Re-*C*), 157.3, 154.8, 151.9, 108.3, 104.3 (4,4′-(NMe$_2$)$_2$bipy), 128.1, 120.2 (*CH* *N*-MeIm), 39.8 (*CH*$_3$ NMe$_2$), 33.5 (*CH*$_3$ *N*-MeIm).

### Synthesis of 15a

$KN(SiMe_3)_2$ (0.14 mL of a 0.7 M solution in toluene, 0.096 mmol) was added to a solution of [Re(*N*-MeIm)(CO)$_3$(4,4′-(NMe$_2$)$_2$bipy)]OTf (**11b**, 65 mg, 0.087 mmol) in THF (20 mL) previously cooled to −78 °C. The color of the solution changed from yellow to red, and the solvent was evaporated to dryness under reduced pressure. The residue was dissolved in $CH_2Cl_2$ (20 mL), filtered through a cannula, and MeOTf (11 μL, 0.096 mmol) was added. The solution was stirred for 15 min. at room temperature, and then evaporated to dryness. The resulting red solid was washed with hexane (3× 15 mL) and dried in vacuo. Yield: 40 mg (61%). IR ($CH_2Cl_2$): 2020, 1914, 1899 $cm^{-1}$ ($\nu_{CO}$). $^1H$ NMR ($CD_2Cl_2$): $\delta = 8.58$ (d, $J = 6.8$ Hz, 2H, $H_{6,6'}$), 7.28 (d, $J = 2.7$ Hz, 2H, $H_{3,3'}$), 6.80 (s, 2H, C*H* *N*-MeIm), 6.60 (dd, $J = 6.8$, 2.7 Hz, 2H, $H_{5,5'}$), 3.53 (s, 6H, C$H_3$ *N*-MeIm), 3.20 (s, 12H, C$H_3$ NMe$_2$). $^{13}C\{^1H\}$ NMR ($CD_2Cl_2$): $\delta = 197.4$ (2*CO*), 192.9 (*CO*), 177.1 (Re-*C*), 156.9, 155.5, 153.2, 108.5, 105.5 (4,4′-(NMe$_2$)$_2$bipy), 123.5 (*CH* *N*-MeIm), 40.1 (*CH*$_3$ NMe$_2$), 39.3 (*CH*$_3$ *N*-MeIm). Elemental analysis (%) calcd for $C_{23}H_{26}F_3N_6O_6ReS$: C 34.46, H 3.46, N 11.10; found: C 34.25, H 3.16, N 10.84.

### Synthesis of 18a

$KN(SiMe_3)_2$ (0.20 mL of a 0.7 M solution in toluene, 0.140 mmol) was added to a solution of [Re(CO)$_3$(*N*-MesIm)(4,4′-Br$_2$bipy)] (**16a**, 100 mg, 0.109 mmol) in THF (20 mL) previously cooled to −78 °C. The color of the solution changed immediately from yellow to red. The IR data of this neutral species, analogous to complex **17b**, in THF are: 2013, 1909, 1896 ($\nu_{CO}$). The solvent was evaporated to dryness under reduced pressure, and a solution of HOTf (12 μL, 0.131 mmol) in $CH_2Cl_2$ (20 mL), previously cooled to −78 °C, was then added. The color of the reaction mixture changed again to yellow, and it was stirred for 10 min, filtered through a cannula, and evaporated to dryness. The resulting yellow solid was washed with hexane (3×15 mL) and dried in vacuo. Yield: 67 mg (67%). IR ($CH_2Cl_2$): 2038, 1936 $cm^{-1}$ ($\nu_{CO}$). $^1H$ NMR ($CD_2Cl_2$): $\delta = 8.78$ (d, $J =$ 6.3 Hz, 1H, $H_{6'}$), 8.35 ($s_{br}$, 1H, $H_6$), 7.68 (d, $J = 6.3$ Hz, 1H, $H_{5'}$), 7.61, 7.56 (s, 1H each, C*H* *N*-MesIm), 3.58 ($s_{br}$, 2H, C$H_2$), 2.44, 1.93, 1.51 (s, 3H each, C$H_3$ *N*-MesIm). $^{13}C\{^1H\}$ NMR ($CD_2Cl_2$): $\delta = 195.2$, 195.0, 194.8 (*CO*), 174.1 ($C_6$), 156.1 ($C_{6'}$), 155.8, 145.7, 142.3, 139.3, 136.0, 134.6, 130.8, 121.8 (4,4′-Br$_2$bipy), 132.1, 126.5 (*CH* *N*-MesIm), 130.8, 130.7 (*N*-MesIm), 130.3 ($C_{5'}$), 125.1 ($C_{3'}$), 117.0 ($C_5$), 74.5 ($C_2$), 38.4 ($C_3$, *C*H$_2$), 21.5, 17.8, 17.5 (*CH*$_3$ *N*-MesIm). Elemental analysis (%) calcd for $C_{26}H_{20}Br_2F_3N_4O_6ReS$: C 33.96, H 2.19, N 6.09; found: C 37.18, H 2.45, N 5.97.

### Synthesis of 21a

$KN(SiMe_3)_2$ (0.20 mL of a 0.7 M solution in toluene, 0.140 mmol) was added to a solution of [Mo($\eta^3$-$C_4H_7$)(CO)$_2$(4,7-Cl$_2$phen)(*N*-MesIm)]OTf (**19a**, 0.100 g, 0.126 mmol) in THF (20 mL) previously cooled to −78 °C. The solvent was evaporated to dryness under reduced pressure, a solution of HOTf (13 μL, 0.151 mmol) in $CH_2Cl_2$ (20 mL) was then added, and the reaction mixture was stirred for 10 min. The reaction mixture was filtered through a cannula and evaporated to a volume of 5 mL. The addition of hexane (20 mL) caused the precipitation of an red solid, which was washed with diethyl ether (2×15 mL) and dried in vacuo. Yield: 0.059 g (59%). IR ($CH_2Cl_2$): 1951, 1867 $cm^{-1}$ ($\nu_{CO}$). $^1H$ NMR ($CD_2Cl_2$): $\delta = 9.12$ (d, $J =$ 5.3 Hz, 1H, $H_9$), 8.23 (d, $J = 8.7$ Hz, 1H, $H_5/H_6$), 7.91 (d, $J = 8.7$ Hz, 1H, $H_6/H_5$), 7.72 (d, $J = 5.3$ Hz, 1H, $H_8$), 7.36 ($s_{br}$, 1H, C*H* *N*-MesIm), 7.09, 6.97 (s, 1H each, Mes), 6.93 (s, 1H, C*H* *N*-MesIm), 5.48 (d, $J =$ 4.7 Hz, 1H, $H_3$), 5.20 ($s_{br}$, 1H, $H_2$), 3.68 ($s_{br}$, 1H, $H_{syn}$ $\eta^3$-$C_4H_7$), 3.40 ($s_{br}$, 1H, $H_{syn}$ $\eta^3$-$C_4H_7$), 2.27, 2.03 (s, 3H each, C$H_3$ *N*-MesIm), 1.64, 1.56 (s, 1H each, $H_{anti}$ $\eta^3$-$C_4H_7$), 1.52 (s, 3H, C$H_3$ $\eta^3$-$C_4H_7$), 1.25 (s, 3H, C$H_3$ *N*-MesIm). $^{13}C\{^1H\}$ NMR ($CD_2Cl_2$): $\delta = 226.2$, 224.1 (*CO*), 153.6, 146.6, 144.2, 142.6, 141.3, 135.0, 134.9, 134.0, 132.8, 130.1, 129.8, 129.3, 127.7, 126.9, 125.7, 124.1, 123.2 (4,7-Cl$_2$phen and *N*-MesIm), 130.7, 124.6 (*CH* *N*-MesIm), 84.3 ($C_2$ $\eta^3$-$C_4H_7$), 60.8, 52.6 ($C_1$ and $C_3$ $\eta^3$-$C_4H_7$), 57.34 ($C_2$ 4,7-Cl$_2$phen), 20.9 (*CH*$_3$ *N*-MesIm), 19.3 (*CH*$_3$ $\eta^3$-$C_4H_7$), 16.8, 16.6 (*CH*$_3$ *N*-MesIm). Elemental analysis (%) calcd for $C_{31}H_{27}Cl_2F_3MoN_4O_5S$: C 47.04, H 3.44, N 7.08; found: C 46.60, H 3.25, N 7.13.

## Acknowledgements

Financial support from Ministerio de Economía *y* Competitividad/FEDER (grant CTQ2015-70231-P), Ministerio de Ciencia, Innovación y Universidades (grant PGC2018-097366-B-100) and Principado de Asturias (grant GRUPIN14-103, and Severo Ochoa predoctoral fellowship to S.F.) is gratefully acknowledged. J.D. thanks CenitS and COMPUTAEX for allowing us the use of supercomputing facilities.

## Conflict of interest

The authors declare no conflict of interest.

**Keywords:** carbene ligands · C–C coupling · molybdenum · rhenium · substituent effects

[1] a) M. Bachrach, T. J. Marks, J. M. Notestein, *ACS Catal.* **2016**, *6*, 1455 – 1476; b) E. Furimsky, F. E. Massoth, *Catal. Rev. Sci. Eng.* **2005**, *47*, 297 – 489; c) R. Prins, *Adv. Catal.* **2001**, *46*, 399 – 464; d) T. C. Ho, *Catal. Rev. Sci. Eng.* **1988**, *30*, 117 – 160.

[2] a) J. B. Bonanno, A. S. Veige, P. T. Wolczanski, E. B. Lobkovsky, *Inorg. Chim. Acta* **2003**, *345*, 173 – 184; b) T. S. Kleckley, J. L. Bennet, P. T. Wolczanski, E. B. Lobkovsky, *J. Am. Chem. Soc.* **1997**, *119*, 247 – 248; c) K. J. Covert, D. R. Neithamer, M. C. Zonnnevylle, R. E. LaPointe, C. P. Schaller, P. T. Wolczanski, *Inorg. Chem.* **1991**, *30*, 2494 – 2508; d) D. R. Neithamer, L. Parkanyi, J. F. Mitchell, P. T. Wolczanski, *J. Am. Chem. Soc.* **1988**, *110*, 4421 – 4423.

[3] a) K. J. Weller, I. Filippov, P. M. Briggs, D. E. Wigley, *Organometallics* **1998**, *17*, 322 – 329; b) K. J. Weller, P. A. Fox, S. D. Gray, D. E. Wigley, *Polyhedron* **1997**, *16*, 3139; c) K. J. Weller, I. Filippov, P. M. Briggs, D. E. Wigley, *J. Organomet. Chem.* **1997**, *528*, 225 – 228; d) K. D. Allen, M. A. Bruck, S. D. Gray, R. P. Kingsborough, D. P. Smith, K. J. Weller, D. E. Wigley, *Polyhedron* **1995**, *14*, 3315 – 3333; e) K. J. Weller, S. D. Gray, P. M. Briggs, D. E. Wigley, *Organometallics* **1995**, *14*, 5588 – 5597; f) S. D. Gray, K. J. Weller, M. A. Bruck, P. M. Briggs, D. E. Wigley, *J. Am. Chem. Soc.* **1995**, *117*, 10678 – 10693; g) S. D. Gray, D. P. Smith, M. A. Bruck, D. E. Wigley, *J. Am. Chem. Soc.* **1992**, *114*, 5462 – 5463.

[4] a) S. Baek, T. Kurogi, D. Kang, M. Kamitani, S. Kwon, D. P. Solowey, C.-H. Chen, M. Pink, P. J. Carroll, D. J. Minidiola, M.-H. Baik, *J. Am. Chem. Soc.* **2017**, *139*, 12804 – 12814; b) A. R. Fout, B. C. Bailey, J. Tomaszewski, D. J. Mindiola, *J. Am. Chem. Soc.* **2007**, *129*, 12640 – 12641; c) B. C. Bailey, H. Fan, J. C. Huffman, M. H. Baik, D. J. Mindiola, *J. Am. Chem. Soc.* **2006**, *128*, 6798 – 6799.

[5] a) M. J. Monreal, S. Kjan, P. L. Diaconescu, *Angew. Chem. Int. Ed.* **2009**, *48*, 8352 – 8355; *Angew. Chem.* **2009**, *121*, 8502 – 8505; b) C. T. Carver, D. Benitez, K. L. Miller, B. N. Williams, E. Tkatchouk, W. A. Goddard III, P. L. Diavonescu, *J. Am. Chem. Soc.* **2009**, *131*, 10269 – 10278; c) C. T. Carver, P. L. Diaconescu, *J. Am. Chem. Soc.* **2008**, *130*, 7558 – 7559.

[6] A similar ring-opening reaction mediated by yttrium alkyl complexes can be found in: a) W. Yi, J. Zhang, S. Huang, L. Weng, X. Zhou, *Chem. Eur. J.* **2014**, *20*, 867 – 876; b) Y. Zhang, J. Zhang, J. Hong, F. Zhang, L. Weng, X. Zhou, *Organometallics* **2014**, *33*, 7052 – 7058.

[7] S. Hu, G. Luo, T. Shima, Y. Luo, Z. Hou, *Nat. Commun.* **2017**, *8*, 1866 – 1873.

[8] K. Murakami, S. Yamada, T. Kaneda, K. Itami, *Chem. Rev.* **2017**, *117*, 9302 – 9332.

[9] P. S. Fier, J. F. Hartwig, *Science* **2013**, *342*, 956 – 960 and references therein.

[10] B. K. Liebov, W. D. Harman, *Chem. Rev.* **2017**, *117*, 13721 – 13755 and references therein.

[11] R. D. Gillard, J. R. Lyons, *J. Chem. Soc. Chem. Commun*. **1973**, 585 – 586.

[12] A review of the contributions to this field carried out by Gillard and related chemistry can be found in: E. C. Constable, *Polyhedron* **2016**, *103*, 295 – 306.

[13] a) K. B. Szpakolski, K. Latham, C. J. Rix, J. M. White, B. Moubaraki, K. S. Murray, *Chem. Eur. J.* **2010**, *16*, 1691 – 1696; b) X.-M. Zhang, M.-L. Tong, X.-M. Chen, *Angew. Chem. Int. Ed.* **2002**, *41*, 1029 – 1031; *Angew. Chem.* **2002**, *114*, 1071 – 1073.

[14] a) S. Fombona, J. Pérez, J. Díaz, L. Riera, *Chem. Eur. J.* **2017**, *23*, 17870 – 17873; b) R. Arévalo, L. Riera, J. Pérez, *Inorg. Chem.* **2017**, *56*, 4249 – 4252; c) R. Arévalo, M. I. Menéndez, R. López, I. Merino, L. Riera, J. Pérez, *Chem. Eur. J.* **2016**, *22*, 17972 – 17975; d) S. Fombona, M. Espinal-Viguri, M. A. Huertos, J. Díaz, R. López, M. I. Menéndez, J. Pérez, L. Riera, *Chem. Eur. J.* **2016**, *22*, 17160 – 17164; e) R. Arévalo, J. Pérez, L. Riera, *Chem. Eur. J.* **2015**, *21*, 3546 – 3549; f) R. Arévalo, J. Pérez, L. Riera, *Inorg. Chem.* **2013**, *52*, 6785 – 6787; g) M. A. Huertos, J. Pérez, L. Riera, *J. Am. Chem. Soc.* **2008**, *130*, 5662 – 5663; h) L. Cuesta, E. Hevia, D. Morales, J. Pérez, V. Riera, E. Rodríguez, D. Miguel, *Chem. Commun.* **2005**, 116 – 117.

[15] A. P. Smith, C. L. Fraser, in *Comprehensive Coordination Chemistry II, Vol. 1* (Eds.: J. A. McCleverty, T. J. Meyer), Elsevier Pergamon, Oxford **2004**, pp. 1 – 23.

[16] a) S. Leelasubcharoen, K. C. Lam, T. E. Concolino, A. L. Rheingold, K. H. Theopold, *Organometallics* **2001**, *20*, 182 – 187; b) L. M. Kobriger, A. K. McMullen, P. E. Fanwicck, I. P. Rothwell, *Polyhedron* **1989**, *8*, 77 – 81.

[17] a) Dearomatization of bipy and phen ligands coordinated to a magnesium center through alkyl or hydride migration from the metal center has been reported: C. Weetman, M. S. Hill, M. F. Mahon, *Polyhedron* **2016**, *103*, 115 – 120; b) The only example of dearomatization of a 2,2′:6′,2″-terpyridine ligand has been found for an $Lu^{III}$ complex: K. C. Jantunen, B. L. Scott, P. J. Hay, J. C. Gordon, J. L. Kiplinger, *J. Am. Chem. Soc.* **2006**, *128*, 6322 – 6323.

[18] The effect of different substituents on the electronic properties of a bipyridine ligand coordinated to $Rh^{III}$ has been computationally studied: D. R. Pahls, J. T. Groves, T. B. Gunnoe, T. R. Cundari, *Organometallics* **2014**, *33*, 1936 – 1944.

[19] See the Supporting Information for further experimental details.

[20] Complexes of the $\{Mo^{II}(\eta^3\text{-allyl})(CO)_2\}$ fragment have been the subject of two recent reviews: a) M. J. Calhorda, P. J. Costa, *Coord. Chem. Rev.* **2017**, *344*, 83 – 100; b) D. E. Ryan, D. J. Cardin, F. Hartl, *Coord. Chem. Rev.* **2017**, *335*, 103 – 149.

[21] $[MoBr(\eta^3\text{-}C_3H_5)(CO)_2(\alpha\text{-diimine})]$ complexes wherein α-diimine is a 4,4′-disubstituted-2,2′-bipyridine or a 2,9-disubstituted-1,10-phenanthroline have been recently reported: M. S. Saraiva, C. D. Nunes, V. Félix, A. P. C. Ribeiro, C. Nieto de Castro, M. J. Calhorda, *Eur. J. Inorg. Chem.* **2018**, 3922 – 3932.

[22] CCDC 1901150 (**2a**), 1901151 (**2b**), 1050350 (**6a**), 1050351 (**7a**), 1901152 (**8b**), 1050353 (**12**), 1901153 (**15a**), 1901154 (**21b**), and 1901155 (**22**) contain the supplementary crystallographic data for this paper. These data are provided free of charge by The Cambridge Crystallographic Data Centre.

[23] Z. Wang, L. Jiang, D. Khairunnisa, B. Mohamed, J. Zhao, T. S. A. Hor, *Coord. Chem. Rev.* **2015**, *293 – 294*, 292 – 326.

[24] M. Brill, J. Díaz, M. A. Huertos, R. López, J. Pérez, L. Riera, *Chem. Eur. J.* **2011**, *17*, 8584 – 8595.

[25] Transformation of a *N*-alkylimidazole ligand into a NH-NHC ligand at an $Mn^{I}$ center can be found in: J. Ruiz, B. F. Perandones, *J. Am. Chem. Soc.* **2007**, *129*, 9298 – 9299.

[26] Nitrogen extrusion on reaction with an electrophile has been published by Mindiola et al. for a completely different fragment (ref. [4]).

[27] The synthesis of $[Re(CO)_3(4,4'\text{-}(OMe)_2bipy)(N\text{-}Rlm)]OTf$ compounds and reactivity towards $KN(SiMe_3)_2$ and afterwards towards HOTf have been published as a preliminary communication (ref. [14d]).

[28] Spectroscopic and structural data of compound **12** are analogous to those found for the products resulting from a deprotonation/protonation sequence of $[Re(CO)_3(4,4'\text{-}(OMe)_2bipy)(N\text{-}Rlm)]OTf$ compounds. For a more detailed discussion, see the preliminary communication (ref. [14d]).

[29] a) S. Kuwata, F. E. Hahn, *Chem. Rev.* **2018**, *118*, 9642 – 9677 and references therein; b) J. Ruiz, D. Sol, J. F. Van der Maelen, M. Vivanco, *Organometallics* **2017**, *36*, 1035 – 1041; c) D. Vagedes, G. Kehr, D. König, K. Wedeking, R. Fröhlich, G. Erker, C. Mück-Lichtenfeld, S. Grimme, *Eur. J. Inorg. Chem.* **2002**, 2015 – 20121; d) A. Wacker, H. Pritzkow, W. Siebert, *Eur. J. Inorg. Chem.* **1998**, 843 – 849.

[30] a) R. Fraser, C. G. C. E. Van Sittert, P. H. van Rooyen, M. Landman, *J. Organomet. Chem.* **2017**, *835*, 60 – 69; b) C.-H. Chen, Y.-H. Liu, S.-M. Peng, J.-T. Chen, S.-T. Liu, *Dalton Trans.* **2012**, *41*, 2747 – 2754; c) M. A. Huertos, J. Pérez, L. Riera, *Chem. Eur. J.* **2012**, *18*, 9530 – 9533; d) T. A. Martin, C. E. Ellul, M. F. Mahon, M. E. Warren, D. Allan, M. K. Whittlesey, *Organometallics* **2011**, *30*, 2200 – 2211; e) M. A. Huertos, J. Pérez, L. Riera, J. Díaz, R. López, *Chem. Eur. J.* **2010**, *16*, 8495 – 8507; f) O. Hiltner, E. Herdtweck, M. Drees, W. A. Herrmann, F. E. Kühn, *Eur. J. Inorg. Chem.* **2009**, 1825 – 1831.

[31] a) M. C. Jahnke, F. E. Hahn, *Coord. Chem. Rev.* **2015**, *293 – 294*, 95 – 115.

[32] a) P. V. Simpson, M. Falasca, M. Massi, *Chem. Commun.* **2018**, *54*, 12429 – 12438; b) C. Hille, F. E. Kühn, *Dalton Trans.* **2016**, *45*, 15 – 31; c) S. J. Hock, L.-A. Schaper, W. A. Herrmann, F. E. Kühn, *Chem. Soc. Rev.* **2013**, *42*, 5073 – 5089.

[33] See, for example: a) S. Oh, J. R. Gallagher, J. T. Miller, Y. Surendranath, *J. Am. Chem. Soc.* **2016**, *138*, 1820 – 1823; b) K. K.-W. Lo, *Acc. Chem. Res.* **2015**, *48*, 2985 – 2995; c) S. Sato, O. Ishitani, *Coord. Chem. Rev.* **2015**, *282 – 283*, 50 – 59; d) A. Zarkadoulas, E. Koutsouri, C. Kefalidi, C. A. Mitsopoulou, *Coord. Chem. Rev.* **2015**, *304 – 305*, 55 – 72; e) L. M. Kiefer, J. T. King, K. J. Kubarych, *Acc. Chem. Res.* **2015**, *48*, 1123 – 1130; f) A. Leonidova, G. Gasser, *ACS Chem. Biol.* **2014**, *9*, 2180 – 2193 and references therein.

[34] DFT calculations have shown that the transformation of $Mn^{I}$ imidazole complexes into NHC species involves an initial attack at a *cis* carbonyl ligand: J. Ruiz, B. F. Perandones, J. F. Van der Maelen, S. García-Granda, *Organometallics* **2010**, *29*, 4639 – 4642.

 

[35] The formation of the imidazoly-2-yl product $\mathbf{P_B}$-***t*Bu** via the $\kappa^2$-*C*,*N*-imidazolyl transition state ($\mathbf{TS_{B2}}$-***t*Bu**) implies a higher Gibbs energy barrier (16.4/14.4 kcal mol$^{-1}$ for *N*-MeIm/*N*-MesIm, respectively).

[36] Note that the electron density is transferred from the bipy ligand through the metal center to the carbonyl ligands, a fact that can be visually appraised by a more pronounced red color for these ligands. The electron-density changes are also experimentally observed in the frequency of the IR $\nu_{CO}$ bands.

[37] No TSs were investigated, as they were not found for the analogous nonsubstituted bipy complexes [Mo($\eta^3$-$C_4H_7$)(CO)$_2$(bipy)(*N*-RIm)] (R = Me, Mes) (ref. [24]).

[38] Imidazol-2-yl formation via pathway 2B is more energetically demanding ($\mathbf{TS_{2B}}$-$\mathbf{NMe_2}$: 18.9 kcal mol$^{-1}$ for *N*-MeIm).

[39] See the Experimental Section for a complete labeling scheme of bipy and phen ligands.

[40] CrysAlis$^{Pro}$ CCD, CrysAlis$^{Pro}$ RED, Oxford Diffraction Ltd., Abingdon, Oxfordshire, UK.

[41] APPEX II, Bruker AXS Inc., Madison, WI, USA, **2004**.

[42] G. M. Sheldrick, *SHELX-97 (SHELXS 97 and SHELXL 97)*, *Programs for Crystal Structure Analyses*, University of Göttingen: Göttingen (Germany), **1996**.

[43] A. Altomare, G. L. Cascarano, C. Giacovazzo, A. Guagliardi, M. C. Burla, G. Polidori, M. Camalli, *J. Appl. Crystallogr.* **1994**, *27*, 435.

[44] A. Altomare, M. C. Burla, M. Camalli, G. L. Cascarano, C. Giacovazzo, A. Guagliardi, A. G. G. Moliterni, G. Polidori, R. Spagna, *J. Appl. Crystallogr.* **1999**, *32*, 115 – 119.

[45] G. M. Sheldrick, *Acta Crystallogr. Sect. A* **2008**, *64*, 112 – 122.

[46] L. J. Farrugia, *J. Appl. Crystallogr.* **1997**, *30*, 565.

[47] Gaussian 09, Revision B.01, M. J. Frisch, G. W. Trucks, H. B. Schlegel, G. E. Scuseria, M. A. Robb, J. R. Cheeseman, G. Scalmani, V. Barone, B. Mennucci, G. A. Petersson, H. Nakatsuji, M. Caricato, X. Li, H. P. Hratchian, A. F. Izmaylov, J. Bloino, G. Zheng, J. L. Sonnenberg, M. Hada, M. Ehara, K. Toyota, R. Fukuda, J. Hasegawa, M. Ishida, T. Nakajima, Y. Honda, O. Kitao, H. Nakai, T. Vreven, J. A. Montgomery, Jr., J. E. Peralta, F. Ogliaro, M. Bearpark, J. J. Heyd, E. Brothers, K. N. Kudin, V. N. Staroverov, R. Kobayashi, J. Normand, K. Raghavachari, A. Rendell, J. C. Burant, S. S. Iyengar, J. Tomasi, M. Cossi, N. Rega, J. M. Millam, M. Klene, J. E. Knox, J. B. Cross, V. Bakken, C. Adamo, J. Jaramillo, R. Gomperts, R. E. Stratmann, O. Yazyev, A. J. Austin, R. Cammi, C. Pomelli, J. W. Ochterski, R. L. Martin, K. Morokuma, V. G. Zakrzewski, G. A. Voth, P. Salvador, J. J. Dannenberg, S. Dapprich, A. D. Daniels, O. Farkas, J. B. Foresman, J. V. Ortiz, J. Cioslowski, D. J. Fox, Gaussian, Inc., Wallingford, CT, **2010**.

[48] a) X. Li, M. J. Frisch, *J. Chem. Theory Comput.* **2006**, *2*, 835 – 839; b) H. B. Schlegel, *Theor. Chem. Acc.* **1984**, *66*, 333 – 340; c) H. B. Schlegel, *J. Comput. Chem.* **1982**, *3*, 214 – 218.

[49] a) G. Scalmani, M. J. Frisch, *J. Chem. Phys.* **2010**, *132*, 114110/1-15; b) J. Tomasi, B. Mennucci, M. T. Cancès, *J. Mol. Struct.* **1999**, *464*, 211 – 226; c) V. Barone, M. Cossi, J. Tomasi, *J. Comput. Chem.* **1998**, *19*, 404 – 417; d) M. T. Cancès, B. Mennucci, J. Tomasi, *J. Chem. Phys.* **1997**, *107*, 3032 – 3041; e) B. Mennucci, J. Tomasi, *J. Chem. Phys.* **1997**, *106*, 5151 – 5158; f) V. Barone, M. Cossi, J. Tomasi, *J. Chem. Phys.* **1997**, *107*, 3210 – 3221.

[50] A. K. Rappé, C. J. Casewit, K. S. Colwell, W. A. Goddard III, W. M. Skiff, *J. Am. Chem. Soc.* **1992**, *114*, 10024 – 10039.

[51] S. Grimme, *J. Comput. Chem.* **2006**, *27*, 1787 – 1799.

[52] W. J. Hehre, L. Radom, J. A. Pople, P. v. R. Schleyer, *Ab Initio Molecular Orbital Theory*, Wiley, New York, **1986**.

[53] P. J. Hay, W. R. Wadt, *J. Chem. Phys.* **1985**, *82*, 270 – 283.

[54] A. W. Ehlers, M. Böhme, S. Dapprich, A. Gobbi, A. Höllwarth, V. Jonas, K. F. Köhler, R. Stegmann, A. Veldkamp, G. Frenking, *Chem. Phys. Lett.* **1993**, *208*, 111 – 114.

[55] D. A. McQuarrie, *Statistical Mechanics*, Harper and Row, New York, **1976**.

[56] R. F. Ribeiro, A. V. Marenich, C. J. Cramer, D. G. Truhlar, *J. Phys. Chem. B* **2011**, *115*, 14556 – 14562.

[57] a) E. Reed, L. A. Curtiss, F. Weinhold, *Chem. Rev.* **1988**, *88*, 899 – 926; b) F. Weinhold, J. E. Carpenter, *The Structure of Small Molecules and Ions* (Eds.: R. Naaman, Z. Vager), Plenum, New York, **1988**, pp. 227 – 236.

[58] *Molecular Electrostatic Potential: Concepts and Applications* (Eds.: J. S. Murray, K. Sen), Elsevier, Amsterdam, **1996**.

Manuscript received: March 6, 2019
Revised manuscript received: April 25, 2019
Accepted manuscript online: April 29, 2019
Version of record online: June 24, 2019

## 5.6 Computational Design of Rhenium(I) Carbonyl Complexes for Anticancer Photodynamic Therapy

Daniel Álvarez, M. Isabel Menéndez, and Ramón López

# Computational Design of Rhenium(I) Carbonyl Complexes for Anticancer Photodynamic Therapy

Daniel Álvarez,[†] M. Isabel Menéndez,[†] and Ramón López[*†]

[†]Departamento de Química Física y Analítica, Facultad de Química, Universidad de Oviedo, C/ Julián Clavería 8, 33006 Oviedo, Spain

ABSTRACT

The effect of pyridocarbazole ligand conjugation and substitution and of the replacement of one CO ligand by phosphines on the spectroscopic properties and photocytoxicity of the [$Re(CO)_3$(pyridocarbazole)(pyridine)] complexes was investigated by means of time-dependent density functional theory (TD-DFT) calculations. The expansion of the pyridocarbazole ligand lowers the HOMO-LUMO energy gap, inducing a bathochromic shift. When present, the electron-withdrawing 1H-pyrrole-2,5-dione heterocycle of the bidentate ligand plays an important role by enhancing the stabilization of the LUMO caused by the rise of the conjugation. The introduction of electron-withdrawing substituents into the pyridine ring of the pyridocarbazole ligand mainly produces a stabilizing effect on the LUMO, whereas the HOMO energy rises primarily when electron-donating substituents are introduced into the indole moiety of the bidentate ligand. Both types of substituents result in a bathochromic shift of the lowest-

lying absorption band, which is even larger if they are combined in the same complex. The removal of the $\pi$-backbonding interaction between Re and the carbonyl *cis* ($CO_{cis}$) to the bidentate ligand when replaced $CO_{cis}$ by phosphines $PMe_3$ and CAP, causes another extra bathochromic shift due to the destabilization of the HOMO, which is specially large with the CAP ligand. The alkylphosphine is merely a spectator ligand in the HOMO, but not the CAP phosphine. Through the combination of $PMe_3$ or CAP ligand with the electron-withdrawing and/or electron-donationg substituents at the pyridocarbazole ligand, we have found several complexes with significant absorption at the therapeutic window. In addition, according to our results on the singlet-triplet energy difference, all of them are able to photosensitize cytotoxic oxygen. Therefore, we propose these complexes as potential candidates for use as PSs in PDT.

## INTRODUCTION

Since Raab's pioneering work on the effects of visible light and acridine dye on paramecia,[1] photodynamic therapy (PDT) has become a significant complementary or alternative well-established approach for cancer treatment.[2-15] PDT offers a temporal and spatial control of the treatment with minimal side effects, which starts with the administration of a photosensitizer (PS, a photoactivatable molecule) followed by excitation of PS by light irradiation at a specific wavelength. The light absorption promotes the PS from its ground singlet state ($S_0$) to an excited singlet state ($S_1$), which is an unstable and short-lived state. As a consequence, the excited PS ($S_1$) can return to its ground state ($S_0$) by converting its energy into heat or fluorescence. Alternatively, the PS can evolve from the $S_1$ state to its excited triplet state ($T_1$) that can transfer its energy by phosphorescence or colliding with other molecules to generate chemically reactive

species (CRS), which kill cancer cells. The mechanisms for CRS formation in PDT are generally classified into two types. In the so-called type I mechanism the PS in its $T_1$ state can react with biological organic substrates to form species like superoxide ($O_2^{\cdot-}$) and hydroperoxyl ($HO_2^{\cdot}$) radicals. The mechanism known as type II mostly implies the reaction of the PS in its $T_1$ state with ground state oxygen ($^3O_2$) by transfer of energy to yield singlet oxygen ($^1O_2$), which is the main molecule causing cellular damage to death by necrosis or apoptosis. Although both mechanisms are believed to occur simultaneously,[4,16] it is widely accepted that the type II mechanism is the predominant one in anticancer PDT treatments.[12,17] As such, the three key elements for the therapeutic efficacy of PDT are the PS, a light of appropriate wavelength, and molecular oxygen. To achieve optimal penetration of light into human body tissues and to generate PS in its triplet state and then produce cytotoxic singlet oxygen, the wavelength of the light must fall in the therapeutic window (around 620-850 nm).[12,18] The lower limit of the therapeutic window is a consequence of light absorption by endogenous biomolecules, whereas the upper limit comes from the fact that the energy gap between ground and excited triplet states of the PS must be higher than energy required (~22.5 kcal/mol) for the transformation $^3O_2$ ($^3\Sigma_g^-$) $\rightarrow$ $^1O_2$ ($^1\Delta_g$).[19,20] The amphiphilic character of PS is also of interest for its efficacy in PDT: its hydrophilicity will facilitate its distribution, and lipophilicity its cellular uptake.[12]

Although PDT has been used against a broad variety of cancers (*i.e.*, bile duct, bladder, brain, esophagus, head, lung, neck, pancreas, prostate, skin, etc.), the number of PSs approved for these treatments is very limited.[12,17,21] Most of these drugs are based on porphyrinoid structures, including porphyrins, chlorins, bacteriochlorins, phthalocyanines, and related structures.[12,17,21] Even though these PS are able to absorb light in the therapeutic window and generate cytotoxic singlet oxygen, they have shown drawbacks such as poor solubility in water, aggregation

tendency in physiological liquids, and the need of an oxygen-rich environment for the production of singlet oxygen.[22-25] As a result, there is great interest in modifying the existing PSs or developing new classes of PS. Among the latter, rhenium(I) tricarbonyl complexes have been explored in recent years as potential candidates for PDT[26-35] due to their rich photophysical and biochemical properties (polarized emission, high photostability, large Stokes shifts, long lifetimes, and biocompatibility),[36-40] which can also be tuned by varying the ligands.

Of particular interest are the structural modifications introduced in the first Re(I) complexes with visible-light-induced anticancer activity reported in 2013.[26,27] In the starting complexes rhenium is coordinated to three carbonyl ligands in *facial* disposition, one pyridyl ligand, and one pyridocarbazole-type bidentate ligand (complexes **I**-**III** in Scheme 1). The expansion of the bidentate ligand shifts the photocytotoxic activity in cancer cells to longer wavelengths when going from complex **I** ($\lambda \geq 330$ nm) to **III** ($\lambda \geq 505$ nm), which is desired for PDT since it allows a deeper tumor penetration.[26] This correlates well with the rise of the maximum wavelength ($\lambda_{max}$) of the lowest-lying absorption band from 373 nm for complex **I** to 512 nm for **III** measured in dimethysulfoxide (DMSO). It was also found that the production of $^1O_2$ by these complexes is crucial to induce photocytotoxicity. Another important factor is the location of the PS inside the cell membrane. In fact, it was discovered that the presence of the 2,2'-bipyridine (bipy) ligand at complex **I** (complex **IV** in Scheme 1) instead of the 2-(2'-pyridyl)indolate ligand produces $^1O_2$ upon exposure to UV light, but not photocytotoxicity since the positive charge of **IV** prevents its localization in the cell membrane.[26] Aiming at getting new Re(I) pyridocarbazole complexes for PDT with improved chemical stability and red-shifted visible-light-induced

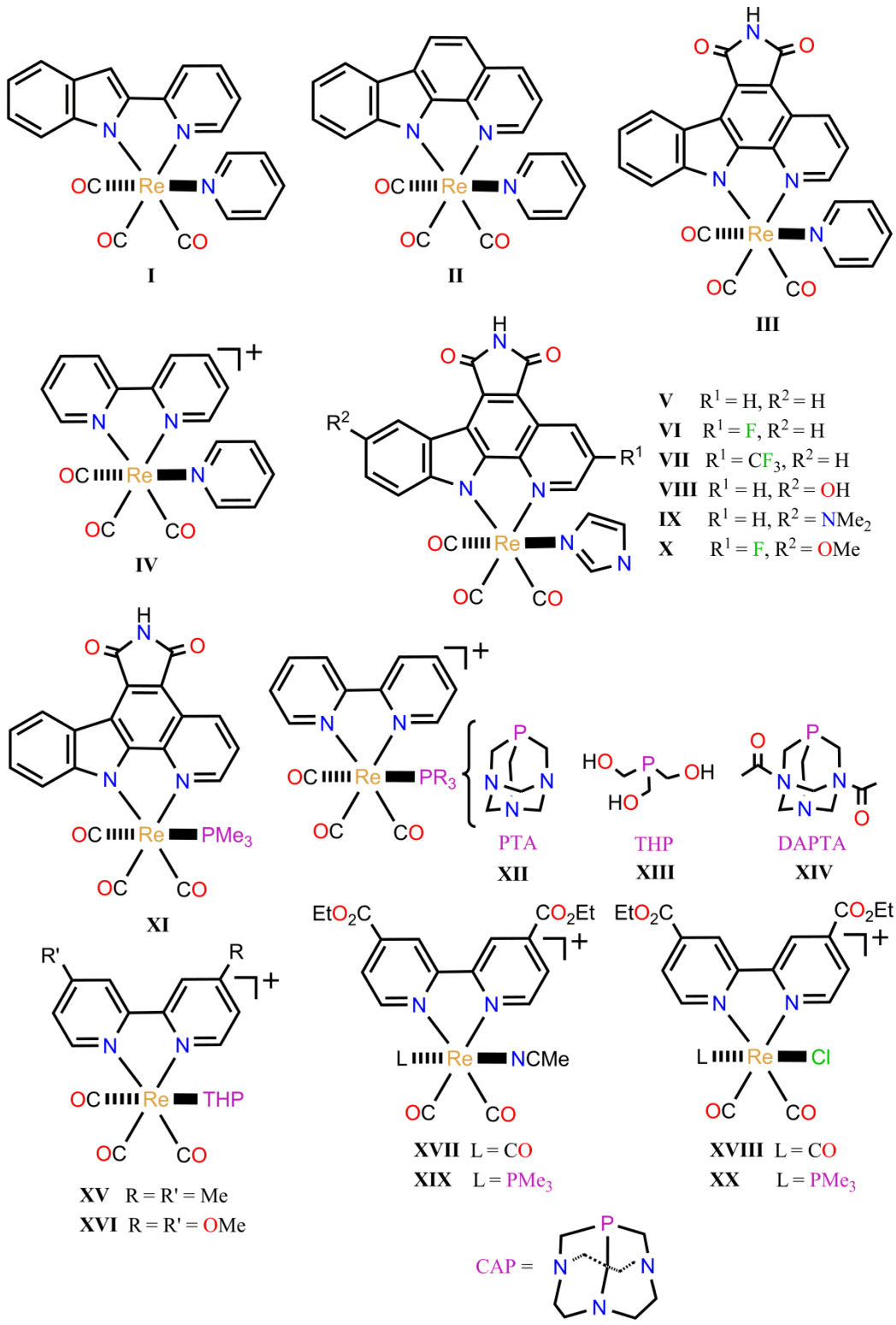


**Scheme 1**. Structure of the rhenium(I) carbonyl complexes **I-XX**. The structure of the phosphines PTA, THP, DAPTA, and CAP is also displayed.

anticancer activity, derivatives of complex **III** were also investigated (complexes **V**-**X** in Scheme 1).[27] The replacement of the strong π-donating pyridine ligand in **III** by the strong σ-donating imidazole one (complex **V** in Scheme 1) does not practically change the value of the longest $\lambda_{max}$ ($\Delta\lambda_{max}$= 1 nm) in DMSO, but it does shift the light-induced toxicity from $\lambda \geq 505$ nm to $\lambda \geq 620$ nm. The presence of $\sigma$-accepting substituents in the 3-position of the pyridine moiety of **V**, complexes **VI** ($R^1$ = F, $R^2$ = H) and **VII** ($R^1$ = $CF_3$, $R^2$ = H) in Scheme 1, further red-shifts the longest $\lambda_{max}$ in DMSO. A similar trend was also obtained when $\pi$-donating substituents are introduced into the 5-position of the indole moiety of **III**, complexes **VIII** ($R^1$ = H, $R^2$ = OH) and **IX** ($R^1$ = H, $R^2$ = $NMe_2$) in Scheme 1. Nonetheless, the latter complexes do not exhibit photocytotoxicity, whereas those containing $\sigma$-accepting groups at the pyridine moiety do. When both types of substituents are simultaneously present at the pyridocarbazole ligand ($R^1$ = F and $R^2$ = OMe, complex **X** in Scheme 1), the longest $\lambda_{max}$ increases from 513 to 552 nm in DMSO when switching from complex **V** to **X** keeping the photoinduced cytotoxic effect at $\lambda \geq 620$ nm. The substitution of the pyridine ligand in **III** by another strong σ-donating ligand like $PMe_3$, complex **XI** in Scheme 1, hardly affects the longest $\lambda_{max}$ ($\Delta\lambda_{max}$ = 3 nm) as in the replacement of pyridine for imidazole, but they differ in that photocytotoxicity now occurs at $\lambda \geq$ 505 nm in both cases. Other phosphine ligands with strong σ-donating character, such as 1,3,5-triaza-7-phosphaadamantane (PTA), *tris*-(hydroxymethyl)phosphine (THP), and 1,4-diacetyl-1,3,7-triaza-5-phosphabicylco[3.3.1]nonane (DAPTA), also appear to have weak effect on the longest $\lambda_{max}$ of Re(I) tricarbonyl complexes bearing bipyridine bidentate ligands (see complexes **XII**-**XIV** in Scheme 1).[33] These compounds show longest $\lambda_{max}$ around 346 nm, which is only 23 nm greater than that obtained for **IV**. However, in contrast to **IV**, complex **XIV** does exhibit cytotoxicity under conditions of light irradiation at 365 nm despite being cationic. This could be related to the

water solubility of this complex conferred by DAPTA. Although, the solubility in water is an important aspect in the design of PSs, it is likely that the electronic character of that phosphine ligand could also be playing a certain role since complexes **XII** and **XIII** are also water-soluble, but without significant photocytotoxicty. Re(I) tricarbonyl complexes bearing the water-soluble phosphine ligand THP also exhibit photocytoxicity at 365 nm when methyl and methoxy substituents are present at the 4 and 4' positions of the bipyridine ligand (complexes **XV** and **XVI** in Scheme 1), whereas the longest $\lambda_{max}$ values hardly change when compared to that obtained for **XIII** ($\Delta\lambda_{max}$ = -5 and -6 nm, respectively).[33] On the other hand, interestingly, a greater effect on the longest $\lambda_{max}$ was found when a phosphine ligand replaces the CO ligand *cis* to a bipyridine-type one instead of pyridine or imidazole ligands. Specifically, the substitution of CO for $PMe_3$ leads to red-shiftings of 100 and 123 nm when going from $[Re(deeb)(CO)_3(NCCH_3)]^+$ and $[Re(deeb)(CO)_3Cl]$ (deeb = 4,4'-diethylester-2,2'-bipyridine) to $[Re(deeb)(CO)_2(PMe_3)(NCCH_3)]^+$ and $[Re(deeb)(CO)_2(PMe_3)Cl]$, respectively (complexes **XVII-XX** in Scheme 1).[41] As the photochemical properties of Re(I) tricarbonyl complexes is mainly controlled by the metal-to-ligand charge transfer (MLCT) transition, that is, the energy difference between the filled Re *d* orbitals and the empty $\pi^*$ orbitals of the bidentate ligand, it was reasoned that the strong σ-donating $PMe_3$ destabilizes the occupied Re *d* orbitals (HOMO of the complex), explaining thus the rise of the longest $\lambda_{max}$ found. In this regard, the use of highly water-soluble phosphine ligands with a very strong electron-donating power, such as 1,4,7-triaza-9-phosphatricyclo[5.3.2.1]tridecane (CAP),[42] could be useful to get new PDT agents based on Re carbonyl pyridocarbazole complexes.

Taking the aforementioned in mind along with the fact that computational chemistry is a reliable tool to obtain and rationalize photophysical and photochemical properties of transition

metal compounds, we undertook a theoretical investigation on the electronic absorption spectra of a series of Re(I) carbonyl pyridocarbazole complexes taking as reference complex **III** in Scheme 1. Aiming at proposing new improved Re(I) complexes for PDT, several aspects will be analyzed: the degree of conjugation and the effect of substituents of the pyridocarbazole ligand, and the replacement of a carbonyl ligand by a highly water-soluble phosphine ligand with a very strong electron-donating power. Such an investigation may provide valuable information for the design of novel Re-based PSs.

## RESULTS AND DISCUSSION

Scheme 2 collects an schematic representation of the Re(I) carbonyl pyridocarbazole complexes investigated in the present work along with the acronyms used in this section. The geometry of all these species was optimized both in the singlet ground state and in the excited triplet state at the B3LYP-D3/6-31+G(d)-LANL2DZ level of theory (see Figure S1), whereas the electronic absorption spectra were obtained at the PCM-TD-M06/6-31+G(d)-LANL2DZ//B3LYP-D3/6-31+G(d)-LANL2DZ level of theory in DMSO solution (see Computational Techniques for details). The computational protocols mentioned above have been chosen after an exhaustive discussion based on validation calculations collected in the Supporting Information. To analyze the influence of the degree of conjugation and the substituents of the pyridocarbazole ligand as well as the replacement of the carbonyl ligand in *cis* disposition to the bidentate ligand by phosphine ones on the spectroscopic and photocytotoxic properties of the Re(I) pyridocarbazole carbonyl complexes, complex **1** in Scheme 2 (**III** in Scheme 1) has been taken as a reference.

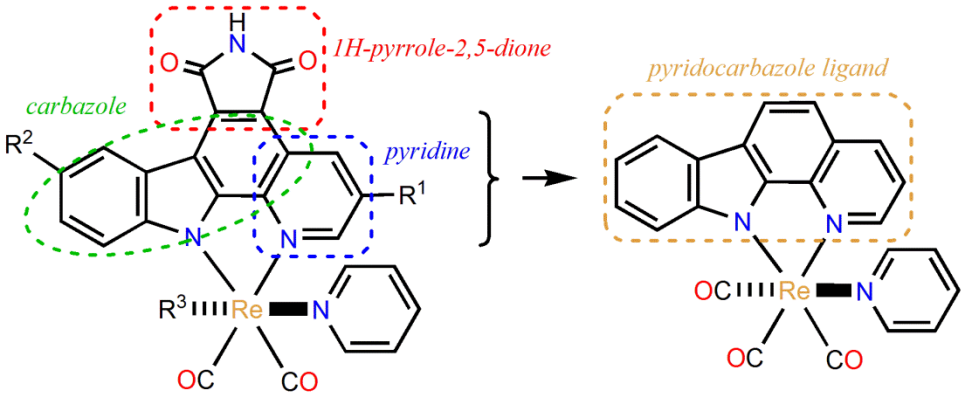


| $R^1$ | $R^2$ | $R^3$ | complex |
|---|---|---|---|
| H | H | CO | **1** |
| $CO_2Et$ | H | CO | **1a** |
| F | H | CO | **1b** |
| H | OMe | CO | **1c** |
| H | $NMe_2$ | CO | **1d** |
| $CO_2Et$ | OMe | CO | **1e** |
| $CO_2Et$ | $NMe_2$ | CO | **1f** |
| $CO_2Et$ | $CO_2Et$ | CO | **1g** |
| F | OMe | CO | **1h** |
| H | H | $PMe_3$ | **1i** |
| H | H | CAP | **1j** |
| $CO_2Et$ | H | $PMe_3$ | **1k** |
| $CO_2Et$ | OMe | $PMe_3$ | **1l** |
| $CO_2Et$ | H | CAP | **1m** |
| $CO_2Et$ | OMe | CAP | **1n** |
| F | H | $PMe_3$ | **1o** |
| F | OMe | $PMe_3$ | **1p** |
| F | H | CAP | **1q** |
| F | OMe | CAP | **1r** |

**Scheme 2**. Structure and notation of the Re(I) carbonyl complexes investigated in this work.

**Influence of the pyridocarbazole ligand conjugation**

Complexes **1**-**3** in Scheme 2 have been selected to analyze the effect of the degree of conjugation of the pyridocarbazole ligand on the absorption properties and the generation of $^1O_2$ of these Re(I) complexes. Figure 1 collects the calculated absorption spectra obtained for complexes **1**-**3** (see also a detailed discussion in the Supporting Information about the reproducibility of the experimental absorption spectra of complexes **1-3** using time-dependent density functional calculations). For the Re(I) complex with the pyridocarbazole ligand containing carbazole, pyridine, and 1H-pyrrole-2,5-dione heterocycles (**1** in Scheme 2), the calculated electronic absorption spectrum collected in Figure 1 presents two clear absorption bands at $\lambda_{max}$ values of 327 nm ($f$ = 0.2133) and 521 nm ($f$ = 0.1459) in good agreement with the two most intense bands experimentally detected for the same compound.[26] The $\lambda_{max}$ value of the most red-shifted band only differs 9 nm from the experimental one. The third low intensity absorption band intermediate to the two previous ones experimentally reported could not be clearly detected in the theoretical spectrum obtained. However, we found that the third most intense excitation energy appears at 390 nm ($f$ = 0.0606), which falls in the region of the least intense absorption band detected experimentally. In accordance with experimental results, the computed absorption spectrum obtained for complex **2**, in which the 1H-pyrrole-2,5-dione heterocycle is not present in the pyridocarbazole ligand, shows two absorption bands at $\lambda_{max}$ values of 341 nm ($f$ = 0.1115) and 446 nm ($f$ = 0.0676) as shown in Figure 1. The latter value fully coincides with the most red-shifted $\lambda_{max}$ reported experimentally.[26] As seen in Figure 1, for Re(I) complex **3** wherein the carbazole benzene ring fused to the pyridine heterocycle of the pyridocarbazole ligand is not present in the bidendate ligand, its electronic absorption spectrum

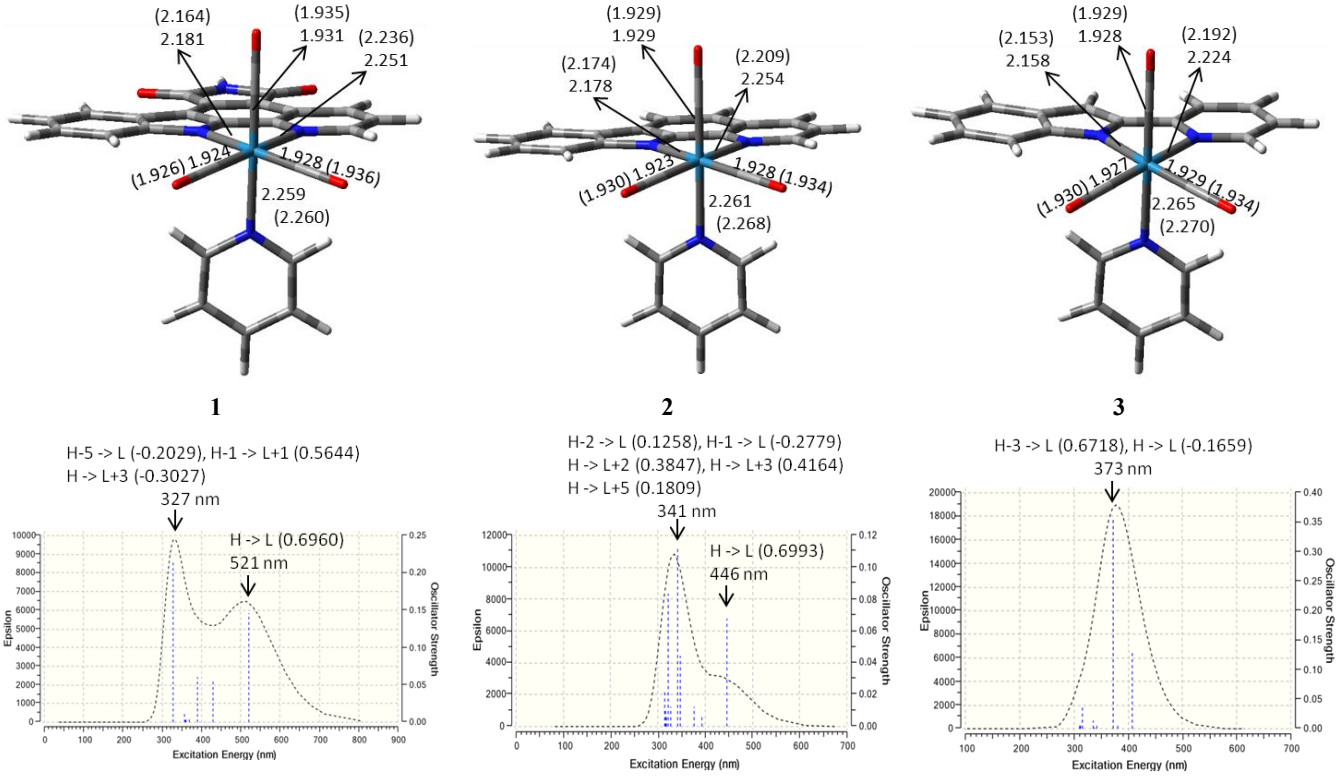


**Figure 1**. Singlet optimized structures and computed electronic absorption spectra in DMSO obtained for Re(I) tricarbonyl pyridyl complexes **1-3**. Some significant bond distances in Å are collected. Data obtained for triplet optimized structures are shown in parentheses. The dominant orbital excitations (coefficients in parenthesis) involved in the main absorption peaks are also displayed.

shows only one absorption band at 373 nm in full agreement with experimental findings as well.[26]

Looking at the most red-shifted absorption band obtained for complexes **1**-**3**, which is the most interesting one of a potential PS for PDT utility purposes, we see that the decrease in the bidentate ligand conjugation when going from complex **1** to **3** results in a hypsochromic shift of the lowest-lying absorption band as experimentally found by Meggers and co-workers.[26] The lowest-lying absorption band for complexes **1** and **2** is due to an electronic transition from the frontier Kohn-Sham orbital HOMO to the LUMO (see Figure 1). As seen in Figure 2, for both complexes, the HOMO is mainly composed of a Re *d* orbital ($d_{\pi}(Re)$) combined with a $\pi^*$ antibonding orbital of one of the CO ligands *cis* to the pyridine one ($\pi^*_{CO}$) and another $\pi^*$ antibonding orbital of the CO ligand *trans* to the pyridine ligand ($\pi^*_{CO}$), denoted here all this as $d_{Re(CO)_2}$, and a $\pi$ bonding orbital of pyridocarbazole ligand ($\pi_{pyridocarbazole}$), whereas the LUMO mainly consists of a $\pi^*$ antibonding orbital of the pyridocarbazole ligand ($\pi^*_{pyridocarbazole}$). In the HOMO, the $\pi_{pyridocarbazole}$ orbital is mainly centered on the carbazole moiety with a small contribution of the pyridyl moiety in both **1** and **2** and of the 1H-pyrrole-2,5-dione ring only in the case of complex **1**. In the LUMO, the $\pi^*_{pyridocarbazole}$ orbital is primarily extended across the pyridyl ring and the carbazole but one benzene ring for both complexes **1** and **2** plus the 1H-pyrrole-2,5-dione heterocycle for complex **1** (see Figure 2). The extra conjugation due to the 1H-pyrrole-2,5-dione ring of the pyridocarbazole ligand in complex **1** compared to **2**

would lead to a stabilization/destabilization of the HOMO/LUMO when switching from the former complex to the latter one and, consequently, a rise of the HOMO-LUMO energy gap ($\Delta E_{H\rightarrow L}$). Although we did find a rise of $\Delta E_{H\rightarrow L}$ of 0.50 eV and a notable destabilization of the LUMO of 0.84 eV from **1** to **2**, it is noteworthy that, contrary to expectations, the HOMO is destabilized 0.34 eV. To rationalize these values, another effect in the bidentate ligand of complex **1** must be taken into account: the electron-withdrawing character of the 1H-pyrrole-2,5-dione ring. Indeed, the loss of this heterocycle results in a destabilization of both the HOMO and the LUMO when going from **1** to **2**. Therefore, this effect together with the conjugation of the bidentate ligand destabilize the LUMO (0.84 eV), but in the case of the HOMO, the electron-withdrawing heterocycle effect is opposite and greater than that of conjugation since the HOMO destabilizes (0.34 eV) from **1** to **2**. The rise of the $\Delta E_{H\rightarrow L}$ value is in the line of the hypsocromic effect of the lowest-lying absorption band found experimentally when going from **1** to **2**.[26] The only absorption band detected for complex **3** is mainly due to the HOMO-1 $\rightarrow$ LUMO transition with a certain participation of the HOMO $\rightarrow$ LUMO one (see Figure 1). The HOMO-1 of complex **3** is very similar to the HOMO of complexes **1** and **2** (see Figure 1), since it is a mixture of the $d_{Re(CO)_2}$ orbital with the $\pi_{\text{pyridoindole}}$ orbital, which is expanded across all the 2-(2'-pyridyl)indolato ligand (see Scheme 2). In accordance with the diminution of the conjugation of the bidentate ligand, the HOMO of complex **3** is 0.11 and 0.45 eV more stable than the HOMO of complexes **1** and **2**, respectively. The HOMO of complex **3** is 0.36 eV higher in energy than its HOMO-1 and mainly differs from it in the $\pi$ bonding

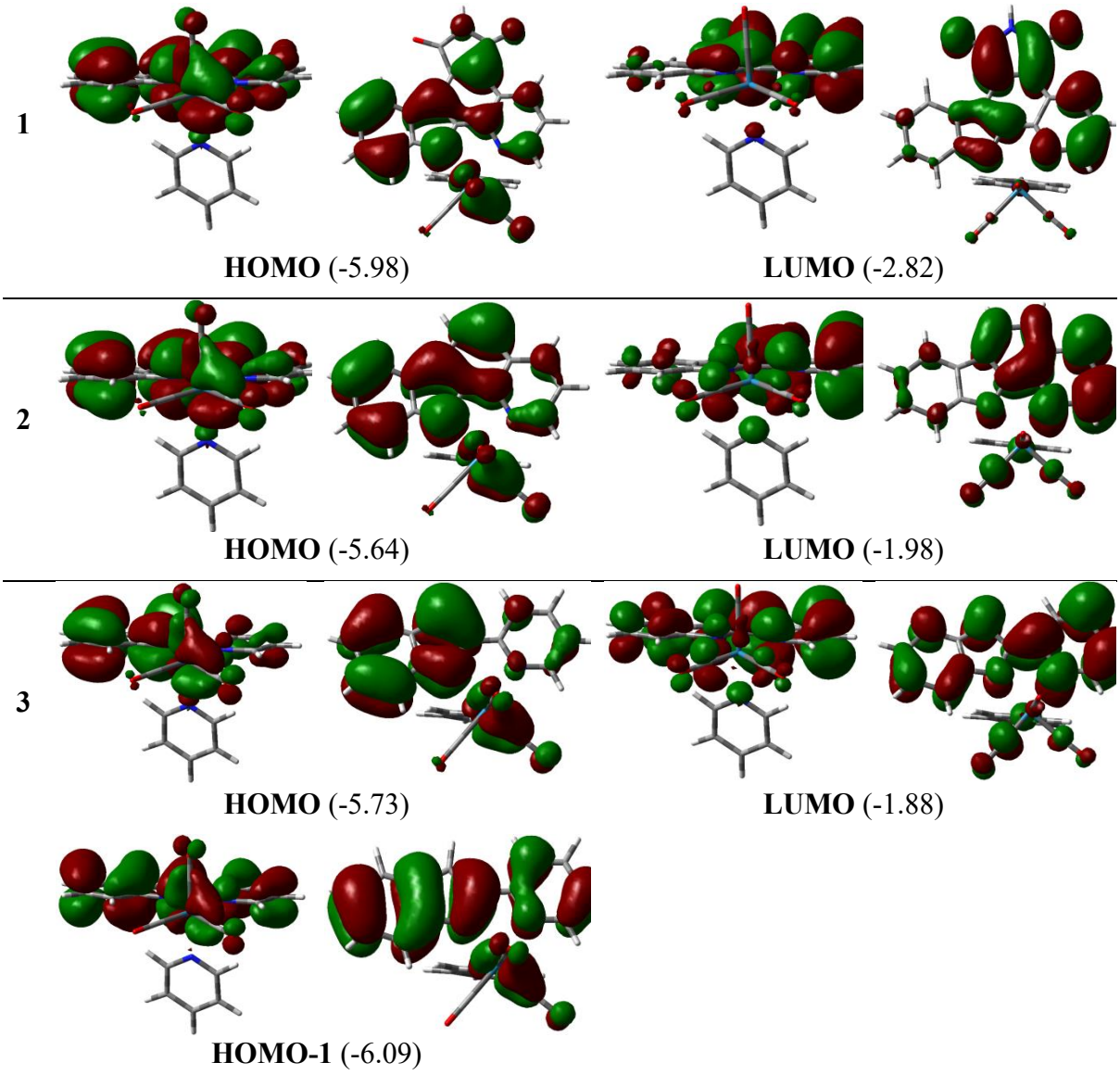


**Figure 2**. Contour maps of the frontier Kohn-Sham orbitals involved in the dominant orbital excitations of the lowest-lying absorption band found for Re(I) tricarbonyl pyridil complexes **1-3**. Orbital energies in eV are shown in parenthesis. Two views are given for each orbital.

orbital of the bidentate ligand. Such an orbital is delocalized across the indole moiety for the HOMO and not across the entire 2-(2'-pyridyl)indolato ligand as indicated for the HOMO-1. Concerning the LUMO, we see in Figure 2 that it is a $\pi*$ antibonding orbital mostly centered on the entire bidentate ligand ($\pi*_{pyridoindole}$) as for complexes **1** and **2**. The absence of a benzene ring in the carbazole heterocycle and the pyrrole one in complex **3** leads to a larger decrease of the conjugation of the bidentate ligand compared to that of complexes **1** and **2**. Consequently, the stability of the LUMO of complex **3** (-1.88 eV) is even lower than that of the analogous orbital of complexes **1** and **2** (-2.82 and -1.98 eV, respectively). The greater instability of the LUMO of complex **3** along with the greater stability of its HOMO-1 and HOMO results in (HOMO-1)-LUMO and HOMO-LUMO energy gaps of 0.69 (0.19) and 1.05 (0.55) eV larger than those obtained for complex **1** (complex **2**), respectively, and, in turn, a decrease of the $\lambda_{max}$ of the lowest-lying absorption band from 521 nm (complex **1**) and 446 nm (complex **2**) to 373 nm (complex **3**). To sum up, the most red-shifted absorption band for complexes **1**-**3** is attributed to a $d_{Re(CO)_2} + \pi_{bidentate} \rightarrow \pi^*_{bidentate}$ transition, so it has a mixed metal-to-ligand charge transfer ($^1$MLCT, $d_{Re(CO)_2} \rightarrow \pi^*_{bidentate}$) and intra-ligand charge transfer ($^1$ILCT, $\pi_{bidentate} \rightarrow \pi^*_{bidentate}$) character.

Although complexes **1**-**3** do not show absorption bands within the therapeutic window (620-850 nm), which limits their use as PSs in PDT, Meggers and co-workers have found that they are capable of producing singlet oxygen when irradiated with light of appropriate

wavelength.[26] Thus, only complex **1** produced singlet oxygen after irradiation with $\lambda \geq 505$ nm, due to the lack of absorption of the other two complexes in this region of the spectrum, whereas all of them did generated such a cytotoxic species upon irradiation with $\lambda \geq 330$ nm. Aiming at examining the ability of complexes **1**-**3** to photosensitize singlet oxygen, we have optimized their structures in the first triplet excited state ($T_1$) and computed the energy gap between $T_1$ and the singlet ground state ($S_0$), $\Delta E_{ST}$. On the whole, the singlet and triplet optimized structures obtained for each complex are very similar. For complex **1**, the bond distances between Re and the N atoms of the indole ($N_{indole}$) and pyridine ($N_{pyridine}$) moieties of the bidentate ligand show the largest discrepancies as they shorten 0.017 and 0.015 Å when passing from the singlet ground state to the first triplet excited one, respectively (see Figure 1). The remaining metal-ligand bond lengths only lengthen between 0.001 and 0.008 Å. For complexes **2** and **3**, the most significant discrepancy was detected only for the Re-$N_{pyridine}$ bond distance, which notably shortens by 0.045 and 0.032 Å when going from the singlet structure to the triplet one, respectively (see Figure 1). The Re-$N_{indole}$ bond length slightly shortens by 0.004 Å (**2**) and 0.005 Å (**3**), whereas the remaining metal-ligand distances lengthen in a range similar to that found for complex **1** (0.001-0.007/0.005 Å for **2**/**3**). The energy difference between the singlet-triplet structures, $\Delta E_{ST}$, obtained for complexes **1**, **2**, and **3** is 38.7, 47.1, and 49.1 kcal/mol, respectively. All these values are notably larger than the minimum energy required, 22.5 kcal/mol,[19,20] to transform $^3O_2$ into $^1O_2$, which is in consonance with the singlet oxygen production reported experimentally for complexes **1**-**3**.[26]

**Effect of substituents at the pyridocarbazole ligand**

Based on the interesting spectroscopic properties experimentally shown by Re(I) carbonyl complexes containing both imidazole plus substituted pyrodicarbazoles[27] and pyridine plus substituted bipyridines,[41] eight Re(I) tricarbonyl pyridyl complexes with substituted pyridocarbazoles (**1a**-**1h** in Scheme 2) have been considered. Complexes **1a** and **1b** contain the electron-accepting $CO_2Et$ and F substituents, $R^1$ in Scheme 2, in the 3-position of the pyridine moiety of the pyridocarbazole ligand, respectively. In complexes **1c** and **1d**, the electron-donating OMe and $NMe_2$ subtituents, $R^2$ in Scheme 2, are present in the 5-position of the indole moiety of the pyridocarbazole ligand, respectively. The remaining complexes **1e**-**1h** have simultaneously both types of substituents at the bidentate ligand, except complex **1g** that contains the same $CO_2Et$ group in both pyridine and indole moieties.

The introduction of substituents into the pyridocarbazole ligand of complex **1** produces hardly any geometrical changes (see Figure S1 and Table S1). For example, the Re-ligand bond distances in complexes **1a**-**1h** compared to the analogous ones in complex **1** only range from -0.004 to 0.003 Å. The general shape of the calculated absorption spectra of complexes **1a**-**1h** also resembles the one previously described for complex **1** (see Figure 3). Two clear absorption bands were located for complexes with $R^1$ = $CO_2Et$, F and $R^2$ = H (**1a** and **1b**, respectively). A similar picture was found for Re(I) compounds with $R^1$ = $CO_2Et$ and $R^2$ = OMe, $CO_2Et$ (**1e** and **1g**, respectively). In the case of $R^1$ = H and $R^2$ = $NMe_2$ (**1d**), three absorption bands were detected. The remaining substituted pyridocarbazole complexes (**1c**, $R^1$ = H and $R^2$ = OMe, **1f**, $R^1$ = $CO_2Et$ and $R^2$ = $NMe_2$,

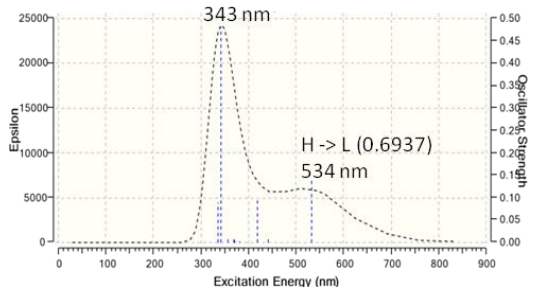


**1a** ($R^1 = CO_2Et$, $R^2 = H$)

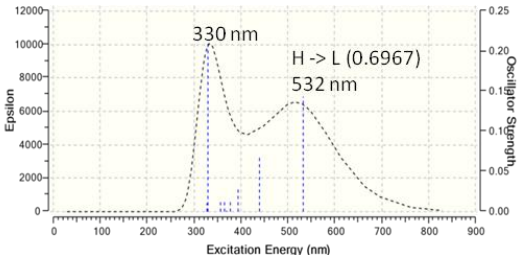


**1b** ($R^1 = F$, $R^2 = H$)

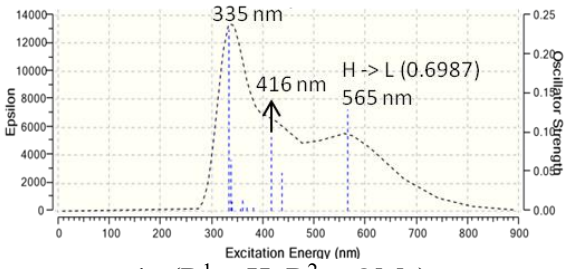


**1c** ($R^1 = H$, $R^2 = OMe$)

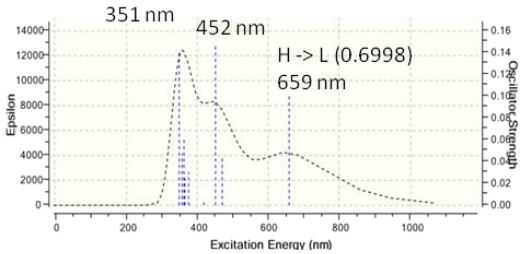


**1d** ($R^1 = H$, $R^2 = NMe_2$)

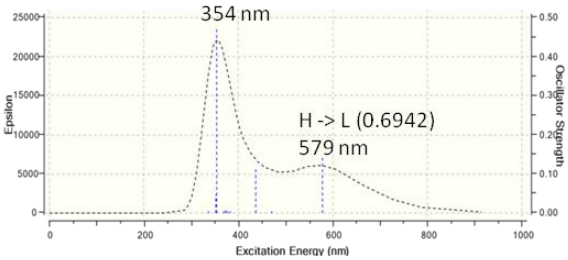


**1e** ($R^1 = CO_2Et$, $R^2 = OMe$)

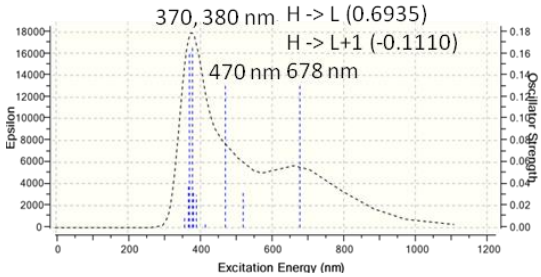


**1f** ($R^1 = CO_2Et$, $R^2 = NMe_2$)

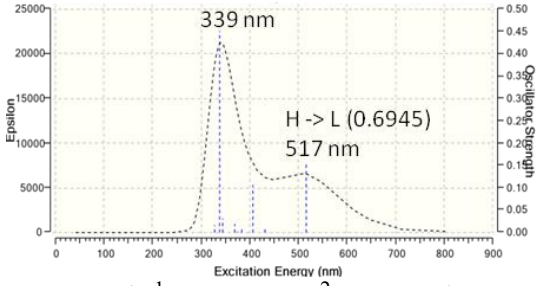


**1g** ($R^1 = CO_2Et$, $R^2 = CO_2Et$)

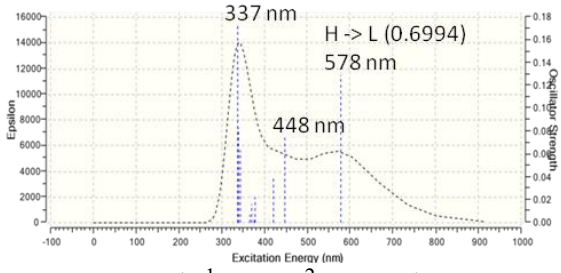


**1h** ($R^1 = F$, $R^2 = OMe$)

**Figure 3**. Computed electronic absorption spectra in DMSO for Re(I) tricarbonyl pyridil complexes bearing substituted pyridocarbazole ligands **1a-1h**. The dominant orbital excitations (coefficients in parenthesis) involved in the most red-shifted absorption peaks are also displayed.

and **1h,** $R^1$ = F and $R^2$ = OMe) display two clear absorption bands and a shoulder between them that could be ascribed to a low intensity absorption band, as for complex **1**. As experimentally found for complex **1** and analogous Re(I) pyridocarbazole complexes bearing the imidazole monodentate ligand instead of the pyridine one,[26,27] the short wavelength absorption band obtained for complexes **1a**-**1h** is the most intense one. It appears in the range between 330nm and 380 nm. The second most intense absorption band has the longest $\lambda_{max}$ ranging from 517 nm to 678 nm. When detected, the intermediate absorption band to the two mentioned above is the least intense by far and varies between 416 and 470 nm.

Focusing on the potential use of these complexes as PSs for PDT, we turn our attention on the variation of the longest $\lambda_{max}$ values obtained for complexes **1a**-**1h** taking as a reference the one obtained for complex **1** (see Figures 1 and 3). According to our results, the introduction of electron-donating groups into the pyridocarbazole indole moiety has a greater effect on the longest $\lambda_{max}$ than that of electron-accepting groups into the pyridine moiety. Specifically, the presence of OMe and, particularly, $NMe_2$ in the indole moiety (complexes **1c** and **1d**, respectively) increases the longest $\lambda_{max}$ by 44 and 138 nm, whereas the presence of $CO_2Et$ and F (complexes **1a** and **1b**, respectively) only increases the longest $\lambda_{max}$ by 13 and 11 nm, respectively. As the $CO_2Et$ group behaves slightly better than the F one, we first consider the simultaneous presence of the former substituent in the pyridocarbazole pyridine moiety with the one of OMe, $NMe_2$, and $CO_2Et$ groups in the 5-position of the indole moiety. For complexes **1e** ($R^1$ = $CO_2Et$, $R^2$ = OMe) and **1f** ($R^1$ =

$CO_2Et$, $R^2 = NMe_2$), we obtain a red-shift of the longest $\lambda_{max}$. This magnitude increases 45 and 144 nm when going from complex **1a** ($R^1 = CO_2Et$, $R^2 = H$) to complexes **1e** ($R^1 = CO_2Et$, $R^2 = OMe$) and **1f** ($R^1 = CO_2Et$, $R^2 = NMe_2$). These values are even larger (by 14 and 19 nm, respectively) when taking the respective complexes **1c** and **1d** as reference. The opposite trend was obtained when another electron-accepting group, $CO_2Et$, is present in the indole moiety, as the longest $\lambda_{max}$ diminishes 17 nm when switching from complex **1a** ($R^1 = CO_2Et$, $R^2 = H$) to complex **1g** ($R^1 = CO_2Et$, $R^2 = CO_2Et$). For the Re(I) complex with $R^1 = F$ and $R^2 = OMe$ (**1h**), the longest $\lambda_{max}$ has a value of 578 nm, which is 46 and 13 nm larger than the analogous ones obtained for complexes **1b** ($R^1 = F$, $R^2 = H$) and **1c** ($R^1 = H$, $R^2 = OMe$), respectively. As for the substituted pyridocarbazole complexes of Re(I) bearing the imidazole ligand, the presence of the $NMe_2$ substituent provides an important red-shift of the lowest-lying absorption band. A rise of the longest $\lambda_{max}$ of 49 nm was found experimentally when going from $[Re(CO)_3(Im)(H,H\text{-pyridocarbazole})]$ to $[Re(CO)_3(Im)(H,NMe_2\text{-pyridocarbazole})]$, whereas a value of 178 nm was obtained when pyridine is the monodentate ligand.

On the other hand, it is noteworthy that complexes **1e** ($R^1 = CO_2Et$, $R^2 = OMe$) and **1h** ($R^1 = F$, $R^2 = OMe$) displays an important red-shift of the lowest-lying absorption band, which are larger than the value of 542 nm reported experimentally for the analogous Re(I) complex containing the imidazole ligand instead of the pyridine one. Taking into account, the phototoxicity reported for analogous complexes, compounds **1e** and **1h** are good

candidates to investigate the possibility of introducing new modifications in the Re complex aiming at looking for new potential candidates for PDT.

As for complex **1**, the lowest-lying absorbance band of the Re(I) compounds **1a**-**1h** is mainly attributed to the HOMO-LUMO transition (see Figure 3). The HOMO of all complexes except those containing the $NMe_2$ substituent, **1d** and **1f**, is essentially the same as that previously described for complex **1**, that is, a mixture of a $d_{Re(CO)_2}$ orbital with a $\pi_{\text{pyridocarbazole}}$ orbital, which is mainly centered on the carbazole and 1H-pyrrole-2,5-dione heterocycles (see Figure 4). The HOMO of complexes **1d** and **1f** is mostly composed of a $\pi_{\text{pyridocarbazole}}$ orbital, which is mainly centered on the indole moiety, with a small contribution of a Re *d* orbital combined with a $\pi^*$ orbital of one CO *trans* to the bidentate ligand. The LUMO of all the complexes is primarily a $\pi^*_{\text{pyridocarbazole}}$ orbital, expanded across all the pyridocarbazole ligand but the benzene ring of indole moiety (see Figure 4). Therefore, on the whole, the HOMO → LUMO transition has a mixed $^1$MLCT and $^1$LLCT ($d_{Re(CO)_2} + \pi_{pyridocarbazole} \rightarrow \pi^*_{pyridocarbazole}$) character for all the complexes except **1d** and **1f**, for which that orbital transition primarily exhibits a $^1$LLCT ($\pi_{pyridocarbazole} \rightarrow \pi^*_{pyridocarbazole}$) character.

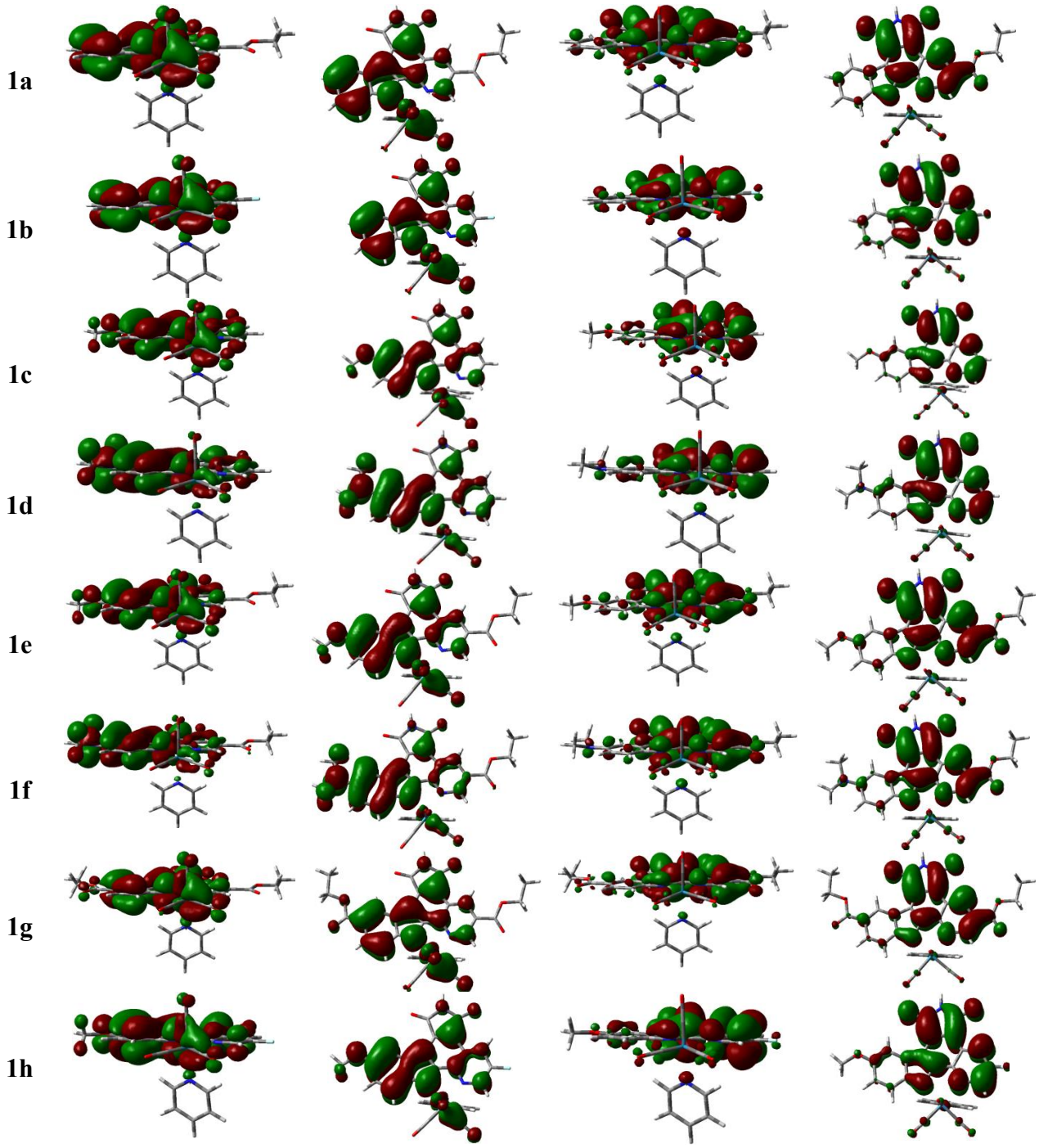


**Figure 4**. Contour maps of the main frontier Kohn-Sham orbitals implied in the dominant orbital excitations of the lowest-lying absorption band found for Re(I) complexes with substituted pyridocarbazoles **1a**-**1h**. Two views are given for each orbital.

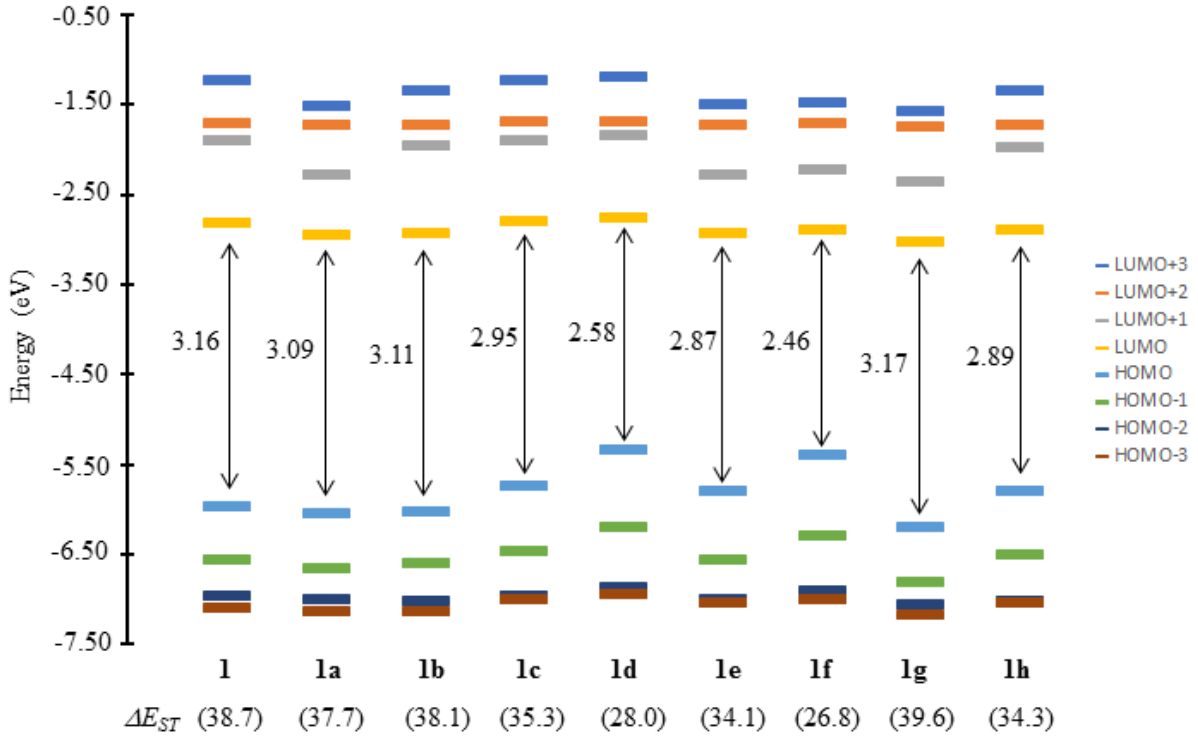


**Figure 5**. Energy diagram of the most relevant Kohn-Sham orbitals for Re(I) complexes **1a-1h** in the singlet ground state along with their corresponding HOMO-LUMO energy gaps in eV. In parenthesis, the difference in electronic energy between the first triplet excited state ($T_1$) and the singlet ground state ($S_0$), $\Delta E_{ST}$, is given in kcal/mol. For comparison purposes, data obtained for complex **1** are also included.

The HOMO of the monosubstitued pyridocarbazole complexes **1a** ($R^1$ = $CO_2Et$) and **1b** ($R^1$ = F) is similar to that of complex **1** (see Figures 2 and 4) as there is no involvement of any substituent orbitals. In consonance with this, the HOMO energy hardly changes when going from complex **1** (-5.98 eV) to complexes **1a** (-6.05 eV) and **1b** (-6.04 eV). The LUMO of the latter complexes displays a greater delocalized $\pi^*_{pyridocarbazole}$ orbital than that of the reference complex owing to the extra participation of $\pi^*$ or $p$ orbitals of the $CO_2Et$ or F substituents, respectively

(see Figure 4). This fact along with the electron-withdrawing character of the substituents explains why the LUMO of complexes **1a** and **1b** stabilizes by 0.14 and 0.11 eV with respect to that of complex **1**. As seen in Figure 5, the greater stabilization of the LUMO compared to that of the HOMO results in a little shortening of the HOMO-LUMO gap of 0.07 eV (complex **1a**) and 0.05 eV (complex **1b**), which explains the rise of the longest $\lambda_{max}$ found by us from complex **1** (521 nm) to complexes **1a** and **1b** (534 and 532 nm, respectively). The presence of OMe and $NMe_2$ substituents in the bidentate indole moiety (complexes **1c** and **1d**, respectively) has more effect on the HOMO of complex **1** than on its LUMO. Indeed, the shape of the latter orbital (-2.82 eV) is similar to that obtained for complexes **1c** (-2.80 eV) and **1d** (-2.77 eV), but their HOMOs are more delocalized due to the involvement of a $\pi^*$ orbital of OMe and $NMe_2$ (see Figure 4). Consequently, the presence of electron-donating substituents in the indole moiety provokes a significant destabilization of the HOMO of complexes **1c** and **1d** by 0.23 and 0.63 eV compared to complex **1**, respectively (see Figure 5). Compared to complex **1**, this destabilization results in a diminution of the HOMO-LUMO energy gap of 0.21 eV and 0.58 eV (complexes **1c** and **1d**, respectively), which coincides with the notable red-shift found for the longest $\lambda_{max}$ of 34 nm (complex **1c**) and 138 nm (complex **1d**). The stronger electron-donating character of $NMe_2$ explains the greater effect of this substituent on the longest $\lambda_{max}$ value. It is also interesting to note that the HOMO destabilization caused by the introduction of electron-donating groups into the indole moiety is more pronounced than the LUMO stabilization generated by the presence of electron-accepting groups in the pyridine moiety. This is in accordance with the experimental findings reported for related Re(I) complexes containing the imidazole monodentate ligand instead of the pyridine one.[27] Based on these results and aiming at red-shifting the longest $\lambda_{max}$ value, we examine Re(I) complexes containing substituents in both the indole and the pyridine

moieties of the pyridocarbazole ligand. Taking as reference complex **1a** ($R^1$ = $CO_2Et$, $R^2$ = H), the introduction of OMe and $NMe_2$ into the indole moiety destabilizes the HOMO and, consequently, the HOMO-LUMO energy gap diminishes 0.22 and 0.63 eV, respectively (see **1e** and **1f** in Figure 5). Yet again, in consonance with this, the longest $\lambda_{max}$ value varies from 534 nm (complex **1**) to 579 nm (complex **1e**) and 678 nm (complex **1f**). By contrast, the addition of the electron-accepting $CO_2Et$ substituent in the indole moiety of complex **1a** stabilizes the HOMO, so the HOMO-LUMO energy gap increases (0.08 eV) and the longest $\lambda_{max}$ value decreases (17 nm). Similar trends are expected for complex **1b** (($R^1$ = F, $R^2$ = H). Indeed, the introduction of the electron-donating OMe group into the indole moiety of complex **1b** leads to a decrease of the HOMO-LUMO energy gap from 3.11 eV to 2.89 eV and the resulting increase of the longest $\lambda_{max}$ value from 532 nm to 578 nm. These variations are similar to those found when replacing F by $CO_2Et$, so both substituents have practically the same effect on the spectroscopic properties of the Re(I) complexes investigated.

We turned now our attention on the capacity of generating singlet oxygen of complexes **1a-1g**. To that end, we optimized the geometry of such complexes in their respective triplet excited states (see Figure S1). Comparing the triplet optimized structures of complexes **1a-1h** to their analogous singlet ones, the geometrical discrepancies obtained are similar to those found in the case of complex **1** (see Table S1). That is, the excitation of the substituted pyridocarbazole complex gives rise to a moderate shortening of the $Re\text{-}N_{indole}$ and $Re\text{-}N_{pyridine}$ bond lengths ranging from 0.009 to 0.023 Å and 0.016 to 0.019 Å, respectively. The remaining Re-ligand bond distances show small variations when going from the singlet ground state to triplet excited one for each complex. Concerning the singlet-triplet energy gap, all the complexes **1a-1g** show $\Delta E_{ST}$ values greater than 22.5 kcal/mol, ranging from 26.8 kcal/mol for complex **1f** to 39.6

kcal/mol for complex **1g** (see Figure 5). Therefore, they should be able to produce singlet oxygen. However, it has been experimentally reported that the formation of singlet oxygen is suppressed for the strong electron-donating $NMe_2$ substituent in the indole moiety.[27] Looking at Figure 4, we reason that it is due to the fact that the contribution of the Re *d* orbital to the HOMO of complexes **1d** and **1f** is practically negligible, changing the nature of the first singlet excited state from $^1$MLCT and $^1$ILCT to just $^1$ILCT. The participation of the metal center in the singlet excited state of potential metal complex-based PSs for PDT should be significant to enhance the intersystem conversion to the triplet state, which is the one that reacts with $^3O_2$.[43,44] Since this is not the case for complexes containing the $NMe_2$ substituent (**1d** and **1f)**, we will no longer consider complexes with that substituent in the following section.

**Effect of replacing the CO *cis* to the pyridocarbazole ligand**

As indicated in the Introduction section, the replacement of a CO ligand in *cis* disposition to a substituted bipyridine ligand, $CO_{cis}$, by $PMe_3$ in the complexes $[Re(deeb)(CO)_3(L)]^n$ (deeb = 4,4'-diethylester-2,2'-bipyridine; L = $NCCH_3$, Cl; $n$ = +1, 0) led to an important bathochromic effect.[41] Based on this fact and aiming at getting substituted pyridocarbazole complexes of Re(I) with $\lambda_{max}$ values longer than the ones obtained in the previous subsection, we designed ten hypothetical Re(I) pyridocarbazole complexes wherein the $CO_{cis}$ ligand is replaced by phosphines $PMe_3$ and CAP (**1i-1r** in Scheme 2). To perform a comprehensive and systematic study, we first replaced the axial CO of complex **1** by phosphines $PMe_3$ and CAP (complexes **1i** and **1j** in Scheme 2, respectively). The CAP ligand has been chosen for its strong electron-donating character and its water solubility.[42] Then, we introduced step by step the $CO_2Et$, F, and OMe substituents into the pyridocarbazole ligands as in the previous section (complexes **1k-1r** in Scheme 2).

As expected, substitution of $CO_{cis}$ by $PMe_3$ or CAP modifies significantly the geometry of complex **1** (see Figure S1 and Table S1). For instance, all Re-ligand distances of complexes **1i-1r** vary moderately or strongly when compared to their analogs of complex **1**, except the bond distance between Re and the N atom of the pyridocarbazole pyridine moiety, which only increases between 0.006 and 0.010 Å. The two Re-CO bond lengths shorten in the range from 0.023 and 0.026 Å, whereas the bond distance between Re and the N atom of the pyridocarbazole indole moiety lengthen in the gap 0.012-0.019 Å. A largest change was found when looking at the distance between Re and the N atom of the pyridine ligand, which notably shortens from 0.032 to 0.035 Å when going from **1** to **1i-1r**. Substitution of the $\pi$-accepting $CO_{cis}$ ligand by another strong $\sigma$-donating one, $PMe_3$ or CAP, alleviates the electron deficiency of Re, thus strengthening the expected well-known backbonding interactions between Re *d* orbitals and $\pi^*$ orbitals of the two remaining CO and the pyridine ligand of complexes **1i-1r** and, consequently, shortening the Re-CO and Re-pyridine distances as described above.[41]

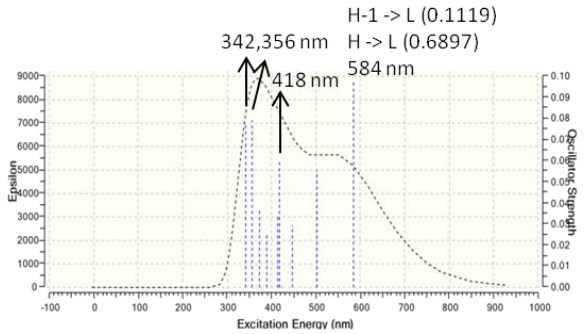


**1i** ($R^1$ = H, $R^2$ = H, $R^3$ = $PMe_3$)

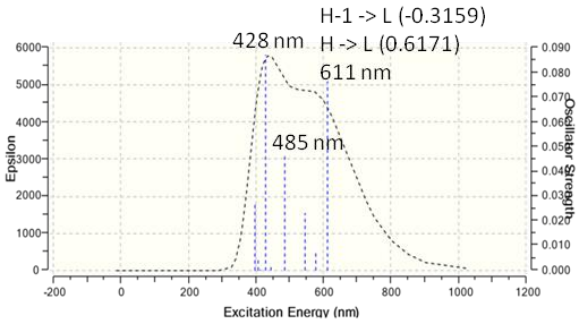


**1j** ($R^1$ = H, $R^2$ = H, $R^3$ = CAP)

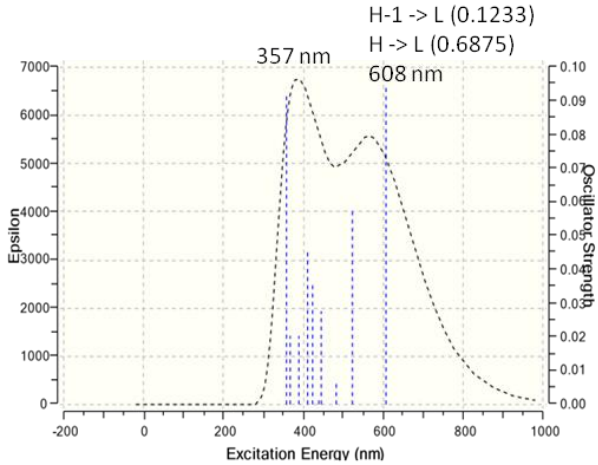


**1k** ($R^1$ = $CO_2Et$, $R^2$ = H, $R^3$ = $PMe_3$)

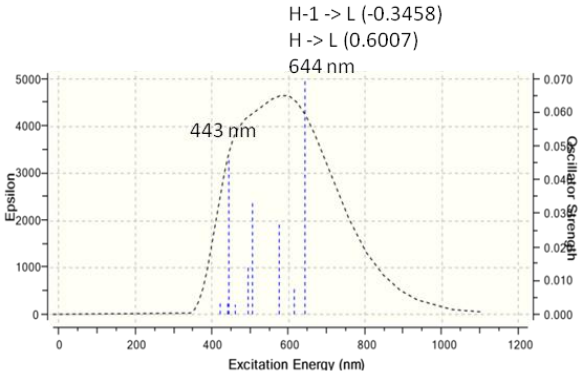


**1m** ($R^1$ = $CO_2Et$, $R^2$ = H, $R^3$ = CAP)

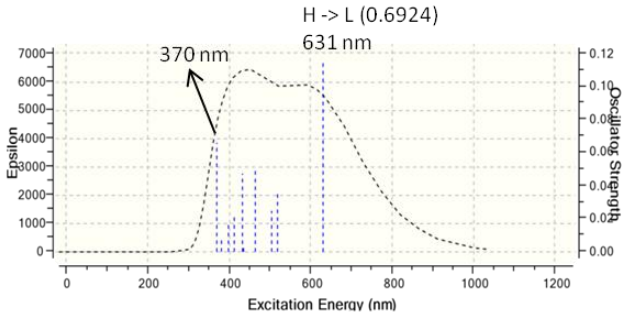


**1l** ($R^1$ = $CO_2Et$, $R^2$ = OMe, $R^3$ = $PMe_3$)

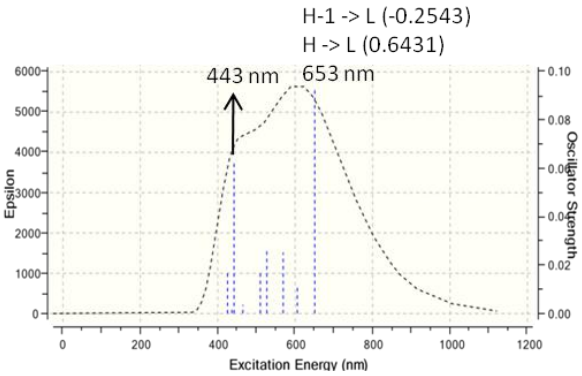


**1n** ($R^1$ = $CO_2Et$, $R^2$ = OMe, $R^3$ = CAP)

**Figure 6**. Computed electronic absorption spectra of some representative Re(I) pyridocarbazole complexes bearing the phosphine ligands $PMe_3$ (**1i**, **1k**, and **1l**) and CAP (**1j**, **1m**, and **1n**). The dominant orbital excitations (coefficients in parenthesis) involved in the most red-shifted absorption peak are also displayed.

The absorption spectrum of complexes **1i**-**1r** displays two absorption bands. As for complexes **1** and **1a**-**1h**, the short wavelength absorption band is more intense than the long one, except for complexes bearing the CAP ligand **1m** ($R^1 = CO_2Et$, $R^2 = H$) and **1n** ($R^1 = CO_2Et$, $R^2 = OMe$), in which the reverse situation occurs (see Figure 6). The intermediate band to the two mentioned above, not well-reproduced for complexes **1a**-**1h**, appears in complexes **1i** ($R^1 = R^2 = H$, $R^3 = PMe_3$) **1j** ($R^1 = R^2 = H$, $R^3 = CAP$), **1p** ($R^1 = F$, $R^2 = OMe$, $R^3 = PMe_3$), and **1q** ($R^1 = F$, $R^2 = H$, $R^3 = CAP$) as a shoulder (see Figures 6 and S2). The $\lambda_{max}$ value of the shorter wavelength absorption band ranges from 342 nm (complex **1i**) to 443 nm (complexes **1m** and **1n**), whereas the $\lambda_{max}$ value of the longer wavelength absorption band varies from 584 nm (complex **1i**) to 653 nm (complex **1n**). Regarding the longest $\lambda_{max}$, we found that the replacement of $CO_{cis}$ by $PMe_3$ or CAP leads to a significant red-shift since the value of 521 nm ($f$ = 0.1459) obtained for complex **1** becomes 584 ($f$ = 0.0979) and 611 ($f$ = 0.0767) nm for complexes **1i** and **1j**, respectively. These values are larger than the best ones obtained for complexes **1e** (579 nm) and **1h** (578 nm). Introducing the same sequence of modifications into the bidentate ligand as in the previous section, we found that the presence of $CO_2Et$ in the pyridine moiety without and with including the OMe substituent in the indole moiety (complexes **1k** and **1l**, respectively) leads to a rise of the longest $\lambda_{max}$ from 584 nm ($f$ = 0.0979, complex **1i**) to 608 nm ($f$ = 0.0945, complex **1k**) and 631 nm ($f$ = 0.1161, complex **1l**). A similar trend was found for complexes bearing the CAP ligands. Specifically, the longest $\lambda_{max}$ of complex **1j** increases from 611 nm ($f$ = 0.0767) to 644 nm ($f$ = 0.0698, complex **1m**) and 653 nm ($f$ = 0.0934, complex **1n**). For the fluoride substituent, we also note that the longest $\lambda_{max}$ rises 17 and 43 nm when going from complex **1i** to complexes bearing the $PMe_3$ ligand **1o** ($R^1$ = F, $R^2$ = H) and **1p** ($R^1$ = F, $R^2$ = OMe),

respectively. For the Re complex containing the CAP ligand, rises of longest $\lambda_{max}$ values of 21 and 34 nm were obtained when going from complex **1j** to complexes **1r** and **1q**, respectively.

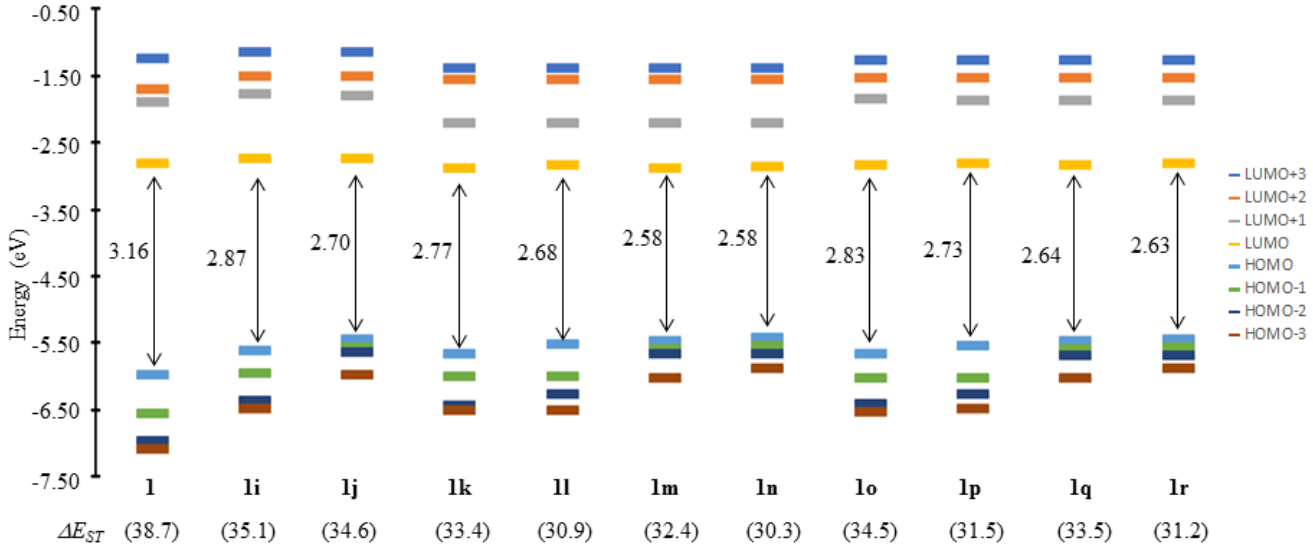


**Figure 7**. Energy diagram of the most relevant Kohn-Sham orbitals for complexes containing phosphine ligands **1i-1r** together with their corresponding HOMO-LUMO energy gaps in eV. In parenthesis, the difference in electronic energy between the first triplet excited state ($T_1$) and the singlet ground state ($S_0$), $\Delta E_{ST}$, is given in kcal/mol. For comparison purposes, data obtained for complex **1** are also included.

The analysis of the computed electronic absorption spectra shows that the lowest-lying absorbance band of all phosphine complexes **1i-1r** is mainly ascribed to the transition HOMO → LUMO (see Figures 6). Nonetheless, the transition HOMO-1 → LUMO also contributes to such an absorbance band, particularly, for complexes **1j**, **1m**, **1n**, **1q**, and **1r** (see Figure 6). Based on this, we will pay attention on the shape of the HOMO and LUMO of complexes **1i-1r** in order to

rationalize the variation of the longest $\lambda_{max}$ values obtained. As depicted in Figure 7, the replacement of $CO_{cis}$ by $PMe_3$ or CAP destabilizes the HOMO of all complexes **1i**-**1r** with respect to that of complex **1** between 0.31 eV (complex **1o**) to 0.53 eV (complexes **1n** and **1r**), whereas the LUMO only varies between +0.08 eV (complex **1i**) and -0.07 eV (complex **1m**) referred to the value of -2.82 eV obtained for complex **1**. As a consequence, the HOMO-LUMO energy gap of the modified Re(I) complexes is smaller than that of complex **1**, thus resulting in a rise of the $\lambda_{max}$ value of the lowest-lying absorption band. A similar trend was also found when replacing $CO_{cis}$ by $PMe_3$ in $[Re(deeb)(CO)_3(L)]^n$.[41] The LUMO of complexes **1i**-**1r** is essentially a $\pi_{pyridocarbazole}$ orbital, as depicted in Figure 8, and follows the same pattern as that found for complex **1** and the analogous substituted pyridocarbazole complexes, which explains the minor variations found for the LUMO energy (see Figure 7). Concerning the HOMO, the absence of $CO_{cis}$ provokes the loss of the corresponding stabilizing backbonding interaction $d_\pi$(Re)-$\pi^*_{CO}$. Indeed, the HOMO of the complexes bearing the $PMe_3$ ligand (**1i**, **1k**, **1l**, **1o**, and **1p**) is composed by a mixture of a Re *d* orbital combined with only one $\pi^*_{CO}$ orbital, denoted now as $d_{Re(CO)}$, and a $\pi_{pyridocarbazole}$ orbital, primarily centered on the indole moiety (see Figure 8). No significant participation of any orbital of $PMe_3$ in the HOMO of complexes containing such a phosphine has been detected (see Figure 8), which coincides with the orbital analysis reported for complexes $[Re(deeb)(CO)_3(L)]^n$ when replacing $CO_{cis}$ by $PMe_3$.[41] However, this picture changes when looking at the composition of the HOMO of complexes with the CAP ligand **1j** ($R^1$ = H, $R^2$ = H), **1m** ($R^1$ = $CO_2Et$, $R^2$ = H), **1n** ($R^1$ = $CO_2Et$, $R^2$ = OMe), **1q** ($R^1$ = F, $R^2$ = H), and **1r** ($R^1$ = F, $R^2$ = OMe). For compounds without substitution (**1j**) and only one substitution (**1m**, $R^1$ = $CO_2Et$, and **1q**, $R^1$ = F) in the pyridocarbazole ligand, the HOMO involves the $d_{Re(CO)}$ combined with a N *p* orbital of the CAP ligand and a very small participation of a $\pi_{pyridocarbazole}$

orbital (see Figure 7). The N *p* orbital interacts in a $\sigma$ bonding fashion with one of the lobes of the Re *d* orbital, recalling one of the typical interactions ascribed to metal-phosphine bonds. For the remaining CAP complexes containing a two-substituted pyridocarbazole (**1n**, $R^1 = CO_2Et$ and $R^2 = OMe$, and **1r**, $R^1 = F$ and $R^2 = OMe$), the HOMO is similar to the previous ones but now the participation of the $\pi_{pyridocarbazole}$ orbital in the description of such a frontier orbital is notable (see Figure 8). Therefore, the replacement of $PMe_3$ by CAP provokes an extra destabilization of the HOMO of pyridocarbazole complexes owing to the interaction between the N atom of the donor CAP ligand and the metal center. Indeed, the HOMO of $PMe_3$ complexes is always more stable than the analogous of CAP ones in the gap between 0.09 and 0.19 eV (see Figure 7). In consonance with this, the HOMO-LUMO energy gaps obtained for $PMe_3$ complexes are larger than the analogous ones found for CAP complexes (see Figure 7), thus explaining why the CAP ligand has a bathochromic effect even greater than the $PMe_3$ ligand. In addition, we also note that the presence of phosphine ligands in Re(I) complexes bearing electron-donating and/or electron-withdrawing substituents in the pyridocarbazole ligand does not change the trends found for the variation of the longest $\lambda_{max}$ when considering the analogous complexes with a $CO_{cis}$ ligand. Thus, both for $PMe_3$ and CAP complexes, the longest $\lambda_{max}$ values were reached when there is double substitution at the pyridocarbazole ligand, that is, complexes **1l**/**1p** ($R^1 = CO_2Et/F$, $R^2 = OMe$, $R^3 = PMe_3$; 631 nm/627 nm) and **1n**/**1r** ($R^1 = CO_2Et/F$, $R^2 = OMe$, $R^3 = CAP$; 653 nm/645 nm).

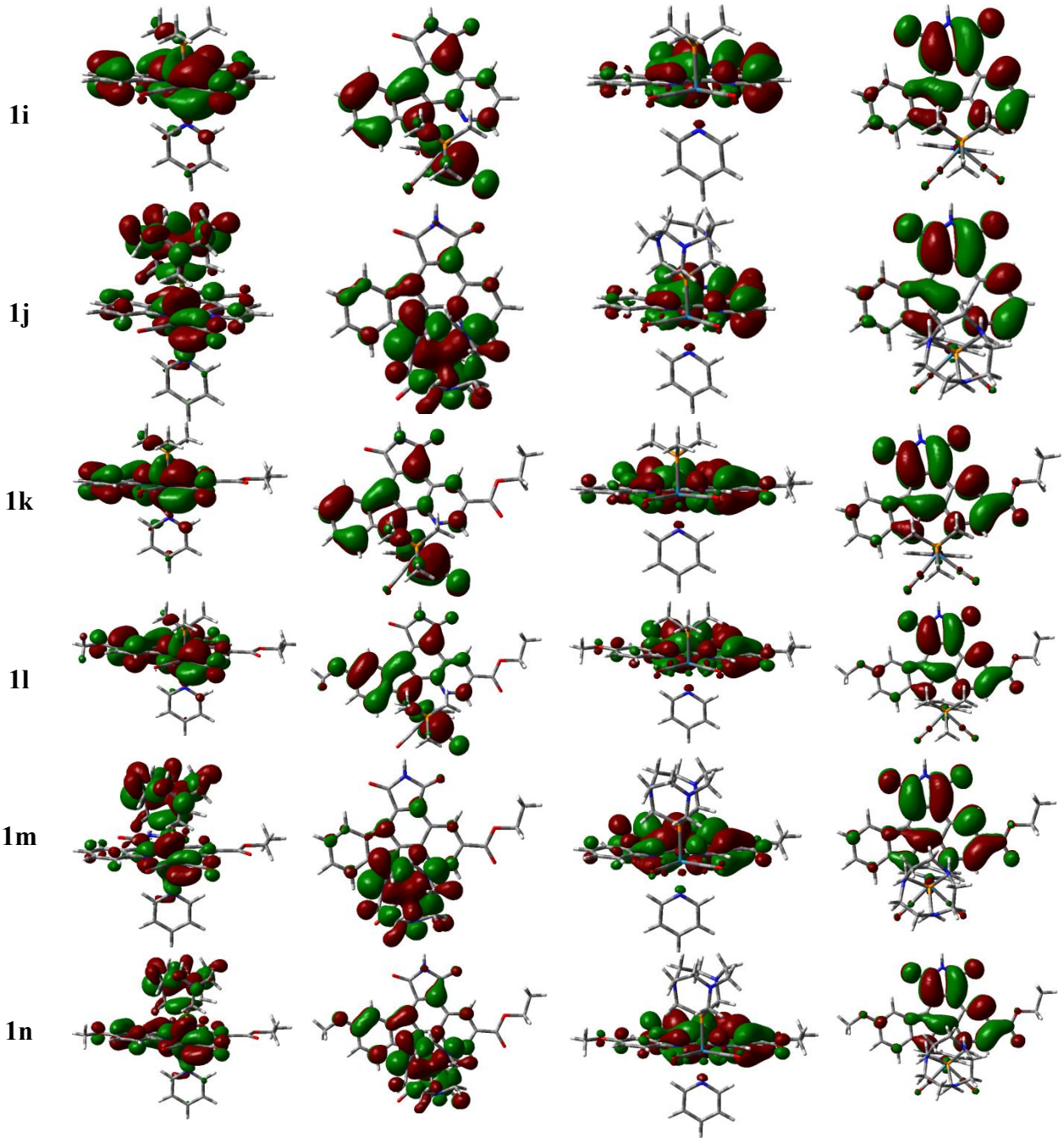


**Figure 8**. Contour maps of the frontier Kohn-Sham orbitals involved in the main orbital transition of the lowest-lying absorption band found for some representative Re(I) dicarbonyl pyridyl complexes containing the phosphine ligands $PMe_3$ (**1i**, **1k**, and **1l**) CAP (**1j**, **1m**, and **1n**). Two views are given for each orbital.

As for complexes **1**-**3** and **1a**-**1h**, we have also examined the ability of phosphine complexes **1i**-**1r** to photosensitize the formation of singlet oxygen. To accomplish this task, we optimized the geometry of such complexes in their respective triplet excited states (see Figure S1). Comparing the triplet optimized structures of complexes **1i**-**1r** to their analogous singlet ones (see Table S1), we found a notable shortening of the distance between Re and the N atom of the indole moiety in the gap 0.059-0.079 Å, whereas an important lengthening (0.021-0.034 Å) was obtained for the distance between Re and the CO located on the same side as the bidentate pyridyl moiety. A moderate shortening (0.009-0.015 Å) was found the distance between Re and the N atom of the bidentate pyridine moiety. The remaining metal-ligand bond lengths of the phosphine complexes hardly changes when going from the singlet species to the triplet ones. Yet again, as displayed in Figure 7, all the phosphine complexes show $\Delta E_{ST}$ values greater than 22.5 kcal/mol, ranging from 30.3 for complex **1n** to 35.1 for complex **1i**. This together with the fact that complexes **1l** ($R^1 = CO_2Et$, $R^2 = OMe$, $R^3 = PMe_3$), **1m** ($R^1 = CO_2Et$, $R^2 = H$, $R^3 = CAP$), **1n** ($R^1 = CO_2Et$, $R^2 = OMe$, $R^3 = CAP$), **1p** ($R^1 = F$, $R^2 = OMe$, $R^3 = PMe_3$), **1q** ($R^1 = F$, $R^2 = H$, $R^3 = CAP$), and **1r** ($R^1 = F$, $R^2 = OMe$, $R^3 = CAP$) present light absorption in the therapeutic window (~ 620-850 nm) lead us to propose them as the preferred PS candidates for their use in PDT. Nonetheless, it is also possible that the remaining phosphine complexes as well as the substituted pyridocarbazole complexes investigated in the previous section, **1a**-**1h**, except those ones containing the $NMe_2$ substituent (**1d** and **1f**) and the complex bearing two $CO_2Et$ substituents (**1g**), could be used as PSs for PDT since they absorb at $\lambda_{max}$ values longer than that found for complex **1**, whose photocytoxicity was detected experimentally at $\lambda \geq 505$ nm.[26]

## CONCLUSIONS

The influence of the pyridocarbazole ligand conjugation and substitution as well as of replacing the carbonyl ligand *cis* ($CO_{cis}$) to the bidentate one by phosphines on the spectroscopic properties and photocytoxicity of complex [$Re(CO)_3$(pyridocarbazole)(pyridine)] has been investigated by using time-dependent density functional theory (TD-DFT) methodology. The analysis of the electronic absorption spectrum obtained for all the complexes investigated shows that the most red-shifted absorption band is mostly ascribed to the HOMO → LUMO transition. This transition has a mixed $^1$MLCT and $^1$ILCT character ($d_{Re(CO)_2} + \pi_{pyridocarbazole} \rightarrow \pi^*_{pyridocarbazole}$) for all the complexes except those containing the electron-donating $NMe_2$ substituent in the indole moiety of the pyridocarbazole ligand and those bearing phosphine ligands. For the former complexes, the HOMO → LUMO transition has a $^1$ILCT character ($\pi_{pyridocarbazole} \rightarrow \pi^*_{pyridocarbazole}$), thus explaining the absence of phototoxicity experimentally reported for analogous complexes bearing imidazole ligands. In the case of complexes containing the phosphine $PMe_3$, although the HOMO → LUMO transition has a mixed $^1$MLCT and $^1$ILCT character ($d_{Re(CO)} + \pi_{pyridocarbazole} \rightarrow \pi^*_{pyridocarbazole}$), the replacement of $CO_{cis}$ by the phosphine has removed the $d_\pi$(Re)-$\pi^*$($CO_{cis}$) backbonding interaction. The spectator role played by the alkylphosphine, typically attributed to phosphine ligands, changes when complexes with the CAP ligand are considered, since this phosphine does participate in the description of HOMO by destabilizing it even more than with the alkylphosphine. Apart from this, it is worth noting that the bidentate ligand participates very little in the HOMO of complexes bearing the CAP ligand, thus suggesting a $^1$MLCT transition.

As expected, the greater the number of conjugated rings in the bidentate ligand, the smaller the HOMO-LUMO energy gap, thus inducing a bathochromic shift as found for closely related Re(I) complexes containing imidazole ligands. More interestingly, the electron-withdrawing nature of the 1H-pyrrole-2,5-dione heterocycle of the bidentate ligand plays an important role by enhancing the stabilization of the LUMO caused by the rise of the conjugation. The introduction of electron-withdrawing substituents into the pyridocarbazole pyridine ring mainly stabilizes the LUMO, whereas the HOMO destabilizes primarily with electron-donating substituents in the pyridocarbazole indole moiety. Both types of substituents result in a bathochromic shift of the most red-shifted absorption band, which is even larger if they are combined in the same complex. Except complexes containing the $NMe_2$ substituent, the replacement of $CO_{cis}$ by $PMe_3$ or CAP has a greater bathochromic shift than the introduction of substituents into the pyridocarbazole ligand due to the loss of one Re-CO bakbonding interactions,. The extra bathochromic shift found for CAP complexes compared to the analogous $PMe_3$ ones is a consequence of the participation of the former phosphine in the description of the HOMO through a $\sigma$-bonding interaction between one lobe of the nitrogen atom of CAP and one of the lobes of a filled *d* orbital of Re. By combining $PMe_3$ or CAP ligand with electron-withdrawing and/or electron-donationg substituents at the pyridocarbazole ligand, we have found several complexes with significant absorption at the therapeutic window. In addition, the calculation of the difference in energy between the first triplet excited state and the singlet ground state obtained for those complexes is greater than 30.0 kcal/mol, clearly above the minimum energy required, 22.5 kcal/mol, to transform triplet oxygen into singlet oxygen, indicating their capacity to photosensitize cytotoxic oxygen. Therefore, these new complexes can be taken into account for use as PSs in PDT.

COMPUTATIONAL DETAILS

Time-Dependent Density Functional Theory (TD-DFT) methodology[45,46] has proven to be reliable for studying UV-vis absorption spectra of Re(I) carbonyl complexes with α-diimine-type ligands.[47-77] A variety of DFT methods together with different basis sets and without or with including solvent effects have been used to that purpose. As TD-DFT computations require the optimization geometry of the stable species, first, and then, the obtaining of their corresponding electronic absorption spectra,[78,79] we describe and justify the levels of theory employed in the present work below.

***Geometry optimization***

The ground-state geometry of all the Re(I) complexes investigated in this work was optimized in the gas phase using the popular hybrid B3LYP functional[80-83] corrected with Grimme's D3 dispersion[84] in conjunction with Pople's 6-31+G(d) basis set for non-metal atoms[85] and the valence double-ζ basis set LANL2DZ plus the effective core potential of Hay and Wadt for the Re atom.[86] The location of the critical points on the potential energy surface was carried out using a modified Schlegel algorithm.[87-89] The nature of the optimized species as global minima was corroborated by means of an analytical calculation of harmonic vibrational frequencies. B3LYP has often been used in conjunction with double-zeta quality basis sets in order to get successful optimized geometries of rhenium carbonyl complexes aiming at carrying out TD-DFT calculations.[47-55,57,67,69,70,75,90-92] The inclusion of dispersion correction is also important to improve the performance of the B3LYP/6-31+G(d)-LANL2DZ level in yielding better optimized geometries. Despite all of this, we compared the B3LYP-D3/6-31+G(d)-LANL2DZ optimized geometry of a Re(I) complex closely related to those investigated in this work, a *N*-benzylated

derivative of the Re(I) tricarbonyl complex containing a pyridine ligand and another pyrido[2,3-*a*]pyrrolo[3,4-*c*]carbazole-5,7(6*H*)-dione ligand, with that reported by X-ray diffraction data.[26] The differences between both geometries show a mean absolute deviation (root mean square deviation) in the bond distances and bond angles involving non-hydrogen atoms of 0.011 Å (0.014 Å) and 0.65º (1.03º), respectively. These relatively small discrepancies corroborate the computational protocol chosen (see the *Validating the computational protocol for geometry optimizations* section in the Supporting Information).

The B3LYP-D3/6-31+G(d)-LANL2DZ level of theory was also employed to optimize all the Re(I) complexes in the first triplet excited state aiming at determining the difference in electronic energy between the triplet excited state and the singlet ground state. To that, the singlet and triplet B3LYP-D3/6-31+G(d)-LANL2DZ energies obtained for each complex were refined at the level used in the TD-DFT computations (see below).

***Electronic absorption spectrum***

The electronic absorption properties of all the Re(I) complexes was investigated by performing PCM-TD-M06/6-31+G(d)-LANL2DZ calculations on the B3LYP-D3/6-31+G(d)-LANL2DZ optimized geometries. That is, TD-DFT computations were carried out using the hybrid meta-GGA M06[93] along with the same basis set as the one used for geometry optimization. Solvent effects of dimethyl sulfoxide (DMSO), the one used in the UV/Vis absorption spectra of the Re(I) complexes **1**-**3** and derivatives (see Scheme 1),[26] were simulated by means of the Polarizable Continuum Model (PCM) taking into account electrostatic, cavitation, dispersion, and repulsion terms in the evaluation of the total energy in solution.[94-100] The first ten lowest excitation energies were only considered in these computations as we are mainly interested in the

lowest-lying absorption band. Apart from the PCM-TD-M06/6-31G(d)-LANL2DZ level, we also considered other computational levels in the TD-DFT computations by replacing M06 by GGA (PBE[101,102]), meta-GGA (TPSS[103], wB97x[104]), hybrid GGA (B3LYP-D3[80-84], PBE0[105], wB97xD[106]), hybrid meta-GGA (M05[107], MN15[108], TPSSh[103,109]), and long-range separate (CAM-B3LYP[110]) functionals. These eleven functionals have been chosen after an extensive revision about the computational protocols commonly used to theoretically investigate the UV-Vis properties of Re(I) carbonyl complexes. As explained in the *Validating the TD-DFT computational level* section in the Supporting Information, our results show that M06 is the most satisfactory functional to reproduce the experimental absorption spectra reported for complexes **1**-**3**. Thus, it should be expected a similar behavior when dealing with Re(I) carbonyl pyridylcarbazole complexes containing small alterations.

All the quantum chemical calculations were performed with the Gaussian 16 (G16) suite of programs.[111]

ASSOCIATED CONTENT

**Supporting Information**

Full DFT and TD-DFT geometry and energy details on all the Re(I) complexes investigated as well as discussion on the validation of the computational protocol used in this work. This material is available free of charge via the Internet at http://pubs.acs.org

AUTHOR INFORMATION

**Corresponding author**

*E-mail: rlopez@uniovi.es

**Notes**

The authors declare no competing financial interest.

ACKNOWLEDGEMENTS

The authors thank Ministerio de Ciencia, Innovación y Universidades (MCIU) of Spain (grant number PGC2018-100013-B-I00) for financial support.

REFERENCES

(1) Raab, O. On the Effect of Fluorescent Substances on Infusoria (German). *Zeitung Biol.* **1900**, *39*, 524-526.

(2) *Photodynamic Therapy: Basic Principles and Clinical Applications*; Henderson, B. W., Dougherty, T. J., Eds.; CRC Press: New York, 1992.

(3) Dougherty, T. J.; Gomer, C. J.; Henderson, B. W.; Jori, G.; Kessel, D.; Korbelik, M.; Moan, J.; Peng, Q. Photodynamic Therapy. *J. Natl. Cancer Inst.* **1998**, *90*, 889-905.

(4) Bonnett, R. *Chemical Aspects of Photodynamic Therapy*; Gordon and Breach Science Publishers: London, 2000.

(5) Hamblin, M. R.; Mroz, P. *Advances in Photodynamic Therapy: Basic, Translational, and Clinical; Engineering in Medicine and Biology*; Artech House: Norwood, MA, 2008.

(6) Agostinis, P.; Berg, K.; Cengel, K. A.; Foster, T. H.; Girotti, A. W.; Gollnick, S. O.; Hahn, S. M.; Hamblin, M. R.; Juzeniene, A.; Kessel, D.; Korbelik, M.; Moan, J.; Mroz, P.; Nowis, D.;

Piette, J.; Wilson, B. C.; Golab, J. Photodynamic Therapy of Cancer: An Update. *CA Cancer J. Clin.* **2011**, *61*, 250-281.

(7) *Handbook of Photomedicine*, 1st ed.; Hamblin, M. R., Huang, Y., Eds.; CRC Press: Boca Raton, FL, 2013.

(8) Allison, R. R. Photodynamic Therapy: Oncologic Horizons. *Future Oncol.* **2014**, *10*, 123-124.

(9) Benov, L. Photodynamic Therapy: Current Status and Future Directions. *Med. Princ. Pract.* **2015**, *24*, 14-28.

(10) Photodynamic Medicine: From Bench to Clinic, 1st ed.; Kostron, H., Hasan, T., Eds.; Royal Society of Chemistry: Cambridge, U.K., 2016.

(11) Abrahamse, H.; Hamblin, M. R. New Photosensitizers for Photodynamic Therapy. *Biochem. J.* **2016**, *473*, 347-364.

(12) van Straten, D.; Mashayekhi, V.; de Bruijn, H.; Oliveira, S.; Robinson, D. Oncologic Photodynamic Therapy: Basic Principles, Current Clinical Status and Future Directions. *Cancers* **2017**, *9*, 19.

(13) Zhang, J.; Jiang, C; Longo, J.P.F.; Azevedo, R.B.; Zhang, H.; Muehlmann, L.A. An Updated Overview on the Development of New Photosensitizers for Anticancer Photodynamic Therapy. *Acta Pharm. Sinica B* **2018**, 8, 137-146.

(14) Ferreira dos Santos, A.; Queiroz-de Almeida, D. R.; Ferreira-Terra, L.; Baptista, M. S.; Labriola, L. Photodynamic Therapy in Cancer Treatment – An Update Review. *J. Cancer Metastasis Treat.* **2019**, *5*, 25.

(15) Muniyandi, K.; George, B.; Parimelazhagan, T.; Abrahamse, H. Role of Photoactive Phytocompounds in Photodynamic Therapy of Cancer. *Molecules*, **2020**, *25*, 4102.

(16) Baptista, M. S.; Cadet, J.; Di Mascio, P.; Ghogare, A. A.; Greer, A.; Hamblin, M. R.; Lorente, C.; Nunez, S. C.; Ribeiro, M. S.; Thomas, A. H.; Vignoni, M.; Yoshimura, T. J. Type I and Type II Photosensitized Oxidation Reactions: Guidelines and Mechanistic Pathways. *Photochem. Photobiol.* **2017**, *93*, 912-919.

(17) Monro, S.; Colón, K.L.; Yin, H.; Roque III, J.; Konda, P.; Gujar, S.; Thummel, R.P.; Lilge, L.; Cameron, C.G.; McFarland, S.A. Transition Metal Complexes and Photodynamic Therapy from a Tumor-Centered Approach: Challenges, Opportunities, and Highlights from the Development of TLD1433. *Chem. Rev.* **2019**, *119*, 797-828.

(18) Szacilowski, K.; Macyk,W.; Drzewiecka-Matuszek, A.; Brindell, M.; Stochel, G. Bioinorganic Photochemistry: Frontiers and Mechanisms. *Chem. Rev.* **2005**, *105*, 2647-2694.

(19) Ogilby, P. R. Singlet Oxygen: There Is Indeed Something New Under the Sun. *Chem. Soc. Rev.* **2010**, *39*, 3181-3209.

(20) Ormon, A. B.; Freeman, H. S. Dye Sensitizers for Photodynamic Therapy. *Materials* **2013**, *6*, 817-840.

(21) Liew, H. S.; Mai, C.-W., Zulkefeli, M.; Madheswaran, T.; Kiew, L. V.; Delsuc, N.; Low, M. L. Recent Emergence of Rhenium(I) Tricarbonyl Complexes as Photosensitisers for Cancer Therapy. *Molecules* **2020**, *25*, 4176.

(22) Brown, J. M. Tumor Hypoxia in Cancer Therapy. *Methods Enzymol.* **2007**, *435*, 295-321.

(23) Juzeniene, A.; Moan, J. The History of PDT in Norway. Part One: Identification of Basic Mechanisms of General PDT. *Photodiagn. Photodyn. Ther.* **2007**, *4*, 3-11.

(24) Bozzini, G.; Colin, P.; Betrouni, N.; Maurage, C. A.; Leroy, X.; Simonin, S.; Martin-Schmitt, C.; Villers, A.; Mordon, S. Efficiency of 5-ALA Mediated Photodynamic Therapy on Hypoxic Prostate Cancer: A Preclinical Study on the Dunning R3327-AT2 Rat Tumor Model. *Photodiagn. Photodyn. Ther.* **2013**, *10*, 296-303.

(25) Nowak-Stepniowska, A.; Pergoł, P.; Padzik-Graczyk, A. Photodynamic Method of Cancer Diagnosis and Therapy-Mechanisms and Applications. *Postep. Biochem.* **2013**, *59*, 53-63.

(26) Kastl, A.; Dieckmann, S.; Wähler, K.; Völker, T.; Kastl, L.; Merkel, A. L.; Vultur, A.; Shanna, B.; Harms, K.; Ocker, M.; Parak, W. J.; Herlyn, M.; Meggers, E. Rhenium Complexes with Visible-Light-Induced Anticancer Activity. *ChemMedChem* **2013**, *8*, 924-927.

(27) Wähler, K.; Ludewig, A.; Szabo, P.; Harms, K.; Meggers, E. Rhenium Complexes with Red-Light-Induced Anticancer Activity. *Eur. J. Inorg. Chem.* **2014**, 807-811.

(28) Leonidova, A.; Gasser, G. Underestimated Potential of Organometallic Rhenium Complexes as Anticancer Agents. *ACS Chem. Biol.* **2014**, *9*, 2180-2193.

(29) Leonidova, A.; Pierroz, V.; Rubbiani, R.; Heier, J.; Ferrari, S.; Gasser, G. Towards Cancer Cell-Specific Phototoxic Organometallic Rhenium(I) Complexes. *Dalton Trans.* **2014**, *43*, 4287-4294.

(30) Gianferrara, T.; Spagnul, C.; Alberto, R.; Gasser, G.; Ferrari, S.; Pierroz, V.; Bergamo, A.; Alessio, E. Towards Matched Pairs of Porphyrin-$Re^{I}/^{99m}Tc^{I}$ Conjugates that Combine

Photodynamic Activity with Fluorescence and Radio Imaging. *ChemMedChem* **2014**, *9*, 1231-1237.

(31) Zhong, F.; Yuan, X.; Zhao, J.; Wang, Q. Visible Light-Harvesting Tricarbonyl Re(I) Complex: Synthesis and Application in Intracellular Photodynamic Effect and Luminescence Imaging. *Sci. China Chem.* **2016**, *59*, 70-77.

(32) Quental, L.; Raposinho, P.; Mendes, F.; Santos, I.; Navarro-Ranninger, C.; Alvarez-Valdes, A.; Huang, H.; Chao, H.; Rubbiani, R.; Gasser, G.; Quiroga, A. G.; Paulo, A. Combining Imaging and Anticancer Properties with New Heterobimetallic Pt(II)/M(I) (M = Re, $^{99m}$Tc) Complexes. *Dalton Trans.* **2017**, *46*, 14523-14536.

(33) Marker, S. C.; MacMillan, S. N.; Zipfel, W. R.; Li, Z.; Ford, P. C.; Wilson, J. J. Photoactivated in Vitro Anticancer Activity of Rhenium(I) Tricarbonyl Complexes Bearing Water-Soluble Phosphines. *Inorg Chem.* **2018**, *57*, 1311-1331.

(34) Yip, A. M.; Shum, J.; Liu, H.; Zhou, H.; Jia, M.; Niu, N.; Li, Y.; Yu, C.; Lo, K. K. W. Luminescent Rhenium(I)–Polypyridine Complexes Appended with a Perylene Diimide or Benzoperylene Monoimide Moiety: Photophysics, Intracellular Sensing, and Photocytotoxic Activity. *Chem. Eur. J.* **2019**, *25*, 8970-8974.

(35) Potocny, A. M.; Teesdale, J. J.; Marangoz, A.; Yap, G. P. A.; Rosenthal, J. Spectroscopic and $^1O_2$ Sensitization Characteristics of a Series of Isomeric Re(bpy)$(CO)_3$Cl Complexes Bearing Pendant BODIPY Chromophores. *Inorg. Chem.* **2019**, *58*, 5042-5050.

(36) Amoroso, A. J.; Coogan, M. P.; Dunne, J. E.; Fernández-Moreira, V.; Hess, J. B.; Hayes, A. J.; Lloyd, D.; Millet, C.; Pope, S. J. A.; Williams, C. Rhenium Fac Tricarbonyl Bisimine

Complexes: Biologically Useful Fluorochromes for Cell Imaging Applications. *Chem. Commun.* **2007**, 3066-3068.

(37) Kumar, A.; Sun, S.-S.; Lees, A. J. *Photophysics and Photochemistry of Organometallic Rhenium Diimine Complexes. In Photophysics of Organometallics*; Lees, A. J., Ed.; Springer: Berlin, 2010; pp 1-36.

(38) Fernández-Moreira, V.; Thorp-Greenwood, F.L.; Coogan, M.P. Application of d6 Transition Metal complexes in Fluorescence Cell Imaging. *Chem. Commun.* **2010**, *46*, 186-202.

(39) Zhao, Q.; Huang, C.; Li, F. Phosphorescent Heavy-Metal Complexes for Bioimaging. *Chem. Soc. Rev.* **2011**, *40*, 2508-2524.

(40) Konkankit, C. C.; Marker, S. C.; Knopf, K. M.; Wilson, J. J. Anticancer Activity of Complexes of the Third-Row Transition Metals, Rhenium, Osmium, and Iridium. *Dalton Trans.* **2018**, *47*, 9934-9974.

(41) Kurtz, D. A.; Brereton, K. R.; Ruoff, K. P.; Tang, H. M.; Felton, G. A. N.; Miller, A. J. M.; Dempsey, J. L. Bathochromic Shifts in Rhenium Carbonyl Dyes Induced through Destabilization of Occupied Orbitals. *Inorg Chem.* **2018**, *57*, 5389-5399.

(42) Britvin, S. N.; Lotnyk, A. Water-Soluble Phosphine Capable of Dissolving Elemental Gold: The Missing Link between 1,3,5-Triaza-7-phosphaadamantane (PTA) and Verkade's Ephemeral Ligand. *J. Am. Chem. Soc.* **2015**, *137*, 5526-5535.

(43) Moitra, T.; Karak, P.; Chakraborty, S.; Ruud, K.; Chakrabarti, S. Behind the Scenes of Spin-Forbidden Decay Pathways in Transition Metal Complexes. *Phys. Chem. Chem. Phys.* **2021,** *23*, 59-81.

(44) Baková, R.; Chergui, M.; Daniel, C.; Jr., A. V.; Záliš, S. Relativistic Effects in Spectroscopy and Photophysics of Heavy-Metal Complexes Illustrated by Spin-Orbit Calculations of $[Re(imidazole)(CO)_3(phen)]^+$. *Coord. Chem. Rev.* **2011,** *255*, 975-989.

(45) Marques, M. A. L.; Gross, E. K. U. Time-dependent Density Functional Theory. *Annu. Rev. Phys. Chem.* **2004**, *55*, 427-455.

(46) Fundamentals of Time-Dependent Density Functional Theory. Marques, M. A. L.; Maitra, N. T.; Nogueira, F. M. S.; Gross, E. K. V.; Rubio, A. Eds., Springer: Heidelberg, **2012**.

(47) Gabrielsson, A.; Busby, M.; Matousek, P.; Towrie, M.; Hevia, E.; Cuesta, L.; Pérez, J.; Záliš, S.; Vlček Jr., A. Electronic Structure and Excited States of Rhenium(I) Amido and Phosphido Carbonyl-Bipyridine Complexes Studied by Picosecond Time-Resolved IR Spectroscopy and DFT Calculations. *Inorg. Chem.* **2006**, *45*, 9789-9797.

(48) Cannizzo, A.; Blanco-Rodríguez, A. M.; El Nahhas, A.; Šebera, J.; Záliš, S.; Vlček Jr., A.; Chergui, M. Femtosecond Fluorescence and Intersystem Crossing in Rhenium(I) Carbonyl-Bipyridine Complexes. *J. Am. Chem. Soc.* **2008**, *130*, 8967-8974.

(49) Li, G.; Parimal, K.; Vyas, S.; Hadad, C. M.; Flood, A. H.; Glusac, K. D. Pinpointing the Extent of Electronic Delocalization in the Re(I)-to-Tetrazine Charge-Separated Excited State using Time-Resolved Infrared Spectroscopy. *J. Am. Chem. Soc.* **2009**, *131*, 11656-11657.

(50) Zhang, T. T.; Jia, J. F.; Wu, H. S. Substituent and Solvent Effects on Electronic Structure and Spectral Property of $ReCl(CO)_3(N\wedge N)$(N∧N = Glyoxime): DFT and TDDFT Theoretical Studies. *J. Phys. Chem. A* **2010**, *114*, 12251-12257.

(51) Záliš, S.; Consani, C.; El Nahhas, A.; Cannizzo, A.; Chergui, M.; Hartl, F.; Vlček Jr., A. Origin of Electronic Absorption Spectra of MLCT-Excited and One-Electron Reduced 2,2'-Bipyridine and 1,10-Phenanthroline Complexes. *Inorg. Chim. Acta.* **2011**, *374*, 578-585.

(52) Zhao, F.; Wang, J. X.; Liu, W. Q.; Wang, Y. B. Electronic Structures and Spectral Properties of Rhenium(I) Tricarbonyl Diimine Complexes with Phosphine Ligands: DFT/TDDFT Theoretical Investigations, *Comput. Theor. Chem.* **2012**, *985*, 90-96.

(53) Chartrand, D.; Castro-Ruiz, C. A.; Hanan, G. S. Diimine Triscarbonyl Re(I) of Isomeric Pyridyl-Fulvene Ligands: An Electrochemical, Spectroscopic, and Computational Investigation. *Inorg. Chem.* **2012**, *51*, 12738-12747.

(54) Xia, H.; Zhao, F.; Liu, W.; Wang, Y. Electronic Structures and Spectral Properties of Rhenium(I) Tricarbonyl Cyclopenta[b]dipyridine Complexes Containing Different Aromatic Ring Groups. *J. Organomet. Chem.* **2013**, *727*, 10-18.

(55) Baranovskii, V. I.; D. A. Maltsev, DFT Study of Potential Energy Surfaces and Conical Intersection Structures of Rhenium(I) Tricarbonyl Diimine Complexes. *Comput. Theor. Chem.* **2014**, *1043*, 71-78.

(56) Blanco-Rodríguez, A. M.; Kvapilová, H.; Sýkora, J; Towrie, M.; Nervi, C.; Volpi, G.; Záliš, S.; Vlček Jr., A. Photophysics of Singlet and Triplet Intraligand Excited States in [ReCl(CO)$_3$(1-(2-pyridyl)-imidazo[1,5-α]pyridine)] Complexes. *J. Am. Chem. Soc.* **2014**, *136*, 5963-5973.

(57) van der Salm, H.; Fraser, M. G.; Horvath, R.; Cameron, S. A.; Barnsley, J. E.; Sun, X. Z.; George, M. W.; Gordon, K. C. Re(I) Complexes of Substituted dppz: A Computational and Spectroscopic Study. *Inorg. Chem.* **2014**, *53*, 3126-3140.

(58) Kondrasenko, I.; Kisel, K. S.; Karttunen, A. J.; Jänis, J.; Grachova, E. V.; Tunik, S. P.; Koshevoy, I. O. Rhenium(I) Complexes with Alkynylphosphane Ligands: Structural, Photophysical, and Theoretical Studies. *Eur. J. Inorg. Chem.* **2015**, 864-875.

(59) Yang, X. Z.; Zhang, T. T.; Wei, J.; Jia, J. F.; Wu, H. S. DFT/TDDFT Studies of the Ancillary Ligand Effects on Structures and Photophysical Properties of Rhenium(I) Tricarbonyl Complexes with the Imidazo[4,5-f]-1,10-Phenanthroline Ligand. *Int. J. Quantum Chem.* **2015**, *115*, 1467-1474.

(60) Eng, J.; Daniel, D. Structural Properties and UV-visible Absorption Spectroscopy of Retinal-Pyridyl-CN Re(I) Carbonyl Bipyridine Complex: A Theoretical Study. *J. Phys. Chem. A* **2015**, *119*, 10645-10653.

(61) Fumanal, M.; Daniel, C. Description of Excited States in $[Re(imidazole)(CO)_3(phen)]^+$ Including Solvent and Spin-Orbit Coupling Effects: Density Functional Theory versus Multiconfigurational Wavefunction Approach. *J. Comput. Chem.* **2016**, *37*, 2454-2466.

(62) Hasheminasab, A.; Dawadi, M. B.; Mehr, H. S.; Herrick, R. S.; Ziegler, C. J. $Re(CO)_3$ Metallopolymers with Complete Metal Monomer Incorporation: Synthetic, Spectroscopic, Electrochemical, and Computational Studies. *Macromolecules*, **2016**, *49*, 3016-3027.

(63) Yang, X. Z.; Wang, Y. L.; Guo, J. Y.; Zhang, T. T.; Jia, J. F.; Wu, H. S. The Effect of Group-Substitution on Structures and Photophysical Properties of Rhenium(I) Tricarbonyl

Complexes with Pyridyltetrazole Ligand: A DFT/TDDFT study. *Mater. Chem. Phys.* **2016**, *178*, 173-181.

(64) Chanawanno, K., Rhoda, H. M.; Hasheminasab, A.; Crandall, L. A.; King, A. J.; Herrick, R. S.; Nemykin, V. N.; Ziegler, C. J. Using Hydrazine to Link Ferrocene with $Re(CO)_3$: A Modular Approach. *J. Organomet. Chem.* **2016**, *818*, 145-153.

(65) Carreño, A.; Gacitúa, M.; Fuentes, J. A.; Páez-Hernández, D.; Peñaloza, J. P.; Otero, C.; Preite, M.; Molins, E.; Swords, W. B.; Meyer, G. J.; Manríquez, J. M.; Polanco, R.; Chávez, I.; Arratia-Pérez, R. Fluorescence Probes for Both Prokaryotic and Eukaryotic Cells Using New Rhenium(I) Tricarbonyl Complexes with an Electron Withdrawing Ancillary ligand. *New J. Chem.* **2016**, *40*, 7687-7700.

(66) Laramée-Milette, B.; Zaccheroni, N.; Palomba, F.; Hanan, G. S. Visible and Near-IR Emissions from $k^2N$- and $k^3N$-Terpyridine Rhenium(I) Assemblies Obtained by an [*n* x 1] Head-to-Tail Bonding Strategy. *Chem. Eur. J.* **2017**, *23*, 6370-6379.

(67) Ramdass, A.; Sathish, V.; Velayudham, M.; Thanasekaran, P.; Umapathy, S.; Rajagopal, S. Luminescent Sensor for Copper(II) Ion Based on Imine Functionalized Monometallic Rhenium(I) Complexes. *Sens. Actuators B* **2017**, *240*, 1216-1225.

(68) Chakraborty, I.; Jimenez, J.; Sameera, W. M. C.; Kato, M.; Mascharak, P. K. Luminescent Re(I) Carbonyl Complexes as Trackable PhotoCORMs for CO Delivery to Cellular Targets. *Inorg. Chem.* **2017**, *56*, 2863-2873.

(69) Shillito, G. E.; Hall, T. B. J.; Preston, D.; Traber, P.; Wu, L.; Reynolds, K. E. A.; Horvath, R.; Sun, X. Z.; Lucas, N. T.; Crowley, J. D.; George, M. W.; Kupfer, S.; Gordon, K. C. Dramatic

Alteration of $^3$ILCT Lifetimes Using Ancillary Ligands in $[Re(L)(CO)_3(phen\text{-}TPA)]^{n+}$ Complexes: An Integrated Spectroscopic and Theoretical Study. *J. Am. Chem. Soc.* **2018**, *140*, 4534-4542.

(70) Whang, D. R.; Apaydin, D. H.; Park; S. Y.; Sariciftci, N. S. An Electron-Reservoir Re(I) Complex for Enhanced Efficiency for Reduction of $CO_2$ to CO. *J. Catal.* **2018**, *363*, 191-196.

(71) Fumanal, M.; Gindensperger, E.; Daniel, C. Ligand Substitution and Conformational Effects on the Ultrafast Luminescent Decay of $[Re(CO)_3(phen)(L)]^+$ (L = Imidazole, Pyridine): Non-Adiabatic Quantum Dynamics. *Phys. Chem. Chem. Phys.* **2018**, *20*, 1134-1141.

(72) Marker, S. C.; MacMillan, S. N.; Zipfel, W. R.; Li, Z.; Ford, P. C.; Wilson, J. J. Photoactivated *In Vitro* Anticancer Activity of Rhenium(I) Tricarbonyl Complexes Bearing Water-Soluble Phosphines. *Inorg. Chem.* **2018**, *57*, 1311-1331.

(73) Klemens, T.; Świtlicka, A.; Szlapa-Kula, A.; Łapok, Ł.; Obłoza, M.; Siwy, M.; Szalkowski, M.; Maćkowski, S.; Libera, M.; Schab-Balcerzak, E.; Machura, B. Tuning Optical Properties of Re(I) Carbonyl Complexes by Modifying Push-Pull Ligands Structure. *Organometallics* **2019**, *38*, 4206-4223.

(74) Favale Jr., J. M.; Danilov, E. O.; Yarnell, J. E.; Castellano, F. N. Photophysical Processes in Rhenium(I) Diiminetricarbonyl Arylisocyanides Featuring Three Interacting Triplet Excited States. *Inorg. Chem.* **2019**, *58*, 8750-8762.

(75) Shillito, G. E.; Preston, D.; Traber, P.; Steinmetzer, J.; McAdam, C. J.; Crowley, J. D.; Wagner, P.; Kupfer, S.; Keith C. Gordon, K. C. Excited-State Switching Frustrates the Tuning of

Properties in Triphenylamine-Donor-Ligand Rhenium(I) and Platinum(II) Complexes. *Inorg. Chem.* **2020**, *59*, 6736-6746.

(76) Auvray, T.; Del Secco, B.; Dubreuil, A.; Zaccheroni, N.; Hanan, G. S. In-Depth Study of the Electronic Properties of NIR-Emissive $\kappa^3$*N*-terpyridine Rhenium(I) Dicarbonyl Complexes. *Inorg. Chem.* **2021**, *60*, 70-79.

(77) Fernández-Terán, R. J.; Sévery, L. Living Long and Prosperous: Productive Intraligand Charge-Transfer States from a Rhenium(I) Terpyridine Photosensitizer with Enhanced Light Absorption. *Inorg. Chem.* **2021**, *60*, 1334-1343.

(78) Adamo, C.; Jacquemin, D. The Calculations of Excited-State Properties with Time-Dependent Density Functional Theory. *Chem. Soc. Rev.* **2013**, *42*, 845-856.

(79) Laurent, A. D.; Adamo, C.; Jacquemin, D. Dye Chemistry with Time-Dependent Density Functional Theory. *Phys. Chem. Chem. Phys.* **2014**, *16*, 14334-14356.

(80) Becke, A. D. Density-Functional Exchange-Energy Approximation with Correct Asymptotic Behavior. *Phys. Rev. A* **1988**, *38*, 3098-3100.

(81) Lee, C.; Yang, W.; Parr, R. G. Development of the Colle-Salvetti Correlation-Energy Formula into a Functional of the Electron Density. *Phys. Rev. B* **1988**, *37*, 785-789

(82) Becke, A. D. Density-Functional Thermochemistry. III. The Role of Exact Exchange. *J. Chem. Phys.* **1993**, *98*, 5648-5652.

(83) Stephens, P. J.; Devlin, F. J.; Chabalowski, C. F.; Frisch, M. J. Ab Initio Calculation of Vibrational Absorption and Circular Dichroism Spectra Using Density Functional Force Fields. *J. Phys. Chem.* **1994**, *98*, 11623-11627.

(84) Grimme, S. A Consistent and Accurate *Ab Initio* Parametrization of Density Functional Dispersion Correction (DFT-D) for the 94 Elements H-Pu. *J. Chem. Phys.* 2010, *132*, 154104.

(85) Hehre, W. J.; Radom, L.; Pople, J. A.; Schleyer, P. v. R. *Ab Initio Molecular Orbital Theory*; Wiley: New York, **1986**.

(86) Hay, P. J.; Wadt, W. R. Ab Initio Effective Core Potentials for Molecular Calculations. Potentials for the Transition Metal Atoms Sc to Hg. *J. Chem. Phys.* **1985**, *82*, 270-283.

(87) Schlegel, H. B. Optimization of Equilibrium Geometries and Transition Structures. *J. Comput. Chem.* **1982**, *3*, 214-218.

(88) Schlegel, H. B. Estimating the Hessian for Gradient-Type Geometry Optimizations. *Theor. Chem. Acc.* **1984**, *66*, 333-340.

(89) Li, X.; Frisch, M. J. Energy-Represented Direct Inversion in the Iterative Subspace within a Hybrid Geometry Optimization Method. *J. Chem. Theory Comput.* **2006**, *2*, 835-839.

(90) Machura, B.; Wolff, M.; Benoist, E.; Coulais, Y. Tricarbonyl Rhenium(I) Complex of Benzothiazole: Synthesis, Spectroscopic Characterization, X-ray Crystal Structure and DFT Calculations. *J. Organomet. Chem.* **2012**, *724*, 82-87.

(91) Sarkar, R.; Rajak, K. K. Synthesis and Characterization of Rhenium(I) Complexes Based on *O*, *N*, *N* Coordinating Ligands: DFT/TDDFT Studies on the Electronic Structures and Spectral Properties. *J. Organomet. Chem.* **2015**, *729*, 1-13.

(92) Harabuchi, Y.; Eng, J.; Gindensperger, E.; Taketsugu, T.; Maeda, S.; Daniel, C. Exploring the Mechanism of Ultrafast Intersystem Crossing in Rhenium(I) Carbonyl Bipyridine Halide

Complexes: Key Vibrational Modes and Spin-Vibronic Quantum Dynamics. *J. Chem. Theory Comput.* **2016**, *12*, 2335-2345.

(93) Zhao, Truhlar, D. G. The M06 Suite of Density Functionals for Main Group Thermochemistry, Thermochemical Kinetics, Noncovalent Interactions, Excited States, and Transition Elements: Two New Functionals and Systematic Testing of Four M06-Class Functionals and 12 Other Functionals. *Theor. Chem. Acc.* **2008**, *120*, 215-241.

(94) Mennucci, B.; Tomasi, J. Continuum Solvation Models: A New Approach to the Problem of Solute's Charge Distribution and Cavity Boundaries. *J. Chem. Phys.* **1997**, *106*, 5151-5158.

(95) Barone, V.; Cossi, M.; Tomasi, J. A New Definition of Cavities for the Computation of Solvation Free Energies by the Polarizable Continuum Model. *J. Chem. Phys.* **1997**, *107*, 3210-3221.

(96) Cancès, M. T.; Mennucci, B.; Tomasi, J. A New Integral Equation Formalism for the Polarizable Continuum Model: Theoretical Background and Applications to Isotropic and Anisotropic Dielectrics. *J. Chem. Phys.* **1997**, *107*, 3032-3041.

(97) Barone, V.; Cossi, M.; Tomasi, J. Geometry Optimization of Molecular Structures in Solution by the Polarizable Continuum Model. *J. Comput. Chem.* **1998**, *19*, 404-417.

(98) Tomasi, J.; Mennucci, B.; Cancès, M. T. The IEF Version of the PCM Solvation Method: An Overview of a New Method Addressed to Study Molecular Solutes at the QM *Ab Initio* Level. *J. Mol. Struct.: THEOCHEM* **1999**, *464*, 211-226.

(99) Scalmani, G.; Frisch, M. J. Continuous Surface Charge Polarizable Continuum Models of Solvation. I. General Formalism. *J. Chem. Phys.* **2010**, *132*, 114110.

(100) Tomasi, J.; Persico, M. Molecular Interactions in Solution: An Overview of Methods Based on Continuous Distributions of the Solvent. *Chem. Rev.* **1994**, *94*, 2027-2094.

(101) Perdew, J. P.; Burke, K.; Ernzerhof, M. Generalized Gradient Approximation Made Simple. *Phys. Rev. Lett.* **1996**, *77*, 3865-3868.

(102) Perdew, J. P.; Burke, K.; Ernzerhof, M. Errata: Generalized Gradient Approximation Made Simple. Phys. Rev. Lett. **1997**, *78*, 1396-1399.

(103) Tao, J.; Perdew, J. P.; Staroverov, V. N.; Scuseria, G. E. Climbing the Density Functional Ladder: Nonempirical Meta-Generalized Gradient Approximation Designed for Molecules and Solids. *Phys. Rev. Lett.* **2003**, *91*, 146401-146405.

(104) Chai, J.-D.; Head-Gordon, M. Systematic Optimization of Long-Range Corrected Hybrid Density Functionals. *J. Chem. Phys.* **2008**, *128*, 084106.

(105) Adamo, C.; Barone, V. Toward Reliable Density Functional Methods without Adjustable Parameters: The PBE0 Model. *J. Chem. Phys.* **1999**, *110*, 6158-6170.

(106) Chai, J. D.; Head-Gordon, M. Long-Range Corrected Hybrid Density Functionals with Damped Atom-Atom Dispersion Corrections. *Phys. Chem. Chem. Phys.* **2008**, *10*, 6615-6620.

(107) Zhao, Y.; Schultz, N. E.; Truhlar, D. G. Exchange-Correlation Functional with Broad Accuracy for Metallic and Nonmetallic Compounds, Kinetics, and Noncovalent Interactions. *J. Chem. Phys.* **2005**, *123*, 161103.

(108) Yu, H. S.; He, X.; Li, S. L.; Truhlar, D. G. MN15: A Kohn-Sham Global-Hybrid Exchange-Correlation Density Functional with Broad Accuracy for Multi-Reference and Single-Reference Systems and Noncovalent Interactions. *Chem. Sci.* **2016**, *7*, 5032-5051.

(109) Staroverov, V. N.; Scuseria, G. E.; Tao, J.; Perdew, J. P. Comparative Assessment of a New Nonempirical Density Functional: Molecules and Hydrogen-Bonded Complexes. *J. Chem. Phys.* **2003**, *119*, 12129-12137.

(110) Yanai, T.; Tew, D. P.; Handy, N. C. A New Hybrid Exchange-Correlation Functional Using the Coulomb-Attenuating Method (CAM-B3LYP). *Chem. Phys. Lett.* **2004**, *393*, 51-57.

(111) Gaussian 16, Revision C.01, Frisch, M. J.; Trucks, G. W.; Schlegel, H. B.; Scuseria, G. E.; Robb, M. A.; Cheeseman, J. R.; Scalmani, G.; Barone, V.; Petersson, G. A.; Nakatsuji, H.; Li, X.; Caricato, M.; Marenich, A. V.; Bloino, J.; Janesko, B. G.; Gomperts, R.; Mennucci, B.; Hratchian, H. P.; Ortiz, J. V.; Izmaylov, A. F.; Sonnenberg, J. L.; Williams-Young, D.; Ding, F.; Lipparini, F.; Egidi, F.; Goings, J.; Peng, B.; Petrone, A.; Henderson, T.; Ranasinghe, D.; Zakrzewski, V. G.; Gao, J.; Rega, N.; Zheng, G.; Liang, W.; Hada, M.; Ehara, M.; Toyota, K.; Fukuda, R.; Hasegawa, J.; Ishida, M.; Nakajima, T.; Honda, Y.; Kitao, O.; Nakai, H.; Vreven, T.; Throssell, K.; Montgomery, J. A., Jr.; Peralta, J. E.; Ogliaro, F.; Bearpark, M. J.; Heyd, J. J.; Brothers, E. N.; Kudin, K. N.; Staroverov, V. N.; Keith, T. A.; Kobayashi, R.; Normand, J.; Raghavachari, K.; Rendell, A. P.; Burant, J. C.; Iyengar, S. S.; Tomasi, J.; Cossi, M.; Millam, J. M.; Klene, M.; Adamo, C.; Cammi, R.; Ochterski, J. W.; Martin, R. L.; Morokuma, K.; Farkas, O.; Foresman, J. B.; Fox, D. J. Gaussian, Inc., Wallingford CT, **2016**.

## 5.7 Assessment of BODIPY-Oxasmaragdyrin Dyads for Dye-Sensitized Solar Cells: Aromaticity, Photosensitization Capability, and Charge Transport

Merlys Borges-Martínez, Daniel Alvarez, Nicolas Montenegro-Pohlhammer, M. Isabel Menendez, Ramon Lopez, and Gloria Cardenas-Jiron

*J. Phys. Chem. C* **2019**, *123*, 19362-19375

THE JOURNAL OF PHYSICAL CHEMISTRY C

Article

Cite This: J. Phys. Chem. C 2019, 123, 19362−19375

pubs.acs.org/JPCC

# Assessment of BODIPY−Oxasmaragdyrin Dyads for Dye-Sensitized Solar Cells: Aromaticity, Photosensitization Capability, and Charge Transport

Merlys Borges-Martínez,[†] Daniel Alvarez,[‡] Nicolas Montenegro-Pohlhammer,[†] M. Isabel Menéndez,[‡] Ramón López,*[,‡] and Gloria Cárdenas-Jirón*[,†]

[†]Laboratory of Theoretical Chemistry, Faculty of Chemistry and Biology, University of Santiago de Chile (USACH), 9170022 Santiago, Chile

[‡]Departamento de Química Física y Analítica, Facultad de Química, Universidad de Oviedo, C/Julián Clavería 8, Oviedo, 33006 Asturias, Spain

Supporting Information

**ABSTRACT:** Dye-sensitized solar cells (DSSC) are presented as an alternative among renewable energies where the dye plays an important role to obtain an effective device. Our goal in this work is to examine the influence of several bridging functional groups between the BODIPY and oxasmaragdyrin systems forming dyads (D), as potential components of DSSC, on the aromatic, photophysical, and charge transport properties. A set of 11 dyads made of the oxasmaragdyrin with 2,6-dimethoxyphenyl and methylamine groups in two of their meso carbons (S) and the 4,4-difluoro-4-bora-3a,4a-diaza-s-indacene (BODIPY, B) moieties that differ in the binding bridge between them has been analyzed with density functional theory (DFT). The geometries were optimized with the B3LYP/6-311G(d,p) level of theory employing D3 Grimme's correction, and a set of six functionals (B3LYP, BHandHLYP, CAM-B3LYP, PBE0, wB97X, TPSSh) was evaluated for reference systems in time-dependent DFT calculations. We found that TPSSh presents the best agreement with the available data of UV−vis spectra, so it was used for calculation of the electronic absorption spectra of the 11 oxasmaragdyrins and 11 dyads. When the bridge between S and B consists of one (D3), two (D5), or three acetylene units (D6), a strong absorption band in the infrared region around 1000 nm can be achieved. These bands correspond to charge-separated excited states that favor a panchromatic absorption in that region. The aromaticity index NICS(0) computed at the macrocycle center ring critical point using the GIAO/B3LYP/6-311G(d,p) level of theory shows in all these systems an aromatic character for the oxasmaragdyrin macrocycle (from −10.7 to −12.4 ppm). We also found that all dyads present a favorable electron injection toward the semiconductor $TiO_2$ because the LUMO energy of the dyad is higher than the conduction band of the semiconductor (−4.3 eV) used in a solar cell. Besides, the HOMO energy of the dyads D3, D5, and D6 is lower than the redox potential (−4.8 eV) of a mediator as the $I^-/I_3^-$ system used to recover it after circulation of electrons. Nonequilibrium Green's function-based calculations performed for a couple of dyads, with (D6) and without (D4) a significant charge transfer band, connected to Au electrodes show that D6 was to be a better conductor, in agreement with the charge transfer results obtained from the photophysical properties. Finally, the Gibbs free energy for the formation of the dyads here investigated is calculated. All of them are shown to be exergonic reactions ($\Delta G_{solution} < 0$), which suggests that these systems could be synthesized.

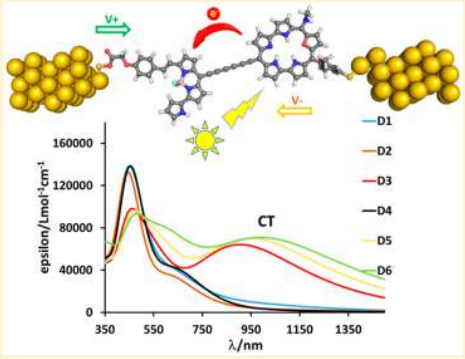


## 1. INTRODUCTION

The search for clean and renewable energy sources is a subject of great interest currently because of the limited life of fossil fuels, the pollution caused by their combustion, and the growing environmental awareness. New technologies for conversion of solar energy into electrical energy by means of dye-sensitized solar cells (DSSC) are a very attractive alternative due to their low cost and high performance.[1−13] In these types of devices the dye plays an important role whenever it meets the following requirements: (a) radiation absorption in the visible−ultraviolet (UV−vis) and near-infrared (NIR) region, (b) large molar absorption coefficients, (c) energy of its lowest unoccupied molecular orbital (LUMO) above the conduction band edge of the semiconductor, with electrons located near the molecular group of the dye anchored to the semiconductor for an efficient electron injection, (d) energy of its highest occupied molecular orbital (HOMO) below the redox mediator for an efficient electron reduction in

Received: May 30, 2019
Revised: July 22, 2019
Published: July 22, 2019







DOI: 10.1021/acs.jpcc.9b05136
J. Phys. Chem. C 2019, 123, 19362−19375

Scheme 1. Molecular structures of (a) Porphyrin, (b) Expanded Porphyrin, and (c) Oxasmaragdyrin

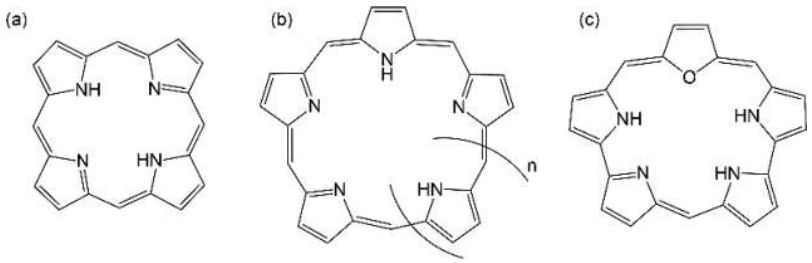


Scheme 2. Reaction for the Synthesis of the BODIPY−Oxasmaragdyrin Dyad[37]

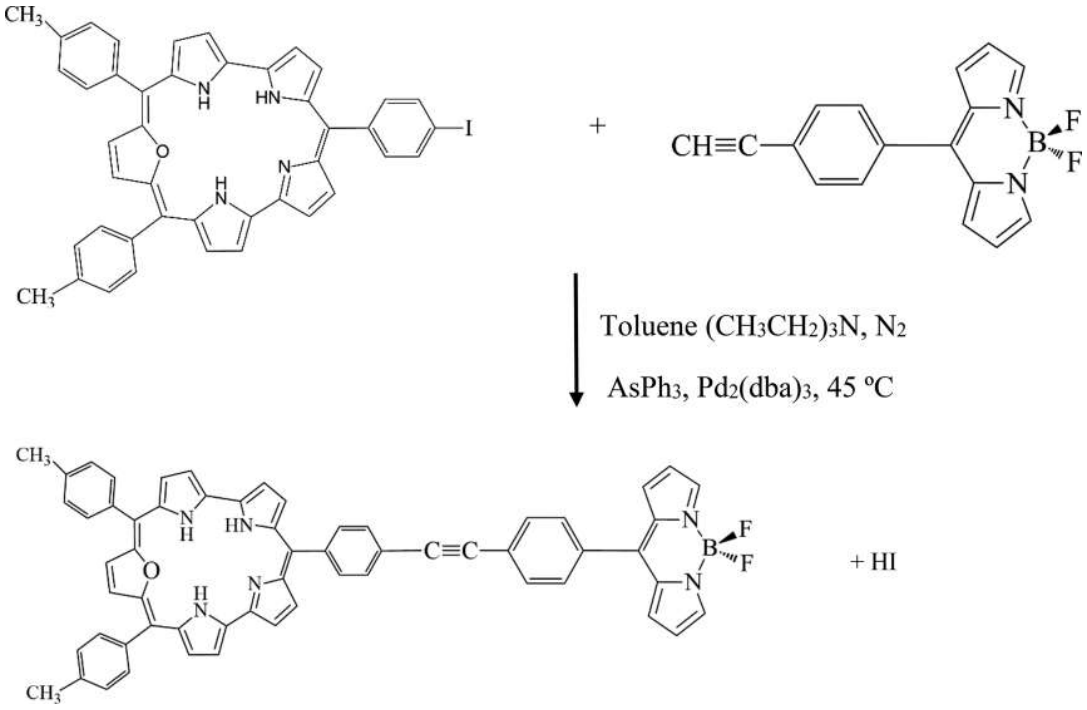


the regeneration of the dye, and (e) absence of aggregation on the semiconductor surface.[14]

Ruthenium complexes started being used as dyes in the DSSC since the pioneering work of Graztel et al.[1−7] However, the limited availability, toxicity, and high cost of ruthenium have led to interest in looking for other efficient dyes for DSSC. Among them, porphyrins are attractive candidates because they have a rigid molecular structure of four pyrrolic rings connected by four bridging meso carbon atoms with high absorption coefficients in the visible region and with many reaction centers (four meso positions and eight beta positions) suitable for introduction of functional groups (see Scheme 1a). Several experimental[15,16] and theoretical[17−20] studies have shown the viability of some porphyrins as dyes for DSSC. Expanded porphyrins containing more than four pyrrole rings or alternative heterocycle subunits (see Scheme 1b) have emerged as functional organic chromophores for a wide range of applications because those structural modifications result in marked changes in the optical, redox, and ion-coordination properties.[21,22] Due to their extended $\pi$-system, expanded porphyrins display red-shifted absorption bands and exceptionally large two-photon absorption cross sections compared to the regular porphyrin. Consequently, they are excellent candidates for near-infrared dyes and nonlinear optical materials. In particular, in recent years there has been growing research on expanded porphyrins consisting of five pyrrole rings in which a pyrrole unit is replaced by a furan named oxasmaragdyrin (see Scheme 1c).

Recent studies have shown the importance of oxasmaragdyrin sensitizer as a compelling material for light-energy-harvesting applications.[23−26] For instance, boryl oxasmaragdyrin offers many advantages, such as simpler synthesis and purification processes, low cost, and moisture stability. Besides, very recently, it has been found that such aromatic core-modified expanded porphyrins are efficient hole-transporting materials (HTMs) for perovskite solar cells (PSCs) as they retard charge recombination and transport the photogenerated hole to the counter electrode.[24]

On the other hand, boron−dipyrromethene units (BODIPY) are also molecular systems commonly used for efficient light capture, mainly in the far visible or UV region of the electromagnetic spectrum. The photophysical properties of BODIPY and derivatives have been previously studied by Jacquemin's and Russo's groups.[27−32] The coupling of oxasmaragdyrins with BODIPY through different types of linkers could also enhance the photosensitization properties of the porphyrin derivatives.[23,33] Experimentally, the effect of spacers or bridges between chromophores has been studied.



DOI: 10.1021/acs.jpcc.9b05136
J. Phys. Chem. C 2019, 123, 19362−19375

**Scheme 3. Molecular Structure of the Dyads (D1-D11) Formed by BODIPY (B) and the Oxasmaragdyrin (S1) without and with Different Bridges**

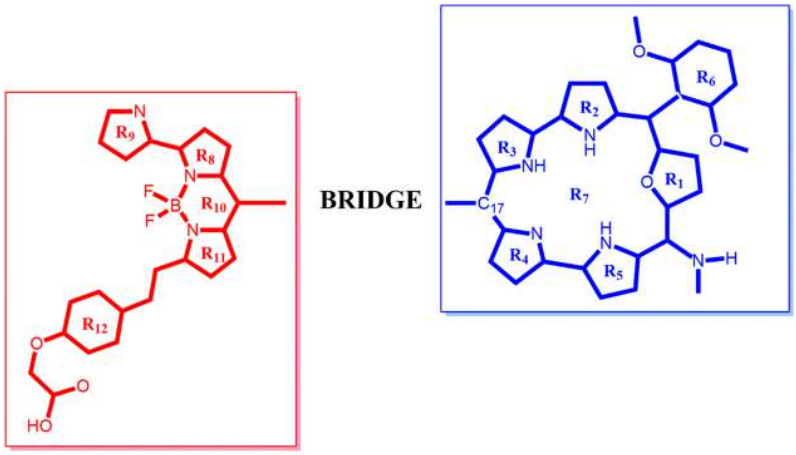


| Notation | Dyad |
|---|---|
| D1 | B—$S_1$ |
| D2 | B—$CH_2$—$CH_2$—$CH_2$—$S_1$ |
| D3 | B—C≡C—$S_1$ |
| D4 | B—$CH_2$—C≡C—$S_1$ |
| D5 | B—C≡C—C≡C—$S_1$ |
| D6 | B—C≡C—C≡C—C≡C—$S_1$ |
| D7 | 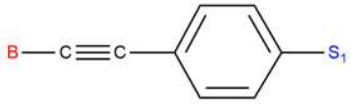 |
| D8 | 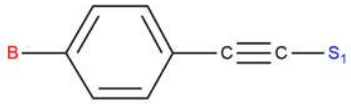 |
| D9 | 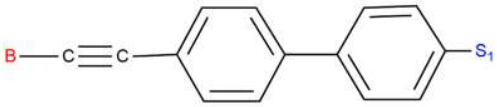 |
| D10 | 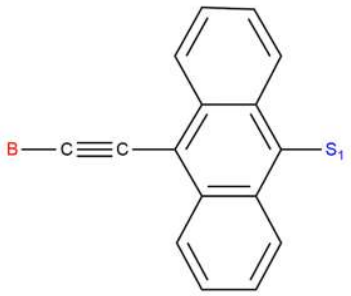 |
| D11 | 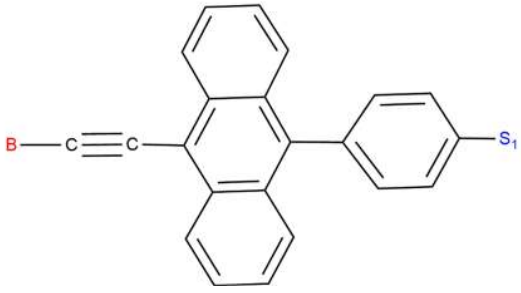 |



DOI: 10.1021/acs.jpcc.9b05136
J. Phys. Chem. C 2019, 123, 19362−19375

Among the bridges that have shown the best results in electronic transfer are those containing acene,[34] thiophene,[35] and phenylethynyl[36] groups.

Recently, the synthesis of a covalently linked BODIPY−oxasmaragdyrin dyad has been reported[37] (see Scheme 2), where 4,4-difluoro-8-(4-ethynylphenyl)-4-bora-3a,4adiaza-s-indacene (BODIPY−CCH) reacts with a 5,10-(4-methylphenyl)-19-(4-iodophenyl)-25-oxasmaragdyrin in the presence of toluene/triethylamine (3:1) and a catalytic mix of $Pd_2(dba)_3$/$AsPh_3$ at 45 °C for 2 h. The reaction has a yield of 65% for the formation of the dyad and is a stable product. The dyad presents absorption in the visible region in the range of 449−706 nm.

Inspired by these authors and the characteristics of these compounds as photosensitizers, we theoretically explored other linkers that could connect both chromophores, as also some structural variations for the dyad components, oxasmaragdyrin and BODIPY. To our knowledge, these kinds of studies applied to BODIPY−oxasmaragdyrin dyads have not yet been reported in the literature.

The oxasmaragdyrin selected in this study has 2,6-dimethoxyphenyl and methylamine groups in two of its meso carbons (S1 in Scheme 3), which are electron-donating groups adequate to achieve the push-up effect of electron density from the porphyrin,[15,16,38] toward the bridge, and eventually to the BODIPY moiety. In addition, the selected BODIPY (4,4-difluoro-4-bora-3a,4a-diaza-s-indacene, B in Scheme 3) is similar to a commercial BODIPY 650/660-succinimidyl ester[39] with a decrease in the size of its side chain. This modification ensures that electronic absorption properties are maintained while saving computational resources.

The main goal of this theoretical research is to propose dyads composed of oxasmaragdyrin and BODIPY that could improve the photosensitization properties of the synthesized dyad displayed in Scheme 2. To that end, we examine the influence of several bridging functional groups between B and S1 on the photophysical properties of the BODIPY−oxasmaragdyrin dyads (see D2−D11 in Scheme 3). For the sake of a simple nomenclature, we include the bridge as part of the oxasmaragdyrin fragment in the dyad named S2−S11. Because of their structural characteristics, we also investigated the aromaticity of these systems and the binding nature between the fragments. A set of bridges between the two chromophores including alkyl, phenyl, and alkynyl groups and a combination of them was considered, evaluating their influence on the geometry, aromaticity, and electronic absorption spectra. Finally, taking into consideration that some dyads present an important charge transfer between the fragments, we investigated the charge transport properties by simulating the dyad connected to gold electrodes to represent a molecular device.

## 2. COMPUTATIONAL METHODS

Optimization of the molecular structure of isolated oxasmaragdyrin S1 and its variants (S2−S11), the isolated BODIPY B, and the corresponding BODIPY−oxasmaragdyrin dyads (D1−D11) was carried out applying density functional theory (DFT) and the B3LYP[40−42] functional as implemented in Gaussian 09[43] (see Scheme 3 for the investigated structures). B3LYP is a hybrid functional that combines the Becke's nonlocal exchange functional, the Hartree−Fock exchange energy, the nonlocal correlation functional of Lee, Yang, and Parr, and the Vosko−Wilk−Nusair fitting to the correlation energy derived from the local spin density approximation. All of the atoms were described with the contracted triple-ζ quality basis set including polarization functions 6-311G-(d,p),[44] while a modified version of the Schlegel algorithm[45−47] was used to locate the energy minima on the potential energy surface. The nature of these critical points was confirmed by analytical computations of harmonic vibrational frequencies. The dispersion interactions in the B3LYP energy computations during the optimization were also taken into account through calculation of the atom-pairwise DFT-D3 dispersion developed by Grimme and co-workers.[48]

Aiming at finding out what factors can influence the sensitization properties of oxasmaragdyrin-type porphyrinic systems, we investigated the electronic absorption spectra and the aromaticity of the oxasmaragdyrins S1−S11 and their corresponding dyads D1−D11. On one hand, B3LYP/6-311G(d,p- optimized geometries were used to calculate the excited electronic spectra applying the time-dependent DFT methodology (TD-DFT),[49,50] where the electronic transitions are considered as verticals Franck−Condon type.

For regular porphyrins and some derivatives the less expensive TD-DFT has been shown to be in better agreement with experiment than the more expensive ab initio configuration interaction (CI), complete active space second-order perturbation theory (CASPT2), or similarity transformed equation-of-motion coupled cluster (STEOM-CC) calculations.[51,52] To obtain reliable electronic spectra, we performed a calibration of some of the most commonly used density functionals in porphyrin-type systems: B3LYP,[40−42] BHandHLYP,[53] CAM-B3LYP,[54] PBE0,[55] TPSSh,[56,57] and wB97x.[58]

To that end, we used as references the electronic absorption spectra experimentally reported for the BODIPY 650/660-succinimidyl ester[39] ($B_{ref}$) and oxasmaragdyrin[59] with phenyl substituents on the three meso carbons ($S_{ref}$) (Scheme S1), which have very similar structures to those of the chromophores of our study. In particular, we compared the electronic absorption spectra calculated with all of the above-mentioned functionals for both the isolated BODIPY ($B_{ref}$) and oxasmaragdyrin ($S_{ref}$) with the corresponding reference spectra. Then, the best functional obtained was used to investigate the electron spectroscopic properties of S1−S11 and D1-D11. In these calculations, a set of 25, 50, and 75 excited states was computed for oxasmaragdyrins (S1−S11), BODIPY, and dyads (D1−D11).

Solvent effects were taken into account in all of the TD-DFT computations with the conductor-like polarizable continuum model (CPCM).[60,61] The dielectric constants of 4.71, 8.93, and 32.61 were used to simulate the chloroform ($CHCl_3$), dichloromethane ($CH_2Cl_2$), and methanol ($CH_3OH$) solvents, respectively. $CH_2Cl_2$ is the solvent used in the TD-DFT computations on the S1−S11 and D1−D11 systems because the experimental absorption spectrum of $S_{ref}$ was obtained in that solvent[59] and the absorption spectrum of BODIPY is relatively insensitive to the solvent.[39] $CHCl_3$ and $CH_3OH$ were only used in the TD-DFT calculations on the dyad shown in Scheme 2 and the isolated BODIPY B to compare them with the electron absorption spectrum reported for $D_{ref}$ and $B_{ref}$ in such solvents, respectively.[52] All of the relevant molecular orbitals involved in the electronic transitions of each system were computed.

On the other hand, the aromaticity of all of the structures located was investigated in terms of the magnetic criterion based on NICS (nucleus-independent chemical shift) calcu-



DOI: 10.1021/acs.jpcc.9b05136
J. Phys. Chem. C 2019, 123, 19362−19375

lations[62,63] using the Gauge-including atomic orbital (GIAO) method in conjunction with the B3LYP/6-311G(d,p) level of theory. NICS values were computed at the ring critical point (RCP) located inside the oxasmaragdyrin macrocycle, NICS(0). Some theoretical studies on related systems recommend computing the NICS not at the geometric center but at the point of lowest density in the ring plane, i.e., at the RCP.[64] This recommendation has proven to be particularly appropriate in the case of heterocyclic or metalloaromatic compounds, where the RCP is usually displaced from the geometric ring center. Here, RCPs were detected by making a topological analysis of the electron density based on the atoms-in-molecules theory of Bader (AIM)[65−67] using the AIMAll program.[68] Although other NICS definitions like that computed at 1 Å above RCP, NICS(1), and its out-of-plane tensor component, NICS(1)zz, were recommended as a better measure of the $\pi$ electron delocalization compared to NICS(0),[69,70] the former indices are not adequate to measure the macrocycle aromaticity of twisted-Hückel conformations of expanded porphyrins.[71] Therefore, in the present work, we only consider NICS(0) values. Magnetically induced current densities were also calculated at the B3LYP/6-311G(d,p) level using the AIMAll program.[72,73] The analyses of calculated current densities and current pathways have proved to be useful for obtaining a more detailed picture of the aromatic pathways in porphyrin systems.[74−76] A better understanding of the aromatic properties may help in designing porphyrinoids with selected properties.

In order to evaluate the electronic transport properties of the dyads, the molecular junction systems composed of each of the aforementioned structures were anchored to two Au(111) nanowires by means of thiol groups. These properties were calculated using the Nanodcal program suite,[77] which is based on a combination of DFT with the Keldysh nonequilibrium Green's function (NEGF) formalism.[78] To this end, the molecular structure of each dyad with two of their terminal hydrogen atoms substituted for S−Au groups was optimized at the DFT level of theory (BP86[40,79]/def2-SVP[80,81]) with the D3 Grimme's dispersion correction. To represent the gold atoms, the relativistic Stuttgart pseudopotentials were employed. Then these atoms were attached to the hollow site of the Au (111) electrode extensions.

For calculation of the transport properties, all of the atoms were represented by a double-$\zeta$-polarized (DZP[82,83]) basis set using the PBE96[84] exchange-correlation functional. The mesh cutoff energy was set to 150 Ry for both the real and the reciprocal space grids in all calculations with a self-consistency tolerance for the convergence of the Hamiltonian and density matrices of $3.6 \times 10^{-6}$ au.

## 3. RESULTS AND DISCUSSION

**3.1. Molecular Structures.** In this section the planarity of the oxasmaragdyrin is analyzed, first as an isolated fragment, then when linked to the different bridges, and finally when those bridges connect the porphyrin derivative with the BODIPY moiety.

From the structural point of view, oxasmaragdyrin (S1) is an expanded porphyrin made of five rings and three meso carbon atoms. As an isolated fragment it strongly deviates from planarity with a root-mean-square deviation (RMSD) of 0.31 Å with respect to the best plane defined by the atoms of the core of the porphyrin that involves the pyrrole rings (see Scheme 3). $\beta$ carbon atoms of R2 and R5 rings stand below the reference plane, yielding a dome geometry for the macrocycle. When bridges are connected to C17 (S2−S11), the planarity of the oxasmaragdyrin macrocycle increases, regardless of the nature of the bridge, as it is reflected in the lower RMSD values collected in Table 1 for S2−S11. These values go from 0.12 (S3, S4, S6) to 0.05 Å (S9). Bridges in S7, S9, S10, and S11 provide a phenyl derivative ring directly linked to S1 and render large planarity of the macrocycle. As an illustration, Figure S1 shows a molecular view of the oxasmaragdyrins with the highest (S1) and lowest (S9) RMSD values. The joining of the BODIPY moiety to the corresponding oxasmaragdyrin hardly affects the planarity of the porphyrin derivative (ΔRMSD is always lower than 0.08 Å, as seen in the last column of Table 1). The only exception is D1, since in this case the unsubstituted nonplanar S1 becomes a C17-substituted oxasmaragdyrin with a degree of planarity very similar to most of the other dyads (its RMSD reduces in 0.21 Å).

**Table 1. Root-Mean Square Deviation (RMSD, Å) of the Non-Hydrogen Atoms of the Oxasmaragdyrin Core to the Best Plane Fitting the Set of Cartesian Coordinates of Such Atoms by a Least-Squares Method for the Different Oxasmaragdyrins and Their Respective Dyads Investigated at the B3LYP/6-311G(d,p) Level and the Difference between them (ΔRMSD, Å)**

| oxasmaragdyrin | RMSD | dyad | RMSD | ΔRMSD |
|---|---|---|---|---|
| S1 | 0.31 | D1 | 0.11 | −0.21 |
| S2 | 0.09 | D2 | 0.15 | 0.06 |
| S3 | 0.12 | D3 | 0.14 | 0.03 |
| S4 | 0.12 | D4 | 0.13 | 0.01 |
| S5 | 0.13 | D5 | 0.11 | −0.02 |
| S6 | 0.12 | D6 | 0.11 | −0.01 |
| S7 | 0.08 | D7 | 0.11 | 0.03 |
| S8 | 0.11 | D8 | 0.14 | 0.03 |
| S9 | 0.05 | D9 | 0.13 | 0.08 |
| S10 | 0.06 | D10 | 0.13 | 0.06 |
| S11 | 0.11 | D11 | 0.11 | 0.00 |

Structurally speaking, it is interesting to mention the relative orientation of both end moieties in the dyads (see Figure S2). In the absence of a bridge, as in D1, the oxasmaragdyrin macrocycle and the BODIPY core lie in almost perpendicular planes. Thus, steric repulsions between neighbor H atoms in the binding region are minimized. A nearly perpendicular orientation of the planes containing both terminal cycles is also found for D2, D4, D7, D8, and D10. In the remaining dyads both units are almost coplanar, although as the length of the bridge increases, their relative orientation depends more on the nature of the bridge than on their own interactions.

**3.2. Spectroscopic Properties.** *Calibration of the Density Functional.* To obtain theoretically the electronic absorption spectra of the dyads and to analyze their corresponding excited states, a calibration method looking for the density functional that best reproduces the experimental data was previously performed for the selected fragments ($S_{ref}$, $B_{ref}$), where the UV−vis spectra are available. Tables 2 and 3 show the characteristic bands calculated for these fragments using the B3LYP, BHandHLYP, CAM-B3LYP, PBE0, wB97X, and TPSSh functionals along with the measured values.[39,59] We include the wavelength (nm), excitation energy (eV), oscillator strength, and deviation of



DOI: 10.1021/acs.jpcc.9b05136
J. Phys. Chem. C 2019, 123, 19362−19375

**Table 2. Excitation Wavelength ($\lambda$) and Energy ($E$), Oscillator Strength ($f$), and Assignment of the Main Absorption Bands of Oxasmaragdyrin ($S_{ref}$) Calculated in $CH_2Cl_2$ and Using the 6-311G(d,p) Basis Set[a]**

| density functional | $\lambda$/nm ($E$/eV), $f$ | band |
|---|---|---|
| B3LYP | 627 (1.98), 0.137 [0.02, 1%] | Q |
| | 600 (2.07), 0.025 [**0.03, 2%**] | Q |
| | 446 (2.78), 1.890 [0.02, 1%] | Soret |
| BHandHLYP | 589 (2.10), 0.022 [0.15, 7%] | Q |
| | 577 (2.15), 0.033 [0.05, 2%] | Q |
| | 403 (3.08), 2.290 [**0.28, 9%**] | Soret |
| CAM-B3LYP | 599 (2.07), 0.030 [0.11, 5%] | Q |
| | 580 (2.14), 0.152 [0.04, 2%] | Q |
| | 404 (3.07) 2.130 [**0.27, 9%**] | Soret |
| PBE0 | 613 (2.02), 0.143 [**0.06, 3%**] | Q |
| | 589 (2.10), 0.026 [0.01, 0,3%] | Q |
| | 436 (2.84), 1.990 [0.04, 2%] | Soret |
| wB97X | 613 (2.02), 0.016 [0.06, 3%] | Q |
| | 521 (2.38) [0.28, 12%] | Q |
| | 375 (3.31), 2.170 [**0.51, 15%**] | Soret |
| TPSSh | 637 (1.95), 0.140 [0.01, 1%] | Q |
| | 605 (2.05), 0.025 [0.05, 2%] | Q |
| | 455 (2.72), 1.820 [**0.07, 3%**] | Soret |
| EXP[b] | 696 (1.78), **633** (1.96) | Q |
| | **591** (2.10), 552 (2.25) | Q |
| | **443** (2.80) | Soret |

[a]Experimental deviation[59] in square parentheses (eV, %). [b]Experimental wavelengths[59] selected for comparison and largest deviations are displayed in bold.

**Table 3. Excitation Wavelength ($\lambda$) and Energy ($E$), Oscillator Strength ($f$), and Assignment of the Main Absorption Bands of BODIPY ($B_{ref}$) Calculated in $CH_3OH$ and Using the 6-311G(d,p) Basis Set[a]**

| density functional | $\lambda$/nm ($E$/eV), $f$ | assignment |
|---|---|---|
| B3LYP | 621 (2.00), 0.854 [0.08, 4%] | 1 |
| | 339 (3.66), 0.399 [0.13, 3%] | 2 |
| | 217 (5.72), 0.319 [**1.41, 25%**] | 3 |
| BHandHLYP | 583 (2.13), 0.906 [**0.21, 10%**] | 1 |
| | 352 (3.52), 0.696 [0.01, 0.4%] | 2 |
| | 296 (4.19), 0.588 [0.11, 3%] | 3 |
| CAM-B3LYP | 589 (2.11), 0.872 [**0.19, 9%**] | 1 |
| | 353 (3.52), 0.744 [0.02, 0.5%] | 2 |
| | 296 (4.19), 0.639 [0.12, 3%] | 3 |
| PBE0 | 610 (2.03), 0.896 [0.11, 6%] | 1 |
| | 331 (3.74), 0.564 [0.21, 6%] | 2 |
| | 212 (5.84), 0.371 [**1.53, 26%**] | 3 |
| wB97X | 578 (2.14), 0.877 [0.22, 10%] | 1 |
| | 323 (3.83), 1.134 [**0.30, 8%**] | 2 |
| | 275 (4.51), 0.373 [0.21, 5%] | 3 |
| TPSSh | 628 (1.98), 0.855 [0.06, 3%] | 1 |
| | 353 (3.51), 0.380 [0.02, 1%] | 2 |
| | 293 (4.24), 0.289 [**0.07, 2%**] | 3 |
| EXP[b] | 646 (1.92), 100[c] | 1 |
| | 351 (3.53), 35.7 | 2 |
| | 288 (4.31), 16.0 | 3 |

[a]Experimental deviation[39] in square parentheses (eV, %). [b]Experimental wavelengths selected for comparison and largest deviation are displayed in bold.[39] [c]Extinction coefficients in %.

the theoretical values with respect to the experimental ones (in eV and %).

For oxasmaragdyrin ($S_{ref}$) we note that all of the functionals predict bands in the visible region, two weak Q bands, and one strong Soret band, as expected for an expanded porphyrin. Obtaining in the calculations two Q bands instead of four occurs because the bands given by TD-DFT are not pure states but a combination of electronic transitions. The Q band at the longest wavelength corresponds in all of the functionals to H-1 → L+1 and H → L transitions of the Q (1−1) and Q (0−0) types, respectively, while the Q band at the lowest wavelength corresponds to H-1 → L and H → L+1 transitions of the type Q (1−0) and Q (0−1) types, respectively.

The theoretical bands for $S_{ref}$ are compared to the Q bands measured at 633 and 591 nm and to the Soret band at 443 nm.[59] The lowest deviations for both types of bands are found for B3LYP (0.03 eV), PBE0 (0.06 eV), and TPSSh (0.07 eV), which for the TD-DFT methodology are considered as negligible errors. These three functionals share the characteristic that they are hybrid functionals with a similar contribution of Hartree−Fock (HF) exact electronic exchange energy, 20%, 28%, and 13%, respectively. Range-separated functionals like CAM-B3LYP and wB97X predict larger errors of up to 0.27 and 0.51 eV, respectively, which may be attributed to the larger contribution of HF exchange for long-range terms of 65% and 100%, respectively. BHandHLYP with 50% HF exchange generates a deviation of up to 0.28 eV, similar to CAM-B3LYP, although somewhat smaller than that of wB97X, and represents an important error for TD-DFT calculations. On the basis of the results it is clear that functionals with a percentage of HF exchange greater than 28% do not describe well the absorption bands of oxasmaragdyrin $S_{ref}$. It is a macrocycle with a strongly covalent electronic structure with high delocalization of $\pi$-electrons. Nonbonding interactions can occur between the lone pairs of the oxygen atoms and the closest inner hydrogen atoms of the pyrrole rings. However, they do not represent interactions of large magnitude.

In the case of BODIPY ($B_{ref}$), all of the functionals predict three bands as experimentally observed (646, 351, and 288 nm), one of them in the visible region and the other two in the UV region. The deviations obtained with the hybrid functionals are much higher than those obtained for $S_{ref}$, 1.41 and 1.53 eV for B3LYP and PBE0, respectively. The TPSSh functional predicts the same small error (0.07 eV) as for $S_{ref}$. The range-separated functionals present a better behavior than for $S_{ref}$ with 0.19 and 0.30 eV deviations for CAM-B3LYP and wB97X, respectively. BHandHLYP predicts similar values to CAM-B3LYP (0.21 eV). In the case of BODIPY, the range-separated functionals lead to a better description of the excited states than for $S_{ref}$. It could be attributed to the $BF_2$ group, where the fluorine atoms present nonbonding interactions as hydrogen bonding with the closer hydrogen atoms.

Taking into consideration all that was mentioned above, TPSSh is the functional showing the best agreement with the experimental data of both oxasmaragdyrin $S_{ref}$ and BODIPY $B_{ref.}$

The same functionals were also tested for the reference dyad ($D_{ref}$) (Schemes 2 and S1c) whose molecular structure is very similar to D7 and D8 of our work (Scheme 3). The molecular structure of $D_{ref}$ was also optimized at the B3LYP/6-311G(d,p) level. We found that all of the functionals show important errors, except TPSSh (0.01 eV), especially for the BODIPY band with deviations in the range of 0.42−0.50 eV. A comparison between the theoretical (TPSSh) and the experimental electronic absorption spectra for $D_{ref}$ is shown



DOI: 10.1021/acs.jpcc.9b05136
J. Phys. Chem. C 2019, 123, 19362−19375

in Figure 1 (see also Table S1). As can be seen, there is an excellent agreement between the experimental and the

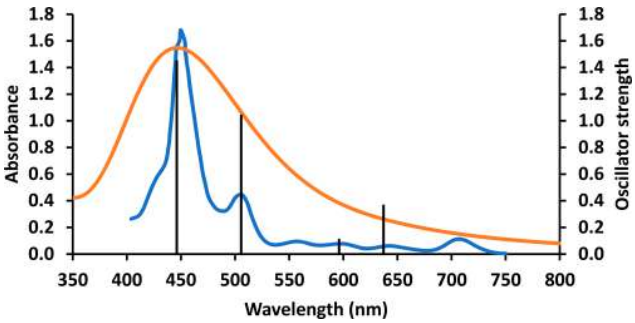


**Figure 1.** Comparison between the experimental (blue) and the theoretical (TPSSh, orange) electronic absorption spectrum of $D_{ref}$. Black lines correspond to the theoretical absorption values for the Soret, Q, and BODIPY bands.

theoretical results for this system. In the 550−710 nm region four small bands assigned as Q bands were observed experimentally. The TPSSh functional predicts two of them with a deviation of 0.01 eV. In addition, both the Soret and the BODIPY bands are well predicted with deviations of 0.05 and 0.01 eV, respectively.

In summary, we demonstrated that the TPSSh functional predicts adequately the optical properties of this kind of molecular systems; therefore, we choose it for making the study of the electronic absorption properties of the new dyads.

*Photophysical Properties.* Calculated photophysical properties for the oxasmaragdyrins S1−S11 and their corresponding dyads D1−D11 shown in Scheme 3 and calculated at the TPSSh/6-311G(d,p) level of theory in $CH_2Cl_2$ are presented in Table 4. Excitation wavelength and energy for each characteristic band of both oxasmaragdyrin and BODIPY fragments are included in that table. Details about the oscillator strength and the electronic transition associated with each band of the dyads are shown in Table S2.

All of these compounds retain the characteristic Q and Soret absorption bands of the reference oxasmaragdyrin $S_{ref}$ as well as the typical visible absorption band of the reference BODIPY $B_{ref}$ in the case of the dyad systems. Let us now discuss the effect of bridging groups on these bands, first for S2−S11 and then for D1−D11.

Concerning the comparison of the photophysical properties of S2−S11 with those of S1, all of the bridges cause an increase of the wavelengths of the Q and Soret bands ($\lambda_Q$ and $\lambda_{Soret}$, respectively) except for S2, that is, linkage of the alkyl group $CH_3-CH_2-CH_2-$ to S1 decreases the two $\lambda_Q$ by 21 and 5 nm, respectively, and $\lambda_{Soret}$ by 6 nm. At S3, with one acetylene (Ace) group bonded to S1, all of the absorption bands are red shifted by 24 and 22 nm (Q bands) and 15 nm (Soret band). Addition of a methyl group at the end of the chain, as in S4, hardly affects the position of the absorption bands with respect to S3. However, addition of either more acetylene units, as in S5 and S6, or a phenyl group, as in S8, increases the $\lambda_Q$ bands between 54 and 83 nm and $\lambda_{Soret}$ by more than 20 nm, which indicates the existence of conjugation between S1 and linkers with an acetylene moiety directly bonded to it.

When a phenyl group is directly attached to S1, as in S7, the two $\lambda_Q$ values hardly increase, while an increase of 21 nm was found for the $\lambda_{Soret}$ value. Similarly, one biphenyl group replacing the phenyl, as in S9, renders $\lambda_Q$ and $\lambda_{Soret}$ values only slightly greater than those of S1. The small effect of the bridges with phenyl and biphenyl connections to S1 comes from the absence of coplanarity between these rings and S1, thus hindering the electron delocalization. Surprisingly, S10 and S11, with an anthracene group in the chain and no possible expansion of the electron density from the oxasmaragdyrin to the nearly perpendicular bridge rings, show $\lambda_Q$ and $\lambda_{Soret}$ values much larger than those of S1, mainly for S10, where the anthracene directly binds to S1.

**Table 4. Excitation Wavelength ($\lambda$) and Energy ($E$) and Assignment of the Main Absorption Bands of the Oxasmaragdyrins S1−S11 and the Corresponding Dyads D1−D11 Calculated at the TPSSh/6-311G(d,p) Level of Theory in the Solution Phase ($CH_2Cl_2$)**

| | $\lambda$/nm ($E$/eV) | band | | $\lambda$/nm ($E$/eV) | band |
|---|---|---|---|---|---|
| S1 | | | D1 | 640 (1.94) | BODIPY |
| | 636 (1.95) | Q | | 635 (1.95) | Q |
| | 588 (2.11) | Q | | 599 (2.07) | Q |
| | 437 (2.84) | Soret | | 438 (2.83) | Soret |
| S2 | | | D2 | 629 (1.97) | BODIPY |
| | 615 (2.02) | Q | | 626 (1.98) | Q |
| | 583 (2.13) | Q | | 587 (2.11) | Q |
| | 431 (2.88) | Soret | | 437 (2.83) | Soret |
| S3 | | | D3 | 555 (2.23) | BODIPY |
| | 660 (1.88) | Q | | 622 (1.99) | Q |
| | 610 (2.03) | Q | | 582 (2.13) | Q |
| | 452 (2.74) | Soret | | 459 (2.70) | Soret |
| S4 | | | D4 | 639 (1.94) | BODIPY |
| | 653 (1.90) | Q | | 662 (1.87) | Q |
| | 608 (2.04) | Q | | 610 (2.03) | Q |
| | 452 (2.74) | Soret | | 453 (2.74) | Soret |
| S5 | | | D5 | 569 (2.18) | BODIPY |
| | 690 (1.80) | Q | | 656 (1.89) | Q |
| | 629 (1.97) | Q | | 581 (2.13) | Q |
| | 459 (2.70) | Soret | | 459 (2.70) | Soret |
| S6 | | | D6 | 585 (2.12) | BODIPY |
| | 719 (1.72) | Q | | 688 (1.80) | Q |
| | 650 (1.91) | Q | | 605 (2.05) | Q |
| | 472 (2.63) | Soret | | 479 (2.59) | Soret |
| S7 | | | D7 | 707 (1.75) | BODIPY |
| | 643 (1.93) | Q | | 642 (1.93) | Q |
| | 596 (2.08) | Q | | 594 (2.09) | Q |
| | 458 (2.71) | Soret | | 448 (2.77) | Soret |
| S8 | | | D8 | 667 (1.86) | BODIPY |
| | 691 (1.79) | Q | | 689 (1.80) | Q |
| | 628 (1.97) | Q | | 624 (1.99) | Q |
| | 470 (2.64) | Soret | | 471 (2.63) | Soret |
| S9 | | | D9 | 705 (1.76) | BODIPY |
| | 640 (1.94) | Q | | 645 (1.92) | Q |
| | 595 (2.08) | Q | | 596 (2.08) | Q |
| | 442 (2.80) | Soret | | 448 (2.77) | Soret |
| S10 | | | D10 | 697 (1.78) | BODIPY |
| | 687 (1.81) | Q | | 675 (1.84) | Q |
| | 625 (1.98) | Q | | 630 (1.97) | Q |
| | 453 (2.74) | Soret | | 453 (2.74) | Soret |
| S11 | | | D11 | 694 (1.79) | BODIPY |
| | 669 (1.85) | Q | | 633 (1.96) | Q |
| | 620 (2.00) | Q | | 596 (2.08) | Q |
| | 449 (2.76) | Soret | | 452 (2.74) | Soret |



DOI: 10.1021/acs.jpcc.9b05136
J. Phys. Chem. C 2019, 123, 19362−19375

Table S2 collects detailed information about the calculated absorption spectra, showing the molecular orbitals (MOs) involved in the transitions. For S9 and mainly S10 and S11 the MO LUMO+2 (L+2) receives electrons in Q and Soret excitations. This orbital is essentially placed in the biphenyl or anthracene moieties, which means that new and low-energy (long wavelength) oxasmaragdyrin → bridge transitions are present.

Let us see now the effect that the bonding of the BODIPY unit to S1−S11 produces on the oxasmaragdyrin absorption bands just described.

For the Soret band the anchorage of B to S1−S11 slightly increases all of the $\lambda_{Soret}$ values in the 0−7 nm range, except for the Ace-phenyl spacer (D7), which causes a decrease of 10 nm when going from S7 to D7. For the Q bands some dyads reduce their $\lambda_Q$ values with respect to those in the corresponding oxasmaragdyrin and others hardly modify them. In the first group, D3, D5, and D6 allow certain B-bridge conjugation that, consequently, reduces the bridge-S one, which explains the reduction in the oxasmaragdyrin $\lambda_Q$ bands. Besides, D10 and mainly D11 also reduce the wavelength of these bands, but now it is due to the presence of large energy transitions starting in the MO HOMO-3 (H-3) located at the anthracene moiety. On the other hand, $\lambda_Q$ values of D1, D2, D4, D7, D8, and D9 keep the value they had in the corresponding oxasmaragdyrins due to isolation of both fragments produced by the nearly perpendicular conformation of close rings (D1, D7, D8, and D9) or by the presence of an alkyl fragment linked with B (D2 and D4). The visible band of B is also affected by the presence of S1−S11. Thus, Table 4 shows that, compared to D1, D2−D6 reduce its value while D7−D11 increase it, making the band of B the one with the largest value. Looking for panchromatism, a large absorption wavelength range is needed, that is, the Soret band, which has the shortest wavelength, should be shifted to even lower values and the band corresponding to the largest wavelength to larger values. Dyads do not significantly reduce the value of the Soret band, while D7−D11 increase the B visible band as just said. Among this group D7 (between 448 and 707 nm) and D9 (between 448 and 705 nm) have the widest absorption range, shifting the gap of isolated oxasmaragdyrin S1 (437−636 nm) toward the IR region.

We also investigated the nature of the bands of both fragments in the dyads in terms of electronic transitions between MOs, and the results are presented in Table S2. The band of isolated BODIPY is mainly a transition H-3 → L or H-2 → L, and it is very similar in the dyads, where the MOs are located in that fragment. In the case of the oxasmaragdyrin fragment, the Q bands are described by the Gouterman orbitals, which are H-1 → L and H → L+1 transitions and H-1 → L+1 transitions. No transitions H → L are found for Q bands in the dyads. Other molecular orbitals such as H-2, L+2, and L+3 also represent a contribution. For the Soret band, we also found H-2 → L+1, H-1 → L+2, H-1 → L+3, and H-2 → L+2 transitions. All of the Q and Soret bands are oxasmaragdyrin → oxasmaragdyrin transitions.

A complete view of the electronic absorption spectra of the dyads D1−D6 is shown in Figures S3 and S4, separated by groups depending of the bridge. Figure S3 shows the systems with an alkyl chain as a bridge, while Figure S4 displays those systems containing rings besides an Acet moiety as bridge.

The appearance in Figure S3 of a wide and intense band at longer wavelengths for dyads D3 (975 nm), D5 (1031 nm), and D6 (1095 nm) is noteworthy , which correspond to separated charge excited states of the oxasmaragdyrin → BODIPY type. In the case of D10 and D11 in Figure S4, the more intense band at about 700 nm corresponds to BODIPY → BODIPY transitions. Charge transfer bands occur at about 990−1200 nm with small oscillator strengths. For comparison, we included D3 in this figure. It is important to mention that analysis of the theoretical absorption spectrum of the dyad $D_{ref}$ shows charge transfer bands in the visible region with very low intensity.

In summary, we have shown that the dyads D3, D5, and D6 present better properties than $D_{ref}$ to be used in dye-sensitized solar cells due to the notorious charge transfer they present.

In order to represent in a more complete manner the excited states we computed the natural transition orbitals (NTO)[85] of the separated charge excited states of the dyads mentioned above (D3, D5, D6). Figure 2 shows NTOs for D6, and Figure S5 presents NTOs for D3 and D5.

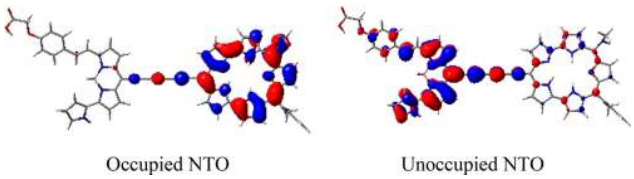


**Figure 2.** Surfaces of natural transition orbitals of the separate charge excited state of dyad D6 computed at the TPSSh/6-311G(d,p) level of theory in the solution phase ($CH_2Cl_2$).

These dyads (D3, D5, D6) show an advantage with respect to other ones in the sense that they absorb in a wider range of the electromagnetic spectrum, achieving a panchromatic absorption and an improvement for being used as photosensitizers in DSSC. The acetylene moiety favors such a panchromatic absorption. The acene groups (D10 and D11) are comparatively less favorable to charge transfer, but they present an increase in the intensity of the BODIPY absorption band (694−697 nm) in the dyad.

**3.3. Aromatic Properties.** The aromaticity of the molecular systems investigated in this work was analyzed on the basis of NICS and magnetically induced density current calculations. All of the species show a ring critical point (RCP) of the electron density inside the macrocycle of the oxasmaragdyrin fragment. The electron density obtained at such an RCP is small and very similar for all of the species studied as the values only vary from 0.0013 to 0.0014 e $Å^{-3}$ (see Table S3 in the Supporting Information).

The aromaticity index NICS(0) calculated at RCP in S1−S11 species varies between −10.7 and −12.4 ppm, thus indicating the aromatic character of the oxasmaragdyrin macrocycle in all of these systems. These values are comparable to the −16.5 ppm value predicted for porphyrins[86] and to the −16.2, −14.9, and −14.1 ppm values predicted for protonated pentaphyrins, sapphyrins, and isosmaragdyrins, respectively.[87,88] As seen in Table 5, taking as reference S1, any group anchored to the C17 atom of this macrocycle (see Scheme 3 for atom numbering) gives rise to a slight increase in the aromaticity of the S1 moiety. For S2−S11 with respect to S1 the greatest increase in the aromaticity was found for S4 (1.1 ppm), S8 (1.1 ppm), S3 (1.4 ppm), S5 (1.6 ppm), and S6 (1.7 ppm). All of these species have in common the presence of at least one triple C≡C bond attached to C17, and the


DOI: 10.1021/acs.jpcc.9b05136
J. Phys. Chem. C 2019, 123, 19362−19375

Table 5. NICS(0), Bond Distances between C17 and the Linker C Atom Bonded to It, HOMO-LUMO Energy Gap ($\Delta E_{H\rightarrow L}$), and Difference in Energy between the LUMO (L′) of $TiO_2$ (−4.3 eV) and the LUMO (L) of S1−S11 and D1−D11 Derivatives ($\Delta E'_{L\rightarrow L'}$) Calculated at the B3LYP/6-311G(d,p) Level of Theory

| species | NICS(0)/ppm | $d$(C17−$C_{linker}$)/Å | $\Delta E_{H\rightarrow L}$/eV | $\Delta E'_{L\rightarrow L'}$/eV |
|---|---|---|---|---|
| S1 | −10.7 | | 2.40 | −2.28 |
| S2 | −11.2 | 1.509 | 2.46 | −2.30 |
| S3 | −12.1 | 1.421 | 2.28 | −2.01 |
| S4 | −11.8 | 1.420 | 2.30 | −2.13 |
| S5 | −12.3 | 1.411 | 2.15 | −1.83 |
| S6 | −12.4 | 1.406 | 2.06 | −1.68 |
| S7 | −11.6 | 1.482 | 2.38 | −2.13 |
| S8 | −11.8 | 1.413 | 2.16 | −1.95 |
| S9 | −11.7 | 1.481 | 2.39 | −2.15 |
| S10 | −11.6 | 1.492 | 2.43 | −2.16 |
| S11 | −11.6 | 1.486 | 2.41 | −2.14 |
| D1 | −12.0 | 1.487 | 1.87 | −1.48 |
| D2 | −11.2 | 1.511 | 1.70 | −1.44 |
| D3 | −12.1 | 1.405 | 1.68 | −1.17 |
| D4 | −12.0 | 1.419 | 1.64 | −1.38 |
| D5 | −12.3 | 1.403 | 1.62 | −1.11 |
| D6 | −12.3 | 1.402 | 1.56 | −1.04 |
| D7 | −11.6 | 1.482 | 1.54 | −1.18 |
| D8 | −12.0 | 1.411 | 1.71 | −1.35 |
| D9 | −11.4 | 1.484 | 1.44 | −1.14 |
| D10 | −11.5 | 1.493 | 1.54 | −1.16 |
| D11 | −11.4 | 1.485 | 1.44 | −1.12 |

greater the number of the alternate C≡C triple bonds, the higher the absolute value of NICS(0) and so the aromaticity.

On the other hand, S7 and S9−S11, with an aromatic ring directly linked to C17, show a moderate rise of the aromaticity index of about 0.9−1.0 ppm. The number and type of the aryl ring do not seem to have a significant influence on the oxasmaragdyrin aromaticity. Finally, the smallest rise in the NICS(0) index was found for S2 (0.5 ppm). NICS(0) values vary from −11.2 to −12.3 ppm. When comparing NICS(0) values for S1−S11 with their corresponding dyads, D1−D11, hardly any change is observed (−0.1−0.2 ppm) except when oxasmaragdyrin is directly linked to BODIPY (1.3 ppm). The presence of the BODIPY moiety does not practically affect the aromaticity of the macrocycle and the trends found for S2−S11 unless when it directly attaches S1.

To get a broader knowledge of the aromaticity of the oxasmaragdyrin fragment in this kind of molecular systems we also carried out magnetically induced current density calculations. To visualize the motion of electrons in such systems, streamline plots of the current densities calculated in a plane placed 1 Å above the molecular plane and current pathways obtained by numerical integration of the current densities passing chemical bonds are shown in Figure 3 (see also Figure S6).

To obtain reliable current density maps the greatest disadvantage comes from the deviation of the planarity of the oxasmaragdyrin macrocycle. Table 1 shows the RMSD of the non-hydrogen atoms of the oxasmaragdyrin macrocycle to the best plane obtained fitting with the Cartesian coordinates of such atoms by the least-squares method. A greater value of RMSD means lower planarity of the oxasmaragdyrin macrocycle. For such kind of nonplanar species it is difficult to define

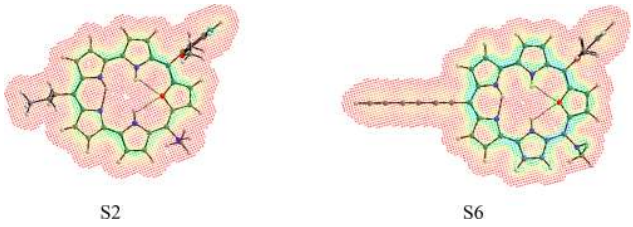


Figure 3. Current density trajectories which intersect a plane 1.0 Å above the nuclear plane of the oxasmaragdyrin macrocycle for S2 and S6 and induced by a magnetic field applied along the +Z axis, i.e., coming out of the page. Arrows indicate the direction of current flow. Arrows in blue are associated with higher current densities, while arrows in red are ascribed to lower current densities. Counterclockwise flow is paramagnetic, whereas clockwise flow is diamagnetic.

accurate current density maps. Under these circumstances we focus on the species showing the largest aromatic index for the oxasmaragdyrin macrocycle, i.e., S6, and on the species displaying the least aromatic index for the macrocycle, i.e., S2 (see density maps for the remaining oxasmaragdyrin compounds in Figure S6). As can be seen in Figure 3, the current density flows through all of the bonds implying the non-hydrogen atoms of the macrocycle of S6 in the clockwise direction, thus indicating the diatropic character of the ring current. Following the clockwise direction, the current density splits at each pyrrole ring into an inner C−N/O and an outer all carbon route. The outer route is preferred over the inner one. The presence of an alkyl group bonded to C17 in S2 decreases the current density flowing along the oxasmaragdyrin macrocycle, in agreement with the smaller NICS(0) index compared to that found in the case of S6, where the current density splits at each ring, with the outer route preferred over the inner one for all of the rings except R4 (see Scheme 3 for ring numbering).

Trying to find an explanation for the above-mentioned trends, we investigated the relationship of the oxasmaragdyrin aromaticity with the planarity of such a macrocycle, the HOMO−LUMO energy gap, and the charge transport (see Tables 1, 5, and S4) of the whole set of molecular systems. In general, apart from S1, there is an anticorrelation between aromaticity and planarity. The smallest degree of planarity of the macrocycle corresponds to S1, which has the lowest absolute value for NICS(0), that is, it is the least aromatic compound. S3−S6 and S8 are also far from planarity (RMSD around 0.12 Å), although they show the largest aromaticity (the absolute value of NICS(0) is greater than or equal to 11.7 ppm). The presence of alternating C≡C triple bonds seems to be better for the electron delocalization from the macrocycle to the bridge. Looking at Table 5, these most aromatic systems, S3−S6 and S8, present the shortest distances between C17 in the oxasmaragdyrin and the bridge (1.421−1.406 Å and 1.405−1.402 Å, respectively), thus confirming a better electron delocalization. The greatest degree of planarity was found for S10 (RMSD = 0.06 Å) and S9 (RMSD = 0.05 Å), which present moderate negative NICS(0) values around −11.6 ppm, indicative of low aromaticity. In these systems the distance between C17 and the bridge is large (1.481 Å for S9 and 1.492 Å for S10), thus indicating no delocalization of the electron density toward the linker. System S2 behaves similarly to the oxasmaragdyrins with an aromatic ring directly linked to S1. It should be noted that dyads show a slight loss of planarity compared to their respective oxasmaragdyrin fragments, except



DOI: 10.1021/acs.jpcc.9b05136
J. Phys. Chem. C 2019, 123, 19362−19375

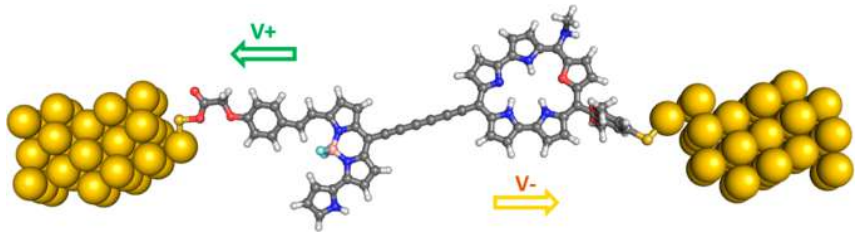


**Figure 4.** Scattering zone atomic structure for the studied molecular junction system composed of Au(111)−D6−Au(111). Both electrodes (yellow) extend to infinity in the transport direction *z*. Dyad is anchored to the electrode by one sulfur atom.

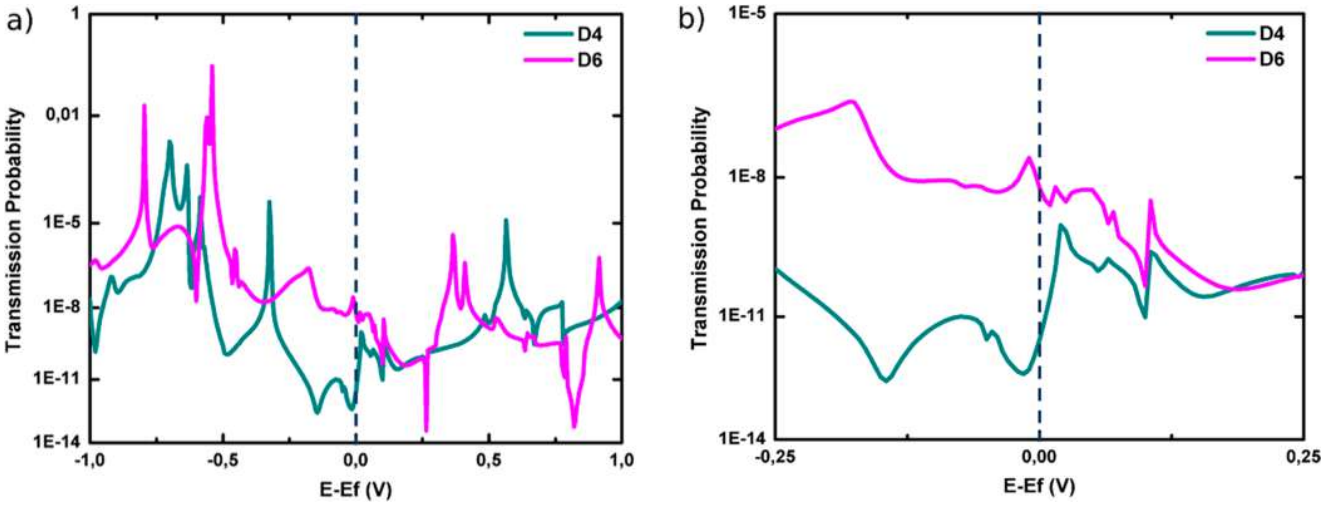


**Figure 5.** (a) Transmission probability for dyads D4 and D6. (b) Enlargement of the energy region closer to the Fermi level.

for D1, D5, and D6. The relationships among planarity, aromaticity, and C17−$C_{bridge}$ bond distance found for S2−S11 also hold for D2−D11.

Concerning the HOMO−LUMO energy gap, for the isolated oxasmaragdyrins the smallest values were found for S6 (2.06 eV), S5 (2.15 eV), and S8 (2.16 eV) and the largest for S11 (2.41 eV) and S10 (2.43 eV). This trend is reversed when analyzing the HOMO−LUMO energy gaps for the corresponding dyads, as D3−D6 show here larger energy gaps than D10 and D11. It should be noted that when going from S1−S11 to the corresponding D1−D11, the HOMO−LUMO energy gap decreases in the range of 0.47−0.97 eV (see Table 5), mainly due to the greater stabilization of the LUMO compared to that of the respective HOMO (see Table S4). We also found that all dyads studied here, with the exception of D1, D2, and D8, present smaller values for the HOMO−LUMO energy gap than $D_{ref}$ (1.71 eV).

The HOMO−LUMO energy gaps obtained for S1−S11 are in line with those obtained for porphyrin and other related systems.[18,89,90] Smaller values were found for the D1−D11 dyads, and this trend is in principle good for DSSC applications.[18] The LUMO energy level of S1−S11 and D1−D11 is always greater than the reported value of −4.3 eV for the edge level conduction band (CB) of $TiO_2$ (LUMO′)[3,91,92] (negative values for the LUMO → LUMO′ energy gap), thus favoring electron injection in the CB of $TiO_2$. For S1−S11 and D1−D11, the most aromatic systems show small LUMO′−LUMO energy gaps.

Indeed, S5 and S6 present energy gaps of −1.83 and −1.68 eV (the smallest in the absence of BODIPY), respectively, while values of −1.11 and −1.04 eV were found in the case of the corresponding dyads. We also note that D11 (−1.12 eV) shows a value similar to that found for D5 and D6. In the case of $D_{ref}$, a similar trend is obtained with a value of −1.21 eV.

For the recovery of the dye after injection and charge transport, a mediator is needed and the dye's HOMO energy level has to be lower than the redox potential of the mediator ($E_{redox}$).[18,89−93] For instance, in the case of the common $I^-/I_3^-$ mediator its redox potential amounts to −4.8 eV.[93] Comparing the HOMO of S1−S11 and D1−D11 with −4.8 eV, D6 (−4.82 eV), D5 (−4.81 eV), and D3 (−4.80 eV), they are the only systems whose HOMO is slightly less than or equal to the reference value. Again, it seems there is a positive correlation between aromaticity and the $HOMO_{dye}-E_{redox}$ energy gap.

**3.4. Charge Transport.** Taking into account the charge transfer (CT) band shown in the absorption spectra, as an illustration, we calculated the electronic transport properties for two dyads: one with a significant CT band (D6) and the other without it (D4). Figure 4 shows the molecular junction system for D6 and the current direction as a function of the voltage sign (see arrows).

For the two studied systems the conductance values obtained through DFT-NEGF methods were very small with values around $10^{-12}$ and $10^{-9}$ $G_0$ for D4 and D6, respectively. However, despite the low conductance of both systems, a remarkable difference in conductivity is seen between them with the conductance of the system presenting D6 as a molecular bridge, around 3 orders of magnitude greater than that of its counterpart featuring D4, thus allowing us to expect that the electron transport is favored on the former. This trend could be confirmed by analyzing the energy-resolved transmission probabilities for both dyads shown in Figure 5a for an


DOI: 10.1021/acs.jpcc.9b05136
J. Phys. Chem. C 2019, 123, 19362−19375

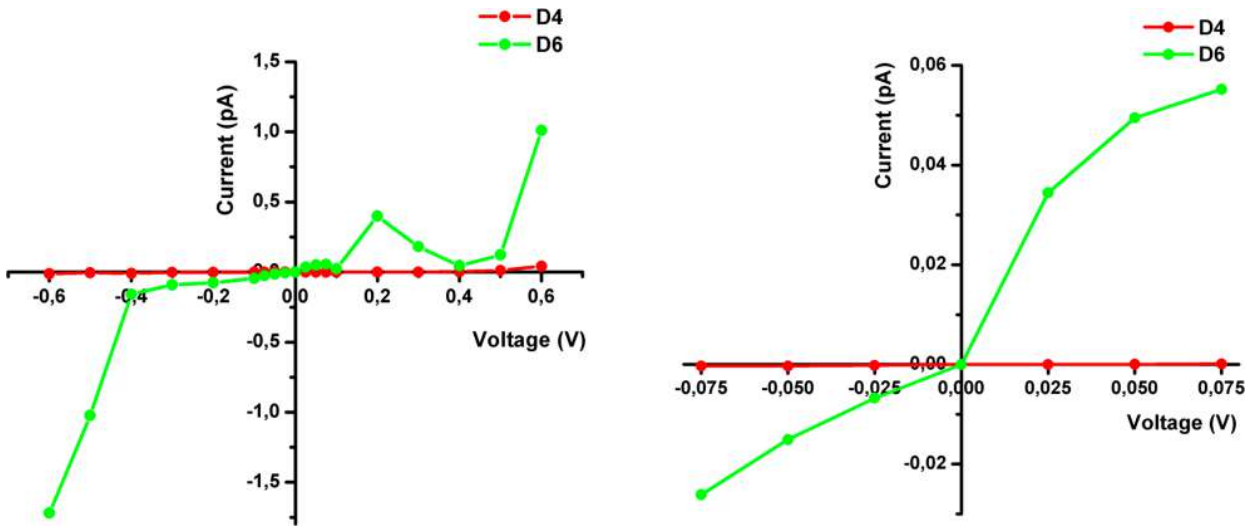


**Figure 6.** Current through Au111−D6(D4)−Au111 molecular device versus bias voltage.

energy range between −1.0 and 1.0 eV with respect to the Fermi level and in more detail from Figure 5b, where the transmission probabilities were depicted from −0.25 to 0.25 eV. It is seen that the system containing D6 has a significantly higher transmission probability in the proximities of the Fermi level, confirming the claim stated above.

The current−voltage ($I$−$V$) profiles obtained for both systems for voltage ranges between −0.6 and 0.6 V and −0.075 and 0.075 V are presented in Figure 6.

Both systems exhibit small current values with strong differences between them for a given voltage, and for the system containing D6 the current is around 2 orders of magnitude greater for all of the studied voltage ranges. This behavior is consistent with the values obtained above for the zero-bias conductance (Figure 6b), where the device composed of D6 shows a conductance of around 3 orders of magnitude greater than the D4 junction. Also, an asymmetric behavior is seen for both systems, with the direction of the current depending on the applied voltage sign. For positive voltage values the current direction is from oxasmaragdyrin to BODIPY and backward if a negative bias voltage is applied. Our results confirm that the acetylene moieties favor the charge transport in the dyad.

**3.5. Formation of the Dyads.** To check if the synthesis of $D_{ref}$ reported by Kalita et al.[37] (see Scheme 2) could be thermodynamically favorable for the synthesis of 11 dyads considered in this work, we calculated the Gibbs free energy change in toluene ($\Delta G_{solution}$) (see Table 6) for the reaction between the corresponding fragments as well as the reference one for comparison purposes (see Scheme S2). For the sake of computational economy, we replaced I by Br, since both are similar good leaving groups.

$\Delta G_{solution}$ values are negative, indicating that formation of the dyads studied here is favorable. It means that all of them are stable and possible to be synthesized in the laboratory. However, dyads D1, D2, D4, and D8 have $\Delta G_{solution}$ values less negative than the reference dyad ($D_{ref}$). The remaining theoretical dyads produce more exergonic reactions than the experimental one, indicating that their stabilities are more favored.

The kind of bonding between BODIPY and oxasmaragdyrin clearly affects the stability of the dyad. Thus, bonding of BODIPY to $sp^3$ (like in D2 and D4) and $sp^2$ (like in D1 and D8) carbon atoms renders less stable dyads, whereas linking of BODIPY to an sp carbon atom (D3, D5, D6, D7, D9, D10, and D11) yields the most stable dyads. This seems to be a factor strongly affecting the exergonic character of the formation reaction of the dyads.

**Table 6. $\Delta G_{solution}$ Values (kcal/mol) for the Formation of the Dyads Calculated at the B3LYP/6-311G(d,p) Level of Theory in Toluene[a]**

| dyad | $\Delta G_{solution}$ | dyad | $\Delta G_{solution}$ |
|---|---|---|---|
| $D_{ref}$[b] | −13.68 | D6 | −21.37 |
| D1 | −9.88 | D7 | −20.92 |
| D2 | −9.74 | D8 | −9.14 |
| D3 | −22.54 | D9 | −20.88 |
| D4 | −4.23 | D10 | −21.29 |
| D5 | −21.85 | D11 | −21.44 |

[a]For comparison purposes, the reference dyad is included . [b]Reference 37.

## 4. CONCLUSIONS

A density functional study of oxasmaragdyrin with 2,6-dimethoxyphenyl and methylamine groups in two of its meso carbons (S1) and the 4,4-difluoro-4-bora-3a,4a-diaza-s-indacene (BODIPY, B) combined with alkyl, alkynyl, and aryl groups or combination of them forming dyads was carried out at the B3LYP/6-311G(d,p) and TPSSh/6-311G(d,p) levels of theory.

The study focused on the study of the influence of several bridging functional groups between B and S1 on a set of properties of the BODIPY−oxasmaragdyrin dyads: UV−vis electron absorption, aromaticity, and charge transport.

Our results show that acetylene moieties as linkers between BODIPY and oxasmaragdyrin in the dyads favor formation of separate charge excited states and also a panchromatic absorption.

On the other hand, evaluation of NICS(0) and the magnetically induced current density for the oxasmaragdyrin fragment in the dyad and in its isolated form showed an agreement in the aromaticity. We found that the higher the aromaticity of the oxasmaragdyrin macrocycle, the greater the



DOI: 10.1021/acs.jpcc.9b05136
J. Phys. Chem. C 2019, 123, 19362−19375

capacity for light harvesting in a broader region of the electromagnetic spectrum. For all of the oxasmaragdyrin fragments and the dyads, the LUMO′−LUMO energy gaps indicate that the electron injection toward $TiO_2$ is favored and the $HOMO_{dye}-E_{redox}$ energy gaps are enough to regenerate the dye. In summary, the results suggest that the investigated dyads may be used in DSSCs.

Using NEGF calculations for the D4 and D6 dyads we showed that the D6 system with three acetylene moieties is a better conductor than D4, in agreement with the charge transfer results obtained from the photophysical properties.

Finally, the exergonic character of the reactions for the formation of the studied dyads, following the Kalita's procedure, suggests that they could be synthesized.

## ■ ASSOCIATED CONTENT

### Supporting Information

The Supporting Information is available free of charge on the ACS Publications website at DOI: 10.1021/acs.jpcc.9b05136.

View of the optimized molecular structures, calculation of the photophysical parameters and assignment of bands, simulated electronic absorption spectra, view of the natural transition orbitals of dyads, calculations of the electron density $\rho(r)$ and Laplacian of $\rho(r)$, graphics of current density trajectories, frontier molecular orbitals (HOMO, LUMO), and proposed reaction for the formation of BODIPY−oxasmaragdyrin dyads (PDF)

## ■ AUTHOR INFORMATION


### Corresponding Authors

*E-mail: rlopez@uniovi.es.

*E-mail: gloria.cardenas@usach.cl.

### ORCID

M. Isabel Menéndez: 0000-0002-5062-4319

Ramón López: 0000-0001-8899-705X

Gloria Cárdenas-Jirón: 0000-0003-4305-8088


### Notes

The authors declare no competing financial interest.

## ■ ACKNOWLEDGMENTS

We are thankful for the financial support from CONICYT/CHILE under FONDECYT Project 1171719 (G.C.-J.) and USACH/CHILE under DICYT 021841CJ Postdoctoral Project (N.M.-P., G.C.-J), Proyecto Fortalecimiento USACH USA1799_CG241216 (G.C.-J.), and DICYT-Universidad de Santiago de Chile. We also acknowledge CONICYT-PCHA/Doctorado Nacional/2015-21150093 for a Doctoral Fellowship for M.B.-M. and for financial support to perform a research stay at the Universidad de Oviedo (Spain) under the supervision of Professor Ramón López, where part of this work was carried out. Powered@NLHPC: This research was partially supported by the supercomputing infrastructure of the NLHPC (ECM-02) of the Universidad de Chile. R.L., M.I.M., and D.A. also thank the Ministerio de Economía y Competitividad (Grant No. CTQ2015-70231-P) and Universidad de Oviedo (Grant No. PAPI-18-PF-05) of Spain for their financial support.

## ■ REFERENCES

(1) Vlachopoulos, N.; Liska, P.; Augustynski, J.; Graetzel, M. Very efficient visible light energy harvesting and conversion by spectral sensitization of high surface area polycrystalline titanium dioxide films. *J. Am. Chem. Soc.* **1988**, *110* (4), 1216−1220.

(2) O'Regan, B.; Grätzel, M. A low-cost, high-efficiency solar cell based on dye-sensitized colloidal TiO2 films. *Nature* **1991**, *353*, 737.

(3) Hagfeldt, A.; Graetzel, M. Light-Induced Redox Reactions in Nanocrystalline Systems. *Chem. Rev.* **1995**, *95* (1), 49−68.

(4) Kay, A.; Grätzel, M. Low cost photovoltaic modules based on dye sensitized nanocrystalline titanium dioxide and carbon powder. *Sol. Energy Mater. Sol. Cells* **1996**, *44* (1), 99−117.

(5) Kalyanasundaram, K.; Grätzel, M. Applications of functionalized transition metal complexes in photonic and optoelectronic devices. *Coord. Chem. Rev.* **1998**, *177* (1), 347−414.

(6) Hagfeldt, A.; Grätzel, M. Molecular Photovoltaics. *Acc. Chem. Res.* **2000**, *33* (5), 269−277.

(7) Grätzel, M. Dye-sensitized solar cells. *J. Photochem. Photobiol., C* **2003**, *4* (2), 145−153.

(8) Smestad, G.; Bignozzi, C.; Argazzi, R. Testing of dye sensitized TiO2 solar cells I: Experimental photocurrent output and conversion efficiencies. *Sol. Energy Mater. Sol. Cells* **1994**, *32* (3), 259−272.

(9) Hagfeldt, A.; Boschloo, G.; Sun, L.; Kloo, L.; Pettersson, H. Dye-Sensitized Solar Cells. *Chem. Rev.* **2010**, *110* (11), 6595−6663.

(10) Vougioukalakis, G. C.; Philippopoulos, A. I.; Stergiopoulos, T.; Falaras, P. Contributions to the development of ruthenium-based sensitizers for dye-sensitized solar cells. *Coord. Chem. Rev.* **2011**, *255* (21), 2602−2621.

(11) Narayan, M. R. Review: Dye sensitized solar cells based on natural photosensitizers. *Renewable Sustainable Energy Rev.* **2011**, *16* (1), 208−215.

(12) Gong, J.; Sumathy, K.; Qiao, Q.; Zhou, Z. Review on dye-sensitized solar cells (DSSCs): Advanced techniques and research trends. *Renewable Sustainable Energy Rev.* **2017**, *68*, 234−246.

(13) Richhariya, G.; Kumar, A.; Tekasakul, P.; Gupta, B. Natural dyes for dye sensitized solar cell: A review. *Renewable Sustainable Energy Rev.* **2017**, *69*, 705−718.

(14) Kalyanasundaram, K.; Grätzel, M. Dye-Sensitized Solar Cells for Direct Conversion of Sunlight to Electricity. *Material Matters* **2009**, *4*, 88.

(15) Odobel, F.; Blart, E.; Lagrée, M.; Villieras, M.; Boujtita, H.; El Murr, N.; Caramori, S.; Alberto Bignozzi, C. Porphyrin dyes for TiO2 sensitization. *J. Mater. Chem.* **2003**, *13* (3), 502−510.

(16) Campbell, W. M.; Burrell, A. K.; Officer, D. L.; Jolley, K. W. Porphyrins as light harvesters in the dye-sensitised TiO2 solar cell. *Coord. Chem. Rev.* **2004**, *248* (13), 1363−1379.

(17) Wang, Q.; Campbell, W. M.; Bonfantani, E. E.; Jolley, K. W.; Officer, D. L.; Walsh, P. J.; Gordon, K.; Humphry-Baker, R.; Nazeeruddin, M. K.; Grätzel, M. Efficient Light Harvesting by Using Green Zn-Porphyrin-Sensitized Nanocrystalline TiO2 Films. *J. Phys. Chem. B* **2005**, *109* (32), 15397−15409.

(18) Balanay, M. P.; Kim, D. H. DFT/TD-DFT molecular design of porphyrin analogues for use in dye-sensitized solar cells. *Phys. Chem. Chem. Phys.* **2008**, *10* (33), 5121−5127.

(19) Dong, H.; Zhou, X.; Jiang, C. Molecular design and theoretical investigation on novel porphyrin derivatives for dye-sensitized solar cells. *Theor. Chem. Acc.* **2012**, *131* (2), 1102.

(20) Xie, M.; Wang, J.; Xia, H.-Q.; Bai, F.-Q.; Jia, R.; Rim, J.-G.; Zhang, H.-X. Theoretical studies on the spectroscopic properties of porphyrin derivatives for dye-sensitized solar cell application. *RSC Adv.* **2015**, *5* (42), 33653−33665.

(21) Tanaka, T.; Osuka, A. Chemistry of meso-Aryl-Substituted Expanded Porphyrins: Aromaticity and Molecular Twist. *Chem. Rev.* **2017**, *117* (4), 2584−2640.

(22) Chatterjee, T.; Srinivasan, A.; Ravikanth, M.; Chandrashekar, T. K. Smaragdyrins and Sapphyrins Analogues. *Chem. Rev.* **2017**, *117* (4), 3329−3376.

(23) Gobeze, H. B.; Kumar, S.; D'Souza, F.; Ravikanth, M. Strongly Coupled Oxasmaragdyrin−BF2 Chelated Dipyrrin Dyads: Syntheses, X-ray Structure, Ground- and Excited-State Charge-Transfer Interactions. *Chem. - Eur. J.* **2017**, *23* (7), 1546−1556.

(24) Mane, S. B.; Sutanto, A. A.; Cheng, C.-F.; Xie, M.-Y.; Chen, C.-I.; Leonardus, M.; Yeh, S.-C.; Beyene, B. B.; Diau, E. W.-G.; Chen, C.-T.; Hung, C.-H. Oxasmaragdyrins as New and Efficient Hole-Transporting Materials for High-Performance Perovskite Solar Cells. *ACS Appl. Mater. Interfaces* **2017**, *9* (37), 31950−31958.
(25) Mane, S. B.; Hu, J.-Y.; Chang, Y.-C.; Luo, L.; Diau, E. W.-G.; Hung, C.-H. Novel expanded porphyrin sensitized solar cells using boryl oxasmaragdyrin as the sensitizer. *Chem. Commun.* **2013**, *49* (61), 6882−6884.
(26) Cárdenas-Jirón, G.; Borges-Martínez, M.; Sikorski, E.; Baruah, T. Excited States of Light-Harvesting Systems Based on Fullerene/Graphene Oxide and Porphyrin/Smaragdyrin. *J. Phys. Chem. C* **2017**, *121* (9), 4859−4872.
(27) Jiang, X.-D.; Guan, J.; Zhao, J.; Le Guennic, B.; Jacquemin, D.; Zhang, Z.; Chen, S.; Xiao, L. Synthesis, structure and photophysical properties of NIR aza-BODIPYs with F/N3/NH2 groups at 1,7-positions. *Dyes Pigm.* **2017**, *136*, 619−626.
(28) Azarias, C.; Russo, R.; Cupellini, L.; Mennucci, B.; Jacquemin, D. Modeling excitation energy transfer in multi-BODIPY architectures. *Phys. Chem. Chem. Phys.* **2017**, *19* (9), 6443−6453.
(29) Grabarz, A. M.; Jędrzejewska, B.; Skotnicka, A.; Murugan, N. A.; Patalas, F.; Bartkowiak, W.; Jacquemin, D.; Ośmiałowski, B. The impact of the heteroatom in a five-membered ring on the photophysical properties of difluoroborates. *Dyes Pigm.* **2019**, *170*, 107481.
(30) Alberto, M. E.; De Simone, B. C.; Russo, N.; Sicilia, E.; Toscano, M. Can BODIPY Dimers Act as Photosensitizers in Photodynamic Therapy? A Theoretical Prediction. *Front. Phys.* **2018**, *6*, 00143.
(31) De Simone, B. C.; Mazzone, G.; Pirillo, J.; Russo, N.; Sicilia, E. Halogen atom effect on the photophysical properties of substituted aza-BODIPY derivatives. *Phys. Chem. Chem. Phys.* **2017**, *19* (3), 2530−2536.
(32) Alberto, M. E.; De Simone, B. C.; Mazzone, G.; Quartarolo, A. D.; Russo, N. Theoretical determination of electronic spectra and intersystem spin-orbit coupling: The case of isoindole-bodipy dyes. *J. Chem. Theory Comput.* **2014**, *10* (9), 4006−4013.
(33) Pareek, Y.; Ravikanth, M. Synthesis and studies of covalently linked BF2-oxasmaragdyrin-BODIPY and BF2-oxasmaragdyrin-ferrocene dyads. *J. Porphyrins Phthalocyanines* **2013**, *17* (01n02), 157−164.
(34) Lin, C.-Y.; Wang, Y.-C.; Hsu, S.-J.; Lo, C.-F.; Diau, E. W.-G. Preparation and Spectral, Electrochemical, and Photovoltaic Properties of Acene-Modified Zinc Porphyrins. *J. Phys. Chem. C* **2010**, *114* (1), 687−693.
(35) Liu, Y.; Xiang, N.; Feng, X.; Shen, P.; Zhou, W.; Weng, C.; Zhao, B.; Tan, S. Thiophene-linked porphyrin derivatives for dye-sensitized solar cells. *Chem. Commun.* **2009**, No. 18, 2499−2501.
(36) Lin, C.-Y.; Lo, C.-F.; Luo, L.; Lu, H.-P.; Hung, C.-S.; Diau, E. W.-G. Design and Characterization of Novel Porphyrins with Oligo(phenylethylnyl) Links of Varied Length for Dye-Sensitized Solar Cells: Synthesis and Optical, Electrochemical, and Photovoltaic Investigation. *J. Phys. Chem. C* **2009**, *113* (2), 755−764.
(37) Kalita, H.; Lee, W.-Z.; Ravikanth, M. Phosphorus Complexes of meso-Triaryl-25-oxasmaragdyrins. *Inorg. Chem.* **2014**, *53* (17), 9431−9438.
(38) Urbani, M.; Grätzel, M.; Nazeeruddin, M. K.; Torres, T. Meso-Substituted Porphyrins for Dye-Sensitized Solar Cells. *Chem. Rev.* **2014**, *114* (24), 12330−12396.
(39) ThermoFisher: https://www.thermofisher.com/cl/es/home/references/molecular-probes-the-handbook/fluorophores-and-their-amine-reactive-derivatives/bodipy-dye-series.html.
(40) Becke, A. D. Density-functional exchange-energy approximation with correct asymptotic behavior. *Phys. Rev. A: At., Mol., Opt. Phys.* **1988**, *38* (6), 3098−3100.
(41) Lee, C.; Yang, W.; Parr, R. G. Development of the Colle-Salvetti correlation-energy formula into a functional of the electron density. *Phys. Rev. B: Condens. Matter Mater. Phys.* **1988**, *37* (2), 785−789.
(42) Becke, A. D. Density-functional thermochemistry. III. The role of exact exchange. *J. Chem. Phys.* **1993**, *98* (7), 5648−5652.
(43) Frisch, M. J.; Trucks, G. W.; Schlegel, H. B.; Scuseria, G. E.; Robb, M. A.; Cheeseman, J. R.; Scalmani, G.; Barone, V.; Mennucci, B.; Petersson, G. A.; et al. *Gaussian 09*; Gaussian, 2009.
(44) Hehre, W. J.; Radom, L.; Pople, J. A.; Schleyer, P. v. R. *Ab Initio Molecular Orbital Theory*; Wiley: New York, 1986.
(45) Schlegel, H. B. Optimization of equilibrium geometries and transition structures. *J. Comput. Chem.* **1982**, *3* (2), 214−218.
(46) Bernhard Schlegel, H. Estimating the hessian for gradient-type geometry optimizations. *Theor. Chim. Acta* **1984**, *66* (5), 333−340.
(47) Li, X.; Frisch, M. J. Energy-Represented Direct Inversion in the Iterative Subspace within a Hybrid Geometry Optimization Method. *J. Chem. Theory Comput.* **2006**, *2* (3), 835−839.
(48) Grimme, S.; Antony, J.; Ehrlich, S.; Krieg, H. A consistent and accurate ab initio parametrization of density functional dispersion correction (DFT-D) for the 94 elements H-Pu. *J. Chem. Phys.* **2010**, *132* (15), 154104.
(49) Furche, F.; Ahlrichs, R. Adiabatic time-dependent density functional methods for excited state properties. *J. Chem. Phys.* **2002**, *117* (16), 7433−7447.
(50) Stratmann, R. E.; Scuseria, G. E.; Frisch, M. J. An efficient implementation of time-dependent density-functional theory for the calculation of excitation energies of large molecules. *J. Chem. Phys.* **1998**, *109* (19), 8218−8224.
(51) Bauernschmitt, R.; Ahlrichs, R. Treatment of electronic excitations within the adiabatic approximation of time dependent density functional theory. *Chem. Phys. Lett.* **1996**, *256* (4), 454−464.
(52) Sundholm, D. Interpretation of the electronic absorption spectrum of free-base porphin using time-dependent density-functional theory. *Phys. Chem. Chem. Phys.* **2000**, *2* (10), 2275−2281.
(53) Becke, A. D. A new mixing of Hartree−Fock and local density-functional theories. *J. Chem. Phys.* **1993**, *98* (2), 1372−1377.
(54) Yanai, T.; Tew, D. P.; Handy, N. C. A new hybrid exchange−correlation functional using the Coulomb-attenuating method (CAM-B3LYP). *Chem. Phys. Lett.* **2004**, *393* (1), 51−57.
(55) Adamo, C.; Barone, V. Toward reliable density functional methods without adjustable parameters: The PBE0 model. *J. Chem. Phys.* **1999**, *110* (13), 6158−6170.
(56) Tao, J.; Perdew, J. P.; Staroverov, V. N.; Scuseria, G. E. Climbing the Density Functional Ladder: Nonempirical Meta−Generalized Gradient Approximation Designed for Molecules and Solids. *Phys. Rev. Lett.* **2003**, *91* (14), 146401.
(57) Staroverov, V. N.; Scuseria, G. E.; Tao, J.; Perdew, J. P. Comparative assessment of a new nonempirical density functional: Molecules and hydrogen-bonded complexes. *J. Chem. Phys.* **2003**, *119* (23), 12129−12137.
(58) Chai, J.-D.; Head-Gordon, M. Systematic optimization of long-range corrected hybrid density functionals. *J. Chem. Phys.* **2008**, *128* (8), 084106.
(59) Narayanan, S. J.; Sridevi, B.; Chandrashekar, T. K.; Englich, U.; Ruhlandt-Senge, K. Core-Modified Smaragdyrins: First Examples of Stable Meso-Substituted Expanded Corrole. *Org. Lett.* **1999**, *1* (4), 587−590.
(60) Barone, V.; Cossi, M. Quantum Calculation of Molecular Energies and Energy Gradients in Solution by a Conductor Solvent Model. *J. Phys. Chem. A* **1998**, *102* (11), 1995−2001.
(61) Cossi, M.; Rega, N.; Scalmani, G.; Barone, V. Energies, structures, and electronic properties of molecules in solution with the C-PCM solvation model. *J. Comput. Chem.* **2003**, *24* (6), 669−681.
(62) Schleyer, P. v. R.; Maerker, C.; Dransfeld, A.; Jiao, H.; van Eikema Hommes, N. J. R. Nucleus-Independent Chemical Shifts: A Simple and Efficient Aromaticity Probe. *J. Am. Chem. Soc.* **1996**, *118* (26), 6317−6318.
(63) Chen, Z.; Wannere, C. S.; Corminboeuf, C.; Puchta, R.; Schleyer, P. v. R. Nucleus-Independent Chemical Shifts (NICS) as an Aromaticity Criterion. *Chem. Rev.* **2005**, *105* (10), 3842−3888.
(64) Morao, I.; Lecea, B.; Cossío, F. P. In-Plane Aromaticity in 1,3-Dipolar Cycloadditions. *J. Org. Chem.* **1997**, *62* (20), 7033−7036.


DOI: 10.1021/acs.jpcc.9b05136
*J. Phys. Chem. C* 2019, 123, 19362−19375

(65) Bader, R. F. W. *Atoms in Molecules. A Quantum Theory*; University Press: Oxford, 1990.
(66) Bader, R. F. W.; Popelier, P. L. A.; Keith, T. A. Theoretical Definition of a Functional Group and the Molecular Orbital Paradigm. *Angew. Chem., Int. Ed. Engl.* **1994**, *33* (6), 620−631.
(67) Popelier, P. L. *Atoms in Molecules: An Introduction*; Prentice Hall: London, 2000.
(68) Keith, T. A. *AIMAll*, Version 11.05.16; T. K. Gristmill Software: Overland Park, KS, 2011. http://aim.tkgristmill.com/.
(69) Schleyer, P. v. R.; Jiao, H.; Hommes, N. J. R. v. E.; Malkin, V. G.; Malkina, O. L. An Evaluation of the Aromaticity of Inorganic Rings: Refined Evidence from Magnetic Properties. *J. Am. Chem. Soc.* **1997**, *119* (51), 12669−12670.
(70) Schleyer, P. v. R.; Manoharan, M.; Wang, Z.-X.; Kiran, B.; Jiao, H.; Puchta, R.; van Eikema Hommes, N. J. R. Dissected Nucleus-Independent Chemical Shift Analysis of π-Aromaticity and Anti-aromaticity. *Org. Lett.* **2001**, *3* (16), 2465−2468.
(71) Stuyver, T.; Perrin, M.; Geerlings, P.; De Proft, F.; Alonso, M. Conductance Switching in Expanded Porphyrins through Aromaticity and Topology Changes. *J. Am. Chem. Soc.* **2018**, *140* (4), 1313−1326.
(72) Keith, T. A.; Bader, R. F. W. Topological analysis of magnetically induced molecular current distributions. *J. Chem. Phys.* **1993**, *99* (5), 3669−3682.
(73) Keith, T. A. Calculation of magnetizabilities using GIAO current density distributions. *Chem. Phys.* **1996**, *213* (1), 123−132.
(74) Valiev, R. R.; Cherepanov, V. N. The influence of benzene rings on aromatic pathways in the porphyrins. *Int. J. Quantum Chem.* **2013**, *113* (23), 2563−2567.
(75) Valiev, R. R.; Fliegl, H.; Sundholm, D. Aromatic Pathways in Carbathiaporphyrins. *J. Phys. Chem. A* **2015**, *119* (7), 1201−1207.
(76) Franzke, Y. J.; Sundholm, D.; Weigend, F. Calculations of current densities and aromatic pathways in cyclic porphyrin and isoporphyrin arrays. *Phys. Chem. Chem. Phys.* **2017**, *19* (20), 12794−12803.
(77) Waldron, D.; Haney, P.; Larade, B.; MacDonald, A.; Guo, H. Nonlinear spin current and magnetoresistance of molecular tunnel junctions. *Phys. Rev. Lett.* **2006**, *96* (16), 166804.
(78) Taylor, J.; Guo, H.; Wang, J. Ab initio modeling of quantum transport properties of molecular electronic devices. *Phys. Rev. B: Condens. Matter Mater. Phys.* **2001**, *63* (24), 245407.
(79) Perdew, J. P. Erratum: Density-functional approximation for the correlation energy of the inhomogeneous electron gas. *Phys. Rev. B: Condens. Matter Mater. Phys.* **1986**, *34* (10), 7406−7406.
(80) Weigend, F.; Ahlrichs, R. Balanced basis sets of split valence, triple zeta valence and quadruple zeta valence quality for H to Rn: Design and assessment of accuracy. *Phys. Chem. Chem. Phys.* **2005**, *7* (18), 3297−3305.
(81) Rappoport, D.; Furche, F. Property-optimized Gaussian basis sets for molecular response calculations. *J. Chem. Phys.* **2010**, *133* (13), 134105.
(82) Ordejón, P.; Artacho, E.; Soler, J. M. Self-consistent order-$N$ density-functional calculations for very large systems. *Phys. Rev. B: Condens. Matter Mater. Phys.* **1996**, *53* (16), R10441−R10444.
(83) Soler, J. M.; Artacho, E.; Gale, J. D.; Garcia, A.; Junquera, J.; Ordejon, P.; Sanchez-Portal, D. The SIESTA method for ab initio order-N materials simulation. *J. Phys.: Condens. Matter* **2002**, *14*, 2745.
(84) Perdew, J. P.; Burke, K.; Ernzerhof, M. Generalized Gradient Approximation Made Simple. *Phys. Rev. Lett.* **1996**, *77* (18), 3865−3868.
(85) Martin, R. L. Natural transition orbitals. *J. Chem. Phys.* **2003**, *118* (11), 4775−4777.
(86) Cyrañski, M. K.; Krygowski, T. M.; Wisiorowski, M.; van Eikema Hommes, N. J. R.; Schleyer, P. v. R. Global and Local Aromaticity in Porphyrins: An Analysis Based on Molecular Geometries and Nucleus-Independent Chemical Shifts. *Angew. Chem., Int. Ed.* **1998**, *37* (1−2), 177−180.
(87) Yoon, Z. S.; Cho, D.-G.; Kim, K. S.; Sessler, J. L.; Kim, D. Nonlinear Optical Properties as a Guide to Aromaticity in Congeneric Pentapyrrolic Expanded Porphyrins: Pentaphyrin, Sapphyrin, Isosmaragdyrin, and Orangarin. *J. Am. Chem. Soc.* **2008**, *130* (22), 6930−6931.
(88) Mack, J. Expanded, Contracted, and Isomeric Porphyrins: Theoretical Aspects. *Chem. Rev.* **2017**, *117* (4), 3444−3478.
(89) Nazeeruddin, M. K.; De Angelis, F.; Fantacci, S.; Selloni, A.; Viscardi, G.; Liska, P.; Ito, S.; Takeru, B.; Grätzel, M. Combined Experimental and DFT-TDDFT Computational Study of Photoelectrochemical Cell Ruthenium Sensitizers. *J. Am. Chem. Soc.* **2005**, *127* (48), 16835−16847.
(90) Lu, X.; Wei, S.; Wu, C.-M. L.; Li, S.; Guo, W. Can Polypyridyl Cu(I)-based Complexes Provide Promising Sensitizers for Dye-Sensitized Solar Cells? A Theoretical Insight into Cu(I) versus Ru(II) Sensitizers. *J. Phys. Chem. C* **2011**, *115* (9), 3753−3761.
(91) Asbury, J. B.; Wang, Y.-Q.; Hao, E.; Ghosh, H. N.; Lian, T. Evidences of hot excited state electron injection from sensitizer molecules to TiO2 nanocrystalline thin films. *Res. Chem. Intermed.* **2001**, *27* (4), 393−406.
(92) Mosurkal, R.; He, J.-A.; Yang, K.; Samuelson, L. A.; Kumar, J. Organic photosensitizers with catechol groups for dye-sensitized photovoltaics. *J. Photochem. Photobiol., A* **2004**, *168* (3), 191−196.
(93) Cahen, D.; Hodes, G.; Grätzel, M.; Guillemoles, J. F.; Riess, I. Nature of Photovoltaic Action in Dye-Sensitized Solar Cells. *J. Phys. Chem. B* **2000**, *104* (9), 2053−2059.


DOI: 10.1021/acs.jpcc.9b05136
*J. Phys. Chem. C* 2019, 123, 19362−19375

# References


[1] Adam, R.; Mon, M.; Greco, R.; Kalinke, L. H. G.; Vidal-Moya, A.; Fernandez, A.; Winpenny, R. E. P.; Doménech-Carbó, A.; Leyva-Pérez, A.; Armentano, D.; Pardo, E.; Ferrando-Soria, J. Self-assembly of catalytically active supramolecular coordination compounds within metal-organic frameworks. *J. Am. Chem. Soc.* **2019,** *141,* 10350–10360.

[2] Glaser, F.; Wenger, O. S. Recent progress in the development of transition-metal based photoredox catalysts. *Coord. Chem. Rev.* **2020,** *405,* 213129.

[3] Pessoa, J. C.; Correia, I. Salan vs. salen metal complexes in catalysis and medicinal applications: Virtues and pitfalls. *Coord. Chem. Rev.* **2019,** *388,* 227–247.

[4] Malinowski, J.; Zych, D.; Jacewicz, D.; Gawdzik, B.; Drzeżdżon, J. Application of coordination compounds with transition metal ions in the chemical industry—a review. *Int. J. Mol. Sci.* **2020,** *21,* 5443.

[5] Holder, E.; Langeveld, B. M. W.; Schubert, U. S. New trends in the use of transition metal-ligand complexes for applications in electroluminescent devices. *Adv. Mater.* **2005,** *17,* 1109–1121.

[6] Quintana, C.; Cifuentes, M. P.; Humphrey, M. G. Transition metal complex/gold nanoparticle hybrid materials. *Chem. Soc. Rev.* **2020,** *49,* 2316–2341.

[7] Roundhill, D. M. *Photochemistry and photophysics of metal complexes;* Plenum Press: New York, 1994.

[8] Lo, K. *Inorganic and Organometallic Transition Metal Complexes with Biological Molecules and Living Cells;* Elsevier Science: Saint Louis, 2016.

[9] Orvig, C.; Abrams, M. J. Medicinal inorganic chemistry: Introduction. *Chem. Rev.* **1999,** *99,* 2201–2204.

[10] Gasser, G.; Ott, I.; Metzler-Nolte, N. Organometallic anticancer compounds. *J. Med. Chem.* **2011,** *54,* 3–25.

[11] Monro, S.; Colón, K. L.; Yin, H.; Roque, J.; Konda, P.; Gujar, S.; Thummel, R. P.; Lilge, L.; Cameron, C. G.; McFarland, S. A. Transition metal complexes and photodynamic therapy from a tumor-centered approach: Challenges, opportunities, and highlights from the development of TLD1433. *Chem. Rev.* **2018,** *119,* 797–828.

[12] Sodhi, R. K. Metal complexes in medicine: An overview and update from drug design perspective. *Canc. Ther. Oncol. Int. J.* **2019,** *14,*.

[13] Hawecker, J.; Lehn, J.-M.; Ziessel, R. Efficient photochemical reduction of $CO_2$ to CO by visible light irradiation of systems containing $Re(bipy)(CO)_3X$ or $Ru(bipy)_3{}^{2+}$-$Co^{2+}$ combinations as homogeneous catalysts. *J. Chem. Soc., Chem. Commun.* **1983,** 536–538.

[14] Hawecker, J.; Lehn, J.-M.; Ziessel, R. Electrocatalytic reduction of carbon dioxide mediated by $Re(bipy)(CO)_3Cl$ (bipy = 2,2′-bipyridine). *J. Chem. Soc., Chem. Commun.* **1984,** 328–330.

[15] Kuninobu, Y.; Takai, K. Organic reactions catalyzed by rhenium carbonyl complexes. *Chem. Rev.* **2011,** *111,* 1938–1953.

[16] Lundin, N. J.; Blackman, A. G.; Gordon, K. C.; Officer, D. L. Synthesis and characterization of a multicomponent rhenium(I) complex for application as an OLED dopant. *Angew. Chem. Int. Ed.* **2006,** *45,* 2582–2584.

[17] Happ, B.; Winter, A.; Hager, M. D.; Schubert, U. S. Photogenerated avenues in macromolecules containing Re(I), Ru(II), Os(II), and Ir(III) metal complexes of pyridine-based ligands. *Chem. Soc. Rev.* **2012,** *41,* 2222–2255.

[18] Zhao, G.-W.; Zhao, J.-H.; Hu, Y.-X.; Zhang, D.-Y.; Li, X. Recent advances of neutral rhenium(I) tricarbonyl complexes for application in organic light-emitting diodes. *Synth. Met.* **2016,** *212,* 131–141.

[19] Lam, S.-T.; Yam, V. W.-W. Synthesis, characterisation and photophysical study of alkynylrhenium(I) tricarbonyl diimine complexes and their metal-ion coordination-assisted metallogelation properties. *Chem. Eur. J.* **2010,** *16,* 11588–11593.

[20] Potocny, A. M.; Teesdale, J. J.; Marangoz, A.; Yap, G. P. A.; Rosenthal, J. Spectroscopic and $^1O_2$ sensitization characteristics of a series of isomeric $Re(bpy)(CO)_3Cl$ complexes bearing pendant BODIPY chromophores. *Inorg. Chem.* **2019,** *58,* 5042–5050.

[21] Komreddy, V.; Ensz, K.; Nguyen, H.; Rillema, D. P. Synthesis and characterization of rhenium(I) 4,4′-dicarboxy-2,2′-bipyridine tricarbonyl complexes for solar energy conversion. *Inorg. Chim. Acta* **2020,** *511,* 119815.

[22] Liu, Z.; He, W.; Guo, Z. Metal coordination in photoluminescent sensing. *Chem. Soc. Rev.* **2013,** *42,* 1568.

[23] Leonidova, A.; Gasser, G. Underestimated potential of organometallic rhenium complexes as anticancer agents. *ACS Chem. Biol.* **2014,** *9,* 2180–2193.

[24] Hostachy, S.; Policar, C.; Delsuc, N. Re(I) carbonyl complexes: Multimodal platforms for inorganic chemical biology. *Coord. Chem. Rev.* **2017,** *351,* 172–188.

[25] Coogan, M. P.; Fernández-Moreira, V. Progress with, and prospects for, metal complexes in cell imaging. *Chem. Commun.* **2014,** *50,* 384–399.

[26] Raszeja, L. J.; Siegmund, D.; Cordes, A. L.; Güldenhaupt, J.; Gerwert, K.; Hahn, S.; Metzler-Nolte, N. Asymmetric rhenium tricarbonyl complexes show superior luminescence properties in live cell imaging. *Chem. Commun.* **2017,** *53,* 905–908.

[27] Huang, Z.; Wilson, J. J. Therapeutic and diagnostic applications of multimetallic rhenium(I) tricarbonyl complexes. *Eur. J. Inorg. Chem.* **2021,** *2021,* 1312–1324.

[28] Marker, S. C.; MacMillan, S. N.; Zipfel, W. R.; Li, Z.; Ford, P. C.; Wilson, J. J. Photoactivated in vitro anticancer activity of rhenium(I) tricarbonyl complexes bearing water-soluble phosphines. *Inorg. Chem.* **2018,** *57,* 1311–1331.

[29] Konkankit, C. C.; Marker, S. C.; Knopf, K. M.; Wilson, J. J. Anticancer activity of complexes of the third row transition metals, rhenium, osmium, and iridium. *Dalton Trans.* **2018,** *47,* 9934–9974.

[30] Liew, H. S.; Mai, C.-W.; Zulkefeli, M.; Madheswaran, T.; Kiew, L. V.; Delsuc, N.; Low, M. L. Recent emergence of rhenium(I) tricarbonyl complexes as photosensitisers for cancer therapy. *Molecules* **2020,** *25,* 4176.

[31] Arévalo, R.; Espinal-Viguri, M.; Huertos, M. A.; Pérez, J.; Riera, L. Dearomatization of transition metal-coordinated N-heterocyclic ligands and related chemistry. **2016,** 47–114.

[32] Cañadas, P.; Ziegler, S.; Fombona, S.; Hevia, E.; Miguel, D.; Pérez, J.; Riera, L. Molybdenum and rhenium carbonyl complexes containing thiolato ligands. *J. Organomet. Chem.* **2019,** *896,* 113–119.

[33] Bond, G. P. Metallocenes. In *Patty's Toxicology*; John Wiley & Sons: New York, 2012.

[34] Waern, J. B.; Harding, M. M. Bioorganometallic chemistry of molybdocene dichloride. *J. Organomet. Chem.* **2004,** *689,* 4655–4668.

[35] Abeysinghe, P. M.; Harding, M. M. Antitumour bis(cyclopentadienyl) metal complexes: titanocene and molybdocene dichloride and derivatives. *Dalton Trans.* **2007,** 3474.

[36] Meléndez, E. Metallocenes as target specific drugs for cancer treatment. *Inorg. Chim. Acta* **2012,** *393,* 36–52.

[37] Meléndez, E. Bioorganometallic chemistry of molybdenocene dichloride and its derivatives. *J. Organomet. Chem.* **2012,** *706-707,* 4–12.

[38] Ahmed, T. J.; Knapp, S. M. M.; Tyler, D. R. Frontiers in catalytic nitrile hydration: Nitrile and cyanohydrin hydration catalyzed by homogeneous organometallic complexes. *Coord. Chem. Rev.* **2011,** *255,* 949–974.

[39] Mao, G.; Huang, Q.; Wang, C. Rhenium-catalyzed annulation reactions. *Eur. J. Org. Chem.* **2017,** *2017,* 3549–3564.

[40] Hua, R.; Jiang, J.-L. Recent development of Rhenium-catalyzed organic synthesis. *Curr. Org. Synth.* **2007,** *4,* 151–174.

[41] Murai, M.; Uemura, E.; Takai, K. Amine-promoted anti-markovnikov addition of 1,3-dicarbonyl compounds with terminal alkynes under Rhenium catalysis. *ACS Catal.* **2018,** *8,* 5454–5459.

[42] Capper, M. S.; Packman, H.; Rehkämper, M. Rhenium-based complexes and in vivo testing: A brief history. *ChemBioChem* **2020,** *21,* 2111–2115.

[43] Suárez, D.; Zakarianezhad, M.; López, R. Insights into the hydrolytic chemistry of molybdocene dichloride based on a theoretical mechanistic study. *Theor. Chem. Acc.* **2013,** *132,*.

[44] Gerbino, D. C.; Hevia, E.; Morales, D.; Clemente, M. E. N.; Pérez, J.; Riera, L.; Riera, V.; Miguel, D. A new reactivity pattern of low-valent transition-metal hydroxo complexes: straightforward synthesis of hydrosulfido complexes via reaction with carbon disulfide. *Chem. Commun.* **2003,** 328.

[45] Cuesta, L.; Gerbino, D. C.; Hevia, E.; Morales, D.; Clemente, M. E. N.; Pérez, J.; Riera, L.; Riera, V.; Miguel, D.; del Río, I.; García-Granda, S. Reactivity of molybdenum and rhenium hydroxo-carbonyl complexes toward organic electrophiles. *Chem. Eur. J.* **2004,** *10,* 1765–1777.

[46] Cuesta, L.; Hevia, E.; Morales, D.; Pérez, J.; Riera, L.; Miguel, D. Reactivity of molybdenum and rhenium hydroxo complexes toward organic electrophiles: Reactions that afford carboxylato products. *Organometallics* **2006,** *25,* 1717–1722.

[47] Fulton, J. R.; Holland, A. W.; Fox, D. J.; Bergman, R. G. Formation, reactivity, and properties of nondative late transition metal-oxygen and -nitrogen bonds. *Acc. Chem. Res.* **2002,** *35,* 44–56.

[48] Gibson, D. H.; Yin, X. Synthesis and reactions of *fac*-Re(dmbpy)$(CO)_3$X (dmbpy = 4,4′-dimethyl-2,2′-bipyridyl; x = COOH, COOMe, H, OH, and OCHO). *J. Am. Chem. Soc.* **1998,** *120,* 11200–11201.

[49] Morales, D.; Clemente, M. E. N.; Pérez, J.; Riera, L.; Riera, V.; Miguel, D. The combination of organometallic [Mo($\eta^3$–allyl)$(CO)_2$(phen)] fragments and hard aquo and hydroxo ligands: Controlled synthesis and structural characterization. *Organometallics* **2002,** *21,* 4934–4938.

[50] Gibson, D. H.; Yin, X.; He, H.; Mashuta, M. S. Synthesis and reactions of *fac*-[Re(dmbpy)$(CO)_3$X] (dmbpy = 4,4′-dimethyl-2,2′-bipyridine; x = COOH, CHO) and their derivatives. *Organometallics* **2002,** *22,* 337–346.

[51] Heard, P. J.; Sroisuwan, P.; Tocher, D. A. Synthesis and reactivity of N, N, N′, N′-tetramethyldiaminomethane complexes of tricarbonylrhenium(I). X-ray molecular structures of [$ReBr(CO)_3$(TMDM)] and [{(bipy)$(CO)_3$}($\mu$-OH)][$SbF_6$]. *Polyhedron* **2003,** *22,* 1321–1327.

[52] Breno, K. L.; Pluth, M. D.; Landorf, C. W.; Tyler, D. R. Aqueous phase organometallic catalysis using $(MeCp)_2Mo(OH)(H_2O)^+$. Intramolecular attack of hydroxide on organic substrates. *Organometallics* **2004,** *23,* 1738–1746.

[53] Hevia, E.; Pérez, J.; Riera, L.; Riera, V.; Miguel, D. Reactive alkoxide complexes of groups 6 and 7 metals. *Organometallics* **2002,** *21,* 1750–1752.

[54] Hevia, E.; Pérez, J.; Riera, L.; Riera, V.; del Río, I.; García-Granda, S.; Miguel, D. Insertion of unsaturated organic electrophiles into molybdenum-alkoxide and rhenium-alkoxide bonds of neutral, stable carbonyl complexes. *Chem. Eur. J.* **2002,** *8,* 4510–4521.

[55] Hevia, E.; Pérez, J.; Riera, V.; Miguel, D. Reactivity of the amido complex [Re(NHpTol)$(CO)_3$(bipy)] toward neutral organic electrophiles. *Organometallics* **2003,** *22,* 257–263.

[56] Cuesta, L.; Hevia, E.; Morales, D.; Pérez, J.; Riera, V.; Rodríguez, E.; Miguel, D. Activation of a 1,10-phenanthroline ligand on a rhenium tricarbonyl complex. *Chem. Commun.* **2005,** 116–117.

[57] Cuesta, L.; Hevia, E.; Morales, D.; Pérez, J.; Riera, V.; Seitz, M.; Miguel, D. Activation of ancillary ligands in the reactions of DMAD with phosphido and alkylideneamido rhenium complexes. *Organometallics* **2005,** *24,* 1772–1775.

[58] Ashby, M. T.; Enemark, J. H. Cycloaddition of alkenes and alkynes to $CpFe(CO)_2PR_2$ to give cyclic Cp(CO)$FePR_2$C−CC−O heterometallacycles. *Organometallics* **1987,** *6,* 1323–1327.

[59] Adams, H.; Bailey, N. A.; Day, A. N.; Morris, M. J.; Harrison, M. M. Reactivity of the metallophosphines [$CpM(CO)_3PPh_2$] (Cp = $\eta$-$C_5H_5$, M = Mo, W) towards alkynes. X-ray crystal structure of [$CpMo(CO)_2$ {$Ph_2PCH(Ph)CO$}]. *J. Organomet. Chem.* **1991,** *407,* 247–258.

[60] Ángel L. Serrano,; Casado, M. A.; Ciriano, M. A.; de Bruin, B.; López, J. A.; Tejel, C. Nucleophilicity and P-C bond formation reactions of a terminal phosphanido iridium complex. *Inorg. Chem.* **2015,** *55,* 828–839.

[61] Antiñolo, A.; García-Yuste, S.; Solera, I. L.; Otero, A.; Flores, J. C. P.; Carmona, R. R.; Villaseñor, E.; Santos, E.; Zuidema, E.; Bo, C. Reactions of alkynes with phosphido niobocenes: a combined experimental and theoretical study. *Dalton Trans.* **2010,** *39,* 1962.

[62] Kaes, C.; Katz, A.; Hosseini, M. W. Bipyridine: the most widely used ligand. a review of molecules comprising at least two 2,2′-bipyridine units. *Chem. Rev.* **2000,** *100,* 3553–3590.

[63] Gillard, R. D.; Lyons, J. R. Equilibria in complexes of heterocyclic ligands. *J. Chem. Soc., Chem. Commun.* **1973,** 585.

[64] Gillard, R. Equilibria in complexes of N-heterocyclic molecules. Part III [1, 2]. An explanation for classical anomalies among complexes of 1,10-phenanthrolines and 2,2′-bi-pyridyls. *Coord. Chem. Rev.* **1975,** *16,* 67–94.

[65] Farver, O.; Moensted, O.; Nord, G. A nuclear magnetic resonance study of the bis(2,2′-bipyridine)platinum(II) cation in basic solution. *J. Am. Chem. Soc.* **1979,** *101,* 6118–6120.

[66] Lay, P. A. Does coordination activate heterocycles toward nucleophilic attack? The importance of $\pi$ interactions between metal ion and ligand. *Inorg. Chem.* **1984,** *23,* 4775–4777.

[67] Blackman, A. Reactions of Coordinated Ligands. In *Advances in Heterocyclic Chemistry*; Elsevier: USA, 1993.

[68] Zhang, X.-M.; Tong, M.-L.; Chen, X.-M. Hydroxylation of N-heterocycle ligands observed in two unusual mixed-valence CuI/CuII complexes. *Angew. Chem. Int. Ed.* **2002,** *41,* 1029–1031.

[69] Kobriger, L. M.; McMullen, A. K.; Fanwick, P. E.; Rothwell, I. P. Complexation and intramolecular alkylation of bipyridyl ligands by $Zr(OAr)_2R_2$ ($R = CH_3, CH_2Ph$) compounds. *Polyhedron* **1989,** *8,* 77–81.

[70] Leelasubcharoen, S.; Lam, K.-C.; Concolino, T. E.; Rheingold, A. L.; Theopold, K. H. Unusual transformations of a bipyridine ligand in attempts to trap a terminal chromium(III) alkylidene. *Organometallics* **2001,** *20,* 182–187.

[71] Jantunen, K. C.; Scott, B. L.; Hay, P. J.; Gordon, J. C.; Kiplinger, J. L. Dearomatization and functionalization of terpyridine by Lutetium(III) alkyl complexes. *J. Am. Chem. Soc.* **2006,** *128,* 6322–6323.

[72] Miller, K. L.; Williams, B. N.; Benitez, D.; Carver, C. T.; Ogilby, K. R.; Tkatchouk, E.; Goddard, W. A.; Diaconescu, P. L. Dearomatization reactions of N-heterocycles mediated by group 3 complexes. *J. Am. Chem. Soc.* **2009,** *132,* 342–355.

[73] Balzarek, C.; Tyler, D. R. Intra- and intermolecular H/D exchange in aqueous solution catalyzed by molybdocenes. *Angew. Chem. Int. Ed.* **1999,** *38,* 2406–2408.

[74] Balzarek, C.; Weakley, T. J. R.; Tyler, D. R. C-H bond activation in aqueous solution: Kinetics and mechanism of H/D exchange in alcohols catalyzed by molybdocenes. *J. Am. Chem. Soc.* **2000,** *122,* 9427–9434.

[75] Breno, K. L.; Tyler, D. R. C-H bond activation in aqueous solution: A linear free energy relationship investigation of the rate-limiting step in the H/D exchange of alcohols catalyzed by a molybdocene. *Organometallics* **2001,** *20,* 3864–3868.

[76] Breno, K. L.; Ahmed, T. J.; Pluth, M. D.; Balzarek, C.; Tyler, D. R. Organometallic chemistry in aqueous solution: Reactions catalyzed by water-soluble molybdocenes. *Coord. Chem. Rev.* **2006,** *250,* 1141–1151.

[77] Ahmed, T. J.; Zakharov, L. N.; Tyler, D. R. Organometallic catalysis in aqueous solution. The hydrolytic activity of a water-soluble ansa-molybdocene catalyst. *Organometallics* **2007,** *26,* 5179–5187.

[78] Ahmed, T. J.; Fox, B. R.; Knapp, S. M. M.; Yelle, R. B.; Juliette, J. J.; Tyler, D. R. Investigation of the reactivity of Pt phosphinito and molybdocene nitrile hydration catalysts with cyanohydrins. *Inorg. Chem.* **2009,** *48,* 7828–7837.

[79] Breno, K. L.; Pluth, M. D.; Tyler, D. R. Organometallic chemistry in aqueous solution. Hydration of nitriles to amides catalyzed by a water-soluble molybdocene, $(MeCp)_2Mo(OH)(H_2O)^+$. *Organometallics* **2003,** *22,* 1203–1211.

[80] Ahmed, T. J.; Tyler, D. R. Effect of solvent on the dimerization of the ansa-molybdocene catalyst $[C_2Me_4Cp_2Mo(OH)(OH_2)][OTs]$. *Organometallics* **2008,** *27,* 2608–2613.

[81] Kuo, L. Y.; Kuhn, S.; Ly, D. First reported aqueous phosphoester bond cleavage promoted by an organometallic complex. *Inorg. Chem.* **1995,** *34,* 5341–5345.

[82] Kuo, L. Y.; Barnes, L. A. Aqueous phosphoester bond cleavage of dimethyl phosphate by $Cp_2MoCl_2$: First reported case of hydrolytic cleavage on an unactivated phosphate diester by an organometallic complex. *Inorg. Chem.* **1999,** *38,* 814–817.

[83] Kuo, L. Y.; Perera, N. M. Paraoxon and parathion hydrolysis by aqueous molybdenocene dichloride $Cp_2MoCl_2$: First reported pesticide hydrolysis by an organometallic complex. *Inorg. Chem.* **2000,** *39,* 2103–2106.

[84] Kuo, L. Y.; Blum, A. P.; Sabat, M. P-S bond scission by bis(cyclopentadienyl)molybdenum(IV) dichloride, $Cp_2MoCl_2(aq)$: First documented example of an organometallic complex hydrolyzing thiophosphinates. *Inorg. Chem.* **2005,** *44,* 5537–5541.

[85] Kuo, L. Y.; Bentley, A. K.; Shariati, Y. A.; Smith, C. P. Phosphonothioate hydrolysis turnover by $Cp_2MoCl_2$ and silver nanoparticles. *Organometallics* **2012,** *31,* 5294–5301.

[86] Tílvez, E.; Cárdenas-Jirón, G. I.; Menéndez, M. I.; López, R. Understanding the hydrolysis mechanism of ethyl acetate catalyzed by an aqueous molybdocene: A computational chemistry investigation. *Inorg. Chem.* **2015,** *54,* 1223–1231.

[87] Tílvez, E.; Menéndez, M. I.; López, R. On the mechanism of the $[Cp_2Mo(OH)(OH_2)]^+$-catalyzed nitrile hydration to amides: A theoretical study. *Organometallics* **2012,** *31,* 1618–1626.

[88] Tílvez, E.; Menéndez, M. I.; López, R. A theoretical investigation on the oxidation of carbon monoxide by an aqueous molybdocene. *Eur. J. Inorg. Chem.* **2012,** *2012,* 4445–4453.

[89] Arévalo, R.; Pérez, J.; Riera, L. Intramolecular nucleophilic addition to the 2 position of coordinated 2,2′-bipyridine by a deprotonated dimethyl sulfide ligand. *Inorg. Chem.* **2013,** *52,* 6785–6787.

[90] Arévalo, R.; Pérez, J.; Riera, L. Deprotonation of coordinated phosphanes in a rhenium complex: C-C coupling with diimine coligands. *Chem. Eur. J.* **2015,** *21,* 3546–3549.

[91] Arévalo, R.; Menéndez, M. I.; López, R.; Merino, I.; Riera, L.; Pérez, J. Nucleophilic additions to coordinated 1,10-phenanthroline intramolecular, intermolecular, reversible, and irreversible. *Chem. Eur. J.* **2016,** *22,* 17972–17975.

[92] Arevalo, R.; López, R.; Falvello, L. R.; Riera, L.; Perez, J. Building C($sp^3$) molecular complexity on 2,2′-bipyridine and 1,10-phenanthroline in rhenium tricarbonyl complexes. *Chem. Eur. J.* **2020,** *27,* 379–389.

[93] Huertos, M. A.; Pérez, J.; Riera, L. Pyridine ring opening at room temperature at a rhenium tricarbonyl bipyridine complex. *J. Am. Chem. Soc.* **2008,** *130,* 5662–5663.

[94] Fombona, S.; Espinal-Viguri, M.; Huertos, M. A.; Díaz, J.; López, R.; Menéndez, M. I.; Pérez, J.; Riera, L. Activation of aromatic C-C bonds of 2,2′-bipyridine ligands. *Chem. Eur. J.* **2016,** *22,* 17160–17164.

[95] Espinal-Viguri, M.; Fombona, S.; Álvarez, D.; Díaz, J.; Menéndez, M. I.; López, R.; Pérez, J.; Riera, L. Regiochemistry control by bipyridine substituents in the deprotonation of ReI and MoII N-alkylimidazole complexes. *Chem. Eur. J.* **2019,** *25,* 9253–9265.

[96] Arévalo, R.; Riera, L.; Pérez, J. Interligand C-C coupling between $\alpha$-methyl N-heterocycles and bipy or phen at rhenium tricarbonyl complexes. *Inorg. Chem.* **2017,** *56,* 4249–4252.

[97] Brill, M.; Díaz, J.; Huertos, M. A.; López, R.; Pérez, J.; Riera, L. Imidazole to NHC rearrangements at molybdenum centers: An experimental and theoretical study. *Chem. Eur. J.* **2011,** *17,* 8584–8595.

[98] Ruiz, J.; Perandones, B. F. Base-promoted tautomerization of imidazole ligands to N-heterocyclic carbenes and subsequent transmetalation reaction. *J. Am. Chem. Soc.* **2007,** *129,* 9298–9299.

[99] Cebollada, A.; Viguri, M. E.; Pérez, J.; Díaz, J.; López, R.; Riera, L. Influence of the N-N coligand: C-C coupling instead of formation of imidazol-2-yl complexes at $\{Mo(\eta^3-allyl)(CO)_2\}$ fragments. Theoretical and experimental studies. *Inorg. Chem.* **2015,** *54,* 2580–2590.

[100] Fombona, S.; Pérez, J.; Díaz, J.; Riera, L. Intermolecular C-C coupling between 1-methyl-1,2,3-triazole and 2,2′-bipyridine or 1,10-phenanthroline in Mo(II) complexes. *Chem. Eur. J.* **2017,** *23,* 17870–17873.

[101] Ghosh, S. Cisplatin: The first metal based anticancer drug. *Bioorg. Chem.* **2019,** *88,* 102925.

[102] Alderden, R. A.; Hall, M. D.; Hambley, T. W. The discovery and development of cisplatin. *J. Chem. Educ.* **2006,** *83,* 728.

[103] Galanski, M.; Jakupec, M.; Keppler, B. Update of the preclinical situation of anticancer platinum complexes: Novel design strategies and innovative analytical approaches. *Curr. Med. Chem.* **2005,** *12,* 2075–2094.

[104] Dasari, S.; Tchounwou, P. B. Cisplatin in cancer therapy: Molecular mechanisms of action. *Eur. J. Pharmacol.* **2014,** *740,* 364–378.

[105] Baik, M.-H.; Friesner, R. A.; Lippard, S. J. Theoretical study of cisplatin binding to purine bases: Why does cisplatin prefer guanine over adenine?. *J. Am. Chem. Soc.* **2003,** *125,* 14082–14092.

[106] Kelland, L. The resurgence of platinum-based cancer chemotherapy. *Nat. Rev. Cancer* **2007,** *7,* 573–584.

[107] Murray, B. S.; Dyson, P. J. Recent progress in the development of organometallics for the treatment of cancer. *Curr. Opin. Chem. Biol.* **2020,** *56,* 28–34.

[108] Bergamo, A.; Sava, G. Ruthenium anticancer compounds: myths and realities of the emerging metal-based drugs. *Dalton Trans.* **2011,** *40,* 7817.

[109] Kostova, I. Titanium and vanadium complexes as anticancer agents. *Anti-Cancer Agents Med. Chem.* **2009,** *9,* 827–842.

[110] Zhang, P.; Sadler, P. J. Advances in the design of organometallic anticancer complexes. *J. Organomet. Chem.* **2017,** *839,* 5–14.

[111] Bauer, E. B.; Haase, A. A.; Reich, R. M.; Crans, D. C.; Kühn, F. E. Organometallic and coordination rhenium compounds and their potential in cancer therapy. *Coord. Chem. Rev.* **2019,** *393,* 79–117.

[112] Konkankit, C. C.; Vaughn, B. A.; Huang, Z.; Boros, E.; Wilson, J. J. Systematically altering the lipophilicity of rhenium(I) tricarbonyl anticancer agents to tune the rate at which they induce cell death. *Dalton Trans.* **2020,** *49,* 16062–16066.

[113] Kermagoret, A.; Morgant, G.; d'Angelo, J.; Tomas, A.; Rousselsel, P.; Bastian, G.; Collery, P.; Desmaële, D. Synthesis, structural characterization and biological activity against several human tumor cell lines of four rhenium(I) diseleno-ethers complexes: $Re(CO)_3Cl(PhSe(CH_2)_2SePh)$, $Re(CO)_3Cl(PhSe(CH_2)_3SePh)$, $Re(CO)_3Cl(HO_2C-CH_2Se(CH_2)_2SeCH_2-CO_2H)$ and $Re(CO)_3Cl(HO_2C-CH_2Se(CH_2)_3SeCH_2-CO_2H)$. *Polyhedron* **2011,** *30,* 347–353.

[114] Philippe, C.; Gerard, B.; Santoni, F.; Ahmed, M.; Ming, W.; Thomas, C.; Alain, T.; Didier, D.; d'Angelo Jean, Uptake and efflux of rhenium in cells exposed to rhenium diseleno-ether and tissue distribution of rhenium and selenium after rhenium diseleno-ether treatment in mice. *Anticancer Res.* **2014,** *34,* 1679–1689.

[115] Collery, P.; Mohsen, A.; Kermagoret, A.; Corre, S.; Bastian, G.; Tomas, A.; Wei, M.; Santoni, F.; Guerra, N.; Desmaële, D.; d'Angelo, J. Antitumor activity of a rhenium (I)-diselenoether complex in experimental models of human breast cancer. *Invest. New Drugs* **2015,** *33,* 848–860.

[116] He, L.; Pan, Z.-Y.; Qin, W.-W.; Li, Y.; Tan, C.-P.; Mao, Z.-W. Impairment of the autophagy-related lysosomal degradation pathway by an anticancer rhenium(I) complex. *Dalton Trans.* **2019,** *48,* 4398–4404.

[117] Wang, F.-X.; Liang, J.-H.; Zhang, H.; Wang, Z.-H.; Wan, Q.; Tan, C.-P.; Ji, L.-N.; Mao, Z.-W. Mitochondria-accumulating rhenium(I) tricarbonyl complexes induce cell death via irreversible oxidative stress and glutathione metabolism disturbance. *ACS Appl. Mater. Interfaces* **2019,** *11,* 13123–13133.

[118] Knopf, K. M.; Murphy, B. L.; MacMillan, S. N.; Baskin, J. M.; Barr, M. P.; Boros, E.; Wilson, J. J. In vitro anticancer activity and in vivo biodistribution of rhenium(I) tricarbonyl aqua complexes. *J. Am. Chem. Soc.* **2017,** *139,* 14302–14314.

[119] Konkankit, C. C.; King, A. P.; Knopf, K. M.; Southard, T. L.; Wilson, J. J. In vivo anticancer activity of a rhenium(I) tricarbonyl complex. *ACS Med. Chem. Lett.* **2019,** *10,* 822–827.

[120] King, A. P.; Marker, S. C.; Swanda, R. V.; Woods, J. J.; Qian, S.-B.; Wilson, J. J. A rhenium isonitrile complex induces unfolded protein response-mediated apoptosis in cancer cells. *Chem. Eur. J.* **2019,** *25,* 9206–9210.

[121] Marker, S. C.; King, A. P.; Granja, S.; Vaughn, B.; Woods, J. J.; Boros, E.; Wilson, J. J. Exploring the in vivo and in vitro anticancer activity of rhenium isonitrile complexes. *Inorg. Chem.* **2020,** *59,* 10285–10303.

[122] Konkankit, C. C.; Lovett, J.; Harris, H. H.; Wilson, J. J. X-ray fluorescence microscopy reveals that rhenium(I) tricarbonyl isonitrile complexes remain intact in vitro. *Chem. Commun.* **2020,** *56,* 6515–6518.

[123] Takeda, H.; Koike, K.; Morimoto, T.; Inumaru, H.; Ishitani, O. Photochemistry and photocatalysis of rhenium(I) diimine complexes. *Adv. Inorg. Chem.* **2011,** *63,* 137–186.

[124] Liu, G.; Hnatowich, D. J. Labeling biomolecules with radiorhenium - a review of the bifunctional chelators. *Anticancer Agents Med. Chem.* **2007,** *7,* 367–377.

[125] Takeda, H.; Ishitani, O. Development of efficient photocatalytic systems for $CO_2$ reduction using mononuclear and multinuclear metal complexes based on mechanistic studies. *Coord. Chem. Rev.* **2010,** *254,* 346–354.

[126] Mazzone, G.; Alberto, M.; Simone, B. D.; Marino, T.; Russo, N. Can expanded bacteriochlorins act as photosensitizers in photodynamic therapy? Good news from density functional theory computations. *Molecules* **2016,** *21,* 288.

[127] Farrer, N. J.; Salassa, L.; Sadler, P. J. Photoactivated chemotherapy (PACT): the potential of excited-state d-block metals in medicine. *Dalton Trans.* **2009,** 10690.

[128] Scott, L. J.; Goa, K. L. Verteporfin. *Drugs Aging* **2000,** *16,* 139–146.

[129] Senge, M. O.; Brandt, J. C. Temoporfin (foscan®, 5,10,15,20-tetra(m-hydroxyphenyl)chlorin)-A second-generation photosensitizer. *Photochem. Photobiol.* **2011,** *87,* 1240–1296.

[130] Rodriguez-Rivera, J.; Rodriguez-Lay, R.; Zegarra-Montes, L.; Benzaghou, F.; Gaillac, B.; Azzouzi, A.; Reis, L.; Palma, P. Extensión de la indicación de terapia fotodinámica dirigida vascular con padeliporfina (WST11): resultados de un estudio multicéntrico latinoamericano del cáncer de próstata. *Actas Urol. Esp.* **2018,** *42,* 632–638.

[131] Baran, T. M. Photofrin ® photodynamic therapy with intratumor photosensitizer injection provides similar tumor response while reducing systemic skin photosensitivity: Pilot murine study. *Lasers Surg. Med.* **2017,** *50,* 476–482.

[132] van Straten, D.; Mashayekhi, V.; de Bruijn, H.; Oliveira, S.; Robinson, D. Oncologic photodynamic therapy: Basic principles, current clinical status and future directions. *Cancers* **2017,** *9,* 19.

[133] Brancaleon, L.; Moseley, H. Laser and non-laser light sources for photodynamic therapy. *Lasers Med. Sci.* **2002,** *17,* 173–186.

[134] Szaciłowski, K.; Macyk, W.; Drzewiecka-Matuszek, A.; Brindell, M.; Stochel, G. Bioinorganic photochemistry: Frontiers and mechanisms. *Chem. Rev.* **2005,** *105,* 2647–2694.

[135] Alberto, M. E.; Simone, B. C. D.; Liuzzi, S.; Marino, T.; Russo, N.; Toscano, M. Iodine substituted phosphorus corrole complexes as possible photosensitizers in photodynamic therapy: Insights from theory. *J. Comput. Chem.* **2020,** *41,* 1395–1401.

[136] Leonidova, A.; Pierroz, V.; Rubbiani, R.; Heier, J.; Ferrari, S.; Gasser, G. Towards cancer cell-specific phototoxic organometallic rhenium(I) complexes. *Dalton Trans.* **2014,** *43,* 4287–4294.

[137] Quental, L.; Raposinho, P.; Mendes, F.; Santos, I.; Navarro-Ranninger, C.; Alvarez-Valdes, A.; Huang, H.; Chao, H.; Rubbiani, R.; Gasser, G.; Quiroga, A. G.; Paulo, A. Combining imaging and anticancer properties with new heterobimetallic Pt(II)/M(I) (M = Re, $^{99m}$Tc) complexes. *Dalton Trans.* **2017,** *46,* 14523–14536.

[138] Gianferrara, T.; Spagnul, C.; Alberto, R.; Gasser, G.; Ferrari, S.; Pierroz, V.; Bergamo, A.; Alessio, E. Towards matched pairs of porphyrin-$Re^{I}/^{99m}Tc^{I}$ conjugates that combine photodynamic activity with fluorescence and radio imaging. *ChemMedChem* **2014,** *9,* 1231–1237.

[139] Kastl, A.; Dieckmann, S.; Wähler, K.; Völker, T.; Kastl, L.; Merkel, A. L.; Vultur, A.; Shannan, B.; Harms, K.; Ocker, M.; Parak, W. J.; Herlyn, M.; Meggers, E. Rhenium complexes with visible-light-induced anticancer activity. *ChemMedChem* **2013,** *8,* 924–927.

[140] Wähler, K.; Ludewig, A.; Szabo, P.; Harms, K.; Meggers, E. Rhenium complexes with red-light-induced anticancer activity. *Eur. J. Inorg. Chem.* **2014,** *2014,* 807–811.

[141] Klfout, H.; Stewart, A.; Elkhalifa, M.; He, H. BODIPYs for dye-sensitized solar cells. *ACS Appl. Mater. Interfaces* **2017,** *9,* 39873–39889.

[142] Saravanan, V.; Ganesan, S.; Rajakumar, P. Synthesis and DSSC application of BODIPY decorated triazole bridged and benzene nucleus cored conjugated dendrimers. *RSC Adv.* **2020,** *10,* 18390–18399.

[143] Yildiz, E. A.; Sevinc, G.; Yaglioglu, H. G.; Hayvali, M. Strategies towards enhancing the efficiency of BODIPY dyes in dye sensitized solar cells. *J. Photochem. Photobiol. A* **2019,** *375,* 148–157.

[144] Zhong, F.; Yuan, X.; Zhao, J.; Wang, Q. Visible light-harvesting tricarbonyl Re(I) complex: synthesis and application in intracellular photodynamic effect and luminescence imaging. *Sci. China Chem.* **2015,** *59,* 70–77.

[145] Ramos, L. D.; de Macedo, L. H.; Gobo, N. R. S.; de Oliveira, K. T.; Cerchiaro, G.; Frin, K. P. M. Understanding the photophysical properties of rhenium(I) compounds coordinated to 4,7-diamine-1,10-phenanthroline: synthetic, luminescence and biological studies. *Dalton Trans.* **2020,** *49,* 16154–16165.

[146] Worl, L. A.; Duesing, R.; Chen, P.; Ciana, L. D.; Meyer, T. J. Photophysical properties of polypyridyl carbonyl complexes of rhenium(I). *J. Chem. Soc., Dalton Trans.* **1991,** 849.

[147] Kurtz, D. A.; Brereton, K. R.; Ruoff, K. P.; Tang, H. M.; Felton, G. A. N.; Miller, A. J. M.; Dempsey, J. L. Bathochromic shifts in rhenium carbonyl dyes induced through destabilization of occupied orbitals. *Inorg. Chem.* **2018,** *57,* 5389–5399.

[148] Gantsho, V. L.; Dotou, M.; Jakubaszek, M.; Goud, B.; Gasser, G.; Visser, H. G.; Schutte-Smith, M. Synthesis, characterization, kinetic investigation and biological evaluation of Re(I) di- and tricarbonyl complexes with tertiary phosphine ligands. *Dalton Trans.* **2020,** *49,* 35–46.

[149] Britvin, S. N.; Lotnyk, A. Water-soluble phosphine capable of dissolving elemental gold: The missing link between 1,3,5-triaza-7-phosphaadamantane (PTA) and verkade's ephemeral ligand. *J. Am. Chem. Soc.* **2015,** *137,* 5526–5535.

[150] Oliva-Chatelain, B. L.; Barron, A. R. "An Introduction to Solar Cell Technology", OpenStax CNX. http://cnx.org/contents/dd0537a2-fb5d-439d-8feb-bf2e50656dae@1, 2011.

[151] O'Regan, B.; Grätzel, M. A low-cost, high-efficiency solar cell based on dye-sensitized colloidal $TiO_2$ films. *Nature* **1991,** *353,* 737–740.

[152] Grätzel, M. Solar energy conversion by dye-sensitized photovoltaic cells. *Inorg. Chem.* **2005,** *44,* 6841–6851.

[153] Rondán-Gómez, V.; Santos, I. M. D. L.; Seuret-Jiménez, D.; Ayala-Mató, F.; Zamudio-Lara, A.; Robles-Bonilla, T.; Courel, M. Recent advances in dye-sensitized solar cells. *Appl. Phys. A* **2019,** *125,*.

[154] Polo, A. S.; Itokazu, M. K.; Iha, N. Y. M. Metal complex sensitizers in dye-sensitized solar cells. *Coord. Chem. Rev.* **2004,** *248,* 1343–1361.

[155] Shalini, S.; Balasundaraprabhu, R.; Kumar, T. S.; Prabavathy, N.; Senthilarasu, S.; Prasanna, S. Status and outlook of sensitizers/dyes used in dye sensitized solar cells (DSSC): a review. *Int. J. Energy Res.* **2016,** *40,* 1303–1320.

[156] Vlachopoulos, N.; Liska, P.; Augustynski, J.; Graetzel, M. Very efficient visible light energy harvesting and conversion by spectral sensitization of high surface area polycrystalline titanium dioxide films. *J. Am. Chem. Soc.* **1988,** *110,* 1216–1220.

[157] Colombo, A.; Dragonetti, C.; Magni, M.; Meroni, D.; Ugo, R.; Marotta, G.; Lobello, M. G.; Salvatori, P.; Angelis, F. D. New thiocyanate-free ruthenium(II) sensitizers with different pyrid-2-yl tetrazolate ligands for dye-sensitized solar cells. *Dalton Trans.* **2015,** *44,* 11788–11796.

[158] Nazeeruddin, M. K.; Kay, A.; Rodicio, I.; Humphry-Baker, R.; Mueller, E.; Liska, P.; Vlachopoulos, N.; Graetzel, M. Conversion of light to electricity by cis-$X_2$bis(2,2′-bipyridyl-4,4′-dicarboxylate)ruthenium(II) charge-transfer sensitizers (X = $Cl^-$, $Br^-$, $I^-$, $CN^-$, and $SCN^-$) on nanocrystalline titanium dioxide electrodes. *J. Am. Chem. Soc.* **1993,** *115,* 6382–6390.

[159] Huang, Y.; Chen, W.-C.; Ghadari, R.; Liu, X.-P.; Fang, X.-Q.; Yu, T.; Kong, F.-T. Highly efficient ruthenium complexes with acetyl electron-acceptor unit for dye sensitized solar cells. *J. Power Sources* **2018,** *396,* 559–565.

[160] Hasselmann, G. M.; Meyer, G. J. Sensitization of nanocrystalline $TiO_2$ by Re(I) polypyridyl compounds. *Z. Phys. Chem.* **1999,** *212,* 39–44.

[161] Hasselmann, G. M.; Meyer, G. J. Diffusion-limited interfacial electron transfer with large apparent driving forces. *J. Phys. Chem. B* **1999,** *103,* 7671–7675.

[162] Chen, Y.; Liu, W.; Jin, J.-S.; Liu, B.; Zou, Z.-G.; Zuo, J.-L.; You, X.-Z. Rhenium(I) tricarbonyl complexes with bispyridine ligands attached to sulfur-rich core: Synthesis, structures and properties. *J. Organomet. Chem.* **2009,** *694,* 763–770.

[163] Zhang, T.-T.; Jia, J.; Wu, H.-S. Theoretical studies of COOH group effect on the performance of rhenium (I) tricarbonyl complexes with bispyridine sulfur-rich core ligand as dyes in DSSC. *Theor. Chem. Acc.* **2012,** *131,*.

[164] Veronese, L.; Procopio, E. Q.; Rossi, F. D.; Brown, T. M.; Mercandelli, P.; Mussini, P.; D'Alfonso, G.; Panigati, M. New dinuclear hydrido-carbonyl rhenium complexes designed as photosensitizers in dye-sensitized solar cells. *New J. Chem.* **2016,** *40,* 2910–2919.

[165] Veronese, L.; Procopio, E. Q.; Moehl, T.; Panigati, M.; Nonomura, K.; Hagfeldt, A. Triarylamine-based hydrido-carboxylate rhenium(I) complexes as photosensitizers for dye-sensitized solar cells. *Phys. Chem. Chem. Phys.* **2019,** *21,* 7534–7543.

[166] Yella, A.; Lee, H.-W.; Tsao, H. N.; Yi, C.; Chandiran, A. K.; Nazeeruddin, M. K.; Diau, E. W.-G.; Yeh, C.-Y.; Zakeeruddin, S. M.; Gratzel, M. Porphyrin-sensitized solar cells with Cobalt (II/III)-based redox electrolyte exceed 12 percent efficiency. *Science* **2011,** *334,* 629–634.

[167] Mathew, S.; Yella, A.; Gao, P.; Humphry-Baker, R.; Curchod, B. F. E.; Ashari-Astani, N.; Tavernelli, I.; Rothlisberger, U.; Nazeeruddin, M. K.; Grätzel, M. Dye-sensitized solar cells with 13 % efficiency achieved through the molecular engineering of porphyrin sensitizers. *Nat. Chem.* **2014,** *6,* 242–247.

[168] Ji, J.-M.; Zhou, H.; Eom, Y. K.; Kim, C. H.; Kim, H. K. 14.2 % efficiency dye-sensitized solar cells by co-sensitizing novel thieno[3,2- b ]indole-based organic dyes with a promising porphyrin sensitizer. *Adv. Energy Mater.* **2020,** *10,* 2000124.

[169] Qin, C.; Mirloup, A.; Leclerc, N.; Islam, A.; El-Shafei, A.; Han, L.; Ziessel, R. Molecular engineering of new thienyl-bodipy dyes for highly efficient panchromatic sensitized solar cells. *Adv. Energy Mater.* **2014,** *4,* 1400085.

[170] Huaulmé, Q.; Aumaitre, C.; Kontkanen, O. V.; Beljonne, D.; Sutter, A.; Ulrich, G.; Demadrille, R.; Leclerc, N. Functional panchromatic BODIPY dyes with near-infrared absorption: design, synthesis, characterization and use in dye-sensitized solar cells. *Beilstein J. Org. Chem.* **2019,** *15,* 1758–1768.

[171] Kandregula, G. R.; Mandal, S.; Ramanujam, K. Molecular engineering of near-infrared active boron dipyrromethene moiety with various donors and acceptors for tuning the absorption behavior and electron injection of the resultant dyes. *J. Photochem. Photobiol. A* **2021,** *410,* 113161.

[172] Kalita, H.; Lee, W.-Z.; Ravikanth, M. Phosphorus complexes of meso-triaryl-25-oxasmaragdyrins. *Inorg. Chem.* **2014,** *53,* 9431–9438.

[173] Jensen, F. *Introduction to computational chemistry;* Wiley: Chichester New York, 1999.

[174] Schrödinger, E. An undulatory theory of the mechanics of atoms and molecules. *Phys. Rev.* **1926,** *28,* 1049–1070.

[175] Born, M.; Oppenheimer, R. Zur quantentheorie der molekeln. *Annalen der Physik* **1927,** *389,* 457-484.

[176] Szabo, A.; Ostlund, N. S. *Modern Quantum Chemistry;* Dover Publications Inc.: New York, 1996.

[177] Mezey, P. *Potential energy hypersurfaces;* Elsevier: Amsterdam New York, 1987.

[178] Cramer, C. *Essentials of computational chemistry : theories and models;* Wiley: Chichester, West Sussex, England Hoboken, NJ, 2004.

[179] Simons, J.; Joergensen, P.; Taylor, H.; Ozment, J. Walking on potential energy surfaces. *J. Phys. Chem.* **1983,** *87,* 2745–2753.

[180] Banerjee, A.; Adams, N.; Simons, J.; Shepard, R. Search for stationary points on surfaces. *J. Phys. Chem.* **1985,** *89,* 52–57.

[181] Baker, J. An algorithm for the location of transition states. *J. Comp. Chem.* **1986,** *7,* 385–395.

[182] Baker, J. An algorithm for geometry optimization without analytical gradients. *J. Comp. Chem.* **1987,** *8,* 563–574.

[183] Byrd, R. H.; Schnabel, R. B.; Shultz, G. A. A trust region algorithm for nonlinearly constrained optimization. *SIAM J. Numer. Anal.* **1987,** *24,* 1152–1170.

[184] Frisch, M. J. *et al.* "Gaussian 16 Revision C.01", 2016 Gaussian Inc. Wallingford CT.

[185] Schlegel, H. B. Optimization of equilibrium geometries and transition structures. *J. Comp. Chem.* **1982,** *3,* 214–218.

[186] Crehuet, R.; Bofill, J. M. The reaction path intrinsic reaction coordinate method and the hamilton-jacobi theory. *J. Chem. Phys.* **2005,** *122,* 234105.

[187] Fukui, K. The path of chemical reactions - the IRC approach. *Acc. Chem. Res.* **1981,** *14,* 363–368.

[188] Gonzalez, C.; Schlegel, H. B. An improved algorithm for reaction path following. *J. Chem. Phys.* **1989,** *90,* 2154–2161.

[189] Gonzalez, C.; Schlegel, H. B. Reaction path following in mass-weighted internal coordinates. *J. Phys. Chem.* **1990,** *94,* 5523–5527.

[190] Slater, J. C. The theory of complex spectra. *Phys. Rev.* **1929,** *34,* 1293–1322.

[191] Roothaan, C. C. J. New developments in molecular orbital theory. *Rev. Mod. Phys.* **1951,** *23,* 69–89.

[192] Hall, G. G. The molecular orbital theory of chemical valency VIII. A method of calculating ionization potentials. *Proc. R. Soc. A* **1951,** *205,* 541–552.

[193] McDonagh, J. L.; Silva, A. F.; Vincent, M. A.; Popelier, P. L. A. Quantifying electron correlation of the chemical bond. *J. Phys. Chem. Lett.* **2017,** *8,* 1937–1942.

[194] Slater, J. C. Molecular energy levels and valence bonds. *Phys. Rev.* **1931,** *38,* 1109–1144.

[195] Boys, S. F. Electronic wave functions - I. A general method of calculation for the stationary states of any molecular system. *Proc. R. Soc. A* **1950,** *200,* 542–554.

[196] Hehre, W. J.; Stewart, R. F.; Pople, J. A. Self-consistent molecular-orbital methods. I. Use of gaussian expansions of Slater-type atomic orbitals. *J. Chem. Phys.* **1969,** *51,* 2657–2664.

[197] Hehre, W. J.; Ditchfield, R.; Pople, J. A. Self-consistent molecular orbital methods. XII. Further extensions of gaussian-type basis sets for use in molecular orbital studies of organic molecules. *J. Chem. Phys.* **1972,** *56,* 2257–2261.

[198] Binkley, J. S.; Pople, J. A.; Hehre, W. J. Self-consistent molecular orbital methods. 21. Small split-valence basis sets for first-row elements. *J. Am. Chem. Soc.* **1980,** *102,* 939–947.

[199] Frisch, M. J.; Pople, J. A.; Binkley, J. S. Self-consistent molecular orbital methods 25. Supplementary functions for gaussian basis sets. *J. Chem. Phys.* **1984,** *80,* 3265–3269.

[200] Dunning, T. H. Gaussian basis sets for use in correlated molecular calculations. I. The atoms boron through neon and hydrogen. *J. Chem. Phys.* **1989,** *90,* 1007-1023.

[201] Cundari, T. R.; Stevens, W. J.; Sommerer, S. O. Effective core potential study of transition metal and lanthanide catalyzed hydrogen exchange. *Chem. Phys.* **1993,** *178,* 235–243.

[202] Cundari, T. R.; Sommerer, S. O.; Strohecker, L. A.; Tippett, L. Effective core potential studies of lanthanide complexes. *J. Chem. Phys.* **1995,** *103,* 7058-7063.

[203] Hay, P. J.; Wadt, W. R. Ab initio effective core potentials for molecular calculations. potentials for the transition metal atoms Sc to Hg. *J. Chem. Phys.* **1985,** *82,* 270–283.

[204] Roy, L. E.; Hay, P. J.; Martin, R. L. Revised basis sets for the LANL effective core potentials. *J. Chem. Theory Comput.* **2008,** *4,* 1029–1031.

[205] Weigend, F.; Ahlrichs, R. Balanced basis sets of split valence, triple zeta valence and quadruple zeta valence quality for H to Rn: Design and assessment of accuracy. *Phys. Chem. Chem. Phys.* **2005,** *7,* 3297.

[206] Balasubramani, S. G. *et al.* TURBOMOLE: Modular program suite for ab initio quantum-chemical and condensed-matter simulations. *J. Chem. Phys.* **2020,** *152,* 184107.

[207] Sherrill, C. D.; Schaefer, H. F. The Configuration Interaction Method: Advances in Highly Correlated Approaches. In *Advances in Quantum Chemistry*; Elsevier: University of Georgia, 1999.

[208] Condon, E. U. The theory of complex spectra. *Phys. Rev.* **1930,** *36,* 1121–1133.

[209] Krylov, A. I. Spin-flip configuration interaction: An electronic structure model that is both variational and size-consistent. *Chem. Phys. Lett.* **2001,** *350,* 522–530.

[210] Schrödinger, E. Quantisierung als eigenwertproblem. *Ann. Phys. (N. Y.)* **1926,** *385,* 437–490.

[211] Møller, C.; Plesset, M. S. Note on an approximation treatment for many-electron systems. *Phys. Rev.* **1934,** *46,* 618–622.

[212] Head-Gordon, M.; Pople, J. A.; Frisch, M. J. MP2 energy evaluation by direct methods. *Chem. Phys. Lett.* **1988,** *153,* 503–506.

[213] Sinanoğlu, O. Many-electron theory of atoms and molecules, electron pairs vs many-electron correlations. *J. Chem. Phys.* **1962,** *36,* 706–717.

[214] Krishnan, R.; Pople, J. A. Approximate fourth-order perturbation theory of the electron correlation energy. *Int. J. Quantum Chem.* **1978,** *14,* 91–100.

[215] Riplinger, C.; Neese, F. An efficient and near linear scaling pair natural orbital based local coupled cluster method. *J. Chem. Phys.* **2013,** *138,* 034106.

[216] Riplinger, C.; Pinski, P.; Becker, U.; Valeev, E. F.; Neese, F. Sparse maps—A systematic infrastructure for reduced-scaling electronic structure methods. II. Linear scaling domain based pair natural orbital coupled cluster theory. *J. Chem. Phys.* **2016,** *144,* 024109.

[217] Löwdin, P.-O. Quantum theory of many-particle systems. I. Physical interpretations by means of density matrices, natural spin-orbitals, and convergence problems in the method of configurational interaction. *Phys. Rev.* **1955,** *97,* 1474–1489.

[218] Neese, F.; Wennmohs, F.; Hansen, A. Efficient and accurate local approximations to coupled-electron pair approaches: An attempt to revive the pair natural orbital method. *J. Chem. Phys.* **2009,** *130,* 114108.

[219] Baerends, E. J.; Ellis, D. E.; Ros, P. Self-consistent molecular Hartree-Fock-Slater calculations I. The computational procedure. *Chem. Phys.* **1973,** *2,* 41–51.

[220] Dunlap, B. I.; Connolly, J. W. D.; Sabin, J. R. On some approximations in applications of X$\alpha$ theory. *J. Chem. Phys.* **1979,** *71,* 3396–3402.

[221] Vahtras, O.; Almlöf, J.; Feyereisen, M. W. Integral approximations for LCAO-SCF calculations. *Chem. Phys. Lett.* **1993,** *213,* 514-518.

[222] Burow, A. M.; Sierka, M.; Mohamed, F. Resolution of identity approximation for the Coulomb term in molecular and periodic systems. *J. Chem. Phys.* **2009,** *131,* 214101.

[223] Duchemin, I.; Li, J.; Blase, X. Hybrid and constrained Resolution-of-Identity techniques for Coulomb integrals. *J. Chem. Theory Comput.* **2017,** *13,* 1199–1208.

[224] Skylaris, C. K.; Gagliardi, L.; Handy, N. C.; Ioannou, A. G.; Spencer, S.; Willetts, A. On the resolution of identity Coulomb energy approximation in density functional theory. *Comput. Theor. Chem.* **2000,** *501-502,* 229–239.

[225] Robert G. Parr, W. Y. *Density-Functional Theory of Atoms and Molecules;* Oxford University Press: New York, 1994.

[226] Thomas, L. H. The calculation of atomic fields. *Math. Proc. Camb. Philos. Soc* **1927,** *23,* 542–548.

[227] Fermi, E. Un metodo statistico per la determinazione di alcune prioprietà dell'atomo. *Rend. Accad. Naz. Lincei* **1927,** *6,* 602–607.

[228] Hohenberg, P.; Kohn, W. Inhomogeneous electron gas. *Phys. Rev.* **1964,** *136,* B864–B871.

[229] Kohn, W.; Sham, L. J. Self-consistent equations including exchange and correlation effects. *Phys. Rev.* **1965,** *140,* A1133–A1138.

[230] Scuseria, G. E.; Staroverov, V. N. Progress in the development of exchange-correlation functionals. In *Theory and Applications of Computational Chemistry*; Elsevier: Rice University, 2005.

[231] Bloch, F. Bemerkung zur elektronentheorie des ferromagnetismus und der elektrischen leitfahigkeit. *Z. Physik* **1929,** *57,* 545–555.

[232] Dirac, P. A. M. Note on exchange phenomena in the Thomas atom. *Proc. Cambridge Phil. Soc.* **1930,** *26,* 376–385.

[233] Vosko, S. H.; Wilk, L.; Nusair, M. Accurate spin-dependent electron liquid correlation energies for local spin density calculations: a critical analysis. *Can. J. Phys.* **1980,** *58,* 1200–1211.

[234] Perdew, J. P.; Wang, Y. Accurate and simple analytic representation of the electron-gas correlation energy. *Phys. Rev. B: Condens. Matter* **1992,** *45,* 13244–13249.

[235] Perdew, J. P.; Yue, W. Accurate and simple density functional for the electronic exchange energy: Generalized gradient approximation. *Phys. Rev. B* **1986,** *33,* 8800–8802.

[236] Perdew, J. P.; Burke, K.; Ernzerhof, M. Generalized Gradient Approximation made simple. *Phys. Rev. Lett.* **1996,** *77,* 3865–3868.

[237] Becke, A. D. Density functional calculations of molecular bond energies. *J. Chem. Phys.* **1986,** *84,* 4524–4529.

[238] Becke, A. D. Density-functional exchange-energy approximation with correct asymptotic behavior. *Phys. Rev. A.* **1988,** *38,* 3098–3100.

[239] Lacks, D. J.; Gordon, R. G. Pair interactions of rare-gas atoms as a test of exchange-energy-density functionals in regions of large density gradients. *Phys. Rev. A.* **1993,** *47,* 4681–4690.

[240] Filatov, M.; Thiel, W. A new gradient-corrected exchange-correlation density functional. *Mol. Phys.* **1997,** *91,* 847–860.

[241] Gill, P. M. W. A new gradient-corrected exchange functional. *Mol. Phys.* **1996,** *89,* 433–445.

[242] Perdew, J. P. *Electronic Structure of Solids 1991;* Akademie Verlag: Berlin, 1991.

[243] Burke, K.; Becke, J. P.; Wang, Y. *Electronic Density Functional Theory: Recent Progress and New Directions;* Plenum: New York, 1997.

[244] Perdew, J. P.; Chevary, J. A.; Vosko, S. H.; Jackson, K. A.; Pederson, M. R.; Singh, D. J.; Fiolhais, C. Atoms, molecules, solids, and surfaces: Applications of the generalized gradient approximation for exchange and correlation. *Phys. Rev. B: Condens. Matter* **1992,** *46,* 6671–6687.

[245] Lee, C.; Yang, W.; Parr, R. G. Development of the Colle-Salvetti correlation-energy formula into a functional of the electron density. *Phys. Rev. B: Condens. Matter* **1988,** *37,* 785–789.

[246] Becke, A. D. Density-functional thermochemistry. IV. A new dynamical correlation functional and implications for exact-exchange mixing. *J. Chem. Phys.* **1996,** *104,* 1040–1046.

[247] Perdew, J. P. Density-functional approximation for the correlation energy of the inhomogeneous electron gas. *Phys. Rev. B: Condens. Matter* **1986,** *33,* 8822–8824.

[248] Wilson, L. C.; Levy, M. Nonlocal wigner-like correlation-energy density functional through coordinate scaling. *Phys. Rev. B: Condens. Matter* **1990,** *41,* 12930–12932.

[249] Tao, J.; Perdew, J. P.; Staroverov, V. N.; Scuseria, G. E. Climbing the density functional ladder: Nonempirical Meta–Generalized Gradient Approximation designed for molecules and solids. *Phys. Rev. Lett.* **2003,** *91,* 146401.

[250] Perdew, J. P.; Kurth, S.; Zupan, A.; Blaha, P. Accurate density functional with correct formal properties: A step beyond the generalized gradient approximation. *Phys. Rev. Lett.* **1999,** *82,* 2544–2547.

[251] Svendsen, P. S.; von Barth, U. Gradient expansion of the exchange energy from second-order density response theory. *Phys. Rev. B* **1996,** *54,* 17402–17413.

[252] Becke, A. D. A new mixing of Hartree-Fock and local density-functional theories. *J. Chem. Phys.* **1993,** *98,* 1372–1377.

[253] Becke, A. D. Density-functional thermochemistry. III. The role of exact exchange. *J. Chem. Phys.* **1993,** *98,* 5648–5652.

[254] Tirado-Rives, J.; Jorgensen, W. L. Performance of B3LYP density functional methods for a large set of organic molecules. *J. Chem. Theory Comput.* **2008,** *4,* 297–306.

[255] Sousa, S. F.; Fernandes, P. A.; Ramos, M. J. General performance of density functionals. *J. Phys. Chem. A* **2007,** *111,* 10439–10452.

[256] Ernzerhof, M.; Scuseria, G. E. Assessment of the Perdew–Burke–Ernzerhof exchange-correlation functional. *J. Chem. Phys.* **1999,** *110,* 5029–5036.

[257] Staroverov, V. N.; Scuseria, G. E.; Tao, J.; Perdew, J. P. Comparative assessment of a new nonempirical density functional: Molecules and hydrogen-bonded complexes. *J. Chem. Phys.* **2003,** *119,* 12129–12137.

[258] Zhao, Y.; Schultz, N. E.; Truhlar, D. G. Exchange-correlation functional with broad accuracy for metallic and nonmetallic compounds, kinetics, and noncovalent interactions. *J. Chem. Phys.* **2005,** *123,* 161103.

[259] Zhao, Y.; Truhlar, D. G. The M06 suite of density functionals for main group thermochemistry, thermochemical kinetics, noncovalent interactions, excited states, and transition elements: two new functionals and systematic testing of four M06-class functionals and 12 other functionals. *Theor. Chem. Acc.* **2007,** *120,* 215–241.

[260] Yu, H. S.; He, X.; Li, S. L.; Truhlar, D. G. MN15: A Kohn–Sham global-hybrid exchange-correlation density functional with broad accuracy for multi-reference and single-reference systems and noncovalent interactions. *Chem. Sci.* **2016,** *7,* 5032-5051.

[261] Becke, A. D. Density-functional thermochemistry. V. Systematic optimization of exchange-correlation functionals. *J. Chem. Phys.* **1997,** *107,* 8554–8560.

[262] Voorhis, T. V.; Scuseria, G. E. A novel form for the exchange-correlation energy functional. *J. Chem. Phys.* **1998,** *109,* 400–410.

[263] Cohen, A. J.; Mori-Sánchez, P.; Yang, W. Challenges for density functional theory. *Chem. Rev.* **2011,** *112,* 289–320.

[264] Jaramillo, J.; Scuseria, G. E.; Ernzerhof, M. Local hybrid functionals. *J. Chem. Phys.* **2003,** *118,* 1068–1073.

[265] Langreth, D. C.; Perdew, J. P. Exchange-correlation energy of a metallic surface: Wave-vector analysis. *Phys. Rev. B* **1977,** *15,* 2884–2901.

[266] Seidl, M.; Perdew, J. P.; Kurth, S. Density functionals for the strong-interaction limit. *Phys. Rev. A.* **2000,** *62,* 012502.

[267] Perdew, J. P.; Kurth, S.; Seidl, M. Exploring the adiabatic connection between weak- and strong-interaction limits in density functional theory. *Int. J. Mod. Phys. B.* **2001,** *15,* 1672–1683.

[268] Ernzerhof, M.; Perdew, J. P.; Burke, K. Coupling-constant dependence of atomization energies. *Int. J. Quantum Chem.* **1997,** *64,* 285–295.

[269] Mori-Sanchez, P.; Cohen, A. J.; Yang, W. Self-interaction-free exchange-correlation functional for thermochemistry and kinetics. *J. Chem. Phys.* **2006,** *124,* 091102.

[270] Savin, A.; Flad, H.-J. Density functionals for the yukawa electron-electron interaction. *Int. J. Quantum Chem.* **1995,** *56,* 327–332.

[271] Leininger, T.; Stoll, H.; Werner, H.-J.; Savin, A. Combining long-range configuration interaction with short-range density functionals. *Chem. Phys. Lett.* **1997,** *275,* 151–160.

[272] Morrell, M. M.; Parr, R. G.; Levy, M. Calculation of ionization potentials from density matrices and natural functions, and the long-range behavior of natural orbitals and electron density. *J. Chem. Phys.* **1975,** *62,* 549.

[273] Song, J.-W.; Tokura, S.; Sato, T.; Watson, M. A.; Hirao, K. An improved long-range corrected hybrid exchange-correlation functional including a short-range gaussian attenuation (LCgau-BOP). *J. Chem. Phys.* **2007,** *127,* 154109.

[274] Yanai, T.; Tew, D. P.; Handy, N. C. A new hybrid exchange–correlation functional using the Coulomb-attenuating method (CAM-b3lyp). *Chem. Phys. Lett.* **2004,** *393,* 51–57.

[275] Toulouse, J.; Colonna, F.; Savin, A. Short-range exchange and correlation energy density functionals: Beyond the local-density approximation. *J. Chem. Phys.* **2005,** *122,* 014110.

[276] Cohen, A. J.; Mori-Sanchez, P.; Yang, W. Development of exchange-correlation functionals with minimal many-electron self-interaction error. *J. Chem. Phys.* **2007,** *126,* 191109.

[277] Peach, M. J. G.; Benfield, P.; Helgaker, T.; Tozer, D. J. Excitation energies in density functional theory: An evaluation and a diagnostic test. *J. Chem. Phys.* **2008,** *128,* 044118.

[278] Grimme, S. Improved second-order Møller–Plesset perturbation theory by separate scaling of parallel- and antiparallel-spin pair correlation energies. *J. Chem. Phys.* **2003,** *118,* 9095–9102.

[279] Grimme, S. Semiempirical hybrid density functional with perturbative second-order correlation. *J. Chem. Phys.* **2006,** *124,* 034108.

[280] Karton, A.; Tarnopolsky, A.; Lamere, J.-F.; Schatz, G. C.; Martin, J. M. L. Highly accurate first-principles benchmark data sets for the parametrization and validation of density functional and other approximate methods. derivation of a robust, generally applicable, double-hybrid functional for thermochemistry and thermochemical kinetics. *J. Phys. Chem. A* **2008,** *112,* 12868–12886.

[281] Flamant, C. "A Brief Summary of Time-Dependent Density Functional Theory", https://canvas.harvard.edu/courses/16134/files/3358020/download? verifier=QXgeniYnL9KG1BGNDQmAe5WRUtkd10ca3ZHv5qyu&wrap=1,.

[282] Marques, M. A. L.; Maitra, N. T.; Nogueira, F. M. S.; Gross, E. K. U.; Rubio, A. *Fundamentals of Time-Dependent Density Functional Theory;* Springer Berlin Heidelberg: New York, 2012.

[283] Runge, E.; Gross, E. K. U. Density-Functional Theory for Time-Dependent systems. *Phys. Rev. Lett.* **1984,** *52,* 997–1000.

[284] Ullrich, C. A.; Gossmann, U. J.; Gross, E. K. U. Time-Dependent Optimized Effective Potential. *Phys. Rev. Lett.* **1995,** *74,* 872–875.

[285] Dobson, J. F.; Bünner, M. J.; Gross, E. K. U. Time-Dependent Density Functional Theory beyond Linear Response: An exchange-correlation potential with memory. *Phys. Rev. Lett.* **1997,** *79,* 1905–1908.

[286] Ullrich, C. A. *Time-Dependent Density-Functional Theory: Concepts and Applications;* Oxford University Press: New York, 2011.

[287] Casida, M. E. Time-Dependent Density Functional Response Theory for Molecules. In *Recent Advances in Density Functional Methods*; World Scientific: Singapore, 1995.

[288] Hirata, S.; Head-Gordon, M. Time-dependent density functional theory within the Tamm–Dancoff approximation. *Chem. Phys. Lett.* **1999,** *314,* 291–299.

[289] Appel, H.; Gross, E. K. U.; Burke, K. Excitations in Time-Dependent Density-Functional Theory. *Phys. Rev. Lett.* **2003,** *90,* 043005.

[290] McQuarrie, D. *Statistical mechanics;* University Science Books: Sausalito, Calif, 2000.

[291] Atkins, P.; Depaula, J.; Keeler, J. *Atkins' Physical Chemistry;* Oxford University Press: UK, 2018.

[292] Ochterski, J. W. "Thermochemistry in *Gaussian*", https://gaussian.com/wp-content/uploads/dl/thermo.pdf, 2000.

[293] Swope, W. C.; Andersen, H. C.; Berens, P. H.; Wilson, K. R. A computer simulation method for the calculation of equilibrium constants for the formation of physical clusters of molecules: Application to small water clusters. *J. Chem. Phys.* **1982,** *76,* 637–649.

[294] Allen, M. P. *Computational soft matter : from synthetic polymers to proteins; Introduction to Molecular Dynamics Simulation;* NIC: Bonn, Germany, 2004.

[295] Rappe, A. K.; Casewit, C. J.; Colwell, K. S.; Goddard, W. A.; Skiff, W. M. UFF, a full periodic table force field for molecular mechanics and molecular dynamics simulations. *J. Am. Chem. Soc.* **1992,** *114,* 10024–10035.

[296] Weiner, S. J.; Kollman, P. A.; Nguyen, D. T.; Case, D. A. An all atom force field for simulations of proteins and nucleic acids. *J. Comput. Chem.* **1986,** *7,* 230–252.

[297] Ponder, J. W.; Case, D. A. Force fields for protein simulations. *Adv. Prot. Chem.* **2003,** *66,* 27–85.

[298] Brooks, B. R.; Bruccoleri, R. E.; Olafson, B. D.; States, D. J.; Swaminathan, S.; Karplus, M. CHARMM: A program for macromolecular energy, minimization, and dynamics calculations. *J. Comput. Chem.* **1983,** *4,* 187–217.

[299] Allured, V. S.; Kelly, C. M.; Landis, C. R. SHAPES empirical force field: new treatment of angular potentials and its application to square-planar transition-metal complexes. *J. Am. Chem. Soc.* **1991,** *113,* 1–12.

[300] Root, D. M.; Landis, C. R.; Cleveland, T. Valence bond concepts applied to the molecular mechanics description of molecular shapes. 1. Application to nonhypervalent molecules of the p-block. *J. Am. Chem. Soc.* **1993,** *115,* 4201–4209.

[301] Maple, J. R.; Cao, Y.; Damm, W.; Halgren, T. A.; Kaminski, G. A.; Zhang, L. Y.; Friesner, R. A. A polarizable force field and continuum solvation methodology for modeling of protein-ligand interactions. *J. Chem. Theory Comput.* **2005,** *1,* 694–715.

[302] Lennard-Jones, J. E. Cohesion. *Proc. Phys. Soc* **1931,** *43,* 461–482.

[303] Wang, J.; Wolf, R. M.; Caldwell, J. W.; Kollman, P. A.; Case, D. A. Development and testing of a general amber force field. *J. Comput. Chem.* **2004,** *25,* 1157–1174.

[304] Seminario, J. M. Calculation of intramolecular force fields from second-derivative tensors. *Int. J. Quantum Chem.* **1996,** *60,* 1271–1277.

[305] Zheng, S.; Tang, Q.; He, J.; Du, S.; Xu, S.; Wang, C.; Xu, Y.; Lin, F. VFFDT: A new software for preparing AMBER force field parameters for metal-containing molecular systems. *J. Chem. Inf. Model.* **2016,** *56,* 811–818.

[306] Sola, M.; Lledos, A.; Duran, M.; Bertran, J.; Abboud, J. L. M. Analysis of solvent effects on the menshutkin reaction. *J. Am. Chem. Soc.* **1991,** *113,* 2873–2879.

[307] Levy, R. M.; Gallicchio, E. COMPUTER SIMULATIONS WITH EXPLICIT SOLVENT: Recent progress in the thermodynamic decomposition of free energies and in modeling electrostatic effects. *Annu. Rev. Phys. Chem.* **1998,** *49,* 531–567.

[308] Skyner, R. E.; McDonagh, J. L.; Groom, C. R.; van Mourik, T.; Mitchell, J. B. O. A review of methods for the calculation of solution free energies and the modelling of systems in solution. *Phys. Chem. Chem. Phys.* **2015,** *17,* 6174–6191.

[309] Tomasi, J.; Mennucci, B.; Cammi, R. Quantum mechanical continuum solvation models. *Chem. Rev.* **2005,** *105,* 2999–3094.

[310] Jorgensen, W. L.; Chandrasekhar, J.; Madura, J. D.; Impey, R. W.; Klein, M. L. Comparison of simple potential functions for simulating liquid water. *J. Chem. Phys.* **1983,** *79,* 926–935.

[311] Zwanzig, R. W. High-temperature equation of state by a perturbation method. I. Nonpolar gases. *J. Chem. Phys.* **1954,** *22,* 1420–1426.

[312] Tomasi, J.; Persico, M. Molecular interactions in solution: An overview of methods based on continuous distributions of the solvent. *Chem. Rev.* **1994,** *94,* 2027-2094.

[313] Wong, M. W.; Wiberg, K. B.; Frisch, M. J. Ab initio calculation of molar volumes: Comparison with experiment and use in solvation models. *J. Comput. Chem.* **1995,** *16,* 385-394.

[314] Foresman, J. B.; Keith, T. A.; Wiberg, K. B.; Snoonian, J.; Frisch, M. J. Solvent effects. 5. Influence of cavity shape, truncation of electrostatics, and electron correlation on ab initio reaction field calculations. *J. Phys. Chem.* **1996,** *100,* 16098-16104.

[315] Bondi, A. Van der Waals volumes and radii. *J. Phys. Chem.* **1964,** *68,* 441–451.

[316] Pauling, L. *The nature of the chemical bond and the structure of molecules and crystals : An introduction to modern structural chemistry;* Cornell University Press: Ithaca, N.Y, 1960.

[317] Pascual-Ahuir, J. L.; Silla, E. GEPOL: An improved description of molecular surfaces. I. Building the spherical surface set. *J. Comput. Chem.* **1990,** *11,* 1047–1060.

[318] Pomelli, C. S.; Tomasi, J. DefPol: New procedure to build molecular surfaces and its use in continuum solvation methods. *J. Comput. Chem.* **1998,** *19,* 1758–1776.

[319] Pierotti, R. A. The solubility of gases in liquids. *J. Phys. Chem.* **1963,** *67,* 1840–1845.

[320] Pierotti, R. A. Aqueous solutions of nonpolar gases. *J. Phys. Chem.* **1965,** *69,* 281–288.

[321] Pierotti, R. A. A scaled particle theory of aqueous and nonaqueous solutions. *Chem. Rev.* **1976,** *76,* 717–726.

[322] Miertuš, S.; Scrocco, E.; Tomasi, J. Electrostatic interaction of a solute with a continuum. a direct utilizaion of AB initio molecular potentials for the prevision of solvent effects. *Chem. Phys.* **1981,** *55,* 117–129.

[323] Cossi, M.; Barone, V. Analytical second derivatives of the free energy in solution by polarizable continuum models. *J. Chem. Phys.* **1998,** *109,* 6246–6254.

[324] Klamt, A.; Schüürmann, G. COSMO: A new approach to dielectric screening in solvents with explicit expressions for the screening energy and its gradient. *J. Chem. Soc., Perkin Trans. 2* **1993,** 799–805.

[325] Barone, V.; Cossi, M. Quantum calculation of molecular energies and energy gradients in solution by a conductor solvent model. *J. Phys. Chem. A* **1998,** *102,* 1995–2001.

[326] Chipman, D. M. Comparison of solvent reaction field representations. *Theor. Chem. Acc.* **2002,** *107,* 80–89.

[327] Cossi, M.; Rega, N.; Scalmani, G.; Barone, V. Energies, structures, and electronic properties of molecules in solution with the C-PCM solvation model. *J. Comput. Chem.* **2003,** *24,* 669–681.

[328] Cancès, E.; Mennucci, B.; Tomasi, J. A new integral equation formalism for the polarizable continuum model: Theoretical background and applications to isotropic and anisotropic dielectrics. *J. Chem. Phys.* **1997,** *107,* 3032–3041.

[329] Mennucci, B.; Cancès, E.; Tomasi, J. Evaluation of solvent effects in isotropic and anisotropic dielectrics and in ionic solutions with a unified integral equation method: Theoretical bases, computational implementation, and numerical applications. *J. Phys. Chem. B* **1997,** *101,* 10506–10517.

[330] Cancès, E.; Mennucci, B. New applications of integral equations methods for solvation continuum models: Ionic solutions and liquid crystals. *J. Math. Chem.* **1998,** *23,* 309–326.

[331] Mennucci, B.; Cammi, R.; Tomasi, J. Excited states and solvatochromic shifts within a nonequilibrium solvation approach: A new formulation of the integral equation formalism method at the self-consistent field, configuration interaction, and multiconfiguration self-consistent field level. *J. Chem. Phys.* **1998,** *109,* 2798–2807.

[332] Klamt, A.; Moya, C.; Palomar, J. A comprehensive comparison of the IEFPCM and SS(v)PE continuum solvation methods with the COSMO approach. *J. Chem. Theory Comput.* **2015,** *11,* 4220–4225.

[333] Chipman, D. M. Charge penetration in dielectric models of solvation. *J. Chem. Phys.* **1997,** *106,* 10194–10206.

[334] Floris, F.; Tomasi, J. Evaluation of the dispersion contribution to the solvation energy. A simple computational model in the continuum approximation. *J. Comput. Chem.* **1989,** *10,* 616–627.

[335] Floris, F. M.; Tomasi, J.; Ahuir, J. L. P. Dispersion and repulsion contributions to the solvation energy: Refinements to a simple computational model in the continuum approximation. *J. Comput. Chem.* **1991,** *12,* 784–791.

[336] Chandler, D.; Andersen, H. C. Optimized cluster expansions for classical fluids. II. Theory of molecular liquids. *J. Chem. Phys.* **1972,** *57,* 1930–1937.

[337] Zhu, W.; Krilov, G. New flexible boundary hybrid solvation models for efficient biomolecular simulations. *J. Mol. Struct. THEOCHEM* **2008,** *864,* 31–41.

[338] Gerogiokas, G.; Calabro, G.; Henchman, R. H.; Southey, M. W. Y.; Law, R. J.; Michel, J. Prediction of small molecule hydration thermodynamics with grid cell theory. *J. Chem. Theory Comput.* **2013,** *10,* 35–48.

[339] Bader, R. *Atoms in molecules: A quantum theory;* Clarendon Press: Oxford, 1990.

[340] Brüggemann, J.; Jacob, C. R. Spin-state dependence of exchange–correlation holes. *Faraday Discuss.* **2020,** *224,* 56–78.

[341] Outeiral, C.; Vincent, M. A.; Pendás, Á. M.; Popelier, P. L. A. Revitalizing the concept of bond order through delocalization measures in real space. *Chem. Sci.* **2018,** *9,* 5517–5529.

[342] Pendás, A. M.; Blanco, M. A.; Francisco, E. Chemical fragments in real space: Definitions, properties, and energetic decompositions. *J. Comput. Chem.* **2006,** *28,* 161–184.

[343] Chen, Z.; Wannere, C. S.; Corminboeuf, C.; Puchta, R.; von Ragué Schleyer, P. Nucleus-independent chemical shifts (NICS) as an aromaticity criterion. *Chem. Rev.* **2005,** *105,* 3842-3888.

[344] von Ragué Schleyer, P.; Maerker, C.; Dransfeld, A.; Jiao, H.; van Eikema Hommes, N. J. R. Nucleus-independent chemical shifts: A simple and efficient aromaticity probe. *J. Am. Chem. Soc.* **1996,** *118,* 6317–6318.

[345] von Ragué Schleyer, P.; Jiao, H.; van Eikema Hommes, N. J. R.; Malkin, V. G.; Malkina, O. L. An evaluation of the aromaticity of inorganic rings: Refined evidence from magnetic properties. *J. Am. Chem. Soc.* **1997,** *119,* 12669–12670.

[346] Bühl, M.; Hirsch, A. Spherical aromaticity of fullerenes. *Chem. Rev.* **2001,** *101,* 1153–1184.

[347] Pernal, K.; Giesbertz, K. J. H. Reduced Density Matrix Functional Theory (RDMFT) and Linear Response Time-Dependent RDMFT (TD-RDMFT). In *Density-Functional Methods for Excited States*; Springer International Publishing: , 2015.

[348] Reed, A. E.; Curtiss, L. A.; Weinhold, F. Intermolecular interactions from a natural bond orbital, donor-acceptor viewpoint. *Chem. Rev.* **1988,** *88,* 899–926.

[349] Parr, R. G.; Yang, W. Density-Functional Theory of the electronic structure of molecules. *Annu. Rev. Phys. Chem.* **1995,** *46,* 701-728 PMID: 24341393.

[350] Geerlings, P.; Proft, F. D.; Langenaeker, W. Conceptual Density Functional Theory. *Chem. Rev.* **2003,** *103,* 1793–1874.

[351] Parr, R. G.; Pearson, R. G. Absolute hardness: companion parameter to absolute electronegativity. *J. Am. Chem. Soc.* **1983,** *105,* 7512–7516.

[352] Sanderson, R. T. Partial charges on atoms in organic compounds. *Science* **1955,** *121,* 207–208.

[353] Domingo, L.; Ríos-Gutiérrez, M.; Pérez, P. Applications of the conceptual density functional theory indices to organic chemistry reactivity. *Molecules* **2016,** *21,* 748.

[354] Koopmans, T. Über die zuordnung von wellenfunktionen und eigenwerten zu den einzelnen elektronen eines atoms. *Physica* **1934,** *1,* 104–113.

[355] Pearson, R. G. Hard and soft acids and bases. *J. Am. Chem. Soc.* **1963,** *85,* 3533–3539.

[356] Pearson, R. G. Acids and bases. *Science* **1966,** *151,* 172–177.

[357] Pearson, R. G.; Songstad, J. Application of the principle of hard and soft acids and bases to organic chemistry. *J. Am. Chem. Soc.* **1967,** *89,* 1827–1836.

[358] Parr, R. G.; Yang, W. Density functional approach to the frontier-electron theory of chemical reactivity. *J. Am. Chem. Soc.* **1984,** *106,* 4049–4050.

[359] Yang, W.; Mortier, W. J. The use of global and local molecular parameters for the analysis of the gas-phase basicity of amines. *J. Am. Chem. Soc.* **1986,** *108,* 5708–5711.

[360] Domingo, L. R.; Aurell, M.; Pérez, P.; Contreras, R. Quantitative characterization of the global electrophilicity power of common diene/dienophile pairs in Diels–Alder reactions. *Tetrahedron* **2002,** *58,* 4417–4423.

[361] Morell, C.; Grand, A.; Toro-Labbé, A. New dual descriptor for chemical reactivity. *J. Phys. Chem. A* **2005,** *109,* 205–212.

[362] Morell, C.; Grand, A.; Toro-Labbé, A. Theoretical support for using the $\delta$f(r) descriptor. *Chem. Phys. Lett.* **2006,** *425,* 342 - 346.

[363] Martínez-Araya, J. I. Why is the dual descriptor a more accurate local reactivity descriptor than Fukui functions?. *J. Math. Chem.* **2014,** *53,* 451–465.

[364] Yang, W.; Parr, R. G. Hardness, softness, and the fukui function in the electronic theory of metals and catalysis.. *Proc. Natl. Acad. Sci. U. S. A.* **1985,** *82,* 6723–6726.

[365] Ruiz, J.; Perandones, B. F.; der Maelen, J. F. V.; García-Granda, S. On the existence of an N-metalated N-heterocyclic carbene: A theoretical study. *Organometallics* **2010,** *29,* 4639–4642.

[366] Simpson, P. V.; Falasca, M.; Massi, M. Properties and prospects for rhenium(I) tricarbonyl N-heterocyclic carbene complexes. *Chem. Comm.* **2018,** *54,* 12429–12438.

[367] Ciccone, L.; Policar, C.; Stura, E. A.; Shepard, W. Human TTR conformation altered by rhenium tris-carbonyl derivatives. *J. Struct. Biol.* **2016,** *195,* 353–364.

[368] Takematsu, K.; Williamson, H.; Blanco-Rodríguez, A. M.; Sokolová, L.; Nikolovski, P.; Kaiser, J. T.; Towrie, M.; Clark, I. P.; Vlček, A.; Winkler, J. R.; Gray, H. B. Tryptophan-accelerated electron flow across a protein–protein interface. *J. Am. Chem. Soc.* **2013,** *135,* 15515–15525.

[369] Zobi, F.; Spingler, B. Post-protein-binding reactivity and modifications of the fac-$[Re(CO)_3]^+$ core. *Inorg. Chem.* **2012,** *51,* 1210–1212.

[370] Binkley, S. L.; Ziegler, C. J.; Herrick, R. S.; Rowlett, R. S. Specific derivatization of lysozyme in aqueous solution with $Re(CO)_3(H_2O)_3{}^+$. *Chem. Commun.* **2010,** *46,* 1203.

[371] Blanco-Rodríguez, A. M.; Busby, M.; Ronayne, K.; Towrie, M.; Grădinaru, C.; Sudhamsu, J.; Sýkora, J.; Hof, M.; Záliš, S.; Bilio, A. J. D.; Crane, B. R.; Gray, H. B.; Vlček, A. Relaxation dynamics of pseudomonas aeruginosa $Re^{I}(CO)_3(\alpha$-diimine$)$(HisX)$^+$ (X = 83, 107, 109, 124, 126)$Cu^{II}$ azurins. *J. Am. Chem. Soc.* **2009,** *131,* 11788–11800.

[372] Shih, C.; Museth, A. K.; Abrahamsson, M.; Blanco-Rodriguez, A. M.; Bilio, A. J. D.; Sudhamsu, J.; Crane, B. R.; Ronayne, K. L.; Towrie, M.; Vlcek, A.; Richards, J. H.; Winkler, J. R.; Gray, H. B. Tryptophan-accelerated electron flow through proteins. *Science* **2008,** *320,* 1760–1762.

[373] Blanco-Rodríguez, A. M.; Busby, M.; Grădinaru, C.; Crane, B. R.; Di Bilio, A. J.; Matousek, P.; Towrie, M.; Leigh, B. S.; Richards, J. H.; Vlček, A.; Gray, H. B. Excited-state dynamics of structurally characterized $[Re^{I}(CO)_3$(phen)(HisX)$]^+$ (x = 83, 109) pseudomonas a eruginosa azurins in aqueous solution. *J. Am. Chem. Soc.* **2006,** *128,* 4365-4370 PMID: 16569013.

[374] Bilio, A. J. D.; Crane, B. R.; Wehbi, W. A.; Kiser, C. N.; Abu-Omar, M. M.; Carlos, R. M.; Richards, J. H.; Winkler, J. R.; Gray, H. B. Properties of photogenerated tryptophan and tyrosyl radicals in structurally characterized proteins containing rhenium(I) tricarbonyl diimines. *J. Am. Chem. Soc.* **2001,** *123,* 3181–3182.

[375] Mai, S.; Gattuso, H.; Fumanal, M.; Muñoz-Losa, A.; Monari, A.; Daniel, C.; González, L. Excited-states of a rhenium carbonyl diimine complex: solvation models, spin–orbit coupling, and vibrational sampling effects. *Phys. Chem. Chem. Phys.* **2017,** *19,* 27240–27250.

[376] Oliveira, B. L.; Moreira, I. S.; Fernandes, P. A.; Ramos, M. J.; Santos, I.; Correia, J. D. Theoretical studies on the binding of rhenium(I) complexes to inducible nitric oxide synthase. *J. Mol. Graph. Model.* **2013,** *45,* 13–25.

[377] Oliveira, B. L.; Morais, M.; Mendes, F.; Moreira, I. S.; Cordeiro, C.; Fernandes, P. A.; Ramos, M. J.; Alberto, R.; Santos, I.; Correia, J. D. G. Re(I) and Tc(I) complexes for targeting nitric oxide synthase: Influence of the chelator in the affinity for the enzyme. *Chem. Biol. Drug. Des.* **2015,** *86,* 1072–1086.

[378] Ritacco, I.; Russo, N.; Sicilia, E. DFT investigation of the mechanism of action of organoiridium(III) complexes as anticancer agents. *Inorg. Chem.* **2015,** *54,* 10801–10810.

[379] Moitra, T.; Karak, P.; Chakraborty, S.; Ruud, K.; Chakrabarti, S. Behind the scenes of spin-forbidden decay pathways in transition metal complexes. *Phys. Chem. Chem. Phys.* **2021,** *23,* 59–81.

[380] Baková, R.; Chergui, M.; Daniel, C.; Jr., A. V.; Záliš, S. Relativistic effects in spectroscopy and photophysics of heavy-metal complexes illustrated by spin-orbit calculations of [Re(imidazole)$(CO)_3$(phen)]$^+$. *Coord. Chem. Rev.* **2011,** *255,* 975–989.